

2010

Characterization of Inorganic Catalysts and Materials by Solid-State NMR

Aaron Rossini
University of Windsor

Follow this and additional works at: <http://scholar.uwindsor.ca/etd>

Recommended Citation

Rossini, Aaron, "Characterization of Inorganic Catalysts and Materials by Solid-State NMR" (2010). *Electronic Theses and Dissertations*. Paper 396.

This online database contains the full-text of PhD dissertations and Masters' theses of University of Windsor students from 1954 forward. These documents are made available for personal study and research purposes only, in accordance with the Canadian Copyright Act and the Creative Commons license—CC BY-NC-ND (Attribution, Non-Commercial, No Derivative Works). Under this license, works must always be attributed to the copyright holder (original author), cannot be used for any commercial purposes, and may not be altered. Any other use would require the permission of the copyright holder. Students may inquire about withdrawing their dissertation and/or thesis from this database. For additional inquiries, please contact the repository administrator via email (scholarship@uwindsor.ca) or by telephone at 519-253-3000ext. 3208.

Characterization of Inorganic Catalysts and Materials by Solid-State NMR

by

Aaron J. Rossini

A Dissertation

Submitted to the Faculty of Graduate Studies
through the Department of Chemistry and Biochemistry
in Partial Fulfilment of the Requirements for
the Degree of Doctor of Philosophy at the
University of Windsor

Windsor, Ontario, Canada

2010

© 2010 Aaron J. Rossini

The Characterization of Inorganic Catalysts and Materials by Solid-state
NMR

by

Aaron J. Rossini

APPROVED BY:

Dr. Robert L. Vold, External Examiner
The College of William and Mary

Dr. Derek O. Northwood
Department of Mechanical, Materials and Automotive Engineering

Dr. Charles L.B. Macdonald
Department of Chemistry and Biochemistry

Dr. Samuel A. Johnson
Department of Chemistry and Biochemistry

Dr. Robert W. Schurko, Advisor,
Department of Chemistry and Biochemistry

Dr. Daniel Heath, Chair of Defense,
Great Lakes Institute of Environmental Research and Department of Biology

Declaration of Co-Authorship / Previous Publications

The majority of the material contained within this document has been previously published in peer-reviewed journals. In accordance with regulations defined by the Faculty of Graduate Studies, this dissertation is presented in manuscript format. I was the principal investigator for all publications, excepting Chapter 8, which was a joint effort with the research group of Prof. Glen G. Briand (Mount Allison University). I had a significant role in the preparation of all manuscripts. I acknowledge my supervisor, Professor Robert W. Schurko, as a co-author in this work as he made significant contributions to the writing/editing of the individual manuscripts and chapters. Portions of the manuscripts upon which Chapters 2 and 8 are based, have been removed from the thesis because they were written by co-authors. Dr. Ivan Hung, a former graduate student in the research group acquired some of the ^{91}Zr and $^{47/49}\text{Ti}$ SSNMR spectra shown in Chapters 3 and 4. All other listed authors on manuscripts contributed through the synthesis of the materials studied, contribution of single crystal X-ray diffraction structures, or contribution of quantum chemical calculation data. The dissertation is based on the following publications:

Chapter 2: A.J. Rossini, R.W. Mills, G.A. Briscoe, E.L. Norton, S.J. Geier, I. Hung, S. Zheng, J. Autschbach and R.W. Schurko, **2009**. Solid-State Chlorine NMR of Group IV Transition Metal Organometallic Complexes. *J. Am. Chem. Soc.*, 131, 3317–3330. DOI: 10.1021/ja808390a

Chapter 3: Aaron J. Rossini, Ivan Hung, Samuel A. Johnson, Carla Slebodnick, Mike Mensch, Paul A. Deck and Robert W. Schurko, **2010**. Solid-State ^{91}Zr

NMR Spectroscopy Studies of Zirconocene Olefin Polymerization Catalyst Precursors, *J. Am. Chem. Soc.*, accepted.

Chapter 4: A.J. Rossini, I. Hung and R.W. Schurko, **2010**. Solid-State $^{47/49}\text{Ti}$ NMR of Titanocene Chlorides. *J. Phys. Chem. Lett.*, DOI: 10.1021/jz1012017.

Chapter 5: A.J. Rossini and R.W. Schurko, **2006**. Experimental and Theoretical Studies of ^{45}Sc NMR Interactions in Solids. *J. Am. Chem. Soc.*, 128, 10391-10402. DOI: 10.1021/ja060477w

Chapter 7: G.G. Briand, A.D. Smith, G. Schatte, A.J. Rossini and R.W. Schurko, **2007**. Probing Lead(II) Bonding Environments in 4-Substituted Pyridine Adducts of $(2,6\text{-Me}_2\text{C}_6\text{H}_3\text{S})_2\text{Pb}$: An X-ray Structural and Solid-State ^{207}Pb NMR Study. *Inorg. Chem.*, 46, 8625-8637. DOI: 10.1021/ic700738w

Chapter 8: A.J. Rossini, H. Hamaed and R.W. Schurko, **2010**. The Application of Frequency Swept Pulses for the Acquisition of Nuclear Quadrupole Resonance Spectra. *J. Magn. Reson.*, 206, 32-40.
DOI:10.1016/j.jmr.2010.05.018

I certify that I have obtained permission from the copyright owner(s) to include the above published material(s) in my thesis. I certify that this thesis, and the research to which it refers, are the product of my own work during my registration as a graduate student at the University of Windsor.

Abstract

This thesis demonstrates the application of solid-state nuclear magnetic resonance (SSNMR) spectroscopy to probe the structure of a variety of inorganic complexes and materials, many of which find applications in catalysis. Particular focus is given to SSNMR spectroscopy of “exotic” and unreceptive NMR nuclei. Complimentary characterization techniques such as quantum chemical calculations and X-ray diffraction experiments are also employed.

The initial focus of the thesis is on the characterization of crystalline molecular metallocenes by ^{35}Cl , $^{47/49}\text{Ti}$ and ^{91}Zr SSNMR spectroscopy. All of these nuclei are considered to be unreceptive for NMR experiments due to a combination of low natural abundance, low resonance (Larmor) frequency and/or extreme broadening by anisotropic NMR interactions. It is demonstrated that with the combination of modern pulsed NMR techniques and high magnetic fields, SSNMR spectra of these nuclei in metallocenes can be rapidly acquired. Correlations are made between the symmetry and structure of the metallocene species, and the observed electric field gradient (EFG) and chemical shift (CS) tensor parameters extracted from the SSNMR spectra. Preliminary results from SSNMR studies of model heterogeneous metallocene catalysts are also presented.

^{45}Sc SSNMR spectroscopy of simple coordination complexes is investigated. Simple coordination complexes were investigated because most previous ^{45}Sc SSNMR studies have been limited to extended systems with poorly defined structures. SSNMR experiments are also employed to investigate the molecular structure of a

heterogeneous scandium catalyst, microencapsulated $\text{Sc}(\text{OTf})_3$.

^{207}Pb SSNMR in conjunction with quantum chemical calculations are used to investigate the electronic structure of a series of lead(II) thiolate complexes. Frequently, lead(II) complexes possess stereochemically-active lone electron pairs. The observed and calculated ^{207}Pb CS tensor parameters are utilized to probe the electronic configuration of the lead(II) complexes.

The utility of frequency swept WURST pulses for the acquisition of nuclear quadrupole resonance (NQR) spectra is investigated. The WURST pulses are demonstrated to be particularly useful for locating a NQR of unknown frequency and for acquiring wide-line NQR spectra. The utility of WURST pulses for optimizing the configuration of NQR/NMR spectrometer systems is also demonstrated.

I would like to dedicate this work to Erin and my family for providing me with support during my post-graduate studies.

Acknowledgements

There are a large number of people who should be acknowledged for making many contributions to the work outlined in this thesis. First and foremost I would like to thank Professor Robert Schurko for affording me the opportunity to work in his research laboratory. Rob initially hired me as a second year undergraduate student to work in his laboratory for the summer. It seems that something piqued my interest during that first summer, as I would later stay on in Rob's laboratory for the following eight years (three undergraduate and five post-graduate). Rob has always been a fair supervisor who has shown a keen interest in my work, even some of my crazier ideas, and has afforded me the chance to attend many scientific conferences.

Given the inordinate amount of time that one spends in the laboratory and office with their fellow graduate students, there are several co-workers who must also be acknowledged. In particular I would like to thank Ivan Hung, who in a way, was my primary supervisor when I first entered the lab. I learned a great deal from Ivan and I often find myself recalling lessons learned from him. In a similar vein, Andy Lo and Cory Widdifield were also more senior members of the laboratory who also taught me a great deal and were always willing to help with any experiments and problems that arose. I would also like to thank many of the other people I worked with over the years such as Joel Tang, Hiyam Hamaed, Bryan Lucier, Marcel Hildebrand, Ryan Mills and Graham Briscoe. I am especially grateful to Marcel for all of the work that he put into the work described in Chapter 7, which was initially his fourth-year Honours project. I would also

like to acknowledge two post-docs, Luke O'Dell and Kris Harris. I had a chance to work with both Luke and Kris towards the end of my graduate studies and I found working with them to be very intellectually stimulating.

In addition to the members of the Schurko group, there are many people at the University of Windsor who I would also like to thank. I am especially grateful to Professors Charles Macdonald and Samuel A. Johnson for both agreeing to serve on my PhD. committee. Both of them have also provided a great deal of advice over the years in matters of synthetic chemistry and crystallography. They are both very patient and were willing to answer any questions regarding synthesis and handling of compounds, no matter how naive my questions were. I would also like to thank the members of the Macdonald group, Benjamin F.T. Cooper, Greg Farrar, Chris Allan and Rajoshree Bandyopadhyay. We shared lab space with the Macdonald group and all of them provided advice and help to me at some point. I would also like to thank the two NMR managers who ran the solution NMR facility, Mike Fuerth and Matt Revington. Mike and Matt both helped with the setup of solids experiments on the 11.7 T instrument in the University NMR facility. Finally, I would like to thank all the members of the University support staff who helped with various aspects of the research. Joe Lichaa is thanked for all of his assistance with various computer problems and members of the Central Machine Shop are thanked for all of the odds and ends which they built. A special thanks goes to Sinisa Jezdic who helped fix various components of the probes and spectrometer many times over the years. Without Sinisa, the spectrometer would undoubtedly reside in a state of disrepair.

I would also like to acknowledge several collaborators from other universities: Prof. Glen Briand (Mount Allison University), Prof. Paul Deck (Virginia Tech) and Prof. Paul Hazendonk (University of Lethbridge). In addition to our formal collaborators, I would like to thank all of the staff at the Canadian National Ultra-High Field Facility for Solids. In particular I would like to thank Victor Terskikh, Eric Ye and Shane Pawsey for acquiring and/or aiding in the acquisition of high field NMR spectra.

Finally, I would like to thank all of my family and friends for their support. I must thank my wife, Erin, for all of her love and support during the writing of this thesis.

Table of Contents

Declaration of Co-Authorship / Previous Publications.....	iii
Abstract	v
Dedication.....	vii
Acknowledgments.....	viii
List of Tables.....	xiv
List of Figures and Schemes	xvi
List of Abbreviations.....	xxviii
List of Symbols.....	xxxii
1 Introduction and Theory.....	1
1.1 Introduction.....	1
1.2 Background and Theoretical Overview.....	2
1.3 The Zeeman Interaction.....	3
1.4 Interactions of Nuclear Spins with Applied RF Fields.....	7
1.5 Relaxation Processes.....	10
1.6 Nuclear Magnetic Shielding and Chemical Shift	12
1.7 Quadrupolar Nuclei and the Quadrupolar Interaction.....	18
1.8 Euler Angles	24
1.9 Direct and Indirect Spin-Spin Coupling	25
1.10 Magic-Angle Spinning	28
1.11 Pulsed NMR Techniques	31
1.12 Quantum Chemical Calculations of NMR Tensor Parameters.....	36
1.13 Nuclear Quadrupole Resonance.....	38
1.14 Context of Research.....	40
1.15 Bibliography.....	44
2 Solid-State Chlorine NMR of Group IV Transition Metal Organometallic Complexes.....	49
2.1 Introduction.....	49
2.2 Experimental	55
2.3 Results and Discussion.....	57
2.4 Conclusions.....	88
2.5 Bibliography.....	90
3 Solid-State ⁹¹Zr NMR Spectroscopy Studies of Zirconocene Olefin Polymerization Catalyst Precursors.....	97
3.1 Introduction.....	97
3.2 Experimental	103
3.3 Results and Discussion.....	106
3.4 Conclusions.....	140

	3.5 Bibliography.....	144
4	Solid-State ^{47/49}Ti NMR of Titanocene Chlorides.....	152
	4.1 Introduction.....	152
	4.2 Experimental	154
	4.3 Results and Discussion.....	155
	4.4 Conclusions.....	168
	4.5 Bibliography.....	170
5	Experimental and Theoretical Studies of ⁴⁵Sc NMR Interactions in Solids	
	176
	5.1 Introduction.....	176
	5.2 Experimental	179
	5.3 Results and Discussion.....	182
	5.4 Conclusions.....	206
	5.5 Bibliography.....	208
6	Multinuclear Solid-State NMR Studies of Polymer Supported Scandium	
	Triflate Catalysts.....	213
	6.1 Introduction.....	213
	6.2 Experimental	216
	6.3 Results and Discussion.....	220
	6.4 Conclusions.....	243
	6.5 Bibliography.....	245
7	Probing Lead(II) Bonding Environments in 4-Substituted Pyridine Adducts	
	of (2,6-Me₂C₆H₃S)₂Pb: A Solid-State ²⁰⁷Pb NMR Study.....	249
	7.1 Introduction.....	249
	7.2 Experimental	251
	7.3 Results and Discussion.....	253
	7.4 Conclusions.....	268
	7.5 Bibliography.....	269
8	The Application of Frequency Swept Pulses for the Acquisition of Nuclear	
	Quadrupole Resonance Spectra.....	276
	8.1 Introduction.....	276
	8.2 Experimental	281
	8.3 Results and Discussion.....	283
	8.4 Conclusions.....	303
	8.5 Bibliography.....	305
9	General Conclusions.....	309

9.1 Preliminary Characterization of Model Heterogeneous Catalysts by ^{91}Zr SSNMR Spectroscopy.....	311
9.2 Bibliography.....	321

Appendices

Appendix A: Supplementary Figures and Tables for Chapter 2.....	323
Appendix B: Supplementary Figures and Tables for Chapter 3.....	329
Appendix C: Supplementary Figures and Tables for Chapter 4.....	358
Appendix D: Supplementary Figures and Tables for Chapter 5.....	366
Appendix E: Supplementary Figures and Tables for Chapter 6.....	374
Appendix F: Supplementary Figures and Tables for Chapter 7.....	388
Appendix G: Supplementary Figures and Tables for Chapter 8.....	401
Vita Auctoris.....	414

List of Tables

Table 2.1. A Summary of Observed ^{35}Cl EFG Tensor Parameters.....	61
Table 2.2. Values of C_Q Calculated from ^{35}Cl NQR Data	62
Table 2.3. Observed ^{35}Cl CS Tensor Parameters and Euler Angles	70
Table 2.4. ^{35}Cl NMR Parameters Calculated with the RHF Method and aug-cc-PVDZ Basis Set	72
Table 2.5. Analysis of NLMO Contributions to EFG Tensors for Cp_2TiCl_2 , CpTiCl_3 and Cp_2ZrCl_2	77
Table 2.6. Observed and Calculated ^{35}Cl NMR Parameters of Cp_2ZrHCl	87
Table 3.1. Experimentally Determined ^{91}Zr EFG and CS Tensor NMR Parameters.....	107
Table 3.2. Average Metrical Parameters of Single Crystal X-ray Diffraction Structures of Zirconocene Complexes.....	108
Table 3.3. Experimental and Calculated ^{91}Zr CS and EFG Tensor Parameters Determined with the B3LYP method and [6s3p3d] Basis Set on Zr.....	127
Table 3.4. Experimentally Determined and Calculated Euler Angles.....	132
Table 4.1. Experimental and Calculated $^{47/49}\text{Ti}$ EFG and CS Tensor Parameters.....	158
Table 5.1. A Summary of Observed ^{45}Sc EFG and CS Tensor Parameters.....	184
Table 5.2. Calculated ^{45}Sc NMR Parameters Showing Best Agreement With Experiment.....	197
Table 5.3. Observed ^{45}Sc NMR Parameters of $\text{Sc}(\text{OTf})_3$, ME $\text{Sc}(\text{OTf})_3$, and $\text{Sc}(\text{OAc})_3$	205
Table 6.1. Experimental ^{45}Sc EFG and CS Tensor Parameters of Crystalline Complexes	221
Table 6.2. Estimates of Sc Loading Levels of ME $\text{Sc}(\text{OTf})_3$ Samples.....	228

Table 6.3. Chemical Shifts and Integrated Intensities of Resonances Employed for Linefitting of MAS ^1H SSNMR Spectra of ME-2.....	232
Table 6.4. Chemical Shifts and Integrated Intensities of Resonances Employed for Linefitting of MAS ^1H - ^{45}Sc TRAPDOR NMR Spectra of ME-2.....	236
Table 7.1. Experimental ^{207}Pb Chemical Shift Tensor Parameters.....	256
Table 7.2. ZORA and Non-relativistic (NR) ADF Calculations of ^{207}Pb MS and CS Tensor Parameters.....	260
Table 7.3. Contributions to paramagnetic shielding from mixing of occ-vir MOs in 1.....	264
Table 8.1. Nuclear Properties.....	284
Table 8.2. Integrated Intensity and Signal to Noise of Single Echo and QCPMG ^{75}As NQR Spectra	294
Table 9.1. Experimental and Calculated ^{91}Zr EFG and CS Tensor NMR Parameters....	316

List of Figures and Schemes

Figure 1.1. (a) The presence of a magnetic field results in quantization of the z -component of nuclear spin angular momentum (shown for an $I = 3/2$ nucleus). This results in distinct nuclear spin states. The energy separation between each of the adjacent nuclear spin states is equivalent, therefore, there is only one transition frequency. (b) The nuclear spin angular momentum precesses about the applied magnetic field.....5

Figure 1.2. (a) The B_1 field appears to be stationary in a frame which rotates at a frequency equal to that of the applied rf field (ω_{Tx}). If the frequency of ω_{Tx} and ω_0 differ, then an effective magnetic field results, which possesses both z - and x' -components. (b) If the frequency ω_{Tx} is close to ω_0 , then the bulk magnetization, \mathbf{M}_Z will precess about the applied field B_1 and be rotated in the y' z -plane (the on resonance case of $\omega_{Tx} = \omega_0$ is shown). The angular displacement (θ_p) of \mathbf{M}_Z depends upon the magnitude of the B_1 field and duration of the applied pulse (τ_p). If the pulse duration is such that $\theta_p = \pi/2$, then the magnetization ends up along y'8

Figure 1.3. (a) Simulated ^{13}C ($I=1/2$) static spectra with $\Omega = 20.0$ ppm and $\delta_{\text{iso}} = 0.0$ ppm. κ affects the position of δ_{22} . Discontinuities correspond to the principal components of the CS tensor. When $\kappa = +1.0$, $\delta_{11} = \delta_{22}$ and when $\kappa = -1.0$, $\delta_{22} = \delta_{33}$. (b) Different orientations of the CS tensor with respect to the magnetic field give rise to distinct transition frequencies (shown on the left). In a powdered sample the tensor will be present in all orientations with respect to a magnetic field, giving rise to a powder pattern.....17

Figure 1.4. The energies of the nuclear spin states under the influence of the first-order quadrupolar interaction and the second-order quadrupolar interaction are shown for a single crystallite orientation. In the presence of the Zeeman interaction there is only a single transition frequency, while the quadrupolar interaction results in multiple transitions. The change in the energy of the nuclear spin states by $\mathcal{H}_Q^{[2]}$ have been exaggerated with respect to those of $\mathcal{H}_Q^{[1]}$22

Figure 1.5. Simulations of static ^{35}Cl SSNMR spectra at 9.4 T ($\nu_0 = 39.160$ MHz). For all simulated spectra $\delta_{\text{iso}} = 0.0$ ppm. (a) Simulated spectra with $\eta_Q = 0.50$ and values of C_Q which range from 0.5 MHz to 7.0 MHz. Vertical scaling factors are indicated to the left of the spectra. (b) Simulated spectra with $C_Q = 5.0$ MHz and η_Q values which range from 0.00 to 1.00.....24

Figure 1.6. Rotation of the CS tensor from the fixed EFG tensor frame of reference (x, y, z) into the PAS of the CS tensor (X, Y, Z). Figure obtained with permission from Dr. Joel A. Tang.....25

Figure 1.7. Representation of the sample orientation for a MAS experiment.....28

Figure 1.8. (a) Simulations of MAS ^{13}C SSNMR spectra employing $\nu_0 = 100.15$ MHz, $\delta_{\text{iso}} = 50$ ppm, $\Omega = 150$ ppm, $\kappa = 0.50$ and various spinning speeds (ν_r , listed next to spectra). The corresponding static spectrum is also shown (bottom). (b) Simulated MAS (top) and static (bottom) ^{35}Cl SSNMR spectra with $\nu_0 = 39.16$ MHz, $\delta_{\text{iso}} = 0.0$ ppm, $C_Q = 3.0$ MHz and $\eta_Q = 0.50$29

Figure 1.9. A schematic of the spin echo pulse sequence (top) and the vector model which illustrates the refocusing of the spins (bottom). An explanation of the sequence is given in the main text.....32

Figure 1.10. (a) Quadrupolar echo pulse sequence. (b) QCPMG pulse sequence. (c) A ^{91}Zr FID obtained with the QCPMG pulse sequence. (d) Fourier transformation of the first spin echo provides a typical spin echo spectrum. (e) Fourier transformation of the entire CPMG echo train gives a spikelet spectrum. The spacing of the spikelets is equal to, τ_{acq}^{-1} , where τ_{acq} is acquisition time of the individual spin echoes.....34

Figure 1.11. The typical pulse sequence employed for cross-polarization experiments. I usually corresponds to a highly abundant high γ nucleus, and S corresponds to nucleus of lower γ . A description of the experiment is given in the text.....35

Figure 1.12. Energy of the nuclear spin states in NMR experiments (Zeeman interaction) and NQR experiments ($B_0 = 0$). Note that the $+m$ and $-m$ spin states are degenerate in the absence of a magnetic field.....38

Scheme 2.1. Organometallic complexes for which solid-state ^{35}Cl NMR spectra have been acquired. The complexes are: bis(cyclopentadienyl)titanium dichloride (Cp_2TiCl_2), cyclopentadienyltitanium trichloride (CpTiCl_3), bis(cyclopentadienyl)zirconium dichloride (Cp_2ZrCl_2), bis(pentamethylcyclopentadienyl)zirconium dichloride ($\text{Cp}^*_2\text{ZrCl}_2$), bis(cyclopentadienyl)hafnium dichloride (Cp_2HfCl_2), methylbis(cyclopentadienyl)zirconium chloride (Cp_2ZrMeCl), Oxobis[bis(cyclopentadienyl)zirconium chloride] [$(\text{Cp}_2\text{ZrCl})_2\mu\text{-O}$], pentamethylcyclopentadienylzirconium trichloride (Cp^*ZrCl_3), cyclopentadienylzirconium trichloride (CpZrCl_3) and bis(cyclopentadienyl)zirconium chloride hydride (Cp_2ZrHCl , Schwartz's reagent).....54

Figure 2.1. Solid-state ^{35}Cl QCPMG NMR spectra and analytical simulations (solid trace) of the spectra of Cp_2TiCl_2 , Cp_2ZrCl_2 , Cp_2HfCl_2 , $\text{Cp}^*_2\text{ZrCl}_2$ and CpTiCl_3 . Satellite transitions are visible in the spectra of Cp_2ZrCl_2 , $\text{Cp}^*_2\text{ZrCl}_2$ and Cp_2HfCl_2 and have been included in simulations of the spectra of $\text{Cp}_2^*\text{ZrCl}_2$ and Cp_2HfCl_2 in order to improve the quality of the fits. The asterisk in the spectrum of $\text{Cp}^*_2\text{ZrCl}_2$ denotes a discontinuity of a satellite transition.....60

Figure 2.2. Solid-state ^{35}Cl QCPMG NMR spectra and analytical simulations (solid trace) of the spectra of Cp_2ZrMeCl and $(\text{Cp}_2\text{ZrCl})_2\mu\text{-O}$. The simulation of the spectrum of $(\text{Cp}_2\text{ZrCl})_2\mu\text{-O}$ includes the satellite transitions. A minor impurity (marked with an asterisk), which is most likely aniline hydrochloride, is visible in the central region of both spectra.....	64
Figure 2.3. Solid-state ^{35}Cl QCPMG NMR spectra and analytical simulations (solid trace) of the spectra of Cp^*ZrCl_3 , CpZrCl_3 . Satellite transitions are visible in the spectra of both complexes. The simulation of the Cp^*ZrCl_3 spectrum utilizes four sites (two bridging and two terminal); representative simulations of bridging and terminal sites are shown (see Figure A1 for all simulations).....	66
Figure 2.4. Solid-state ^{35}Cl NMR spectra of CpTiCl_3 , Cp_2ZrCl_2 and Cp^*ZrCl_3 acquired at 21.1 T and analytical simulations of the spectra. Piece-wise QCPMG spectra have been acquired for CpTiCl_3 and Cp_2ZrCl_2 . A piece-wise Hahn-echo spectrum was acquired for Cp^*ZrCl_3 . Representative simulations of the bridging and terminal sites are shown for Cp^*ZrCl_3	69
Figure 2.5. The cluster model used for Gaussian 03 calculations on CpZrCl_3 . The chlorine sites in Table 2.4 of the manuscript are labelled. Selected bond lengths are also shown. Sites 1 and 2 are symmetry related and magnetically distinct in this model, but not in the crystal structure. Sites 3 and 4 are also magnetically distinct in the cluster model, but not in the crystal structure. Therefore, averages of the calculated NMR parameters from the pairs of sites have been used in the analytical simulation of the spectrum.....	73
Figure 2.6. EFG tensor orientations in Cp_2TiCl_2 and Cp^*ZrCl_3 . The tensor orientations are shown for the terminal and bridging Cl sites of Cp^*ZrCl_3 . The orientations are taken from the calculations listed in Table 2.4.....	75
Figure 2.7. Images of NLMOs which are the main contributors to the observed ^{35}Cl EFGs in Cp_2TiCl_2 and CpTiCl_3 . The contributions of the individual NLMOs to the observed ^{35}Cl EFGs are described in Table 2.5.....	80
Figure 2.8. Images of NLMOs which are the main contributors to the observed ^{35}Cl EFGs in Cp_2ZrCl_2 . The contributions of the individual NLMOs to the observed ^{35}Cl EFGs are described in Table 2.5.....	82

Figure 2.9. Solid-state ^{35}Cl NMR spectra of Cp_2ZrHCl acquired at 9.4 T and 21.1 T and analytical simulations of the spectra. Simulations with (solid red trace) and without (dashed blue trace) the effects of CSA are shown. The effects of ^1H decoupling on an individual sub-spectrum from 9.4 T are shown in the inset. The application of ^1H decoupling greatly increases the number of echoes that may be acquired and leads to a dramatic increase in signal to noise84

Figure 2.10. The structure of Cp_2ZrHMe and models of the solid-state structure of Cp_2ZrHCl . Cartesian coordinates of atomic positions are given in the original publication86

Scheme 3.1. Schematic representation of compounds which have been studied by solid-state ^{91}Zr NMR: bis(cyclopentadienyl)zirconium dichloride [Cp_2ZrCl_2], bis(pentamethylcyclopentadienyl)zirconium dichloride [$\text{Cp}^*_2\text{ZrCl}_2$ (**1**)], bis(cyclopentadienyl)zirconium dibromide [Cp_2ZrBr_2 (**2**)], bis(trimethylsilylcyclopentadienyl)zirconium dibromide [$(\text{Me}_3\text{SiC}_5\text{H}_4)_2\text{ZrBr}_2$ (**3**)], [$\text{O}(\text{Me}_2\text{SiC}_5\text{H}_4)_2\text{ZrBr}_2$ (**4**)], [$(1,3\text{-C}_5\text{H}_3)(\text{SiMe}_2\text{OSiMe}_2)_2(1,3\text{-C}_5\text{H}_3)\text{ZrBr}_2$ (**5**)], bis(indenyl)zirconium dichloride [$\text{Ind}_2\text{ZrCl}_2$ (**6**)], bis(cyclopentadienyl)methylzirconium chloride [Cp_2ZrMeCl (**7**)], bis(cyclopentadienyl)dimethylzirconium [Cp_2ZrMe_2 (**8**)], and the active polymerization catalyst [$\text{Cp}_2\text{ZrMe}][\text{MeB}(\text{C}_6\text{F}_5)_3]$ (**9**).....102

Scheme 3.2. The reaction of excess amounts of methylalumoxane (MAO) with a catalyst precursor (Cp_2ZrCl_2) results in the abstraction of the chloride ligands and methylation of the zirconium center leading to the formation of **7** and **8**. Further abstraction of a methyl group by MAO results in a cationic zirconocene with a vacant coordination site (the active polymerization catalyst) and generation of an anionic methyl-MAO adduct.....120

Figure 3.1. MAS ^{91}Zr SSNMR spectra (black traces) of (a) Cp_2ZrCl_2 at $\nu_{\text{rot}} = 15000$ Hz, (b) **1** [$\text{Cp}^*_2\text{ZrCl}_2$] at $\nu_{\text{rot}} = 10000$ Hz, (c) **2** [Cp_2ZrBr_2] at $\nu_{\text{rot}} = 10000$ Hz, (d) **3** [$(\text{Me}_3\text{SiC}_5\text{H}_4)_2\text{ZrBr}_2$] at $\nu_{\text{rot}} = 15500$ Hz, (e) **4** [$\text{O}(\text{Me}_2\text{SiC}_5\text{H}_4)_2\text{ZrBr}_2$] at $\nu_{\text{rot}} = 11000$ Hz and (f) **5** [$(1,3\text{-C}_5\text{H}_3)(\text{SiMe}_2\text{OSiMe}_2)_2(1,3\text{-C}_5\text{H}_3)\text{ZrBr}_2$] at $\nu_{\text{rot}} = 10000$ Hz. Corresponding analytical simulations (red traces) are shown beneath all experimental spectra. All spectra were acquired at 9.4 T. Asterisks denote spinning sidebands.....109

Figure 3.2. Static ^{91}Zr SSNMR spectra acquired at 9.4 T (bottom) and 21.1 T (top) of (a) Cp_2ZrCl_2 , (b) **1** [$\text{Cp}^*_2\text{ZrCl}_2$] and (c) **2** [Cp_2ZrBr_2]. Analytical simulations (red traces) which include the effects of CSA and Euler angles are overlayed on the experimental spectra.....114

Figure 3.3. Static ^{91}Zr SSNMR spectra acquired at fields of 9.4 T (bottom) and 21.1 T (top) of (a) **4** [$\text{O}(\text{Me}_2\text{SiC}_5\text{H}_4)_2\text{ZrBr}_2$] and (b) **5** [$(1,3\text{-C}_5\text{H}_3)(\text{SiMe}_2\text{OSiMe}_2)_2(1,3\text{-C}_5\text{H}_3)\text{ZrBr}_2$]. The 21.1 T spectrum of **4** was acquired with the QCPMG sequence due to limited sample quantity. Both a spikelet spectrum and an echo spectrum resulting from co-addition of the echoes in the time domain are shown for **4**. Analytical simulations (red traces) which include the effects of CSA and Euler angles are overlaid on the experimental spectra.....116

Figure 3.4. Static ^{91}Zr SSNMR spectra and analytical simulations of **6** [$\text{Ind}_2\text{ZrCl}_2$] acquired at fields of 21.1 T (top) and 9.4 T (bottom). (a) Analytical simulation employing a single site overlaid on the experimental WURST-QCPMG spectrum. (b) Deconvolution of the individual sites of the two site simulation. (c) Analytical simulation employing two-sites overlaid on the experimental WURST-QCPMG spectrum. (d) Simulation of the experimental pattern employing a single site. (e) Analytical simulation employing two sites overlaid on experimental piece-wise QCPMG spectrum. The satellite transitions of nearby $^{35/37}\text{Cl}$ resonances are much more intense in the 9.4 T spectrum and obscure the ^{91}Zr signal.....118

Figure 3.5. Static solid-state ^{91}Zr NMR spectra of **7** [Cp_2ZrMeCl] acquired with the WURST-QCPMG sequence at fields of 21.1 T (top) and 9.4 T (bottom). (a) Deconvolution of the individual sites employed in the two site simulation. (b) Two site analytical simulation (red trace) overlaid on the experimental spectrum formed by time domain co-addition of the echoes in the WURST-QCPMG echo train. (c) Two site analytical simulation overlaid on the experimental WURST-QCPMG spikelet spectrum. (d) Deconvolution of the individual sites employed in the two site simulation. (e) Two site analytical simulation (red trace) overlaid on the experimental piece-wise WURST-QCPMG spikelet spectrum.....122

Figure 3.6. Static ^{91}Zr SSNMR spectra of **8** [Cp_2ZrMe_2] and **9** [$\text{Cp}_2\text{ZrMe}][\text{MeB}(\text{C}_6\text{F}_5)_3$]. Analytical simulations (red traces) overlaid on the experimental WURST-QCPMG spectra of **8** acquired at fields of (a) 21.1 T and (b) 9.4 T. (c) Analytical simulation (red trace) overlaid on the experimental WURST-QCPMG spectrum of **9** acquired at a field of 21.1 T. Experiments on **9** were attempted at 9.4 T, however no signal could be observed. This is due to the large breadth of the central transition powder pattern at this field.....124

Figure 3.7. Theoretical ^{91}Zr EFG and MS tensor orientations in the molecular frames of (a) Cp_2ZrCl_2 , (b) **7** [Cp_2ZrMeCl] and (c) **8** [Cp_2ZrMe_2]. All tensor orientations are taken from the calculations which employ idealized Cp rings. The tensor orientation for Cp_2ZrCl_2 has been taken from site 1. The tensor orientation for Cp_2ZrMeCl has been taken from calculations on site 2 of the new structure (see text for full explanation).....133

Figure 3.8. Theoretical ^{91}Zr EFG and MS tensor orientations in the molecular frames of (a) **9**, (b) **1** [$\text{Cp}^*_2\text{ZrCl}_2$], (c) **2** [Cp_2ZrBr_2], (d) **4** [$\text{O}(\text{Me}_2\text{SiC}_5\text{H}_4)_2\text{ZrBr}_2$], (e) **5** [$(1,3\text{-C}_3\text{H}_3)(\text{SiMe}_2\text{OSiMe}_2)_2(1,3\text{-C}_3\text{H}_3)\text{ZrBr}_2$] and (f) **6** [$\text{Ind}_2\text{ZrCl}_2$]. All tensor orientations are taken from the calculations which employ idealized Cp rings. The tensor orientation for complex **2** has been taken from site 1.....136

Figure 3.9. Values of ^{91}Zr EFG tensor parameters obtained from B3LYP calculations on structures with variable Zr-Cl and Zr-Me carbon bond lengths. The bond lengths were varied in increments of 0.05 Å. Calculated (a) C_Q and (b) η_Q values when both of the Zr-X (X = Cl, Me) bond lengths in Cp_2ZrCl_2 and **8** [Cp_2ZrMe_2] are varied. Calculated (c) C_Q and (d) η_Q values when the Zr-Me bond length of **7** [Cp_2ZrMeCl] is varied and when the bridging Zr-Me bond length of [Cp_2ZrMe][BMe_4] is varied. The model complex, [Cp_2ZrMe][BMe_4], was created by replacing the three pentafluorophenyl groups of **9** with Me groups. Crystallographic bond lengths are marked with open circles and squares. Atomic coordinates with idealized Cp rings were employed for all calculations. Coordinates from site 1 of Cp_2ZrCl_2 and site 2 of **7** of the respective crystal structures were employed.....138

Scheme 4.1. Titanocene chloride complexes for which $^{47/49}\text{Ti}$ SSNMR spectra have been acquired: Cp_2TiCl_2 (**1**), $\text{Cp}^*_2\text{TiCl}_2$ (**2**), CpTiCl_3 (**3**), Cp^*TiCl_3 (**4**).....153

Figure 4.1. Experimental MAS $^{47/49}\text{Ti}$ SSNMR spectra (black traces) of Cp_2TiCl_2 (**1**), $\text{Cp}^*_2\text{TiCl}_2$ (**2**), CpTiCl_3 (**3**) and Cp^*TiCl_3 (**4**) acquired at 21.1 T [$\nu_0(^{49}\text{Ti}) = 50.75$ MHz] and spectra of **3** and **4** acquired at 9.4 T [$\nu_0(^{49}\text{Ti}) = 22.53$ MHz]. Sample spinning speeds are given in the figure. Analytical simulations are overlaid on the experimental spectra (red traces). All spectra at 21.1 T were acquired with a standard rotor synchronized 90° - 180° echo pulse sequence. Asterisks denote spinning sidebands. The inset of the spectrum of **4** shows the ^{49}Ti isotropic peak that is obtained when the single high-frequency spinning sideband and the two nearest low-frequency spinning sidebands are added onto the isotropic peak. Spectra at 9.4 T were acquired with the DFS-echo (**3**) and DFS-QCPMG (**4**) pulse sequences. The spectrum of **4** was formed by co-adding the QCPMG echoes in the time domain, followed by Fourier transformation of the resultant echo. Additional experimental details are provided in Appendix C.....157

Figure 4.2. Static $^{47/49}\text{Ti}$ SSNMR spectra of Cp_2TiCl_2 (**1**), $\text{Cp}^*_2\text{TiCl}_2$ (**2**), CpTiCl_3 (**3**) and Cp^*TiCl_3 (**4**) acquired at 21.1 T and 9.4 T. Analytical simulations (red traces) are overlaid on the experimental spectra (black traces). De-convolutions of the ^{49}Ti (green traces) and ^{47}Ti (blue traces) powder pattern simulations are also shown. Spectra at 21.1 T were acquired with a standard echo sequence. Spectra of **1** and **2** at 9.4 T were acquired with the DFS-QCPMG pulse sequence161

Figure 4.3. EFG and CS tensor orientations for **1** to **4** obtained from quantum chemical calculations. The Euler angles associated with these tensor orientations are listed in Table

4.1. Methyl groups and hydrogen atoms bound to the Cp rings have been omitted for clarity.....166

Scheme 5.1. Scandium complexes for which solid-state ^{45}Sc NMR spectra have been acquired.....179

Figure 5.1. Solid-state ^{45}Sc NMR spectra and analytical simulations of $\text{Sc}(\text{acac})_3$ and $\text{Sc}(\text{TMHD})_3$. (a) MAS spectrum of $\text{Sc}(\text{acac})_3$, $\nu_{\text{rot}} = 15$ kHz. Inset, a SIMPSON simulation utilizing ideal pulses and processed with 100 Hz of exponential line broadening. (b) Static spectra of $\text{Sc}(\text{acac})_3$ at 9.4 T and 11.75 T. The static spectrum at 9.4 T was acquired with a 90° - 90° echo. (c) MAS RAPT-Echo spectrum of $\text{Sc}(\text{TMHD})_3$, $\nu_{\text{rot}} = 15$ kHz. (d) Static spectra of $\text{Sc}(\text{THMD})_3$ at 9.4 T and 11.75 T.....185

Figure 5.2. Solid-state ^{45}Sc NMR spectra and analytical simulations of $\text{Sc}(\text{NO}_3)_3 \cdot 5\text{H}_2\text{O}$ and $\text{Sc}(\text{OAc})_3$. (a) MAS spectrum of $\text{Sc}(\text{NO}_3)_3 \cdot 5\text{H}_2\text{O}$, $\nu_{\text{rot}} = 8$ kHz. (b) Static spectra of $\text{Sc}(\text{NO}_3)_3 \cdot 5\text{H}_2\text{O}$ at 9.4 T and 11.75 T. (c) MAS spectrum of $\text{Sc}(\text{OAc})_3$, $\nu_{\text{rot}} = 8$ kHz. (d) Static spectra of $\text{Sc}(\text{OAc})_3$ at 9.4 T and 11.75 T acquired with a 90° - 90° echo.....188

Figure 5.3. Solid-state ^{45}Sc NMR spectra and analytical simulations of $\text{ScCl}_3 \cdot 6\text{H}_2\text{O}$ and $\text{ScCl}_3 \cdot 3\text{THF}$. (a) MAS spectrum of $\text{ScCl}_3 \cdot 6\text{H}_2\text{O}$, $\nu_{\text{rot}} = 10$ kHz. (b) Static spectra of $\text{ScCl}_3 \cdot 6\text{H}_2\text{O}$ at 9.4 T and 11.75 T. (c) MAS spectrum of $\text{ScCl}_3 \cdot 3\text{THF}$, $\nu_{\text{rot}} = 12.5$ kHz. (d) Static spectra of recrystallized $\text{ScCl}_3 \cdot 3\text{THF}$ at 9.4 T and 11.75 T acquired with a 90° - 90° echo.....190

Figure 5.4. Solid-state ^{45}Sc NMR spectra of $\text{ScCl}_3 \cdot 3\text{THF}$ (first sample). (a) MQMAS contour plot, $\nu_{\text{rot}} = 8$ kHz. (b) The two resolved sites from cross-sections of the indirect dimension and analytical simulations. (c) MAS spectrum ($\nu_{\text{rot}} = 15$ kHz) and the simulated pattern that results from addition of the individually simulated patterns. (d) Static spectra.....192

Figure 5.5. Solid-state ^{45}Sc NMR spectra of ScCp_3 and simulations. (a) MAS spectrum, $\nu_{\text{rot}} = 12$ kHz. (b) Static spectra at 9.4 T and 11.75 T.....194

Figure 5.6. ^{45}Sc chemical shift and magnetic shielding scales. The magnetic shielding scale was generated from the RHF/6-311G** on Sc series of calculations. The theoretical result for ScCp_3 has been omitted.....195

Figure 5.7. Proposed EFG and CS tensor orientations. (a) $\text{Sc}(\text{acac})_3$ (b) $\text{Sc}(\text{TMHD})_3$ (c) $\text{Sc}(\text{NO}_3)_3 \cdot 5\text{H}_2\text{O}$ (d) $\text{Sc}(\text{OAc})_3$ (e) $\text{ScCl}_3 \cdot 6\text{H}_2\text{O}$ (f) $\text{ScCl}_3 \cdot 3\text{THF}$ (g) ScCp_3199

Figure 5.8. Solid-state ^{45}Sc NMR spectra and analytical simulations of $\text{Sc}(\text{OTf})_3$ and ME $\text{Sc}(\text{OTf})_3$. (a) MAS spectrum of $\text{Sc}(\text{OTf})_3$, $\nu_{\text{rot}} = 4$ kHz. (b) Static spectra of $\text{Sc}(\text{OTf})_3$ at 9.4 T and 11.75 T. (c) MAS spectrum of ME $\text{Sc}(\text{OTf})_3$, $\nu_{\text{rot}} = 4$ kHz. (b) Static spectra of

Sc(OTf)₃ at 9.4 T (AMDFS-Hahn Echo) and 11.75 T.....204

Figure 5.9. Proposed model of Sc(OTf)₃ (left) and the known structure of Sc(OAc)₃ (right). Fluorine and hydrogen atoms have been omitted for clarity.....205

Figure 6.1. MAS (left) and static (right) ⁴⁵Sc SSNMR spectra acquired at 9.4 T. Analytical simulations of the spectra (red traces) are overlaid on top of the experimental spectra (black traces). (a) MAS spectrum of Sc(OTf)₃ at a sample spinning speed of $\nu_{\text{rot}} = 4.0$ kHz and (b) static spectrum of Sc(OTf)₃. (c) MAS spectrum of Sc(OAc)₃ at $\nu_{\text{rot}} = 8.0$ kHz and (d) static spectrum with ¹H decoupling. (e) MAS spectrum of Sc(OTf)₃•8H₂O at $\nu_{\text{rot}} = 8.0$ kHz and (f) static spectrum with ¹H decoupling. Spinning sidebands are indicated with asterisks. ⁴⁵Sc EFG and CS tensor parameters extracted from simulations are listed in Table 1. All static spectra were acquired with a 90°-90° echo sequence. 90°-90° echo static spectra of Sc(OTf)₃ and Sc(OTf)₃•8H₂O at 11.7 T were acquired in order to confirm the ⁴⁵Sc CS tensor parameters and Euler angles (Figure E1).....221

Figure 6.2. Structures of (a) Sc(OAc)₃, (b) Sc(OTf)₃ and (c) Sc(OTf)₃•8H₂O. Hydrogen and fluorine atoms have been omitted for clarity from the structures of Sc(OAc)₃ and Sc(OTf)₃. Experimental (black trace) powder X-ray diffraction patterns of (d) Sc(OAc)₃, (e) Sc(OTf)₃ and (f) Sc(OTf)₃•8H₂O. Powder X-ray diffraction patterns calculated (red trace) from the corresponding single crystal X-ray diffraction structures are shown for Sc(OAc)₃ and Sc(OTf)₃•8H₂O. Single crystal XRD structures of Sc(OAc)₃ and Sc(OTf)₃•8H₂O have been previously published [references 43 and 50]. The oxygen atoms labelled O_C possess fractionally occupancies of 0.67 in the single crystal XRD structure of Sc(OTf)₃•8H₂O, leading to eight-coordinate Sc. There is no crystal structure of Sc(OTf)₃ available. The model of Sc(OTf)₃ presented herein, is based upon our ⁴⁵Sc SSNMR spectra and the powder X-ray diffraction patterns.....223

Figure 6.3. MAS and static ⁴⁵Sc SSNMR spectra of Sc(OTf)₃•8H₂O and the commercial sample of ME Sc(OTf)₃ acquired at 9.4 T. (a) MAS spectrum of Sc(OTf)₃•8H₂O at a sample spinning speed of $\nu_{\text{rot}} = 8.0$ kHz and (b) static spectra with and (c) without ¹H decoupling. (d) MAS spectrum of ME Sc(OTf)₃ at $\nu_{\text{rot}} = 12.0$ kHz and (e) static spectra with and (f) without ¹H decoupling. All static spectra were acquired with a DFS 90°-180° echo pulse sequence.....225

Figure 6.4. MAS (left) and static (right) ⁴⁵Sc SSNMR spectra of Sc(OTf)₃•8H₂O and samples of ME Sc(OTf)₃ prepared with various synthetic procedures. All spectra were acquired at 9.4 T. Spectra of (a) Sc(OTf)₃•8H₂O, (b) ME Sc(OTf)₃ prepared by microencapsulating Sc(OTf)₃•8H₂O in PS under an inert atmosphere (ME-1), (c) ME Sc(OTf)₃ prepared under ambient atmosphere (ME-2), (d) ME Sc(OTf)₃ prepared under inert conditions (ME-3), and (e) ME Sc(OTf)₃ prepared with fully deuterated PS (ME ScOTf₃-d₈) under ambient conditions. All static spectra were acquired with a DFS 90°-90° echo sequence and ¹H decoupling (except where noted) and all MAS spectra were

acquired with a DFS 90°- 180° echo sequence. Static ⁴⁵Sc SSNMR spectra of Sc(OTf)₃•8H₂O and ME Sc(OTf)₃-d₈ acquired without ¹H decoupling are also shown.....227

Figure 6.5. MAS ¹H SSNMR spectra of (a) pure PS (PS), (b) PS recovered from cyclohexane, (c) PS recovered from cyclohexane and hexanes, (d) PS recovered from cyclohexane, hexanes, and acetonitrile, and (e) ME-2. A line-fitting simulation (red trace) is overlaid on the experimental spectrum of ME-2 (black trace). (f) Deconvolution of the individual sites employed in the line-fitting simulation. All spectra were acquired with a Bloch decay pulse sequence (90° pulse-acquire), $\nu_{rot} = 13.5$ kHz, 32 scans and a recycle delay of 20 s which is required to obtain full recovery of longitudinal magnetization.....231

Figure 6.6. MAS ¹H-⁴⁵Sc TRAPDOR SSNMR spectra of ME-2. (a) control experiment with no ⁴⁵Sc irradiation, (b) dephasing experiment with irradiation of ⁴⁵Sc during the τ_1 period and (c) the difference spectrum resulting from subtraction of the dephasing spectrum from the control spectrum (intensity increased by a factor of 4). Linefitting simulations (red trace) are overlaid on the experimental spectra (black trace). (d) A deconvolution of the three sites employed in the linefitting simulations. $\nu_{rot} = 12.5$ kHz and a recycle delay of 20 s were employed. A τ_1 value of 240 s was used, corresponding to 3 rotor cycles, and a ⁴⁵Sc rf field (ν_1) of 108 kHz was applied during the τ_1 period of the dephasing experiment.....234

Figure 6.7. Experimental PXRD patterns obtained from (a) anhydrous Sc(OTf)₃, (b) Sc(OTf)₃•8H₂O, (c) Sc(OTf)₃•xH₂O, (d) ME-1, (e) ME-2, and (f) solvent-treated PS.....238

Figure 6.8. MAS ¹H SSNMR spectra (left) and static ⁴⁵Sc SSNMR 90°-180° echo spectra (right) of a sample of ambient ME-2 which has been exposed to air. The sample was exposed to air for total times of (a) 0 hours, (b) 20 hours, (c) 2 days and (d) 15 days. For exposure times of 20 hours and 2 days the static ⁴⁵Sc SSNMR spectra are shown with and without ¹H decoupling. For the exposure time of 15 days, the static ⁴⁵Sc SSNMR spectra were acquired with selective and non-selective 90° and 180° ⁴⁵Sc pulses (and no ¹H decoupling).....239

Figure 6.9. PXRD patterns acquired from a sample of ambient ME Sc(OTf)₃ which was exposed to air. The total exposure time is listed to the right of each PXRD pattern242

Figure 6.10. Proposed structural model of ME Sc(OTf)₃. This model is highly schematized and qualitative. Sc(OTf)₃ is hydrated when it undergoes microencapsulation in PS and is incorporated as nanocrystalline domains of Sc(OTf)₃•8H₂O. The PS groups and cyclohexane molecules are spatially proximate to the surface of the nanocrystalline Sc(OTf)₃•8H₂O domains. The cyclohexane molecules undergo translational/rotational

motions.....243

Scheme 7.1. Schematic drawings of lead thiolate structures, including (2,6-Me₂C₆H₃S)₂Pb(py)₂ (**1**), [(2,6-Me₂C₆H₃S)₂Pb(pyOMe)]₂ (**2**) and (2,6-Me₂C₆H₃S)₂Pb(pyNMe₂) (**3**) (py = pyridine; pyOMe = 4-methoxypyridine; pyNMe₂ = 4-dimethylaminopyridine). Additional views of the structures are shown in Figure 7.3.....251

Figure 7.1. ¹H-²⁰⁷Pb VACP/MAS NMR spectra of **1**, **2** and **3** each acquired at three spinning speeds (v_{rot}). Dashed lines indicate δ_{iso} . A recycle delay of 10 s was used for all spectra and 2004 to 8428 scans were acquired. The relative vertical scaling of the spectra is given on the left.....255

Figure 7.2. ¹H-²⁰⁷Pb CP/CPMG static NMR spectra (black trace) of compounds **1**, **2**, and **3**. Analytical simulations (solid red trace) are overlaid on the experimental spectra. The CS tensor parameters obtained from the simulations are given in Table 7.1.....257

Figure 7.3. Lead CS tensor orientations for complexes **1**, **2** and **3**. The tensor orientations have been generated from the ZORA calculations.....262

Figure 7.4. The occupied and virtual MOs of **1** that make significant contributions to the paramagnetic shielding term. A partial MO diagram indicating the magnetic-dipole allowed transitions between the occupied and virtual orbitals that are pictured is also shown. The MOs are visualized at the 97% electron density level.....265

Figure 7.5. A representation of the rotation of vir MOs 139 and 143 of **1**. The axes of rotation correspond to the directions of σ_{11} and σ_{22} in the molecular frame. Only Pb, S and N atoms are shown.....267

Figure 8.1. Schematic representations of the pulse sequences employed for the acquisition of NQR spectra. (a) Hahn-Echo with 90° excitation pulse and 180° or 90° refocusing pulse. (b) QCPMG sequence with 90° excitation pulse and a train of 180° refocusing pulses (reference 35). (c) The composite echo sequence of Odin (reference 54). (d) WURST-QCPMG sequence with excitation and refocusing pulses with 90° pulses of equal length and sweep rate. Note that for WURST echo spectra the WURST-QCPMG sequence (reference 64) was employed with only a single refocusing pulse and the first echo was acquired (N = 1).....277

Figure 8.2. Integrated intensity of the ⁷⁵As NQR spectra of As₂O₃ (arsenolite) as a function of transmitter offset from the resonance frequency for the 90°-180° echo, 90°-90° echo, composite echo and WURST echo pulse sequences. For each transmitter offset the probe was tuned using reflected power measurements available in Spinsight, followed by acquisition of the spectra with the five pulse sequences. For clarity the intensity points

have been connected by lines for the 90°-180° echo and WURST echo spectra.....285

Figure 8.3. Integrated intensity of the ⁷⁵As NQR spectra of As₂O₃ acquired when the probe has been tuned on resonance (116.234 MHz), tuned +300 kHz off resonance (116.534 MHz), and when the probe is tuned +300 kHz off resonance and the pulse widths have been re-calibrated. The transmitter was set to the resonant frequency (116.234 MHz) in all cases. Spectra were acquired with the four different pulse sequences. When the probe is tuned +300 kHz off resonance and re-calibrated pulses are employed, the II of the NQR spectra is 1.3 to 1.4 times larger.....292

Figure 8.4. Integrated intensity of the ³⁵Cl NQR spectra of 4-chloropyridine as a function of transmitter offset from the resonance frequency for the 90°-180° echo, 90°-90° echo, composite echo and WURST echo. For each transmitter offset the probe was tuned using reflected power measurements available in Spinsight. Spectra with the four pulse sequences were then acquired. For clarity the intensity points have been connected by lines for the 90°-180° echo and WURST echo spectra.....296

Figure 8.5. Integrated intensity of the ³⁵Cl NQR spectra of 4-chloropyridine acquired when the probe has been tuned on resonance (35.352 MHz), tuned -200 kHz off resonance (35.152 MHz) and when the probe is tuned -200 kHz off resonance and the pulse widths have been re-calibrated. The transmitter was set to the resonant frequency (35.352 MHz) in all cases. Spectra were acquired with the four different pulse sequences. When the probe is tuned -200 kHz off resonance and re-calibrated pulses are employed, the II of the NQR spectra is 1.64 to 1.67 times larger.....298

Figure 8.6. Wideline ^{63/65}Cu NQR spectrum of the broad resonance of CuCN centered around 37.9 MHz. (a) "Point-by-point" spectrum (see text for details) acquired with the QCPMG pulse sequence and low power pulses (10 μs 90° pulse). A transmitter increment of 120 kHz was employed and 15 echoes were acquired (1.3 hours total acquisition time). (b) QCPMG spikelet spectrum and echo spectrum formed from time domain co-addition of the echoes. A transmitter increment of 120 kHz and high-power 90° pulses (0.7 μs) were employed. 12 sub-spectra were required to form the total pattern (1.3 hours total acquisition time). (c) WURST-QCPMG spikelet spectrum and echo spectrum formed from time domain co-addition of the echoes. A transmitter increment of 250 kHz was employed and 6 sub-spectra were required to form the total pattern (0.8 hours total acquisition time).....301

Scheme 9.1. Preparation of surface supported zirconocenes. Molecular analogs to the surface supported species are also shown.....312

Figure 9.1. Static ^{91}Zr SSNMR spectra of (a) $\text{Cp}_2\text{ZrCl}(\text{SiO}_2)$ (**1-Cl**) and (b) $\text{Cp}_2\text{ZrMe}(\text{SiO}_2)$ (**2-Me**) acquired at 18.8 T. Analytical simulations are overlaid on the experimental spectra (solid red traces). Both spectra were acquired with sample temperatures of 10 K, 30 second recycle delays and 512 transients (4.3 hours) per sub-spectrum (50 kHz transmitter offset). 11 sub-spectra and 13 sub-spectra were acquired to form the total spectra of $\text{Cp}_2\text{ZrCl}(\text{SiO}_2)$ and $\text{Cp}_2\text{ZrMe}(\text{SiO}_2)$, respectively. A simulation with $\Omega = 0$ ppm (dashed blue trace) is shown for $\text{Cp}_2\text{ZrMe}(\text{SiO}_2)$. (c) Static ^{91}Zr SSNMR WURST-QCPMG spectrum of $\text{Cp}_2\text{ZrCl}(\text{OSiMe}_3)$ at 9.4 T (black trace). The asterisk denotes a small amount of Cp_2ZrCl_2 . Partway through the acquisition of sub-spectra it was necessary to alter the probe configuration, resulting in uneven intensities in the individual sub-spectra, and leading to intensity differentials between the experimental and simulated spectra.....315

Figure 9.2. (a) Structure of $\text{Cp}_2\text{Zr}(\text{OSiMe}_3)$ with coordinates based upon the single crystal XRD structure of $\text{Cp}_2\text{Zr}(\text{OSiMe}_2(\text{CH}_2\text{Cl}))$. (b) Geometry optimized structure of $\text{Cp}_2\text{Zr}(\text{OSiMe}_3)$. (c) Geometry optimized model of **1-Cl**. The Cp_2ZrCl fragment was bonded to a SiO_2 cluster based upon the structure of β -cristabollite. Atomic coordinates for the SiO_2 fragment were taken from Blanc et al. Each of the terminal oxygen atoms was capped with a single H atom.....318

List of Abbreviations

acac	acetylacetonate
ADF	Amsterdam Density Functional
AMDFS	amplitude modulated double frequency sweep
BHP	Bühl, Hopp, von Philipsborn
B3LYP	Becke's three parameter hybrid functionals using the correlation functional of Lee, Yang and Parr
Cp	cyclopentadienyl
Cp*	pentamethylcyclopentadienyl
Cp'	cyclopentadienyl of any substitution pattern
CP	cross-polarization
CP/CPMG	cross-polarization Carr-Purcell Meiboom-Gill
CPMG	Carr-Purcell Meiboom-Gill
CS	chemical shift
CSA	chemical shift anisotropy
CT	central transition
DFS	double frequency sweep
DNP	dynamic nuclear polarization
EDX	energy dispersive X-ray
EFG	electric field gradient
FID	free induction decay
FWHH	full width at half height
GIAO	gauge including atomic orbitals
II	integrated intensity
Ind	indenyl
MAO	methyalumoxane
MAS	magic angle spinning

ME	microencapsulated
MG	Meiboom-Gill
MOs	molecular orbitals
MQMAS	multiple-quantum magic angle spinning
MS	magnetic shielding
n.a.	natural abundance
NLMO	natural localized molecular orbital
NMR	nuclear magnetic resonance
NQR	nuclear quadrupole resonance
NR	non-relativistic
OAc	acetate
occ	occupied
OTf	trifluoromethanesulfonate
PAS	principal axis system
ppm	part per million
PS	polystyrene
PXRD	powder X-ray diffraction
QCPMG	quadrupolar Carr-Purcell Meiboom-Gill
QI	quadrupolar interaction
Q-factor	quality factor
RF	radiofrequency
RHF	restricted Hartree-Fock
SEM	scanning electron microscopy
S/N	signal to noise ratio
SSNMR	solid-state nuclear magnetic resonance
ST	satellite transitions

THF	tetrahydrofuran
TMHD	2,2,6,6-tetramethyl-3,5-heptanedionato
TPPM	two pulse phase modulated
TRAPDOR	transfer of populations in double resonance
VACP	variable amplitude cross-polarization
vir	virtual
WURST	wideband uniform rate smooth truncated
ZORA	zeroth-order regular approximation

List of Symbols

α, β, γ	Euler angles
B_0	static applied magnetic field
B_1	alternating magnetic field applied in the form of a pulse
B_{eff}	effective magnetic field
C_Q	quadrupolar coupling constant
ΔE	energy separation
δ_{iso}	isotropic chemical shift
$\delta_{11}, \delta_{22}, \delta_{33}$	principal components of the chemical shielding tensor
e	the charge of an electron
γ	gyromagnetic ratio
h	Planck's constant
\hbar	Planck's constant divided by 2π
η_Q	electric field gradient asymmetry parameter
I	nuclear spin quantum number
I	nuclear spin angular momentum vector
I_x, I_y, I_z	x, y or z -component of nuclear spin angular momentum
k	Boltzmann's constant
M	macroscopic magnetization
M_x, M_y, M_z	components of macroscopic magnetization
m_1	nuclear Zeeman spin-state
μ	magnetic dipole moment
ν	frequency of radiation
ν_1	nutaton frequency of applied rf fields in Hz
ν_0	Larmor frequency in Hz
ν_Q	quadrupolar frequency in Hz

v_{rot}	sample spinning speed
Q	quadrupole moment
σ_{iso}	isotropic magnetic shielding
σ_{d}	isotropic diamagnetic shielding
σ_{p}	isotropic paramagnetic shielding
σ_{so}	isotropic shielding due to spin-orbit interaction
$\sigma_{11}, \sigma_{22}, \sigma_{33}$	principal components of the magnetic shielding tensor
τ	time delays within pulse sequences
T	temperature
T_1	longitudinal relaxation time constant
T_2	transverse relaxation time constant
T_2^*	effective transverse relaxation time constant
UW	ultra-wideline
V_{11}, V_{22}, V_{33}	principal components of the EFG tensor
ω_1	nutaton frequency of applied rf fields in radians per second
ω_0	Larmor frequency in radians per second
ω_{Tx}	frequency of applied rf fields in radians per second
ω_{Q}	quadrupolar frequency in radians per second

Chapter 1: Introduction and Theory

1.1 Introduction

The space quantization of electron spin and nuclear spin were first discovered over 80 years ago by Stern and Gerlach in the early 1920's and early 1930's.¹⁻⁵ Their experiments were conducted with beams of silver atoms and molecular hydrogen in inhomogeneous magnetic fields. From these experiments it was possible to measure the magnetic moments of the electron and proton nuclei. Rabi proposed and conducted further atomic and molecular beam experiments in the late 1930's.⁶⁻⁹ Rabi took the additional step of applying electromagnetic radiation to induce transitions between the nuclear spin states, marking the first demonstrations of nuclear magnetic resonance (NMR). In the late 1940's the research groups of Bloch and Purcell independently undertook experiments which allowed for the detection of ¹H NMR signals by the application of radiofrequency (*rf*) fields to condensed matter samples in static magnetic fields.¹⁰⁻¹⁶ Until the early 1950's, NMR was principally used as tool by physicists to test the predictions of quantum mechanics and to measure the spin angular momentum (*I*) and magnetic moments (μ) of various nuclei. Underscoring the importance of these early experiments, Nobel prizes in physics were awarded to Stern in 1943, Rabi in 1944, and Purcell and Bloch in 1952.

In the mid-1950's the chemical shift was observed when distinct ¹H resonances were recorded for ethanol.¹⁷ Shortly thereafter, the utility of solution NMR for the rapid assessment of molecular structure was realized. With this key discovery in hand and the

implementation of modern pulsed NMR techniques by Ernst in the 1960's and 1970's,^{18, 19} NMR quickly found applications in diverse areas such as magnetic resonance imaging, synthetic chemistry, analytical chemistry, materials science and biochemistry.^{20, 21}

Many of the early (and now routine) NMR experiments employ ubiquitous and/or receptive spin-1/2 nuclei such as ^1H , ^{13}C and ^{19}F . However, many of the elements in the periodic table possess NMR-active nuclei which are classified as “unreceptive” due to their combination of low gyromagnetic ratio (γ), low natural abundance (n.a.), unfavourable relaxation characteristics, large chemical shielding anisotropies (CSA) and/or large quadrupole moments (Q). These unreceptive NMR nuclei can potentially be used to probe the structures of a myriad number of inorganic complexes which have far reaching applications in research areas such as catalysis, energy conversion, and biochemistry. The primary focus of this thesis is upon developing and utilizing solid-state NMR (SSNMR) spectroscopy of unreceptive and/or “exotic” nuclei to characterize the structure of inorganic complexes and materials, many of which find applications in catalysis. The background for the individual systems and the motivation for their study are provided in the introduction sections of the individual chapters.

The contents of this section are derived from are a number of excellent texts and reviews which explain the theoretical aspects of NMR spectroscopy, in various levels of detail, to which the reader is referred.²²⁻³²

1.2 Background and Theoretical Overview

The NMR phenomenon arises due to the interaction of nuclear magnetic dipole

moments with external magnetic fields. There are additional internal interactions arising from the presence of neighbouring nuclear spins and electrons that affect the energy of the nuclear spin states, and hence the appearance of the NMR spectra that are obtained. A Hamiltonian that describes the principal interactions of NMR, and hence, the energy of the nuclear spin states of a diamagnetic system placed in a magnetic field can be written:

$$\mathcal{H}_{\text{Total}} = \mathcal{H}_{\text{Z}} + \mathcal{H}_{\text{MS}} + \mathcal{H}_{\text{Q}} + \mathcal{H}_{\text{DD}} + \mathcal{H}_{\text{J}} \quad (1)$$

where \mathcal{H}_{Z} is the Zeeman interaction, \mathcal{H}_{MS} is the nuclear magnetic shielding interaction, \mathcal{H}_{Q} is the quadrupolar interaction, \mathcal{H}_{DD} represents direct dipolar coupling and \mathcal{H}_{J} represents indirect spin-spin coupling. Each of these interactions are discussed below in detail.

1.3 The Zeeman Interaction

Nuclei which possess a nuclear spin quantum number (I) greater than 0 intrinsically possess nuclear spin angular momentum (\mathbf{I} , the bold face indicates that it is a vector quantity), which is proportional to a nuclear magnetic dipole moment ($\boldsymbol{\mu}$):

$$\boldsymbol{\mu} = \gamma \mathbf{I} \quad (2)$$

Here, γ is the constant of proportionality known as the gyromagnetic ratio, which relates the magnitude of $\boldsymbol{\mu}$ to \mathbf{I} . The sign of γ can be negative or positive, with a positive gamma indicating that $\boldsymbol{\mu}$ is aligned in the same direction as \mathbf{I} and a negative γ indicating the

opposite. The magnitude of \mathbf{I} is:

$$|\mathbf{I}| = \hbar[I(I+1)]^{1/2} \quad (3)$$

Classically, the energy of a magnetic dipole in an external magnetic field (\mathbf{B}) depends upon its orientation:

$$E = -\boldsymbol{\mu} \cdot \mathbf{B} = -\mu B \cos(\theta) \quad (4)$$

where θ is the angle which describes the angle which $\boldsymbol{\mu}$ makes with \mathbf{B} (the latter is usually assumed to be directed along the z -axis). Therefore, it is energetically favourable for $\boldsymbol{\mu}$ to align with the applied field \mathbf{B} ($\theta = 0$), while it is unfavourable for $\boldsymbol{\mu}$ to oppose \mathbf{B} ($\theta = \pi$ radians).

Now consider a nuclear magnetic dipole placed in a magnetic field (\mathbf{B}_0) which is directed along the z -axis and possesses no x - or y - components [$\mathbf{B}_0 = (0, 0, B_0)$]. In an analogous manner to the classical expression, there are different energies associated with the possible orientations of $\boldsymbol{\mu}$ with respect to the magnetic field. However, unlike the classical case it is found that for a nucleus the orientations of $\boldsymbol{\mu}$ are quantized, that is, the expectation values of the z -component of nuclear spin angular momentum (I_z) are restricted to discrete values. For a spin I nucleus, there are $2I+1$ possible values of I_z . The possible values of I_z are termed nuclear spin states and are described by the quantum number m_I , where $m_I = I, I-1, \dots, -I$. In a magnetic field the nuclear spin states are non-degenerate (Figure 1.1), and the Hamiltonian describing this interaction and the energy of the respective nuclear spin states are given by:

$$\mathcal{H}_Z = -\hat{I}_Z \hbar \gamma B_0, \quad (5)$$

$$E_{m_1} = -m_1 \hbar \gamma B_0 = -m_1 \hbar \omega_0 \quad (6)$$

The quantity γB_0 has units of rad s^{-1} and is known as the Larmor frequency (ω_0).

Classically, this corresponds to the frequency at which the nuclear spin angular momentum precesses about the magnetic field. This precession occurs over a conical path, which possess a fixed angle between the nuclear spin angular momentum vector and

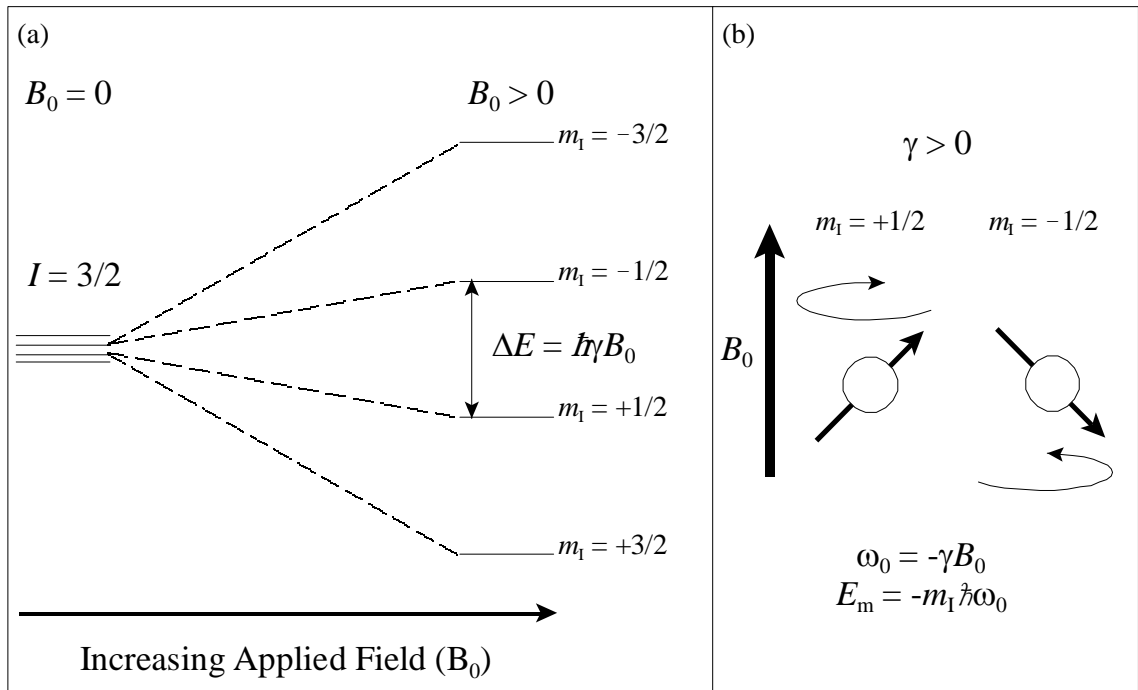


Figure 1.1. (a) The presence of a magnetic field results in quantization of the z -component of nuclear spin angular momentum (shown for an $I = 3/2$ nucleus). This results in distinct nuclear spin states. The energy separation between each of the adjacent nuclear spin states is equivalent, therefore, there is only one transition frequency. (b) The nuclear spin angular momentum precesses about the applied magnetic field.

the applied field for a given m_I (Figure 1b). The Larmor frequency defines the frequency of radiation which is necessary in order to induce transitions between the adjacent nuclear spin states ($\Delta E = h\nu$, *vide infra*). Under the influence of the Zeeman interaction, there is only one transition frequency for a spin I nucleus, as the separation of each nuclear spin state is equivalent and only transitions with $\Delta m_I = 1$ are formally allowed.

Only an isolated spin in a magnetic field has been considered thus far; however, when an NMR experiment is performed one must employ a sample which contains a large number of spins (typically $> 10^{15}$ spins). As a result of the small magnitude of μ , the energy differences between the spin states are very small. For most NMR experiments the magnitude of the thermal energy (kT) is much larger than the energy of the Zeeman interaction. For this reason, there is only a slight tendency for the spins to align with the field in the lower energy orientation. The ratio of the populations of the individual spin states in a bulk sample can be determined from the Boltzmann distribution:

$$\frac{N_\alpha}{N_\beta} = e^{\frac{\Delta E}{kT}} = e^{\frac{\hbar\gamma B_0}{kT}} \quad (7)$$

For an $I=1/2$ nucleus with positive γ , β corresponds to $m_I = -1/2$ and α to $m_I = +1/2$, N_α refers to the number of nuclei populating a lower energy nuclear spin state, and N_β the number populating a higher energy spin state. For a collection of ^1H nuclei in an applied magnetic field of 9.4 T ($\nu_0 \approx 400$ MHz) and a temperature of 295 K, the ratio of N_α/N_β is equal to 1.000065102. This illustrates how small the differences in the energies, and subsequently the population differences of the nuclear spin states are. Finally, it is

important to note that the nuclear spins are not restricted to distinct quantum states (i.e., every spin in the sample is aligned or opposed to the field); rather the individual spins exist in superpositions of the allowed quantum states.

While the population differences between the spin states are very small, the slight tendency for the nuclei within the sample to orient such that their magnetic dipole moments are aligned along the magnetic field, gives rise to a bulk macroscopic magnetization (\mathbf{M}). The magnitude of the observable NMR signal is directly proportional to the magnitude of the projection of \mathbf{M} along the z-axis (M_z), necessitating the use of relatively large sample sizes (e.g., samples containing at least *ca.* 10^{15} nuclear spins). The signal of the NMR experiment can be increased by working at high magnetic fields, cooling the sample to low temperatures and by utilizing nuclei which possess large gyromagnetic (γ) ratios, as all of these factors will also lead to an increase in the magnitude of N_α/N_β , and consequently a larger M_z .

1.4 Interactions of Nuclear Spins with Applied RF Fields

Before further discussing the NMR interactions it is necessary to understand how nuclear spins respond to applied radiofrequency fields. In a typical NMR experiment, a sample is placed into a small coil which is located inside of a large homogeneous static magnetic field. Once in the field, the sample attains an equilibrium value of M_z , after a period of time which is dictated by the relaxation properties of the nuclei. A pulse of alternating current of finite duration (τ_p), which oscillates at a transmitter frequency (ω_{Tx}) equal to, or similar to ω_0 of the nucleus, is passed through the coil. This generates an

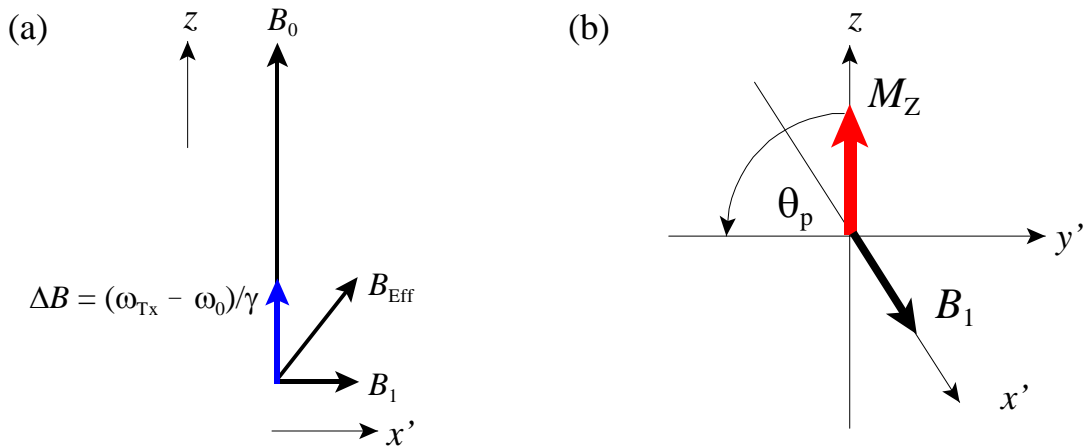


Figure 1.2. (a) A component of the B_1 field appears to be stationary in a frame which rotates at a frequency equal to that of the applied rf field (ω_{Tx}). If the frequency of ω_{Tx} and ω_0 differ, then an effective magnetic field results, which possesses both z - and x' -components. (b) If the frequency ω_{Tx} is close to ω_0 , then the bulk magnetization, M_Z will precess about the applied field B_1 and be rotated in the y' z -plane (the on resonance case of $\omega_{Tx} = \omega_0$ is shown). The angular displacement (θ_p) of M_Z depends upon the magnitude of the B_1 field and duration of the applied pulse (τ_p). If the pulse duration is such that $\theta_p = \pi/2$, then the magnetization ends up along $-y'$.

oscillating magnetic field (B_1). The coil is designed/oriented such that the B_1 field will possess a component which is *perpendicular* to the direction of the large static magnetic field (B_0). For a solenoidal coil oriented such that its cylindrical axis is perpendicular to B_0 , the B_1 field will also be perpendicular to B_0 (in the xy -plane).

At this point it is convenient to consider a frame which rotates about the z -axis with angular frequency ω_{Tx} . The x and y coordinates of this rotating frame are denoted x' and y' . In this rotating frame, a component of the B_1 field appears as a stationary field which is aligned along x' . If the frequency of the applied field (ω_{Tx}) is equal to that of the Larmor frequency ($\omega_{Tx} = \omega_0$), then magnetic dipole moments of the individual nuclei will precess about the applied B_1 field. A component of M_Z is rotated into the xy -plane by the B_1 field, yielding transverse magnetization (i.e., M_X and M_Y). If the frequency of ω_{Tx} and

ω_0 differ, then this reduces the magnitude of the x' -component of B_1 field, and results in an effective magnetic field (B_{eff}) which has both z - and x' -components (or y' -components depending upon the phase of the pulse). If one defines the quantity $\Delta B = (\omega_{\text{Tx}} - \omega_0)/\gamma$, then the orientation of B_{eff} in the rotating frame is found by vector summation of B_1 and ΔB (Figure 2a). If there is a large difference between the frequency of the applied pulse (ω_{Tx}) and the Larmor frequency (ω_0), then the pulse will be less effective at generating transverse magnetization (*vide infra*).

The magnitude of B_1 depends upon the amount of current which is passed through the coil; if a large current is passed through the coil then a large B_1 field will be obtained. The magnitude of the B_1 field is usually quantified by the nutation frequency, $\omega_1 = \gamma B_1$, which describes the rate at which magnetization will precess about B_1 fields applied on resonance. Large B_1 fields result in higher nutation frequencies, which are capable of exciting NMR signals with larger frequency offsets. This is a very important consideration for the acquisition of wideline SSNMR spectra, where very large differences between the transmitter and resonance frequencies commonly occur. Knowledge of the nutation frequency is very important, as it also determines the duration of pulses necessary to obtain optimal signal. If an on-resonance pulse of duration τ_p and strength ω_1 is applied, M_z will be rotated through an angle (θ_p):

$$\theta_p = \omega_1(\tau_p) \quad (8)$$

When the duration of the pulse is chosen so that $\theta_p = \pi/2$ rad, then M_z is converted into transverse magnetization (in the case of Figure 2b, $-M_y$). Power levels of the pulses are

experimentally calibrated by recording a series of spectra with pulses of variable durations at a constant power setting (B_1). Maximum signal corresponds to the $\pi/2$ - or 90° -pulse, as this will generate the maximum amount of initial transverse magnetization. It should be noted that many experiments also rely upon π -pulses, which are double the duration of $\pi/2$ pulses.

In the simplest NMR experiments, a single $\pi/2$ pulse is applied to the sample. After the pulse, transverse magnetization generated remains in the xy -plane and precesses about B_0 . In turn, this induces an alternating current in the sample coil. This induced current is then recorded by a receiver to form a time-domain signal, which is subsequently digitized, and transferred to a computer where it is Fourier transformed to construct a frequency-domain NMR spectrum.

1.5 Relaxation Processes

Relaxation processes will only be briefly addressed here. There are two main types of relaxation commonly encountered in NMR spectroscopy: longitudinal, or spin-lattice relaxation and transverse relaxation. Phenomenological descriptions of both processes are provided by the Bloch equations.¹³ The interested reader is referred to other more advanced descriptions of relaxation.³³⁻³⁵

Consider the case of an ensemble of ^1H nuclei; when the sample is initially placed into a magnetic field, the nuclear spins will have no preferred orientation within the sample, and hence there will be no macroscopic magnetization. Due to random molecular motion, the nuclear spins experience an enormous number of small fluctuating local

magnetic fields which cause the nuclear spins to gradually change their orientations such that there is an excess of spins populating the α spin state. Eventually, M_z reaches the equilibrium value (M_0) predicted from the Boltzmann distribution. This buildup of M_z is known as longitudinal relaxation and is described by the time constant T_1 . For nuclei in solution, T_1 is usually on the order of seconds, although it may range from μs for paramagnetic complexes, to hours or days for nuclei in some solids. The T_1 of the nucleus dictates the amount of time which one must wait in between scans, and hence strongly influences the total time required for NMR experiments. The magnitude of M_z is related to T_1 via an exponential relationship, therefore, in order to obtain complete relaxation ($M_z = M_0$) one must wait approximately $5 T_1$ periods.

In a manner analogous to longitudinal relaxation, the transverse magnetization generated by an applied pulse will also undergo relaxation. After the pulse is applied, the transverse magnetization precesses in the xy -plane, however, its magnitude decreases over time and it eventually decays to zero. This occurs due to the individual nuclear spins acquiring random orientations (phases) within the xy -plane which leads to a loss of coherence. This process is known as transverse relaxation and is described by the time constant T_2 . Transverse relaxation results from molecular motion and fluctuating magnetic fields, as for longitudinal relaxation, as well as static time-independent local fields which result in different precession frequencies. T_2 is always less than T_1 and is typically on the order of ms to s. A long T_2 is desirable as this provides sufficient time for the power of the pulse to dissipate in the probe and allows the signal to be recorded without interference. Long T_2 's are also beneficial as they allow the magnetization to be

repeatedly refocused, as in the Carr-Purcell Meiboom-Gill pulse sequence,^{36,37} which is a useful approach for signal enhancement.

1.6 Nuclear Magnetic Shielding and Chemical Shift

The nuclear magnetic shielding (MS) phenomenon was first observed in 1950 in ¹⁹F and ¹⁴N NMR experiments.^{38,39} In 1951 three distinct ¹H resonances were observed for the methyl (-CH₃), methylene (-CH₂) and alcohol (-OH) hydrogen nuclei of ethanol, and their frequency differences were referred to as chemical shifts (CS).¹⁷ These discoveries spurred the further development of NMR spectroscopy as a tool for the evaluation of molecular structure.

The magnetic shielding (MS) interaction arises due to induced circulation of electrons around the nucleus. Since electrons are charged particles, their circulation about the nucleus induces a magnetic field which alters the local field at the nucleus. The total isotropic magnetic shielding (σ_{iso}) describes the magnitude of this induced field. The effect of magnetic shielding is to effect the apparent magnitude of B_0 and concomitantly alter ω_0 :

$$\omega_0 = (1 - \sigma_{\text{iso}})\gamma B_0 \quad (9)$$

σ_{iso} is unitless and usually positive, and its magnitude is typically on the order of parts per million (ppm, 10^{-6}). The “iso” subscript refers to the isotropic (or average) MS, since the MS interaction is usually anisotropic in nature (*vide infra*).

The theoretical basis of the MS interaction was described in the early 1950's

shortly after the observation of the chemical shift.⁴⁰⁻⁴² σ_{iso} is usually broken down into diamagnetic ($\sigma_{d,\text{iso}}$) and paramagnetic ($\sigma_{p,\text{iso}}$) contributions:

$$\sigma_{\text{iso}} = \sigma_{d,\text{iso}} + \sigma_{p,\text{iso}} \quad (10)$$

Diamagnetic contributions ($\sigma_{d,\text{iso}}$) typically shield the nucleus from the external field ($\sigma_d > 0$), and paramagnetic contributions ($\sigma_{p,\text{iso}}$) typically deshield the nucleus ($\sigma_{p,\text{iso}} < 0$).

Diamagnetic shielding arises due to circulation of electrons in the ground state orbitals, which is induced by the applied static magnetic field. For a given nucleus, the values of σ_d show little variation between different chemical species. Paramagnetic shielding, is also induced by the static magnetic field and arises due to the mixing of low lying excited electronic states (virtual orbitals) with ground electronic states (occupied orbitals). σ_p strongly depends upon the oxidation state of the element as well as the symmetry of the nuclear site. Consequently, variations in σ_p are responsible for the differences in MS (and CS) observed for different chemical species. The σ_p term is usually highly anisotropic in nature and is responsible for the anisotropic nature of total MS. For heavy nuclei relativistic effects lead to a significant spin-orbit contribution (σ_s) to the total shielding which must also be taken into account.⁴³⁻⁴⁶ For an in depth discussion of these various shielding terms see Chapter 8 where the contributions of the various shielding terms to the MS of ^{207}Pb in a series of lead(II) thiolate complexes are discussed.

In order to understand how MS affects the appearance of NMR spectra it is necessary to consider the Hamiltonian which describes this interaction:

$$\mathcal{H}_{\text{MS}} = -\hbar\gamma \mathbf{I} \cdot \ddot{\boldsymbol{\sigma}} \cdot \mathbf{B} \quad (11)$$

\mathbf{I} and \mathbf{B} are vector quantities describing the nuclear spin angular momentum and the direction of applied field, respectively. From this equation it can be seen that the MS interaction varies with the nuclear spin orientation relative to the external magnetic field. $\ddot{\boldsymbol{\sigma}}$ is second-rank tensor that describes the MS of the nucleus in the molecular frame:

$$\ddot{\boldsymbol{\sigma}} = \begin{pmatrix} \sigma_{xx} & \sigma_{xy} & \sigma_{xz} \\ \sigma_{yx} & \sigma_{yy} & \sigma_{yz} \\ \sigma_{zx} & \sigma_{zy} & \sigma_{zz} \end{pmatrix} \quad (12)$$

Individual MS tensor components (σ_{ij}) describe the shielding in the direction i that results from application of a magnetic field along direction j . The MS tensor can be transformed to its own principal axis system (PAS) by removing the antisymmetric portion of $\ddot{\boldsymbol{\sigma}}$ and diagonalizing the symmetric portion. This yields $\ddot{\boldsymbol{\sigma}}_{\text{PAS}}$:

$$\ddot{\boldsymbol{\sigma}}_{\text{PAS}} = \begin{pmatrix} \sigma_{11} & 0 & 0 \\ 0 & \sigma_{22} & 0 \\ 0 & 0 & \sigma_{33} \end{pmatrix} \quad (13)$$

The orientation of the PAS within the molecular frame can sometimes be rationalized by considering the symmetry at the nuclear site. The directions corresponding to the principal components of σ_{PAS} will usually align with molecular symmetry elements (e.g., rotational axes, mirror planes, etc.). The principal components are ordered such that $\sigma_{11} \leq$

$\sigma_{22} \leq \sigma_{33}$ (i.e., from lowest to highest shielding). The isotropic shielding can be calculated from the principal tensor components:

$$\sigma_{\text{iso}} = \frac{(\sigma_{11} + \sigma_{22} + \sigma_{33})}{3} \quad (14)$$

The zero point of the MS scale is a bare nucleus which does not have any electrons associated with it (e.g., for ^{13}C , $\sigma_{\text{iso}}(\text{C}^{6+}) = 0$ ppm). Experimentally, it is usually impossible to measure the resonance frequency of a bare nucleus. Therefore, σ_{iso} values can not be easily determined for nuclei in atoms and molecules, as the ω_0 corresponding to $\sigma = 0.0$ ppm cannot be measured. For this reason, the chemical shift (CS) scale is employed. The CS scale (δ) is constructed by assigning a reference material an arbitrary shift (often $\delta_{\text{iso}} = 0$ ppm) and then measuring the Larmor frequency (ν_{sample}) of the compound of interest and the standard ($\nu_{\text{reference}}$). If the two resonance frequencies are known, then the isotropic chemical shift (δ_{iso}) can be determined:

$$\delta_{\text{iso}} = \frac{(\nu_{\text{sample}} - \nu_{\text{reference}})}{(\nu_{\text{reference}} \times 10^6)} = \frac{\sigma_{\text{iso, sample}} - \sigma_{\text{iso, reference}}}{1 - \sigma_{\text{iso, reference}}} \approx \sigma_{\text{iso, sample}} - \sigma_{\text{iso, reference}} \quad (15)$$

δ_{iso} is approximately equal to the difference in the shielding values of the nucleus in the sample ($\sigma_{\text{iso, sample}}$) and the shielding values of the nucleus in the reference ($\sigma_{\text{iso, reference}}$).

The principal components of the MS tensor (σ_{kk}) can also be converted to the principal components of the CS tensor (δ_{kk}) in this manner:

$$\delta_{kk} = \frac{\sigma_{\text{iso, reference}} - \sigma_{kk, \text{ sample}}}{1 - \sigma_{\text{iso, reference}}} \quad (16)$$

Note that the principal components of the CS tensor are ordered such that $\delta_{11} \geq \delta_{22} \geq \delta_{33}$, from highest CS (least shielded) to lowest CS (most shielded).

As previously mentioned, the CS tensor is anisotropic in nature. A number of conventions have been developed to describe the magnitude of the chemical shift anisotropy (CSA) as well as the symmetry of the CS tensor. These conventions aim to make it simpler to compare CS tensors measurements between different complexes and nuclei. In this thesis, the Maryland convention is used to specify the CS tensors.^{47, 48} This convention employs three different parameters which are all derived from the principal components of the CS tensor: δ_{iso} , the span (Ω) and the skew (κ):

$$\delta_{\text{iso}} = \frac{\delta_{11} + \delta_{22} + \delta_{33}}{3} \quad (17)$$

$$\Omega = \delta_{11} - \delta_{33} \approx \sigma_{11} - \sigma_{33} \quad (18)$$

$$\kappa = \frac{3(\delta_{22} - \delta_{\text{iso}})}{\Omega}, \quad -1 \leq \kappa \leq +1 \quad (19)$$

δ_{iso} corresponds to the average value of the principal components of the CS tensor and corresponds to the chemical shift which is measured from solution NMR spectra. Ω

describes the magnitude of the CSA and is always a positive number. κ ranges from +1 to -1 and describes the axial symmetry of the CS tensor (e.g., if $\kappa = +1$ then $\delta_{22} = \delta_{11}$ and if $\kappa = -1$ then $\delta_{22} = \delta_{33}$).

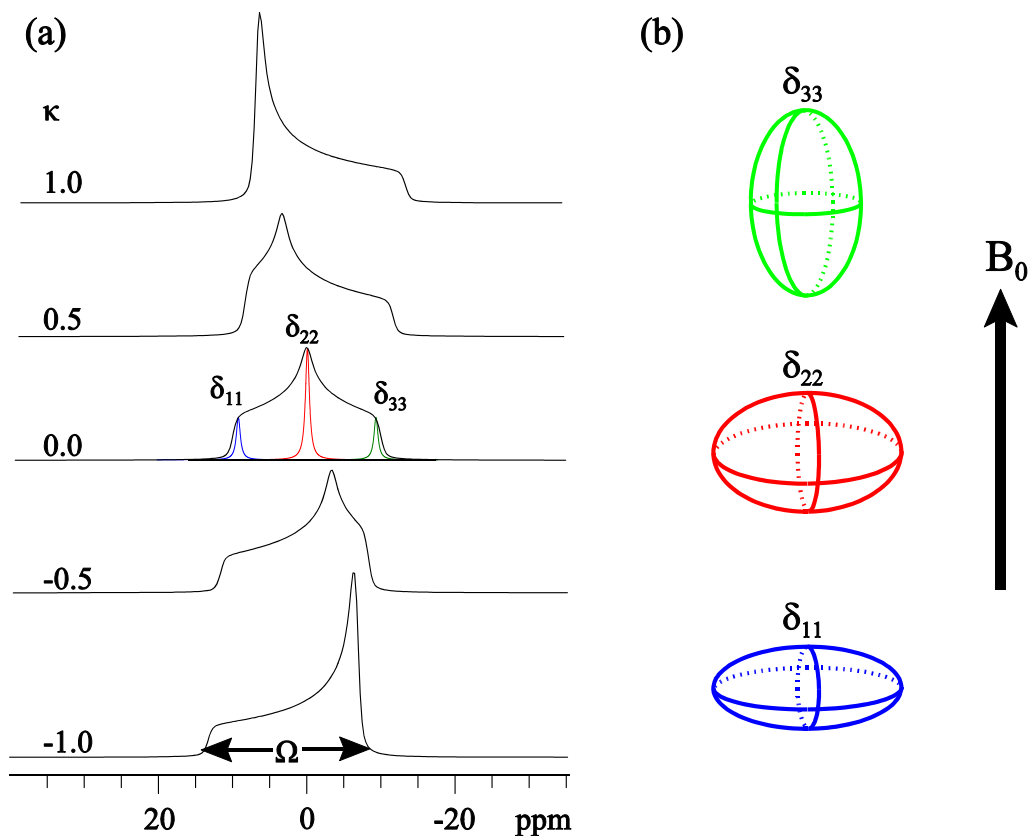


Figure 1.3. (a) Simulated ^{13}C ($I=1/2$) static spectra with $\Omega = 20.0$ ppm and $\delta_{\text{iso}} = 0.0$ ppm. κ affects the position of δ_{22} . Discontinuities correspond to the principal components of the CS tensor. When $\kappa = +1.0$, $\delta_{11} = \delta_{22}$ and when $\kappa = -1.0$, $\delta_{22} = \delta_{33}$. (b) Different orientations of the CS tensor with respect to the magnetic field give rise to distinct transition frequencies (shown on the left). In a powdered sample the tensor will be present in all orientations with respect to a magnetic field, giving rise to a powder pattern.

The influence of these parameters on the appearance of NMR spectra are now addressed. In solution NMR experiments, the the effects of CSA are averaged to zero (although it may broaden the spectrum via relaxation effects) because the molecules containing the nuclei of interest usually experience rapid isotropic tumbling in solution. This leads to the observation of a single relatively narrow resonance with a chemical shift of δ_{iso} . Conversely, when acquiring SSNMR spectra one normally works with powdered samples in which the molecules are not undergoing rapid isotropic motion. A crystalline powdered sample contains a random array of crystallites, and hence every possible orientation of the molecule (and CS tensors) with respect to the magnetic field exists (Figure 1.3). The anisotropic nature of the CS interaction leads to the broadening of SSNMR spectra of powdered samples, resulting in so-called powder patterns. Examples of static ^{13}C SSNMR powder patterns which result from CSA are shown in Figure 1.3a. The shape of the powder patterns is controlled by the CS tensor parameters. The breadth of the powder pattern in ppm is equal to Ω , while κ determines the location of the central discontinuity (which corresponds to δ_{22}) and δ_{iso} is the centre of gravity of the powder pattern.

1.7 Quadrupolar Nuclei and the Quadrupolar Interaction

The quadrupolar interaction is observed for nuclei with $I > 1/2$ (e.g., $I = 1, 3/2, 5/2$, etc.). In a quadrupolar nucleus, the nuclear charge is non-spherically distributed, giving rise to a nuclear quadrupole moment (Q).^{22, 49} The quadrupolar interaction occurs due to the interaction of Q with any surrounding electric field gradients (EFGs). EFGs

arise from the non-spherically symmetric distribution of charges or electron density (i.e., from atoms and bonds) surrounding the nucleus. At any nucleus about which the molecular geometry is non-spherical there will exist a non-zero EFG.^{50,51} The EFG about a nucleus in the molecular frame is described by a symmetric (e.g., $V_{xy} = V_{yx}$) second-rank tensor $\ddot{\mathbf{V}}$:

$$\ddot{\mathbf{V}} = \begin{pmatrix} V_{xx} & V_{yx} & V_{zx} \\ V_{xy} & V_{yy} & V_{zy} \\ V_{xz} & V_{yz} & V_{zz} \end{pmatrix} \quad (20)$$

Diagonalization of the EFG tensor transforms the EFG to its PAS:

$$\ddot{\mathbf{V}}_{\text{PAS}} = \begin{pmatrix} V_{11} & 0 & 0 \\ 0 & V_{22} & 0 \\ 0 & 0 & V_{33} \end{pmatrix} \quad (21)$$

The EFG tensor is described by three principal components ordered such that $|V_{11}| \leq |V_{22}| \leq |V_{33}|$. The EFG tensor is also traceless [$V_{11} + V_{22} + V_{33} = 0$].

The magnitude of the quadrupolar interaction is described by the quadrupolar coupling constant and the quadrupolar frequency (both in units of Hz):

$$C_Q = \frac{eQV_{33}}{h}, \quad \nu_Q = \frac{3C_Q}{2I(2I - 1)} \quad (22)$$

For most quadrupolar nuclei residing in non-spherically symmetric environments, C_Q is

on the order of MHz and in extreme cases may approach the magnitude of the ν_0 . The EFG asymmetry parameter, η_Q , describes the axial symmetry of the EFG tensor:

$$\eta_Q = \frac{V_{11} - V_{22}}{V_{33}}, \quad 0 \leq \eta_Q \leq 1 \quad (23)$$

The cases where $\eta_Q = 0$ ($V_{11} = V_{22}$) and $\eta_Q = 1$ ($V_{11} = 0, V_{22} = -V_{33}$) correspond to axially symmetric EFG tensors.

The total Hamiltonian describing the quadrupolar interaction is³⁰:

$$\mathcal{H}_Q = \frac{eQ}{2I(2I - 1)\hbar} \mathbf{I} \cdot \ddot{\mathbf{V}} \cdot \mathbf{I} = \frac{eQ}{6I(2I - 1)\hbar} \sum_{\alpha, \beta = X, Y, Z} V_{\alpha\beta} \left[\frac{3}{2} (\hat{I}_\alpha \hat{I}_\beta + \hat{I}_\beta \hat{I}_\alpha) - \delta_{\alpha\beta} \hat{I}^2 \right] \quad (24)$$

Expansion of the $\mathbf{I} \cdot \ddot{\mathbf{V}} \cdot \mathbf{I}$ term on the left by matrix multiplication and use of the fact, $V_{\alpha\beta} = V_{\beta\alpha}$, leads to the form of the Hamiltonian on the right. If ν_0 is on the order of 10 times larger than ν_Q , then the quadrupolar interaction may be treated as a perturbation of the Zeeman interaction, allowing for the terms on the right hand side of equation (22) which do not commute with I_z to be discarded. The quadrupolar Hamiltonian is then expanded into a series using perturbation theory:

$$\mathcal{H}_Q = \mathcal{H}_Q^{[1]} + \mathcal{H}_Q^{[2]} + \dots \quad (25)$$

If ν_Q is relatively small then only the first-order quadrupolar interaction [$\mathcal{H}_Q^{[1]}$] needs to be considered. The main effect of the quadrupolar interaction is to perturb the energies of the Zeeman spin states (m_l):

$$E_m = E_{Z,m} + E_{Q,m}^{[1]} + E_{Q,m}^{[2]} \quad (26)$$

where E_m is the total energy of a given spin state m , $E_{Z,m}$ is the energy of the Zeeman interaction and $E_m^{[1]}$ and $E_m^{[2]}$ correspond to the energy corrections associated with the first-order and second-order quadrupolar interaction, respectively.³⁰ The correction of the energy of spin-state m due to the first order quadrupolar interaction is given by:^{30, 52, 53}

$$E_{Q,m}^{[1]} = \frac{e^2 q Q}{4I(2I - 1)} [3m^2 - I(I+1)] F(\theta, \varphi) \quad (27)$$

where:

$$F(\theta, \varphi) = \frac{1}{2} [(3\cos^2\theta - 1) + \frac{1}{2}\eta_Q \sin^2\theta \cos 2\varphi] \quad (28)$$

The angles θ and φ are polar angles which describe the orientation of the PAS of the EFG tensor with respect to the external magnetic field (θ describes the angle V_{33} forms with \mathbf{B}_0). If the magnitude of v_Q is relatively large, then the second-order quadrupolar interaction will also significantly effect the energy of the nuclear spin states, and the correction is given by:^{30, 52, 53}

$$E_{Q,m}^{[2]} = - \left(\frac{e^2 q Q}{4I(2I - 1)} \right)^2 \frac{m}{\omega_0} \times F_2(\theta, \varphi, m, I) \quad (29)$$

where $F_2(\theta, \varphi, m, I)$ is:

$$\begin{aligned}
F_2(\theta, \varphi, m, I) = & \left[-\frac{1}{5}(I(I+1) - 3m^2)(3 + \eta_Q^2) \right. \\
& + \frac{1}{28}(8I(I+1) - 12m^2 - 3)[(\eta_Q^2 - 3)(3\cos^2\theta - 1) + 6\eta_Q\sin^2\theta\cos 2\varphi] \\
& + \frac{1}{8}(18I(I+1) - 34m^2 - 5)\left[\frac{1}{140}(18 + \eta_Q^2)(35\cos^4\theta - 30\cos^2\theta + 3) \right. \\
& \left. \left. \times \frac{3}{7}\eta_Q^2\sin^2\theta(7\cos^2\theta - 1)\cos 2\varphi + \frac{1}{4}\sin^4\theta\cos 4\varphi \right] \right] \quad (30)
\end{aligned}$$

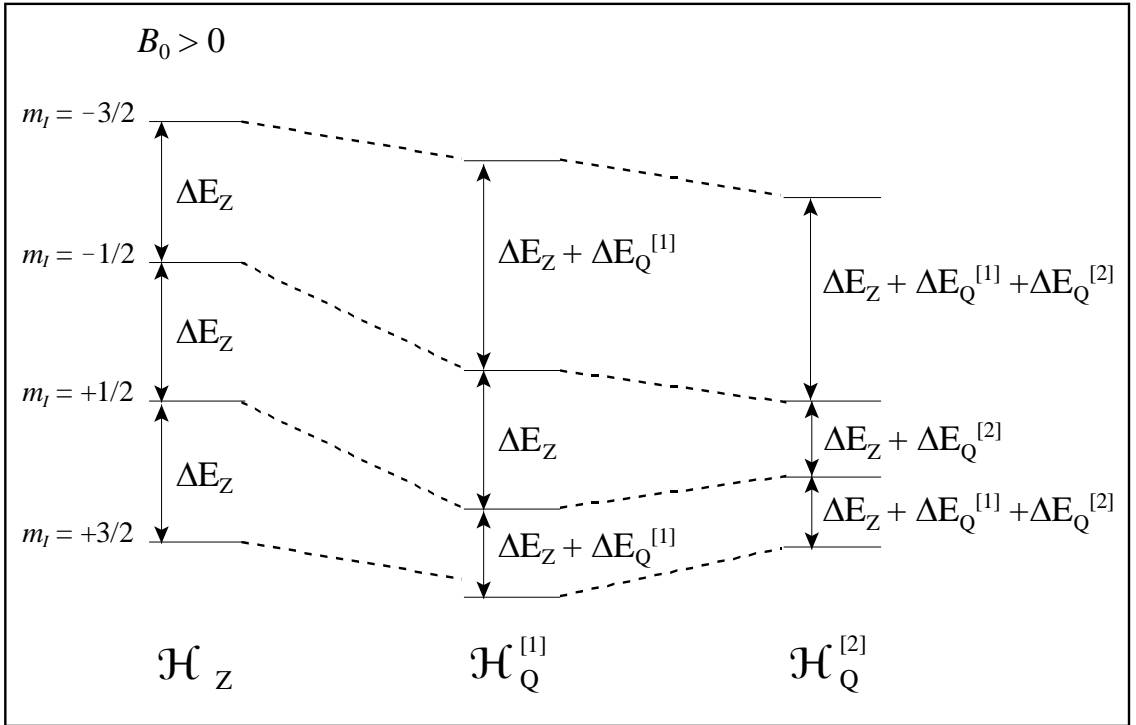


Figure 1.4. The energies of the nuclear spin states under the influence of the first-order quadrupolar interaction and the second-order quadrupolar interaction are shown for a single crystallite orientation. In the presence of the Zeeman interaction there is only a single transition frequency, while the quadrupolar interaction results in multiple transitions. The change in the energy of the nuclear spin states by $\mathcal{H}_Q^{[2]}$ have been exaggerated with respect to those of $\mathcal{H}_Q^{[1]}$.

In NMR spectroscopy, the energies that are observed correspond to transitions between adjacent spin states (Figure 1.4). In order to understand the appearance of the

SSNMR spectrum, it is necessary to consider the difference in energy between the adjacent nuclear spin states (e.g., $\Delta m = \pm 1$). Although the energy of the individual spin states are perturbed, the first-order quadrupolar interaction does *not* perturb the energy of the central transition (CT, $m = +1/2 \rightarrow m = -1/2$). Consequently, the CT remains unaffected by the first-order quadrupolar interaction. However, all satellite transitions (ST, $m \rightarrow m - 1, m \neq +1/2$) are perturbed by the first-order quadrupolar interaction. For large values of ν_Q , the second order quadrupolar interaction becomes significant and perturbs the CT and further perturbs the ST.

From equations (27) and (29) it can be seen that the energy of the nuclear spin states strongly depends upon the magnitude of the quadrupolar interaction and the orientation of the EFG tensor of the nucleus with respect to the magnetic field. For a powdered sample, there will be many crystallites present which will possess EFG tensors in every possible orientation. Therefore, powder patterns which possess characteristic lineshapes are observed in the static SSNMR spectra of quadrupolar nuclei. Usually only the CT powder patterns are observed in SSNMR spectra of quadrupolar nuclei, as the ST powder patterns are normally broadened beyond detection by the first order quadrupolar interaction. Simulations of static CT powder patterns for ^{35}Cl ($I = 3/2$) are shown in Figure 1.5. Based upon their shapes it is possible to obtain the EFG tensor parameters C_Q and η_Q . C_Q and η_Q provide a measure of the spherical symmetry and the axial symmetry of the EFG tensor at the nuclear site, respectively. Numerous examples of SSNMR spectra of quadrupolar nuclei are found in the subsequent chapters of the thesis.

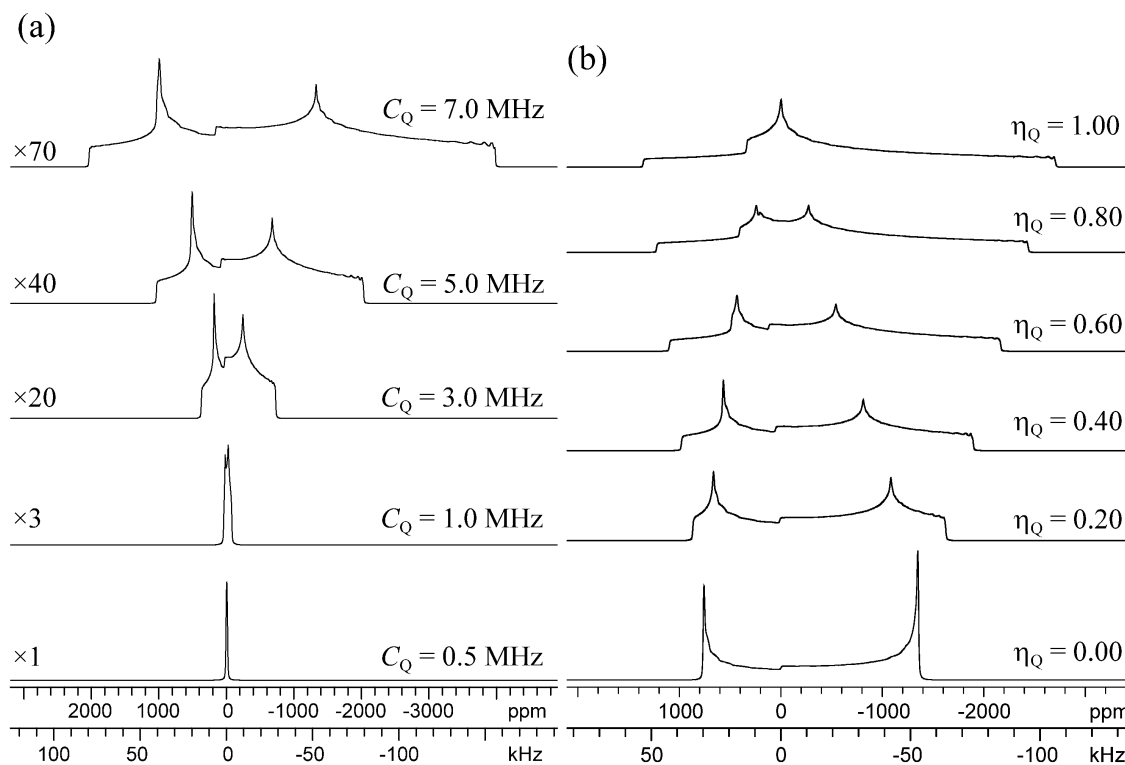


Figure 1.5. Simulations of static ^{35}Cl SSNMR spectra at 9.4 T ($\nu_0 = 39.160$ MHz). For all simulated spectra $\delta_{\text{iso}} = 0.0$ ppm. (a) Simulated spectra with $\eta_Q = 0.50$ and values of C_Q which range from 0.5 MHz to 7.0 MHz. Vertical scaling factors are indicated to the left of the spectra. (b) Simulated spectra with $C_Q = 5.0$ MHz and η_Q values which range from 0.00 to 1.00.

1.8 Euler Angles

Many quadrupolar nuclei possess significant CSA. In these cases, the appearance of the central-transition powder patterns are profoundly affected by the relative orientation of the CS and EFG tensors.^{54, 55} The Euler angles, α , β and γ , are used to describe the relative orientation of the two tensors, and describe the series of two-dimensional rotations necessary to translate one of the tensors back into its own PAS system. Figure 1.6 shows the rotations necessary to translate the CS tensor to its own

PAS from a frame which is coincident with the PAS of the EFG tensor. Examples of static SSNMR spectra of quadrupolar nuclei influenced by Euler angles are shown in the subsequent chapters of the thesis.

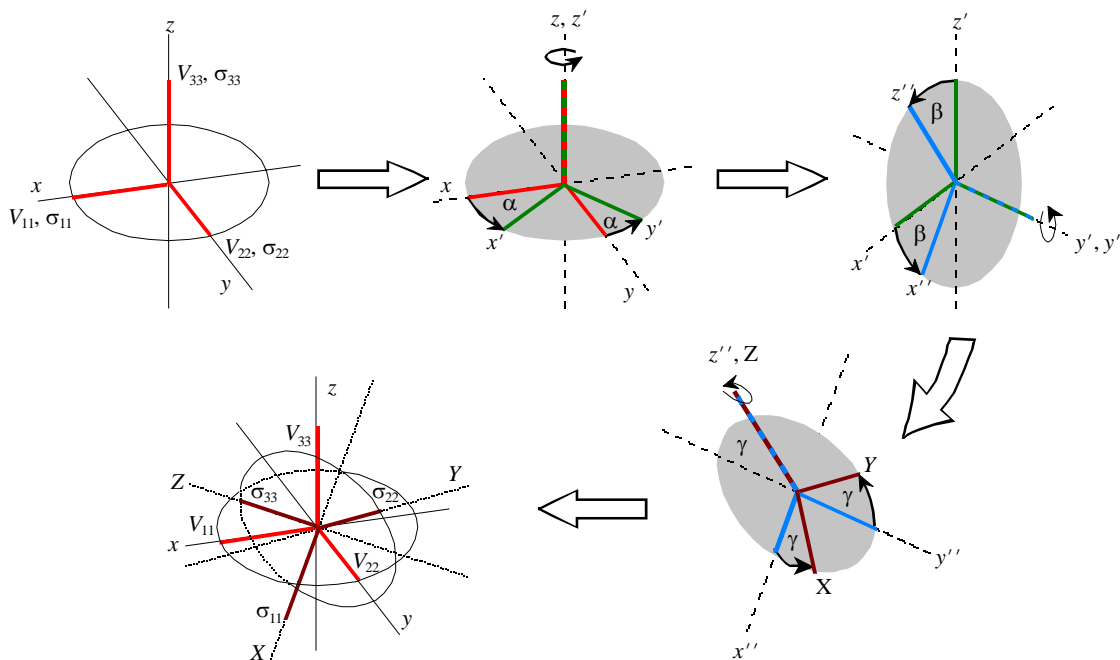


Figure 1.6. Rotation of the CS tensor from the fixed EFG tensor frame of reference (x , y , z) into the PAS of the CS tensor (X , Y , Z). Figure obtained with permission from Dr. Joel A. Tang.

1.9 Direct and Indirect Spin-Spin Coupling

The direct spin-spin coupling and indirect spin-spin coupling interactions are not discussed in great detail here, as these interactions are not heavily involved in the SSNMR experiments conducted in this thesis.

Direct spin-spin coupling, or dipolar coupling, arises from the through space interactions of the magnetic moments of two nuclei. The total dipolar coupling Hamiltonian in Cartesian tensor form is given by:

$$\mathcal{H}_{\text{DD}} = -2\mathbf{I}\cdot\ddot{\mathbf{D}}\cdot\mathbf{S}, \quad \ddot{\mathbf{D}} = -\begin{pmatrix} -\frac{d}{2} \\ -\frac{d}{2} \\ +d \end{pmatrix} \quad (31)$$

where $\ddot{\mathbf{D}}$ is a traceless first-rank tensor and d is the dipolar coupling constant:

$$d = -\hbar \left(\frac{\mu_0}{4\pi} \right) \frac{\gamma_I \gamma_S}{r^3} \quad (32)$$

d is in units of Hz, and r is the distance between nuclei I and S . d describes the magnitude of the dipolar interaction. From (32) it can be seen that d is proportional to the γ of the two coupled nuclei and is inversely proportional to the cube of the internuclear distance (r). This means that dipolar couplings are very large for closely spaced high- γ nuclei. For example, ^1H nuclei contained in organic moieties usually experience dipolar couplings on the order of tens of kHz, and subsequently, ^1H SSNMR spectra are normally very broad. The influence of the ^1H dipolar coupling on the SSNMR spectra of heteronuclei is normally removed by the application of heteronuclear decoupling schemes and/or magic-angle spinning (MAS, *vide infra*). Dipolar coupling is also exploited to obtain signal enhancement with the cross-polarization experiment.

Indirect spin-spin coupling (J -coupling) is similar to the dipolar interaction, however, the coupling of the two nuclei is mediated by chemical bonds rather than through space. The Hamiltonian describing J -coupling is²⁴:

$$\mathcal{H}_{\text{DD}} = -2\pi\mathbf{I}\cdot\ddot{\mathbf{J}}\cdot\mathbf{S} \quad (33)$$

where $\ddot{\mathbf{J}}$ is a second-rank anti-symmetric tensor that describes the magnitude of the scalar coupling for different orientations of the nucleus, I , with respect to the magnetic field.

The magnitude of the coupling is usually described by a coupling constant, J_{IS} , which is equal to the average of the principal components of the $\ddot{\mathbf{J}}$. The magnitude of the coupling is proportional to the γ values of the two coupled nuclei. In cases where the Fermi contact mechanism is dominant, J_{IS} is proportional to the amount of s -orbital overlap between the atoms which contain the nuclei. Frequently a reduced coupling constant (K_{IS}) is reported:

$$K_{IS} = \frac{4\pi^2 J_{IS}}{\hbar\gamma_I\gamma_S} \quad (34)$$

K_{IS} is independent of the magnitudes of γ of the two coupled nuclei and allows for comparisons of coupling constants for different nuclei to be made. Because J -coupling is mediated by chemical bonds, comparison of the K_{IS} values can provide insight into the nature of bonding between different atoms.⁵⁶

J -couplings are commonly encountered in solution NMR experiments and are used in order to determine connectivity within molecular systems. Normally, J -couplings are only observed in SSNMR spectra when MAS (*vide infra*) experiments are employed. MAS experiments usually average the anisotropic components of $\ddot{\mathbf{J}}$ so that only the isotropic coupling constant is observed, although it is sometimes possible to observe the

anisotropic portions of J -couplings (ΔJ).⁵⁷ J -couplings are usually on the order of several hundred Hz; however if heavy nuclei are involved they may be on the order of kHz.

NMR Techniques

1.10 Magic-Angle Spinning

MAS is a technique used for the acquisition of high resolution SSNMR spectra. For solution NMR experiments, high resolution is naturally afforded by isotropic molecular motion, which averages many of the anisotropic NMR interactions. In order to obtain “solution-like” SSNMR spectra, MAS is employed. In MAS experiments the sample is rapidly spun (*ca.* 3-70 kHz) about an axis oriented at 54.74° with respect to the magnetic field (Figure 1.7).^{58,59} The magic angle is

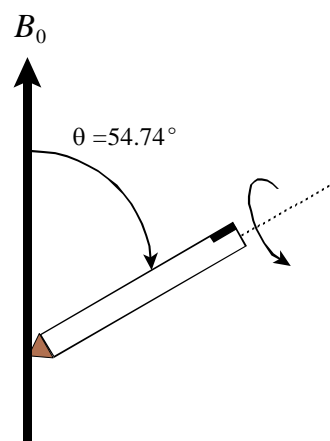


Figure 1.7. Representation of the sample orientation for a MAS experiment.

derived from the term, $3\cos^2\theta - 1$; which is zero when $\theta = 54.74^\circ$. All of the first-order anisotropic NMR interactions have an orientation dependence which is described by this geometric term. Rapid spinning of powdered samples at the magic angle results in partial or complete averaging of these anisotropic interactions. When a powdered sample is spun at the magic angle each crystallite possesses an average orientation of $\langle 3\cos^2\theta - 1 \rangle$ over the course of one full rotation period (where θ corresponds to the angle between B_0 and largest principal component of the interaction tensor). As a rule of thumb, if the

sample is spun at a rate in Hz on the order of the anisotropic component of the interaction, then the anisotropic NMR interaction is represented by its isotropic value in the SSNMR spectrum. The specific applications of MAS for the acquisition of SSNMR spectra influenced by the CS and quadrupolar interactions are now discussed.

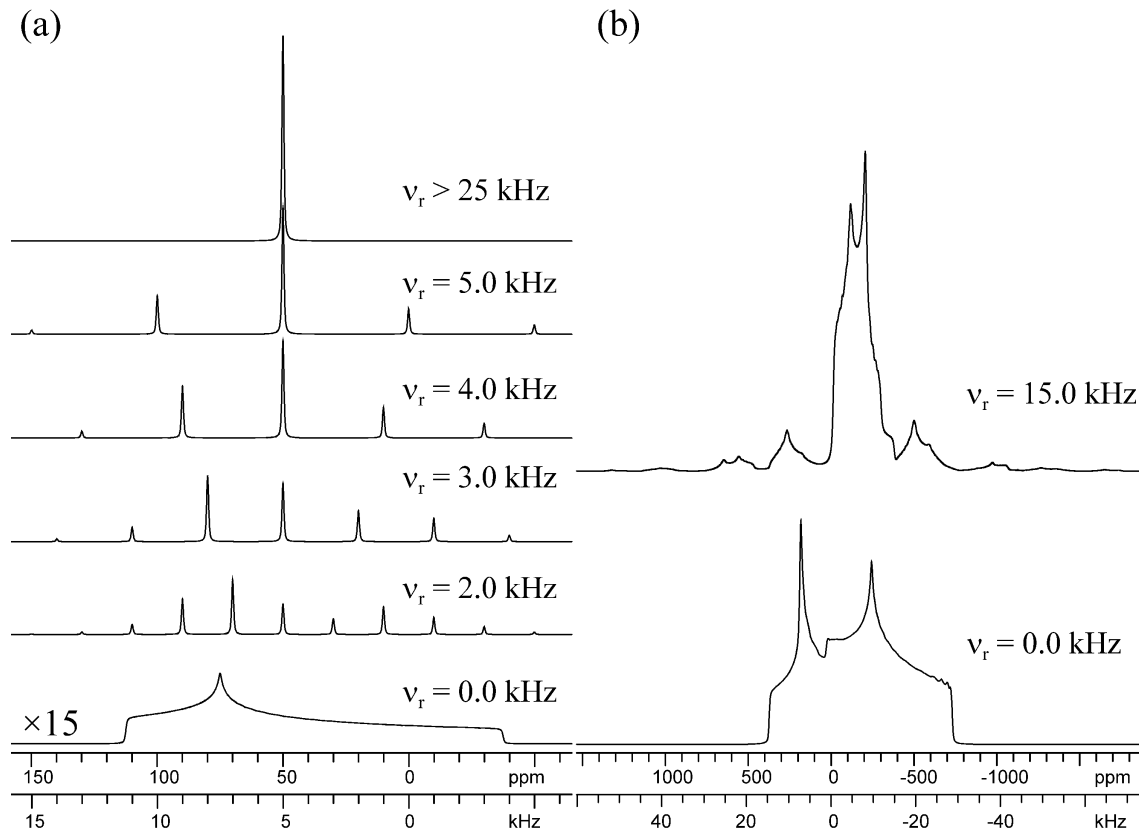


Figure 1.8. (a) Simulations of MAS ^{13}C SSNMR spectra employing $\nu_0 = 100.15$ MHz, $\delta_{\text{iso}} = 50$ ppm, $\Omega = 150$ ppm, $\kappa = 0.50$ and various spinning speeds (ν_r , listed next to spectra). The corresponding static spectrum is also shown (bottom). (b) Simulated MAS (top) and static (bottom) ^{35}Cl SSNMR spectra with $\nu_0 = 39.16$ MHz, $\delta_{\text{iso}} = 0.0$ ppm, $C_Q = 3.0$ MHz and $\eta_Q = 0.50$.

The broadening of SSNMR spectra due to CSA is described by a $3\cos^2\theta - 1$ term; therefore, MAS can potentially completely average the broadening due to CSA. When MAS is performed on a nucleus solely influenced by CSA, a spectrum containing a sharp

isotropic peak is obtained (Figure 1.8a). Depending upon the sample spinning speed (v_{rot}) employed, there are additional peaks offset from the isotropic peak at integer multiples of the sample spinning speed. These peaks are known as spinning sidebands and their intensities are determined by the CS tensor. It is possible to determine the principal components of the CS tensor via Herzfeld-Berger analysis, which takes v_{rot} and the spinning sideband intensities into account.⁶⁰ From a practical standpoint, MAS provides a large degree of signal enhancement in comparison to experiments conducted on static samples, since the signal intensity is concentrated into the relatively sharp isotropic peaks and spinning sidebands.

For quadrupolar nuclei, the broadening due to first-order quadrupolar interaction is also dependent upon $3\cos^2\theta - 1$, where θ corresponds to the angle between V_{33} and B_0 . MAS can effectively average the first-order quadrupolar interaction; however, the second-order quadrupolar interaction is only partially averaged, due to its complex angular dependence (29). CT powder patterns are observed for the MAS SSNMR spectra of quadrupolar nuclei, however, their breadths are reduced by a factor of *ca.* 3 - 4 compared to the static CT powder patterns. Comparisons of static and MAS SSNMR spectra of a half-integer spin quadrupolar nucleus are shown in Figure 1.8b. In most cases, the lineshape of the MAS powder patterns of quadrupolar nuclei only depends upon C_Q , η_Q and δ_{iso} . This simplifies the extraction of EFG tensor parameters from these patterns, as the influence of CSA and Euler angles are removed. Consequently only three parameters are necessary to properly fit the MAS spectrum. Although, in certain cases if the CSA is large then intensity from the MAS CT powder pattern may be distributed into the

spinning sidebands. Signal enhancement is also afforded due to narrowing of the MAS quadrupolar powder patterns, with respect to the corresponding static powder patterns.

1.11 Pulsed NMR Techniques

The magnitude of the signal and the information content of NMR spectra are ultimately controlled by the pulse sequence which is used to create the time-domain signal. For example, double-resonance techniques are routinely employed to enhance the signal of NMR spectra by means of polarization transfer from abundant high- γ nuclei. The continued development of new methods and pulse sequences continues to be an area of intense research within NMR spectroscopy. The basic features of several pulse sequences which have been employed to acquire the SSNMR spectra shown in the subsequent chapters are now discussed.

In the most basic NMR experiment, a single $\pi/2$ pulse is applied to the sample, and the resultant time domain signal is then recorded. Due to the rapid relaxation behaviour of some nuclei, and the non-ideal characteristics of NMR probe electronics, this experiment is not always viable. For example, when trying to observe an NMR spectrum of a broad resonance the signal will rapidly dephase following the application of the pulse. In such cases it may not be possible to blank the probe (dissipate the power of the pulse) and turn on the receiver quickly enough to record the rapidly decaying NMR signal. One solution to this problem is to use an echo experiment.

Echo Pulse Sequences. In 1950 Irwin Hahn introduced the spin-echo experiment (Figure 1.9).⁶¹ In a typical echo experiment a $\pi/2$ pulse is applied to create transverse

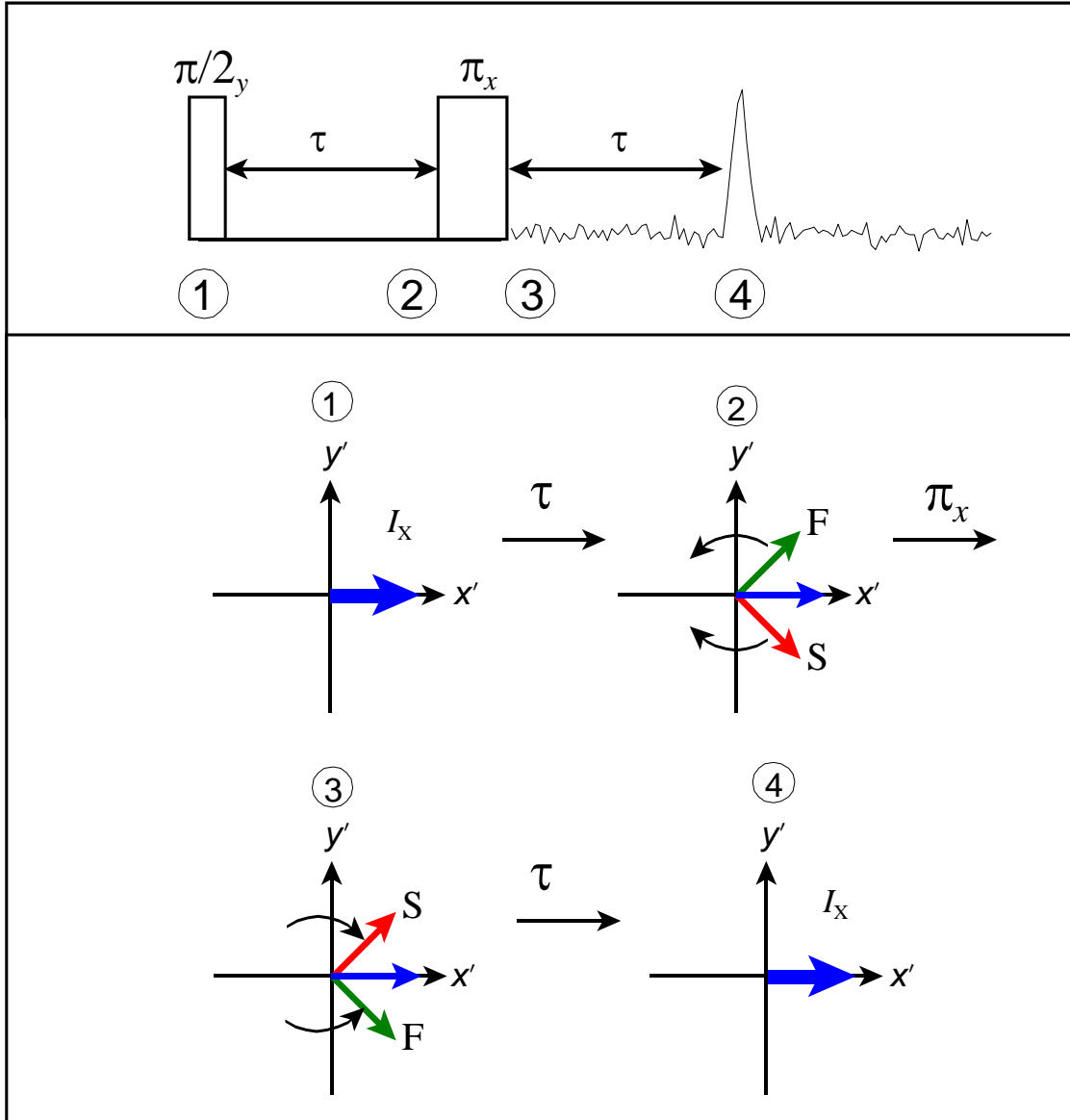


Figure 1.9. A schematic of the spin echo pulse sequence (top) and the vector model which illustrates the refocusing of the spins (bottom). An explanation of the sequence is given in the main text.

magnetization. The $\pi/2$ pulse is followed by an echo dephasing period (τ). During t , vectors representing different offset frequencies are visualized to be precessing about the z -axis (B_0). The precession of a fast component (F, positive transmitter offset), an on resonance frequency (zero offset), and a slow component (S, negative transmitter offset)

of the transverse magnetization in the rotating frame. The second pulse refocuses the initial transverse magnetization and leads to the formation of a spin echo at time τ after refocusing pulse is applied. Echo pulse sequences are normally applied whenever broad lines are encountered as they provide enough recovery time for the probe to record the entire signal.

Shortly after Hahn's description of the spin-echo experiment the Carr-Purcell Meiboom-Gill (CPMG) experiment was introduced as a method to measure T_2 .^{36, 37} Following these initial experiments, the CPMG pulse sequence was frequently employed to measure slow molecular motions and chemical exchange in both solution and liquid-crystal media.⁶²⁻⁷¹ Subsequent applications employed the CPMG sequence for signal enhancement.⁷¹⁻⁷³ In the late 1990's, the phase cycle of the CPMG pulse sequence was modified and the sequence was employed to acquire high signal to noise SSNMR spectra of quadrupolar nuclei.⁷⁴ This modified form of the sequence is termed quadrupolar CPMG (QCPMG).⁷⁴ The QCPMG pulse sequence is similar to a Hahn echo sequence; however a train of π -pulses follows the first spin echo (Figure 1.10). This generates a series of spin echoes and allows one to record multiple spin echoes per scan, leading to a large signal enhancement. The resulting CPMG echo trains can be Fourier transformed to provide a "spikelet" spectrum (Figure 1e). Alternatively, all of the echoes can be summed in the time domain to produce a single spin echo, which is then subsequently Fourier transformed to give a standard echo spectrum. The spikelet spectrum is useful as it focuses intensity into the narrow spikelets and gives rise to higher S/N. The QCPMG sequence is very useful for acquiring SSNMR spectra of broad powder patterns which are

characterized by inherently short T_2^* values and relatively long T_2 values.

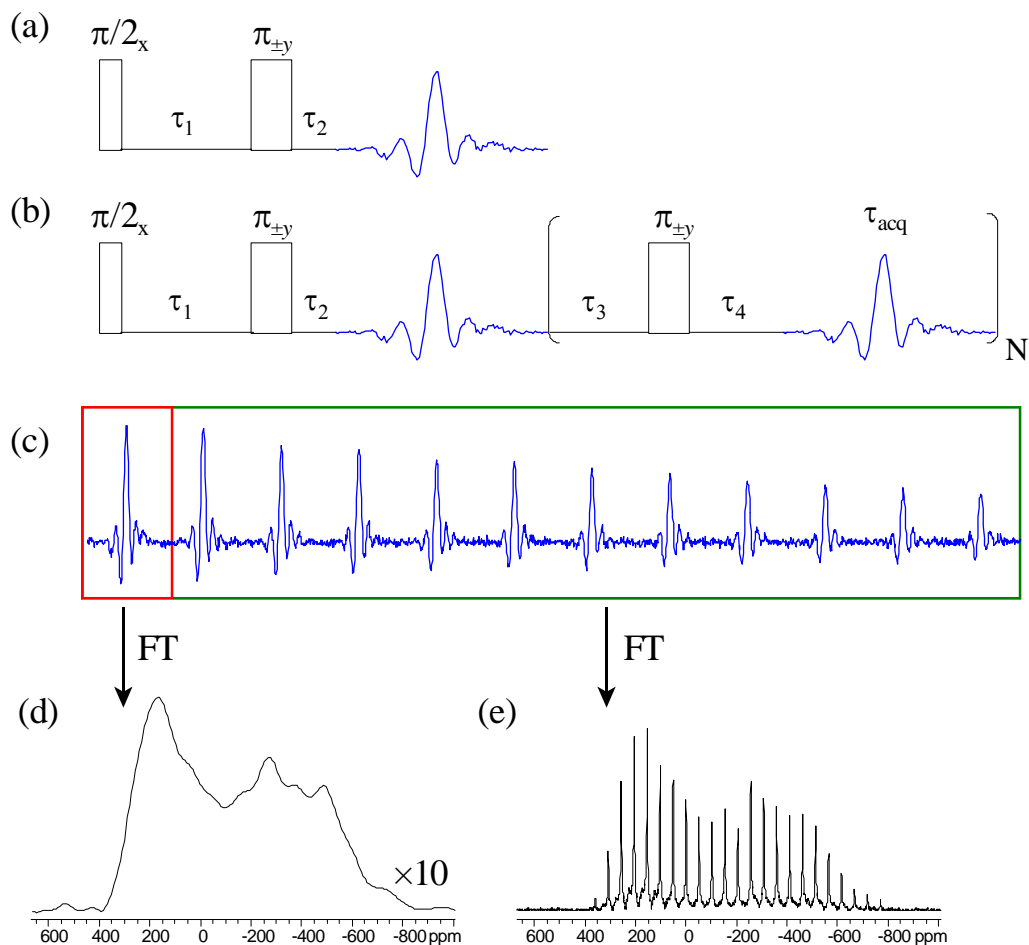


Figure 1.10. (a) Quadrupolar echo pulse sequence. (b) QCPMG pulse sequence. (c) A ^{91}Zr FID obtained with the QCPMG pulse sequence. (d) Fourier transformation of the first spin echo provides a typical spin echo spectrum. (e) Fourier transformation of the entire CPMG echo train gives a spikelet spectrum. The spacing of the spikelets is equal to, τ_{acq}^{-1} , where τ_{acq} is acquisition time of the individual spin echoes.

Recently a modified version of the QCPMG sequence, known as WURST-QCPMG has been developed.^{75, 76} This pulse sequence is similar to the standard QCPMG sequence, however, the sequence employs frequency swept (wideband uniform rate

smooth truncated, WURST) pulses in the place of conventional rectangular pulses. The WURST pulses are applied at a fixed transmitter frequency, with the frequency sweep achieved via simultaneous modulation of the pulse amplitude and phase of the pulses.⁷⁷⁻⁷⁹ The duration of the WURST pulses (*ca.* 50 μ s) is typically much longer than conventional rectangular pulses. The WURST-QCPMG sequence is extremely useful for the acquisition of wideline SSNMR spectra as the superior excitation bandwidths affords a large reduction in the number of sub-spectra which must be acquired. Applications of the WURST-QCPMG sequence are demonstrated in the subsequent chapters of the thesis. In particular, Chapter 9 details the application of WURST pulses for the acquisition of nuclear quadrupole resonance (NQR) spectra.

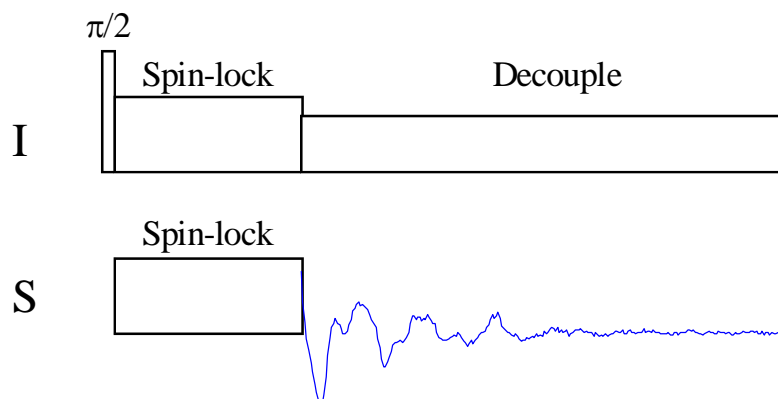


Figure 1.11. The typical pulse sequence employed for cross-polarization experiments. I usually corresponds to a highly abundant high γ nucleus, and S corresponds to nucleus of lower γ . A description of the experiment is given in the text.

Cross-Polarization. Cross-polarization (CP) is routinely employed to enhance the signal to noise of NMR spectra of nuclei which possess low natural abundance and low γ (e.g., ^{13}C , ^{15}N and ^{29}Si). The signal enhancement arises by transferring polarization from highly abundant, high γ nuclei such as ^1H and ^{19}F . The pulse sequence employed for

typical CP experiments is shown in Figure 1.11.⁸⁰⁻⁸² A $\pi/2$ pulse is applied to the abundant nucleus (I), which is then followed by a spin-locking pulse on both I and the unresponsive nucleus (S). The duration of the spin-locking pulse is known as the contact time. The strength of the rf fields applied during the contact time are carefully chosen to fulfill the Hartman-Hahn matching condition, which under static conditions is⁸³:

$$\omega_{1I} = \omega_{1S} \quad (34)$$

If this condition is fulfilled, then there will be an efficient transfer of polarization from the I spins to dipolar coupled S spins. The maximum gain in signal is proportional to the ratio of γ_I/γ_S . The Hartman-Hahn matching condition varies for MAS experiments, and is altered when considering spin pairs involving quadrupolar nuclei.^{83, 84} Additional time savings are realized with CP experiments because the recycle delays depend upon the T_1 of the abundant I spin, which are typically shorter than those of the rare S spin. Recently, CP has been coupled with the CPMG pulse sequence to yield the CP/CPMG sequence.⁸⁵⁻⁸⁸ This pulse sequence combines the signal enhancement characteristics of both sequences, and enables the rapid acquisition of both static wide-line SSNMR spectra of spin-half and quadrupolar nuclei.

1.12 Quantum Chemical Calculations of NMR Tensor Parameters

Quantum chemical calculations have become an increasingly valuable tool in many areas of chemistry. Many different methods and models have been developed for calculating the energy of atoms and molecules, and from most of these methods it is

possible to obtain NMR parameters such as J -couplings, magnetic shielding and electric field gradients. Quantum chemical calculations of NMR properties remains a fertile area of research within the computational chemistry community.⁸⁹⁻⁹⁷ With regards to NMR tensor calculations for solids, the continued development of DFT plane-wave methods capable of performing calculations on periodic structures appears to be very promising.^{98.}⁹⁹ Within this thesis, a variety of computational methods have been employed to calculate NMR tensor parameters. These include ab initio methods (Hartree Fock), hybrid density functional (DFT),¹⁰⁰⁻¹⁰² and pure DFT methods as implemented in the Gaussian 03¹⁰³ and Amsterdam Density Functional Theory (ADF)¹⁰⁴ software packages. The theoretical basis and overviews of these methods are summarized elsewhere.^{89, 105-107}

Calculations of NMR tensor parameters are useful for several reasons: (1) They can be used to generate the orientations of the NMR tensors within molecular frames, providing insight into the origin of the observed anisotropic NMR tensor parameters. (2) They can be used to relate the calculated NMR tensor parameters to the electronic and molecular structures of the complexes. For example, in Chapter 8, the large CSAs that are observed and calculated for a series of lead(II) complexes are related to the presence of stereochemically active electron lone pairs. (3) They can be used to construct models of systems with unknown molecular structures.

SSNMR spectra, in conjunction with calculations of NMR parameters can potentially be used to identify molecular structures. For example, NMR tensor parameters can be calculated for a series of structural models. The experimental NMR tensor parameters can then be compared to the calculated and the most probable

structures can be identified. However, if such an approach is used, it is important to first benchmark the accuracy of computational methods. This can be accomplished by

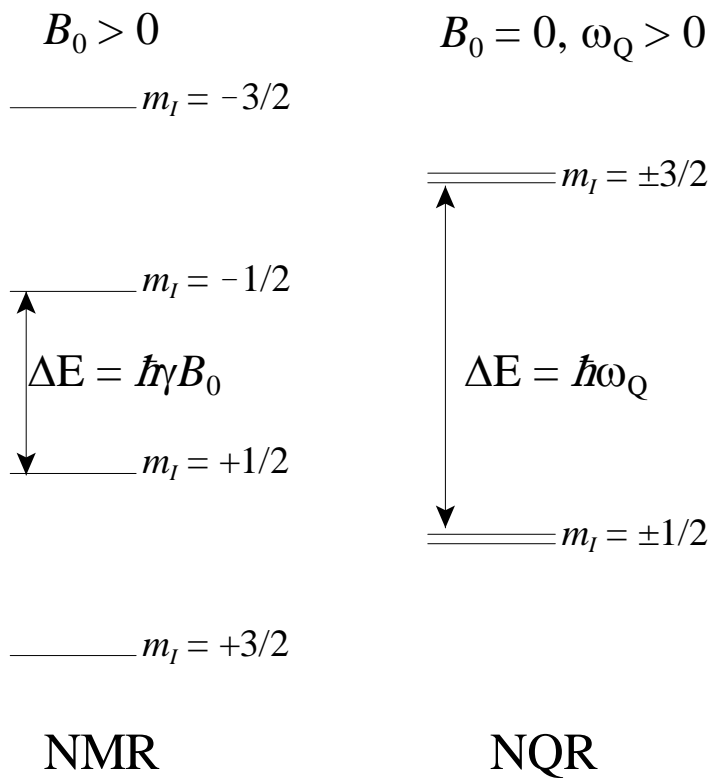


Figure 1.12. Energy of the nuclear spin states in NMR experiments (Zeeman interaction) and NQR experiments ($B_0 = 0$). Note that the $+m$ and $-m$ spin states are degenerate in the absence of a magnetic field.

performing calculations of NMR tensor parameters on crystalline complexes which have been characterized by SSNMR and single-crystal XRD. This approach is extensively demonstrated throughout the thesis.

1.13 Nuclear Quadrupole Resonance

Nuclear quadrupole resonance (NQR) is a technique which is closely associated with NMR. The NQR phenomenon is observed for quadrupolar nuclei in the absence of a magnetic field, and hence is often referred to as “zero-field” NMR.^{49, 108-110} In NQR, the nuclear spin states are quantized by the quadrupolar interaction rather than by a magnetic field (Figure 1.12). Consequently, there are several differences from NMR spectroscopy. The largest component of the electric field gradient (V_{33}) acts as the axis of quantization for the individual nuclear spin-states, resulting in precession of the nuclear spins about V_{33} . Therefore, the NQR frequency is determined entirely by the magnitude of ω_Q , which is related to the magnitude of V_{33} (C_Q) and the value of η_Q . This can be problematic, because C_Q is determined by the symmetry at the nuclear site and can take on values which range from zero MHz to thousands of MHz, depending upon the nucleus in question. Therefore, if one does not have some *a priori* knowledge of the NQR frequency, a great deal of time must be devoted to searching for the resonance frequency. NQR experiments on amorphous or disordered systems are also very challenging. This is because atomic/molecular level disorder gives rise to a range of C_Q values, which in turn gives rise to a range of NQR frequencies and correspondingly broad NQR spectra. Finally, NQR experiments are restricted to solid samples in most cases, because in solution isotropic molecular motion results in an averaging of the quadrupolar interaction.

NQR does have several advantages and complements SSNMR experiments in several ways. For example, if ω_Q is large, broad powder patterns are observed for the SSNMR spectra of quadrupolar nuclei; however, the NQR spectrum consists of a single, relatively sharp resonance. This is because the quantization axis is oriented in the same

direction with respect to the molecular/crystalline frame of each crystallite. Therefore, the NQR frequencies of the individual crystallites do not possess any orientation dependence and sharp resonances are observed. Further, for very large values of C_Q , the NQR frequency is relatively high. This results in more favourable Boltzmann distributions, and correspondingly larger NQR signals. Additional details on NQR experiments are provided in the introduction to Chapter 8.

1.14 Context of Research

In this thesis SSNMR spectroscopy is employed to characterize an array of inorganic complexes and materials. Emphasis is placed upon characterizing materials with applications in catalysis using SSNMR spectroscopy of exotic and unreceptive nuclei. With the increasing availability of high field NMR spectrometers throughout the world and the continued development of pulsed NMR techniques, SSNMR spectroscopy of nearly any unreceptive nucleus is becoming feasible. SSNMR spectra of these nuclei could potentially provide information that is both unique and complementary to that obtained from other techniques. In particular, this approach can be useful for the characterization of heterogeneous catalysts.

There is a lack of previous SSNMR studies in the literature for many of the unreceptive nuclei which could potentially be useful for characterizing heterogeneous catalysts (e.g., ^{35}Cl , $^{47/49}\text{Ti}$, ^{91}Zr). Therefore, it is necessary to investigate well-defined crystalline systems in order to make correlations between molecular structure and the anisotropic NMR interactions measured from the SSNMR spectra. In this regard, systems

which have been previously studied by single-crystal X-ray diffraction are useful, as their atomic coordinates are precisely known. These systems are also ideal for testing the accuracy of quantum chemical calculation methods for calculating NMR tensor parameters. The crystalline systems are also suitable for benchmarking new SSNMR methods and observation strategies prior to investigating complex catalyst systems.

Chapters 2 to 4 focus on the characterization of group IV metallocene complexes, due to their varied applications in homogeneous and heterogeneous catalysis. The acquisition of ^{35}Cl SSNMR spectra of the metallocene complexes is described in Chapter 2, where it is shown that the ^{35}Cl SSNMR spectra are sensitive to molecular structure. On the basis of the observed ^{35}Cl spectra of Cp_2ZrHCl , we are able to prove that the complex possesses a dimeric structure in the solid-state. We have also demonstrated that ^{35}Cl SSNMR spectra of metallocenes can be acquired in a matter of minutes at high magnetic fields (21.1 T).

Chapter 3 focuses on the acquisition of ^{91}Zr SSNMR spectra of zirconocenes. It is demonstrated that the magnitude of C_Q is very sensitive to the local environment of the Zr nucleus and can be utilized to identify the key intermediates involved in the formation of highly active olefin polymerization catalysts. We also demonstrate that wide-line ^{91}Zr SSNMR spectra can be acquired in experiment times on the order of minutes at 21.1 T. Methods suitable for the accurate quantum chemical calculations of ^{91}Zr NMR tensor parameters are also identified. Chapter 4 details the acquisition of $^{47/49}\text{Ti}$ SSNMR spectra of titanocenes. This represents the first example of a molecular system which has been studied by $^{47/49}\text{Ti}$ SSNMR. We demonstrate that it is straightforward to acquire $^{47/49}\text{Ti}$

SSNMR spectra at high magnetic fields with standard echo techniques.

Chapter 5 focuses on the application of ^{45}Sc SSNMR spectroscopy to characterize scandium coordination complexes. Prior to the study presented in Chapter 5, there were very few ^{45}Sc SSNMR studies conducted on well-defined systems. Correlations between the observed ^{45}Sc NMR tensor parameters and molecular symmetry and structure are made. Preliminary investigations of some heterogeneous scandium based catalysts are also shown.

The work in Chapter 6 is an extension of that done in Chapter 5 on the characterization of a polymer supported scandium catalyst. ^{45}Sc SSNMR experiments are employed to investigate the structure of microencapsulated (ME) $\text{Sc}(\text{OTf})_3$. Additional ^1H , ^{19}F and ^{13}C SSNMR and PXRD experiments provide information that is complimentary to that obtained from the ^{45}Sc NMR spectra, allowing for structural models of ME complexes to be proposed.

In Chapter 7, solid-state ^{207}Pb NMR experiments are applied in combination with density functional theory (DFT) calculations to provide insight into the nature of bonding in a series of lead(II) thiolate complexes. The lead NMR experiments reveal some of the largest chemical shift anisotropies (CSA) observed in lead coordination complexes to date. DFT calculations are utilized to demonstrate that the CS tensor is primarily influenced by mixing of occupied MOs localized on the sulfur and lead atoms with virtual MOs largely comprised of lead 6p-orbitals.

In Chapter 8, the application of WURST pulses for the acquisition of NQR spectra is investigated. ^{75}As and ^{35}Cl NQR spectra acquired with the WURST echo sequence are

compared to those acquired with standard echo sequences and echo sequences which employ composite refocusing pulses. The WURST echo sequence is demonstrated to possess superior excitation bandwidths in comparison to the pulse sequences which employ conventional monochromatic rectangular pulses. The utility of WURST pulses for the acquisition of wide-line NQR spectra is also demonstrated by acquiring part of the $^{63/65}\text{Cu}$ NQR spectrum of CuCN.

Finally, Chapter 9 is a preliminary ^{91}Zr SSNMR study of model heterogeneous catalysts. ^{91}Zr SSNMR spectra of zirconocenes immobilized on silica surface have been acquired at natural isotopic abundance with the combination of cryogenic temperatures and high magnetic fields. Quantum chemical calculations are used to construct models of the heterogeneous catalysts and calculate ^{91}Zr NMR tensor parameters.

1.15 Bibliography

- (1) Estermann, I.; Stern, O., *Z. Phys.* **1933**, 85, 17-24.
- (2) Estermann, I.; Frisch, R.; Stern, O., *Nature* **1933**, 132, 169-170.
- (3) Knauer, F.; Stern, O., *Z. Phys.* **1926**, 39, 780-786.
- (4) Gerlach, W.; Stern, O., *Z. Phys.* **1922**, 9, 353-355.
- (5) Gerlach, W.; Stern, O., *Z. Phys.* **1921**, 8, 110-111.
- (6) Rabi, I. I.; Millman, S. P.; Kusch, P.; Zacharias, J. R., *Phys. Rev.* **1939**, 55, 526-535.
- (7) Rabi, I. I., *Phys. Rev.* **1937**, 51, 652-654.
- (8) Rabi, I. I.; Zacharias, J. R.; Millman, S. P.; Kusch, P., *Phys. Rev.* **1937**, 53, 652-654.
- (9) Kellogg, J. M. B.; Rabi, I. I.; Ramsey, N. F.; Zacharias, J. R., **1939**, 56, 728-743.
- (10) Purcell, E. M.; Torrey, H. C.; Pound, R. V., *Phys. Rev.* **1946**, 69, 37-8.
- (11) Purcell, E. M.; Pound, R. V.; Bloembergen, N., *Phys. Rev.* **1946**, 70, 980-987.
- (12) Purcell, E. M.; Bloembergen, N.; Pound, R. V., *Phys. Rev.* **1946**, 70, 988.
- (13) Bloembergen, N.; Purcell, E. M.; Pound, R. V., *Nature* **1947**, 160, 475-6.
- (14) Bloch, F., *Phys. Rev.* **1946**, 70, 460-74.
- (15) Bloch, F.; Hansen, W. W.; Packard, M., *Phys. Rev.* **1946**, 70, 474-85.
- (16) Bloch, F.; Levinthal, E. C.; Packard, M. E., *Phys. Rev.* **1947**, 72, 1125-6.
- (17) Arnold, J. T.; Dharmatti, S. S.; Packard, M. E., *J. Chem. Phys.* **1951**, 507.
- (18) Ernst, R. R.; Anderson, W. A., *Rev. Sci. Instrum.* **1966**, 37, (1), 93-+.
- (19) Aue, W. P.; Bartholdi, E.; Ernst, R. R., *J. Chem. Phys.* **1976**, 64, (5), 2229-2246.
- (20) Jonas, J.; Gutowsky, H. S., *Ann. Rev. Phys. Chem.* **1980**, 31, 1-27.
- (21) Emsley, J. W.; Feeney, J., *Prog. Nucl. Magn. Reson.* **1995**, 28, 1-9.
- (22) Slichter, C. P., *Principles of Magnetic Resonance*. 3rd ed.; New York, 1990.
- (23) Mehring, M., *Principles of High Resolution NMR in Solids*. 2nd ed.; Springer-Verlag: 1983.
- (24) Levitt, M. H., *Spin Dynamics*. Second ed.; John Wiley & Sons: Chichester, 2008.
- (25) Keeler, J., *Understanding NMR Spectroscopy*. John Wiley & Sons: Chichester, 2005.
- (26) Schmidt-Rohr, K.; Spiess, H. W., *Multidimensional Solid-state NMR and Polymers*. Academic Press: San Diego, 1994.

- (27) Fukushima, E.; Roeder, S. B. W., *Experimental Pulse NMR*. Addison-Wesley Publishing Company, Inc.: Reading, 1981.
- (28) Abragam, A.; Goldman, M., *Nuclear Magnetism: order and disorder*. Clarendon Press: Oxford, 1982.
- (29) Fyfe, C. A., *Solid State NMR For Chemists*. C.F.C. Press: Guelph, 1983.
- (30) Duer, M. J., *Introduction to Solid-State NMR Spectroscopy*. Blackwell: Oxford, 2004.
- (31) Mackenzie, K. J. D.; Smith, M. E., *Multinuclear Solid-State NMR of Inorganic Materials*. Pergamon: Oxford, 2002.
- (32) Stejskal, E. O.; Memory, J. D., *High Resolution NMR in the Solid State*. Oxford University Press: New York, 1994.
- (33) Farrar, T. C.; Becher, E. D., *Pulse and FT NMR - Intro to Theory and Methods*. Academic Press: New York, 1971.
- (34) Wasylishen, R. E., NMR Relaxation and Dynamics. In *NMR Spectroscopy Techniques*, Dybowski, C.; Lichter, R. L., Eds. New York, 1987; pp 45-91.
- (35) Bloembergen, N.; Purcell, E. M.; Pound, R. V., *Phys. Rev.* **1948**, 73, (7), 679-712.
- (36) Meiboom, S.; Gill, D., *Rev. Sci. Inst.* **1958**, 29, 688-691.
- (37) Carr, H. Y.; Purcell, E. M., *Phys. Rev.* **1954**, 94, 630-638.
- (38) Proctor, W. G.; Yu, F. C., *Phys. Rev.* **1950**, 77, 717.
- (39) Dickinson, W. C., *Phys. Rev.* **1950**, 77, 736-737.
- (40) Ramsey, N. F., *Phys. Rev.* **1950**, 78, 699-703.
- (41) Ramsey, N. F., *Phys. Rev.* **1951**, 83, 540-1.
- (42) Ramsey, N. F., *Phys. Rev.* **1952**, 86, 243-6.
- (43) Schreckenbach, G.; Ziegler, T., *International Journal of Quantum Chemistry* **1997**, 61, (6), 899-918.
- (44) van Lenthe, E.; Baerends, E. J.; Snijders, J. G., *Journal of Chemical Physics* **1993**, 99, (6), 4597-4610.
- (45) Fukui, H.; Baba, T.; Inomata, H., *Journal of Chemical Physics* **1996**, 105, (8), 3175-3186.

- (46) Wolff, S. K.; Ziegler, T., *Journal of Chemical Physics* **1998**, 109, (3), 895-905.
- (47) Jameson, C. J., *Solid State Nucl. Magn. Reson.* **1998**, 11, (3-4), 265-268.
- (48) Mason, J., *Solid State Nucl. Magn. Reson.* **1993**, 2, (5), 285-288.
- (49) Lucken, E. A. C., *Nuclear Quadrupole Coupling Constants*. Academic Press: London, 1969; p 360.
- (50) Akitt, J. W.; McDonald, W. S., *J. Magn. Reson.* **1984**, 58, (3), 401-412.
- (51) Knop, O.; Palmer, E. M.; Robinson, R. W., *Acta Crystallogr. Sect. A* **1975**, A 31, (JAN1), 19-31.
- (52) Cohen, M. H.; Reif, F., *Solid-State Physics* **1957**, 5, 321.
- (53) Abragam, A., *The Principles of Nuclear Magnetism*. In Clarendon Press: Oxford, 1983; p Chapter VII.
- (54) Power, W. P.; Wasylishen, R. E.; Mooibroek, S.; Pettitt, B. A.; Danchura, W., *J. Phys. Chem.* **1990**, 94, (2), 591-598.
- (55) Cheng, J. T.; Edwards, J. C.; Ellis, P. D., *J. Phys. Chem.* **1990**, 94, (2), 553-561.
- (56) Autschbach, J.; Le Guennic, B., *J. Chem. Educ.* **2007**, 84, 156-171.
- (57) Wasylishen, R. E., In *Encyclopedia of Nuclear Magnetic Resonance*, Grant, D. M.; Harris, R. K., Eds. Wiley, Inc.: Chichester, UK, 1996; pp 1685-1695.
- (58) Andrew, E. R.; Bradbury, A.; Eades, R. G., *Nature* **1958**, 182, 1659.
- (59) Andrew, E. R.; Bradbury, A.; Eades, R. G., *Nature* **1959**, 183, 1802.
- (60) Herzfeld, J.; Berger, A. E., *J. Chem. Phys.* **1980**, 73, 6021-6030.
- (61) Hahn, E. L., *Phys. Rev.* **1950**, 80, 580-594.
- (62) Bloom, M.; Sternin, E., *Biochemistry* **1987**, 26, (8), 2101-2105.
- (63) Allerhan, A.; Gutowsky, H. S., *J. Chem. Phys.* **1965**, 42, (5), 1587-1588.
- (64) Bloom, M.; Reeves, L. W.; Wells, E. J., *J. Chem. Phys.* **1965**, 42, (5), 1615-1616.
- (65) Gutowsky, H. S.; Vold, R. L.; Wells, E. J., *J. Chem. Phys.* **1965**, 43, (11), 4107-4108.
- (66) Allerhan, A.; Thiele, E., *J. Chem. Phys.* **1966**, 45, (3), 902-903.
- (67) Carver, J. P.; Richards, R. E., *J. Magn. Reson.* **1972**, 6, (1), 89-90.
- (68) Jen, J., *J. Magn. Reson.* **1978**, 30, (1), 111-128.

- (69) Lankhorst, D.; Schrieffer, J.; Leyte, J. C., *J. Magn. Reson.* **1983**, 51, (3), 430-437.
- (70) Vega, A. J., *J. Magn. Reson.* **1985**, 65, (2), 252-267.
- (71) Swanson, S.; Ganapathy, S.; Kennedy, S.; Henrichs, P. M.; Bryant, R. G., *J. Magn. Reson.* **1986**, 69, (3), 531-534.
- (72) Cheng, J. T.; Ellis, P. D., *J. Phys. Chem.* **1989**, 93, (6), 2549-2555.
- (73) Garroway, A. N., *J. Magn. Reson.* **1977**, 28, (3), 365-371.
- (74) Larsen, F. H.; Jakobsen, H. J.; Ellis, P. D.; Nielsen, N. C., *J. Phys. Chem. A* **1997**, 101, (46), 8597-8606.
- (75) O'Dell, L. A.; Schurko, R. W., *Chem. Phys. Lett.* **2008**, 464, (1-3), 97-102.
- (76) O'Dell, L. A.; Rossini, A. J.; Schurko, R. W., *Chem. Phys. Lett.* **2009**, 468, (4-6), 330-335.
- (77) Bhattacharyya, R.; Frydman, L., *J. Chem. Phys.* **2007**, 127, (19).
- (78) Tannus, A.; Garwood, M., *NMR Biomed.* **1997**, 10, (8), 423-434.
- (79) Bohlen, J. M.; Rey, M.; Bodenhausen, G., *J. Magn. Reson.* **1989**, 84, (1), 191-197.
- (80) Gibby, M. G., et al., *Chem. Phys. Lett.* **1972**, 17, (1), 80-84.
- (81) Pines, A.; Waugh, J. S.; Gibby, M. G., *Chem. Phys. Lett.* **1972**, 15, (3), 373-374.
- (82) Pines, A.; Waugh, J. S.; Gibby, M. G., *J. Chem. Phys.* **1972**, 56, (4), 1776-1777.
- (83) Hartmann, S. R.; Hahn, E. L., *Phys. Rev.* **1962**, 128, (5), 2042-2053.
- (84) Vega, S., *Phys. Rev. A* **1981**, 23, 3152.
- (85) Hung, I.; Rossini, A. J.; Schurko, R. W., *J. Phys. Chem. A* **2004**, 108, (34), 7112-7120.
- (86) Lipton, A. S.; Sears, J. A.; Ellis, P. D., *J. Magn. Reson.* **2001**, 151, (1), 48-59.
- (87) Lipton, A. S.; Heck, R. W.; Sears, J. A.; Ellis, P. D., *J. Magn. Reson.* **2004**, 168, (1), 66-74.
- (88) Siegel, R.; Nakashima, T. T.; Wasylshen, R. E., *J. Phys. Chem. B* **2004**, 108, (7), 2218-2226.
- (89) Calculation of NMR and EPR Parameters. Eds., Kaupp, M. J.; Buhl, M.; Malkin, V. G., Eds. Wiley: Weinheim, 2004.
- (90) Autschbach, J.; Zheng, S. H.; Schurko, R. W., *Concepts Magn. Reson. Part A* **2010**,

- 36A, (2), 84-126.
- (91) Zurek, E.; Autschbach, J., *Int. J. Quantum Chem.* **2009**, 109, (14), 3343-3367.
- (92) Casabianca, L. B.; De Dios, A. C., *J. Chem. Phys.* **2008**, 128, (5).
- (93) Autschbach, J., *Coord. Chem. Rev.* **2007**, 251, (13-14), 1796-1821.
- (94) Bagno, A.; Saielli, G., *Theor. Chem. Acc.* **2007**, 117, (5-6), 603-619.
- (95) Ziegler, T.; Autschbach, J., *Chem. Rev.* **2005**, 105, (6), 2695-2722.
- (96) Schreckenbach, G.; Ziegler, T., *Theor. Chem. Acc.* **1998**, 99, (2), 71-82.
- (97) Ziegler, T., *Chem. Rev.* **1991**, 91, (5), 651-667.
- (98) Yates, J. R.; Pickard, C. J.; Mauri, F., *Phys. Rev. B* **2007**, 76, (2), 024401-11.
- (99) Pickard, C. J.; Mauri, F., *Phys. Rev. B* **2001**, 63, (24), 245101-13.
- (100) Becke, A. D., *Phys. Rev. A* **1988**, 38, (6), 3098-3100.
- (101) Becke, A. D., *J. Chem. Phys.* **1993**, 98, (7), 5648-5652.
- (102) Lee, C. T.; Yang, W. T.; Parr, R. G., *Phys. Rev. B* **1988**, 37, (2), 785-789.
- (103) Frisch, M. J. et al. *Gaussian 03*, Revision B.03; Gaussian, Inc.: Pittsburgh, PA, 2003.
- (104) Baerends, E. J. et al. *ADF2007*, SCM, Theoretical Chemistry, Vrije Universiteit: Amsterdam.
- (105) Levine, I. N., *Quantum Chemistry*. 5th ed.; Prentice-Hall: Upper Saddle River, NJ, 2000.
- (106) Leach, A. R., *Molecular Modelling, Principles and Application*. Pearson: Harlow UK, 2001.
- (107) McQuarrie, D. A.; Simon, J. D., *Physical Chemistry, A Molecular Approach*. University Science Books: Sausalito, California, 1997.
- (108) Das, T. P.; Hahn, E. L., *Nuclear Quadrupole Resonance Spectroscopy*. Academic Press: New York, 1958; Vol. 1, p 223.
- (109) Drago, R. S., Nuclear Quadrupole Resonance Spectroscopy. In *Physical Methods in Chemistry*, Saunders College Publishing: 1977; pp 510-529.
- (110) Semin, G. K.; Babushkina, T. A.; Yakobson, G. G., *Nuclear Quadrupole Resonance in Chemistry*. John Wiley and Sons: New York, 1975; p 517.

Chapter 2: Solid-State Chlorine NMR of Group IV Transition Metal Organometallic Complexes

2.1 Introduction

The “metallocene revolution” has been used to describe the increased use of transition metal metallocene catalysts in industrial olefin polymerization processes over the last fifteen years.¹⁻⁴ Metallocene catalysts have found use as homogeneous catalysts, which are dissolved in solution and reacted with the olefin, or as heterogeneous catalysts, which are immobilized on a support material and applied in gas or slurry phase processes. The single-site nature of the metallocene catalysts allows for the rational improvement and tuning of the polymerization performance by modification of the surface-supported organometallic species; however, this requires that “the interactions and mechanisms at work on the support surface during the immobilization, activation, and polymerization steps must be understood.”⁴

Solid-state NMR spectroscopy has previously been applied to examine the nature and structure of surface-supported organometallic complexes, as well as their cocatalysts, such as AlMe_3 , methylalumoxane (MAO) and borane complexes.⁵⁻¹⁵ The majority of these studies have utilized solid-state ^1H , ^{13}C and ^{29}Si NMR. Solid-state ^{13}C NMR studies have clearly demonstrated that cyclopentadienyl ligands remain bound to the metal upon immobilization on surfaces, and that metal-bound alkyl ligands may be transferred to Lewis acid sites on alumina and silica supports.^{6-8, 12, 14, 15} While this information provides much insight into the catalytic processes, there are still many uncertainties regarding the exact nature of the metal-surface bond and cocatalyst-metal-surface interactions. For

example, immobilizing the metallocene pre-catalyst onto the support and subsequent activation with cocatalyst often gives different polymers than contacting the support with cocatalyst, followed by immobilization of the metallocene.³

In light of this, and the fact that the organometallic metal centre is believed to be the active catalytic site in most cases, we have been investigating metallocene structure and dynamics from the perspective of solid-state NMR of quadrupolar metal nuclei. Examples of these previous studies include, ⁹¹Zr, ⁹³Nb and ¹³⁹La SSNMR, of metallocene systems that are similar to or commonly used as polymerization pre-catalysts.¹⁶⁻¹⁸ Several solution NMR studies of quadrupolar metal nuclei in transition metal metallocenes have prefaced and inspired our studies.¹⁹⁻²⁴ We have found that the NMR spectra of these half-integer quadrupolar nuclei are responsive to both subtle and dramatic changes in molecular structure, and should serve as excellent probes of metallocene chemistry in homogeneous catalysts and actual heterogeneous catalysts.

Chlorine is frequently found as a ligand in organometallic transition metal complexes, including many of those important in catalytic polymerization processes, and may act as a useful NMR probe. There are two naturally occurring NMR-active nuclei of chlorine, ³⁵Cl and ³⁷Cl, both of which are spin $I = 3/2$ nuclei, and high natural abundance [n.a.(³⁵Cl) = 75.78 % and n.a.(³⁷Cl) = 24.22 %]. They are considered to be low gyromagnetic ratio (“low γ ”) nuclei [$\nu_0(^{35}\text{Cl}) = 39.19$ MHz and $\nu_0(^{37}\text{Cl}) = 32.62$ MHz at 9.4 T] and possess relatively small quadrupole moments [$Q(^{35}\text{Cl}) = -8.165$ fm² and $Q(^{37}\text{Cl}) = -6.435$ fm²].²⁵ The ³⁵Cl nucleus is preferred for most NMR experiments because of its higher receptivity; however, acquisition of ³⁷Cl NMR spectra is sometimes

useful, since ^{35}Cl and ^{37}Cl powder patterns are affected to different extents by anisotropic quadrupolar and chemical shielding parameters, allowing for the measurement of chlorine chemical shielding anisotropy (CSA).

Bryce and Sward have recently presented a thorough review of solid-state NMR of quadrupolar halogen nuclei.²⁶ To date, there are approximately 80 publications featuring solid-state $^{35/37}\text{Cl}$ NMR. Despite the relatively favourable nuclear properties of both chlorine isotopes and the ubiquity of chlorine in many chemical systems, the application of chlorine NMR is usually limited to systems in which chlorine atoms reside in environments of high spherical symmetry. The quadrupolar interaction is greatly reduced in such environments, resulting in small quadrupolar coupling constants ($C_Q = 0.1 - 6.0$ MHz) and correspondingly narrow, easily acquired powder patterns.^{27, 28} There are numerous representative examples of such systems for which ^{35}Cl SSNMR spectra have been acquired, including ionic metal chlorides,²⁹⁻³¹ perchlorates,³² amino acid hydrochlorides,³³⁻³⁶ and HCl pharmaceuticals.³⁷

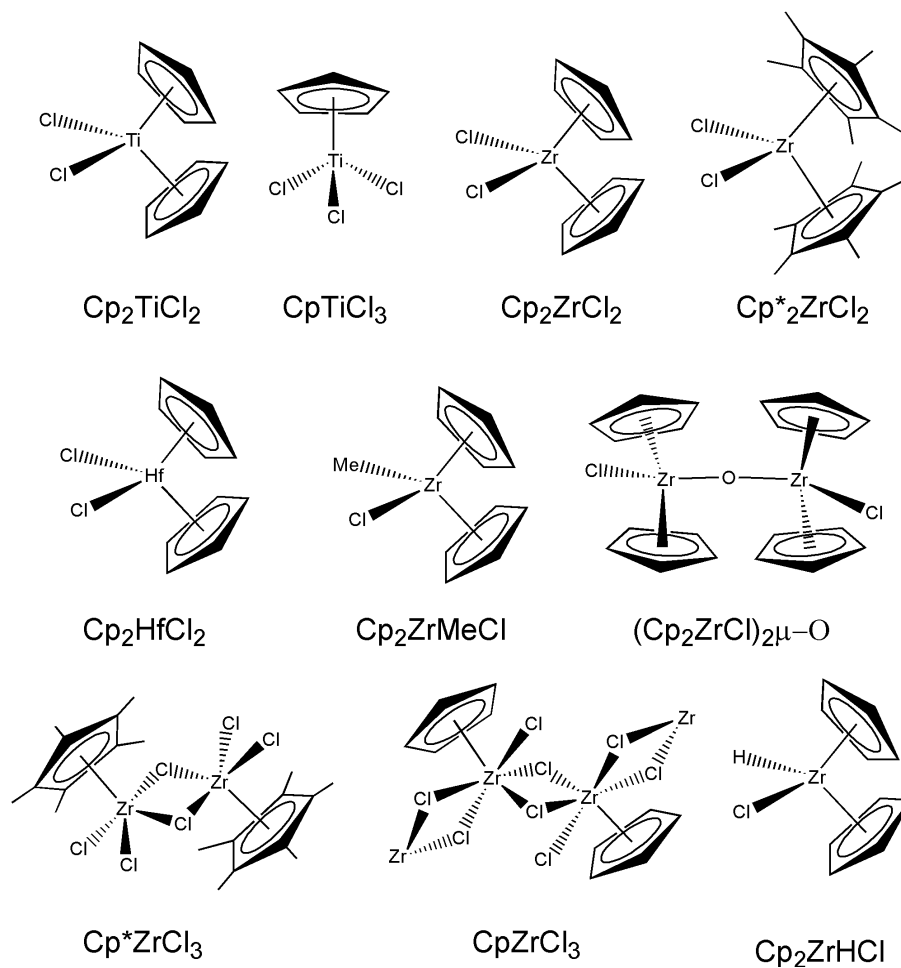
In many systems the chlorine atoms reside in terminal or bridging environments with low spherical symmetry, and the ^{35}Cl nuclei experience correspondingly large quadrupolar interactions. In these cases, second-order quadrupolar broadening can result in powder patterns that are hundreds to thousands of kHz in breadth, complicating spectral acquisition with routine methods. Nuclear quadrupole resonance³⁸ (NQR) is predominantly used for the determination of larger values of $C_Q(^{35}\text{Cl})$, e.g., ca. 10 MHz and larger; however, specialized NQR experiments³⁹⁻⁴¹ must be performed in order to obtain the EFG asymmetry parameter, η_Q , and the chemical shift parameters are only

available from ^{35}Cl NMR experiments. Single-crystal NMR has traditionally been the preferred method for the determination of ^{35}Cl chemical shift (CS) and electric field gradient (EFG) parameters for systems with large $C_Q(^{35}\text{Cl})$ values; however, this method is limited since it relies on the isolation of large single crystals. For example, single-crystal ^{35}Cl NMR spectra of *para*-dichlorobenzene reveal that $C_Q = 73.96$ MHz and $\eta_Q = 0.071$,⁴² corresponding to a central transition powder pattern of more than 10 MHz in breadth at 21.1 T. Many other systems possess chlorine nuclei with more moderate values of C_Q for which SSNMR spectra of powdered samples may be obtained. To date, the largest value of C_Q measured by solid-state ^{35}Cl NMR on a powdered sample is that of aluminum trichloride ($C_Q = 9.4$ MHz),⁴³ which has a ^{35}Cl powder pattern with a breadth of over 250 kHz at 14.1 T. ^{35}Cl quadrupolar parameters for halogenated transition metal metallocenes fall in this intermediate regime. For instance, ^{35}Cl NQR spectra acquired by Bryukhova et al.,^{44, 45} revealed values of C_Q ranging from ca. 16 MHz in CpTiCl_3 to 24 MHz in Cp_2TiCl_2 , corresponding to ^{35}Cl SSNMR powder patterns between ca. 1 to 3 MHz in breadth at moderate magnetic field strengths (e.g., 9.4 T).

The extreme breadths of such ^{35}Cl powder patterns necessitates the use of frequency-stepped NMR techniques,⁴⁶⁻⁵³ where separate spin-echoes are acquired at evenly spaced transmitter frequencies. The total spectrum is then formed either by plotting the echo intensities as a function of transmitter frequency,^{46, 48, 49, 51} or by Fourier transforming the spin echoes and co-adding/projecting the sub-spectra.^{47, 50, 52, 53} While this methodology is successful for acquiring broad powder patterns, the inherently low signal to noise of broadened NMR spectra leads to lengthy experimental times. Recently,

the Carr-Purcell Meiboom-Gill (CPMG) sequence^{54, 55} has been re-introduced as a method for the signal enhancement of NMR spectra of quadrupolar nuclei (the QCPMG sequence).⁵⁶⁻⁶⁰ The combination of the QCPMG pulse sequence and frequency-stepped techniques is especially useful for the rapid acquisition of extremely broad powder patterns.^{16, 18, 50, 61-63}

The current work involves three major facets. First, we demonstrate the application of ultra-wideline QCPMG (UW-QCPMG) for the rapid acquisition of solid-state ³⁵Cl NMR spectra of early transition metal organometallic compounds (Scheme 2.1) moderate (9.4 T) and high magnetic fields (21.1 T). Second, the origin of the observed ³⁵Cl NMR parameters are examined with quantum chemical methods, including Hartree-Fock (HF) and density functional theory (DFT). For the first time, the contributions of individual occupied MOs to the EFG tensors are analysed within a natural localized molecular orbital (NLMO) framework. Differences in the metal first-coordination sphere (e.g., Cp₂ZrCl₂ vs. Cp₂ZrMeCl) and the profound impact on the observed ³⁵Cl NMR parameters are discussed in detail. Finally, application of our methodology (i.e, the combination of wideline ³⁵Cl SSNMR and quantum chemical calculations) is demonstrated in the characterization of an important organometallic reagent, Cp₂ZrHCl (Schwartz's reagent), whose solid-state structure is hitherto unknown.



Scheme 2.1. Organometallic complexes for which solid-state ^{35}Cl NMR spectra have been acquired. The complexes are: bis(cyclopentadienyl)titanium dichloride (Cp_2TiCl_2), cyclopentadienyltitanium trichloride (CpTiCl_3), bis(cyclopentadienyl)zirconium dichloride (Cp_2ZrCl_2), bis(pentamethylcyclopentadienyl)zirconium dichloride ($\text{Cp}^*_2\text{ZrCl}_2$), bis(cyclopentadienyl)hafnium dichloride (Cp_2HfCl_2), methylbis(cyclopentadienyl)zirconium chloride (Cp_2ZrMeCl), Oxobis[bis(cyclopentadienyl)zirconium chloride] [$(\text{Cp}_2\text{ZrCl})_2\mu\text{-O}$], pentamethylcyclopentadienylzirconium trichloride (Cp^*ZrCl_3), cyclopentadienylzirconium trichloride (CpZrCl_3) and bis(cyclopentadienyl)zirconium chloride hydride (Cp_2ZrHCl , Schwartz's reagent).

2.2 Experimental

Sample Preparation. Samples of Cp_2TiCl_2 , CpTiCl_3 , Cp_2ZrCl_2 , $\text{Cp}_2^*\text{ZrCl}_2$, Cp_2ZrHCl and Cp^*ZrCl_3 were obtained from Strem Chemicals Inc. Samples of Cp_2HfCl_2 and CpZrCl_3 were obtained from Sigma-Aldrich. All commercially obtained samples were used without purification. $(\text{Cp}_2\text{ZrCl})_2\mu\text{-O}$ was synthesized according to published procedures.⁶⁴ Cp_2ZrMeCl was obtained from the synthesised sample of $(\text{Cp}_2\text{ZrCl})_2\mu\text{-O}$ by the previously published method.⁶⁵ The bulk purity of $(\text{Cp}_2\text{ZrCl})_2\mu\text{-O}$ and Cp_2ZrMeCl was confirmed by powder X-ray diffraction. All samples were handled in a nitrogen atmosphere glovebox, except for Cp_2HfCl_2 , CpZrCl_3 and $(\text{Cp}_2\text{ZrCl})_2\mu\text{-O}$ which were handled in an argon filled glove bag.

Solid-state NMR. Solid-state ^{35}Cl NMR spectra were acquired on a wide-bore Oxford 9.4 T magnet [$\nu_0(^1\text{H}) = 400$ MHz, $\nu_0(^{35}\text{Cl}) = 39.16$ MHz] with a Varian Infinity Plus console running Spinsight software. High field ^{35}Cl NMR spectra were acquired on a standard-bore 21.15 T magnet [$\nu_0(^1\text{H}) = 900$ MHz, $\nu_0(^{35}\text{Cl}) = 88.2$ MHz] with a Bruker Avance II console running TopSpin software. ^{35}Cl NMR experiments at 9.4 T were acquired with a Varian/Chemagnetics 5 mm HX static probe. Experiments at 21.1 T were conducted on a home-built single channel 5 mm probe. All samples were finely ground, packed into filed 5 mm glass NMR tubes, capped and sealed with parafilm. ^{35}Cl chemical shifts were reported with respect to an infinitely dilute solution of $\text{NaCl}(\text{aq})$ ($\delta_{\text{iso}} = 0.0$ ppm) by the use of a secondary standard of $\text{NaCl}(\text{s})$ for which $\delta_{\text{iso}} = -45.37$ ppm.³³ Pulse calibrations were performed on a saturated solution of $\text{NaCl}(\text{aq})$ and central-transition selective $\pi/2$ pulse widths were calculated by scaling the solution pulse widths by a factor

of a half, i.e. $(I + 1/2)^{-1}$. The QCPMG pulse sequence of the form $\{\pi/2 - [\tau - \pi - \tau - \text{acquire}]_N\}$ was used for the acquisition of ^{35}Cl NMR spectra.⁵⁶ The number of refocusing π pulses varied from 20 to 162 depending upon the sample (Tables A1 and A2). All spectra were processed on a personal computer with the Nuts program from Acorn Software. The FIDs of sub-spectra were left-shifted where necessary, apodized using a Gaussian function of less than 100 Hz, digitally filtered to remove frequencies outside of 200 kHz, Fourier transformed and magnitude calculated. The individual sub-spectra were then co-added to form the total pattern. Curved baselines are visible in some spectra and are apparent when relatively low signal to noise sub-spectra are co-added to generate total NMR spectra. The curved baselines will not affect the positions of discontinuities, and hence, will not affect the NMR parameters extracted from simulations. Analytical simulations of solid-state ^{35}Cl NMR spectra were performed using the WSolids computer program.⁶⁶

Quantum chemical Calculations. Calculations of CS and EFG tensors were performed using Gaussian 03.⁶⁷ Molecular coordinates were input from structures determined by single-crystal X-ray diffraction experiments and proton positions were geometry-optimized. Calculations were carried out using restricted Hartree-Fock (RHF) and hybrid density functional theory (DFT) employing the hybrid B3LYP functional.⁶⁸ The Dunning type basis sets indicated in the text were utilized for Cl.^{69,70} The 6-311G** basis set was employed for Ti, C, H, and O. The Zr-5F3 basis set of Huzinaga was employed for Zr.⁷¹ The LANL2DZ electron core potential (ECP) basis set of Hay and Wadt was employed on Hf for calculations on Cp_2HfCl_2 .^{72,73} CS tensors were calculated

using the gauge-including atomic orbitals (GIAO) method.^{74, 75} HCl was chosen as a chemical shielding standard and calculated chemical shieldings were converted to shifts as described in Table 2.3.⁷⁶ The natural localized molecular orbital (NLMO) EFG analysis were performed with the Amsterdam Density Functional (ADF) program.⁷⁷⁻⁷⁹ ADF calculations utilized the B3LYP functional with all-electron doubly-polarized triple- ζ basis sets on all atoms.

X-ray Diffraction Experiments. Details on single crystal X-ray diffraction experiments are provided in the original publication.⁸⁰ Samples for powder X-ray diffraction were placed into 1.0 mm glass capillary tubes and flame sealed. Powder X-ray diffraction patterns were collected using a Bruker AXS HI-STAR system using a General Area Detector Diffractions System. The X-ray source was Cu K α radiation (1.540598 Å) and an area detector using a 2θ range between 4.0° to 65.0° was employed. Powder X-ray diffraction patterns were simulated with the Powder Cell software package.⁸¹

2.3 Results and Discussion

Solid-state ³⁵Cl NMR spectroscopy. Before the individual complexes are discussed, there are some common features of the ³⁵Cl NMR spectra that should be addressed. First, very broad powder patterns are observed for all of the complexes at 9.4 T (Figures 2.1-2.3) and 21.1 T (Figure 2.4), with minimum breadths of 1 MHz and 500 kHz, respectively. Second, given the breadth of the ³⁵Cl powder patterns, chemically similar (e.g., comparable bond lengths, angles, etc.) but crystallographically distinct chlorine sites cannot be resolved in the ³⁵Cl NMR spectra, meaning that the spectra

essentially correspond to those of single chlorine sites, and their simulations represent average values of the NMR parameters. However, it is possible to resolve chlorine sites in different bonding environments (e.g., bridging and terminal chlorine sites in CpZrCl_3 , *vide infra*). Third, despite the large breadths of the ^{35}Cl static powder patterns, which range from ca. 1.0 to 2.5 MHz at 9.4 T, the spectra can be acquired in a piece-wise manner with the QCPMG pulse sequence within a reasonable time frame (e.g., 1.6 hours to 28 hours). This is due to the generally long ^{35}Cl transverse relaxation time constants (T_2) which permit the acquisition of long echo trains. Finally, once the total patterns have been formed by co-addition of the sub-spectra, analytical simulations provide values of C_Q , η_Q and δ_{iso} (Table 2.1). The effects of chlorine chemical shielding anisotropy (CSA) are negligible at 9.4 T (Figure A1), but can be detected at 21.1 T, to yield the span, Ω , and skew, κ , of the chemical shift tensor. The positions of the discontinuities are crucial for accurately determining the quadrupolar parameters, which dominate the broad second-order central transitions, while the chemical shielding parameters are somewhat less influential. Variations in intensity across these patterns can arise from a variety of sources, including small CSA contributions, interference from satellite transitions, overlap of resonances from similar but magnetically distinct chlorine sites, heteronuclear dipolar interactions, and so forth.

Cp₂MCl₂ Series. All of the group IV Cp_2MCl_2 (M = Ti, Zr or Hf) single crystal X-ray structures contain two distinct molecules in the asymmetric unit, with four crystallographically and magnetically distinct chlorine sites.⁸²⁻⁸⁴ The M-Cl bond lengths and Cl-M-X bond angles are similar for all chlorine sites, which results in powder

patterns that essentially correspond to that of a single site for each complex. Quantum chemical calculations (*vide infra*) and NQR spectra acquired by Bryukhova et al. confirm this for the Cp_2MCl_2 series.⁴⁵

The solid-state ^{35}Cl NMR spectrum of Cp_2TiCl_2 consists of a second-order powder pattern that is ca. 2.5 MHz wide (Figure 2.1). Several distinct discontinuities are visible in the experimental spectrum and all are readily reproduced by the analytical simulation, yielding $C_Q = 22.1$ MHz, $\eta_Q = 0.61$ and $\delta_{\text{iso}} = 500$ ppm (Table 2.1). Given the magnitude of the quadrupolar interaction, the error in the measured value of δ_{iso} is large at 9.4 T.

The ^{35}Cl NMR spectrum of Cp_2ZrCl_2 is best simulated with $C_Q = 16.0$ MHz, $\eta_Q = 0.72$ and $\delta_{\text{iso}} = 300$ ppm. ^{35}Cl and ^{91}Zr satellite transitions are visible at the low frequency end (right side) of the powder pattern. The spectrum of Cp_2HfCl_2 is simulated with $C_Q = 17.1$ MHz, $\eta_Q = 0.65$ and $\delta_{\text{iso}} = 400$ ppm. The breadth of the ^{35}Cl powder patterns of Cp_2ZrCl_2 and Cp_2HfCl_2 (~1.6 MHz) are drastically reduced in comparison to that of Cp_2TiCl_2 . The total spectrum of Cp_2ZrCl_2 was acquired in 1.6 hours at 9.4 T because of the combination of a favourable T_2 and relatively narrow powder pattern width.

Within the Cp_2MCl_2 series there are several trends evident in the ^{35}Cl NMR parameters. The values of C_Q observed for Cp_2ZrCl_2 and Cp_2HfCl_2 are much smaller than that observed for Cp_2TiCl_2 . Increases in the average M-Cl bond lengths of Cp_2ZrCl_2 (2.45 Å)⁸² and Cp_2HfCl_2 (2.42 Å)⁸³ as compared to the average Ti-Cl bond lengths (2.37 Å) of

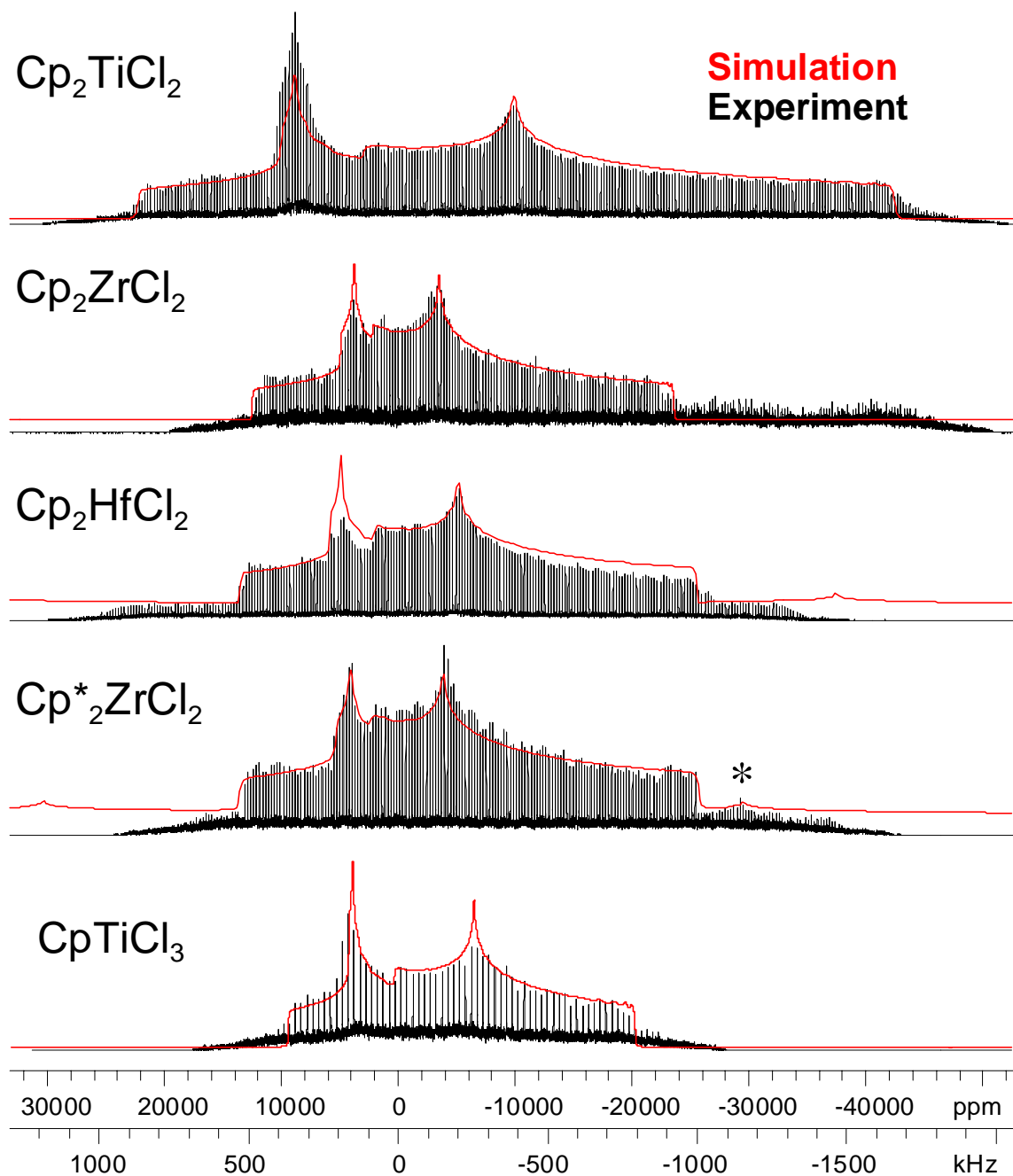


Figure 2.1. Solid-state ^{35}Cl QCPMG NMR spectra and analytical simulations (solid trace) of the spectra of Cp_2TiCl_2 , Cp_2ZrCl_2 , Cp_2HfCl_2 , $\text{Cp}^*_2\text{ZrCl}_2$ and CpTiCl_3 . Satellite transitions are visible in the spectra of Cp_2ZrCl_2 , $\text{Cp}^*_2\text{ZrCl}_2$ and Cp_2HfCl_2 and have been included in simulations of the spectra of $\text{Cp}_2^*\text{ZrCl}_2$ and Cp_2HfCl_2 in order to improve the quality of the fits. The asterisk in the spectrum of $\text{Cp}^*_2\text{ZrCl}_2$ denotes a discontinuity of a satellite transition.

Cp_2TiCl_2 are expected to lead to reductions in the largest component of the EFG tensor, V_{33} , however, the deformation of core and valence atomic orbitals by covalent bonding interactions must also be considered.³⁸ Relationships between M-Cl bonding and V_{33} are addressed in the theoretical section.

Table 2.1. A Summary of Observed ^{35}Cl EFG Tensor Parameters

Compound	C_Q (MHz) ^a	η_Q ^b	δ_{iso} (ppm) ^c
Cp_2TiCl_2	22.1(5) ^d	0.61(3)	500(500)
Cp_2ZrCl_2	16.0(5)	0.72(4)	300(150)
Cp_2HfCl_2	17.1(4)	0.65(5)	400(500)
$\text{Cp}^*_2\text{ZrCl}_2$	16.7(4)	0.73(3)	400(400)
CpTiCl_3	15.5(4)	0.54(5)	500(150)
Cp_2ZrMeCl	13.7(4)	0.75(10)	400(400)
$(\text{Cp}_2\text{ZrCl})_2\mu\text{-O}$	16.3(4)	0.43(7)	300(400)
Cp^*ZrCl_3 [site 1]	12.8(5)	0.10(10)	400(200)
Cp^*ZrCl_3 [site 2]	13.3(5)	0.12(10)	400(200)
Cp^*ZrCl_3 [site 3]	14.6(5)	0.88(10)	200(200)
Cp^*ZrCl_3 [site 4]	14.0(5)	0.80(10)	200(200)
CpZrCl_3 [multiple sites] ^e	14.8 - 18.6	0.7 - 0.8	300
Cp_2ZrHCl	19.7(3)	0.20(4)	80(50)

^a $C_Q = eQV_{33}/h$, ^b $\eta_Q = (V_{11} - V_{22})/V_{33}$, ^c $\delta_{\text{iso}} = (\delta_{11} + \delta_{22} + \delta_{33})/3$. ^dThe uncertainty in the last digit(s) of each value is denoted in brackets. ^eDetails are given in the text.

The value of C_Q for Cp_2TiCl_2 is the largest observed in this series of complexes, and corresponds to a regime where the quadrupolar interaction is approaching the magnitude of the Zeeman interaction. However, the analytical simulations produced by the WSolids computer program are based on the high-field approximation, where the

Larmor frequency (ν_0) is assumed to be an order of magnitude larger than (ν_Q) quadrupolar frequency, allowing the latter to be treated as a perturbation on the former. Of course, this raises questions about the validity of the simulations. Fortunately, ν_Q has been measured for this complex and others via NQR.^{44,45} The value of ν_Q is related to C_Q for an $I = 3/2$ nucleus by:

$$C_Q = \frac{2\nu_Q}{\sqrt{1 + \frac{\eta_Q^2}{3}}} \quad (1)$$

In all cases the experimentally determined values of C_Q are within experimental error of the values predicted from NQR spectra (Table 2.2).⁸⁵

Table 2.2. Values of C_Q Calculated from ³⁵Cl NQR Data

Compound	Range of ν_Q values (MHz) ^a	Average ν_Q (MHz) ^a	Average NQR C_Q (MHz) ^b	NMR C_Q (MHz)
Cp ₂ TiCl ₂	11.787 - 12.090	11.91	22.46	22.1(5)
CpTiCl ₃	7.970 and 7.984	7.97	15.28	15.5(4)
Cp ₂ ZrCl ₂	8.558 - 8.756	8.68	16.04	16.0(5)
Cp ₂ MoCl ₂	16.875 - 17.273	17.13	32.92	-
Cp ₂ WCl ₂	17.723 - 18.063	17.84	34.28	-

^a Taken from refs 44 and 45. NQR measurements for Cp₂TiCl₂, Cp₂ZrCl₂ and CpTiCl₃ were conducted at 293.5 K. An average of the values of ν_Q for crystallographically distinct sites has been used to calculate the NQR C_Q . ^b Calculated using equation 1 with values of ν_Q taken from NQR experiments and values of η_Q from NMR experiments.

Cp^{*}₂ZrCl₂. Analytical simulation of the ³⁵Cl NMR spectrum of Cp^{*}₂ZrCl₂ yields $C_Q = 16.7$ MHz, $\eta_Q = 0.73$ and $\delta_{iso} = 400$ ppm. The fit of the spectrum was aided by the detection of a discontinuity in the satellite transition on the low frequency side of the

powder pattern. The single crystal X-ray structure reveals Zr-Cl bond lengths (2.46 Å) similar to those of Cp_2ZrCl_2 , and correspondingly similar ^{35}Cl NMR parameters are observed.⁸⁶ There is a slight difference in the values of C_Q , suggesting that ^{35}Cl NMR may be able to detect differences in the Cp ligand framework.

CpTiCl₃. Simulation of the ^{35}Cl NMR spectra of CpTiCl_3 (Figure 2.1) yields $C_Q = 15.5$ MHz, $\eta_Q = 0.54$ and $\delta_{\text{iso}} = 500$ ppm. The values of C_Q and η_Q are significantly different than those obtained for Cp_2TiCl_2 , demonstrating the sensitivity of ^{35}Cl NMR parameters to differences in the first coordination sphere of the metal. It should also be recognized that the signal to noise ratio of the ^{35}Cl NMR spectrum of CpTiCl_3 is much lower than that of Cp_2TiCl_2 due to a much shorter T_2 in the former, which results in a shorter echo train and acquisition of fewer echoes.

The previously reported ^{35}Cl NQR spectra of CpTiCl_3 display two distinct quadrupolar frequencies,⁴⁴ inconsistent with the single crystal X-ray structure reported by Engelhardt et al.,⁸⁷ which identifies three magnetically and crystallographically distinct chlorine sites. We have reported a newly refined structure which possesses two distinct Cl sites, in agreement with the NQR data.⁸⁰ The new single-crystal X-ray structure reveals Ti-Cl bond lengths (2.22 Å) that are 0.15 Å shorter (on average) than those observed for Cp_2TiCl_2 (2.37 Å).

In a purely electrostatic (ionic) model, shorter Ti-Cl bond lengths would lead to larger C_Q values; V_{33} is proportional to the cube of the interatomic distance(s) ($1/r^3$) under the point charge approximation.³⁸ However, the value of C_Q observed for CpTiCl_3 is significantly smaller than that of Cp_2TiCl_2 . The difference between values of C_Q in these

two species must therefore arise from differences in Ti-Cl covalent bonding. In this light, Bryukhova has previously ascribed the lower C_Q in CpTiCl_3 to increased Ti-Cl π -bonding in comparison to Cp_2TiCl_2 .^{44,45} This hypothesis is further discussed in the quantum chemical calculations section.

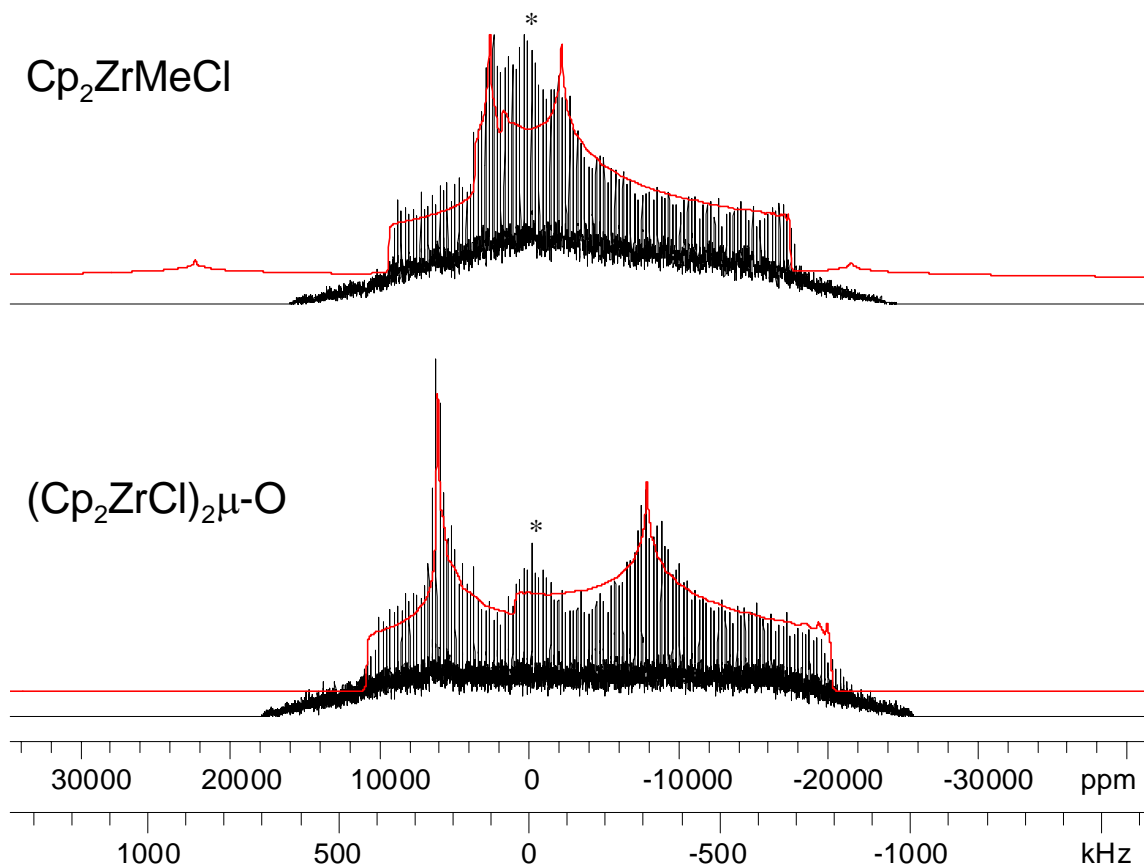


Figure 2.2. Solid-state ^{35}Cl QCPMG NMR spectra and analytical simulations (solid trace) of the spectra of Cp_2ZrMeCl and $(\text{Cp}_2\text{ZrCl})_2\mu\text{-O}$. The simulation of the spectrum of $(\text{Cp}_2\text{ZrCl})_2\mu\text{-O}$ includes the satellite transitions. A minor impurity (marked with an asterisk), which is most likely aniline hydrochloride, is visible in the central region of both spectra.

Cp₂ZrMeCl. It has been proposed that the alkylation of an organometallic complex by an activator or cocatalyst increases the activity of surface-supported

organometallic species.^{3,4} Solid-state ^{35}Cl NMR may be useful to monitor the abstraction of chloride ligands by cocatalysts and quantify the amounts of chlorinated metallocene centres remaining after activation. Analytical simulations reveal $C_Q = 13.7$ MHz, $\eta_Q = 0.75$ and $\delta_{\text{iso}} = 400$ ppm (Figure 2.2). This complex possesses the smallest value of C_Q observed in this series of complexes. Cp_2ZrMeCl has a lower C_Q than Cp_2ZrCl_2 , likely due to changes in the Zr-Cl bond lengths induced by the presence of the methyl ligand (i.e., 2.49 Å and 2.45 Å, respectively).⁸⁸ It should be noted that a minor impurity is visible, resulting in a relatively poor fit of the central part of the pattern. This impurity signal is most likely due to a small amount of aniline hydrochloride which was formed in the synthesis of the compound.

$(\text{Cp}_2\text{ZrCl})_2\mu\text{-O}$. The oxo-bridged complex $(\text{Cp}_2\text{ZrCl})_2\mu\text{-O}$ is a synthetic precursor to Cp_2ZrMeCl and is the product of the hydrolysis of Cp_2ZrMeCl .⁶⁵ The ^{35}Cl NMR parameters obtained from the spectrum are $C_Q = 16.3$ MHz, $\eta_Q = 0.43$ and $\delta_{\text{iso}} = 300$ ppm. The observed value of η_Q is significantly lower than those observed for the other zirconium complexes. A minor amount of impurity is visible in the spectrum (*vide supra*).

Cp^*ZrCl_3 . Cp^*ZrCl_3 is a dimer with three magnetically distinct chlorine sites in its crystal structure.⁸⁹ Two of the chlorine atoms are terminally bound to Zr and the third site bridges adjacent Zr centres. The spectrum of Cp^*ZrCl_3 is distinct from those of the previous complexes (Figure 2.3). Specifically, the central discontinuities of the powder pattern are not readily observable and ‘shoulders’ are apparent at the edges of the

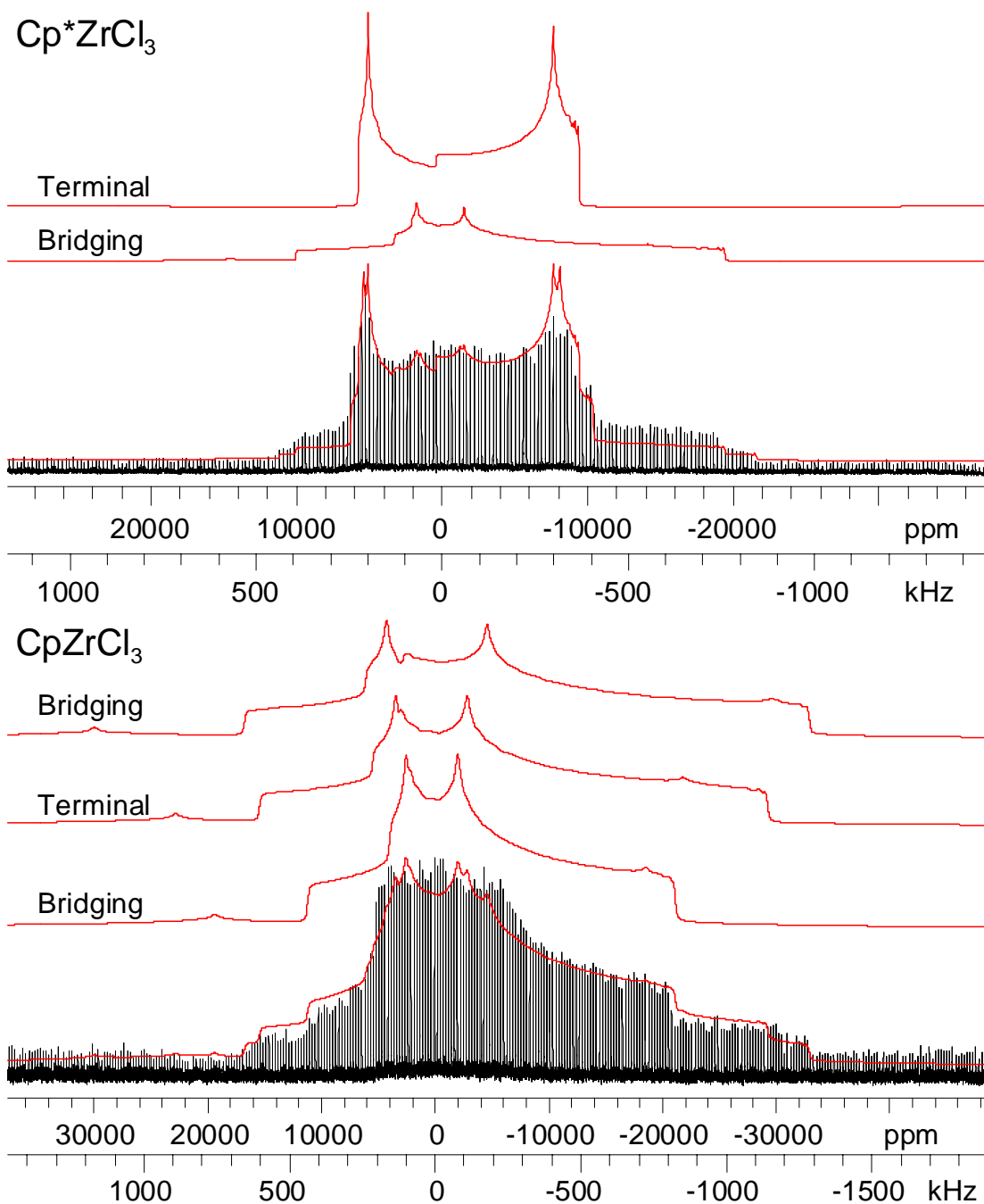


Figure 2.3. Solid-state ^{35}Cl QCPMG NMR spectra and analytical simulations (solid trace) of the spectra of Cp^*ZrCl_3 , CpZrCl_3 . Satellite transitions are visible in the spectra of both complexes. The simulation of the Cp^*ZrCl_3 spectrum utilizes four sites (two bridging and two terminal); representative simulations of bridging and terminal sites are shown (see Figure A2 for all simulations).

spectrum. An accurate simulation of the experimental spectrum is more difficult to obtain and larger uncertainties are associated with the NMR parameters, because the observed powder pattern corresponds to both bridging and terminal chlorine sites. The general features of the spectrum can be reproduced by a simple simulation which employs high- and low- η_Q powder patterns in a 1:2 intensity ratio, both of which possess similar values of C_Q (Figure A2), however, in order to properly account for the shoulders a four site simulation must be used (two bridging and two terminal sites with 1:2 intensity ratios). The inclusion of an additional bridging site (with an η_Q value near 1) disagrees with the current crystal structure, but it is required to reproduce the shoulder features of the spectrum. The ratio of intensities suggests that the low η_Q pattern corresponds to the terminal chloride ligands and quantum chemical calculations confirm this (*vide infra*). The NMR parameters obtained for both Cp^*ZrCl_3 and $(\text{Cp}_2\text{ZrCl})_2\mu\text{-O}$ suggests that the observation of lower values of η_Q may be used to identify the terminal chloride ligands of dimers (this information is absent from standard NQR experiments). It is also interesting to note the extremely high values of η_Q observed for the bridging ligands of the complex.

CpZrCl₃. CpZrCl_3 is a coordination polymer in the solid-state.⁸⁷ The crystal structure reveals three magnetically distinct chlorine sites, with bridging and terminal chloride ligands present in a 2:1 ratio. The ^{35}Cl NMR spectrum is relatively broad and lacks central discontinuities; however, several shoulders are visible at the sides of the spectrum (Figure 2.3). The number of magnetically distinct sites and lack of features make it difficult, if not impossible, to determine the NMR parameters of the individual sites. However, the appearance of the spectrum is clearly distinct from those of the

complexes which possess only terminal chlorine ligands, and despite its complexity, can be utilized to differentiate between monomeric and oligomeric metallocene species. Quantum chemical calculations of ^{35}Cl EFG tensors (*vide infra*) can be used to provide parameters which adequately reproduce the experimental spectrum, though there is some disagreement in the positions of the discontinuities of the experimental and simulated spectra.

Solid-State ^{35}Cl NMR spectra acquired at 21.1 T. It is expected that the use of high magnetic fields will be very beneficial for ^{35}Cl NMR for two reasons: first, the signal to noise of an NMR experiment is proportional to the square of the magnetic field (B_0^2), greatly reducing the time required to acquire each sub-spectrum; and second, the breadths of the ^{35}Cl powder patterns will be inversely proportional to B_0 , greatly reducing the number of sub-spectra which must be acquired. The ^{35}Cl NMR spectra of CpTiCl_3 , Cp_2ZrCl_2 and Cp^*ZrCl_3 at 21.1 T are shown in Figure 2.4. The QCPMG spectra of CpTiCl_3 and Cp_2ZrCl_2 were acquired in 13 and 7 minutes, respectively, at 21.1 T, as compared to 11 and 1.6 hours at 9.4 T.

The breadths of the ^{35}Cl powder patterns acquired at 21.1 T are reduced to approximately half of the breadths of the corresponding spectra acquired at 9.4 T, consistent with powder patterns dominated by the second-order quadrupolar interaction; however, if spectra are simulated without accounting for chlorine CSA, a relatively poor fit is obtained (dashed trace, Figure 2.4). Simulations of the ^{35}Cl SSNMR spectra from 21.1 T which include the CS tensor parameters, Ω and κ , and the Euler angles, α , β and γ , which describe the relative orientations of the CS and EFG tensors⁹⁰ (Table 2. 3) result in

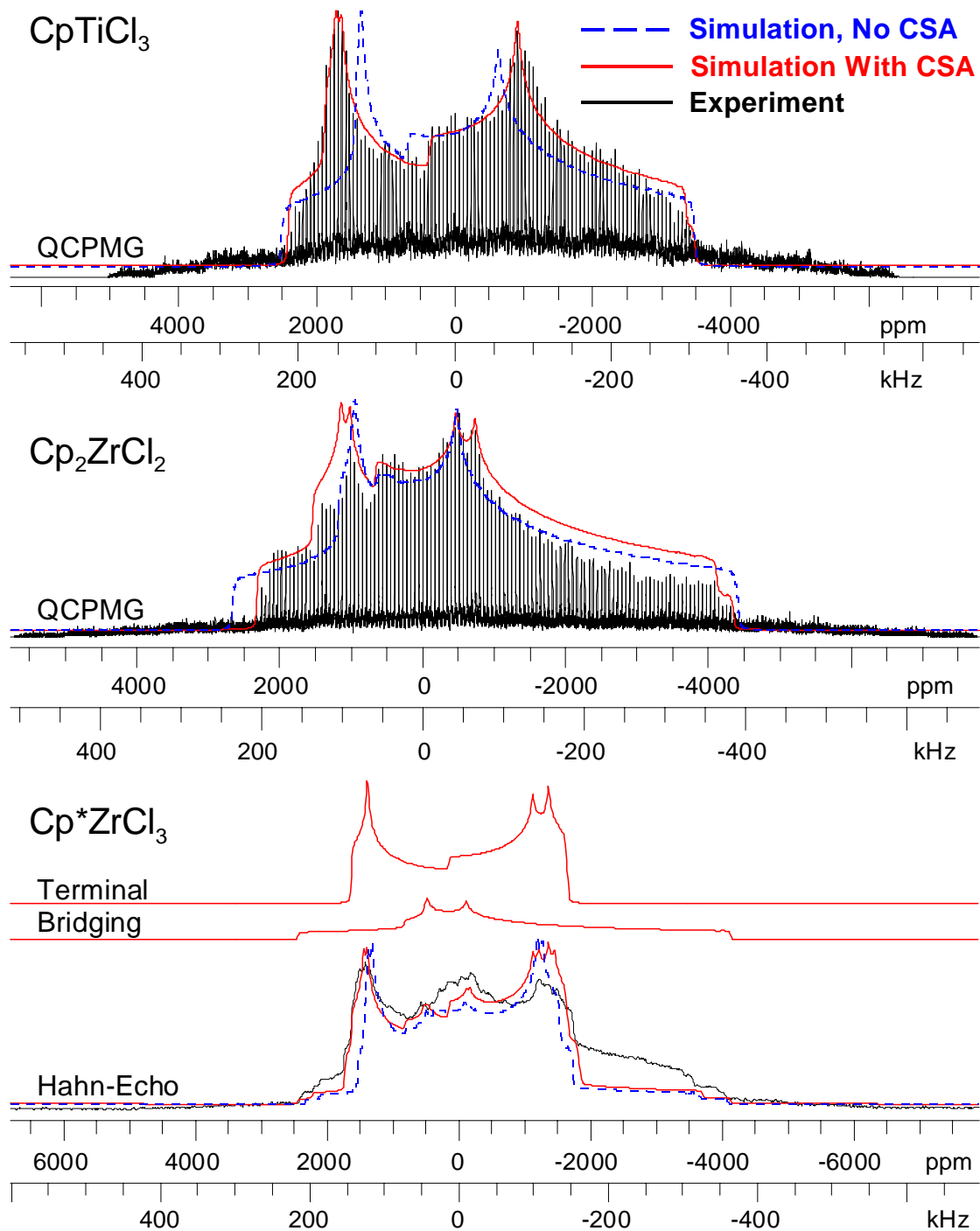


Figure 2.4. Solid-state ^{35}Cl NMR spectra of CpTiCl_3 , Cp_2ZrCl_2 and Cp^*ZrCl_3 acquired at 21.1 T and analytical simulations of the spectra. Piece-wise QCPMG spectra have been acquired for CpTiCl_3 and Cp_2ZrCl_2 . A piece-wise Hahn-echo spectrum was acquired for Cp^*ZrCl_3 . Representative simulations of the bridging and terminal sites are shown for Cp^*ZrCl_3 .

improved fits of the experimental spectra of CpTiCl₃ and Cp₂ZrCl₂ and Cp*ZrCl₃ (solid trace, Figure 2.4). However, the reader is cautioned that the errors associated with Ω , κ and the Euler angles are large in all cases due to the relative magnitude of the quadrupolar and chemical shielding interactions. Due to the overlap of multiple distinct chlorine sites in Cp*ZrCl₃ the uncertainties associated with the CS tensors parameters and Euler angles are especially large. In general the observed values of Ω are several times larger than those observed for amino acid hydrochlorides ($\Omega < 150$ ppm) and alkaline earth chlorides ($\Omega < 75$ ppm),^{29, 35, 36} however, given the low local symmetry about the chlorine nuclei in the organometallic complexes, the large values of Ω are expected and are predicted by quantum chemical calculations. Finally, simulations of the spectra at 9.4 T are seen to be largely unaffected by the inclusion of CSA (Figure A1).

Table 2.3. Observed ³⁵Cl CS Tensor Parameters and Euler Angles

Compound	δ_{iso} (ppm) ^a	Ω (ppm) ^b	κ ^c	α (°) ^d	β (°)	γ (°)
CpTiCl ₃	500(150)	750(400)	-0.4(5)	80(30)	5(15)	5(30)
Cp ₂ ZrCl ₂	300(150)	800(500)	0.0(5)	2(10)	72(20)	-70(20)
Cp*ZrCl ₃ [site 1, 2]	400(200)	500(400)	0.4(8)	10(90)	15(30)	0(90)
Cp*ZrCl ₃ [site 3, 4]	200(200)	200(200)	- ^e	-	-	-

^aDefined in Table 2.1. ^b $\Omega = \delta_{11} - \delta_{33}$. ^c $\kappa = 3(\delta_{22} - \delta_{\text{iso}})/\Omega$. ^dThe Rose convention is used for the Euler angles.^{91, 92} ^eThe overlap of sites and small CSA make it difficult to estimate κ and the Euler angles for the bridging sites.

Quantum Chemical Calculations. First principles calculations of ³⁵Cl NMR parameters are extremely useful as they may provide insight into the origin of the observed NMR parameters and/or aid in the interpretation of ³⁵Cl NMR data from systems which are not amenable to X-ray diffraction techniques. The origin of the observed ³⁵Cl

C_Q values are further investigated within the framework of a NLMO analysis.

Computations were performed with the Gaussian 03⁶⁷ and ADF codes.⁷⁷⁻⁷⁹

Gaussian 03 Calculations of Chlorine NMR Parameters. Chlorine basis sets for the accurate calculation of $^{35/37}\text{Cl}$ EFG and CS tensor parameters have previously been suggested by Bryce et al.³⁶ Both B3LYP and RHF calculations, which employ the cc-pVDZ, cc-pVDZ DK or aug-cc-pVDZ chlorine basis sets, yield EFG tensor parameters that are in excellent agreement with the experimental values (Tables 2.4). There are several notable trends in the calculated values that should be discussed. Calculations employing the RHF method and aug-cc-pVDZ basis set on chlorine consistently yield values of C_Q that are within $\pm 5\%$ of the experimental values for all of the monomeric complexes, with the exception of Cp_2ZrMeCl ; however, the theoretical values of η_Q and δ_{iso} are typically lower than the experimental values. On the other hand, B3LYP calculations generally produce more accurate values of δ_{iso} , while overestimating the values of C_Q , η_Q , and Ω .

Theoretically calculated ^{35}Cl EFG tensors are distinct for terminal and bridging chlorine sites, helping to account for their disparate EFG parameters. For instance, in the dimeric Cp^*ZrCl_3 species, theoretical values of C_Q are similar in magnitude for both the bridging and terminal chlorine sites; however, for the terminal chlorine, the sign of C_Q is negative and η_Q is predicted to be near 0 (i.e., V_{33} is the unique component of the EFG tensor), whereas for the bridging chlorine, the sign of C_Q is positive and the η_Q is near 1 (V_{11} is the unique component).

Table 2.4. ^{35}Cl NMR Parameters Calculated with the RHF Method and aug-cc-pVDZ Basis Set^a

Compound	Method/Cl basis set ^b	Site	C_Q (MHz) ^c	η_Q	δ_{iso} (ppm) ^d	Ω (ppm) ^{e,f}	κ ^{e,f}
Cp_2TiCl_2	experimental	-	22.1	0.62	500		
	RHF/aug-cc-pVDZ	1	-23.0	0.46	216	958	0
	RHF/aug-cc-pVDZ	2	-23.3	0.46	210	958	0.1
CpTiCl_3	experimental	-	15.5	0.54	500	750	-0.4
	RHF/aug-cc-pVDZ	1	-15.6	0.45	470	909	-0.2
	RHF/aug-cc-pVDZ	2	-15.5	0.44	478	902	-0.2
	RHF/aug-cc-pVDZ	3	-15.5	0.45	474	901	-0.3
Cp_2ZrCl_2	experimental	-	16	0.72	300	800	0
	RHF/aug-cc-pVDZ	1	-16.4	0.58	158	740	0.1
	RHF/aug-cc-pVDZ	2	-15.9	0.59	173	733	0
$\text{Cp}^*_2\text{ZrCl}_2$	experimental	-	16.7	0.73	400		
	RHF/aug-cc-pVDZ	1	-16.1	0.46	204	571	-0.5
Cp_2HfCl_2	experimental	-	17.1	0.65	400		
	RHF/aug-cc-pVDZ	1	-17.3	0.56	131	608	0.2
	RHF/aug-cc-pVDZ	2	-17.1	0.56	145	613	0.1
Cp_2ZrMeCl	experimental	-	13.7	0.75	400		
	RHF/aug-cc-pVDZ	1	-15.3	0.66	168	775	-0.1
$(\text{Cp}_2\text{ZrCl})_2(\mu\text{-O})$	experimental	-	16.3	0.43	300		
	RHF/aug-cc-pVDZ	1	-15.9	0.45	72	545	0.2
	RHF/aug-cc-pVDZ	2	-15.4	0.40	65	454	0.2
Cp^*ZrCl_3	experimental	1	12.8	0.10	400	500	0.4
	experimental	2	13.3	0.12	400	500	0.4
	experimental	3	14.6	0.88	200	200	0
	experimental	4	14	0.80	200	200	0
	RHF/aug-cc-pVDZ	1	-13.1	0.06	320	472	-0.2
	RHF/aug-cc-pVDZ	2	-12.0	0.07	335	478	-0.1
	RHF/aug-cc-pVDZ	3, 4	12.1	0.95	131	40	-0.4
CpZrCl_3	experimental	1, 2	14.8	0.80	400		
	experimental	3, 4	18.6	0.75	150		
	experimental	5	17.4	0.80	500		
	RHF/aug-cc-pVDZ	1	-15.7	0.75	257	528	-0.3
	RHF/aug-cc-pVDZ	2	-14.7	0.89	192	386	-0.2
	RHF/aug-cc-pVDZ	3	19.8	0.72	77	178	-0.6
	RHF/aug-cc-pVDZ	4	18.7	0.72	77	160	-0.4
RHF/aug-cc-pVDZ	5	-17.4	0.72	341	688	-0.8	

^a Additional computational results can be found in the original publication. ^b See the experimental section for details on the basis sets used on other atoms. ^c Only the magnitude of C_Q can be measured experimentally. For definitions of all NMR parameters refer to Table 2.1. ^d The theoretical values of δ_{iso} were determined by comparison to the shielding values of HCl calculated with the corresponding method and basis sets. The equation used was, $\delta_{\text{iso}} = \sigma_{\text{iso}}(\text{HCl}) - \sigma_{\text{iso}} + 28$ ppm. ^e Experimental CSA parameters are available only for compounds for which a spectrum at 21.1 T was recorded. ^f Defined in Table 2.3.

Calculations on CpZrCl_3 are complicated because it exists as a coordination polymer in the solid-state. A cluster with a charge of -2 , containing 3 zirconium centres, 3 Cp rings and 9 chlorine atoms was used for calculations on CpZrCl_3 (Figure 2.5). The five chlorine atoms bound to the central Zr unit provide an adequate model of the chlorine atoms in the full coordination polymer structure. However, there is one key difference between the cluster model and crystal structure: the cluster contains five magnetically distinct chlorine sites, while the crystal structure contains only three distinct chlorine sites. For this reason, the NMR parameters calculated for the pairs of bridging sites have been averaged to obtain values used for the analytical simulation. The resulting analytical

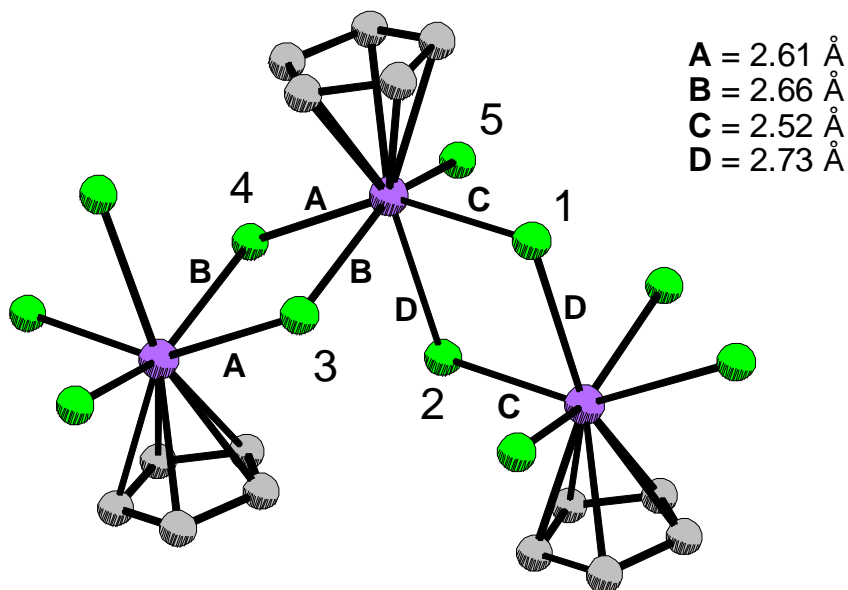


Figure 2.5. The cluster model used for Gaussian 03 calculations on CpZrCl_3 . The chlorine sites in Table 2.4 of the manuscript are labelled. Selected bond lengths are also shown. Sites 1 and 2 are symmetry related and magnetically distinct in this model, but not in the crystal structure. Sites 3 and 4 are also magnetically distinct in the cluster model, but not in the crystal structure. Therefore, averages of the calculated NMR parameters from the pairs of sites have been used in the analytical simulation of the spectrum.

simulation adequately reproduces the features of the experimental spectrum (Figure 2.3 and Table 2.4), particularly the ‘shoulders’ that are visible at the sides of the spectrum.

There are also some interesting features of the calculated NMR parameters for this complex. The two pairs of bridging chloride ligands possess significantly different calculated EFG and CS tensor parameters (see Table 2.4). Most notably, for one pair (sites 1 and 2) the values of C_Q are negative (-15.7 MHz and -14.7 MHz), and for the other pair (sites 3 and 4) the values of C_Q are positive and slightly larger in magnitude (19.8 MHz and 18.7 MHz). The EFG and CS tensor parameters of sites 1 and 2 are similar to those of the terminal chlorine sites observed in other complexes. The single-crystal X-ray structure⁸⁷ reveals that the site 1 and 2 chloride ligands are opposite to Cp rings, and each makes a short (2.52 Å) and a long (2.73 Å) contact with the zirconium centres that they bridge. It would appear that the presence of a distant second zirconium centre has little effect on the ³⁵Cl NMR parameters, making the NMR parameters of sites 1 and 2 more similar to those observed for terminal chloride ligands. Conversely, the geometry of sites 3 and 4 is similar to that of the bridging site observed in Cp*ZrCl₃ with two relatively equal contacts to each zirconium centre (2.66 and 2.61 Å). This explains the similarity of the NMR parameters of sites 3 and 4 of CpZrCl₃ to those for the bridging site of Cp*ZrCl₃.

The visualization of calculated orientations of EFG tensors within molecular frames can provide insight into the origin of the observed EFG tensor parameters. Several chlorine EFG tensor orientations are shown in Figure 2.6. The EFG tensor orientation of Cp₂TiCl₂ is representative of terminal chlorine sites. The largest component of the EFG,

V_{33} , nearly parallel to the Ti-Cl bond (V_{33} -Cl-Ti angle of 4.3°). Since V_{33} is directed near the metal-Cl bond in Cp_2TiCl_2 , the observation that longer M-Cl bond lengths lead to smaller C_Q values in the Cp_2MCl_2 series is to be expected. The chlorine EFG tensor orientations for Cp^*ZrCl_3 , which possesses both bridging and terminal chloride ligands, are also pictured in Figure 2.6. The EFG orientation of the terminal site is similar to that of Cp_2TiCl_2 (V_{33} -Cl-Zr angle of 6.1°). Conversely, for the bridging site, V_{33} is directed perpendicular to Zr-Cl-Zr plane (angle of 86° with respect to the Zr-Cl-Zr plane). Similar V_{33} orientations have been calculated for aluminum EFGs where V_{33} is oriented perpendicular to the horizontal mirror plane of trigonal planar systems.⁶¹ Cartesian coordinates for EFG tensor orientations are provided in the original publication.

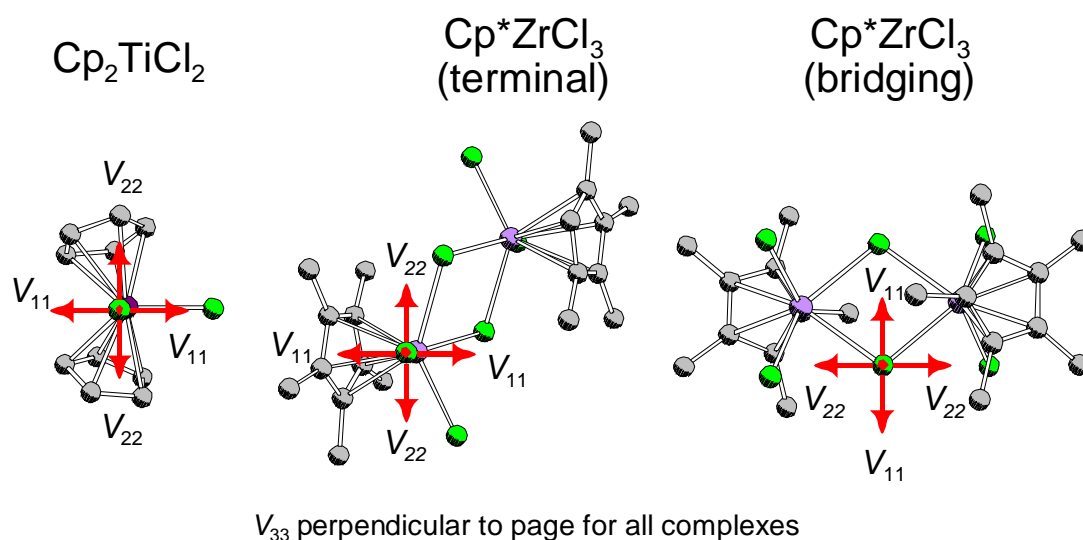


Figure 2.6. EFG tensor orientations in Cp_2TiCl_2 and Cp^*ZrCl_3 . The tensor orientations are shown for the terminal and bridging Cl sites of Cp^*ZrCl_3 . The orientations are taken from the calculations listed in Table 2.4.

ADF NLMO Analysis of EFG Tensors. In order to further probe the origins of the observed ^{35}Cl EFG tensor parameters we have undertaken an NLMO analysis,^{93,94} i.e. we have determined the contributions of individual NLMOs to the observed ^{35}Cl EFGs. Computations were performed with a developer's version of the ADF code, version 2007.⁷⁷⁻⁷⁹ For the present work, a new module has been developed for a molecular orbital (MO) based analysis of EFG tensors, using either delocalized or localized MOs.⁹⁵ A similar approach for the analysis of NMR spin-spin coupling constants and chemical shifts has been demonstrated and thoroughly discussed by Autschbach.⁹⁶⁻⁹⁹

For the NLMO analysis quadrupole coupling constants are obtained from $C_Q = eQ \cdot V_{33}/h$, such that the NLMO contributions for V_{33} are directly related to C_Q . In the analysis, contributions smaller than an arbitrary threshold of 5% of V_{33} are omitted to keep the amount of data at a manageable level. The information available from the NLMO analysis is similar to that from NBO analysis, and includes classification of the NLMO (e.g. bonding, core and lone pair orbitals), the composition of the NLMOs in terms of atomic orbitals (AOs), and a measure of how well the molecular wavefunction is described by a given Lewis structure (as indicated by the occupancy numbers). NLMO EFG analyses for Cp_2TiCl_2 , CpTiCl_3 and Cp_2ZrCl_2 are examined and compared in order to understand the origins of the chlorine EFG tensors in terms of localized MOs for which individual intuitive bonding, lone pair, and core contributions to the EFG can be obtained. The generally delocalized, canonical MOs available from standard HF and DFT calculations are not as convenient for such an analysis since many of these MOs may

Table 2.5. Analysis of NLMO Contributions to EFG Tensors for Cp₂TiCl₂, CpTiCl₃ and Cp₂ZrCl₂

Compound	Exp. V_{33} (a.u.) ^a	Calc. V_{33} (a.u.)	NLMO Number <i>b</i>	Electron Pair Type ^c	Occ. ^d	NLMO Composition ^e	V_{33} Lewis	V_{33} non-	V_{33} Total		
							(a.u.)	Lewis (a.u.)	(a.u.) ^f		
Cp ₂ TiCl ₂	1.152	1.386	36	core	2	100 Cl (100 2 <i>p</i>)	79.634	0.020	79.654		
			37	core	2	100 Cl (100 2 <i>p</i>)	52.764	0.013	52.777		
			38	core	2	100 Cl (100 2 <i>p</i>)	-132.225	-0.013	-132.238		
							Sum of core orbital contributions		0.173	0.020	0.193
			54	lone pair, nb	1.97	1.2 Ti (24.6 4 <i>s</i> , 74 3 <i>d</i>), 98.7 Cl (70.5 3 <i>s</i> , 29.5 3 <i>p</i>)		-2.112	-0.055	-2.167	
			55	lone pair, π	1.92	2.7 Ti (99.4 3 <i>d</i>), 96.1 Cl (100 3 <i>p</i>)		4.577	-0.200	4.377	
			56	lone pair, π	1.83	8.7 Ti (99.3 3 <i>d</i>), 90.6 Cl (99.3 3 <i>p</i>)		4.140	-0.245	3.895	
			57	lone pair, σ	1.61	21.1 Ti (10.8 4 <i>s</i> , 88.6 3 <i>d</i>), 76.5 Cl (28.7 3 <i>s</i> , 71.0 3 <i>p</i>)		-5.362	0.619	-4.743	
							Sum of all Cl lone pair/bonding orbital contributions		1.243	0.119	1.362
			62	Cp-Ti, σ/π	1.05	17.9 Ti (99.2 3 <i>d</i>), 1.9 Cl (28.4 3 <i>s</i> , 70.8 3 <i>p</i>), 80.1 Cp C		0.018	-0.103	-0.085	
				Sum of all NLMO contributions		1.434	0.036	1.470			
CpTiCl ₃	0.808	0.789	20	core	2	100 Ti (100 3 <i>s</i>)	-0.066	0.000	-0.066		
			22	core	2	100 Ti (100 3 <i>p</i>)	-0.041	0.002	-0.039		
			26	core	2	100 Ti (100 3 <i>p</i>)	-0.058	0.003	-0.055		
							Sum of Ti core orbital contributions		-0.165	0.005	-0.160
			29	core	2	100 Cl (100 2 <i>p</i>)	-62.120	-0.001	-62.121		
			30	core	2	100 Cl (100 2 <i>p</i>)	79.956	0.009	79.965		
			31	core	2	100 Cl (100 2 <i>p</i>)	-17.743	0.001	-17.742		

							Sum of Cl core orbital contributions	0.093	0.009	0.102
			47	lone pair, nb	1.98	1.0 Ti (9.4 4s, 89.6 3d), 99.0 Cl (68.4 3s, 31.6 3p)		-2.138	-0.045	-2.183
			48	lone pair, π	1.79	9.2 Ti (99.3 3d), 89.2 Cl (100 3p)		4.323	-0.257	4.066
			49	lone pair, σ/π	1.69	13.1 Ti (11.3 4s, 87.7 3d), 84.5 Cl (11.8 3s, 88 3p)		-3.618	0.695	-2.923
			1	bond, σ/π	1.99	13.5 Ti (16.4 4s, 83.1 3d), 86.3 Cl (18.3 3s, 81.5 3p)		1.766	-0.074	1.692
							Sum of Cl lone pair/bonding orbital contributions	0.333	0.319	0.652
			53	Cp-Ti, π	0.1	79.6 Cp C, 17.5 Ti (97.1 3d), 2.1 Cl (91.5 3p)		-0.010	0.105	0.095
							Sum of all NLMO contributions	0.251	0.438	0.689
Cp ₂ ZrCl ₂	0.834	0.895	28	core	2	99.5 Zr (99.99 4s)		-0.054	0.000	-0.054
			37	core	2	100 Zr (100 4p)		-0.052	0.005	-0.048
			50	core	2	100 Cl (100 2p)		77.536	0.018	77.554
			51	core	2	100 Cl (100 2p)		56.132	0.016	56.148
			52	core	2	100 Cl (100 2p)		-133.574	0.014	-133.560
							Sum of Cl core orbital contributions	0.094	0.048	0.142
			67	lone pair, nb	1.98	1.0 Zr (13.4 5s, 85.5 4d), 98.9 Cl (63.4 3s, 36.6 3p)		-2.677	0.014	-2.663
			68	lone pair, π	1.91	3.9 Zr (98.6 4d), 95.0 Cl (99.9 3p), 0.9 Cp C		4.624	-0.241	4.383
			69	lone pair, π	1.85	7.8 Zr (98.7 4d), 91.7 Cl (1.0 3s, 98.9 3p)		4.074	-0.286	3.788
			70	lone pair, σ	1.7	15.3 Zr (15.1 5s, 84.2 4d), 83.5 Cl (35.5 3s, 64.3 3p)		-5.213	0.553	-4.660
							Sum of Cl lone pair/bonding orbital contributions	0.808	0.040	0.848
							Sum of all NLMO contributions	0.796	0.092	0.888

^aThe experimental values of C_Q have been converted to V_{33} values. The sign of V_{33} can not be determined experimentally. ^bThis is the index number assigned by the NBO program. ^cThis is the label assigned by the NBO program. Bond refers to a bonding pair of electrons, core to a non-bonding pair of electrons in the sub-shell below the valence shell, and lone pair to an electron lone pair localized on Cl. The chlorine electron lone pairs have also been qualitatively described as non-bonding (nb) or participating in Ti-Cl π - or σ -bonding. ^dOcc refers to the occupancy of the parent NBO of the NLMO, the analysis data is for the NLMO. Occupancies less than 2 indicate deviation away from an ideal Lewis structure. ^eThe number before the atom symbol indicates the percentage composition of each NLMO in terms of atomic orbitals from the given atom(s). The contribution of each atom is then broken down by percentage orbital type (eg. *s, p, d*). ^fThe V_{33} summed from all printed NLMO contributions differs from the calculated V_{33} due to the exclusion of many small contributions which are not printed.

contribute to a local bonding environment with large contributions of opposite signs.

The output from the NLMO EFG analysis of Cp_2TiCl_2 is discussed in detail below in order to clarify the contents of Table 2.5. The experimentally determined and calculated values of V_{33} are shown in columns 2 and 3 of the table. The chlorine site with the calculated value of V_{33} closest to experimental value of V_{33} has been chosen for analysis. There are 8 NLMOs shown in column 4 (54-57 are shown in Figure 2.7), since they make contributions to V_{33} larger than 5% of the total value of V_{33} . Columns 5 and 6 indicate the electron pair type and occupancy, respectively. The 'NLMO Composition' in column 7 provides a percentage composition of the NLMOs in terms of atomic orbitals from individual atoms as printed by the NBO program. The contributions of each atom are further decomposed into percentage contributions from specific atomic orbitals (e.g., $2s$, $3d$). The Lewis, non-Lewis and total contributions to V_{33} made by each NLMO are given in the columns 8, 9 and 10.

NLMOs 36-38 are completely comprised of core Cl $2p$ orbitals. The individual Lewis contributions of NLMOs 36-38 to V_{33} are very large; however, because they correspond to a closed $2p$ shell, their combined contribution to V_{33} amounts to only 0.193 a.u. A filled sub-shell of AOs should make no net contribution to the EFG tensor due to its spherical symmetry; however, in this case, the non-zero contribution of orbitals 36-38 to V_{33} arises from the deformation of these orbitals by nearby atoms and bonds. The small combined contributions of the core Cl NLMOs is seen for both of the other systems. NLMOs 54-57, primarily composed of Cl $3s$ and $3p$ AOs, contribute 1.362 a.u. to V_{33} , representing a large portion of the total of 1.470 a.u. NLMOs 54 and 57 make large

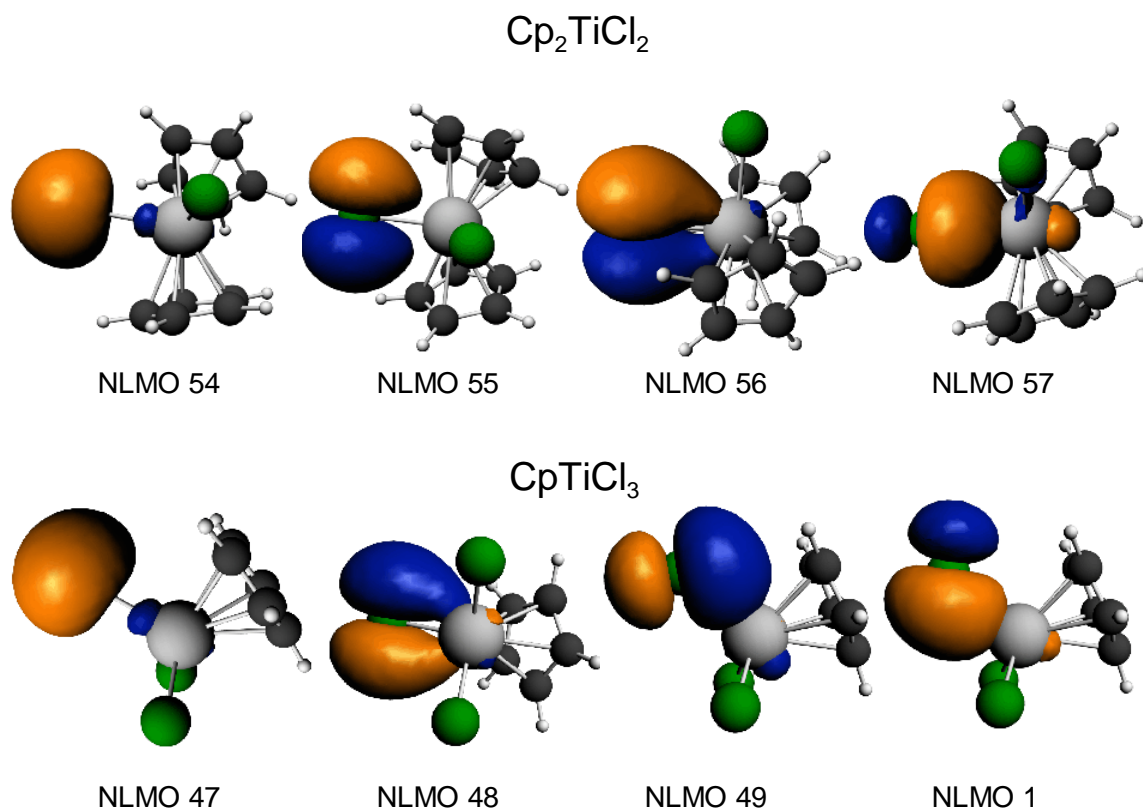


Figure 2.7. Images of NLMOs which are the main contributors to the observed ^{35}Cl EFGs in Cp_2TiCl_2 and CpTiCl_3 . The contributions of the individual NLMOs to the observed ^{35}Cl EFGs are described in Table 2.5.

negative contributions to V_{33} , and represent a non-bonding electron lone pair and Ti-Cl σ -bond, respectively. NLMOs 55 and 56 make large positive contributions to V_{33} , and represent lone pairs which participate in Ti-Cl π -bonding. It is evident that NLMO 56 represents a greater degree of Ti-Cl π -bonding than NLMO 55 as indicated by the lower occupancy (1.833 vs. 1.924) of its parent NBO and its larger fraction of Ti character (8.7 % vs. 2.7%). It also makes a smaller contribution to V_{33} than NLMO 55 (3.895 a.u. vs. 4.377 a.u.).

Bryukhova has previously hypothesized that increased Ti-Cl π -bonding leads to a

decrease in the observed $^{35/37}\text{Cl}$ EFGs.^{44,45} This hypothesis was used to explain the large decrease in C_Q observed when comparing the ^{35}Cl NQR data from CpTiCl_3 and Cp_2TiCl_2 . It is interesting to see if this hypothesis can be confirmed by comparing the NLMO-EFG analyses of Cp_2TiCl_2 and CpTiCl_3 . The NLMO-EFG analysis of CpTiCl_3 is shown in Table 2.5 and NLMOs 47-49 and 1 are shown in Figure 2.7.

Minor negative contributions to V_{33} from core Ti AOs are observed for CpTiCl_3 , which likely arise because of much shorter Ti-Cl bond lengths compared to Cp_2TiCl_2 . The majority of V_{33} is seen to once again arise from contributions from the valence Cl AOs and Ti-Cl bonding orbitals which are described by NLMOs 47-49 and 1. The non-bonding Cl lone pair orbital, NLMO 47, and one of the π -bonding electron lone pairs, NLMO 48, make contributions to V_{33} similar in sign and magnitude to their counterparts in Cp_2TiCl_2 (NLMOs 54 and 55, respectively). However, the remaining two Cl electron lone pairs of CpTiCl_3 are quite different from those of Cp_2TiCl_2 . NLMO 49 is classified as a “lone pair” by the NBO program, however, it is evident that NLMO 49 represents a significant degree of Ti-Cl bonding based upon its appearance and low occupancy (1.693). The contribution to V_{33} from NLMO 49 is -2.923 a.u., which is of the same sign and lower in magnitude than that from the σ -bonding lone pair of Cp_2TiCl_2 (NLMO 57, -4.743 a.u.). NLMO 1 is classified as a bonding orbital and possesses a high occupancy (1.986). The V_{33} contribution of NLMO 1 (1.692 a.u.) is of the same sign as that of the π -bonding lone pair of Cp_2TiCl_2 (NLMO 56); however, the magnitude of the contribution is significantly lower. The V_{33} contributions of NLMOs 1 and 49 of CpTiCl_3 total -1.231 a.u. as compared to the total of -0.848 a.u. of NLMOs 56 and 57 of Cp_2TiCl_2 . In

summary, it is clear from the visualization of NLMOs 48, 49 and 1 of CpTiCl_3 and the much lower parent NBO occupancies for NLMOs 48 and 49 that there is much more π -bonding in CpTiCl_3 than in Cp_2TiCl_2 . By comparing the NLMOs and EFG tensors in CpTiCl_3 and Cp_2TiCl_2 , it is clear that the decreased V_{33} contributions from the CpTiCl_3 NLMOs arise from increased Ti-Cl π -bonding character, in agreement with Bryukhova's hypothesis,^{44, 45} which is based upon the semi-empirical Townes-Daily theory.¹⁰⁰

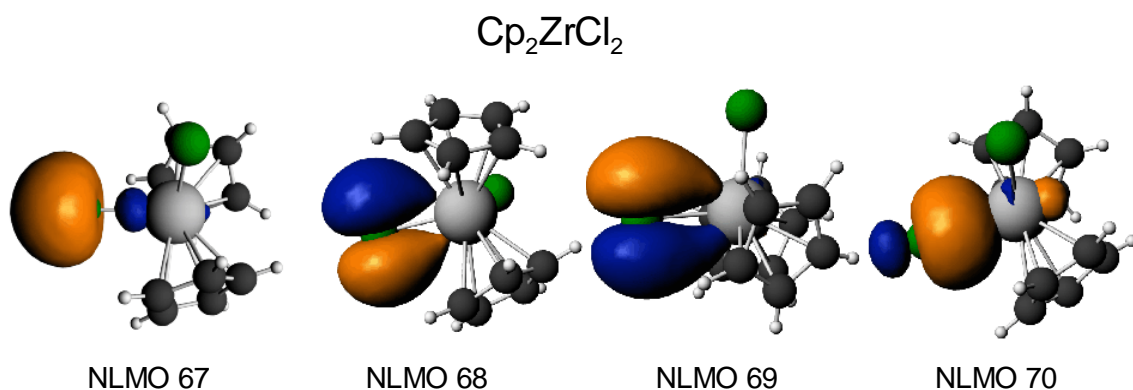


Figure 2.8. Images of NLMOs which are the main contributors to the observed ^{35}Cl EFGs in Cp_2ZrCl_2 . The contributions of the individual NLMOs to the observed ^{35}Cl EFGs are described in Table 2.5.

Finally, the NLMO analysis of Cp_2ZrCl_2 is compared to that of Cp_2TiCl_2 , in order to explain the large differences in their C_Q values. The reduced C_Q in Cp_2ZrCl_2 occurs for the following reasons: minor negative contributions to V_{33} are seen to arise from NLMO 28 and 37, which are comprised of core Zr $4s$ and $4p$ AOs. The major reduction in C_Q seems to arise from the valence Cl $3s$ and $3p$ orbitals, NLMOs 67-70 (Figure 2.8), where the contributions to V_{33} are reduced by 0.514 a.u. This is mainly due to a large increase in the magnitude of the negative contribution (-2.663 a.u.) from the non-bonding Cl electron

lone pair, NLMO 67. The non-bonding lone pair is of much higher p -character in Cp_2ZrCl_2 (36.6 %) than in Cp_2TiCl_2 (29.5%), resulting in a more asymmetric distribution of charge, and a larger negative contribution to V_{33} .

Solid-state ^{35}Cl NMR Spectroscopy and Quantum Chemical Modelling of Cp_2ZrHCl . Cp_2ZrHCl was first synthesized in 1970's^{64, 101, 102} and the utility of the compound as a reagent for hydrogenation, halogenation and carbon-carbon bond forming reactions was quickly realized.^{103, 104} Development of new reactions which utilize the complex continues today.¹⁰⁵⁻¹⁰⁷ There is currently no known single-crystal or powder X-ray diffraction structure of Schwartz's reagent (Cp_2ZrHCl). In order to probe the solid-state structure of this important reagent, the solid-state ^{35}Cl NMR spectrum has been acquired and quantum chemical calculations on several models have been performed, following the methodologies discussed above.

The solid-state ^{35}Cl NMR spectra and analytical simulations of Cp_2ZrHCl are shown in Figure 2.9. The spectra very closely conform to that of a standard quadrupolar powder pattern, indicating that the powdered sample is crystalline (powder X-ray diffraction also confirms this, Figure A3) and contains one type of chlorine ligand. The ^{35}Cl NMR spectrum at 9.4 T is best simulated with $C_Q = 19.7$ MHz, $\eta_Q = 0.20$ and $\delta_{\text{iso}} = 80$ ppm (Table 2.1). Simulations of the spectra at 21.1 T utilize $\Omega = 400$ ppm, $\kappa = 0.5$ (Table 2.6), and non-zero Euler angles [$\alpha = \gamma = 0(30)^\circ$, $\beta = 85(30)^\circ$]. The chlorine CSA is much smaller than that observed for Cp_2ZrCl_2 and CpTiCl_3 .

Previously acquired IR spectra of Cp_2ZrHCl and Cp_2ZrDCl suggest the hydride ligands bind in a bridging manner, implying that the complex exists as an oligomer in the

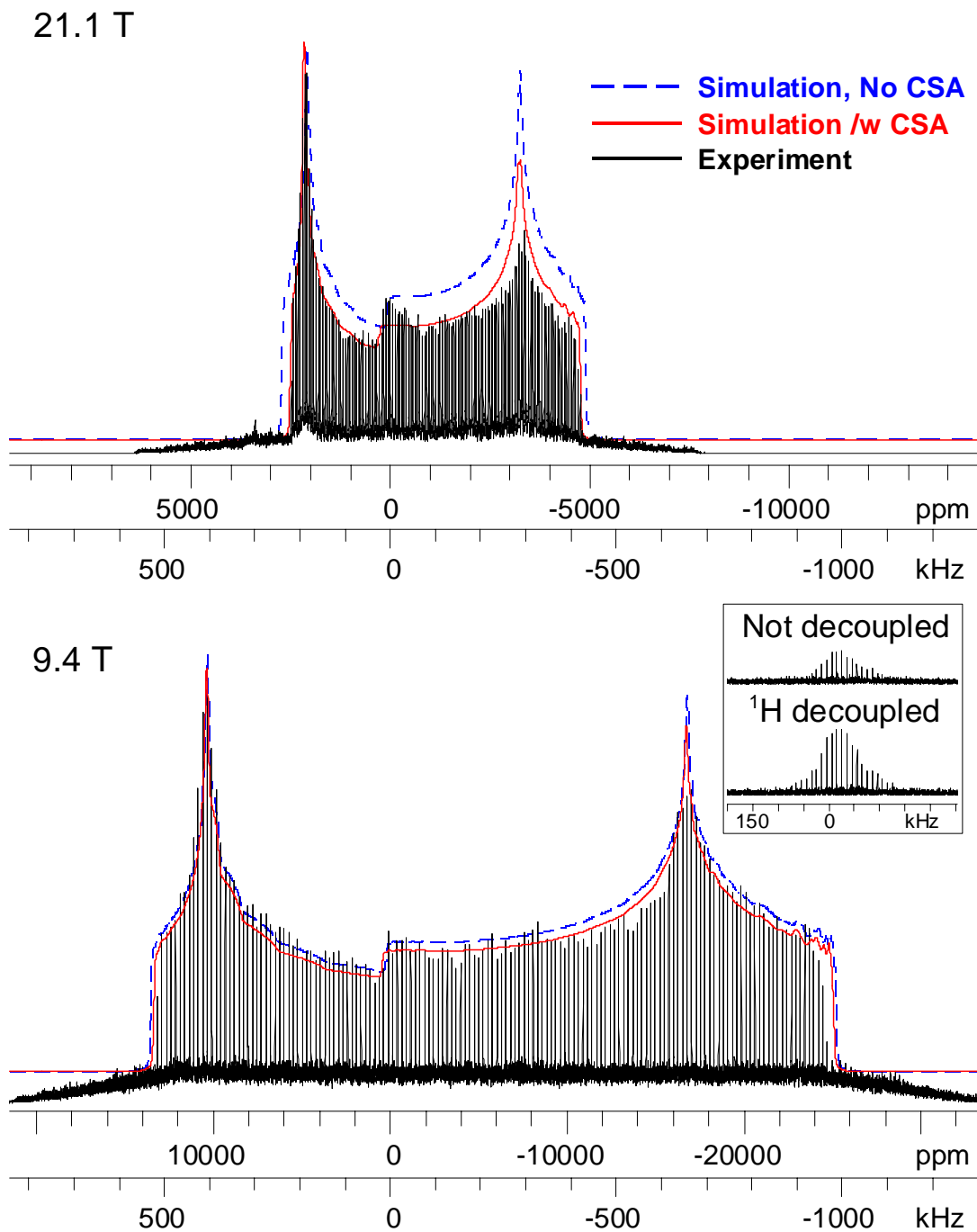


Figure 2.9. Solid-state ^{35}Cl NMR spectra of Cp_2ZrHCl acquired at 9.4 T and 21.1 T and analytical simulations of the spectra. Simulations with (solid red trace) and without (dashed blue trace) the effects of CSA are shown. The effects of ^1H decoupling on an individual sub-spectrum from 9.4 T are shown in the inset. The application of ^1H decoupling greatly increases the number of echoes that may be acquired and leads to a dramatic increase in signal to noise.

solid state.^{64, 102} The observed ^{35}Cl NMR parameters unequivocally confirm this hypothesis. The value of C_Q is significantly larger than that observed for Cp_2ZrCl_2 . The observed value of η_Q is similar to the low values of η_Q observed for the terminal chloride ligands of Cp^*ZrCl_3 and $(\text{Cp}_2\text{ZrCl})_2\mu\text{-O}$, and distinct from the intermediate to high η_Q values observed in all of the monomeric complexes which possess terminal chloride ligands. This indicates that the complex is a dimer which contains bridging hydride ligands and terminal chloride ligands. The application of ^1H decoupling during the acquisition of the sub-spectra greatly lengthens the time for which echoes can be acquired with the QCPMG sequence. This subsequently improves the signal to noise of the spectrum (inset of Figure 2.9 and Figure A4) and indicates the proximity of the hydride and chlorine atoms.

In order to confirm the model derived from experiment, quantum chemical calculations of ^{35}Cl EFG and CS tensors were performed on a series of model structures. As a starting point for developing our structural models, a search of the Cambridge Structural Database (CSD) for other bis(cyclopentadienyl)zirconium hydride complexes was performed. A single crystal X-ray structure was found for methyl-bis(cyclopentadienyl)zirconium hydride (Cp_2ZrHMe),¹⁰⁸ which exists as a dimer in the solid-state. Given the similarity of the molecular structures of Cp_2ZrCl_2 and Cp_2ZrMeCl , Cp_2ZrHMe is a reasonable starting point for modelling the solid-state structure of Cp_2ZrHCl . Monomeric bis(cyclopentadienyl)zirconium chloride hydride and dihydride structures were also located, however all of these complexes contained bulky, substituted Cp' ligands, which have a strong influence on the structure and chemistry in general.^{109, 110}

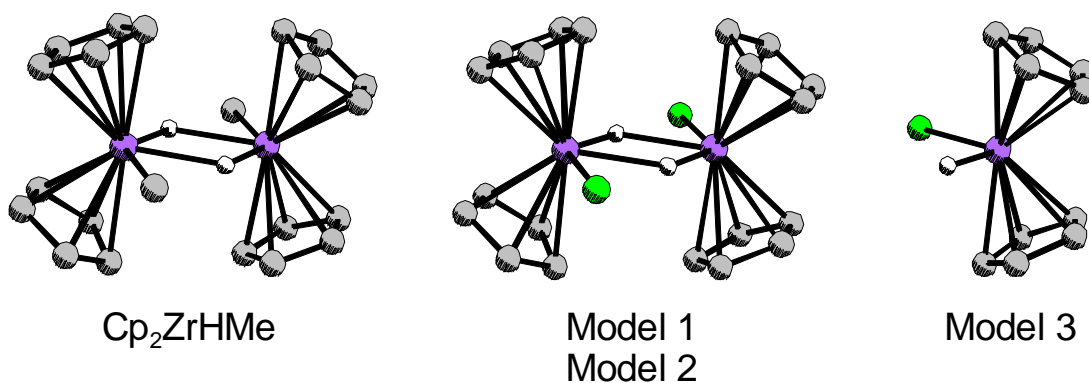


Figure 2.10. The structure of Cp_2ZrHMe and models of the solid-state structure of Cp_2ZrHCl . Cartesian coordinates of atomic positions are given in the original publication.

Two models were constructed from the crystal structure of Cp_2ZrHMe (Figure 2.10). The positions of the Zr, hydride and Cp carbon atoms are not altered in both models. In Model 1, the methyl ligand is replaced with a chloride ligand. The positions of Cl and Cp H atoms were geometry optimized. Optimized Cl-Zr bond lengths of 2.61 Å (RHF) and 2.56 Å (B3LYP) were obtained and calculations with both methods result in an angular displacement of the Cl ligand by ca. 2° from the position of the methyl carbon. Calculations of ^{35}Cl NMR parameters from Model 1 yield reasonable agreement with the experimental parameters (Table 2.6). Model 2 is identical to Model 1, except the Zr-Cl bond lengths are set to a more reasonable distance of 2.46 Å, based upon the terminal Zr-Cl bond lengths observed in other zirconium complexes. The calculated EFG tensor parameters of Model 2 are in better agreement with the experimental values than those of Model 1. The success of the calculations on Models 1 and 2 at reproducing the experimental NMR parameters suggest that they are accurate representations of the

molecular structure.

Powder X-ray diffraction results also support the proposed structure model of Cp_2ZrHCl . The observed powder X-ray diffraction pattern of Cp_2ZrHCl bears a striking resemblance to that which is predicted from the single crystal X-ray structure of Cp_2ZrHMe (Figure A3). If the methyl group in the crystal structure of Cp_2ZrHMe is removed and a Cl atom is placed at the methyl carbon position, the powder X-ray diffraction pattern predicted from this ‘rough crystal structure’ of Cp_2ZrHCl is seen to provide an extremely close match with the experimental diffraction pattern. While a full Rietveld refinement of Cp_2ZrHCl is beyond the scope of this study, the diffraction results suggests that the proposed dimer structure of Cp_2ZrHCl is correct and that it crystallizes in the same space group as Cp_2ZrHMe with very similar unit cell parameters.

Table 2.6. Observed and Calculated ^{35}Cl NMR Parameters of Cp_2ZrHCl

Compound	Method/basis set	C_Q (MHz) ^a	η_Q	δ_{iso} (ppm)	Ω (ppm)	κ
Cp_2ZrHCl	Experimental	19.7	0.20	80	400(250)	0.5(5)
Model 1	RHF/aug-cc-pVDZ	-20.9	0.08	-40	318	0.9
	B3LYP/aug-cc-pVDZ	-23.1	0.15	124	485	0.7
Model 2	RHF/aug-cc-pVDZ	-18.9	0.12	6	351	0.9
	B3LYP/aug-cc-pVDZ	-21.1	0.18	154	476	0.8
Model 3	RHF/aug-cc-pVDZ	11.5	0.94	224	793	-0.3
	B3LYP/aug-cc-pVDZ	13.4	0.55	482	1074	-0.2

^aSee Table 2.1 for definitions of parameters.

Finally, to demonstrate that the ^{35}Cl NMR parameters are distinct for monomeric and dimeric species, a third model was constructed from the crystal structure of the monomeric complex, Cp_2ZrMeCl (Figure 2.10). The methyl ligand was replaced with a

hydride, and the hydride and chloride positions were optimized. Calculations on Model 3 result in values of C_Q and η_Q that show very poor agreement with experimental values. Further, the B3LYP values of δ_{iso} for Models 1 and 2 are in good agreement with the experimental parameters, while calculated values for Model 3 are not. The calculated values of Ω and κ from Models 1 and 2 are quite distinct from those of Model 3 as well, demonstrating the potential of CS tensor parameters for distinguishing between monomeric and dimeric structures.

2.4 Conclusions

Extremely broad ^{35}Cl NMR spectra of early transition organometallic complexes can be acquired using the QCPMG sequence in 2 and 28 hours of experimental times at a moderate magnetic field of 9.4 T. The acquisition of ^{35}Cl spectra at 21.1 T results in an order of magnitude reduction of experimental times as compared to those of 9.4 T. It is possible to acquire a high quality ^{35}Cl spectra of Cp_2ZrCl_2 and CpTiCl_3 in less than 13 minutes at 21.1 T due to the increase in signal to noise and the reduction in the breadth of the ^{35}Cl powder patterns. This suggests that it is possible to utilize ^{35}Cl NMR spectroscopy to probe surface supported organometallic complexes, despite the low loading levels (approximately 5 weight % catalyst or less). The ^{35}Cl NMR parameters act as sensitive probes of molecular structure because of their dependence upon the number and types of ligands coordinated to the metal centre(s) to which they are bound. Chlorine CSA is quite large and may be observed in high field NMR spectra. Quantum chemical

calculations can accurately reproduce the experimentally observed NMR parameters. In particular, the NLMO-EFG analyses should shed much light on the relationships between EFG tensors and molecular symmetry and bonding. NMR spectra, powder X-ray diffraction data and theoretical methods demonstrate that Cp_2ZrHCl exists as a dimer in the solid-state and possesses a structure similar to that of Cp_2ZrHMe . The tandem of ^{35}Cl NMR spectroscopy and quantum chemical calculations will ultimately allow one to examine the molecular structure of surface supported organometallics.

While this work has focussed on the ^{35}Cl NMR spectroscopy of early transition metal metallocenes it is clear that the methods describe herein can easily be extended to characterization of countless chlorine-containing main group and transition metal coordination compounds. Lucken has summarized the values of $\nu_Q(^{35}\text{Cl})$ obtained from NQR spectra of chloride complexes of B, Al, Ga, Si, Sn, Sb, and Bi and the corresponding values of $C_Q(^{35}\text{Cl})$ for these complexes range from approximately 9 MHz (Al complexes) to 40 MHz (Si, Sn, and Sb complexes).³⁸ The values of $\nu_Q(^{35}\text{Cl})$ observed for late transition metal complexes (e.g. Re, Os, Pt) indicate that rapid acquisition of ^{35}Cl SSNMR spectra of these complexes is also feasible. The combination of high magnetic fields (e.g., 21.1 T) and new NMR techniques designed to increase excitation bandwidths^{111, 112} should permit comprehensive structural characterization of inorganic species in a variety of solid phases by ^{35}Cl SSNMR, especially those for which single crystal data is unavailable.

2.5 Bibliography

- (1) Soga, K., *Macromol. Symp.* **1996**, 101, 281-288.
- (2) Sinclair, K. B.; Wilson, R. B., *Chem. Ind.* **1994**, (21), 857-862.
- (3) Hlatky, G. G., *Chem. Rev.* **2000**, 100, (4), 1347-1376.
- (4) Severn, J. R.; Chadwick, J. C.; Duchateau, R.; Friederichs, N., *Chem. Rev.* **2005**, 105, (11), 4073-4147.
- (5) He, M. Y.; Xiong, G. X.; Toscano, P. J.; Burwell, R. L.; Marks, T. J., *J. Am. Chem. Soc.* **1985**, 107, (3), 641-652.
- (6) Toscano, P. J.; Marks, T. J., *J. Am. Chem. Soc.* **1985**, 107, (3), 653-659.
- (7) Toscano, P. J.; Marks, T. J., *Langmuir* **1986**, 2, (6), 820-823.
- (8) Dahmen, K. H.; Hedden, D.; Burwell, R. L.; Marks, T. J., *Langmuir* **1988**, 4, (5), 1212-1214.
- (9) Vasnetsov, S. A.; Nosov, A. V.; Mastikhin, V. M.; Zakharov, V. A., *J. Mol. Catal.* **1989**, 53, (1), 37-41.
- (10) Sishta, C.; Hathorn, R. M.; Marks, T. J., *J. Am. Chem. Soc.* **1992**, 114, (3), 1112-1114.
- (11) Reven, L., *J. Mol. Catal.* **1994**, 86, (1-3), 447-477.
- (12) Ahn, H.; Marks, T. J., *J. Am. Chem. Soc.* **2002**, 124, (24), 7103-7110.
- (13) Atiqullah, M.; Akhtar, M. N.; Faiz, M.; Moman, A.; Abu-Raqabah, A. H.; Khan, J. H.; Wazeer, M. I., *Surf. Interface Anal.* **2006**, 38, (10), 1319-1327.
- (14) Joubert, J.; Delbecq, F.; Sautet, P.; Le Roux, E.; Taoufik, M.; Thieuleux, C.; Blanc, F.; Coperet, C.; Thivolle-Cazat, J.; Basset, J. M., *J. Am. Chem. Soc.* **2006**, 128, (28), 9157-9169.
- (15) Jezequel, M.; Dufaud, V.; Ruiz-Garcia, M. J.; Carrillo-Hermosilla, F.; Neugebauer, U.; Niccolai, G. P.; Lefebvre, F.; Bayard, F.; Corker, J.; Fiddy, S.; Evans, J.; Broyer, J. P.; Malinge, J.; Basset, J. M., *J. Am. Chem. Soc.* **2001**, 123, (15), 3520-3540.
- (16) Hamaed, H.; Lo, A. Y. H.; Lee, D. S.; Evans, W. J.; Schurko, R. W., *J. Am. Chem.*

- Soc.* **2006**, 128, (39), 12638-12639.
- (17) Lo, A. Y. H.; Bitterwolf, T. E.; Macdonald, C. L. B.; Schurko, R. W., *J. Phys. Chem. A* **2005**, 109, (32), 7073-7087.
- (18) Hung, I.; Schurko, R. W., *J. Phys. Chem. B* **2004**, 108, (26), 9060-9069.
- (19) Hao, N.; Sayer, B. G.; Denes, G.; Bickley, D. G.; Detellier, C.; McGlinchey, M. J., *J. Magn. Reson.* **1982**, 50, (1), 50-63.
- (20) Dormond, A.; Fauconet, M.; Leblanc, J. C.; Moise, C., *Polyhedron* **1984**, 3, (7), 897-900.
- (21) Berger, S.; Bock, W.; Marth, C. F.; Raguse, B.; Reetz, M. T., *Magn. Reson. Chem.* **1990**, 28, (6), 559-60.
- (22) Buhl, M.; Hopp, G.; von Philipsborn, W.; Beck, S.; Prosenč, M. H.; Rief, U.; Brintzinger, H. H., *Organometallics* **1996**, 15, (2), 778-785.
- (23) von Philipsborn, W., *Chem. Soc. Rev.* **1999**, 28, (2), 95-105.
- (24) Pinkas, J.; Lycka, A.; Sindelar, P.; Gyepes, R.; Varga, V.; Kubista, J.; Horacek, M.; Mach, K., *J. Mol. Catal. A-Chem.* **2006**, 257, (1-2), 14-25.
- (25) Harris, R. K.; Becker, E. D.; De Menezes, S. M. C.; Goodfellow, R.; Granger, P., *Pure Appl. Chem.* **2001**, 73, (11), 1795-1818.
- (26) Bryce, D. L.; Sward, G. D., *Magn. Reson. Chem.* **2006**, 44, (4), 409-450.
- (27) Akitt, J. W.; McDonald, W. S., *J. Magn. Reson.* **1984**, 58, (3), 401-412.
- (28) Kentgens, A. P. M., *Geoderma* **1997**, 80, (3-4), 271-306.
- (29) Bryce, D. L.; Bultz, E. B., *Chem.-Eur. J.* **2007**, 13, (17), 4786-4796.
- (30) Kanda, T., *J. Phys. Soc. Jpn.* **1955**, 10, 85-8.
- (31) Yamagata, Y., *J. Phys. Soc. Jpn.* **1964**, 19, (1), 10-23.
- (32) Skibsted, J.; Jakobsen, H. J., *Inorg. Chem.* **1999**, 38, (8), 1806-1813.
- (33) Bryce, D. L.; Gee, M.; Wasylishen, R. E., *J. Phys. Chem. A* **2001**, 105, (45), 10413-10421.
- (34) Gervais, C.; Dupree, R.; Pike, K. J.; Bonhomme, C.; Profeta, M.; Pickard, C. J.;

- Mauri, F., *J. Phys. Chem. A* **2005**, 109, (31), 6960-6969.
- (35) Bryce, D. L.; Sward, G. D., *J. Phys. Chem. B* **2006**, 110, (51), 26461-26470.
- (36) Bryce, D. L.; Sward, G. D.; Adiga, S., *J. Am. Chem. Soc.* **2006**, 128, (6), 2121-2134.
- (37) Hamaed, H.; Pawlowski, J. M.; Cooper, B. F. T.; Fu, R.; Eichhorn, S. H.; Schurko, R. W., *J. Am. Chem. Soc.* **2008**, 130, (33), 11056-11065.
- (38) Lucken, E. A. C., *Nuclear Quadrupole Coupling Constants*. Academic Press: London, 1969; p 360.
- (39) Ramachandran, R.; Oldfield, E., *J. Chem. Phys.* **1984**, 80, (2), 674-677.
- (40) Harbison, G. S.; Slokenbergs, A.; Barbara, T. M., *J. Chem. Phys.* **1989**, 90, (10), 5292-5298.
- (41) Harbison, G. S.; Slokenbergs, A., *Z. Naturforsch. Sect. A-J. Phys. Sci.* **1990**, 45, (3-4), 575-580.
- (42) Creel, R. B.; Von Meerwall, E.; Griffin, C. F.; Barnes, R. G., *J. Chem. Phys.* **1973**, 58, (11), 4930-5.
- (43) Sandland, T. O.; Du, L.-S.; Stebbins, J. F.; Webster, J. D., *Geochim. Cosmochim. Acta* **2004**, 68, (24), 5059-5069.
- (44) Bryukhova, E. V.; Semin, G. K.; Alimov, I. M.; Nesmeyan, A. N.; Nogina, O. V.; Dubovits, V. A.; Kuznetso, S. I., *J. Organomet. Chem.* **1974**, 81, (2), 195-199.
- (45) Kuznetsov, S. I.; Bryukhova, E. V.; Khotsyanova, T. L.; Semin, G. K., *Z. Naturforsch. Sect. A-J. Phys. Sci.* **1994**, 49, (4-5), 627-629.
- (46) Rhodes, H. E.; Wang, P. K.; Stokes, H. T.; Slichter, C. P.; Sinfelt, J. H., *Phys. Rev. B* **1982**, 26, (7), 3559-3568.
- (47) Sparks, S. W.; Ellis, P. D., *J. Am. Chem. Soc.* **1986**, 108, (12), 3215-3218.
- (48) Bastow, T. J., *Z. Naturforsch. Sect. A-J. Phys. Sci.* **1994**, 49, (1-2), 320-328.
- (49) Bastow, T. J.; Smith, M. E., *Solid State Nucl. Magn. Reson.* **1992**, 1, (4), 165-174.
- (50) Lipton, A. S.; Wright, T. A.; Bowman, M. K.; Reger, D. L.; Ellis, P. D., *J. Am. Chem. Soc.* **2002**, 124, (20), 5850-5860.

- (51) Kennedy, M. A.; Vold, R. L.; Vold, R. R., *J. Magn. Reson* **1991**, 92, (2), 320-331.
- (52) Medek, A.; Frydman, V.; Frydman, L., *J. Phys. Chem. A* **1999**, 103, (25), 4830-4835.
- (53) Massiot, D.; Farnan, I.; Gautier, N.; Trumeau, D.; Trokiner, A.; Coutures, J. P., *Solid State Nucl. Magn. Reson.* **1995**, 4, (4), 241-248.
- (54) Meiboom, S.; Gill, D., *Rev. Sci. Inst.* **1958**, 29, 688-691.
- (55) Carr, H. Y.; Purcell, E. M., *Phys. Rev.* **1954**, 94, 630-638.
- (56) Larsen, F. H.; Jakobsen, H. J.; Ellis, P. D.; Nielsen, N. C., *J. Phys. Chem. A* **1997**, 101, (46), 8597-8606.
- (57) Cheng, J. T.; Ellis, P. D., *J. Phys. Chem.* **1989**, 93, (6), 2549-2555.
- (58) Larsen, F. H.; Jakobsen, H. J.; Ellis, P. D.; Nielsen, N. C., *Mol. Phys.* **1998**, 95, (6), 1185-1195.
- (59) Larsen, F. H.; Jakobsen, H. J.; Ellis, P. D.; Nielsen, N. C., *Chem. Phys. Lett.* **1998**, 292, (4-6), 467-473.
- (60) Larsen, F. H.; Jakobsen, H. J.; Ellis, P. D.; Nielsen, N. C., *J. Magn. Reson.* **1998**, 131, (1), 144-147.
- (61) Tang, J. A.; Masuda, J. D.; Boyle, T. J.; Schurko, R. W., *ChemPhysChem* **2006**, 7, (1), 117-131.
- (62) Hung, I.; Rossini, A. J.; Schurko, R. W., *J. Phys. Chem. A* **2004**, 108, (34), 7112-7120.
- (63) Lipton, A. S.; Bergquist, C.; Parkin, G.; Ellis, P. D., *J. Am. Chem. Soc.* **2003**, 125, (13), 3768-3772.
- (64) Wailes, P. C.; Weigold, H., *J. Organomet. Chem.* **1970**, 24, (2), 405-411.
- (65) Wailes, P. C.; Weigold, H.; Bell, A. P., *J. Organomet. Chem.* **1971**, 33, (2), 181-188.
- (66) Eichele, K.; Wasylishen, R. E. *WSolids: Solid-State NMR Spectrum Simulation*, 2001.
- (67) Frisch, M. J. e. a. *Gaussian 03*, Rev. B.03; Gaussian, Inc.: Pittsburgh, 2003.
- (68) Lee, C.; Yang, W.; Parr, R. G., *Phys. Rev. B* **1988**, 37, 785-789.

- (69) Woon, D. E.; Dunning, T. H., *J. Chem. Phys.* **1995**, 103, (11), 4572-4585.
- (70) Dunning, T. H., *J. Chem. Phys.* **1989**, 90, (2), 1007-1023.
- (71) Huzinaga, S., *Gaussian Basis Sets for Molecular Calculations*. Elsevier: New York, 1984.
- (72) Hay, P. J.; Wadt, W. R., *J. Chem. Phys.* **1985**, 82, (1), 270-283.
- (73) Hay, P. J.; Wadt, W. R., *J. Chem. Phys.* **1985**, 82, (1), 299-310.
- (74) Ditchfield, R., *Mol. Phys.* **1974**, 27, 789-807.
- (75) Wolinski, K.; Hinton, J. F.; Pulay, P., *J. Am. Chem. Soc.* **1990**, 112, (23), 8251-8260.
- (76) Gee, M.; Wasylishen, R. E.; Laaksonen, A., *J. Phys. Chem. A* **1999**, 103, (50), 10805-10812.
- (77) Baerends, E. J.; Autschbach, J.; Berces, A.; Bickelhaupt, F. M.; Bo, C.; Boerrigter, P. M.; Cavallo, L.; Chong, D. P.; Deng, L.; Dickson, R. M.; Ellis, D. E.; van Faassen, M.; Fan, L.; Fischer, T. H.; Fonseca Guerra, C.; van Gisbergen, S. J. A.; Groeneveld, J. A.; Gritsenko, O. V.; Gruning, M.; Harris, F. E.; van den Hoek, P.; Jacob, C. R.; Jacobsen, H.; Jensen, L.; van Kessel, G.; Kootstra, F.; van Lenthe, E.; McCormack, D. A.; Michalak, A.; Neugebauer, J.; Osinga, V. P.; Patchkovskii, S.; Philipsen, P. H. T.; Post, D.; Pye, C. C.; Ravenek, W.; Ros, P.; Schipper, P. R. T.; Schreckenbach, G.; Snijders, J. G.; Sol`a, M.; Swart, M.; Swerhone, D.; te Velde, G.; Vernooijs, P.; Versluis, L.; Visscher, L.; Visser, O.; Wang, F.; Wesolowski, T. A.; van Wezenbeek, E.; Wiesenekker, G.; Wolff, S. K.; Woo, T. K.; Yakovlev, A. L.; Ziegler, T. *ADF2007*, SCM, Theoretical Chemistry, Vrije Universiteit: Amsterdam.
- (78) Fonseca Guerra, C.; Snijders, J. G.; te Velde, G.; Baerends, E. J., *Theor. Chem. Acc.* **1998**, 99, (6), 391-403.
- (79) Velde, G. T.; Bickelhaupt, F. M.; Baerends, E. J.; Guerra, C. F.; Van Gisbergen, S. J. A.; Snijders, J. G.; Ziegler, T., *J. Comput. Chem.* **2001**, 22, (9), 931-967.
- (80) Rossini, A. J.; Mills, R. W.; Briscoe, G. A.; Norton, E. L.; Geier, S. J.; Hung, I.; Zheng, S.; Autschbach, J.; Schurko, R. W., *J. Amer. Chem. Soc.* **2009**, 131, (9), 3317-3330.

- (81) Kraus, W.; Nolze, G. *PowderCell for Windows*, Federal Institute for Materials Research and Testing: Berlin, Germany, 2000.
- (82) Repo, T.; Klinga, M.; Mutikainen, I.; Su, Y.; Leskela, M.; Polamo, M., *Acta Chem. Scand.* **1996**, 50, (12), 1116-1120.
- (83) Soloveichik, G. L.; Arkhireeva, T. M.; Bel'skii, V. K.; Bulychev, B. M., *Metalloorganicheskaya Khimiya* **1988**, 1, (1), 226-30.
- (84) Nieger, M.; Hupfer, H., *Private Communication* **1999**, CSD Code: CDCPTI04.
- (85) Kuznetsov, S. I.; Bryukhova, E. V.; Semin, G. K., *Izvestiya Akademii Nauk Sssr Seriya Fizicheskaya* **1981**, 45, (3), 476-486.
- (86) Bohme, U.; Rittmeister, B., *Private Communication* **1998**, CSD Code: GEJPEQ.
- (87) Engelhardt, L. M.; Papasergio, R. I.; Raston, C. L.; White, A. H., *Organometallics* **1984**, 3, (1), 18-20.
- (88) Hunter, W. E.; Hrcncir, D. C.; Bynum, R. V.; Penttila, R. A.; Atwood, J. L., *Organometallics* **1983**, 2, (6), 750-755.
- (89) Martin, A.; Mena, M.; Palacios, F., *J. Organomet. Chem.* **1994**, 480, (1-2), C10-C11.
- (90) Power, W. P.; Wasylshen, R. E.; Mooibroek, S.; Pettitt, B. A.; Danchura, W., *J. Phys. Chem.* **1990**, 94, (2), 591-598.
- (91) Arfken, G., *Mathematical Methods for Physicists*. 3rd ed.; Academic Press: New York, 1985.
- (92) Rose, M. E., *Elementary Theory of Angular Momentum*. Wiley: New York, 1957.
- (93) Bohman, J. A.; Weinhold, F.; Farrar, T. C., *J. Chem. Phys.* **1997**, 104, 1173-1184.
- (94) Weinhold, F., Natural Bond Orbital Methods. In *Encyclopedia of Computational Chemistry*, von Rague Schleyer, P., Ed. John Wiley & Sons: Chichester, UK, 1998; Vol. 3, pp 1792-1811.
- (95) Autschbach, J.; Zheng, S. H.; Schurko, R. W., *Concepts Magn. Reson. Part A* **36A**, (2), 84-126.
- (96) Autschbach, J., *J. Chem. Phys.* **2007**, 127, (12), 124106-11.

- (97) Autschbach, J., *J. Chem. Phys.* **2008**, 128, (16), 164112-11.
- (98) Autschbach, J.; Le Guennic, B., *J. Chem. Educ.* **2007**, 84, (1), 156-171.
- (99) Boshalaa, A. M. A.; Simpson, S. J.; Autschbach, J.; Zheng, S., *Inorg. Chem.* **2008**, 47, (20), 9279-9292.
- (100) Townes, C. H.; Dailey, B. P., *J. Chem. Phys.* **1949**, 17, 782-96.
- (101) Wailes, P. C.; Weigold, H.; Bell, A. P., *J. Organomet. Chem.* **1971**, 27, (3), 373-378.
- (102) Kautzner, B.; Wailes, P. C.; Weigold, H., *J. Chem. Soc., Chem. Commun.* **1969**, (19), 1105.
- (103) Schwartz, J.; Labinger, J. A., *Angew. Chem.-Int. Edit. Engl.* **1976**, 15, (6), 333-340.
- (104) Hart, D. W.; Schwartz, J., *J. Am. Chem. Soc.* **1974**, 96, (26), 8115-8116.
- (105) Spletstoser, J. T.; White, J. M.; Tunoori, A. R.; Georg, G. I., *J. Am. Chem. Soc.* **2007**, 129, (11), 3408-3419.
- (106) Wipf, P.; Nunes, R. L., *Tetrahedron* **2004**, 60, (6), 1269-1279.
- (107) Wipf, P.; Jahn, H., *Tetrahedron* **1996**, 52, (40), 12853-12910.
- (108) Harlan, C. J.; Bott, S. G.; Barron, A. R., *J. Chem. Soc.-Dalton Trans.* **1997**, (4), 637-641.
- (109) Bradley, C. A.; Lobkovsky, E.; Keresztes, I.; Chirik, P. J., *J. Am. Chem. Soc.* **2006**, 128, (19), 6454-6467.
- (110) Pool, J. A.; Bradley, C. A.; Chirik, P. J., *Organometallics* **2002**, 21, (6), 1271-1277.
- (111) Bhattacharyya, R.; Frydman, L., *J. Chem. Phys.* **2007**, 127, (19), 194503-8.
- (112) O'Dell, L. A.; Schurko, R. W., *Chem. Phys. Lett.* **2008**, 464, (1-3), 97-102.

Chapter 3: Solid-State ^{91}Zr NMR Spectroscopy Studies of Zirconocene Olefin Polymerization Catalyst Precursors

3.1 Introduction

Cyclopentadienyl (Cp) transition metal complexes (metallocenes) have found increasing use as both homogeneous and heterogeneous olefin polymerization catalysts in industrial processes over the last 15 to 20 years.¹⁻⁵ Metallocene catalysts offer several advantages over the traditional heterogeneous Ziegler-Natta⁶⁻⁹ (i.e., TiCl_4 supported on MgCl_2) and Philips^{7, 10, 11} (i.e., CrO_x supported on SiO_2) catalysts, such as generally higher polymerization activities and resultant polymers with narrow molecular weight distributions and potentially higher molecular weights. The tacticity of the resulting polymers can also be easily controlled via judicious alteration of the Cp ligand framework.^{2, 5, 12, 13} All of these advantages can be attributed to the “single site” nature of the metallocene catalysts, standing in stark contrast to the heterogeneous Ziegler-Natta and Philips catalysts, which possess several different active surface sites that give rise to correspondingly non-uniform polymers. In particular, zirconium metallocene derivatives (zirconocenes) have probably attracted the most research interest due to their practical properties, which include stability at conventional polymerization temperatures, low relative cost of materials and high catalytic activities.⁵

For most industrial processes heterogeneous catalysts are preferred. For this reason, metallocenes and other organometallic catalysts are frequently immobilized onto inorganic support materials (e.g., SiO_2 , MgCl_2 , Al_2O_3). A cocatalyst, usually methylaluminoxane (MAO), may be contacted with the support before or after

immobilization of the metallocene.^{3,4} However, the insolubility and disordered nature of the surface-supported metallocene pre-catalysts and cocatalysts prevent their characterization by standard techniques, such as X-ray diffraction (XRD) and solution NMR spectroscopy. Classical surface chemistry characterization techniques such as IR,¹⁴⁻¹⁸ XPS,^{16, 19-21} and MAS ¹H, ¹³C and ²⁹Si SSNMR^{15, 16, 18, 22-28} spectroscopy have frequently been employed to study supported organometallic complexes and cocatalysts. Data obtained from these techniques have revealed that the peripheral Cp ligands remain coordinated to the metal centre upon immobilization and that alkyl groups bound to the metal center may be transferred to Lewis acid sites on the support. However, there are several ambiguities regarding the interactions between the metallocene pre-catalyst and cocatalyst in both homogeneous and heterogeneous systems. For example, (MAO) is the preferred cocatalyst for zirconocenes in industrial olefin polymerization; however, its molecular structure remains poorly understood.^{3,4, 29-32} Studies by Jordan, Marks and Rausch on dimethyl zirconocene and tris- and tetra(pentafluorophenyl)boron adducts have demonstrated that the generation of a zirconocene-cocatalyst ion pair of the form $[\text{Cp}_2\text{ZrMe}^+][\text{A}^-]$ is required to generate an active olefin polymerization catalyst.³³⁻³⁸ Solution ¹³C and ⁹¹Zr NMR^{39, 40} and solid-state ¹³C NMR experiments⁴¹ conducted on MAO-zirconocene adducts with low Al:M (M = Zr, Ti) ratios (*ca.* 5-20) have demonstrated that the reaction between metallocene dichlorides and MAO results in the formation of similar cationic zirconocenes. However, in order to obtain highly active catalysts very large MAO:zirconocene ratios are required (typically 10² to 10⁴:1).^{38, 42} The catalyst structure at high MAO:zirconocene ratios also remains poorly understood.³⁸

Similarly, intermediate species of the type $\text{Cp}_2\text{Zr(R)(olefin)}^+$ are generally assumed to form during the polymerization process.^{5,43} For all of these reasons, the development of additional tools capable of probing the structure of zirconocenes would be invaluable.

Our group has been investigating the possibility of utilizing solid-state NMR (SSNMR) spectra of quadrupolar (nuclear spin, $I > 1/2$) metal nuclei in metallocenes to probe the structures and identities of a variety of metallocene species, including some which are utilized in olefin polymerization. Our previous studies on model crystalline metallocene systems include ^{139}La SSNMR of tris(cyclopentadienyl)lanthanides, ^{93}Nb SSNMR of a variety of half-sandwich niobocenes, and ^{91}Zr SSNMR of bis(cyclopentadienyl)zirconium dichloride (Cp_2ZrCl_2).⁴⁴⁻⁴⁶ The SSNMR spectra of metal nuclei that lie at the “heart” of these metallocenes have allowed us to examine the electronic environment and molecular symmetry from the perspective of the central metal atom. Additionally, we have also recently presented a ^{35}Cl SSNMR study of crystalline group IV metallocene chloride complexes.⁴⁷ Because of our success with these bulk crystalline systems, and the importance of zirconocenes in heterogeneous catalytic production of polyolefins, it seems that ^{91}Zr SSNMR is a logical choice for the characterization of immobilized metallocene catalysts.

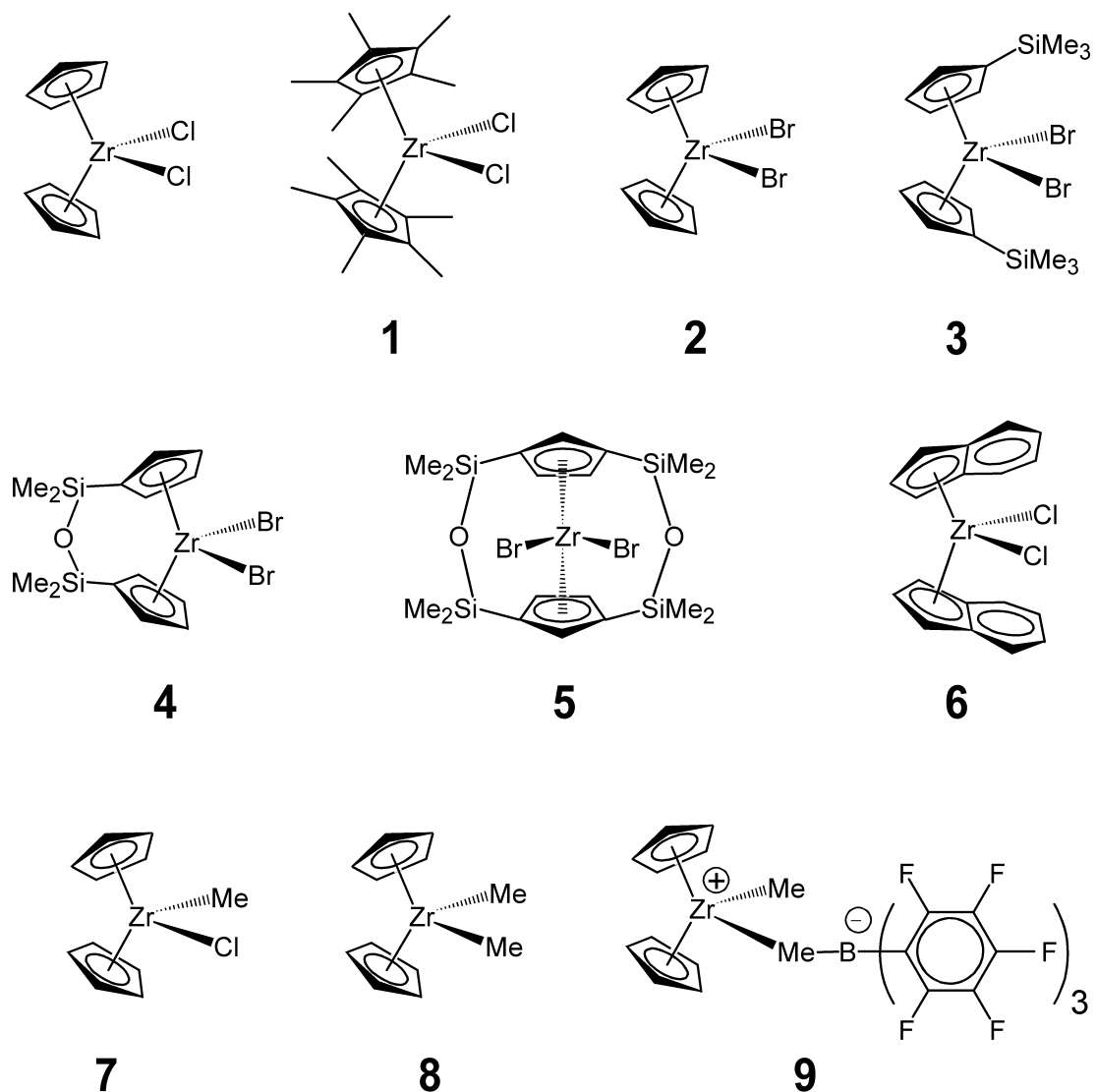
Owing to advances in hardware and pulse sequence programming, as well as the increased availability of high field NMR spectrometers, there has been a recent flurry of activity in the acquisition of SSNMR spectra of unresponsive quadrupolar nuclei⁴⁸⁻⁵⁶ such as ^{91}Zr (*vide infra*). Notably, the significant signal to noise (S/N) enhancement brought about by the quadrupolar Carr-Purcell Meiboom-Gill (QCPMG) pulse sequence⁵⁷ has

encouraged much of this work. Recently, Bhattacharyya and Frydman demonstrated the use of adiabatic frequency swept pulses (WURST pulses)^{58,59} for the acquisition of wide-line SSNMR spectra of quadrupolar nuclei.⁶⁰ Our research group has combined this approach with the QCPMG protocol and developed the WURST-QCPMG experiment.⁶¹⁶² We have found that WURST-QCPMG, in combination with frequency stepped acquisition, is the most efficient method to date for the acquisition of ultra-wide-line SSNMR powder patterns of quadrupolar nuclei (which we define as patterns > 250 kHz in breadth, which require frequency-stepped experiments, specialized pulse sequences and/or hardware, high magnetic fields, etc. for their acquisition). These techniques are vital for ⁹¹Zr SSNMR studies because many zirconium compounds exhibit large quadrupolar interactions (⁹¹Zr quadrupole coupling constants, C_Q , typically range from 10 to 30 MHz) which result in extremely broad central transition (CT) patterns.

There are relatively few NMR studies of zirconium compounds in the condensed phase owing to the relatively low sensitivity of ⁹¹Zr ($I = 5/2$), which has a moderate quadrupole moment ($Q(^{91}\text{Zr}) = -1.76(3) \times 10^{-29} \text{ m}^2$),⁶³ a low natural abundance (11.23%) and a relatively low magnetogyric ratio ($-2.49750 \times 10^7 \text{ rad T}^{-1} \text{ s}^{-1}$). Previous studies have been limited to extended systems such as zirconium oxides, phosphates, silicates and halides.⁶⁴⁻⁷⁶ Our previous work on Cp_2ZrCl_2 remains the only example of a molecular system studied by ⁹¹Zr SSNMR.⁴⁵ Therefore, it is of importance to initially characterize model zirconocene compounds in order to correlate the structural features of metallocenes with the NMR interaction tensor parameters obtained from experimental NMR spectra. These model systems will also aid in determining the most suitable quantum chemical

methods for the accurate calculation of ^{91}Zr NMR parameters, which should permit future theoretical predictions of unknown metallocene structures.

Herein, we report a comprehensive ^{91}Zr SSNMR study of a series of zirconocenes, which serve as precursors for the preparation of heterogeneous and homogeneous catalysts (compounds **1-8**, Scheme 3.1). We have also acquired the ^{91}Zr SSNMR spectrum of an active polymerization catalyst $[\text{Cp}_2\text{ZrMe}][\text{MeB}(\text{C}_6\text{F}_5)_3]$ (**9**). These samples were examined in order to obtain the ^{91}Zr electric field gradient (EFG) and chemical shift (CS) tensor parameters for a diverse range of zirconocene structural motifs. Extensive quantum chemical calculations of ^{91}Zr EFG and CS tensor parameters are presented herein, and are used to rationalize the origin of the observed NMR parameters and related to the molecular and electronic structures of the complexes. Quantum chemical calculations conducted with variable Zr-X (X = Cl, Me) bond lengths were performed in order to understand the large differences observed in the EFG tensor parameters of several complexes. Previous solution ^{91}Zr NMR studies have prefaced and inspired this current work.⁷⁷⁻⁸² In particular, Bühl, Hopp, von Philipsborn (BHP) and co-workers have studied compounds **1, 2, 3, 7, 8** and other compounds analogous to **4** and **5** using solution ^{91}Zr NMR and quantum mechanical calculations;⁷⁹ therefore, we will often refer to their work for comparison with the results presented here.



Scheme 3.1. Schematic representation of compounds which have been studied by solid-state ^{91}Zr NMR: bis(cyclopentadienyl)zirconium dichloride [Cp_2ZrCl_2], bis(pentamethylcyclopentadienyl)zirconium dichloride [$\text{Cp}^*_2\text{ZrCl}_2$ (**1**)], bis(cyclopentadienyl)zirconium dibromide [Cp_2ZrBr_2 (**2**)], bis(trimethylsilylcyclopentadienyl)zirconium dibromide [$(\text{Me}_3\text{SiC}_5\text{H}_4)_2\text{ZrBr}_2$ (**3**)], [$\text{O}(\text{Me}_2\text{SiC}_5\text{H}_4)_2\text{ZrBr}_2$ (**4**)], [$(1,3\text{-C}_5\text{H}_3)(\text{SiMe}_2\text{OSiMe}_2)_2(1,3\text{-C}_5\text{H}_3)\text{ZrBr}_2$ (**5**)], bis(indenyl)zirconium dichloride [$\text{Ind}_2\text{ZrCl}_2$ (**6**)], bis(cyclopentadienyl)methylzirconium chloride [Cp_2ZrMeCl (**7**)], bis(cyclopentadienyl)dimethylzirconium [Cp_2ZrMe_2 (**8**)], and the active polymerization catalyst [$\text{Cp}_2\text{ZrMe}^+[\text{MeB}(\text{C}_6\text{F}_5)_3]^-$] (**9**).

3.2 Experimental

Samples. Samples of Cp_2ZrCl_2 , $\text{Cp}^*_2\text{ZrCl}_2$ (**1**) and $\text{Ind}_2\text{ZrCl}_2$ (**6**) were purchased from Strem Chemicals, Inc. and used without purification. Samples of Cp_2ZrBr_2 (**2**), $(\text{Me}_3\text{SiC}_5\text{H}_4)_2\text{ZrBr}_2$ (**3**),⁸³ $\text{O}(\text{Me}_2\text{SiC}_5\text{H}_4)_2\text{ZrBr}_2$ (**4**),⁸³ $(\text{O}(\text{Me}_2\text{Si})_2\text{C}_5\text{H}_3)_2\text{ZrBr}_2$ (**5**),⁸³ Cp_2ZrMeCl (**7**),⁸⁴ Cp_2ZrMe_2 (**8**),⁸⁵ and $[\text{Cp}_2\text{ZrMe}][\text{MeB}(\text{C}_6\text{F}_5)_3]$ (**9**)³⁷ were synthesized according to previously published literature procedures and characterized by ^1H , ^{13}C and ^{19}F solution NMR.

Solid-State NMR Spectroscopy. NMR experiments were performed on a Varian Infinityplus NMR console with an Oxford 9.4 T wide bore magnet for which the ^{91}Zr resonance frequency (ν_0) is 37.16 MHz. Typical central transition selective 90° pulse widths of *ca.* 2.0 μs (corresponding to radio frequency fields of ~ 40 kHz) were employed along with pulse delays between 0.7 s and 2.0 s. Between 6500 and 150000 transients were acquired. Continuous wave ^1H decoupling was applied for most MAS and static experiments. For the acquisition of static and MAS spectra a Hahn echo sequence with a 16-step phase cycle was employed.⁵⁷ Double frequency sweep (DFS)^{86, 87} or fast radio-frequency amplitude modulated⁸⁸ (FAM) schemes were employed for some of the ^{91}Zr static and MAS spectra in order to provide signal enhancement and reduce experimental times at 9.4 T. For the acquisition of broad static ^{91}Zr NMR spectra the QCPMG pulse sequence⁵⁷ and WURST-QCPMG⁶⁰⁻⁶² pulse sequences were employed. MAS ^{91}Zr NMR spectra were typically acquired at spinning frequencies (ν_{rot}) between 10000 and 15000 Hz. 5.0 mm outer diameter (o.d.) ZrO_2 rotors were employed for acquisition of MAS spectra. Teflon or Delrin 5.0 mm o.d. sample tubes and shortened glass NMR tubes were

used for non-spinning experiments. Zirconium chemical shifts were referenced to a concentrated dichloromethane (CH_2Cl_2) solution of Cp_2ZrCl_2 ($\delta_{\text{iso}} = 0.0$ ppm). A complete list of experimental details can be found in Appendix B (Tables B1 - B5).

High-field static NMR experiments were performed on a 21.1 T Bruker Avance II NMR spectrometer for which $\nu_0(^{91}\text{Zr}) = 83.7$ MHz. Samples were placed in sealed shortened 5.0 mm or 4.0 mm o.d. glass NMR tubes or a 10 o.d. mm teflon sample tube. Spectra were acquired on home built 5 mm or 10 mm single channel probes or a Bruker 4 mm MAS HX probe. The Hahn echo, QCPMG or WURST-QCPMG pulse sequences were employed.

Spectral Simulations. Analytical simulations of NMR spectra were performed with the WSOLIDS software package.⁸⁹ The convention used for the specification of the chemical shift (CS) tensors is: $\delta_{11} \geq \delta_{22} \geq \delta_{33}$; $\delta_{\text{iso}} = (\delta_{11} + \delta_{22} + \delta_{33})/3$; $\Omega = \delta_{11} - \delta_{33}$; $\kappa = 3(\delta_{22} - \delta_{\text{iso}})/\Omega$. The convention used for specification of electric field gradient (EFG) tensors is: $|V_{33}| \geq |V_{22}| \geq |V_{11}|$; $C_Q = eQV_{33}/h$; $\eta_Q = (V_{11} - V_{22})/V_{33}$. The Rose convention is used to describe the order and direction of Euler angle rotations, which describe the relative orientation of the EFG and CS tensors.^{90, 91}

Theoretical Calculations. Calculations of EFG tensors were performed using Gaussian 03⁹² employing molecular coordinates for isolated molecules resolved by X-ray diffraction.^{79, 93, 94} Atomic coordinates for **5** were obtained from a preliminary single crystal XRD structure. In all cases idealized hydrogen atom positions were employed. For some calculations, “idealized” Cp ring coordinates were employed (see discussion section for details). Computations were carried out using the restricted Hartree-Fock

(RHF), and hybrid density functional theory methods (B3LYP).⁹⁵⁻⁹⁷ Several all-electron basis sets on zirconium were employed (see Appendix B), including (17s13p9d)^{98,99} contracted to [12s9p5d], with two sets of diffuse *p* functions¹⁰⁰ ($\alpha_p = 0.11323$ and 0.04108) and one diffuse *d* function ($\alpha_d = 0.0382$),⁷⁹ and (17s11p8d) contracted to [6s3p3d] or [12s7p4d].⁹⁸ The double-zeta basis set of Dunning was employed for Cl.¹⁰¹ Additional Cl basis sets were also tested. The 6-311G** basis sets included with Gaussian 03 were used for all other atoms. Calculations with all electron basis sets on Br were also attempted (see Appendix B). These Br basis sets include (13s10p1d) contracted to [4s3p1d],¹⁰² the triple-zeta basis set of Dunning¹⁰³ and the quadruple-zeta [11s7p4d]¹⁰⁴ and triple-zeta [8s6p2d]⁹⁹ basis sets of Ahlrich. Most basis sets were obtained from the EMSL Basis Set Exchange.¹⁰⁵ Quadrupolar coupling constants were converted from atomic units (a.u.) to Hz by multiplying the largest component of the EFG tensor, V_{33} , by $eQ/h \times 9.71736 \times 10^{21} \text{ V m}^{-2}$, where $Q(^{91}\text{Zr}) = -1.76(3) \times 10^{-29} \text{ m}^2$,⁶³ and $e = -1.602188 \times 10^{-19} \text{ C}$. The EFGShield program was used to extract Euler angles and generate EFG and CS tensor orientations from the Gaussian 03 output.¹⁰⁶

X-ray Diffraction Experiments. Results from single crystal X-ray diffraction experiments are provided in Appendix B (Figures B1-B3 and Tables B6 - B8). Samples for powder X-ray diffraction (PXRD) experiments were placed into 0.7 mm glass capillary tubes and flame sealed. PXRD patterns were collected using a Bruker AXS HI-STAR system using a General Area Detector Diffractions System. The X-ray source was Cu K α radiation (1.540598 Å) and an area detector using a 2 θ range between 4.0° to 65.0° was employed. PXRD patterns were simulated with the PowderCell software package.¹⁰⁷

3.3 Results and Discussion

MAS ⁹¹Zr Solid-State NMR Spectra. MAS ⁹¹Zr SSNMR spectra of Cp₂ZrCl₂ and complexes **1** - **5** are pictured in Figure 3.1. Before the spectra of individual complexes are discussed, there are several general observations to be made. Those complexes which feature coordination by unsubstituted or substituted Cp ligands (denoted as Cp') and halogens possess relatively small ⁹¹Zr quadrupolar coupling constants resulting in relatively narrow static and MAS ⁹¹Zr powder patterns (**6** being the exception, *vide infra*). This allows for central-transition (CT) MAS ⁹¹Zr SSNMR spectra of complexes **1** - **5** to be acquired at a moderate magnetic field strength (9.4 T) and at sample spinning speeds below 15 kHz. All of the MAS ⁹¹Zr SSNMR spectra are clearly influenced by second-order quadrupolar broadening. The ⁹¹Zr EFG parameters (C_Q and η_Q) and isotropic chemical shift values (δ_{iso}) derived from simulation of these spectra are compiled in Table 3.1. The isotropic chemical shifts for **1** - **5** are in good agreement with values measured by BHP using solution ⁹¹Zr NMR.⁷⁹ It is apparent that MAS ⁹¹Zr SSNMR spectra can serve as a powerful tool for identification of zirconocenes, as variations in the ring substitution, type of halide, and overall symmetry of the molecule have an obvious influence on the lineshape of the spectra, with observed C_Q values ranging from 2.4 MHz to 6.35 MHz and η_Q values ranging from near 0 to near 1. In order to relate the molecular structures to the observed ⁹¹Zr NMR parameters, we have compiled the average bond lengths and inter-ligand angles from the single crystal XRD structures in Table 3.2.

Table 3.1. Experimentally Determined ^{91}Zr EFG and CS Tensor NMR Parameters

Compound	δ_{iso} (ppm)	$ C_Q $ (MHz) ^a	η_Q ^b	Ω (ppm) ^c	κ ^d	α (°)	β (°)	γ (°)
Cp_2ZrCl_2 ^e (site 1)	21(5)	6.2(3)	0.18(10)	340(40)	-0.6(3)	90(35)	86(10)	2(10)
Cp_2ZrCl_2 (site 2)	21(5)	6.5(3)	0.30(10)	350(40)	-0.7(3)	90(35)	86(10)	3(10)
$\text{Cp}^*_2\text{ZrCl}_2$ 1	208(2)	2.6(1)	0.22(10)	235(25)	-0.75(20)	20(40)	90(25)	90(10)
Cp_2ZrBr_2 2 ^f	128(10)	2.4(3)	0.40(20)	550(50)	-0.55(20)	40(90)	0(90)	0(90)
$(\text{Me}_3\text{Si}-\text{C}_5\text{H}_4)_2\text{ZrBr}_2$ 3	154(5)	4.7(1)	0.88(4)	-	-	-	-	-
$\text{O}(\text{Me}_2\text{SiC}_5\text{H}_4)_2\text{ZrBr}_2$ 4	143(3)	2.5(1)	0.68(7)	620(70)	-0.8(2)	40(20)	90(15)	35(40)
$(1,3-\text{C}_5\text{H}_3)(\text{SiMe}_2\text{OSiMe}_2)_2(1,3-\text{C}_5\text{H}_3)\text{ZrBr}_2$ 5	163(7)	3.9(2)	0.25(9)	530(60)	-0.55(20)	40(20)	30(15)	85(10)
$\text{Ind}_2\text{ZrCl}_2$ 6 (single site fit) ^g	20(50)	31.5(15)	0.33(20)	700(300)	0.6(9)	20(10)	75(15)	-40(40)
6 (two site fit, site 1)	60(50)	32.0(10)	0.25(20)	200(400)	-0.3(8)	80(60)	60(40)	4(60)
6 (two site fit, site 2)	60(50)	30.7(10)	0.38(20)	200(400)	-0.3(8)	80(60)	60(40)	4(60)
Cp_2ZrMeCl 7 (site 1)	230(100)	23.3(10)	0.35(10)	900(500)	-0.6(8)	5(70)	15(45)	85(70)
Cp_2ZrMeCl 7 (site 2)	230(100)	20.0(30)	0.75(15)	1000(500)	0.8(9)	80(40)	20(20)	5(40)
Cp_2ZrMe_2 8	475(40)	28.0(3)	0.40(4)	1750(300)	-0.9(3)	80(40)	90(5)	0(5)
$[\text{Cp}_2\text{ZrMe}][\text{MeB}(\text{C}_6\text{F}_5)_3]$ 9	350(100)	39.0(8)	0.76(6)	1000(400)	0.2(5)	90(10)	80(15)	86(40)

^a $C_Q = eQV_{33}/h$. ^b $\eta_Q = (V_{11} - V_{22})/V_{33}$. ^c $\Omega = \delta_{33} - \delta_{11}$. ^d $\kappa = 3(\delta_{22} - \delta_{\text{iso}})/\Omega$. ^eWe have previously studied this compound by ^{91}Zr SSNMR, see reference 45. ^fEstimated parameters from overlapping sites (see text for details). ^gSee text for details regarding single site and two site fits.

Table 3.2. Average Metrical Parameters of Single Crystal X-ray Diffraction Structures of Zirconocene Complexes^a

Compound	$r(\text{Zr-Hal})$ (Å)	$r(\text{Zr-Me})$ (Å)	$\angle \text{X-Zr-X}$ (°)	$r(\text{Zr-Cp}'_{\text{Cent}})$ (Å)	$\angle \text{Cp}'_{\text{Cent-Zr-Cp}'_{\text{Cent}}}$ (°)	Reference
Cp ₂ ZrCl ₂	2.45	-	97.0	2.20	129.3	[93]
Cp* ₂ ZrCl ₂ 1	2.46	-	95.4	2.26	130.9	[107]
(Me ₄ EtCp) ₂ ZrCl ₂ ^b	2.44	-	94.6	2.25	137.0	[122]
Cp ₂ ZrBr ₂ 2 ^c	2.61	-	96.7	2.19	129.0	[79]
(Me ₃ SiC ₅ H ₄) ₂ ZrBr ₂ 3	2.61	-	94.2	2.20	128.1	[112]
O(Me ₂ SiC ₅ H ₄) ₂ ZrBr ₂ 4	2.61	-	98.0	2.20	131.2	This work
(1,3-C ₅ H ₃)(SiMe ₂ OSiMe ₂) ₂ (1,3-C ₅ H ₃) ZrBr ₂ 5	2.60	-	96.7	2.19	130.4	This work
(1,3-C ₅ H ₃)(SiMe ₂ OSiMe ₂) ₂ (1,3-C ₅ H ₃) ZrBr ₂ 5 (123 K)	2.60	-	99.0	2.20	130.6	This work
Ind ₂ ZrCl ₂ 6	2.44	-	94.7	2.23	128.3	[93]
Cp ₂ ZrMeCl 7 ^d	2.51	2.23	94.5	2.21	131.4	This work
Cp ₂ ZrMeCl 7	2.49	2.36	95.1	2.21	131.1	[94]
Cp ₂ ZrMe ₂ 8	-	2.28	95.5	2.26	132.5	[94]
[Cp ₂ ZrMe][MeB(C ₆ F ₅) ₃] 9 ^e	-	2.25, 2.56	87.7	2.20	131.1	[119]

^a Parameters have been taken from previously reported single crystal X-ray diffraction structures. The parameters for **4**, **5** and **7** are taken from the structures reported in this work. ^b Quantum chemical calculations utilizing coordinates from the published crystal structure of **1** gave poor agreement with experimental NMR tensor parameters. Calculations employing atomic coordinates from (Me₄EtCp)₂ZrCl₂ gave much better results, therefore, we have listed the metrical parameters of this complex. ^c Conformation 2 of the second site in the asymmetric unit has been disregarded because the Cp_{cent}-Zr bond distance is significantly longer (2.21 Å) than the other distances in the structure. ^d The second methyl position in the asymmetric unit has been disregarded because the Zr-Me distance is abnormally short (2.176 Å). ^e The second Zr-Me distance reported corresponds to the methyl group which is bridging between the Zr and B atoms.

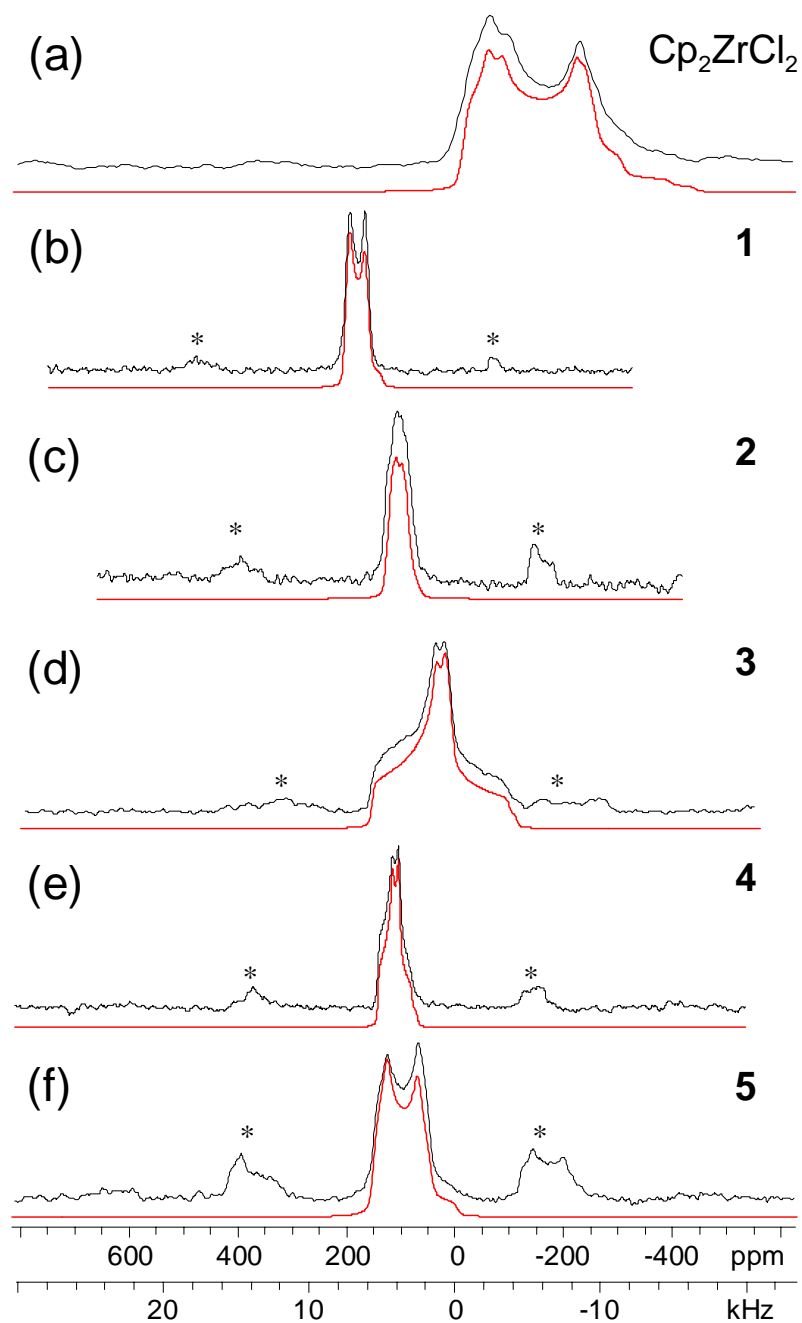


Figure 3.1. MAS ^{91}Zr SSNMR spectra (black traces) of (a) Cp_2ZrCl_2 at $\nu_{\text{rot}} = 15000$ Hz, (b) **1** [$\text{Cp}^*_2\text{ZrCl}_2$] at $\nu_{\text{rot}} = 10000$ Hz, (c) **2** [Cp_2ZrBr_2] at $\nu_{\text{rot}} = 10000$ Hz, (d) **3** [$(\text{Me}_3\text{SiC}_5\text{H}_4)_2\text{ZrBr}_2$] at $\nu_{\text{rot}} = 15500$ Hz, (e) **4** [$\text{O}(\text{Me}_2\text{SiC}_5\text{H}_4)_2\text{ZrBr}_2$] at $\nu_{\text{rot}} = 11000$ Hz and (f) **5** [$(1,3\text{-C}_5\text{H}_3)(\text{SiMe}_2\text{OSiMe}_2)_2(1,3\text{-C}_5\text{H}_3)\text{ZrBr}_2$] at $\nu_{\text{rot}} = 10000$ Hz. Corresponding analytical simulations (red traces) are shown beneath all experimental spectra. All spectra were acquired at 9.4 T. Asterisks denote spinning sidebands.

We previously acquired the MAS ^{91}Zr SSNMR spectrum of Cp_2ZrCl_2 at 9.4 T.⁴⁵ For the present work, a MAS spectrum was acquired at 21.1 T in an attempt to resolve two separate signals corresponding to the two distinct sites observed in the single crystal X-ray diffraction structure.⁹³ Multiple magnetic fields are useful for resolving overlapping sites, because broadening of the CT powder pattern due to the second order quadrupolar interaction and chemical shift dispersion are inversely and directly proportional to B_0 , respectively. The spectrum acquired at 21.1 T possesses a distinct “splitting” of the high frequency discontinuity of the CT powder pattern, indicative of the presence of two sites (Figure B4). A simulation employing two sites yielded similar values of C_Q (6.2 MHz and 6.5 MHz) and η_Q (0.18 and 0.30), and identical values of $\delta_{\text{iso}} = 21$ ppm, which is unsurprising given the similarity of the two Zr environments. The parameters obtained from the MAS spectra are similar to those previously reported by our research group.

The spectrum of **1** (Figure 3.1b) is characterized by a ^{91}Zr quadrupole coupling constant that is smaller than that of Cp_2ZrCl_2 by a factor of 2.4. The value of η_Q for **1** is similar to that observed for Cp_2ZrCl_2 , and δ_{iso} is approximately 180 ppm more positive. Examination of the crystal structures^{93, 108} of Cp_2ZrCl_2 and **1** reveals a slight lengthening in the average Zr-Cp' centroid and Zr-Cl distances in **1** compared to Cp_2ZrCl_2 , which is likely due to the steric bulk of the Cp* rings in **1**. A decrease in C_Q with lengthening of the metal-Cp' centroid distance is consistent with observations made from variable-temperature experiments on linear sodocenes¹⁰⁹ and CpK.¹¹⁰ BHP have also used ab initio calculations to demonstrate that the decrease in C_Q of **1** compared to Cp_2ZrCl_2 is caused

largely by the electronic effects of the highly basic Cp* ligand.⁷⁹

The MAS ⁹¹Zr SSNMR spectrum of **2** (Figure 3.1c) appears to show the overlap of narrow patterns from two distinct zirconium species. The observation of more than one zirconium site is in agreement with the existence of two distinct molecules in the asymmetric unit of **2**.⁷⁹ Unfortunately, the chemical shift dispersion at B₀ = 9.4 T is insufficient to resolve the nonequivalent sites of **2**, even with a high-resolution solid-state NMR technique such as triple-quantum (3Q) multiple-quantum (MQ) MAS^{111, 112} (Figure B5). Nevertheless, by considering the approximate width of the pattern, it is possible to make rough estimates of the maximum C_Q, as well as δ_{iso} and η_Q. The simulation of the MAS ⁹¹Zr SSNMR spectrum employs two sites which possess identical EFG tensor parameters and distinct δ_{iso} values of 125 ppm and 132 ppm. A MAS ⁹¹Zr SSNMR spectrum of **2** was also acquired at 21.1 T (Figure B6); however, even at this field, there is still insufficient resolution of the two sites. Nonetheless, acquisition of MAS and static ⁹¹Zr SSNMR spectra at two magnetic fields still allows for the accurate determination of the EFG tensor parameters (*vide infra*).

The average δ_{iso} of **2** is 128.5 ppm, which is *ca.* 100 ppm higher than that observed for Cp₂ZrCl₂. The η_Q value of **2** is similar to Cp₂ZrCl₂, while the C_Q value is approximately 2.5 times smaller, in accordance with the narrower ⁹¹Zr solution NMR linewidths observed by BHP for **2**. The Cp-Zr bond lengths and Cp-Zr-Cp angles are similar in both Cp₂ZrCl₂ and **2**, suggesting that the reduction in C_Q can be attributed to the increased lengths of Zr-Br bonds in comparison to Zr-Cl bonds (averages of 2.61 Å and 2.45 Å, respectively). This is further addressed in the quantum chemical calculation

section below.

The MAS ^{91}Zr SSNMR spectra of the zirconocene dibromides, **3**, **4** and **5** are shown in Figures 3.1d, 3.1e, and 3.1f, respectively. Complex **3** has a silane moiety on the Cp rings, while **4** and **5** have *ansa*-bridging siloxane moieties on the Cp ring. The observed values of δ_{iso} are between 143 and 163 ppm, which are near the value observed for **2** (128.5 ppm). The C_Q values are larger than those observed for **2**, but smaller than that observed for Cp_2ZrCl_2 . The values of η_Q are observed to be near 0 (**5**, $\eta_Q = 0.25$), intermediate (**4**, $\eta_Q = 0.68$) and near 1 (**3**, $\eta_Q = 0.88$), despite the superficial similarities in molecular structure for the three complexes, which have similar Zr-Cp' and Zr-Br bond lengths and Cp'-Zr-Cp' and Br-Zr-Br angles¹¹³ (Table 3.2), suggesting that the differences in the EFG tensor parameters may be due to inductive effects of the various silane substituents. In this regard, Bercaw and co-workers have performed a comprehensive spectroscopic and theoretical study of *ansa*-bridged zirconocene complexes and found that the electronic structure of the Cp'-zirconium bonds can be significantly affected by *ansa* bridges.¹¹⁴

Compounds **3**, **4** and **5** comprise a set of structures which model zirconocenes that have been tethered to a surface *via* reactive ancillary moieties. The conformation of **3** reflects zirconocene molecules prior to adsorption, while **4** and **5** serve as models of surface-tethered species. These results show great promise for using ^{91}Zr SSNMR for the characterization of surface-tethered zirconocenes, since (i) large changes in the substitution and conformation of the Cp' rings, such as for **3**, **4** and **5**, do not appear to cause large increases in C_Q , which would render simple MAS NMR experiments

untenable due to broadening of the MAS powder patterns, and (ii) MAS ^{91}Zr NMR spectra show sensitivity to slight changes in coordination and molecular geometry.

Static ^{91}Zr SSNMR Spectra. We have previously demonstrated that Cp_2ZrCl_2 possesses a significant ^{91}Zr chemical shift anisotropy (CSA); hence, CSA and associated Euler angles¹¹⁵⁻¹¹⁸ must be considered in simulations of static ^{91}Zr SSNMR spectra.⁴⁵ The broadening of CT powder patterns of half integer quadrupolar nuclei by the second-order quadrupolar interaction is inversely proportional to B_0 , while the broadening due to CSA is directly proportional to B_0 . Static spectra of all complexes have been acquired at two magnetic fields, in order to confirm the values of CS tensor parameters, the span (Ω) and skew (κ), and the Euler angles, which describe the relative orientations of the CS and EFG tensors. When the CSA and quadrupolar interaction are similar in magnitude, the Euler angles can influence the position and intensity of the discontinuities of the static powder patterns. The CS tensor parameters and Euler angles determined from the simulations are reported in Table 3.1.

The static ^{91}Zr SSNMR spectra of Cp_2ZrCl_2 , **1** and **2** acquired at 9.4 T and 21.1 T, and their analytical simulations are shown in Figure 3.2. The CS tensor parameters presented herein for Cp_2ZrCl_2 are $\Omega = 340$ and 350 ppm and $\kappa = -0.60$ and -0.70 , for sites 1 and 2, respectively. These parameters are slightly different from our previous values ($\Omega = 430$ ppm and $\kappa = -0.55$), due to the increased sensitivity of the spectrum acquired at 21.1 T to changes in the CS tensor parameters. The observation of a κ values near -1 indicates that the distinct component of the CS tensor is δ_{11} (and that δ_{22} and δ_{33} are similar in value). κ values near -1 are observed for most of these complexes,

suggesting that this is a general feature of zirconocenes.

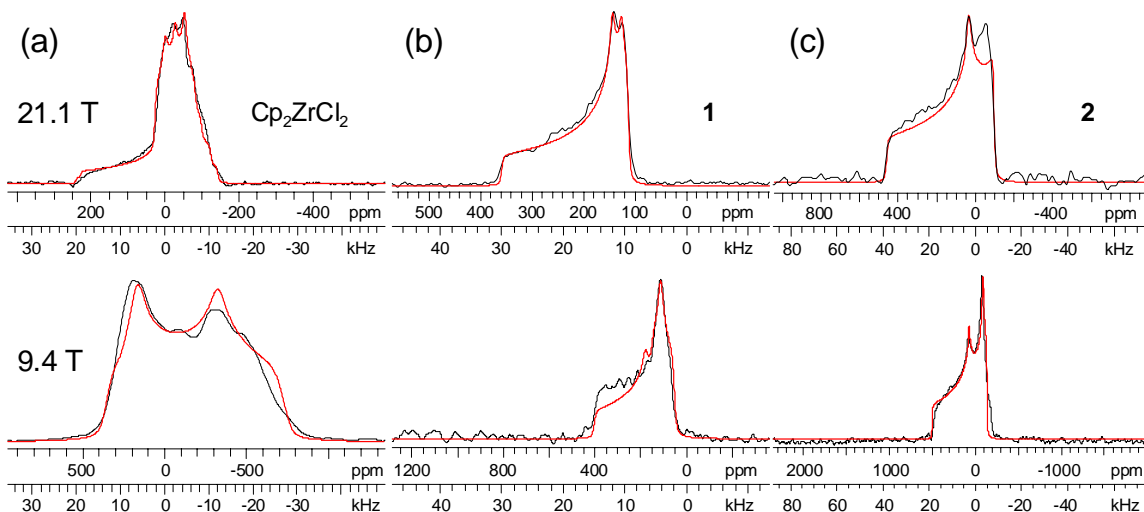


Figure 3.2. Static ^{91}Zr SSNMR spectra acquired at 9.4 T (bottom) and 21.1 T (top) of (a) Cp_2ZrCl_2 , (b) **1** [Cp^*ZrCl_2] and (c) **2** [Cp_2ZrBr_2]. Analytical simulations (red traces) which include the effects of CSA and Euler angles are overlaid on the experimental spectra.

The static spectra of **1** reveal that $\Omega = 235$ ppm and $\kappa = -0.75$. The symmetry of the CS tensor of **1** is similar to that of Cp_2ZrCl_2 , as indicated by κ , however, the value of Ω is reduced. The value of δ_{iso} for **1** indicates that the Zr nucleus is significantly deshielded with respect to Cp_2ZrCl_2 . The Zr-Cl distances of **1** are similar to those of Cp_2ZrCl_2 , suggesting that the differences in δ_{iso} and Ω arise from the increased basicity of the Cp^* ligand in comparison to the Cp ligands. The Euler angle β is near 90° for both **1** and Cp_2ZrCl_2 . β describes the angle separating the largest principal component of the EFG tensor (V_{33}) and the most shielded component of the CS tensor (δ_{33}) (meaning in this case they are perpendicular to one another). Calculated tensor orientations are discussed in the quantum chemical calculations section.

The static spectra of complex **2** reveals $\kappa = -0.6$, which is similar to Cp_2ZrCl_2 and **1**, but $\Omega = 550$ ppm, which is significantly larger than those of the chlorinated complexes. It is worth noting that the simulations of Cp_2ZrBr_2 provide a relatively poor match with the low frequency discontinuity of the static spectrum acquired at 21.1 T. Simulation of this spectrum is more difficult because of the presence of the two crystallographic sites with distinct NMR parameters, and the small quadrupolar interaction. For this reason, the uncertainties in Euler angles are large however, the breadths of the static spectra at both fields allows accurate measurements of Ω and κ to be obtained. With respect to the large zirconium CSA and small C_Q , the MAS ^{91}Zr SSNMR spectrum acquired at 21.1 T is of particular interest, possessing an extensive spinning sideband manifold not commonly observed for ^{91}Zr (Figure B6).

The static spectra of **4** and **5** are shown in Figure 3.3. The values of Ω obtained from these spectra are 530 ppm and 620 ppm, respectively. These CS tensor parameters are similar to those obtained from the other brominated species, **2**; however, the Euler angles of **4** and **5** are substantially different: β is near 90° and γ is 35° for **4**, while β is 30° and γ is near 90° for **5**. The similarity of their CS tensor parameters and their distinct n_Q values suggest that the EFG tensor is oriented differently within the molecular frames of these complexes (this is further addressed in the quantum chemical calculation section). Unfortunately, static spectra of **3** could not be obtained due to limited sample quantity and sample degradation. In summary, the MAS and static ^{91}Zr spectra of Cp_2ZrCl_2 and compounds **1** through **5** suggest that the solid-state ^{91}Zr NMR spectra of brominated zirconocenes are generally characterized by more positive δ_{iso} values and

larger Ω values than those of chlorinated zirconocenes, while the C_Q values are generally similar in magnitude.

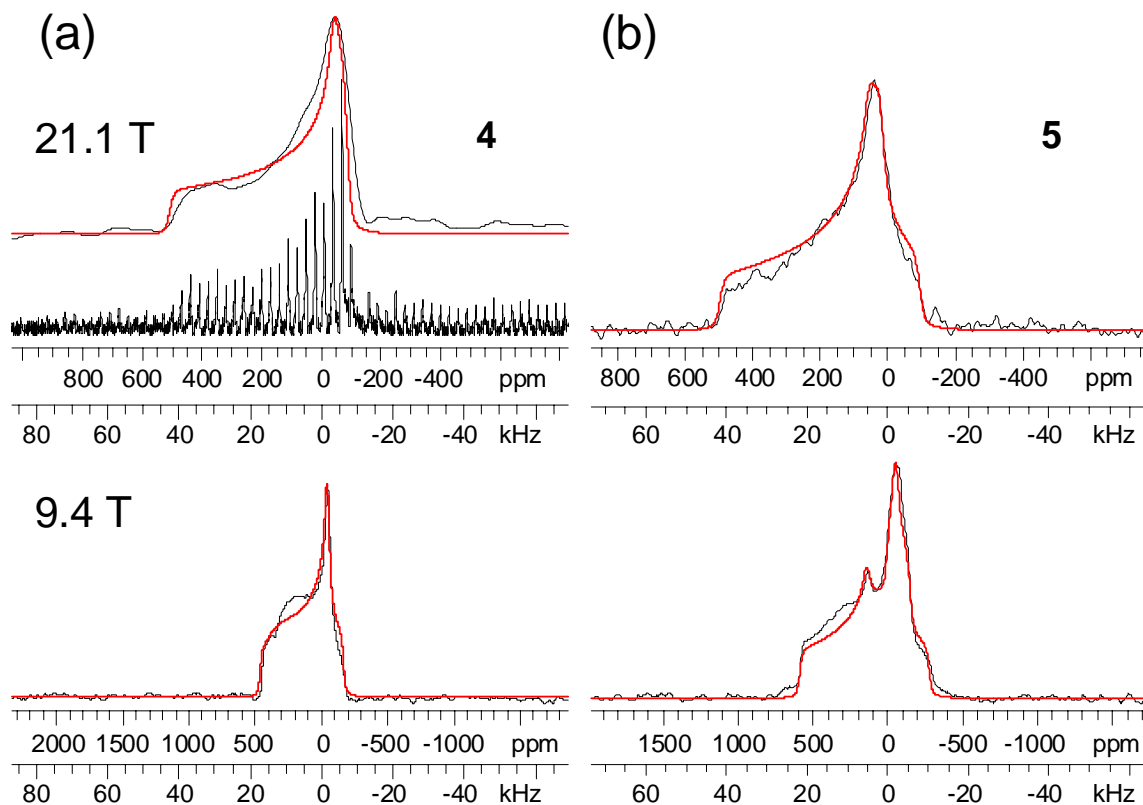


Figure 3.3. Static ^{91}Zr SSNMR spectra acquired at fields of 9.4 T (bottom) and 21.1 T (top) of (a) **4** [$\text{O}(\text{Me}_2\text{SiC}_5\text{H}_4)_2\text{ZrBr}_2$] and (b) **5** [$(1,3\text{-C}_5\text{H}_3)(\text{SiMe}_2\text{OSiMe}_2)_2(1,3\text{-C}_5\text{H}_3)\text{ZrBr}_2$]. The 21.1 T spectrum of **4** was acquired with the QCPMG sequence due to limited sample quantity. Both a spikelet spectrum and an echo spectrum resulting from co-addition of the echoes in the time domain are shown for **4**. Analytical simulations (red traces) which include the effects of CSA and Euler angles are overlaid on the experimental spectra.

In order to control the tacticity of the polymers produced by metallocene catalysts, it is necessary to alter the structure and symmetry of the coordinating Cp ligands.^{1,2,119} This is often accomplished by preparing metallocenes with modified Cp ligands such as the indenyl (Ind) and fluorenyl ligands. The static ^{91}Zr NMR spectra of the bis(indenyl)

complex, **6**, acquired at 9.4 T and 21.1 T are shown in Figure 3.4. Spectra acquired at 9.4 T display significant overlap with the $^{35/37}\text{Cl}$ satellite transitions,⁴⁷ making it difficult to resolve the static ^{91}Zr powder pattern at this field. This problem is lessened at 21.1 T due to a greater separation between the Larmor frequencies of $^{35/37}\text{Cl}$ and ^{91}Zr . When a simulation with only a single site is employed, poor agreement with the intensities of the experimental spectrum is observed (Figure 3.4a). The single site simulation also requires the use of a large value of Ω (700 ppm), in order to obtain the “splitting” of the two high-frequency discontinuities, which is much larger than the other chloride complexes (single site fit listed in Table 3.1). A simulation employing two sites (Figure 3.4b and 3.4c) results in an improved fit of the experimental spectrum and employs more realistic Ω values (200 ppm for each site). However, the previously published single crystal XRD structure shows the presence of only one magnetically distinct Zr site.⁹³ Solution ^1H and ^{13}C NMR spectroscopy confirm the sample is pure, and that the second pattern does not arise from an impurity (Figure B7). The single crystal X-ray data was acquired at 153 K while the ^{91}Zr NMR spectra presented herein were acquired at room temperature, so it is possible that the second site is a result of temperature-dependent polymorphism. In fact, a powder XRD pattern measured at room temperature (Figure B8) reveals the sample is highly crystalline; however, the experimental pattern does not match that predicted from the low temperature crystal structure, confirming the possible existence of a different phase at room temperature.

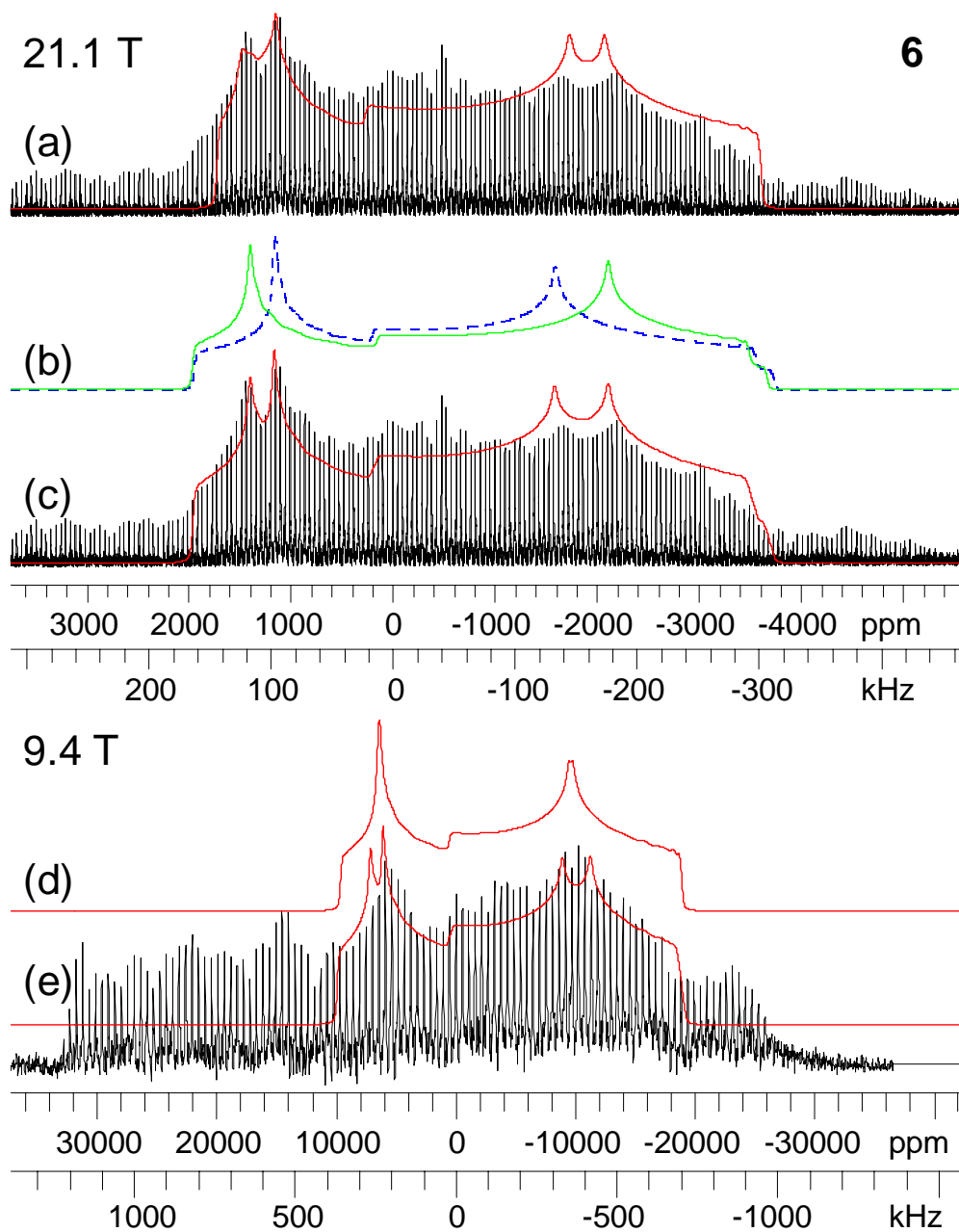
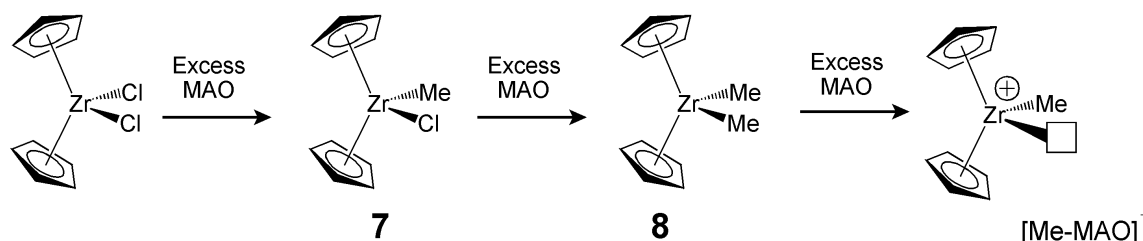


Figure 3.4. Static ^{91}Zr SSNMR spectra and analytical simulations of **6** $[\text{Ind}_2\text{ZrCl}_2]$ acquired at fields of 21.1 T (top) and 9.4 T (bottom). (a) Analytical simulation employing a single site overlaid on the experimental WURST-QCPMG spectrum. (b) Deconvolution of the individual sites of the two site simulation. (c) Analytical simulation employing two-sites overlaid on the experimental WURST-QCPMG spectrum. (d) Simulation of the experimental pattern employing a single site. (e) Analytical simulation employing two sites overlaid on experimental piece-wise QCPMG spectrum. The satellite transitions of nearby $^{35/37}\text{Cl}$ resonances are much more intense in the 9.4 T spectrum and obscure the ^{91}Zr signal.

Regardless of whether a one- or two-site fit is employed for **6**, a value of C_Q (>30 MHz) much larger than those observed for the other halogen complexes is obtained. Quantum chemical calculations employing atomic coordinates from the single-crystal XRD structure predict a large C_Q (*vide infra*) of *ca.* 30 MHz suggesting that our simulations are valid (this assumes, of course, that the local structure of **6** is similar in both polymorphs). This provides confidence that the two-site fit is correct and that the CS tensor parameters and Euler angles are similar to those determined for the other chloride complexes. However, these parameters are associated with large uncertainties due to overlap of the two sites and the large magnitude of C_Q . **6** possesses Zr-Cl distances and Cl-Zr-Cl angles similar to those observed for Cp_2ZrCl_2 and **1**, suggesting that the large difference in C_Q must then be due to the asymmetry of the indenyl ligands. It has been noted that the two carbon atoms common to the five- and six-membered rings within the indenyl ligands possess much longer C-Zr bond lengths [average $r(\text{Zr-C})$ of 2.599 Å] than the Zr-C bond lengths of the three carbon atoms [average $r(\text{Zr-C})$ of 2.486 Å] exclusive to the five-membered ring.⁹³ The large asymmetry in Zr-Cp carbon atom bond lengths is not observed for the other complexes, suggesting that this is the most likely source of the large increase in C_Q for **6**.

Complexes **7** to **9** were investigated because of their roles in the olefin polymerization process (Scheme 3.2). In industrial olefin polymerization processes, a chlorinated form of the metallocene precatalyst, such as Cp_2ZrCl_2 , is reacted with an excess of the cocatalyst, MAO (10^2 to 10^4 equivalents) in order to generate an active catalyst.^{3, 4, 38} The role of MAO is to abstract the chloride ligands and transfer methyl

ligands to the zirconium centers, resulting in the monomethyl and dimethyl complexes, **7** and **8**. MAO also serves as an activator by further abstracting a coordinated methyl group from the zirconium center, leading to a cationic complex, which is the active polymerization catalyst. In this case, complex **9** will serve as a mimic of the active catalyst site that is generated by MAO (i.e., a cationic zirconocene).



Scheme 3.2. The reaction of excess amounts of methylalumoxane (MAO) with a catalyst precursor (Cp_2ZrCl_2) results in the abstraction of the chloride ligands and methylation of the zirconium center leading to the formation of **7** and **8**. Further abstraction of a methyl group by MAO results in a cationic zirconocene with a vacant coordination site (the active polymerization catalyst) and generation of an anionic methyl-MAO adduct.

The static ^{91}Zr NMR spectra of **7** acquired at magnetic fields of 9.4 T and 21.1 T seem to indicate the presence of two distinct Zr sites (Figure 3.5); however, a previously published single crystal XRD structure contains only one magnetically distinct Zr site.⁹⁴ An abnormally long Zr-methyl carbon distance [$r(\text{Zr-Me}) = 2.36 \text{ \AA}$] was observed in this structure, suggesting that the methyl and chlorine positions may be disordered.⁹⁴ We obtained a new single crystal XRD structure of **7**, which has been modelled with disordered methyl carbon and chlorine positions, resulting in two magnetically distinct Zr sites with uneven occupancies. The new structure possesses a $r(\text{Zr-Me})$ of 2.227 \AA (occupancy of 0.616) and a $r(\text{Zr-Me})$ of 2.176 \AA (occupancy of 0.384) for the two distinct

Zr sites. The latter distance seems unrealistically short and is probably a by-product of limited resolution in the XRD experiments. Extensive characterization with both powder XRD, solution ^{13}C , ^1H and ^{91}Zr NMR and ^{13}C SSNMR experiments confirms the sample of **7** was of high purity (see Figures B9-B14), and that the presence of a second powder pattern in the static ^{91}Zr SSNMR spectrum is not due to an impurity phase.

Simulations of the experimental spectra of **7** employing two sites of equal integrated intensity are shown in Figure 3.5. For both sites, $\delta_{\text{iso}} = 230$ ppm while values of Ω (900 and 1000 ppm) and C_Q (23.3 and 20.0 MHz) are similar in magnitude; however, the two sites have very distinct η_Q values (for site 1, $\eta_Q = 0.35$ and for site 2, $\eta_Q = 0.75$) and Euler angles, perhaps reflecting the uneven occupancies and slightly differing Zr environments indicated by the single-crystal structure. Simulated spectra at both fields possess low frequency discontinuities which are slightly more intense than those of the experimental spectra; even if the Euler angles and CS tensor parameters are freely varied, it is not possible to produce a fit of the 9.4 T spectrum which possesses a low frequency discontinuity of the appropriate intensity. We are uncertain of the origin of the broadening of the discontinuities and non-ideal intensities at 9.4 T; however, this spectrum is still useful for determining C_Q and η_Q . Hence, though there are large uncertainties associated with the experimental EFG and CS tensor parameters of **7**, the static ^{91}Zr SSNMR spectra are distinct from those of the other complexes, and still provide a useful “fingerprint” of this complex.

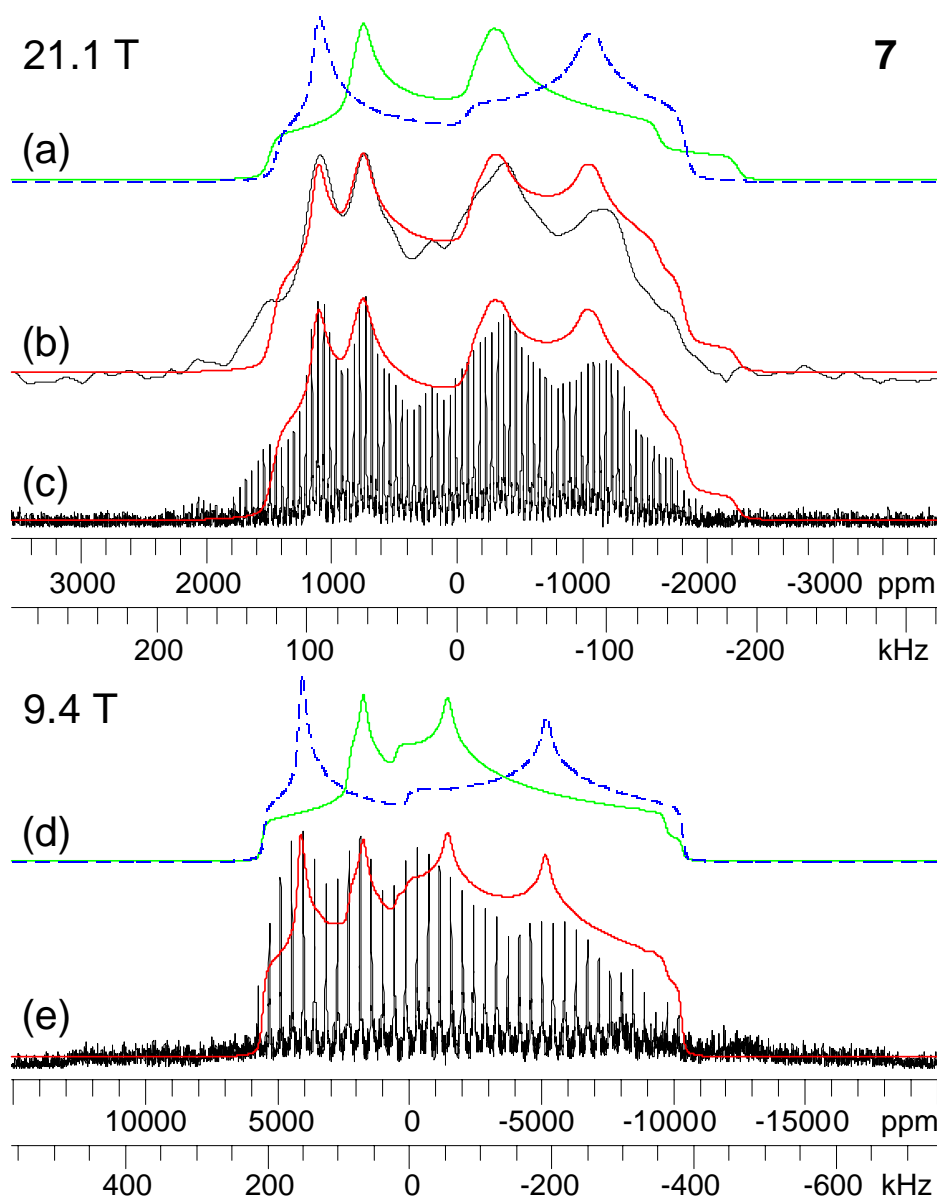


Figure 3.5. Static solid-state ^{91}Zr NMR spectra of **7** [Cp_2ZrMeCl] acquired with the WURST-QCPMG sequence at fields of 21.1 T (top) and 9.4 T (bottom). (a) Deconvolution of the individual sites employed in the two site simulation. (b) Two site analytical simulation (red trace) overlaid on the experimental spectrum formed by time domain co-addition of the echoes in the WURST-QCPMG echo train. (c) Two site analytical simulation overlaid on the experimental WURST-QCPMG spikelet spectrum. (d) Deconvolution of the individual sites employed in the two site simulation. (e) Two site analytical simulation (red trace) overlaid on the experimental piece-wise WURST-QCPMG spikelet spectrum.

The static ^{91}Zr wideline QCPMG NMR spectrum of **8** exhibits a powder pattern with a breadth of 850 kHz at 9.4 T (Figure 3.6b), which yields a large C_Q of 27.9 MHz, and an η_Q value of 0.41, similar to that of Cp_2ZrCl_2 . The Euler angles of **8** are found to be nearly identical to those of Cp_2ZrCl_2 . A very large span of $\Omega = 1750$ ppm is obtained from simulations of the static spectra at both fields. The large C_Q value of **8** is consistent with the broad signal (FWHH of 2530 Hz at 300 K) observed in the solution ^{91}Zr NMR spectrum of **8** by BHP, and agrees qualitatively with their theoretical calculations;⁷⁹ specifically, that **8** should have a C_Q larger than Cp_2ZrCl_2 by a factor of *ca.* 3. The difference of *ca.* 450 ppm in the δ_{iso} values of **8** and Cp_2ZrCl_2 in the solid-state is similar to the difference of approximately 500 ppm that is observed in solution ^{91}Zr NMR spectra (Figure B13). Comparison of the crystal structures of Cp_2ZrCl_2 and **8** reveal that the Zr-Cp centroid (Zr-Cp_{cent}) distances and Cp-Zr-Cp angles are similar; however, the Zr-Me bond is much shorter than the Zr-Cl bond [$r(\text{Zr-Me}) = 2.28 \text{ \AA}$ and $r(\text{Zr-Cl}) = 2.47 \text{ \AA}$].⁹⁴ The larger C_Q observed in **8** compared to that of Cp_2ZrCl_2 is likely due to the shorter bond lengths; however, the differences in the electronic structure of the two ligands also play an important role (this is further investigated in the theoretical section). It should be noted that the spectrum at 21.1 T was acquired with a single transmitter offset with the WURST-QCPMG technique (with ^1H decoupling) in a total time of 1.1 hours, suggesting that the study of samples with dilute zirconium contents and broad resonances is feasible at natural abundance.

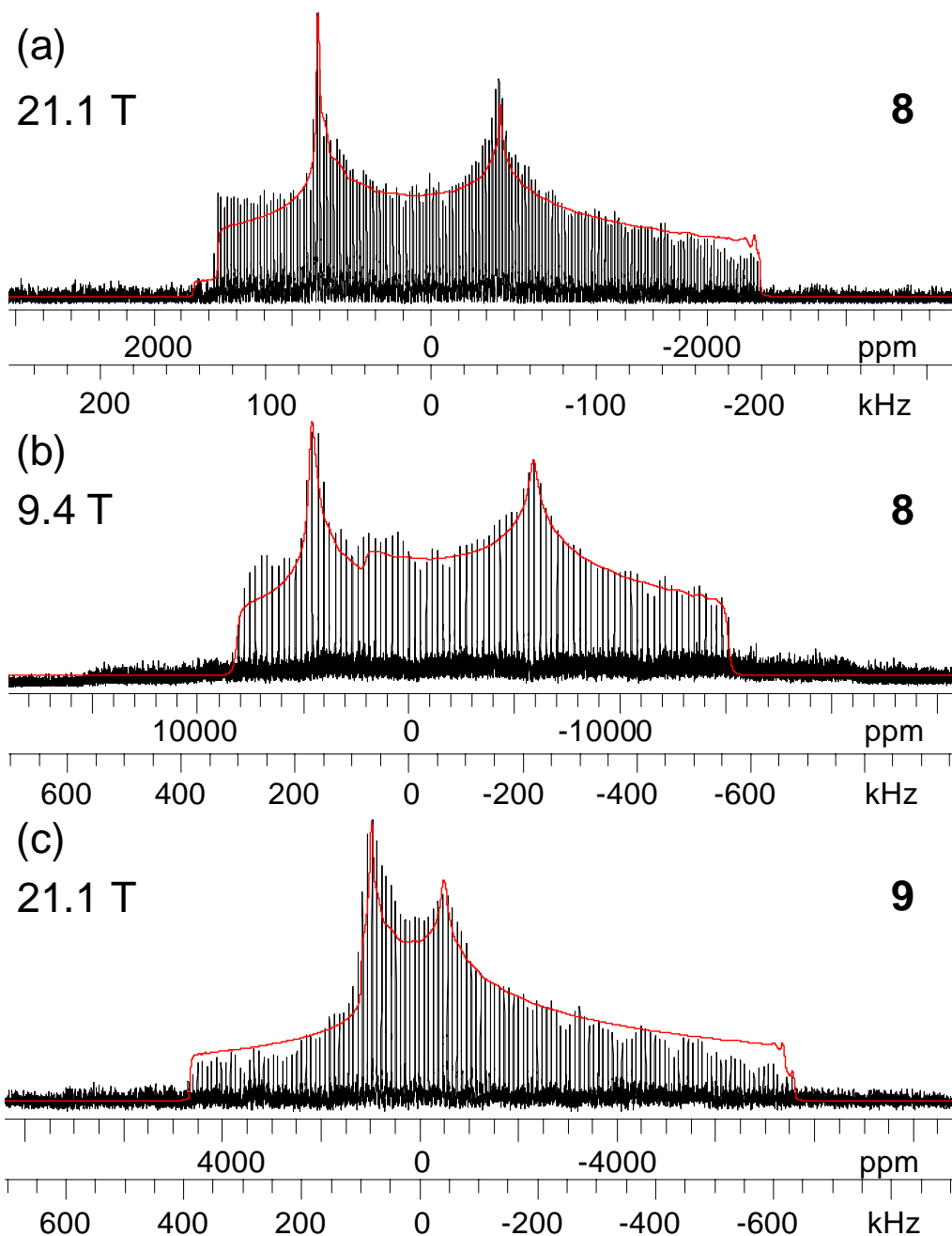


Figure 3.6. Static ^{91}Zr SSNMR spectra of **8** [Cp_2ZrMe_2] and **9** [Cp_2ZrMe][$\text{MeB}(\text{C}_6\text{F}_5)_3$]. Analytical simulations (red traces) overlaid on the experimental WURST-QCPMG spectra of **8** acquired at fields of (a) 21.1 T and (b) 9.4 T. (c) Analytical simulation (red trace) overlaid on the experimental WURST-QCPMG spectrum of **9** acquired at a field of 21.1 T. Experiments on **9** were attempted at 9.4 T, however no signal could be observed. This is due to the large breadth of the central transition powder pattern at this field.

The static ^{91}Zr SSNMR spectrum of **9** at 21.1 T is shown in Figure 3.6c. The spectrum reveals an extremely large C_Q value of 39.0 MHz and an η_Q value of 0.76. This C_Q is significantly larger than those observed for **7** and **8** and slightly smaller than the value of 44.7 MHz measured for K_2ZrF_6 , which is the largest $C_Q(^{91}\text{Zr})$ measured by NMR to date.⁷⁶ The Zr-methyl carbon bond lengths are highly asymmetric for this complex; the methyl group which is bound solely to Zr possesses $r(\text{Zr-Me}) = 2.25 \text{ \AA}$, while the methyl group which bridges the adjacent Zr and B atoms possesses $r(\text{Zr-Me}) = 2.56 \text{ \AA}$.¹²⁰ Presumably, the large increase in C_Q for **9** arises due to the reduction in spherical symmetry about the zirconium centre as compared to complex **8**. A sizable value of $\Omega = 1000 \text{ ppm}$ is also observed, although this is reduced in comparison to **8**. The Euler angles are similar to those observed for Cp_2ZrCl_2 and **8**, with the exception of γ which is found to be near 90° for **9**. The observation of large C_Q and η_Q values distinct from those of the catalyst precursors, Cp_2ZrCl_2 , **7** and **8**, suggests that ^{91}Zr solid-state NMR can readily distinguish the polymerization active cationic zirconocenes, although samples containing a mixture of the species would give rise to complicated ^{91}Zr NMR spectra. The spectrum of **9** was acquired with the WURST-CPMG pulse sequence (with ^1H decoupling) and required 8 sub-spectra at 21.1 T to form the total pattern giving a total acquisition time of slightly over 9 hours. Acquisition of spectra at 9.4 T was attempted, however, no signal was observed. This is unsurprising given that the static ^{91}Zr spectrum of **9** at a field of 9.4 T would exceed 2 MHz in breadth and the long experiment times required at 21.1 T. This suggests that ^{91}Zr SSNMR studies of catalytically active zirconocenes in heterogeneous catalysts systems with dilute zirconium contents would be extremely challenging (though

not impossible) and require high fields and cryogenic temperatures, and possibly isotopic enrichment, to be feasible.

Theoretical Calculations. BHP have presented extensive quantum chemical calculations of ^{91}Zr EFG and CS tensors for a large series of zirconocenes.⁷⁹ They obtained the best results by using DFT methods, and basis sets similar to those employed herein. BHP estimated the magnitude of the largest component of the EFG tensor (V_{33}) based upon the observed linewidths of solution ^{91}Zr NMR spectra and were able to successfully reproduce the relative magnitudes of V_{33} with quantum chemical calculations. However, the V_{33} values calculated by BHP are *ca.* two to three times greater in magnitude than those determined from the C_Q values obtained from our ^{91}Zr SSNMR spectra (Table 3.3). The ^{91}Zr EFG tensor parameters obtained from SSNMR spectra are much more accurate than those obtained from solution ^{91}Zr NMR spectra, where under the assumptions of the extreme-narrowing limit, it is necessary to estimate the correlation time (τ_c) and η_Q .^{79, 121, 122}

A summary of results obtained from B3LYP calculations performed on atomic coordinates obtained from single crystal XRD structures is presented in Table 3.3. Extensive tests of Zr, Cl and Br basis sets were performed on Cp_2ZrCl_2 and **2** (Tables B9 and B10). Regardless of the basis sets and methods employed, relatively poor agreement between the experimentally determined and calculated EFG tensor parameters, C_Q and η_Q , is generally observed when coordinates from single crystal X-ray structures are employed in the calculations for Cp_2ZrCl_2 and complexes **1** to **5** (Table 3.3). Examination of the individual crystal structures of the complexes reveals that there is a substantial variation

Table 3.3. Experimental and Calculated ^{91}Zr CS and EFG Tensor Parameters Determined with the B3LYP method and [6s3p3d] Basis Set on Zr^a

Compound	Site/Structure	V_{33}	C_Q	η_Q	δ_{iso}	Ω	κ^e
Cp_2ZrCl_2	experimental site 1	0.150	6.2	0.18	21	350	-0.7
	experimental site 2	0.157	6.5	0.30	21	340	-0.6
	1/X-ray ^f	-0.249	-10.3	0.22	35	499	-0.5
	2/X-ray	-0.262	-10.8	0.19	18	511	-0.6
	1/ideal Cp ^f	-0.134	-5.6	0.22	21	454	-0.6
	2/ideal Cp	-0.147	-6.1	0.30	21	456	-0.6
$\text{Cp}^*_2\text{ZrCl}_2$ 1	experimental	0.063	2.6	0.22	208	235	-0.8
	1/X-ray	0.137	5.7	0.75	178	335	0.7
	1/ideal Cp	-0.239	-9.9	0.22	384	352	0.8
	1/X-ray (Me_4EtCp) ^g	-0.117	-4.8	0.56	179	251	-0.8
	1/ideal (Me_4EtCp) ^g	0.072	3.0	0.23	164	286	-0.5
Cp_2ZrBr_2 2	experimental	0.058	2.4	0.40	127	550	-0.6
	1/X-ray	-0.151	-6.2	0.86	132	811	-0.6
	2/X-ray conf. 1	0.137	5.6	0.67	136	728	-0.7
	2/X-ray conf. 2	0.030	1.2	0.58	158	728	-0.6
	1/ideal Cp	-0.032	-1.3	0.57	156	700	-0.7
	2/ideal Cp conf. 1	-0.038	-1.6	0.39	142	692	-0.7
	2/ideal Cp conf. 2	-0.049	-2.0	0.16	162	707	-0.7
$(\text{Me}_3\text{SiC}_5\text{H}_4)_2\text{ZrBr}_2$ 3	experimental	0.114	4.7	0.88	154	-	-
	1/X-ray	-0.169	-7.0	0.76	132	634	-0.9
	1/ideal Cp	0.107	4.4	0.56	118	589	-1.0
$\text{O}(\text{Me}_2\text{SiC}_3\text{H}_4)_2\text{ZrBr}_2$ 4	experimental	0.061	2.5	0.68	143	620	-0.8
	1/X-ray	0.098	4.0	0.70	143	707	-0.7
	1/ideal Cp	-0.104	-4.3	0.54	133	692	-0.7
$(1,3\text{-C}_5\text{H}_3)(\text{SiMe}_2\text{OSiMe}_2)_2$	experimental	0.095	3.9	0.25	163	530	-0.6
	1/X-ray	-0.094	-3.9	0.88	114	620	-0.7
$(1,3\text{-C}_5\text{H}_3)\text{ZrBr}_2$ 5	1/ideal Cp	-0.109	-4.5	0.31	98	637	-0.5
$\text{Ind}_2\text{ZrCl}_2$ 6	experimental site 1	0.779	32.0	0.25	60	200	-0.3
	experimental site 2	0.748	30.7	0.38	56	200	-0.3
	1/X-ray	-0.729	-30.1	0.08	64	332	-0.3
Cp_2ZrMeCl 7	experimental site 1	0.563	23.3	0.35	230	900	-0.6
	experimental site 2	0.484	20.0	0.75	230	1000	0.8
	1/X-ray	0.535	22.1	0.23	325	1205	-0.6
	1/ideal Cp	0.477	19.7	0.07	334	1194	-0.6
	1/new X-ray ^h	0.870	36.0	0.18	318	1287	-0.5
	2/new X-ray	0.811	33.6	0.09	329	1259	-0.6
	1/new ideal Cp	0.875	36.2	0.03	317	1250	-0.5
2/new ideal Cp	0.731	30.2	0.02	329	1247	-0.5	
Cp_2ZrMe_2 8	experimental	0.677	27.9	0.41	475	1750	-0.9

	1/X-ray	-0.714	-29.5	0.20	622	1873	-0.9
	1/ideal Cp	-0.615	-25.4	0.29	624	1842	-1.0
[Cp ₂ ZrMe][MeB(C ₆ F ₅) ₃] 9	experimental	0.946	39.0	0.76	350	1000	0.2
	1/X-ray	-0.887	-36.7	0.96	325	1066	-0.4
	1/ideal Cp	-0.952	-39.4	0.81	334	1049	-0.4

^a Additional computational results can be found in Tables B9 to B13. See text for details on basis sets used in the calculations. The 6s3p3d basis set was used for Zr, cc-pVDZ for Cl and 6-311G** on Br. ^b See the experimental section for details on the basis sets used on other atoms. ^c Only the magnitude of C_Q can be measured experimentally. For definitions of all NMR parameters refer to Table 3.1. ^d The theoretical values of δ_{iso} were determined by comparison to the magnetic shielding values calculated from calculations on Cp₂ZrCl₂ which utilized ideal Cp rings and the corresponding method and basis sets (Table B2). The equation used was, $\delta_{\text{iso}} = \sigma_{\text{iso}}(\text{Cp}_2\text{ZrCl}_2 \text{ ideal Cp}) - \sigma_{\text{iso}}(x) + 21$ ppm. ^e Defined in Table 3.1. ^f "X-ray" refers to calculations with Cp carbon atom coordinates determined from single crystal XRD structures. "ideal Cp" refers to calculations where idealized Cp carbon atom coordinates have been used. See text for details. ^g These calculations employ coordinates from the single crystal XRD structure of (Me₂EtCp)₂ZrCl₂, where the Et groups have been replaced with Me groups. ^h These calculations employ coordinates from the single crystal XRD structure of Cp₂ZrMeCl presented in this work.

in the interatomic carbon-carbon distances; for example, in Cp₂ZrCl₂ the C-C distances range from 1.364 Å to 1.414 Å. There are also deviations of the Cp rings from planarity, as indicated by torsional angles of four carbons in the Cp rings. Distortions of up to 2.19° are observed in the crystal structure of Cp₂ZrCl₂ (this is typical of torsional angles observed in the other complexes). For this reason calculations with "idealized" Cp rings were attempted. In these calculations, the crystallographically refined Cp ring structures have been replaced with perfectly flat Cp rings (0° torsional angles) with all C-C distances set to 1.40 Å and C-C-C internal angles of 108°. The crystallographically determined Zr-Cp_{Cent} distances have been retained.

Calculations which employ such idealized Cp rings lead to significantly reduced V_{33} and C_Q values for Cp₂ZrCl₂, **1**, **2**, and **3**, and yield much better agreement with experimental values of C_Q (Table 3.3 and Tables B11 and B12). All of these complexes possess small V_{33} values, and minor deviations in the Cp' carbon atom positions would be expected to reduce the symmetry around the Zr atom and give rise to larger EFGs;

however, it is somewhat surprising to observe that minor deviations in the positions of the carbons within the Cp rings can lead to two- to four-fold differences in the magnitude of V_{33} . For complexes **4** and **5**, calculations on structures with ideal Cp rings lead to only slight differences in the calculated EFG and CS tensor parameters. Complexes **7**, **8** and **9** feature coordination by methyl ligands and possess values of C_Q greater than 20 MHz. The use of ideal Cp rings leads to changes in calculated values of C_Q by 3 to 4 MHz compared to calculations utilizing X-ray coordinates for Cp carbon atoms. This suggests that the large values of V_{33} observed for **7**, **8** and **9** relative to those of the halogenated zirconocenes mainly arise from the presence of the methyl ligands coordinated to Zr rather than from differences in the Cp carbon positions (*vide infra*). Calculations utilizing X-ray coordinates for Cp' carbon atoms and the idealized Cp' rings yield very similar CS tensor parameters for all complexes. In summary, calculations utilizing idealized Cp' rings with Zr-Cp'_{Cent} distances determined from X-ray structures should be used for quantum chemical calculations of ^{91}Zr EFG tensor parameters of zirconocenes.

Discrepancies and observations about the quantum chemical calculations of NMR tensor parameters for some of the individual complexes are now briefly discussed. Our initial quantum chemical calculations on **1** employed atomic coordinates from the previously published single-crystal X-ray structure.¹⁰⁸ These calculations resulted in ^{91}Zr NMR tensor parameters showing poor agreement with experimental values, regardless of whether X-ray or idealized Cp* rings were utilized. An X-ray crystal structure of **1** was unavailable at the time of BHP's study, so the authors used atomic coordinates from the previously published crystal structure of bis(tetramethylethylcyclopentadienyl)zirconium

dichloride¹²³ [(Me₄EtCp)₂ZrCl₂] to construct a model of **1**, by replacing the ethyl groups on both Cp ligands with methyl groups. With this approach, they observed good agreement between the calculated and experimental values of δ_{iso} for **1**.⁷⁹ We have taken a similar approach, and our calculations yield ⁹¹Zr NMR tensor parameters in excellent agreement with experimental values (Table 3.3). The largest differences evident in the crystal structures of **1** and (Me₄EtCp)₂ZrCl₂ are the Cp'_{Cent}-Zr-Cp'_{Cent} angles (130.9° and 137.0°, respectively, Table 3.2). The success of these calculations suggest to us that there may be an error in the previously determined crystal structure of **1**.

The crystal structure of **2** has two crystallographically distinct Zr atoms (sites 1 and 2); in addition, site 2 has two Cp ring conformations which differ by rotation of one of the Cp rings about its five-fold axis by an angle of 30°, as well as different Zr-Cp_{Cent} distances (2.185 Å and 2.213 Å for conformations 1 and 2 respectively). Calculations of EFG tensor parameters for **2** reveal C_Q and η_Q values which differ by greater than 20% for sites 1 and 2. There is a significant variation in calculated C_Q and η_Q values for the two distinct Cp ring conformations of site 2; however, the Zr-Cp_{Cent} distance of conformation 2 is significantly longer than the other distances within the structure, and casts doubt on the accuracy of the crystal structure. This suggests that the two resonances observed in the MAS ⁹¹Zr NMR spectrum arise from the two crystallographically distinct Zr sites, rather than from distinct conformations of the Cp rings.

Calculations on **7** employing coordinates from the previously published single crystal XRD structure yield much smaller C_Q values than those obtained from the crystal structure presented herein. The major difference between the two structures is a

significantly shorter $r(\text{Zr-Me})$ in the new structure (2.23 Å versus 2.36 Å). Simulations of the static ^{91}Zr SSNMR spectra of **7** required two sites with disparate ^{91}Zr NMR tensor parameters in order to produce reasonable fits of the experimental spectra. The calculations on our new crystal structure suggests that the only parameter which should vary significantly between the two sites is C_Q , with both sites possessing similar η_Q and CS tensor parameters, suggesting that the latter parameters are not highly dependent upon $r(\text{Zr-Me})$.

Our new single-crystal XRD structure of **7** indicates that the Me and Cl positions are disordered. Calculations on twelve-molecule clusters of **7** were performed to see how the presence of neighbouring molecular units affects the calculated EFG tensor parameters. Calculations were performed on two clusters (Figure B15). In both cases the central molecule of the cluster corresponds to site 2 (i.e., $r(\text{Zr-Me}) = 2.23$ Å and $r(\text{Zr-Cl}) = 2.51$ Å) and X-ray coordinates of the Cp carbon atoms were used. In cluster 1, all neighbouring units correspond to site 2 of the single crystal XRD structure (i.e., all neighbouring units possess $r(\text{Zr-Me}) = 2.23$ Å and $r(\text{Zr-Cl}) = 2.51$ Å). In cluster 2, four of the neighbouring units correspond to site 1 (i.e., $r(\text{Zr-Me}) = 2.18$ Å and $r(\text{Zr-Cl}) = 2.51$ Å). The four neighbouring units that were changed in cluster 2 were chosen because their Me or Cl ligands were directed toward the central molecule of the cluster. Calculations on both cluster 1 and 2 result in calculated values of C_Q for the central molecule which are similar in magnitude to that calculated for an isolated molecule, however, the η_Q value calculated for cluster 1 is 0.66 (Table B14). The η_Q values calculated for cluster 2 and the isolated molecule are near 0. This suggests that the orientation of the neighbouring

molecules can effect the EFG tensor, and that the high η_Q site observed in the experimental spectra of **7** may originate from the disorder in the orientation of the neighbouring molecules within the crystal lattice.

Table 3.4. Experimentally Determined and Calculated Euler Angles^a

Compound	Method/Structure	α (°)	β (°)	γ (°)
Cp ₂ ZrCl ₂	experiment site 1	90(35)	86(10)	2(10)
	experiment site 2	90(35)	86(10)	3(10)
	site 1 ideal Cp	103	89	1
	site 2 ideal Cp	108	88	-1
Cp* ₂ ZrCl ₂ 1	experiment	20(40)	90(25)	90(10)
	ideal (Me ₄ EtCp)	-20	82	90
Cp ₂ ZrBr ₂ 2	experiment	40(90)	0(90)	0(90)
	site 1 ideal Cp	1	82	103
O(Me ₂ SiC ₅ H ₄) ₂ ZrBr ₂ 4	experiment	40(20)	90(15)	35(40)
	ideal Cp	98	56	-91
(1,3-C ₅ H ₃)(SiMe ₂ OSiMe ₂) ₂ (1,3-C ₅ H ₃)ZrBr ₂ 5	experiment	40(20)	30(15)	85(10)
	ideal Cp	17	20	87
Ind ₂ ZrCl ₂ 6 (two site fit, site 1)	experiment	80(60)	60(40)	4(60)
Ind ₂ ZrCl ₂ 6 (two site fit, site 2)	experiment	80(60)	60(40)	4(60)
	ideal Cp	80	60	0
Cp ₂ ZrMeCl 7 (site 1)	experiment	5(70)	15(45)	85(70)
Cp ₂ ZrMeCl 7 (site 2)	experiment	80(40)	20(20)	5(40)
	site 2 ideal Cp	36	6	97
Cp ₂ ZrMe ₂ 8	experiment	80(40)	90(5)	0(5)
	ideal Cp	93	89	1
[Cp ₂ ZrMe][MeB(C ₆ F ₅) ₃] 9	experiment	90(10)	80(15)	86(40)
	ideal Cp	-90	63	90

^aEuler angle conventions are specified in the experimental section.

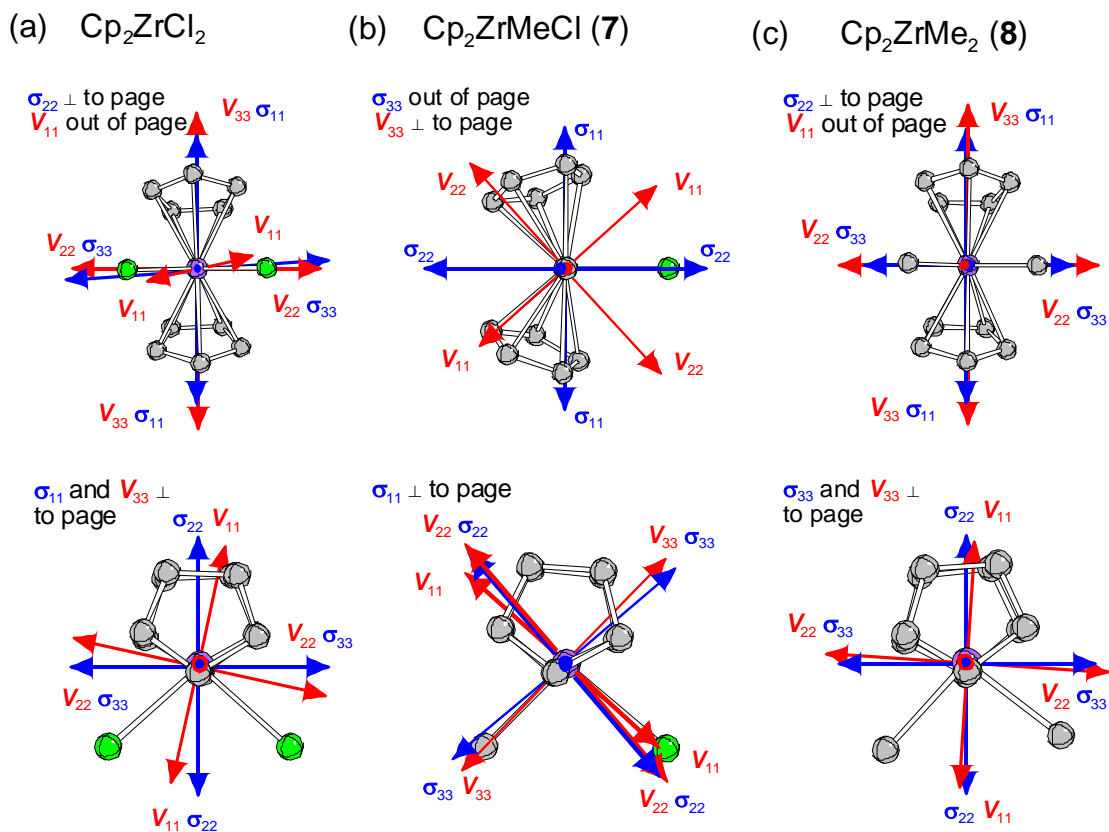


Figure 3.7. Theoretical ^{91}Zr EFG and MS tensor orientations in the molecular frames of (a) Cp_2ZrCl_2 , (b) **7** [Cp_2ZrMeCl] and (c) **8** [Cp_2ZrMe_2]. All tensor orientations are taken from the calculations which employ idealized Cp rings. The tensor orientation for Cp_2ZrCl_2 has been taken from site 1. The tensor orientation for **7** has been taken from calculations on site 2 of the new structure (see text for full explanation).

The theoretically obtained ^{91}Zr EFG and magnetic shielding (MS) tensor orientations within the molecular frames are now discussed (Figures 3.7 and 3.8). Euler angles extracted from the quantum chemical calculations are shown in Table 3.4. For all complexes, the least shielded component of the MS tensor (σ_{11}) is oriented in a direction approximately perpendicular to the X-Zr-X plane (X = Me, Cl, Br). Nuclear deshielding in this direction arises from magnetic dipole induced mixing of occupied and virtual

molecular orbitals (MOs) within the X-Zr-X plane (i.e., virtual MOs of high Zr *d* atomic orbital character and occupied Zr-X σ - (X = CH₃, Cl, Br) and π -bonding (X = Cl, Br) MOs). This is consistent with previous Hückel MO calculations on bent metallocene complexes by Lauher and Hoffman, which show that Zr-X σ and π MOs are the highest occupied MOs in these complexes, and that their electron densities are largely concentrated within or about the X-Zr-X plane.¹²⁴ The only exception we note is **6**, where a significant deviation away from normality is observed (σ_{11} forms a torsional angle of *ca.* 78° with the Cl-Zr-Cl plane); this may arise from the positioning of the indenyl rings.

The tensor orientations for the series of complexes found in Scheme 3.2 (Cp₂ZrCl₂ and **7** - **9**) are discussed first. Quantum chemical calculations predict similar orientations of EFG tensors for Cp₂ZrCl₂ (Figure 3.7a) and **8** (Figure 3.7c): V_{11} and V_{22} lie approximately within the X-Zr-X (X = Me, Cl) plane and V_{33} is directed towards the Cp rings forming torsional angles with the X-Zr-X plane of 88.4° and 90.3° for X = Me and X = Cl, respectively. The tensor orientations presented for Cp₂ZrCl₂ are similar to those previously reported by our research group.⁴⁵ The EFG orientations in Cp₂ZrCl₂ and **8** are consistent with experimental values of η_Q being closer to 0 than 1, which indicate that V_{33} is the distinct component, oriented in an electronic environment different from those of V_{11} and V_{22} . For both complexes, the least shielded component of the MS tensor (σ_{11}) is approximately co-linear with the largest component of the EFG tensor (V_{33}), and the most shielded component (σ_{33}) is predicted to lie in the X-Zr-X plane near V_{22} ; this is consistent with the Euler angles of $\alpha \approx \beta \approx 90^\circ$ obtained from simulations of the static ⁹¹Zr NMR spectra.

Complex **7** possesses a similar MS tensor orientation to the other compounds where σ_{11} is oriented normal to the Me-Zr-Cl plane, while σ_{22} and σ_{33} are approximately contained within the Me-Zr-Cl plane, near the Zr-Cl and Zr-Me bonds, respectively (Figure 3.7b, bottom). However, the EFG tensor orientation in **7** is distinct from that of the other complexes; V_{33} is oriented such that it is coincident with the Zr-Me bond, while V_{11} and V_{22} make angles of approximately 45° with respect to the Me-Zr-Cl plane (Figure 3.7b, top). The orientation of V_{33} along the Zr-Me bond suggests that the increase in C_Q observed for **7** compared to that of Cp_2ZrCl_2 can be attributed to the asymmetry of the Zr-Me and Zr-Cl bonds. Unfortunately, given the uncertainty regarding the simulations of the static NMR spectra of **7**, it is difficult to compare experimental and calculated Euler angles, although a calculated value of β near zero is distinct from the other complexes. The EFG and MS tensor orientation for **9** are shown in Figure 3.8a. The η_Q value near 1 is consistent with the orientation of V_{11} towards the Cp rings, with V_{33} and V_{22} oriented near the Zr-Me carbon bonds (V_{33} is directed towards the bridging methyl group). This suggests that the large C_Q observed for this complex results in part from the asymmetry of the Zr-Me carbon bond lengths (*vide infra*).

Complexes **1 - 5** are all characterized by small C_Q values (less than that of Cp_2ZrCl_2) and η_Q values which vary from near 0 to near 1. For all of these complexes, V_{33} is oriented such that it is contained within or near the X-Zr-X plane (Figure 3.8b - e, orientations for **3** not shown), although the direction of V_{33} within this plane is variable and seems to be uncorrelated to the predicted sign of C_Q or value of η_Q . We posit that this is because when V_{33} is small, subtle differences in ligand positions can result in completely

different EFG tensor orientations. In complex **6**, V_{33} is directed towards the carbon atoms which are common to the five and six-membered rings of the indenyl ligands (Figure 3.8f). The average Zr-C bond lengths of 2.599 Å of the two carbon atoms, are much longer than the average Zr-C bond length 2.489 Å of the three carbon atoms exclusive to the five-membered ring. This supports the notion that the large increase in C_Q for **6** as compared to Cp_2ZrCl_2 can be attributed to the asymmetric binding of the indenyl ligands.

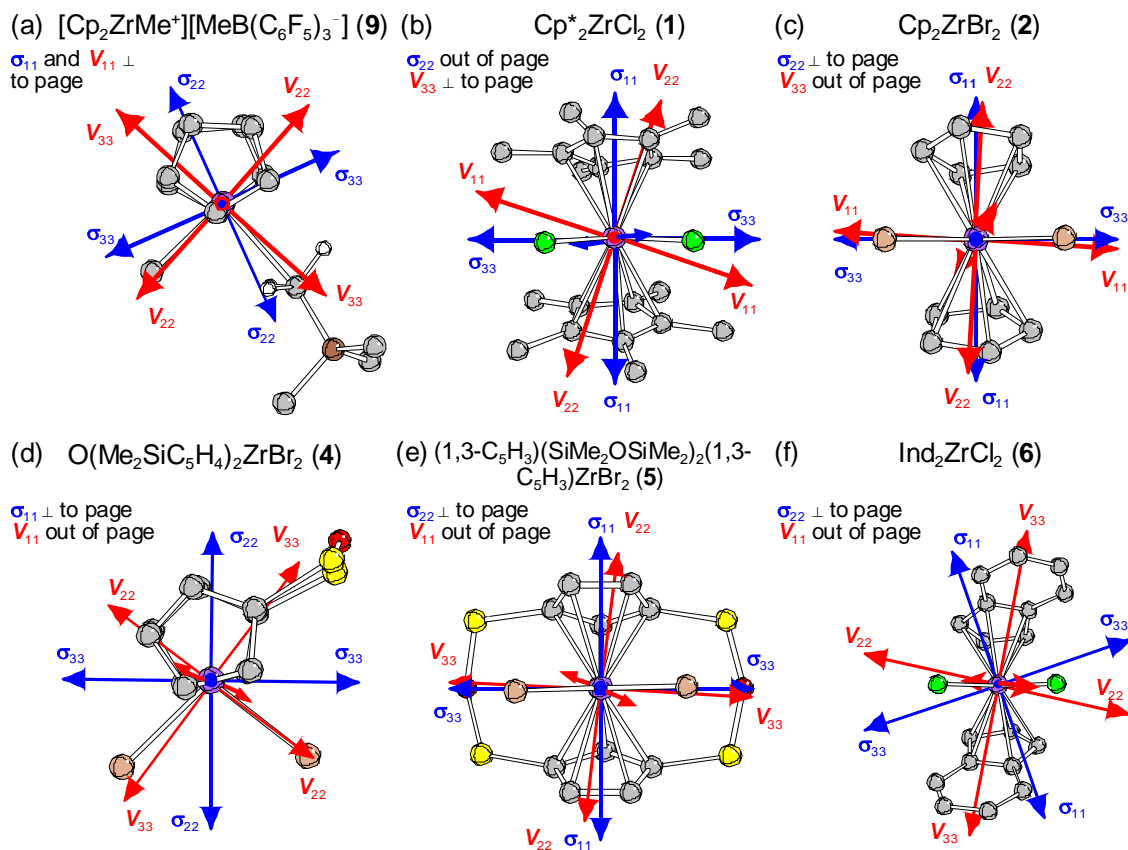


Figure 3.8. Theoretical ^{91}Zr EFG and MS tensor orientations in the molecular frames of (a) **9**, (b) **1** [$\text{Cp}^*_2\text{ZrCl}_2$], (c) **2** [Cp_2ZrBr_2], (d) **4** [$\text{O}(\text{Me}_2\text{SiC}_5\text{H}_4)_2\text{ZrBr}_2$], (e) **5** [$(1,3\text{-C}_5\text{H}_3)(\text{SiMe}_2\text{OSiMe}_2)_2(1,3\text{-C}_5\text{H}_3)\text{ZrBr}_2$] and (f) **6** [$\text{Ind}_2\text{ZrCl}_2$]. All tensor orientations are taken from the calculations which employ idealized Cp rings. The tensor orientation for complex **2** has been taken from site 1.

Finally, due to the importance of Cp_2ZrCl_2 and complexes **7** - **9** in olefin polymerization catalysis, it is important to further probe the origin of the large differences observed and predicted in the values of C_Q and η_Q in this series. We have calculated the EFG tensor parameters for structures with variable Zr-X (X = Cl, Me) bond lengths, since all of these complexes possess similar $\text{Cp}_{\text{Cent}}\text{-Zr}$ bond lengths, $\text{Cp}_{\text{Cent}}\text{-Zr-Cp}_{\text{Cent}}$ angles and X-Zr-X angles (Table 3.2). A plot of calculated C_Q values as a function of Zr-X bond lengths is shown in Figure 3.9a for Cp_2ZrCl_2 and **8**. Cp_2ZrCl_2 and **8** possess crystallographically determined average Zr-X bond lengths of $r(\text{Zr-Cl}) = 2.45 \text{ \AA}$ and $r(\text{Zr-Me}) = 2.28 \text{ \AA}$, respectively. As the Zr-X bonds are *symmetrically shortened* (e.g., both Zr-Cl bond lengths are decreased in length by the same amount for Cp_2ZrCl_2) from their crystallographic distances, C_Q remains negative and is observed to steadily increase in magnitude for both complexes (Figure 3.9a). As both bond lengths are symmetrically increased from their crystallographic distances, C_Q is observed to approach zero, then become positive and steadily increase in magnitude. η_Q remains relatively constant for Cp_2ZrCl_2 over the full range of Zr-Cl bond lengths employed in calculations, while for **8**, a steady increase in η_Q is observed as the average Zr-Me bond lengths are symmetrically increased from 1.98 \AA to 2.58 \AA (Figure 3.9b).

It is interesting to note that when the Zr-Me distances in **8** are set approximately equal to the crystallographic Zr-Cl distances of Cp_2ZrCl_2 , the calculated values of C_Q for **8** are nearly double those of Cp_2ZrCl_2 (Figure 3.9a). This suggests that the electronic nature of the Zr-X bonding, and not only the bond lengths, has an major effect on the magnitude of C_Q . This is not surprising considering that Cl ligands possess electron lone pairs

capable of ligand-to-metal π -donation, whereas Me ligands do not. In summary, the increase in C_Q observed for **8** compared to that of Cp_2ZrCl_2 is primarily due to both the relatively short Zr-Me bond lengths and the differing electronic structures of these bonds.

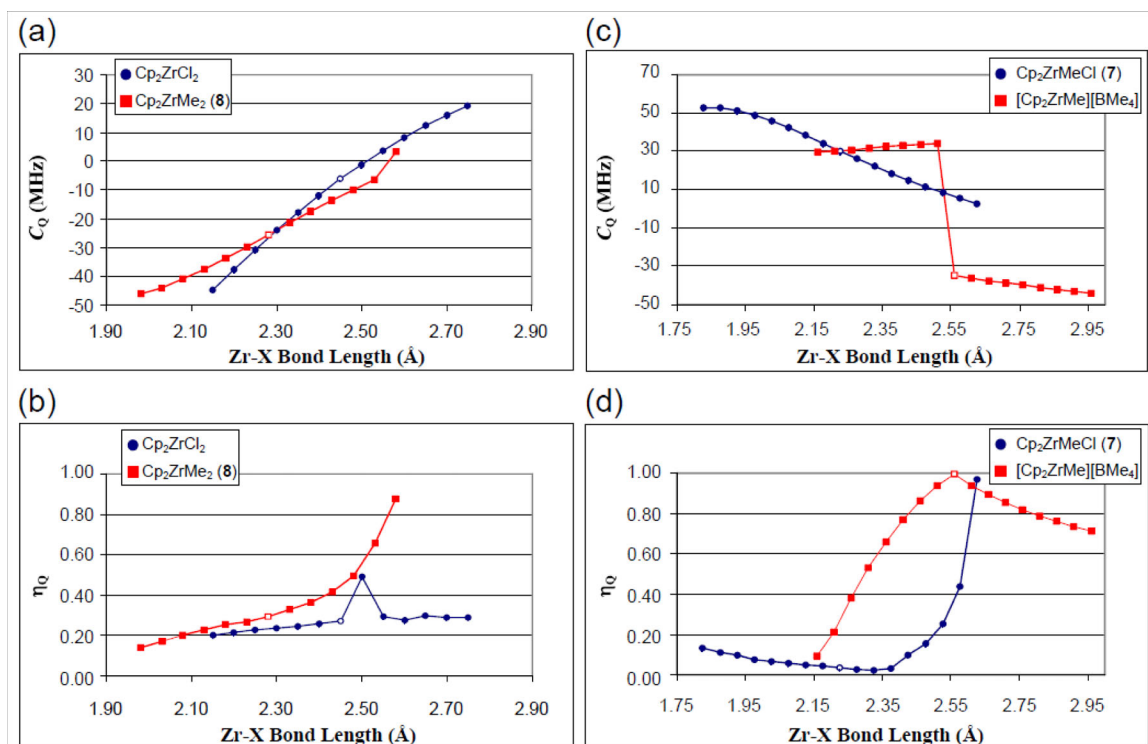


Figure 3.9. Values of ^{91}Zr EFG tensor parameters obtained from B3LYP calculations on structures with variable Zr-Cl and Zr-Me carbon bond lengths. The bond lengths were varied in increments of 0.05 \AA . Calculated (a) C_Q and (b) η_Q values when both of the Zr-X ($X = \text{Cl}, \text{Me}$) bond lengths in Cp_2ZrCl_2 and **8** [Cp_2ZrMe_2] are varied. Calculated (c) C_Q and (d) η_Q values when the Zr-Me bond length of **7** [Cp_2ZrMeCl] is varied and when the bridging Zr-Me bond length of $[\text{Cp}_2\text{ZrMe}][\text{BMe}_4]$ is varied. The model complex, $[\text{Cp}_2\text{ZrMe}][\text{BMe}_4]$, was created by replacing the three pentafluorophenyl groups of **9** with Me groups. Crystallographic bond lengths are marked with open circles and squares. Atomic coordinates with idealized Cp rings were employed for all calculations. Coordinates from site 1 of Cp_2ZrCl_2 and site 2 of **7** of the respective crystal structures were employed.

Calculations of ^{91}Zr EFG tensors are also helpful in understanding the significant differences in the values of η_Q for the two structurally similar (but magnetically distinct) Zr sites in **7**. Since there is some uncertainty associated with the crystallographically determined values of $r(\text{Zr-Me})$ for **7** (*vide supra*), EFG tensor parameter calculations were performed on a model structure of **7** in which $r(\text{Zr-Me})$ was altered, while $r(\text{Zr-Cl})$ was held constant at its crystallographically determined value (Figure 3.9c and 3.9d). These calculations reveal that C_Q is positive and steadily decreases in magnitude as $r(\text{Zr-Me})$ is increased in length from 1.83 Å to 2.63 Å. Calculations predict C_Q values near the experimentally determined values of 20.0 and 23.3 MHz when $r(\text{Zr-Me})$ is *ca.* 2.33 Å (0.1 Å longer than the crystallographic bond length). The value of η_Q is relatively constant and near 0 when $r(\text{Zr-Me})$ is less than 2.48 Å, but at longer $r(\text{Zr-Me})$, the value of η_Q rapidly approaches 1. This suggests that the high η_Q site observed in the static ^{91}Zr SSNMR spectra is not arising from disorder in the position of the methyl group. Calculations on twelve-molecule clusters of **7** (*vide supra*) suggest that this variation in η_Q arises from longer range electrostatic interactions which depend upon the orientation of the Me and Cl ligands in neighbouring molecules.

In order to probe the origins of the large C_Q and high η_Q observed for **9**, EFG tensor parameters were calculated for a model complex which is analogous to **9**, $[\text{Cp}_2\text{ZrMe}][\text{BMe}_4]$. The $r(\text{Zr-Me})$ of the bridging Me group was then varied (the BMe_3 group was also moved by the same amount), while the terminal $r(\text{Zr-Me})$ was fixed at the crystallographic distance observed for **9** (2.25 Å). As the bridging $r(\text{Zr-Me})$ is increased from 2.16 Å to 2.51 Å, C_Q (which is positive) steadily increases in magnitude (Figure

3.9c). At $r(\text{Zr-Me}) = 2.56 \text{ \AA}$, C_Q becomes negative, and steadily increases in magnitude as the bond length is increased. The change in the sign of C_Q occurs because V_{22} and V_{33} are similar in magnitude and opposite in sign (corresponding to η_Q values near 1) for $r(\text{Zr-Me})$ near 2.56 \AA , and further increases in $r(\text{Zr-Me})$ causes the V_{22} and V_{33} principal components to switch directions and leads to a sign change for C_Q . η_Q is observed to fluctuate between 0 and 1 over the range of $r(\text{Zr-Me})$ (Figure 3.9d), with η_Q values greater than 0.70 observed at $r(\text{Zr-Me})$ greater than 2.41 \AA . When $r(\text{Zr-Me}) = 2.56 \text{ \AA}$, $C_Q = -35 \text{ MHz}$ and $\eta_Q = 1.0$ are predicted, similar to the experimentally obtained EFG tensor parameters for **9**. Therefore, the large value of C_Q observed for **9** and the η_Q values close to 1 arise from unequal Zr-Me bond lengths for the bridging and terminal methyl groups. When the bridging $r(\text{Zr-Me})$ is equal to 2.26 \AA , both the bridging and terminal $r(\text{Zr-Me})$ are approximately equal and are similar to those of **8**. In this case, C_Q is calculated to be 30.9 MHz for $[\text{Cp}_2\text{ZrMe}][\text{BMe}_4]$, while C_Q is calculated to be -25.6 MHz for **8**. This suggests that when the hydrogen atoms of the bridging Me group are directed towards the Zr centre, an increase in $|C_Q|$ will also occur.

3.4 Conclusions

The use of ^{91}Zr SSNMR and quantum mechanical calculations has allowed for the examination of the ^{91}Zr quadrupolar and chemical shift interactions in zirconocenes possessing Cp ligands of varying substitution patterns and different heteroligands (i.e., Cl, Br, Me). The combination of QCPMG and/or WURST-QCPMG pulse sequences with

frequency-stepped techniques facilitates the acquisition of broad static patterns that span hundreds of kilohertz (i.e., spectra of **6**, **7**, **8** and **9**). In general, halide complexes are characterized by small C_Q values, while the coordination of methyl ligands leads to larger C_Q values. The increase in C_Q by a factor of *ca.* 4.4 for **8** as compared to Cp_2ZrCl_2 is explained on the basis of shortened bond lengths Zr-X bond lengths. Isotropic ^{91}Zr chemical shifts are seen to closely parallel those previously observed in solution ^{91}Zr NMR spectra, and allow for variations in the Cp ring substitution patterns as well as the types of heteroligands coordinated to the metal to be differentiated. Consistent with our previous ^{91}Zr SSNMR study of Cp_2ZrCl_2 , simulations of static spectra at both high (9.4 T) and ultrahigh fields (21.1 T) require that CSA and Euler angles be accounted for. CSA is observed to be very sensitive to the nature of the heteroligand; Ω is seen to increase for the ligand series Cl, Br, and Me, affording another parameter which allows for insight into zirconocene structure and bonding. Methods for the accurate calculation of ^{91}Zr EFG and CS tensor parameters have been identified and show excellent agreement with experimental values. Visualization of EFG and MS tensor orientations within the molecular frames obtained from quantum chemical calculations allows for the origin of the NMR interactions to be rationalized.

The purpose of studying compounds **3** - **5** was to mimic the structures of zirconocene species before (**3**) and after (**4** and **5**) chemisorption to surface materials via the ancillary functional groups of the Cp ligands. Cp_2ZrCl_2 and complexes **7** - **9** were studied in order to demonstrate that solid-state ^{91}Zr NMR can differentiate the key intermediates that result from the reaction of MAO with a pre-catalyst (Cp_2ZrCl_2). This

may also allow for the interactions between MAO and zirconocenes to be probed in the future, for both homogeneous and heterogeneous catalysts. The ability of solid-state ^{91}Zr NMR to distinguish Cp_2ZrCl_2 and complexes **7**, **8** and **9** is of importance if industrial heterogeneous olefin polymerization catalysts are to be examined in the future. We have also recently demonstrated that the acquisition of solid-state ^{35}Cl NMR spectra of zirconocenes is feasible and can provide complimentary insight into zirconocene structure.⁴⁷ The combination of quantum chemical calculations and ^{91}Zr and ^{35}Cl SSNMR should allow for the structure of immobilized zirconocenes with ambiguous structures to be probed.

The acquisition of ^{91}Zr NMR spectra of heterogeneous catalyst systems will prove challenging due to the dilution of the ^{91}Zr nuclei (typical heterogeneous catalysts are 0.5 - 5% Zr by mass). For samples which possess narrow central-transition powder patterns (e.g., Cp_2ZrCl_2) it is possible to acquire static spectra in a matter of minutes at 21.1 T with standard echo sequences, suggesting that the acquisition of solid-state ^{91}Zr spectra of heterogeneous catalysts featuring narrow resonances is feasible with standard techniques. However, if the halide ligands are replaced during immobilization and/or the metallocene structure is significantly altered, a large increase in the breadth of the NMR pattern is expected (compare spectra of Cp_2ZrCl_2 and **8**). The combination of WURST-QCPMG and ultrahigh magnetic fields allows for the acquisition of ultra-wideline solid-state ^{91}Zr NMR spectra of **7**, **8**, and **9** in total experimental times of 4.6, 1.1 and 9.1 hours, respectively. Therefore, the acquisition of solid-state ^{91}Zr NMR spectra of heterogeneous catalysts possessing broad ^{91}Zr resonances would be a considerable challenge. In these cases ^{91}Zr

isotopic enrichment and/or cryogenic temperatures in combination with ^1H cross-polarization QCPMG (CP/QCPMG) pulse sequences would be necessary in order to enhance the signal of NMR experiments.^{51, 52, 125} This approach has been pioneered and extensively demonstrated by Ellis and Lipton for SSNMR studies of quadrupolar metal nuclei present in extremely low concentrations in the active sites of metallo-proteins.¹²⁶⁻¹²⁸

3.5 Bibliography

- (1) Soga, K., *Macromol. Symp.* **1996**, 101, 281-288.
- (2) Coates, G. W., *J. Chem. Soc.-Dalton Trans.* **2002**, (4), 467-475.
- (3) Hlatky, G. G., *Chem. Rev.* **2000**, 100, (4), 1347-1376.
- (4) Severn, J. R.; Chadwick, J. C.; Duchateau, R.; Friederichs, N., *Chem. Rev.* **2005**, 105, (11), 4073-4147.
- (5) Janiak, C., *Metallocene Catalysts for Olefin Polymerization*. In *Metallocenes: Synthesis, Reactivity, Applications*, Togni, A.; Halterman, R. L., Eds. Wiley-VCH Verlag GmbH: Weinheim, 1998; Vol. 2, pp 547-623.
- (6) Bohm, L. L., *Angew. Chem. Int. Ed.* **2003**, 42, (41), 5010-5030.
- (7) Zecchina, A.; Groppo, E.; Bordiga, S., *Chem. Eur. J.* **2007**, 13, (9), 2440-2460.
- (8) Soga, K.; Shiono, T., *Prog. Polym. Sci.* **1997**, 22, (7), 1503-1546.
- (9) Kim, S. H.; Somorjai, G. A., *Proc. Natl. Acad. Sci. U. S. A.* **2006**, 103, (42), 15289-15294.
- (10) Groppo, E.; Lamberti, C.; Bordiga, S.; Spoto, G.; Zecchina, A., *Chem. Rev.* **2005**, 105, (1), 115-183.
- (11) Theopold, K. H., *Eur. J. Inorg. Chem.* **1998**, (1), 15-24.
- (12) Miller, S. A.; Bercaw, J. E., *Organometallics* **2006**, 25, (15), 3576-3592.
- (13) Wild, F.; Zsolnai, L.; Huttner, G.; Brintzinger, H. H., *J. Organomet. Chem.* **1982**, 232, (3), 233-247.
- (14) Panchenko, V. N.; Danilova, I. G.; Zakharov, V. A.; Paukshtis, E. A., *Kinet. Catal.* **2004**, 45, (4), 547-553.
- (15) Joubert, J.; Delbecq, F.; Sautet, P.; Le Roux, E.; Taoufik, M.; Thieuleux, C.; Blanc, F.; Coperet, C.; Thivolle-Cazat, J.; Basset, J. M., *J. Am. Chem. Soc.* **2006**, 128, (28), 9157-9169.
- (16) Atiqullah, M.; Akhtar, M. N.; Faiz, M.; Moman, A.; Abu-Raqabah, A. H.; Khan, J. H.; Wazeer, M. I., *Surf. Interface Anal.* **2006**, 38, (10), 1319-1327.

- (17) Panchenko, V. N.; Semikolenova, N. V.; Danilova, I. G.; Paukshtis, E. A.; Zakharov, V. A., *J. Mol. Catal. A-Chem.* **1999**, 142, (1), 27-37.
- (18) Blanc, F.; Thivolle-Cazat, J.; Basset, J. M.; Coperet, C.; Hock, A. S.; Tonzetich, Z. J.; Schrock, R. R., *J. Am. Chem. Soc.* **2007**, 129, (5), 1044-1045.
- (19) Bianchini, D.; dos Santos, J. H. Z.; Uozumi, T.; Sano, T., *J. Mol. Catal. A-Chem.* **2002**, 185, (1-2), 223-235.
- (20) Eisen, M. S.; Marks, T. J., *J. Am. Chem. Soc.* **1992**, 114, (26), 10358-10368.
- (21) Atiqullah, M.; Faiz, M.; Akhtar, M. N.; Salim, M. A.; Ahmed, S.; Khan, J. H., *Surf. Interface Anal.* **1999**, 27, (8), 728-734.
- (22) Ahn, H.; Marks, T. J., *J. Am. Chem. Soc.* **2002**, 124, (24), 7103-7110.
- (23) Jezequel, M.; Dufaud, V.; Ruiz-Garcia, M. J.; Carrillo-Hermosilla, F.; Neugebauer, U.; Niccolai, G. P.; Lefebvre, F.; Bayard, F.; Corker, J.; Fiddy, S.; Evans, J.; Broyer, J. P.; Malinge, J.; Basset, J. M., *J. Am. Chem. Soc.* **2001**, 123, (15), 3520-3540.
- (24) Le Roux, E.; Chabanas, M.; Baudouin, A.; de Mallmann, A.; Coperet, C.; Quadrelli, E. A.; Thivolle-Cazat, J.; Basset, J. M.; Lukens, W.; Lesage, A.; Emsley, L.; Sunley, G. J., *J. Am. Chem. Soc.* **2004**, 126, (41), 13391-13399.
- (25) Reven, L., *J. Mol. Catal.* **1994**, 86, (1-3), 447-477.
- (26) Vasnetsov, S. A.; Nosov, A. V.; Mastikhin, V. M.; Zakharov, V. A., *J. Mol. Catal.* **1989**, 53, (1), 37-41.
- (27) Blanc, F.; Basset, J. M.; Coperet, C.; Sinha, A.; Tonzetich, Z. J.; Schrock, R. R.; Solans-Monfort, X.; Clot, E.; Eisenstein, O.; Lesage, A.; Emsley, L., *J. Am. Chem. Soc.* **2008**, 130, (18), 5886-5900.
- (28) Blanc, F.; Coperet, C.; Lesage, A.; Emsley, L., *Chem. Soc. Rev.* **2008**, 37, (3), 518-526.
- (29) Bryant, P. L.; Butler, L. G.; Reyes, A. P.; Kuhns, P., *Solid State Nucl. Magn. Reson.* **2000**, 16, (1-2), 63-67.
- (30) Negureanu, L.; Hall, R. W.; Butler, L. G.; Simeral, L. A., *J. Am. Chem. Soc.* **2006**, 128, (51), 16816-16826.

- (31) Wu, F. J.; Simeral, L. S.; Mrse, A. A.; Eilertsen, J. L.; Negureanu, L.; Gan, Z. H.; Fronczek, F. R.; Hall, R. W.; Butler, L. G., *Inorg. Chem.* **2007**, 46, (1), 44-47.
- (32) Stellbrink, J.; Niu, A. Z.; Allgaier, J.; Richter, D.; Koenig, B. W.; Hartmann, R.; Coates, G. W.; Fetters, L. J., *Macromolecules* **2007**, 40, (14), 4972-4981.
- (33) Jordan, R. F.; Dasher, W. E.; Echols, S. F., *J. Am. Chem. Soc.* **1986**, 108, (7), 1718-1719.
- (34) Jordan, R. F.; Bajgur, C. S.; Willett, R.; Scott, B., *J. Am. Chem. Soc.* **1986**, 108, (23), 7410-7411.
- (35) Chien, J. C. W.; Tsai, W. M.; Rausch, M. D., *J. Am. Chem. Soc.* **1991**, 113, (22), 8570-8571.
- (36) Yang, X. M.; Stern, C. L.; Marks, T. J., *J. Am. Chem. Soc.* **1991**, 113, (9), 3623-3625.
- (37) Yang, X. M.; Stern, C. L.; Marks, T. J., *J. Am. Chem. Soc.* **1994**, 116, (22), 10015-10031.
- (38) Chen, E. Y. X.; Marks, T. J., *Chem. Rev.* **2000**, 100, (4), 1391-1434.
- (39) Tritto, I.; Li, S. X.; Sacchi, M. C.; Locatelli, P.; Zannoni, G., *Macromolecules* **1995**, 28, (15), 5358-5362.
- (40) Siedle, A. R.; Lamanna, W. M.; Newmark, R. A.; Schroepfer, J. N., *J. Mol. Catal. A-Chem.* **1998**, 128, (1-3), 257-271.
- (41) Sishta, C.; Hathorn, R. M.; Marks, T. J., *J. Am. Chem. Soc.* **1992**, 114, (3), 1112-1114.
- (42) Babushkin, D. E.; Semikolenova, N. V.; Zakharov, V. A.; Talsi, E. P., *Macromol. Chem. Phys.* **2000**, 201, (5), 558-567.
- (43) Tritto, I.; Donetti, R.; Sacchi, M. C.; Locatelli, P.; Zannoni, G., *Macromolecules* **1999**, 32, (2), 264-269.
- (44) Hamaed, H.; Lo, A. Y. H.; Lee, D. S.; Evans, W. J.; Schurko, R. W., *J. Am. Chem. Soc.* **2006**, 128, (39), 12638-12639.
- (45) Hung, I.; Schurko, R. W., *J. Phys. Chem. B* **2004**, 108, (26), 9060-9069.
- (46) Lo, A. Y. H.; Bitterwolf, T. E.; Macdonald, C. L. B.; Schurko, R. W., *J. Phys. Chem.*

A **2005**, 109, (32), 7073-7087.

(47) Rossini, A. J.; Mills, R. W.; Briscoe, G. A.; Norton, E. L.; Geier, S. J.; Hung, I.; Zheng, S.; Autschbach, J.; Schurko, R. W., *J. Amer. Chem. Soc.* **2009**, 131, (9), 3317-3330.

(48) Dybowski, C.; Bal, S., *Anal. Chem.* **2008**, 80, (12), 4295-4300.

(49) Mackenzie, K. J. D.; Smith, M. E., *Multinuclear Solid-State NMR of Inorganic Materials*. First ed.; Pergamon: Oxford, 2002.

(50) Kentgens, A. P. M., *Geoderma* **1997**, 80, (3-4), 271-306.

(51) Lipton, A. S.; Heck, R. W.; Sears, J. A.; Ellis, P. D., *J. Magn. Reson.* **2004**, 168, (1), 66-74.

(52) Lipton, A. S.; Sears, J. A.; Ellis, P. D., *J. Magn. Reson.* **2001**, 151, (1), 48-59.

(53) Smith, M. E., Recent progress in solid-state NMR of low-gamma nuclei. In *Annual Reports on Nmr Spectroscopy, Vol 43*, 2001; Vol. 43, pp 121-175.

(54) Smith, M. E.; van Eck, E. R. H., *Prog. Nucl. Magn. Reson. Spectrosc.* **1999**, 34, (2), 159-201.

(55) Ashbrook, S. E.; Duer, M. J., *Concepts Magn. Reson. Part A* **2006**, 28A, (3), 183-248.

(56) Wasylishen, R. E.; Bernard, G. M., Solid-state NMR Spectroscopy in Organometallic Chemistry. In *Comprehensive Organometallic Chemistry III*, Crabtree, R. H.; Mingos, D. M. P.; Parkin, G., Eds. Elsevier: Oxford, 2007; Vol. 1, pp 451-482.

(57) Larsen, F. H.; Jakobsen, H. J.; Ellis, P. D.; Nielsen, N. C., *J. Phys. Chem. A* **1997**, 101, (46), 8597-8606.

(58) Kupce, E.; Freeman, R., *J. Magn. Reson. Ser. A* **1995**, 115, (2), 273-276.

(59) Kupce, E.; Freeman, R., *J. Magn. Reson. Ser. A* **1996**, 118, (2), 299-303.

(60) Bhattacharyya, R.; Frydman, L., *J. Chem. Phys.* **2007**, 127, (19), 194503, 8 pages.

(61) O'Dell, L. A.; Rossini, A. J.; Schurko, R. W., *Chem. Phys. Lett.* **2009**, 468, (4-6), 330-335.

(62) O'Dell, L. A.; Schurko, R. W., *Chem. Phys. Lett.* **2008**, 464, (1-3), 97-102.

- (63) Kello, V.; Pyykko, P.; Sadlej, A. J.; Schwerdtfeger, P.; Thyssen, J., *Chem. Phys. Lett.* **2000**, 318, (1-3), 222-231.
- (64) Bastow, T. J., *J. Phys.-Condes. Matter* **1990**, 2, (29), 6327-6330.
- (65) Zhu, J. F.; Lin, Z.; Yan, Z. M.; Huang, Y. N., *Chem. Phys. Lett.* **2008**, 461, (4-6), 260-265.
- (66) Yan, Z. M.; Kirby, C. W.; Huang, Y. N., *J. Phys. Chem. C* **2008**, 112, (23), 8575-8586.
- (67) Armelao, L.; Gross, S.; Muller, K.; Pace, G.; Tondello, E.; Tsetsgee, O.; Zattin, A., *Chem. Mat.* **2006**, 18, (25), 6019-6030.
- (68) Dajda, N.; Dixon, J. M.; Smith, M. E.; Carthey, N.; Bishop, P. T., *Phys. Rev. B* **2003**, 67, (2), 024201, 9 pages.
- (69) Bastow, T. J.; Forwood, C. T.; Gibson, M. A.; Smith, M. E., *Phys. Rev. B* **1998**, 58, (6), 2988-2997.
- (70) Hartmann, P.; Scheler, G., *Z. Naturforsch. Sect. A-J. Phys. Sci.* **1995**, 50, (1), 90-94.
- (71) Bastow, T. J.; Hobday, M. E.; Smith, M. E.; Whitfield, H. J., *Solid State Nucl. Magn. Reson.* **1994**, 3, (2), 49-57.
- (72) Dec, S. F.; Davis, M. F.; Maciel, G. E.; Bronnimann, C. E.; Fitzgerald, J. J.; Han, S. S., *Inorg. Chem.* **1993**, 32, (6), 955-959.
- (73) Bastow, T. J.; Smith, M. E.; Stuart, S. N., *Chem. Phys. Lett.* **1992**, 191, (1-2), 125-129.
- (74) Hartman, J. S.; Koffyberg, F. P.; Ripmeester, J. A., *J. Magn. Reson.* **1991**, 91, (2), 400-404.
- (75) Bastow, T. J.; Smith, M. E., *Solid State Nucl. Magn. Reson.* **1992**, 1, (4), 165-174.
- (76) Pauvert, O.; Fayon, F.; Rakhmatullin, A.; Kramer, S.; Horvatic, M.; Avignant, D.; Berthier, C.; Deschamps, M.; Massiot, D.; Bessada, C., *Inorg. Chem.* **2009**, 48, (18), 8709-8717.
- (77) Bohme, U.; Thiele, K. H.; Rufinska, A., *Z. Anorg. Allg. Chem.* **1994**, 620, (8), 1455-1462.

- (78) Benn, R.; Rufinska, A., *J. Organomet. Chem.* **1984**, 273, (3), C51-C54.
- (79) Buhl, M.; Hopp, G.; vonPhilipsborn, W.; Beck, S.; Prosenc, M. H.; Rief, U.; Brintzinger, H. H., *Organometallics* **1996**, 15, (2), 778-785.
- (80) Siedle, A. R.; Newmark, R. A.; Gleason, W. B.; Lamanna, W. M., *Organometallics* **1990**, 9, (4), 1290-1295.
- (81) Sayer, B. G.; Hao, N.; Denes, G.; Bickley, D. G.; McGlinchey, M. J., *Inorg. Chim. Acta* **1981**, 48, (1), 53-55.
- (82) Sayer, B. G.; Thompson, J. I. A.; Hao, N.; Birchall, T.; Eaton, D. R.; McGlinchey, M. J., *Inorg. Chem.* **1981**, 20, (11), 3748-3750.
- (83) Deck, P. A.; Fisher, T. S.; Downey, J. S., *Organometallics* **1997**, 16, (6), 1193-1196.
- (84) Hawrelak, E. J.; Deck, P. A., *Organometallics* **2004**, 23, (1), 9-11.
- (85) Jantunen, K. C.; Scott, B. L.; Kiplinger, J. L., *J. Alloy. Compd.* **2007**, 444, 363-368.
- (86) Iuga, D.; Schafer, H.; Verhagen, R.; Kentgens, A. P. M., *J. Magn. Reson.* **2000**, 147, (2), 192-209.
- (87) Kentgens, A. P. M.; Verhagen, R., *Chem. Phys. Lett.* **1999**, 300, (3-4), 435-443.
- (88) Madhu, P. K.; Goldbourt, A.; Frydman, L.; Vega, S., *J. Chem. Phys.* **2000**, 112, (5), 2377-2391.
- (89) Eichele, K.; Wasylishen, R. E. *WSolids: Solid-State NMR Spectrum Simulation*, 2001.
- (90) Arfken, G., *Mathematical Methods for Physicists*. 3rd ed.; Academic Press: New York, 1985.
- (91) Rose, M. E., *Elementary Theory of Angular Momentum*. Wiley: New York, 1957.
- (92) Frisch, M. J.; et al. *Gaussian 03*, Revision B.03; Gaussian, Inc.: Pittsburgh, PA, 2003.
- (93) Repo, T.; Klinga, M.; Mutikainen, I.; Su, Y.; Leskela, M.; Polamo, M., *Acta Chem. Scand.* **1996**, 50, (12), 1116-1120.
- (94) Hunter, W. E.; Hrcir, D. C.; Bynum, R. V.; Penttila, R. A.; Atwood, J. L., *Organometallics* **1983**, 2, (6), 750-755.

- (95) Becke, A. D., *J. Chem. Phys.* **1993**, 98, (7), 5648-5652.
- (96) Becke, A. D., *Phys. Rev. A* **1988**, 38, (6), 3098-3100.
- (97) Lee, C. T.; Yang, W. T.; Parr, R. G., *Phys. Rev. B* **1988**, 37, (2), 785-789.
- (98) Horn, H., 1991, Computational Chemistry List, Ltd.
<http://www.ccl.net/cca/data/basis-sets/karlsruhe-old/zr.shtml>
- (99) Schafer, A.; Horn, H.; Ahlrichs, R., *J. Chem. Phys.* **1992**, 97, (4), 2571-2577.
- (100) Walch, S. P.; Bauschlicher, C. W.; Nelin, C. J., *J. Chem. Phys.* **1983**, 79, (7), 3600-3602.
- (101) Woon, D. E.; Dunning, T. H., *J. Chem. Phys.* **1993**, 98, (2), 1358-1371.
- (102) Huzinaga, S., *Gaussian Basis Sets for Molecular Calculations*. Elsevier: New York, 1984.
- (103) Wilson, A. K.; Woon, D. E.; Peterson, K. A.; Dunning, T. H., *J. Chem. Phys.* **1999**, 110, (16), 7667-7676.
- (104) Weigend, F.; Furche, F.; Ahlrichs, R., *J. Chem. Phys.* **2003**, 119, (24), 12753-12762.
- (105) Feller, D., *J. Comput. Chem.* **1996**, 17, (13), 1571-1586.
- (106) Adiga, S.; Aebi, D.; Bryce, D. L., *Can. J. Chem.-Rev. Can. Chim.* **2007**, 85, (7-8), 496-505.
- (107) Bohme, U.; Rittmeister, B., *Private Communication* **1998**, CSD Code: GEJPEQ.
- (108) Willans, M. J.; Schurko, R. W., *J. Phys. Chem. B* **2003**, 107, (22), 5144-5161.
- (109) Widdifield, C. M.; Schurko, R. W., *J. Phys. Chem. A* **2005**, 109, (31), 6865-6876.
- (110) Medek, A.; Frydman, L., *J. Braz. Chem. Soc.* **1999**, 10, (4), 263-277.
- (111) Medek, A.; Harwood, J. S.; Frydman, L., *J. Am. Chem. Soc.* **1995**, 117, (51), 12779-12787.
- (112) Antinolo, A.; Lappert, M. F.; Singh, A.; Winterborn, D. J. W.; Engelhardt, L. M.; Raston, C. L.; White, A. H.; Carty, A. J.; Taylor, N. J., *J. Chem. Soc.-Dalton Trans.* **1987**, (6), 1463-1472.
- (113) Zachmanoglou, C. E.; Docrat, A.; Bridgewater, B. M.; Parkin, G.; Brandow, C. G.;

- Bercaw, J. E.; Jardine, C. N.; Lyall, M.; Green, J. C.; Keister, J. B., *J. Am. Chem. Soc.* **2002**, 124, (32), 9525-9546.
- (114) Cheng, J. T.; Edwards, J. C.; Ellis, P. D., *J. Phys. Chem.* **1990**, 94, (2), 553-561.
- (115) Chu, P. J.; Gerstein, B. C., *J. Chem. Phys.* **1989**, 91, (4), 2081-2101.
- (116) Power, W. P.; Wasylishen, R. E.; Mooibroek, S.; Pettitt, B. A.; Danchura, W., *J. Phys. Chem.* **1990**, 94, (2), 591-598.
- (117) Bryce, D. L., Tensor Interplay. In *Encyclopedia of Magnetic Resonance*, Harris, R. K.; Wasylishen, R. E., Eds. Wiley: 2008; pp 1-11.
- (118) Coates, G. W., *Chem. Rev.* **2000**, 100, (4), 1223-1252.
- (119) Guzei, I. A.; Stockland, R. A.; Jordan, R. F., *Acta Crystallogr. Sect. C-Cryst. Struct. Commun.* **2000**, 56, 635-636.
- (120) Harris, R. K., Quadrupolar Effects. In *Nuclear Magnetic Resonance Spectroscopy*, Longman Scientific & Technical: Essex, pp 131-141.
- (121) Abragam, A., In *The Principles of Nuclear Magnetism*, Oxford University: 1961; pp 264-353.
- (122) Kurz, S.; Heyhawkins, E., *Z. Kristall.* **1993**, 205, 61-67.
- (123) Lauher, J. W.; Hoffmann, R., *J. Am. Chem. Soc.* **1976**, 98, (7), 1729-1742.
- (124) Ellis, P. D.; Lipton, A. S., Low-temperature solid-state NMR spectroscopy. A strategy for the direct observation of quadrupolar nuclides of biological interest. In *Annual Reports on Nmr Spectroscopy, Vol 60*, 2007; Vol. 60, pp 1-38.
- (125) Lipton, A. S.; Heck, R. W.; Primak, S.; McNeill, D. R.; Wilson, D. M.; Ellis, P. D., *J. Am. Chem. Soc.* **2008**, 130, (29), 9332-9341.
- (126) Lipton, A. S.; Heck, R. W.; de Jong, W. A.; Gao, A. R.; Wu, X. J.; Roehrich, A.; Harbison, G. S.; Ellis, P. D., *J. Am. Chem. Soc.* **2009**, 131, (39), 13992-13999.
- (127) Lipton, A. S.; Heck, R. W.; Hernick, M.; Fierke, C. A.; Ellis, P. D., *J. Am. Chem. Soc.* **2008**, 130, (38), 12671-12679.

Chapter 4: Solid-State $^{47/49}\text{Ti}$ NMR of Titanocene Chlorides

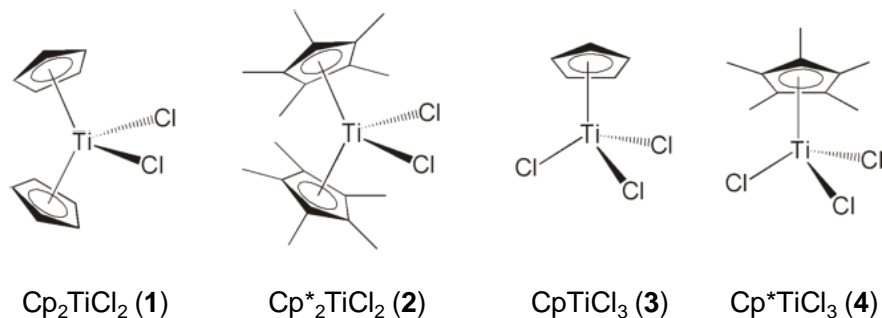
4.1 Introduction

Early transition metal metallocene complexes are highly active catalysts for olefin polymerization, affording better control over the stereospecificity and molecular weight distributions of resulting polymers than the traditional heterogeneous $\text{TiCl}_4/\text{MgCl}_2$ Ziegler-Natta system.¹⁻⁴ While certain metallocenes can be dissolved in polymerization media and used as homogeneous catalysts, they are also employed as heterogeneous catalysts on support materials such as alumina and silica.^{1,3} The solubilized homogeneous catalysts are amenable to traditional structural, kinetic and mechanistic studies; however, the active sites of supported catalysts are often difficult to characterize.^{1,3} We have demonstrated that solid-state NMR (SSNMR) spectra of metal quadrupolar nuclei that lie at the “hearts” of metallocenes can act as sensitive probes of molecular structure and dynamics,⁵⁻⁹ and could therefore find use for characterizing heterogeneous catalysts. In this regard, $^{47/49}\text{Ti}$ SSNMR could potentially serve as a powerful probe of molecular structure for titanocene-based heterogeneous catalysts.

Titanium possesses two NMR-active nuclei, ^{47}Ti ($I = 5/2$) and ^{49}Ti ($I = 7/2$),¹⁰ both of which are unreceptive owing to their low natural abundances [n.a. (^{47}Ti) = 7.44%, n.a. (^{49}Ti) = 5.41%], moderate quadrupole moments [$Q(^{47}\text{Ti}) = 29.0 \text{ fm}^2$, $Q(^{49}\text{Ti}) = 24.0 \text{ fm}^2$] and low gyromagnetic ratios [$\gamma(^{47}\text{Ti}) = -1.5105 \times 10^7 \text{ rad s}^{-1} \text{ T}^{-1}$, $\gamma(^{49}\text{Ti}) = -1.51095 \times 10^7 \text{ rad s}^{-1} \text{ T}^{-1}$].¹⁰ ^{49}Ti is preferred for SSNMR experiments, as the central-transition (CT) powder patterns are significantly narrower due to its slightly smaller quadrupole moment and higher nuclear spin. However, the similarity of the gyromagnetic ratios of ^{47}Ti and ^{49}Ti complicates the acquisition and analysis of SSNMR spectra: the difference

of the Larmor frequencies is so small that the ^{49}Ti and ^{47}Ti resonances are located ca. 267 ppm apart, which often results in overlapping CT powder patterns. Despite these difficulties there are numerous examples of $^{47/49}\text{Ti}$ solution¹¹⁻²⁵ and solid-state²⁶⁻⁴⁸ NMR found in the literature, reflecting the myriad number of important systems containing titanium.

To date, most $^{47/49}\text{Ti}$ SSNMR studies have been restricted to oxides and other extended solids. In this work, we report the first application of $^{47/49}\text{Ti}$ SSNMR for the structural characterization of molecular titanium-containing complexes. Before complex solid catalysts can be investigated by SSNMR of quadrupolar nuclei such as $^{47/49}\text{Ti}$, fundamental studies on well-characterized crystalline species are required. To this end, MAS and static $^{47/49}\text{Ti}$ SSNMR spectra of the titanocenes, Cp_2TiCl_2 (**1**), $\text{Cp}^*_2\text{TiCl}_2$ (**2**), CpTiCl_3 (**3**), and Cp^*TiCl_3 (**4**) have been acquired (Scheme 4.1). Quantum chemical calculations of NMR tensor parameters are also presented.



Scheme 4.1. Titanocene chloride complexes for which $^{47/49}\text{Ti}$ SSNMR spectra have been acquired: Cp_2TiCl_2 (**1**), $\text{Cp}^*_2\text{TiCl}_2$ (**2**), CpTiCl_3 (**3**) and Cp^*TiCl_3 (**4**).

4.2 Experimental Methods

Samples of **1** to **4** were purchased from Strem Chemicals Inc. and used without purification. All samples were finely ground into powders and packed into zirconia rotors or shortened glass NMR tubes under an inert N₂ atmosphere. ^{47/49}Ti SSNMR spectra were acquired on a 21.1 T Bruker Avance II NMR spectrometer at the Canadian National Ultrahigh-Field Facility and a 9.4 T Varian InfinityPlus. A complete listing of experimental details is given in Appendix C (Tables C1-C4). Experiments at 9.4 T were conducted with Chemagnetics 5 mm HXY MAS, 4 mm HXY and 5 mm static probes equipped with a Chemagnetics low- γ tuning box. Experiments at 21.1 T were acquired with a Bruker 4 mm HX MAS probe and home-built single-channel static 5 mm and 7 mm probes. Pulse width calibrations were performed on saturated solutions of **1** dissolved in CH₂Cl₂. Chemical shifts were referenced to neat TiCl₄(*l*) [$\delta_{\text{iso}}(^{49}\text{Ti}) = 0.0$ ppm] *via* an external standard of powdered SrTiO₃ [$\delta_{\text{iso}}(^{49}\text{Ti}) = -843$ ppm].²⁸ Experiments at 21.1 T employed standard echo sequences for acquisition. Experiments at 9.4 T employed DFS-echo^{49, 50} or DFS-QCPMG^{51, 52} pulse sequences for signal enhancement. Analytical simulations of MAS and static ^{47/49}Ti SSNMR spectra were performed with the WSolids program.⁵³ The Rose convention is used to describe the direction and order of the Euler angles which describe the CS and EFG tensor orientation.^{54, 55} The SIMPSON program was employed for numerical simulations of the MAS ⁴⁹Ti SSNMR spectrum of **4** (Figure C2).⁵⁶

Quantum chemical calculations of NMR tensor parameters were performed with the Gaussian 03⁵⁷ software package and employed molecular coordinates for isolated molecules resolved from single-crystal X-ray diffraction structures.⁵⁸⁻⁶¹ In all cases, the

hydrogen atoms were fixed to idealized positions prior to calculations. Both restricted Hartree-Fock (RHF) and hybrid density functional theory (B3LYP) calculations were performed.⁶²⁻⁶⁴ Several Ti basis sets⁶⁵ were tested and results from these calculations are given in Appendix C. The double- ζ basis set of Dunning⁶⁶ was employed for Cl and the 6-311G** basis set was employed for C and H. Additional ab initio plane-wave density functional calculations were performed using the CASTEP NMR program (Table C5).^{67, 68}

4.3 Results and Discussion

Solid-state ^{47/49}Ti NMR Spectroscopy. Magic angle spinning (MAS) ^{47/49}Ti SSNMR spectra of compounds **1** to **4** acquired at 21.1 T are shown in Figure 4.1. At 21.1 T, spectra of **1**, **3** and **4** could be acquired in relatively short experimental times (< 1.5 hours). The spectrum of **2** required *ca.* 32000 scans (1 day) due to the increased breadth of its MAS powder pattern and the reduced Ti content. The ⁴⁹Ti MAS spectra of **1** and **2** display characteristic second-order quadrupolar CT powder patterns, indicative of sizable quadrupolar interactions. From the simulations of these patterns, it is possible to obtain C_Q , η_Q and δ_{iso} (Table 4.1). For both **1** and **2**, the ⁴⁷Ti powder patterns are obscured due to their comparably larger breadths and subsequently lower signal-to-noise ratios. Simulations of the ⁴⁷Ti powder patterns which utilize a $C_Q(^{47}\text{Ti})$ that has been scaled by the ratio of ⁴⁷Ti and ⁴⁹Ti quadrupole moments, indicate that much faster sample spinning speeds are necessary to prevent sideband overlap. For this reason the reported ^{47/49}Ti NMR tensor parameters are based upon simulations of the MAS ⁴⁹Ti CT powder patterns, with the MAS ⁴⁷Ti CT patterns providing additional constraints on these parameters. It should be noted

that the crystal structure of **1** contains two crystallographically distinct titanium sites with similar local environments.⁵⁸ As a result, the ^{47/49}Ti NMR spectrum of **1** is composed of two very similar powder patterns which can be simulated with a single set of quadrupolar and chemical shift parameters. Quantum chemical calculations also confirm the similarities between the sites (*vide infra*).

In comparison to **1** and **2**, the MAS ^{47/49}Ti CT powder patterns of the trichloride species, **3** and **4**, are relatively narrow, and at 21.1 T, it is difficult to accurately extract values of C_Q and η_Q . The ⁴⁷Ti powder patterns of **3** and **4** are slightly broader and can be used to estimate C_Q and η_Q , although with large uncertainties. In order to obtain accurate measurements of C_Q and η_Q for **3** and **4**, additional MAS spectra were recorded at 9.4 T (Figure 4.1, bottom). The CT powder patterns are considerably broader than those obtained at 21.1 T, and exhibit features typical of a strong second-order quadrupolar interaction. From these spectra, EFG tensor parameters of $C_Q = 1.6$ MHz and $\eta_Q = 0.95$ and $C_Q = 3.0$ MHz and $\eta_Q = 0.35$ were obtained for **3** and **4**, respectively, comparable to the small $C_Q(^{95}\text{Mo})$ values observed for a similar “piano-stool” complex, $(\text{Me}_3\text{C}_6\text{H}_3)\text{Mo}(\text{CO})_3$.⁶⁹ Experimental times at 9.4 T were significantly greater than those at 21.1 T. The MAS ^{47/49}Ti SSNMR spectrum of **3** was acquired in 2 hours (3680 scans, 2 s pulse delay) with a DFS-echo pulse sequence, while the spectrum of **4** was acquired in ca. 21 hours (25000 scans, 3 s pulse delay) with a DFS-QCPMG sequence.

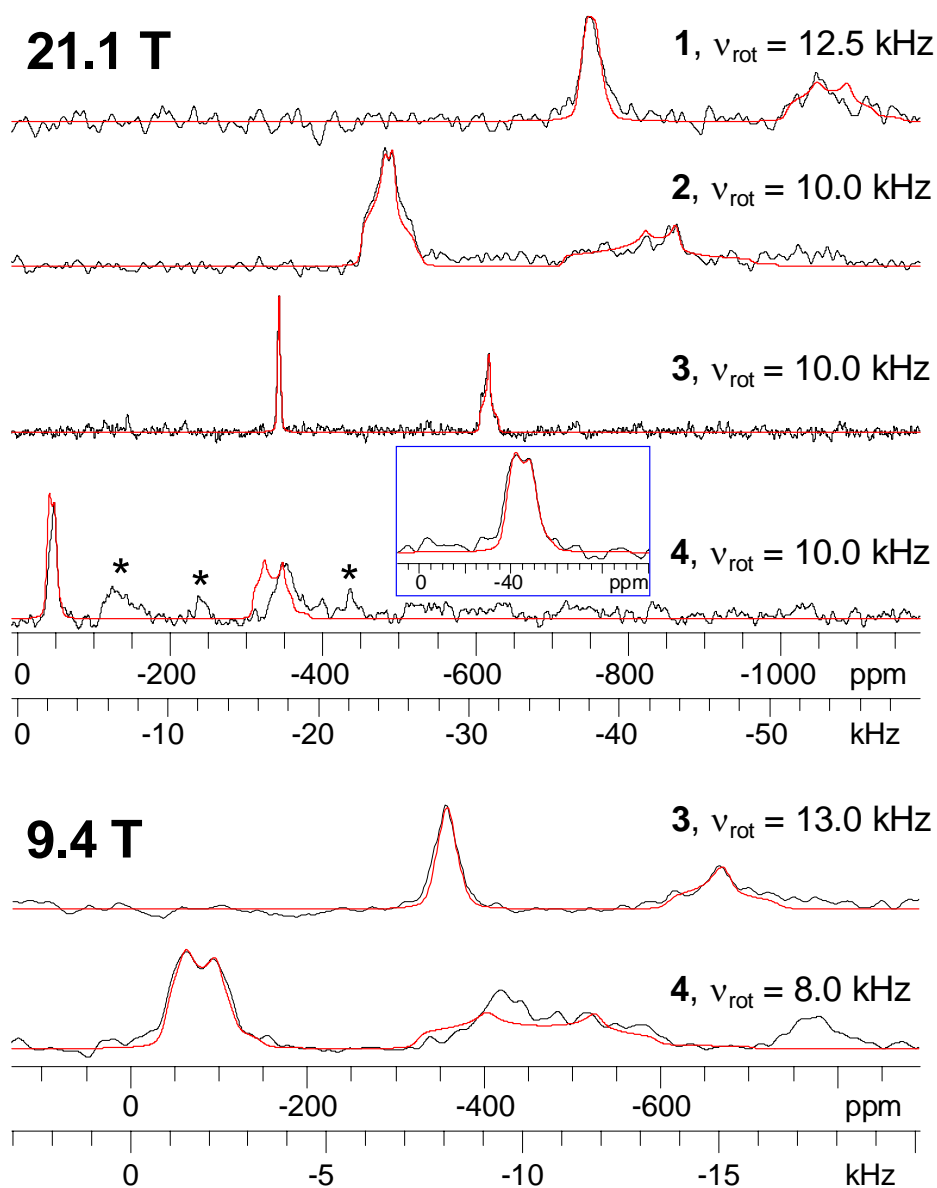


Figure 4.1. Experimental MAS $^{47/49}\text{Ti}$ SSNMR spectra (black traces) of Cp_2TiCl_2 (**1**), Cp^*TiCl_2 (**2**), CpTiCl_3 (**3**) and Cp^*TiCl_3 (**4**) acquired at 21.1 T [$\nu_0(^{49}\text{Ti}) = 50.75$ MHz] and spectra of **3** and **4** acquired at 9.4 T [$\nu_0(^{49}\text{Ti}) = 22.53$ MHz]. Sample spinning speeds are given in the figure. Analytical simulations are overlaid on the experimental spectra (red traces). All spectra at 21.1 T were acquired with a standard rotor synchronized 90° - 180° echo pulse sequence. Asterisks denote spinning sidebands. The inset of spectrum **4** shows the ^{49}Ti isotropic peak that is obtained when the single high-frequency spinning sideband and the two nearest low-frequency spinning sidebands are added onto the isotropic peak. Spectra at 9.4 T were acquired with the DFS-echo (**3**) and DFS-QCPMG (**4**) pulse sequences. The spectrum of **4** was formed by co-adding the QCPMG echoes in the time domain, followed by Fourier transformation of the resultant echo. Additional experimental details are provided in Appendix C.

Table 4.1. Experimental and Calculated $^{47/49}\text{Ti}$ EFG and CS Tensor Parameters

Complex/Method/ Structure	$\delta_{\text{iso}}(^{49}\text{Ti})$ (ppm) ^a	$C_Q(^{49}\text{Ti})$ (MHz) ^b	η_Q ^b	Ω (ppm) ^c	κ ^c	α (°) ^d	β (°)	γ (°)
Cp₂TiCl₂ (1)/Experiment	-732(5)	4.2(4)	0.45(30)	275(50)	0.65(30)	20(70)	20(20)	-10(90)
1/RHF/Site 1 Ideal Cp ^e	-689	-6.1	0.21	166	0.7	63	82	9
1/RHF/Site 1 X-ray ^e	-737	-2.0	0.55	252	0.2	-	-	-
1/RHF/Site 2 Ideal Cp	-692	-6.0	0.16	168	0.7	-	-	-
1/RHF/Site 2 X-ray	-715	4.2	0.95	230	0.3	-	-	-
1/B3LYP/Site 1 Ideal Cp	-678	3.8	0.16	526	-0.3	-	-	-
1/B3LYP/Site 1 X-ray	-729	7.8	0.07	588	-0.4	-	-	-
1/B3LYP/Site 2 Ideal Cp	-680	3.8	0.12	530	-0.3	-	-	-
1/B3LYP/Site 2 X-ray	-708	8.3	0.04	576	-0.3	-	-	-
Cp*₂TiCl₂ (2)/Experiment	-449(4)	5.5(3)	0.72(10)	165(60)	-0.1(8)	80(40)	90(30)	-5(60)
2/RHF/Ideal Cp	-478	-5.9	0.40	101	-0.1	154	19	37
2/RHF/X-ray	-479	-6.5	0.42	138	-0.4	-	-	-
2/B3LYP/Ideal Cp	-399	-4.0	0.67	327	-0.1	-	-	-
2/B3LYP/X-ray	-401	6.4	0.83	317	0.1	-	-	-
CpTiCl₃ (3)/Experiment	-341(2)	1.6(2)	0.95(10)	85(10)	0.8(2)	50(30)	12(12)	10(40)
3/RHF/Ideal Cp	-200	3.8	0.46	44	-0.5	-	-	-
3/RHF/X-ray	-214	3.8	0.60	43	-0.2	71	86	171
3/B3LYP/Ideal Cp	-239	8.5	0.19	375	-0.8	-	-	-
3/B3LYP/X-ray	-253	8.5	0.24	369	-0.8	-	-	-
Cp*TiCl₃ (4)/Experiment	-33(3)	3.0(3)	0.35(10)	650(75)	0.9(3)	30(90)	0(10)	0(90)
4/RHF/Ideal Cp	-33	1.2	0.62	394	0.9	43	63	26
4/RHF/X-ray	-33	1.4	0.57	414	1.0	-	-	-
4/B3LYP/Ideal Cp	-33	2.6	0.77	102	0.7	-	-	-
4/B3LYP/X-ray	-33	2.1	0.62	138	0.7	-	-	-
Cp ₂ TiMe ₂ /Experiment	-	-	-	-	-	-	-	-
Cp ₂ TiMe ₂ /RHF/Ideal Cp	-218	22.5	0.79	1809	-1.0	-	-	-
Cp ₂ TiMe ₂ /RHF/X-ray	-234	25.5	0.84	1811	-1.0	-	-	-

^aThe shifts are referenced to neat $\text{TiCl}_4(l)$ [$\delta_{\text{iso}}(^{49}\text{Ti}) = 0.0$ ppm] via a secondary external standard of solid SrTiO_3 for which $\delta_{\text{iso}}(^{49}\text{Ti}) = -843$ ppm. The value of $\delta_{\text{iso}}(^{47}\text{Ti}) = \delta_{\text{iso}}(^{49}\text{Ti}) - 267$ ppm. Calculated isotropic magnetic shielding (MS) values (σ_{iso}) were converted to δ_{iso} values by subtracting the calculated MS values from those calculated for **4**, $\delta_{\text{iso}} = \sigma_{\text{iso}}(\mathbf{4}) - \sigma_{\text{iso}}(\text{complex}) - 33$ ppm. ^bThe EFG tensor is defined by three principal components ordered such that $|V_{11}| \leq |V_{22}| \leq |V_{33}|$ where, $C_Q = eQV_{33}/h$ and $0.0 \leq \eta_Q = (V_{11} - V_{22})/V_{33} \leq 1.0$. The value of $C_Q(^{47}\text{Ti}) = 1.21C_Q(^{49}\text{Ti})$. ^cThe CS tensor is described by three principal components ordered such that $\delta_{11} \geq \delta_{22} \geq \delta_{33}$ where, $\delta_{\text{iso}} = (\delta_{11} + \delta_{22} + \delta_{33})/3$, $\Omega = \delta_{11} - \delta_{33}$ and $\kappa = 3(\delta_{22} - \delta_{\text{iso}})/\Omega$. ^dThe Rose convention is used to describe the Euler angles. Uncertainties associated with the last digits of the experimental NMR parameters are given in parentheses. ^eQuantum chemical calculations employed atomic coordinates obtained from single crystal X-ray diffractions structures. The “X-ray” and “Ideal Cp” labels indicate whether XRD coordinates of the Cp carbon atoms were employed or whether idealized Cp rings were employed (see main text).

Complex **4** possesses a relatively large $^{47/49}\text{Ti}$ chemical shift anisotropy (CSA, *vide infra*), which further disperses spectral intensity into the spinning sidebands and affects the shape of the isotropic CT pattern; therefore, it is necessary to sum the sideband intensity into the isotropic position to obtain an undistorted CT pattern (inset, Figure 4.1).⁷⁰ The spectrum of **4** at 9.4 T does not require the addition of spinning sidebands into the isotropic

pattern due to an increase in the relative magnitude of the quadrupolar interaction with respect to the CSA.

The trends in the titanium isotropic chemical shifts mirror those observed in previous solution NMR studies.^{14-17, 21-23, 25} An increase in δ_{iso} is observed for the Cp* complexes in comparison to the analogous Cp complexes, and the mono-Cp' species possess higher chemical shifts than the bis-Cp' species (Cp' refers to a Cp ligand of any substitution pattern). The differences in δ_{iso} of **3** and **4** have previously been correlated to the absorption maxima (λ_{max}) of UV-visible spectra, which are 380 and 437 nm for **3** and **4**, respectively.^{14, 25} It is well known that smaller energy separations between occupied and virtual-orbitals give rise to larger paramagnetic shielding interactions, and hence more positive chemical shifts (increased deshielding).⁷¹⁻⁷⁷ Thus, correlations between δ_{iso} and λ_{max} are observed when the MOs that make large contributions to the nuclear magnetic shielding are the same MOs involved in optical transitions.

A comparison of the ^{47/49}Ti EFG tensor parameters obtained from solid-state and solution ^{47/49}Ti NMR experiments is not as straightforward. In solution, the values of C_Q are estimated from the full widths at half height (FWHH) of the ^{47/49}Ti peaks, under the approximation of the extreme narrowing limit. Furthermore, the values of η_Q cannot be accurately determined from solution NMR spectra (many instances of predicting C_Q values from FWHHs rely on the assumption is that $\eta_Q = 0$, which is most often not the case). Nonetheless, the previously measured FWHH values from solution ^{47/49}Ti NMR spectra of **1** to **3** correlate well with the relative magnitudes of C_Q obtained from the corresponding solid-state NMR spectra, and the values of $C_Q(^{49}\text{Ti})$ are slightly larger for the bis-Cp' species in comparison to those of the mono-Cp' species.^{14, 22, 25} However, FWHH values

obtained from solution NMR spectra of **4** suggest that it possesses a smaller C_Q than that of **3**,^{22, 25} which is not the case in the solid state. Both **3** and **4** possess very small quadrupolar coupling constants; therefore, the differences in the magnitude of C_Q may be a result of subtle structure deviations and/or long range intermolecular electrostatic interactions. However, given the limitations of the approximations described above, it is more likely that the solid-state measurement of C_Q is simply more accurate. For complexes **1**, **2** and **4**, η_Q -values are not close to either 0 or 1, indicating that all of the components of the EFG tensor are distinct from one another. For **3**, η_Q is close to 1, indicating that V_{11} is the distinct component of the EFG tensor and $V_{22} \approx -V_{33}$).

The values of $C_Q(^{49}\text{Ti})$ obtained for **1** to **4** are on the smaller end of the range previously measured from SSNMR spectra of non-cubic oxides and other extended solids, where $C_Q(^{49}\text{Ti})$ is found to range from 2.6 to 24.0 MHz.³⁶ Similarly, in our ^{91}Zr SSNMR study of bis-Cp zirconocene dihalide complexes, we found that $C_Q(^{91}\text{Zr})$ was relatively small compared to those of oxides and related systems.⁹ This indicates that the ground state electronic environment at the metal atoms in d^0 metallocene halide complexes are of comparatively higher spherical symmetry than those of the metal oxides.

Titanium CSA has previously been observed for several titanates ($\Omega = 22 - 180$ ppm)³⁶ and the rutile phase of TiO_2 ($\Omega = 30$ ppm).⁴³ Furthermore, our previous ^{91}Zr SSNMR studies of zirconocenes,^{5, 9} ^{45}Sc SSNMR study of coordination complexes⁷⁸ and extensive ^{51}V SSNMR studies of Polenova et al.⁷⁹⁻⁸³ have indicated that CSAs are substantial for the nuclei of the elements directly adjacent to Ti in the periodic table. In order to measure the CS tensor parameters, the span (Ω) and skew (κ), static $^{47/49}\text{Ti}$ SSNMR spectra of **1** to **4** were acquired at 21.1 T and 9.4 T (Figure 4.2). The static spectra also

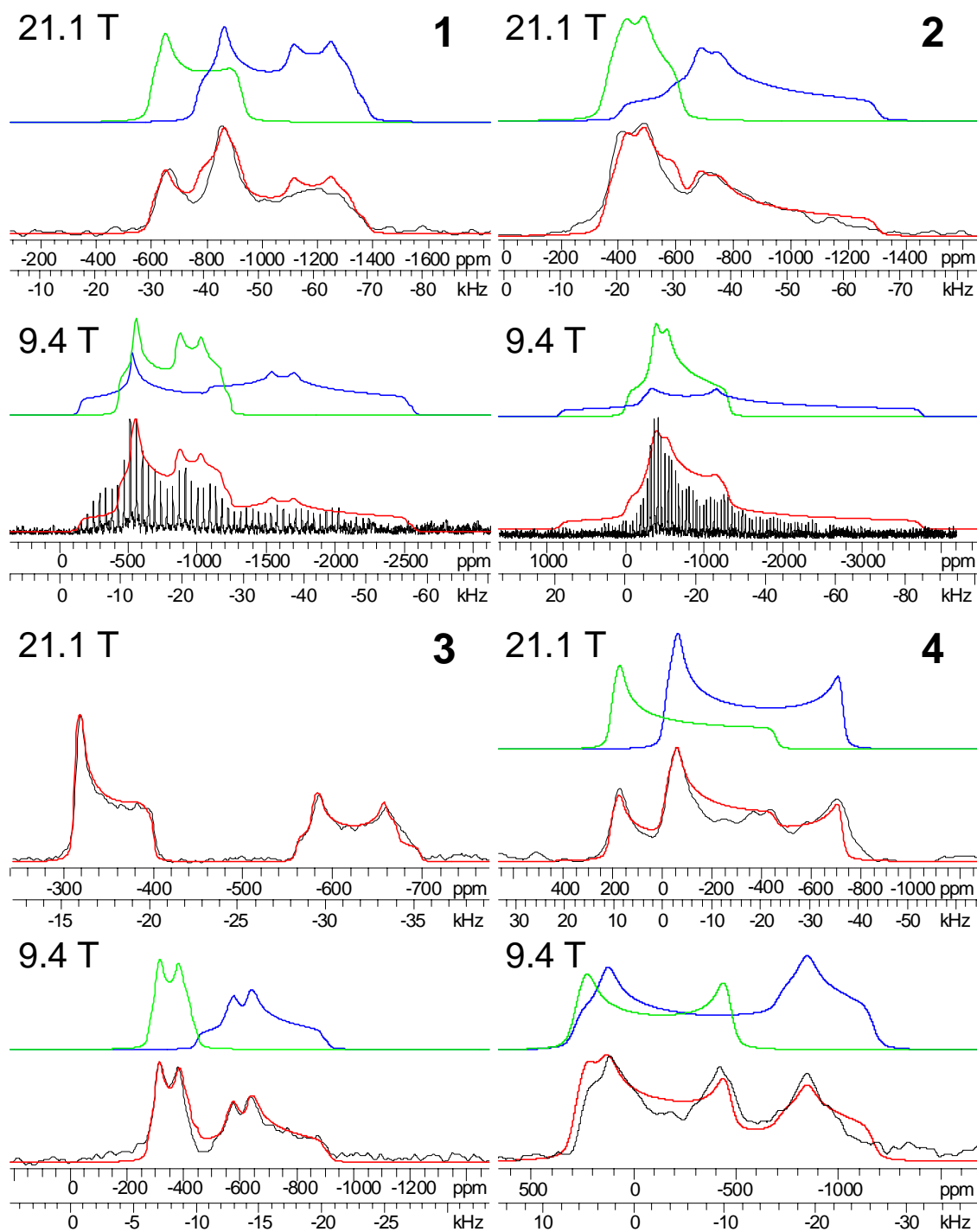


Figure 4.2. Static $^{47/49}\text{Ti}$ SSNMR spectra of Cp_2TiCl_2 (**1**), $\text{Cp}^*_2\text{TiCl}_2$ (**2**), CpTiCl_3 (**3**) and Cp^*TiCl_3 (**4**) acquired at 21.1 T and 9.4 T. Analytical simulations (red traces) are overlaid on the experimental spectra (black traces). De-convolutions of the ^{49}Ti (green traces) and ^{47}Ti (blue traces) powder pattern simulations are also shown. Spectra at 21.1 T were acquired with a standard echo sequence. Spectra of **1** and **2** at 9.4 T were acquired with the DFS-QCPMG pulse sequence.

serve to confirm EFG tensor parameters isolated from MAS spectra, and allow for the determination of the Euler angles which describe the relative orientation of the EFG and CS tensors in each complex.

The appearance of the static spectra are indicative of the presence of substantial titanium CSA (Figure 4.2); it is not possible to simulate the static powder patterns using only the quadrupolar interaction (Figure C1). For all static spectra, ^{47}Ti and ^{49}Ti powder patterns are observed to overlap, except for the spectrum of **3** acquired at 21.1 T. Overlap of the patterns can complicate simulations of the static spectra; however, with spectra from two magnetic fields it is possible to obtain reasonably accurate measurements of the CS tensors. If more accurate measurements of the CS tensors and Euler angles are desired, QCPMG experiments which employ pulses with nutation angles designed to give a spectrum with only one of the $^{47/49}\text{Ti}$ nuclei may be employed.⁴³ However, acquisition times for the static spectra were significantly longer than those for the MAS spectra, due to much wider dispersion of the signal intensity in the former. At 21.1 T, static echo spectra were acquired in 3 to 20 hours, while at 9.4 T, DFS-echo and DFS/QCPMG pulse sequences were used, with experiment times on the order of days.

From the static spectra, Ω is found to range from 85 ppm (**3**) to 650 ppm (**4**). The Ω of **1** is greater than **2** (Cp vs. Cp*), while for **3** and **4** the opposite is observed. The value of Ω for **4** is substantially larger than those of the other complexes, as well as those previously reported for other systems ($\Omega \leq 180$ ppm).³⁶ As mentioned above, the MAS spectrum of **4** possesses a number of intense spinning sidebands not observed in any of the other MAS spectra, consistent with this large CSA. SIMPSON simulations of the $^{47/49}\text{Ti}$ MAS spectra with variable values of Ω , confirm the unusually large value of $\Omega = 650$ ppm (Figure C2).

The values of κ are close to +1 for **1**, **3** and **4**, indicating that the CS tensors are all nearly axially symmetric (i.e., $\delta_{11} \approx \delta_{22}$, and δ_{33} is the distinct component of each CS tensor). Axial symmetry of the CS tensor is expected for **3** and **4**, given that these complexes possess pseudo- C_3 rotational axes. This is similar to the κ values near +1 measured for the ^{55}Mn and ^{95}Mo SSNMR spectra of piano-stool, arene-metal complexes.^{69,}
⁸⁴ However, it is interesting to note that for a series of bis-Cp zirconocene dihalide complexes analogous to **1** and **2**, we have found that κ is always close to -1 (a full discussion of this is beyond the scope of this paper).⁹ For **2**, $\kappa = -0.1$, which indicates that the three principal components of the CS tensor are unequal and approximately evenly spaced, although there is large uncertainty associated with the experimental value of κ . In summary, titanium CSA is found to be relatively large for **1** to **4**, and distinct values of Ω are observed for each complex, suggesting that this parameter can act as a useful secondary probe of molecular structure.

Quantum chemical calculations. Results from the quantum chemical calculations of titanium EFG and magnetic shielding (MS) tensors are shown in Table 4.1. We note that quantum chemical calculations provide the principal components of the MS tensor (σ_{ii}), which can then be converted to CS tensor parameters for comparison to experimental results (see footnote of Table 4.1). A number of methods and basis set combinations were tested, and summarized in Appendix C (Tables C5-C8). In addition, we have performed calculations with atomic coordinates which employ “idealized” Cp rings. In these calculations, the crystallographically determined Cp centroid distances have been retained; however, perfectly planar Cp rings with ideal C-C bond lengths (1.40 Å) and C-C-C angles (108°) have been employed. We have found this approach necessary to obtain accurate

quantum chemical calculations of ^{91}Zr EFG tensor parameters of zirconocenes.⁹ In general, RHF and B3LYP calculations which employ Ahlrichs valence double- ζ polarized (pVDZ) basis set⁶⁵ on Ti give the best agreement between experiment and theory, although calculations of some EFG and CS tensor parameters are not satisfactory. In particular, calculated values of C_Q , η_Q and Ω are poor for many of the complexes. Given the small size of the data set, it is also not clear whether the use of ideal Cp ring coordinates gives superior results to those which employ Cp ring coordinates determined by X-ray crystallography.

The RHF calculations are clearly superior for the calculation of the CS tensor parameters, yielding nearly quantitative values of δ_{iso} and correctly predicting the symmetry of the CS tensor (κ) for **1**, **2** and **4**. While the calculations do not accurately predict the values of Ω , they do correctly predict the relative values for complexes **1** to **4** (i.e., Ω for **4** > **1** > **2** > **3**). B3LYP calculations yield accurate values of δ_{iso} ; however, calculated values of Ω and κ show poor agreement with experimental values.

Both RHF and B3LYP calculations yield C_Q and η_Q values which show relatively poor agreement with the experimental data. The calculations are able to correctly predict that C_Q is relatively small for **1** – **4**; however, they are unable to predict the relative magnitudes of C_Q within the series. Accurate calculations of ^{45}Sc and ^{51}V EFG tensor parameters have previously been demonstrated,^{78-80, 82, 85} and Ti is a relatively light element for which relativistic effects should be minimal. This suggests that calculations of titanium EFG tensors should be straightforward. It may be that because C_Q is relatively small for **1** to **4**, minor errors in the calculated EFG tensor principal components (V_{ii}) lead to substantial errors in both C_Q and η_Q . Periodic plane-wave DFT calculations were also attempted for **1**

to **4** (Table C9); however, the calculated NMR tensor parameters also show poor agreement with experiment. All of this data suggests that more quantum chemical methods and functionals should be tested in the future in order to identify suitable methods for calculations of $^{47/49}\text{Ti}$ NMR tensor parameters.

Finally, we present calculated EFG and MS tensor orientations for **1** to **4** (Figure 4.3). The tensor orientations provide insight into the origin of the observed anisotropic NMR interactions and allow for correlations between the NMR interaction tensors and molecular symmetry and structure. The orientation of the calculated EFG tensors in **1** and **2** are similar. The orientation of V_{33} perpendicular to the Cl-Ti-Cl plane arises because the *electric field* is large in the direction of the chloride ligands, but small along the direction of the Cp ligands, giving rise to the large *gradient*. We have previously calculated that the magnitude of V_{33} significantly increases as the Zr-Cl bond lengths of Cp_2ZrCl_2 are shortened.⁹ In fact, the EFG and MS tensor orientations calculated for **1** are similar to those previously calculated for Cp_2ZrCl_2 .⁹ At this time, we do not comment on the orientation of the EFG tensors for **3** and **4**, as the calculated values of C_Q and η_Q show relatively poor agreement with experiment, though they are shown for reference in Figure 4.3.

For the Cp complexes, **1** and **3**, σ_{11} , the least shielded components of the MS tensors, are oriented towards the Cp ring carbon atom which lies above the Ti atom. For **1**, σ_{11} , is oriented such that it is approximately perpendicular to the Cl-Ti-Cl plane. Deshielding along this direction likely arises from mixing of high energy occupied Ti-Cl bonding molecular orbitals with low-lying unoccupied *d*-orbitals, both of which are located in the Cl-Ti-Cl plane. It is known that paramagnetic deshielding arises due to magnetic

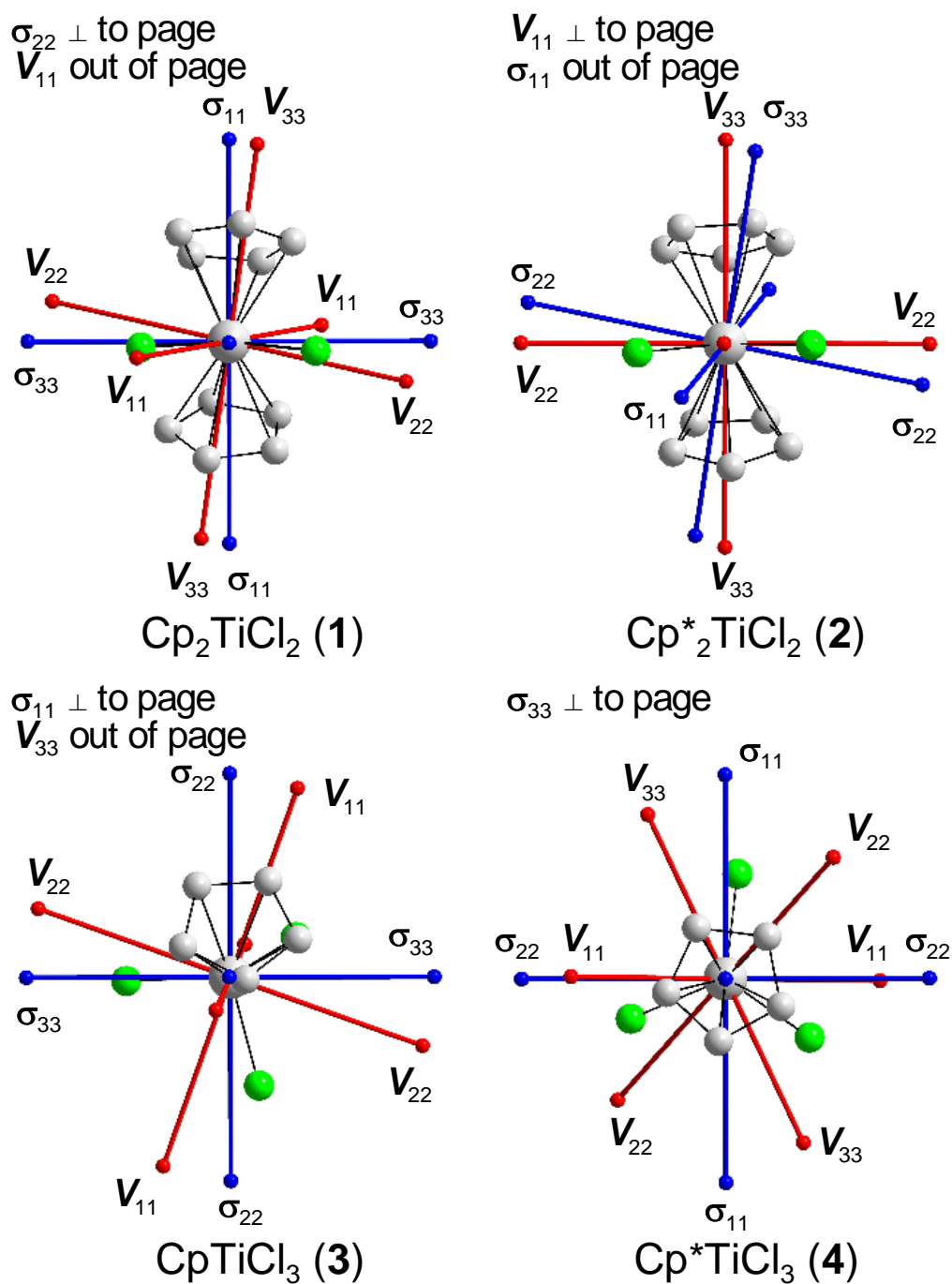


Figure 4.3. EFG and CS tensor orientations for **1** to **4** obtained from quantum chemical calculations. The Euler angles associated with these tensor orientations are listed in Table 4.1. Methyl groups and hydrogen atoms bound to the Cp rings have been omitted for clarity.

field induced mixing of occupied and virtual molecular orbitals,⁷¹⁻⁷⁷ and deshielding contributions are largest in the direction perpendicular to the plane of mixing. In this regard, Hoffman has previously presented Hückel calculations which demonstrate that the valence molecular orbitals in titanocenes correspond to Cl-Ti σ - and π -bonding orbitals.⁸⁶

In **2**, the most shielded component of the MS tensor, σ_{33} is directed towards a Cp* carbon atom which lies above the Ti atom, while in **4**, σ_{33} is directed towards the centroid of the Cp* ligand. The distinct orientations of the MS tensors for **2** and **4** compared to **1** and **3** suggest that the energies and symmetries of the molecular orbitals are undoubtedly influenced by the increased basicity of the Cp* ligand in comparison to the Cp ligands. The orientations of σ_{11} and σ_{22} for both **2** and **4** suggests deshielding primarily arises due to mixing of high energy occupied or low-lying virtual orbitals of Ti-Cp* bonding character, which is also consistent with the observations of more positive δ_{iso} values for the Cp* complexes. As noted above, previous UV-Vis measurements on **3** and **4** have found that λ_{max} occurs at longer wavelengths in the latter. If the MOs that make large *anisotropic* contributions to the nuclear magnetic shielding are the same MOs involved in optical transitions, then it is anticipated that decreased energy separations between these MOs will lead to a larger titanium CSA in **4** than **3**.

Finally, EFG and CS tensor calculations were also performed for Cp₂TiMe₂ (**5**), which is a species important to catalytic processes involving titanocenes. In order to obtain active metallocene olefin polymerization catalysts, it is necessary to treat them with an activator or co-catalyst, such as methylaluminoxane (MAO).^{1,3} MAO abstracts the chloride ligands, replaces them with methyl ligands, and subsequently abstracts a methyl group to generate a catalytically active, coordinatively unsaturated, cationic metallocene. We have

previously observed that Cp_2ZrMe_2 possesses relatively large values of $C_Q(^{91}\text{Zr}) = 28.0$ MHz and $\Omega(^{91}\text{Zr}) = 1750$ ppm.⁹ Consistent with these findings, quantum chemical calculations indicate that **5** has a very large C_Q (ca. 22-25 MHz) and CSA ($\Omega > 1800$ ppm). From these calculations it is clear that $^{47/49}\text{Ti}$ SSNMR spectra very distinct from those of **1** and **2** would be observed for methyl titanocenes. However, due to the large C_Q and Ω values, Cp_2TiMe_2 would be expected to possess a wide $^{47/49}\text{Ti}$ SSNMR spectrum of ca. 300-400 kHz in breadth at 21.1 T, the acquisition of which would be difficult, and beyond the scope of the current work.

4.4 Conclusions

MAS and static $^{47/49}\text{Ti}$ SSNMR spectra were acquired for complexes **1** to **4**, each yielding unique sets of EFG and CS tensor parameters. C_Q values for these complexes are small with respect to the known range of C_Q values. All of the complexes possess significant titanium CSAs, affording another set of NMR parameters which can be used to provide insight into their molecular and electronic structures. Quantum chemical calculations can accurately predict δ_{iso} for **1** – **4**; however, further computational methods and basis sets must be evaluated in order to obtain better agreement between experimental and theoretical $^{47/49}\text{Ti}$ NMR parameters.

At an ultrahigh magnetic field of 21.1 T, it is possible to acquire MAS and static $^{47/49}\text{Ti}$ SSNMR spectra in several hours with standard echo techniques. However, at a moderate magnetic field of 9.4 T, signal-enhancement techniques are required for the acquisition of $^{47/49}\text{Ti}$ SSNMR spectra, and acquisition times remain on the order of days. The lengthy experiment times required to obtain adequate signal-to-noise ratios suggest that

$^{47/49}\text{Ti}$ SSNMR experiments on systems with low Ti contents, such as heterogeneous catalysts, would be very challenging. However, isotopic labeling in conjunction with cross-polarization (CP)-CPMG experiments at cryogenic temperatures could enable the acquisition of $^{47/49}\text{Ti}$ spectra of heterogeneous catalysts. Ellis and Lipton have extensively utilized this approach to acquire SSNMR spectra of metalloproteins, which contain dilute concentrations of low- γ nuclei such as ^{25}Mg and ^{67}Zn .⁸⁷⁻⁹¹ CP from ^1H could be especially beneficial for $^{47/49}\text{Ti}$ given that the maximum theoretical signal enhancement is $\gamma_{\text{H}}/\gamma_{^{49}\text{Ti}} = -17.7$. In addition, the differences in CP Hartmann-Hahn matching conditions which arise from the different spins of ^{47}Ti and ^{49}Ti could be useful for selectively exciting only one of the isotopes.^{92, 93} In an analogous manner to CP experiments, the development of dynamic nuclear polarization (DNP) experiments may also be very beneficial for SSNMR studies of unresponsive nuclei such as $^{47/49}\text{Ti}$, as the maximum signal enhancement is, $\gamma_e/\gamma_{^{49}\text{Ti}} = 11654$.^{94, 95} These signal-enhancing methods and the sensitivity of $^{47/49}\text{Ti}$ NMR parameters to differences in molecular structure make $^{47/49}\text{Ti}$ SSNMR very appealing for continued study of such systems.

4.5 Bibliography

- (1) Hlatky, G. G., *Chem. Rev.* **2000**, 100, (4), 1347-1376.
- (2) Kaminsky, W.; Laban, A., *Appl. Catal. A-Gen.* **2001**, 222, (1-2), 47-61.
- (3) Severn, J. R.; Chadwick, J. C.; Duchateau, R.; Friederichs, N., *Chem. Rev.* **2005**, 105, (11), 4073-4147.
- (4) Soga, K.; Shiono, T., *Prog. Polym. Sci.* **1997**, 22, (7), 1503-1546.
- (5) Hung, I.; Schurko, R. W., *J. Phys. Chem. B* **2004**, 108, (26), 9060-9069.
- (6) Hamaed, H.; Lo, A. Y. H.; Lee, D. S.; Evans, W. J.; Schurko, R. W., *J. Am. Chem. Soc.* **2006**, 128, (39), 12638-12639.
- (7) Lo, A. Y. H.; Bitterwolf, T. E.; Macdonald, C. L. B.; Schurko, R. W., *J. Phys. Chem. A* **2005**, 109, (32), 7073-7087.
- (8) Widdifield, C. M.; Schurko, R. W., *J. Phys. Chem. A* **2005**, 109, (31), 6865-6876.
- (9) Rossini, A. J.; Hung, I.; Johnson, S. A.; Mensch, M.; Deck, P. A.; Schurko, R. W., *J. Am. Chem. Soc.* **2010**, Submitted.
- (10) Harris, R. K.; Becker, E. D.; De Menezes, S. M. C.; Goodfellow, R.; Granger, P., *Pure Appl. Chem.* **2001**, 73, (11), 1795-1818.
- (11) Foris, A., *Magn. Reson. Chem.* **2000**, 38, (12), 1044-1046.
- (12) Fedotov, M. A.; Zekovets, G. A.; Gavrilov, V. Y., *Zh. Neorg. Khim.* **1999**, 44, (6), 973-976.
- (13) Boyle, T. J.; Alam, T. M.; Mechenbier, E. R.; Scott, B. L.; Ziller, J. W., *Inorg. Chem.* **1997**, 36, (15), 3293-3300.
- (14) Hafner, A.; Okuda, J., *Organometallics* **1993**, 12, (3), 949-50.
- (15) Hafner, A.; Duthaler, R. O.; Marti, R.; Rihs, G.; Rothe-Streit, P.; Schwarzenbach, F., *J. Am. Chem. Soc.* **1992**, 114, (7), 2321-36.
- (16) Traill, P. R.; Young, C. G., *J. Magn. Reson.* **1990**, 90, (3), 551-6.
- (17) Berger, S.; Bock, W.; Marth, C. F.; Raguse, B.; Reetz, M. T., *Magn. Reson. Chem.* **1990**, 28, (6), 559-60.
- (18) Finch, W. C.; Anslyn, E. V.; Grubbs, R. H., *J. Am. Chem. Soc.* **1988**, 110, (8), 2406-13.

- (19) Chi, K. M.; Frerichs, S. R.; Philson, S. B.; Ellis, J. E., *J. Am. Chem. Soc.* **1988**, 110, (1), 303-4.
- (20) McGlinchey, M. J.; Bickley, D. G., *Polyhedron* **1985**, 4, (6), 1147-8.
- (21) Gassman, P. G.; Campbell, W. H.; Macomber, D. W., *Organometallics* **1984**, 3, (3), 385-7.
- (22) Dormond, A.; Fauconet, M.; Leblanc, J. C.; Moise, C., *Polyhedron* **1984**, 3, (7), 897-900.
- (23) Hao, N.; Sayer, B. G.; Denes, G.; Bickley, D. G.; Detellier, C.; McGlinchey, M. J., *J. Magn. Reson.* **1982**, 50, (1), 50-63.
- (24) Kidd, R. G.; Matthews, R. W.; Spinney, H. G., *J. Am. Chem. Soc.* **1972**, 94, (19), 6686-9.
- (25) Erben, M.; Ruzicka, A.; Picka, M.; Pavlik, I., *Magn. Reson. Chem.* **2004**, 42, (4), 414-417.
- (26) Forbes, C. E.; Hammond, W. B.; Cipollini, N. E.; Lynch, J. F., *J. Chem. Soc., Chem. Commun.* **1987**, (6), 433-6.
- (27) Bastow, T. J., *J. Phys. Condens. Matter* **1989**, 1, (30), 4985-91.
- (28) Dec, S. F.; Davis, M. F.; Maciel, G. E.; Bronnimann, C. E.; Fitzgerald, J. J.; Han, S. S., *Inorg. Chem.* **1993**, 32, (6), 955-9.
- (29) Bastow, T. J.; Forwood, C. T.; Gibson, M. A.; Smith, M. E., *Phys. Rev. B* **1998**, 58, (6), 2988-2997.
- (30) Bastow, T. J.; Gibson, M. A.; Forwood, C. T., *Solid State Nucl. Magn. Reson.* **1998**, 12, (4), 201-209.
- (31) Bastow, T. J.; Whitfield, H. J., *Chem. Mater.* **1999**, 11, (12), 3518-3520.
- (32) Kiyama, T.; Fujisawa, S.; Saitoh, H.; Itoh, M.; Kodama, K.; Takigawa, M., *Physica B* **2003**, 329, 733-735.
- (33) Zalar, B.; Laguta Valentin, V.; Blinc, R., *Phys. Rev. Lett.* **2003**, 90, (3), 037601.
- (34) Kiyama, T.; Itoh, M., *Phys. Rev. Lett.* **2003**, 91, (16), 7202-6.
- (35) Ganapathy, S.; Gore, K. U.; Kumar, R.; Amoureux, J. P., *Solid State Nucl. Magn. Reson.* **2003**, 24, (2-3), 184-195.

- (36) Padro, D.; Jennings, V.; Smith, M. E.; Hoppe, R.; Thomas, P. A.; Dupree, R., *J. Phys. Chem. B* **2002**, 106, (51), 13176-13185.
- (37) Gervais, C.; Smith, M. E.; Pottier, A.; Jolivet, J. P.; Babonneau, F., *Chem. Mater.* **2001**, 13, (2), 462-467.
- (38) Crevoiserat, S.; Lehnert, T.; Dimitropoulos, C.; Gotthardt, R., *Metallofizika i Noveishie Tekhnologii* **2001**, 23, (Spets. Vyp.), 182-187.
- (39) Bastow, T. J.; Whitfield, H. J., *Solid State Commun.* **2001**, 117, (8), 483-488.
- (40) Bastow, T. J.; Doran, G.; Whitfield, H. J., *Chem. Mater.* **2000**, 12, (2), 436-439.
- (41) Koyama, T.; Sugita, H.; Wada, S.; Miyatani, K.; Tanaka, T.; Ishikawa, M., *Physica B* **2000**, 284-288, 1513-1514.
- (42) Bastow, T. J., *Z. Naturforsch., A: Phys. Sci.* **2000**, 55, (1/2), 291-297.
- (43) Larsen, F. H.; Farnan, I.; Lipton, A. S., *J. Magn. Reson.* **2006**, 178, 228-236.
- (44) Toberer, E. S.; Epping, J. D.; Chmelka, B. F.; Seshadri, R., *Chem. Mat.* **2006**, 18, (26), 6345-6351.
- (45) Wagner, G. W.; Procell, L. R.; Munavalli, S., *J. Phys. Chem. C* **2007**, 111, (47), 17564-17569.
- (46) MacKenzie, K. J. D.; Smith, M. E., *Multinuclear Solid-state NMR of Inorganic Materials*. Pergamon: Oxford, 2002.
- (47) Brauniger, T.; Madhu, P. K.; Pampel, A.; Reichert, D., *Solid State Nucl. Magn. Reson.* **2004**, 26, (3-4), 114-120.
- (48) Zhu, J. F.; Trefiak, N.; Woo, T. K.; Huang, Y. N., *J. Phys. Chem. C* **2009**, 113, (23), 10029-10037.
- (49) Kentgens, A. P. M.; Verhagen, R., *Chem. Phys. Lett.* **1999**, 300, (3-4), 435-443.
- (50) Iuga, D.; Schafer, H.; Verhagen, R.; Kentgens, A. P. M., *J. Magn. Reson.* **2000**, 147, (2), 192-209.
- (51) Schurko, R. W.; Hung, I.; Widdifield, C. M., *Chem. Phys. Lett.* **2003**, 379, (1-2), 1-10.
- (52) Larsen, F. H.; Jakobsen, H. J.; Ellis, P. D.; Nielsen, N. C., *J. Phys. Chem. A* **1997**, 101, (46), 8597-8606.

- (53) Eichele, K.; Wasylishen, R. E. *WSolids: Solid-State NMR Simulation Package*, V1.17.28; 2001.
- (54) Arfken, G., *Mathematical Methods for Physicists*. 3rd ed.; Academic Press: New York, 1985.
- (55) Rose, M. E., *Elementary Theory of Angular Momentum*. Wiley: New York, 1957.
- (56) Bak, M.; Rasmussen, J. T.; Nielsen, N. C., *J. Magn. Reson.* **2000**, 147, (2), 296-330.
- (57) Frisch, M. J.; Trucks, G. W.; Schlegel, H. B.; Scuseria, G. E.; Robb, M. A.; Cheeseman, J. R.; Montgomery, J., J. A.; Vreven, T.; Kudin, K. N.; Burant, J. C. *Gaussian 03*, Revision B.03; Gaussian, Inc.: Pittsburgh, PA, 2003.
- (58) Clearfield, A.; Warner, D. K.; Saldarriagamolina, C. H.; Ropal, R.; Bernal, I., *Can. J. Chem.-Rev. Can. Chim.* **1975**, 53, (11), 1622-1629.
- (59) McKenzie, T. C.; Sanner, R. D.; Bercaw, J. E., *J. Organomet. Chem.* **1975**, 102, (4), 457-466.
- (60) Pevec, A., *Acta Chim. Slov.* **2003**, 50, (2), 199-200.
- (61) Rossini, A. J.; Mills, R. W.; Briscoe, G. A.; Norton, E. L.; Geier, S. J.; Hung, I.; Zheng, S.; Autschbach, J.; Schurko, R. W., *J. Am. Chem. Soc.* **2009**, 131, (9), 3317-3330.
- (62) Becke, A. D., *Phys. Rev. A* **1988**, 38, (6), 3098-3100.
- (63) Becke, A. D., *J. Chem. Phys.* **1993**, 98, (7), 5648-5652.
- (64) Lee, C. T.; Yang, W. T.; Parr, R. G., *Phys. Rev. B* **1988**, 37, (2), 785-789.
- (65) Schafer, A.; Horn, H.; Ahlrichs, R., *J. Chem. Phys.* **1992**, 97, (4), 2571-2577.
- (66) Woon, D. E.; Dunning, T. H., *J. Chem. Phys.* **1993**, 98, (2), 1358-1371.
- (67) Clark, S. J.; Segall, M. D.; Pickard, C. J.; Hasnip, P. J.; Probert, M. J.; Refson, K.; Payne, M. C., *Z. Kristall.* **2005**, 220, (5-6), 567-570.
- (68) Profeta, M.; Mauri, F.; Pickard, C. J., *J. Am. Chem. Soc.* **2003**, 125, (2), 541-548.
- (69) Bryce, D. L.; Wasylishen, R. E., *Phys. Chem. Chem. Phys.* **2002**, 4, (15), 3591-3600.
- (70) Wu, G.; Zhu, J. F.; Mo, X.; Wang, R. Y.; Terskikh, V., *J. Am. Chem. Soc.* **2010**, 132, (14), 5143-5155.
- (71) Widdifield, C. M.; Schurko, R. W., *Concepts Magn. Reson. Part A* **2009**, 34A, (2), 91-123.

- (72) Schreckenbach, G.; Ziegler, T., *J. Phys. Chem.* **1995**, 99, (2), 606-611.
- (73) Grutzner, J. B., Chemical Shift Theory. Orbital Symmetry and Charge Effects on Chemical Shifts. In *Recent Advances in Organic NMR Spectroscopy*, Lambert, J. B.; Rittner, R., Eds. Norell Press: Landisville, 1987; pp 17-42.
- (74) Forgeron, M. A. M.; Wasylshen, R. E., *J. Am. Chem. Soc.* **2006**, 128, (24), 7817-7827.
- (75) Feindel, K. W.; Ooms, K. J.; Wasylshen, R. E., *Phys. Chem. Chem. Phys.* **2007**, 9, (10), 1226-1238.
- (76) Wiberg, K. B.; Hammer, J. D.; Zilm, K. W.; Keith, T. A.; Cheeseman, J. R.; Duchamp, J. C., *J. Org. Chem.* **2004**, 69, (4), 1086-1096.
- (77) Wiberg, K. B.; Hammer, J. D.; Zilm, K. W.; Cheeseman, J. R.; Keith, T. A., *J. Phys. Chem. A* **1998**, 102, (45), 8766-8773.
- (78) Rossini, A. J.; Schurko, R. W., *J. Am. Chem. Soc.* **2006**, 128, (32), 10391-10402.
- (79) Ooms, K. J.; Bolte, S. E.; Baruah, B.; Choudhary, M. A.; Crans, D. C.; Polenova, T., *Dalton Trans.* **2009**, (17), 3262-3269.
- (80) Bolte, S. E.; Ooms, K. J.; Polenova, T.; Baruah, B.; Crans, D. C.; Smee, J. J., *J. Chem. Phys.* **2008**, 128, (5), 052317-052328.
- (81) Ooms, K. J.; Bolte, S. E.; Smee, J. J.; Baruah, B.; Crans, D. C.; Polenova, T., *Inorg. Chem.* **2007**, 46, (22), 9285-9293.
- (82) Pooransingh-Margolis, N.; Renirie, R.; Hasan, Z.; Wever, R.; Vega, A. J.; Polenova, T., *J. Am. Chem. Soc.* **2006**, 128, (15), 5190-5208.
- (83) Huang, W. L.; Todaro, L.; Yap, G. P. A.; Beer, R.; Francesconi, L. C.; Polenova, T., *J. Am. Chem. Soc.* **2004**, 126, (37), 11564-11573.
- (84) Ooms, K. J.; Feindel, K. W.; Terskikh, V. V.; Wasylshen, R. E., *Inorg. Chem.* **2006**, 45, (21), 8492-8499.
- (85) Ooms, K.; Polenova, T.; Shough, A. M.; Doren, D. J.; Nash, M. J.; Lobo, R. F., *J. Phys. Chem. C* **2009**, 113, (24), 10477-10484.
- (86) Lauher, J. W.; Hoffmann, R., *J. Am. Chem. Soc.* **1976**, 98, (7), 1729-1742.

- (87) Larsen, F. H.; Lipton, A. S.; Jakobsen, H. J.; Nielsen, N. C.; Ellis, P. D., *J. Am. Chem. Soc.* **1999**, 121, (15), 3783-3784.
- (88) Lipton, A. S.; Buchko, G. W.; Sears, J. A.; Kennedy, M. A.; Ellis, P. D., *J. Am. Chem. Soc.* **2001**, 123, (5), 992-993.
- (89) Lipton, A. S.; Sears, J. A.; Ellis, P. D., *J. Magn. Reson.* **2001**, 151, (1), 48-59.
- (90) Lipton, A. S.; Heck, R. W.; Sears, J. A.; Ellis, P. D., *J. Magn. Reson.* **2004**, 168, (1), 66-74.
- (91) Lipton, A. S.; Heck, R. W.; Primak, S.; McNeill, D. R.; Wilson, D. M.; Ellis, P. D., *J. Am. Chem. Soc.* **2008**, 130, (29), 9332-9341.
- (92) Walter, T. H.; Turner, G. L.; Oldfield, E., *J. Magn. Reson.* **1988**, 76, (1), 106-120.
- (93) Vega, S., *Phys. Rev. A* **1981**, 23, (6), 3152-3173.
- (94) Rosay, M.; Tometich, L.; Pawsey, S.; Bader, R.; Schauwecker, R.; Blank, M.; Borchard, P. M.; Cauffman, S. R.; Felch, K. L.; Weber, R. T.; Temkin, R. J.; Griffin, R. G.; Maas, W. E., *Phys. Chem. Chem. Phys.* **2010**, 12, (22), 5850-5860.
- (95) Griffin, R. G.; Prisner, T. F., *Phys. Chem. Chem. Phys.* **2010**, 12, (22), 5737-5740.

Chapter 5: Experimental and Theoretical Studies of ^{45}Sc NMR Interactions in Solids

5.1 Introduction

The chemistry of scandium has not been explored to the extent of other transition metals due to the relatively high costs of materials and its limited reactivity arising from restriction to the +3 oxidation state. The use of scandium in both inorganic and organometallic chemistry has recently received more attention, as observed by the increasing number of compounds that have been synthesized and characterized by single-crystal X-ray diffraction and other methods.^{1,2} Scandium is found in an assortment of materials, such as alloys,³ inorganic materials,⁴⁻⁹ ferroelectric relaxors and ceramics.¹⁰⁻¹⁵ Scandium complexes are also used in a number of organic syntheses and polymerization reactions. Certain Sc(III) complexes, due to the extreme electron deficiency at the Sc atom, act as some of the strongest Lewis acids among transition metal complexes. For instance, scandium triflate is extensively used in organic synthesis to catalyse a wide variety of reactions.^{16,17} There is also increasing interest in the organometallic chemistry of scandium, since Sc-C bonds are especially susceptible to insertion reactions involving unsaturated molecules. Active scandium catalysts for the copolymerisation of ethylene with styrene or norbornene have been synthesized.^{18,19} Further advances have also been made with the incorporation of non-cyclopentadienyl ligand systems.^{20,21} Given the increased interest in scandium chemistry, development of solid-state ^{45}Sc NMR spectroscopy for characterization of molecular structure and dynamics in both crystalline

and disordered materials is of great importance.

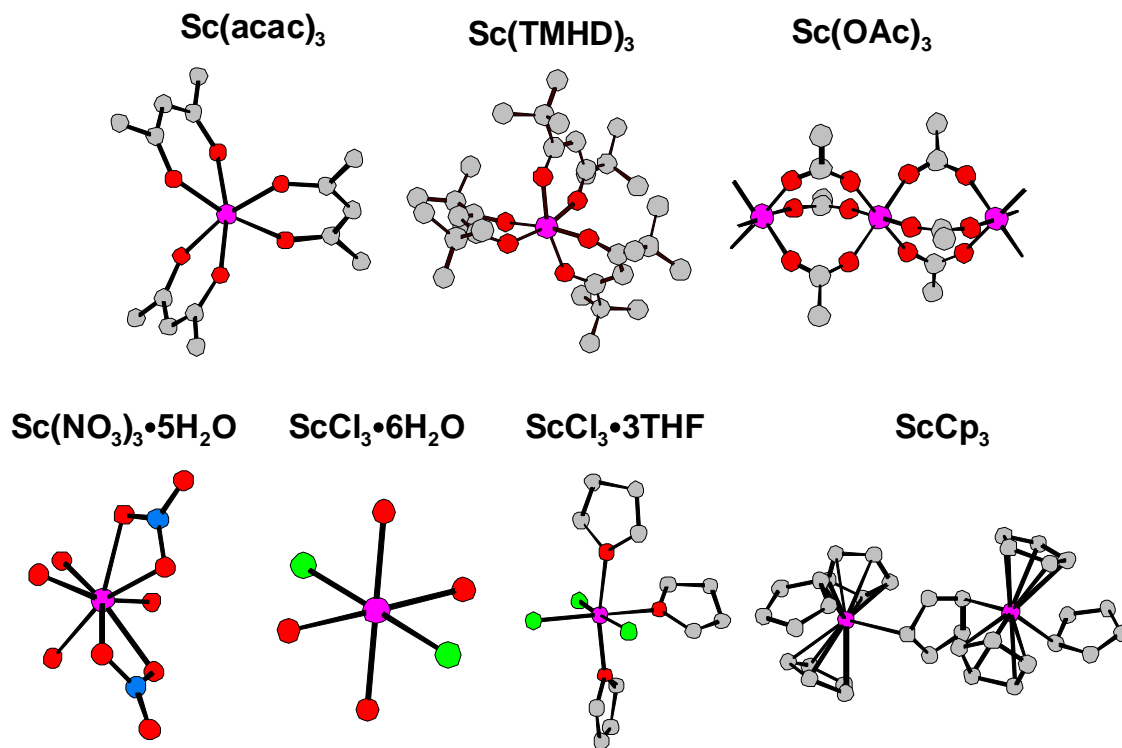
Scandium has one naturally occurring NMR active isotope, ^{45}Sc , which is 100% naturally abundant, possesses a gyromagnetic ratio of $6.50880 \times 10^7 \text{ rad T}^{-1} \text{ s}^{-1}$ (close to ^{13}C), a nuclear spin of $I = 7/2$, and a moderate nuclear quadrupole moment (Q) of $0.22 \times 10^{-28} \text{ m}^2$. These factors result in a relative receptivity of 1780 in comparison to ^{13}C , making ^{45}Sc an excellent nucleus for NMR experimentation. Solid-state ^{45}Sc NMR spectra are normally comprised of relatively broad powder patterns which result from anisotropic NMR interactions. The quadrupolar interaction (QI) normally determines the appearance of such spectra, though the effects of chemical shift anisotropy (CSA) also significantly influence the appearance of the spectra. ^1H - ^{45}Sc dipolar coupling can be observed in some instances. While the presence of these interactions generally complicate solid-state NMR spectra and increase acquisition times, they also act as a rich source of information on molecular structure and dynamics.

Several solution ^{45}Sc NMR studies have established a chemical shift range of approximately 250 ppm.²²⁻³⁵ By contrast, there are few reported examples of solid-state ^{45}Sc NMR, and even fewer in which chemical shift (CS) and electric field gradient (EFG) tensor parameters have been measured. In a preliminary study by Thompson and Oldfield, the isotropic scandium chemical shift (δ_{iso}), ^{45}Sc quadrupolar coupling constant (C_Q) and the electric field gradient asymmetry parameter (η_Q) of $\text{Sc}(\text{OAc})_3$ (OAc = acetate) and $\text{ScCl}_3 \cdot 6\text{H}_2\text{O}$ were measured.³⁶ Solid-state ^{45}Sc NMR was also utilized by Han et al. to observe hydrogen diffusion in hexagonally close packed scandium metal,³⁷ by Kataoka et al. to observe temperature-induced phase transitions in $\text{Sc}(\text{OAc})_3$ ³⁸ and by Koyama et al.,

who examined a ternary superconductor, $\text{Sc}_5\text{Co}_4\text{Si}_{10}$.³⁹ Several NMR studies on ferroelectric relaxors⁴⁰⁻⁴³ and a variety of Sc-containing alloys and materials of mixed compositions^{4, 9, 44, 45} have also been reported. In addition, due to the favourable NMR characteristics, ^{45}Sc NMR has been employed for the design and optimization of pulse sequences for spin (I) 7/2 nuclei.⁴⁶⁻⁴⁸

In this paper we report a comprehensive solid-state ^{45}Sc NMR study of scandium coordination complexes, in an effort to gain an understanding of the relationship between scandium coordination environments and the observed NMR parameters. The complexes under study are pictured in Scheme 1 (hydrogen atoms and molecules not bound to scandium are omitted for clarity). These complexes are $\text{Sc}(\text{acac})_3$, $\text{Sc}(\text{TMHD})_3$, $\text{Sc}(\text{OAc})_3$, $\text{Sc}(\text{NO}_3)_3 \cdot 5\text{H}_2\text{O}$, $\text{ScCl}_3 \cdot 6\text{H}_2\text{O}$, $\text{ScCl}_3 \cdot 3\text{THF}$, and ScCp_3 (acac = acetylacetonate, TMHD = 2,2,6,6-tetramethyl-3,5-heptanedionato, THF = tetrahydrofuran and Cp = cyclopentadienyl). All of these complexes have crystal structures which were previously reported or are reported for the first time herein. These complexes were chosen because they afford a range of coordination environments about the scandium nucleus leading to the observation of an assortment of distinct CS and EFG tensor parameters. Quantum mechanical calculations of NMR interaction tensors are utilized to examine the orientation of NMR tensors within molecular frames, and to help rationalize the origin of scandium NMR interactions. We also demonstrate the application of solid-state ^{45}Sc NMR for probing unknown molecular structures, including the Lewis acid catalyst $\text{Sc}(\text{OTf})_3$ and a polystyrene microencapsulated (ME) form of $\text{Sc}(\text{OTf})_3$ (OTf = SO_3CF_3). Application of solid-state NMR to the ME- $\text{Sc}(\text{OTf})_3$ is of particular interest, since

structural changes imparted by microencapsulation increase the catalytic activity of $\text{Sc}(\text{OTf})_3$ in carbon-carbon bond-forming reactions.



Scheme 5.1. Scandium complexes for which solid-state ^{45}Sc NMR spectra have been acquired.

5.2 Experimental

Sample Preparation. Samples of tris(cyclopentadienyl) scandium (ScCp_3) and scandium chloride hexahydrate ($\text{ScCl}_3 \cdot 6\text{H}_2\text{O}$) were purchased from Sigma-Aldrich Canada, Ltd. and used without purification. A sample of scandium acetate hydrate ($\text{Sc}(\text{OAc})_3 \cdot x\text{H}_2\text{O}$) was acquired from Sigma-Aldrich Canada, Ltd. and was recrystallized from a 5.0 M aqueous solution of acetic acid and dried in vacuo to produce anhydrous

scandium acetate ($\text{Sc}(\text{OAc})_3$). Samples of tris(2,2,6,6-tetramethyl-3,5-heptanedionato) scandium ($\text{Sc}(\text{TMHD})_3$), scandium nitrate pentahydrate ($\text{Sc}(\text{NO}_3)_3 \cdot 5\text{H}_2\text{O}$), scandium trifluoromethanesulfonate ($\text{Sc}(\text{OTf})_3$) and scandium trifluoromethanesulfonate microencapsulated in a styrene polymer (ME $\text{Sc}(\text{OTf})_3$) were purchased from Strem Chemicals, Inc., and used without further purification. Samples of scandium tris(acetylacetonate) ($\text{Sc}(\text{acac})_3$) and scandium chloride tris(tetrahydrofuran) ($\text{ScCl}_3 \cdot 3\text{THF}$) were synthesized in the research laboratories of Prof. Warren Piers at the University of Calgary using standard procedures.^{49, 50} A second sample of $\text{ScCl}_3 \cdot 3\text{THF}$ was prepared by adding anhydrous ScCl_3 to an excess of THF. The sample was then dried in vacuo and used without further purification. All samples were finely ground, packed into 4 mm outer diameter zirconia rotors and sealed with airtight caps under a nitrogen or argon atmosphere. The $\text{Sc}(\text{acac})_3$ and $\text{Sc}(\text{TMHD})_3$ samples were prepared in a similar manner outside of the glovebox.

Solid-state NMR Spectroscopy. Solid-state ^{45}Sc , ^{13}C and ^{19}F NMR spectra were acquired on a Varian Infinity Plus spectrometer with an Oxford 9.4 T ($\nu_0(^1\text{H}) = 400$ MHz) wide-bore magnet. Additional ^{45}Sc static spectra were acquired on a Bruker Avance 500 spectrometer with an 11.75 T ($\nu_0(^1\text{H}) = 500$ MHz) magnet. ^{45}Sc chemical shifts were reported with respect to an external standard solution of 0.11 molal (moles of solute/kg of solvent) ScCl_3 in 0.05 M HCl ($\delta_{\text{iso}} = 0.0$ ppm). As there is currently no universally applied scandium NMR standard, this sample was chosen due to the sharp peak observed in its solution NMR spectrum, and the insensitivity of the scandium chemical shift to changes in hydrogen chloride concentrations from 0.05 M to 1.0 M.²³ ^{13}C chemical shifts

were referenced to tetramethylsilane ($\delta_{\text{iso}} = 0.0$ ppm) by using the high-frequency peak of adamantane as a secondary reference ($\delta_{\text{iso}} = 38.57$ ppm). ^{19}F chemical shifts were referenced to fluorotrichloromethane ($\delta_{\text{iso}} = 0.0$ ppm) by setting the ^{19}F resonance of Teflon ($\delta_{\text{iso}} = -122.0$ ppm) as a secondary reference.

Central-transition selective $\pi/2$ pulse widths were calculated by scaling the non-selective pulses by a factor of a quarter, i.e., $(I + 1/2)^{-1}$. Unless otherwise noted, a quadrupolar echo pulse sequence of the form $\{\pi/2_x - \tau_1 - \pi_{\pm y} - \tau_2 - \text{acquire}\}$ was used for the acquisition of ^{45}Sc NMR spectra. Static ^{45}Sc NMR spectra of $\text{Sc}(\text{acac})_3$, $\text{Sc}(\text{OAc})_3$ and $\text{ScCl}_3 \cdot 3\text{THF}$ were also acquired with a echo pulse sequence of the form $\{\pi/2_x - \tau_1 - \pi/2_{\pm y} - \tau_2 - \text{acquire}\}$ (90° - 90° echo). Rotary-assisted polarization transfer (RAPT)⁵¹ and amplitude-modulated double frequency sweep (AM-DFS)⁵² pulse sequences were employed for the acquisition of selected spectra. ^{45}Sc NMR experiments were conducted at $\nu_0(^{45}\text{Sc}) = 97.4$ MHz (9.4 T) and 122.0 MHz (11.75 T). The rf fields used for acquisition of the static ^{45}Sc NMR spectra were generally set to one half of the pattern width in order to avoid lineshape distortions.⁵³ All experimental parameters can be found in Table D1. Analytical simulations of ^{45}Sc solid-state NMR spectra were performed using WSolids⁵⁴ and numerical simulations were performed using SIMPSON.⁵⁵

^{13}C NMR spectra were acquired using Hahn-echo and variable-amplitude cross-polarization MAS (VACP/MAS) pulse sequences. $^1\text{H} \rightarrow ^{13}\text{C}$ CP was performed on all samples for the acquisition of ^{13}C spectra, except for the $\text{Sc}(\text{OTf})_3$ samples, for which $^{19}\text{F} \rightarrow ^{13}\text{C}$ CP was applied. The TPPM⁵⁶ decoupling sequence was employed in all cases. Solid-state ^{19}F NMR spectra were acquired with a rotor-synchronized Hahn-echo pulse

sequence.

Quantum Chemical Calculations. Calculations of CS and EFG tensors were performed using Gaussian 03⁵⁷ running on two Dell Precision workstations running Red Hat Linux 9.0. Molecular coordinates were input from structures determined by single-crystal X-ray diffraction experiments and proton positions were geometry-optimized for most structures. Calculations were carried out using restricted Hartree-Fock (RHF) and hybrid density functional theory (DFT) employing the B3LYP functional.⁵⁸ The basis sets 6-31G**, 6-31+G**, 6-311G** and 6-311+G** were used for all calculations. All-electron basis sets on scandium were also employed for calculations on Sc(acac)₃.⁵⁹ CS tensors were calculated using the gauge-including atomic orbitals (GIAO) method.^{60,61} [Sc(H₂O)₆]³⁺ was chosen to model the magnetic shielding (MS) of the solution standard,⁶² and absolute shieldings were converted to shifts as described in Tables 5.1 and 5.2.

X-ray Diffraction Experiments. Powdered ScCl₃•3THF, Sc(OAc)₃ and Sc(OTf)₃ were packed into 1.0 mm glass capillary tubes under nitrogen and flame sealed. Powder X-ray diffraction patterns were collected using a Bruker AXS HI-STAR system using a General Area Detector Diffractions System. The X-ray source employed was a Cu K α radiation (1.540598 Å) with an area detector using a 2 θ range between 4.0° to 65.0°. Powder X-ray diffraction patterns were simulated with the Powder Cell software package.⁶³

5.3 Results and Discussion

In the first part of this section, a detailed discussion of ⁴⁵Sc NMR spectroscopy of

scandium coordination compounds is presented. In all of the cases discussed herein, it is possible to utilize MAS to almost completely average the scandium CSA, while partially averaging the second-order QI. Therefore, the values of C_Q , η_Q , and δ_{iso} can be readily obtained by analytical simulations of the ^{45}Sc MAS NMR central transition spectra (Table 5.1). Static ^{45}Sc NMR spectra allow for the measurement of both quadrupolar (C_Q and η_Q) and CS tensor parameters (δ_{iso} , as well as the span, Ω , and the skew, κ), as well as the Euler angles (α , β , and γ) which describe the relative orientation of EFG and CS tensors (see Table 5.1 for definitions of these parameters). Static spectra acquired at a second field are used to confirm the observed CS tensor parameters and Euler angles.^{64,65} The shapes of the static powder patterns are sensitive to the pulse sequences and rf fields used in their acquisition (Figure D1); fortunately, the locations of discontinuities, which are paramount for determination of spectral parameters, are largely unaffected by these factors. To the best of our knowledge, there are no previous reports of scandium CSA in the literature. Spectral simulations presented throughout the paper account for scandium CSA; for comparison, spectral simulations that neglect the presence of CSA are found in the Appendix D (Figure D2). In the second part of this section, theoretically calculated CS and EFG tensors, and their orientations and origins, are investigated in depth. In the final part of this section, we examine the application of ^{45}Sc NMR to structurally characterize systems for which crystallographic and/or other structural data are unavailable. Details of crystal structure determinations are given in the original publication.⁶⁶

Table 5.1. A Summary of Observed ^{45}Sc EFG and CS Tensor Parameters

Compound	C_Q (MHz) ^a	η_Q ^b	δ_{iso} (ppm) ^c	Ω (ppm) ^d	κ ^e	α (°)	β (°)	γ (°)
$\text{Sc}(\text{acac})_3$	13.0(3) ^f	0.22(3)	82(1)	70(10)	-0.7(2)	90(15)	83(4)	0(5)
$\text{Sc}(\text{TMHD})_3$	13.1(2)	0.93(2)	89.5(10)	110(20)	-0.7(3)	0(10)	15(15)	90(5)
$\text{Sc}(\text{NO}_3)_3 \cdot 5\text{H}_2\text{O}$	6.2(2)	0.75(5)	-18.5(10)	60(10)	-0.8(1)	80(15)	10(10)	65(15)
$\text{Sc}(\text{OAc})_3$	4.6(2)	0.18(6)	-6.2(8)	73(5)	0.65(10)	0(45)	7(3)	90(45)
$\text{ScCl}_3 \cdot 6\text{H}_2\text{O}$	3.9(2)	0.77(9)	125.4(5)	180(10)	0.9(1)	45(10)	30(5)	40(10)
$\text{ScCl}_3 \cdot 3\text{THF}$	8.4(2)	0.30(5)	202(1)	200(20)	-0.1(3)	85(35)	4(4)	12(25)
Cp_3Sc	8.3(2)	0.88(4)	62.8(8)	135(15)	0.0(3)	-24(10)	73(8)	130(15)

The CS tensor is described by three principal components ordered such that $\delta_{11} \leq \delta_{22} \leq \delta_{33}$. The EFG tensor is described by three principal components ordered such that $|V_{11}| \leq |V_{22}| \leq |V_{33}|$. ^a $C_Q = eQV_{33}/h$, ^b $\eta_Q = (V_{11} - V_{22})/V_{33}$, ^c $\delta_{jj} = (\sigma_{\text{iso, ref}} - \sigma_{jj})(10^6)/(1 - \sigma_{\text{iso, ref}}) \approx \sigma_{\text{iso, ref}} - \sigma_{jj}$ where $jj = 11, 22$ or 33 , $\delta_{\text{iso}} = (\delta_{11} + \delta_{22} + \delta_{33})/3$, ^d $\Omega = \delta_{11} - \delta_{33}$, ^e $\kappa = 3(\delta_{22} - \delta_{\text{iso}})/\Omega$, ^f The uncertainty in the last digit of each value is denoted in brackets.

Solid-State ^{45}Sc NMR Experiments. **Sc(acac)₃.** The solid-state ^{45}Sc MAS NMR spectrum of the central transition (Figure 5.1a) is simulated with $C_Q = 13.0$ MHz, $\eta_Q = 0.22$, and $\delta_{\text{iso}} = 82$ ppm. Experimental and simulated static ^{45}Sc NMR spectra of $\text{Sc}(\text{acac})_3$ acquired at two different magnetic field strengths (Figure 5.1b) reveal that $\Omega = 70$ ppm and $\kappa = -0.7$ (all Euler angles are tabulated in Table 5.1). The “shoulder” on the low-frequency side of the MAS spectrum is not predicted by the analytical simulation; however, a numerical simulation using SIMPSON reveals that this shoulder is due to the presence of an underlying satellite transition (Figure 5.1a, inset).

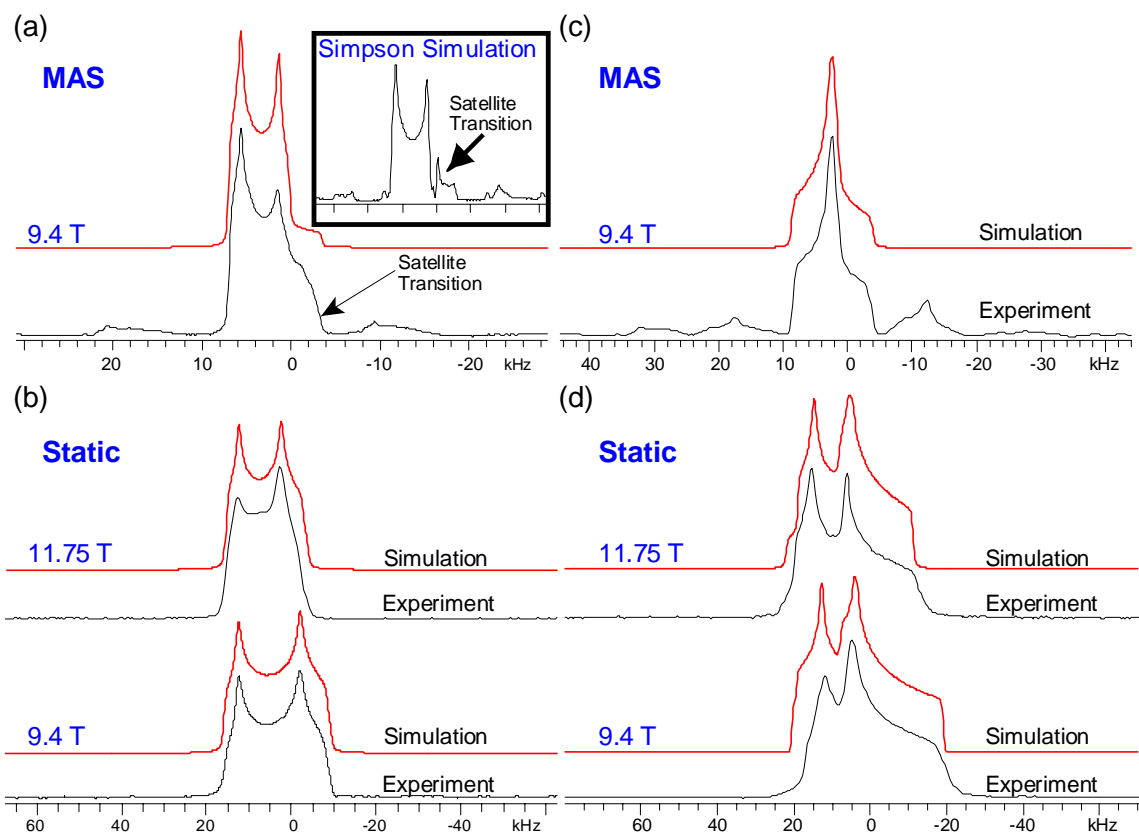


Figure 5.1. Solid-state ^{45}Sc NMR spectra and analytical simulations of $\text{Sc}(\text{acac})_3$ and $\text{Sc}(\text{TMHD})_3$. (a) MAS spectrum of $\text{Sc}(\text{acac})_3$, $\nu_{\text{rot}} = 15$ kHz. Inset, a SIMPSON simulation utilizing ideal pulses and processed with 100 Hz of exponential line broadening. (b) Static spectra of $\text{Sc}(\text{acac})_3$ at 9.4 T and 11.75 T. The static spectrum at 9.4 T was acquired with a 90° - 90° echo. (c) MAS RAPT-Echo spectrum of $\text{Sc}(\text{TMHD})_3$, $\nu_{\text{rot}} = 15$ kHz. (d) Static spectra of $\text{Sc}(\text{TMHD})_3$ at 9.4 T and 11.75 T.

The nature of the EFG and CS tensors and their relation to one another as well as the molecular frame can be rationalized by considering the molecular structure. The scandium atom is coordinated by six oxygen atoms from the three bidentate acetylacetonato ligands.⁶⁷ Inspection of the crystal structure reveals that the coordination sphere formed by the oxygen atoms more closely resembles a trigonal anti-prism, and deviates considerably from octahedral geometry (and therefore spherical symmetry).² There are only minor variations in the Sc-O bond lengths (~ 0.02 Å); however, deviations

of up to 10° from ideal octahedral angles are observed in the O-Sc-O bond angles. In this respect, the observation of a relatively large C_Q is not surprising (this is the second largest value of C_Q observed in this series of complexes). The value of η_Q is closer to zero than one, indicating that V_{33} is the pseudo-unique component of the EFG tensor. The appreciable span indicates that the scandium magnetic shielding is anisotropic, and the skew indicates that σ_{11} is the pseudo-unique component (i.e., the values of σ_{22} and σ_{33} are closer to one another than σ_{11} and σ_{22}). The Euler angles indicate that the largest component of the EFG tensor which defines the magnitude of the quadrupolar interaction, V_{33} , is nearly coincident with σ_{11} , the principal component of the MS tensor which describes the direction of least magnetic shielding. Given the near-axial symmetry of each tensor, one would expect that V_{33} and σ_{11} are aligned near the pseudo three-fold axis of the molecule. Proposed tensor orientations are investigated further in the discussion of ab initio calculations for this molecule and all remaining systems.

Sc(TMHD)₃. Simulation of the ^{45}Sc MAS NMR spectrum of $\text{Sc}(\text{TMHD})_3$ (Figure 5.1c), reveals $C_Q = 13.1$ MHz and $\delta_{\text{iso}} = 89.5$ ppm. Simulation of the static ^{45}Sc NMR spectra (Figure 5.1d) yield parameters similar to those observed in $\text{Sc}(\text{acac})_3$, with $\Omega = 110$ ppm and $\kappa = -0.7$; however, the Euler angles are different. The ligands and their coordination to Sc in $\text{Sc}(\text{acac})_3$ and $\text{Sc}(\text{TMHD})_3$ are analogous, so that the observation of similar values of δ_{iso} and C_Q are not surprising. However, $\eta_Q = 0.93$, which indicates that V_{11} is the most distinct component of the EFG tensor and is oriented along or near the two-fold molecular axis, in contrast to $\text{Sc}(\text{acac})_3$. The difference in relative tensor orientations between the two complexes can be explained by comparison of the crystal

structures. In $\text{Sc}(\text{acac})_3$, each of the ligands forms an approximately planar six-membered ring with the scandium centre; however, in $\text{Sc}(\text{TMHD})_3$, there is a 22° deviation away from planarity in two of the three six-membered rings. The molecule is now more properly described as possessing C_2 symmetry, and this difference in symmetry is the major cause of the distinct EFG tensor orientation. The low value of β also means that V_{33} and σ_{33} are closely oriented, unlike in $\text{Sc}(\text{acac})_3$. Thus, changes in the geometry of the ligand at a distance from the scandium centre have dramatically affected the relative orientation of the EFG and CS tensors.

$\text{Sc}(\text{NO}_3)_3 \cdot 5\text{H}_2\text{O}$. The ^{45}Sc MAS NMR spectrum of $\text{Sc}(\text{NO}_3)_3 \cdot 5\text{H}_2\text{O}$ (Figure 5.2a) reveals a much narrower powder pattern than those observed for the diketonato compounds. From the MAS and static spectra (Figure 5.2b) the measured parameters are, $C_Q = 6.2$ MHz, $\eta_Q = 0.75$, $\delta_{\text{iso}} = -18.5$ ppm, $\Omega = 60$ ppm and $\kappa = -0.8$. The ^{45}Sc nucleus is highly shielded in comparison to the distorted octahedral environments discussed above, and a relatively small scandium CSA is also observed. The observation of a relatively small C_Q is unexpected, given the considerably non-spherical coordination environment about scandium that is revealed in the single crystal X-ray structure.⁶⁶ However, inspection of the Sc-O bond lengths reveals that they are longer than those observed in $\text{Sc}(\text{acac})_3$ and $\text{Sc}(\text{OAc})_3$ (the Sc-O bonds of water and the nitrate ligands are on average 0.14 Å and 0.21 Å longer, respectively). The decreased EFG must therefore result from the increased Sc-O bond distances. Similar observations have been made in numerous systems where increased bond lengths and augmented ionic character tend to result in lowering of C_Q , since the magnitude of V_{33} is proportional to $1/r^3$ in a simple point charge

model.^{68, 69}

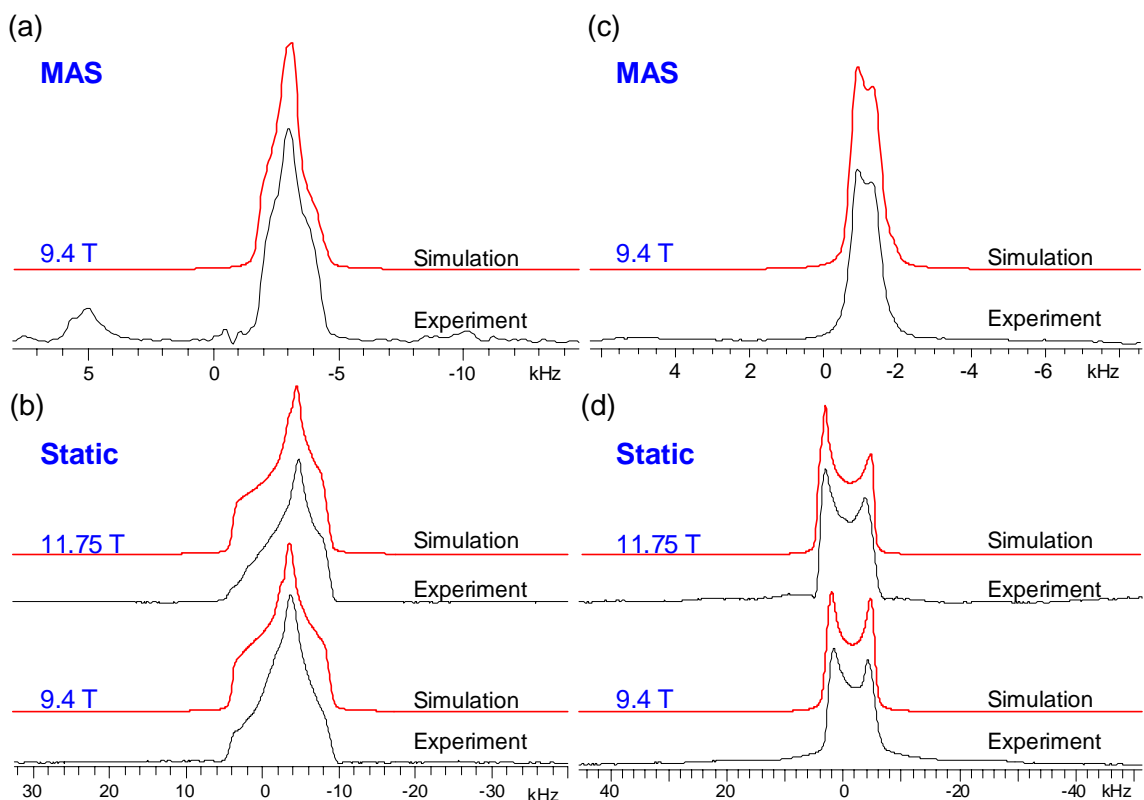


Figure 5.2. Solid-state ^{45}Sc NMR spectra and analytical simulations of $\text{Sc}(\text{NO}_3)_3 \cdot 5\text{H}_2\text{O}$ and $\text{Sc}(\text{OAc})_3$. (a) MAS spectrum of $\text{Sc}(\text{NO}_3)_3 \cdot 5\text{H}_2\text{O}$, $\nu_{\text{rot}} = 8$ kHz. (b) Static spectra of $\text{Sc}(\text{NO}_3)_3 \cdot 5\text{H}_2\text{O}$ at 9.4 T and 11.75 T. (c) MAS spectrum of $\text{Sc}(\text{OAc})_3$, $\nu_{\text{rot}} = 8$ kHz. (d) Static spectra of $\text{Sc}(\text{OAc})_3$ at 9.4 T and 11.75 T acquired with a 90° - 90° echo.

$\text{Sc}(\text{OAc})_3$. MAS and static ^{45}Sc NMR spectra of $\text{Sc}(\text{OAc})_3$ reveal a relatively narrow central transition (Figure 5.2c and 5.2d), and simulations yield $C_Q = 4.6$ MHz, $\eta_Q = 0.18$, $\delta_{\text{iso}} = -6.2$ ppm, $\Omega = 73$ ppm, $\kappa = 0.65$. Solid-state ^{45}Sc NMR spectra of $\text{Sc}(\text{OAc})_3$ have been reported previously by Thompson and Oldfield, as well as Kataoka et al. Both groups reported $C_Q = 5$ MHz and $\eta_Q = 0$ from simulations of static central transition spectra.^{36, 38} Kataoka reported a refined $C_Q = 4.45$ MHz based upon a simulation of satellite transitions, which is closer to our result. In both papers, the effects of CSA were

neglected in the simulations, and η_Q was assumed to be zero. From the appearance of our static spectra, it is apparent that scandium CSA is present and the EFG tensor is non-axial. These factors must be accounted for to properly simulate the static spectra.

The previously determined X-ray crystal structure⁷⁰ reveals a coordination polymer structure, with a unique Sc atom in a six-coordinate environment that results from bridging acetate ligands (powder XRD patterns (Figure D3) confirms that recrystallization successfully produced anhydrous $\text{Sc}(\text{OAc})_3$). The Sc-O bond lengths are similar to those in $\text{Sc}(\text{acac})_3$; however, the $\text{Sc}(\text{acac})_3$ metal environment is nearly octahedral, with all *trans*-O-Sc-O bond angles equal to 180° and *cis*-O-Sc-O bond angles deviating only slightly from 90° ($\pm 3.5^\circ$). The relatively small C_Q can be accounted for by the nearly spherically symmetric arrangement of oxygen atoms about the scandium. The δ_{iso} and Ω are similar to that of $\text{Sc}(\text{NO}_3)_3 \cdot 5\text{H}_2\text{O}$, but the ^{45}Sc nucleus is relatively shielded from the external magnetic field compared to those in $\text{Sc}(\text{acac})_3$ and $\text{Sc}(\text{TMHD})_3$, which have distorted octahedral oxygen coordination environments. The symmetry of both the CS and EFG tensors is quite distinct from that of $\text{Sc}(\text{NO}_3)_3 \cdot 5\text{H}_2\text{O}$, which is to be expected given their structural differences. The value of η_Q for $\text{Sc}(\text{OAc})_3$ indicates that V_{33} is the distinct component of the EFG tensor, and κ indicates that σ_{33} is the unique component of the CS tensor. The low value of β indicates that V_{33} and σ_{33} are nearly co-linear and are likely directed along the C_3 axis of the molecule, in the direction of propagation of the

polymer structure.

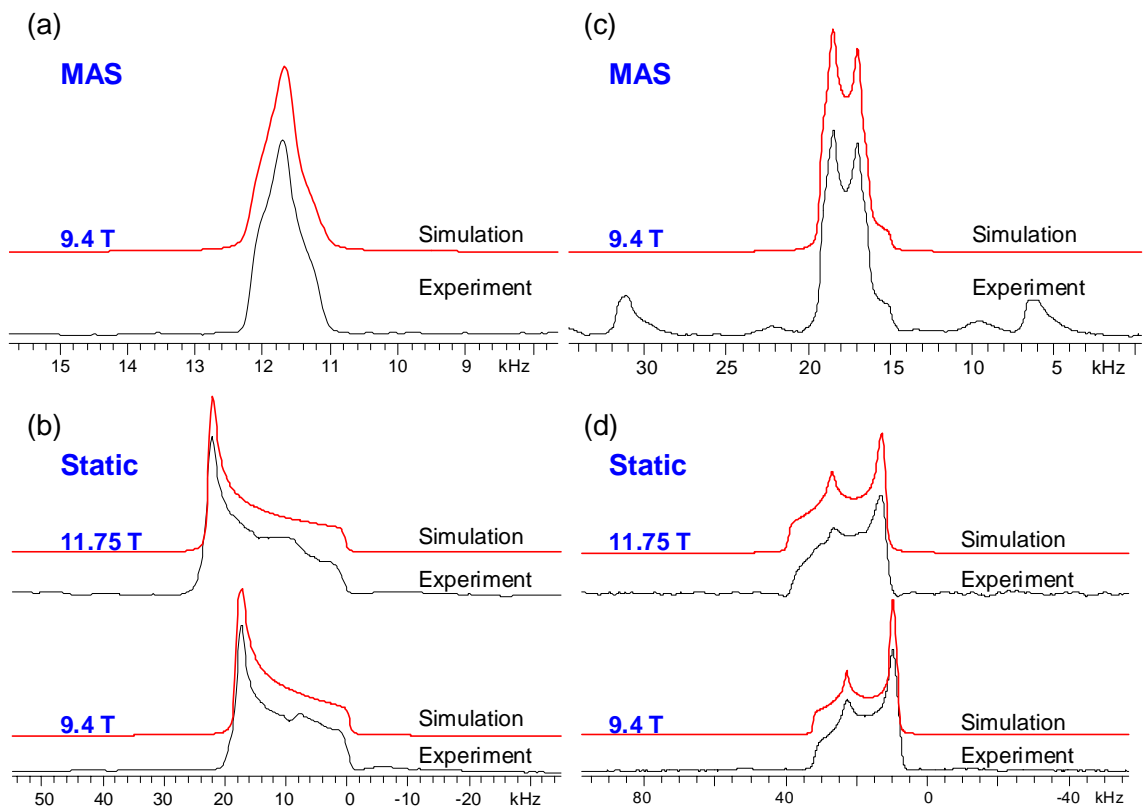


Figure 5.3. Solid-state ^{45}Sc NMR spectra and analytical simulations of $\text{ScCl}_3 \cdot 6\text{H}_2\text{O}$ and $\text{ScCl}_3 \cdot 3\text{THF}$. (a) MAS spectrum of $\text{ScCl}_3 \cdot 6\text{H}_2\text{O}$, $\nu_{\text{rot}} = 10$ kHz. (b) Static spectra of $\text{ScCl}_3 \cdot 6\text{H}_2\text{O}$ at 9.4 T and 11.75 T. (c) MAS spectrum of re-crystallized $\text{ScCl}_3 \cdot 3\text{THF}$, $\nu_{\text{rot}} = 12.5$ kHz. (d) Static spectra of recrystallized $\text{ScCl}_3 \cdot 3\text{THF}$ at 9.4 T and 11.75 T acquired with a 90° - 90° echo.

$\text{ScCl}_3 \cdot 6\text{H}_2\text{O}$. The ^{45}Sc MAS NMR spectrum of $\text{ScCl}_3 \cdot 6\text{H}_2\text{O}$ (Figure 5.3a) reveals a very narrow powder pattern with a breadth of ca. 1 kHz, with $C_Q = 3.9$ MHz, $\eta_Q = 0.77$ and $\delta_{\text{iso}} = 125.4$ ppm. Static spectra (Figure 5.3b) reveal a large span, $\Omega = 180$ ppm, and a nearly axial CS tensor, $\kappa = 0.9$. The static spectra contain a distortion that is unaccounted for in the lineshape of the static simulations at both fields, which likely arises from a small amount of impurity, as opposed to incomplete excitation or intramolecular

dynamics. The EFG parameters for $\text{ScCl}_3 \cdot 6\text{H}_2\text{O}$ are different than those reported by Thompson and Oldfield,³⁶ who found that $C_Q = 14$ MHz and $\eta_Q = 0.60$, based upon the acquisition and simulation of a static ^{45}Sc NMR spectrum. The differences in their parameters from ours could arise from their neglect of scandium CSA and the absence of ^{45}Sc MAS NMR data. It is also unclear whether proton decoupling was applied in their NMR experiments, which has adverse effects on the appearance of the ^{45}Sc static NMR powder pattern in this case (Figure D4).

This complex possesses the smallest observed C_Q and largest Ω in the series of compounds studied herein. These two observations can be rationalized in terms of molecular structure. The crystal structure for $\text{ScCl}_3 \cdot 6\text{H}_2\text{O}$ was not previously reported and our initial assumption was that the scandium atom would be coordinated by six oxygen atoms. While this structural model is consistent with the quadrupolar data, it is inconsistent with the high isotropic shift and large span. Refinement of the crystal structure of $\text{ScCl}_3 \cdot 6\text{H}_2\text{O}$ reveals a highly symmetrical coordination environment about scandium, involving two Cl and four O atoms which form a $[\text{ScCl}_2(\text{H}_2\text{O})_4]^+$ unit of approximately D_{4h} symmetry. The two Sc-Cl distances are equivalent and the angle separating them is 180.0° , while there is less than 1.0° deviation from ideal octahedral O-Sc-O angles. In this respect, the observations of a relatively small C_Q and large scandium CSA is not surprising. The large span and axially symmetric skew indicate that σ_{33} is likely oriented near the Sc-Cl bond axis, and that there are large paramagnetic deshielding contributions perpendicular to this axis.

$\text{ScCl}_3 \cdot 3\text{THF}$. ^{45}Sc NMR spectra were acquired from two different samples of

ScCl₃•3THF (Figures 5.3 and 5.4). Initial ⁴⁵Sc MAS NMR spectra acquired from this compound revealed the presence of two distinct scandium sites. A ⁴⁵Sc multiple-quantum MAS (MQMAS) NMR experiment⁷¹ was performed in order to resolve the overlapping sites observed in the first sample (Figure 5.4a), with simulations (Figure 5.4b) yielding $C_Q = 8.5$ MHz, $\eta_Q = 0.32$ and $\delta_{\text{iso}} = 201.5$ ppm (site 1) and $C_Q = 8.5$ MHz, $\eta_Q = 0.50$ and $\delta_{\text{iso}} = 211$ ppm (site 2). Simulated spectra are co-added to simulate the observed MAS spectra (Figure 5.4c). The overlapping static powder patterns render determination of the CS tensor parameters and Euler angles difficult (Figure 5.4d).

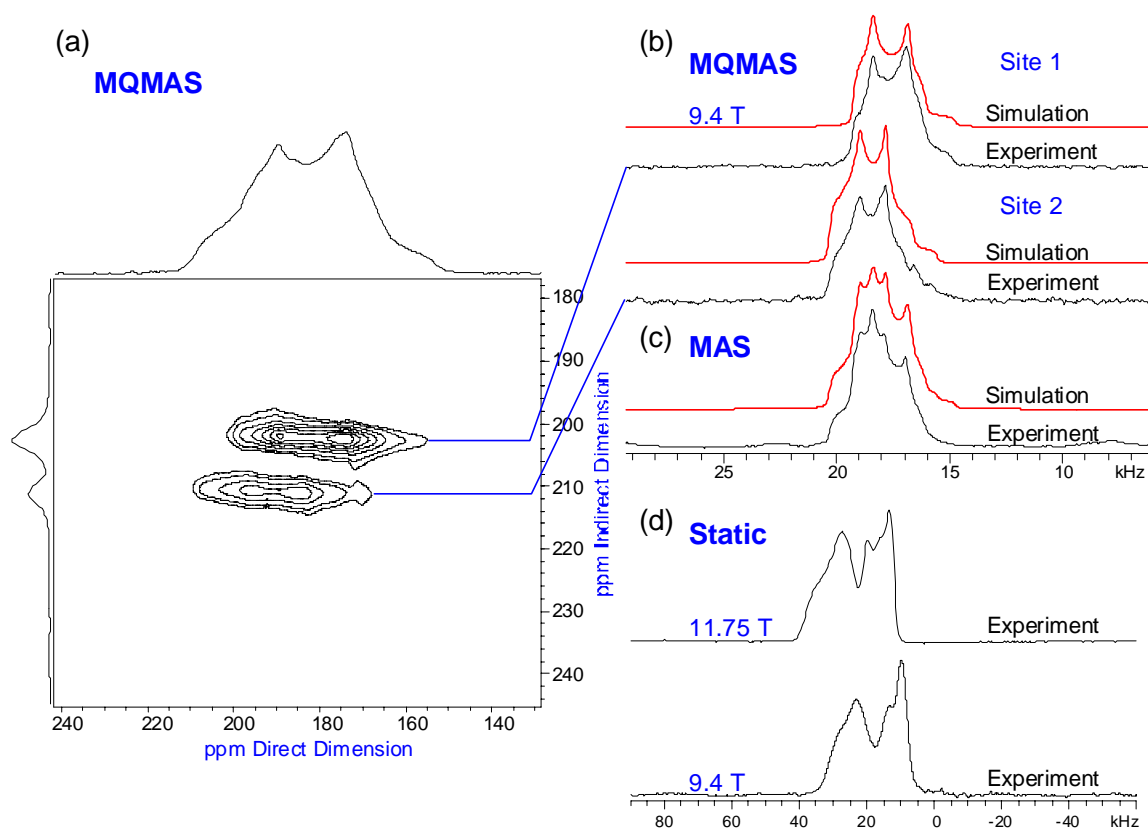


Figure 5.4. Solid-state ⁴⁵Sc NMR spectra of ScCl₃•3THF (first sample). (a) MQMAS contour plot, $\nu_{\text{rot}} = 8$ kHz. (b) The two resolved sites from cross-sections of the indirect dimension and analytical simulations. (c) MAS spectrum ($\nu_{\text{rot}} = 15$ kHz) and the simulated pattern that results from addition of the individually simulated patterns. (d) Static spectra.

The observation of two scandium sites in the NMR spectra was surprising because the previously reported crystal structure indicates that only one crystallographically and magnetically distinct Sc site should be present.⁴⁹ The powder XRD pattern (Figure D3) indicates that this sample is highly crystalline, though additional high intensity peaks indicate that there is a second crystalline phase present. The presence of impurities in this sample is unlikely, given the roughly equal NMR signal intensities and the similar NMR parameters of the two scandium sites. Re-crystallization of anhydrous ScCl₃ in an excess of THF was performed. NMR spectra acquired from this second sample yielded one scandium resonance as expected (Figures 5.3c and 5.3d), and spectra are simulated with $C_Q = 8.4$ MHz, $\eta_Q = 0.30$, $\delta_{iso} = 202$ ppm, $\Omega = 200$ ppm and $\kappa = -0.1$. The powder XRD pattern of the re-crystallized sample closely matches the predicted pattern. Clearly, the combination of ⁴⁵Sc MQMAS NMR and powder XRD is extremely useful for differentiating Sc sites in similar coordination environments.

ScCl₃•3THF consists of a scandium atom coordinated by three chlorine atoms and three THF molecules in a meridional fashion. The large positive chemical shift (the highest in this series) and large span are consistent with the notion that replacement of an oxygen with chlorine in the first coordination sphere results in magnetic deshielding of the scandium nucleus. The Sc-Cl bonds are considerably more covalent than Sc-O bonds; as such, there are increased paramagnetic shielding contributions perpendicular to the Sc-Cl bond axes. Given the meridional arrangement of Cl and O atoms, σ_{11} should be oriented in a direction perpendicular to all three Sc-Cl bonds. The non-axial κ indicates that the CS tensor does not have a pseudo-unique component. The skew, the moderate

value of C_Q and the non-axial η_Q are all consistent with the meridional arrangement of Cl and O atoms in the in the first coordination sphere.

ScCp₃. This compound represents a departure from all other systems studied herein, and is mentioned as an aside. Given current interest in organometallic scandium compounds,¹⁸⁻²¹ solid-state ⁴⁵Sc NMR could be a useful method to gain insight into their molecular structure and dynamics. In this regard, ScCp₃ is a good entry point for studies upon π -coordinated systems. Herein we present some preliminary room-temperature NMR data. Analytical simulation of ⁴⁵Sc MAS (Figure 5.5a) and static (Figure 5.5b) NMR spectra of ScCp₃ yield $\delta_{\text{iso}} = 62.8$ ppm, $C_Q = 8.3$ MHz, $\eta_Q = 0.88$ and $\Omega = 135$ ppm, $\kappa = 0.0$. The discontinuities in static spectra are difficult to resolve at both 9.4 T and 11.75 T, increasing the errors in the CS tensor parameters and Euler angles. The appearance of the spectra are suggestive of some intramolecular dynamics, though this is beyond the scope of the current paper (see ¹³C NMR data in Figure D5).

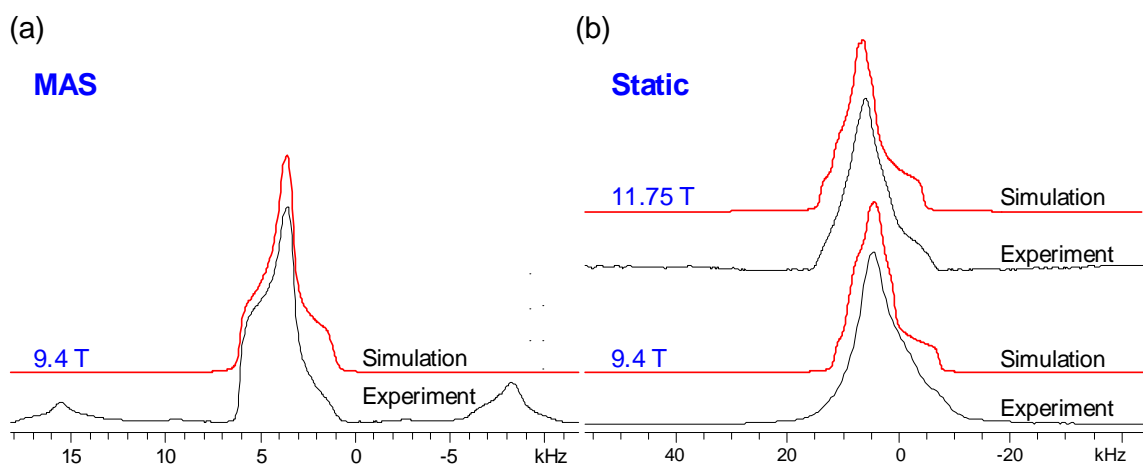


Figure 5.5. Solid-state ⁴⁵Sc NMR spectra of ScCp₃ and simulations. (a) MAS spectrum, $\nu_{\text{rot}} = 12$ kHz. (b) Static spectra at 9.4 T and 11.75 T.

The structure of ScCp₃ consists of two η^5 -Cp rings and two η^1 -Cp rings. The η^1 -

Cp rings bridge two adjacent scandium atoms leading to the formation of polymeric chains. In the majority of NMR studies of metal nuclei in metallocene systems⁷²⁻⁷⁶ the values of δ_{iso} typically occur far to the low-frequency end of the chemical shift range, consistent with nuclei which are highly shielded from the magnetic field. In this respect, the “mid-range” δ_{iso} for this metallocene system is unusual. The η^5 -Cp rings are likely responsible for significant magnetic shielding of the ^{45}Sc nucleus, while the η^1 -Cp must result in some degree of deshielding. With the absence of other organometallic species for comparison, it is difficult to assess the origin of the moderate value of C_Q .

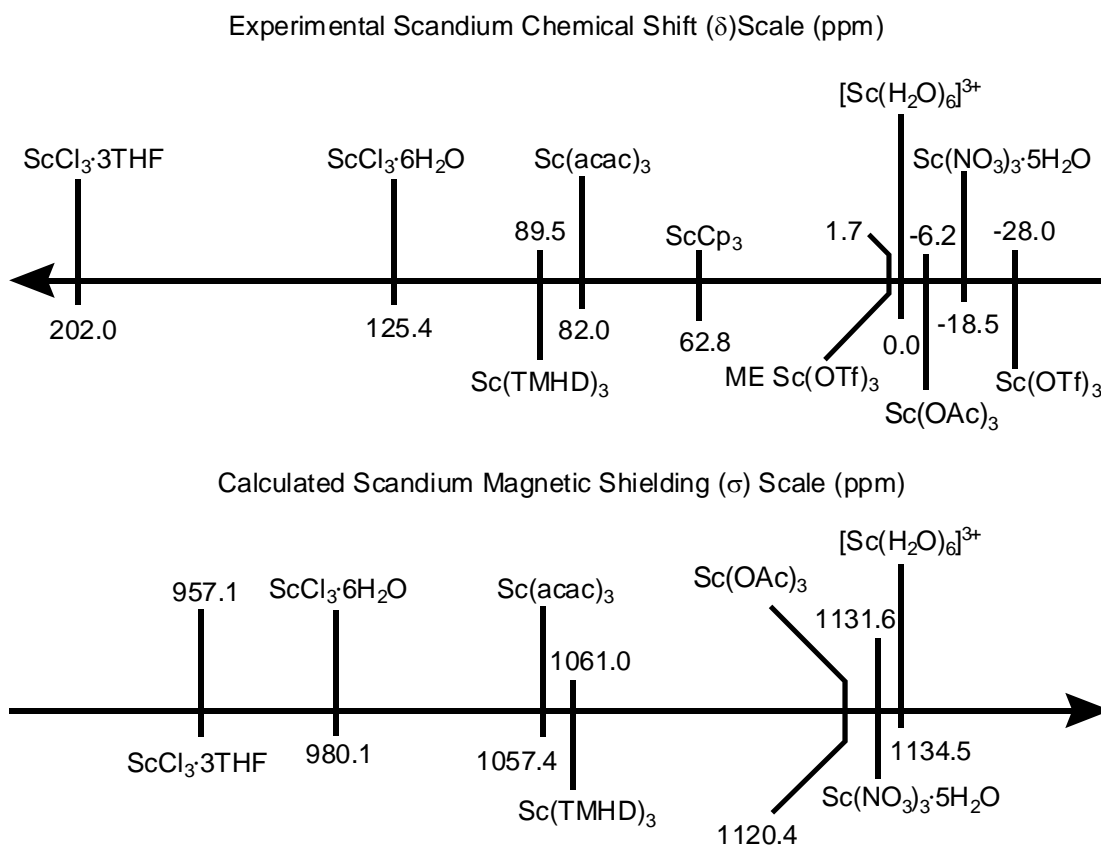


Figure 5.6. ^{45}Sc chemical shift and magnetic shielding scales. The magnetic shielding scale was generated from the RHF/6-311G** on Sc series of calculations. The theoretical result for ScCp_3 has been omitted.

Summary of Observed ^{45}Sc NMR Parameters. To aid in illustrating the observed trends, a chemical shift scale has been constructed from all of the complexes studied herein (Figure 5.6). Magnetic deshielding is observed upon replacement of oxygen with chlorine; for instance, the isotropic chemical shift of scandium in $\text{ScCl}_3 \cdot 6\text{H}_2\text{O}$ is 125 ppm (coordination by two chlorine atoms), while the observed shift of $\text{ScCl}_3 \cdot 3\text{THF}$ is 202 ppm (coordination by three chlorine atoms). Sc-Cl bonding must play a significant role in making paramagnetic shielding contributions and increasing the span of the scandium CS tensors. A trend in the observed values of Ω is also observed: coordination of scandium by more than one type of atom or by ligands engaging in multiple binding modes (eg. ScCp_3) is seen to result in sizable Ω values.

A correlation between molecular symmetry and size of C_Q is also observed. A C_Q of 2.02 MHz in hexagonally closed packed Sc metal has been previously observed,³⁷ which is reflective of the spherically symmetric scandium environment. Compounds that possess coordination environments with bond-angles close to ideal octahedral angles, such as $\text{Sc}(\text{OAc})_3$ and $\text{ScCl}_3 \cdot 6\text{H}_2\text{O}$, are seen to possess relatively small values of C_Q . Distortions away from octahedral symmetry result in an increase in C_Q as observed in $\text{Sc}(\text{acac})_3$ and $\text{Sc}(\text{TMHD})_3$. Values of η_Q near zero or one are observed when symmetry elements such as rotational axes are present.

The aforementioned trends illustrate the utility of solid-state ^{45}Sc NMR for the analysis of molecular structure. Values of C_Q can be used to gauge the spherical symmetry of the ground state electronic structure about a scandium nucleus, while the values of δ_{iso} and Ω can be used to provide information about the nature of the ligands that are bound to

scandium and their modes of bonding. The presence of symmetry elements, such as rotational axes and mirror planes, are reflected in the values of η_Q and κ , as well as in the Euler angles.

Table 5.2. Calculated ^{45}Sc NMR Parameters Showing Best Agreement With Experiment

Compound/Method	C_Q (MHz) ^a	η_Q	δ_{iso} (ppm) ^b	Ω (ppm)	κ	α (°)	β (°)	γ (°)
Sc(acac)₃	13.0(3)	0.22(3)	82(1)	70(10)	-0.7(2)	90(15)	83(4)	0(5)
RHF/6-311G** on Sc	-11.6	0.44	77	61.3	-0.69	89	85	1
B3LYP/6-311G**	-12.3	0.40	101.8	95.1	-0.67	85	85	2
Sc(TMHD)₃	13.1(2)	0.93(2)	89.5(10)	110(20)	-0.7(3)	0(10)	15(15)	90(5)
RHF/6-311+G** on Sc	14.4	0.67	76.1	82.5	0.57	90	68	0
B3LYP/6-311G** on Sc	15.3	0.71	98.4	118.8	0.36	90	5	0
Sc(NO₃)₃•5H₂O	6.2(2)	0.75(5)	-18.5(10)	60(10)	-0.8(1)	80(15)	10(10)	65(15)
RHF/6-311G**	-5.6	0.72	7.3	58.9	-0.74	51	39	75
B3LYP/6-311+G**	-5.8	0.96	46.4	70.9	0.20	25	33	89
Sc(OAc)₃	4.6(2)	0.18(6)	-6.2(8)	73(5)	0.65(10)	0(45)	7(3)	90(45)
RHF/6-311G**	3.3	0.18	15.8	24.9	0.86	1	6	90
B3LYP/6-311G**	4.6	0.00	-19.4	102.6	0.99	0	0	90
ScCl₃•6H₂O	3.9(2)	0.77(9)	125.4(5)	180(10)	0.9(1)	45(10)	30(5)	40(10)
RHF/6-311G** on Sc	5.3	0.78	154.4	228.9	0.96	51	26	40
B3LYP/6-311+G** on Sc	5.3	0.74	231.3	486.2	0.98	52	25	38
ScCl₃•3THF	8.4(2)	0.30(5)	202(1)	200(20)	-0.1(3)	85(35)	4(4)	12(25)
RHF/6-311G** on Sc	9.7	0.26	176.8	157.8	-0.11	80	5	12
B3LYP/6-311G**	10.0	0.35	303.0	316.7	-0.26	73	4	18
ScCp₃	8.3(2)	0.88(4)	62.8(8)	135(15)	0.0(3)	-24(10)	73(8)	130(15)
RHF/6-311G** on Sc	-8.5	0.90	-74.6	86.1	-0.02	60	43	20
B3LYP/6-311+G** on Sc	-7.9	0.74	115.1	300.5	-0.34	-47	36	36

^a Only the magnitude of C_Q can be measured experimentally. For definitions of all NMR parameters refer to Table 5.1.

^b The theoretical isotropic shifts were calculated by comparison of the calculated shielding to that calculated from a geometry optimized model of $[\text{Sc}(\text{H}_2\text{O})_6]^{3+}$ at the appropriate level of theory.

^c In cases where the basis set used for scandium is explicitly stated the 6-31G** basis set was employed on all other atoms.

Quantum Chemical Calculations of ^{45}Sc Interaction Tensors. Ab initio

calculations are performed to predict the orientations of the CS and EFG tensors in the molecular frames (Figure 5.7). This allows for relationships between the observed ^{45}Sc NMR parameters and molecular structure and symmetry to be confirmed and/or established. Calculated EFG and CS tensor parameters showing the best agreement with experimental values are presented for $\text{Sc}(\text{acac})_3$, $\text{Sc}(\text{TMHD})_3$, $\text{Sc}(\text{NO}_3)_3 \cdot 5\text{H}_2\text{O}$, $\text{Sc}(\text{OAc})_3$, $\text{ScCl}_3 \cdot 6\text{H}_2\text{O}$, $\text{ScCl}_3 \cdot 3\text{THF}$ and ScCp_3 in Table 5.2. Calculations on $\text{Sc}(\text{acac})_3$ employing the basis sets of Huzinaga⁵⁹ and the results of all other calculations are given in the original publication.⁶⁶ Cartesian coordinate files containing the orientation of the EFG and CS tensors for each compound are provided with the original publication.⁶⁶

$\text{Sc}(\text{acac})_3$ and $\text{Sc}(\text{TMHD})_3$. Calculations performed upon $\text{Sc}(\text{acac})_3$ generally produce results which are in good agreement with the experimentally observed parameters. The B3LYP/6-311G** calculation on $\text{Sc}(\text{acac})_3$ orients the largest component of the EFG tensor, V_{33} , and least shielded component of the CS tensor, σ_{11} , coincident with the pseudo- C_3 axis, in agreement with our proposed orientation based on the experimental values of κ and η_Q . The theoretical Euler angles are found to be in excellent agreement with experimentally determined angles. Similar tensor orientations have been observed in $\text{Co}(\text{acac})_3$ and $\text{Al}(\text{acac})_3$, both of which have analogous molecular geometries.^{77, 78}

All calculations performed upon $\text{Sc}(\text{TMHD})_3$ predict intermediate positive values of κ , distinct from the experimentally determined value of -0.7. V_{11} is the pseudo-unique component of the EFG tensor (Figure 5.7b) and is oriented near the pseudo- C_2 axis of the

molecule and σ_{22} , while V_{33} and σ_{33} are nearly coincident and directed toward the bent ligands. The theoretical Euler angles are close to the observed angles (if β is near zero, α and γ are approximately interchangeable). The calculations are correctly predicting the orientation of the EFG and CS tensors within the molecular frame, but consistently underestimate σ_{22} and overestimate σ_{33} .

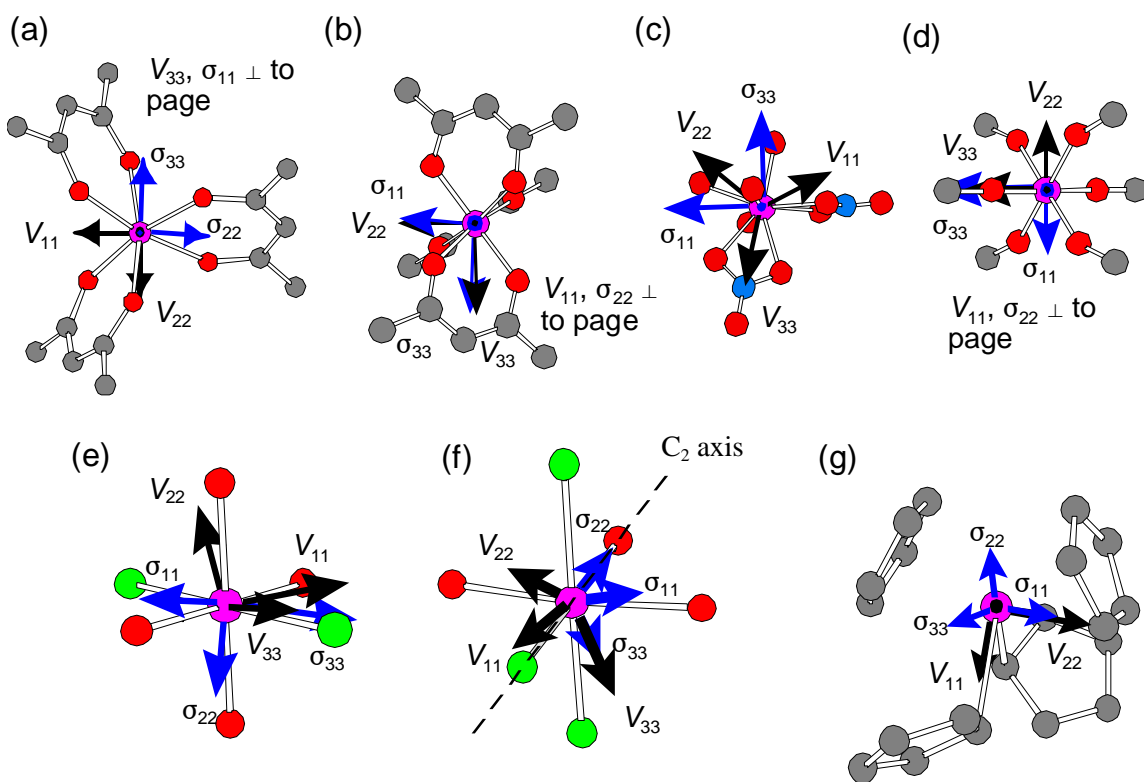


Figure 5.7. Proposed EFG and CS tensor orientations. (a) $\text{Sc}(\text{acac})_3$ (b) $\text{Sc}(\text{TMHD})_3$ (c) $\text{Sc}(\text{NO}_3)_3 \cdot 5\text{H}_2\text{O}$ (d) $\text{Sc}(\text{OAc})_3$ (e) $\text{ScCl}_3 \cdot 6\text{H}_2\text{O}$ (f) $\text{ScCl}_3 \cdot 3\text{THF}$ (g) ScCp_3 .

$\text{Sc}(\text{NO}_3)_3 \cdot 5\text{H}_2\text{O}$ and $\text{Sc}(\text{OAc})_3$. Calculations performed upon $\text{Sc}(\text{NO}_3)_3 \cdot 5\text{H}_2\text{O}$ yield several results which are close to the experimental values. There are no discernable symmetry elements present, with the exception of a pseudo-mirror plane, that could account for the observation of such a small value of C_Q . As mentioned earlier, the most

reasonable explanations for the small C_Q , despite the lack of spherical symmetry, are the increased Sc-O distances. It is notable that V_{33} is oriented in the direction of one of the nitrogen atoms in a nitrate group (Figure 5.7c), though it is uncertain why this is the case. The calculated orientation of the CS tensor conforms to the symmetry of the atomic arrangement and is oriented such that the σ_{11} and σ_{33} are contained in the pseudo-mirror plane formed by the nitrate ligands.

In $\text{Sc}(\text{OAc})_3$, calculations successfully predict that V_{33} and σ_{33} are the pseudo-distinct components (Figure 5.7d), and reveals that they are nearly co-linear with the C_3 axis of the molecule. Thus, the tensors are aligned in the direction of chain propagation of this coordination polymer and are clearly constrained by the symmetry of the molecule. The predicted Euler angles are in excellent agreement with the experimental values.

$\text{ScCl}_3 \cdot 6\text{H}_2\text{O}$ and $\text{ScCl}_3 \cdot 3\text{THF}$. The experimental and theoretical parameters obtained for $\text{ScCl}_3 \cdot 6\text{H}_2\text{O}$ indicate that V_{11} and σ_{33} are the pseudo-unique components, and the value of α indicates they are not closely aligned (Figure 5.7e). The values of η_Q indicate that V_{11} is the pseudo-unique component, and should be aligned along or near the C_4 axis of the molecule; however, this is not the case. The theoretical prediction aligns V_{33} at ca. 27° from the C_4 axis, with V_{11} and V_{22} oriented approximately 27° and 18° away from Sc-O bonds (C_2 axes), respectively. The theoretical CS tensor places σ_{33} along the Sc-Cl bond, approximately 26° from V_{33} , which is consistent with σ_{33} being the unique component of the CS tensor, while σ_{11} and σ_{22} are in the ScO_4 plane, oriented near the Sc-O bonds. Close agreement is observed between the experimental and predicted NMR tensor parameters and tensor orientations.

The orientation of the CS tensor in $\text{ScCl}_3 \cdot 6\text{H}_2\text{O}$ which gives rise to high magnetic shielding along the Cl-Sc-Cl axis and deshielding in the ScO_4 plane can be explained using Ramsey's description of contributions to paramagnetic shielding. The paramagnetic shielding tensor at a nucleus, A , is given as⁷⁹:

$$\sigma_{A\alpha\beta}^p = -\frac{\mu_0 e^2}{4\pi 2m^2} \sum_{k \neq 0} (E_k - E_0)^{-1} \times [\langle 0 | \sum_i L_{i\alpha} | k \rangle \langle k | \sum_i \frac{L_{iA\beta}}{r_{iA}^3} | 0 \rangle + \langle 0 | \sum_i \frac{L_{iA\alpha}}{r_{iA}^3} | k \rangle \langle k | \sum_i L_{i\beta} | 0 \rangle]$$

where $E_k - E_0$ is the energy difference between occupied ($|0\rangle$) and virtual ($|k\rangle$) MOs, and L_i and L_{iA} are the orbital angular momentum operators of the i th electron with respect to the gauge origin and nucleus, respectively. The angular momentum operators describe the mixing of occupied and virtual MOs via rotation about an axis perpendicular to a plane containing the MOs, which can be visualized as physical rotation of charge about an applied magnetic field.

Magnetic shielding along the Cl-Sc-Cl axis is high since the occupied and virtual MOs in the ScO_4 plane are far apart in energy and do not have the appropriate symmetry for magnetic-dipole allowed mixing; as a result, the paramagnetic contribution to deshielding perpendicular to the ScO_4 plane is minimal. Conversely, deshielding arising from paramagnetic contributions in the plane are high, since there are energetically similar MOs of appropriate symmetry in the ScO_2Cl_2 planes which are available for mixing. The large Ω and high δ_{iso} are consistent with this qualitative model, and are not observed in any of the complexes which do not have Sc-Cl bonds.

For $\text{ScCl}_3 \cdot 3\text{THF}$, the calculated value of η_Q is in good agreement with the observed value and indicates that V_{33} is the pseudo-unique component of the tensor. V_{33} is nearly coincident with the Cl-Sc-Cl pseudo-axis ($\angle 174.5^\circ$), whereas V_{11} coincides with the C_2 axis of the molecule formed by O-Sc-Cl axis ($\angle 179.4^\circ$) (Figure 5.7f). It is important to note that σ_{33} is oriented near the Cl-Sc-Cl axis (\perp to the ClScO_3 plane), σ_{22} near the Cl-Sc-O axis (\perp to the Cl_2ScO_2 plane), and σ_{11} near the O-Sc-O axis (\perp to the Cl_3ScO plane). This is consistent with arguments above, where the large paramagnetic deshielding contributions are generated perpendicular to the plane with the most coordinated Cl atoms. A detailed MO analysis is beyond the scope of the current study.

ScCp₃. Calculated and observed EFG parameters of ScCp_3 are in good agreement. Calculations were carried out using a $[\text{ScCp}_4]$ cluster (Figure 5.7g), and reveal that V_{11} is nearly coincident with one of the η^1 -Cp-Sc bonds, and that V_{33} is oriented in the direction of propagation of the metallocene polymer. The observation of a high value of η_Q , which indicates that V_{11} is the unique component of the EFG tensor, is not surprising in this context. It is difficult to comment on the observed CS tensor orientation; nonetheless, it is of interest to note that the calculations do predict a relatively large span. The predicted isotropic shifts fluctuate widely between the B3LYP and RHF calculations, perhaps suggesting that use of an isolated cluster in this instance is insufficient to properly model the CS tensor.

Summary of Ab Initio Calculations. Inspection of all the calculations reveals that the RHF method is generally superior to the B3LYP method. The former typically result in both CS and EFG tensor parameters that are close to the experimentally observed

values, while the latter do not correctly predict CS tensor parameters in most cases. In the case of extended systems (i.e., coordination polymers like $\text{Sc}(\text{OAc})_3$ and $\text{ScCl}_3 \cdot 6\text{H}_2\text{O}$) calculations upon isolated small charged clusters are sufficient to accurately calculate the observed ^{45}Sc EFG and CS tensor parameters, indicating that the interactions are mainly intramolecular in origin. Examination of the calculated isotropic shifts reveals that the RHF calculations typically result in errors of less than ± 25 ppm with larger basis sets (with the exception of ScCp_3), while the B3LYP calculations generally produce poorer agreement and greatly overestimate the effects of coordination by chlorine on chemical shifts.

Solid-State ^{45}Sc NMR Experiments on $\text{Sc}(\text{OTf})_3$ and ME $\text{Sc}(\text{OTf})_3$. The following section represents a preliminary study of $\text{Sc}(\text{OTf})_3$ and ME $\text{Sc}(\text{OTf})_3$. The interested reader is directed to Chapter 6 where a more thorough study of $\text{Sc}(\text{OTf})_3$ and ME $\text{Sc}(\text{OTf})_3$ is described. With our new data in Chapter 6 it is clear that some of our original hypotheses regarding the structure of ME $\text{Sc}(\text{OTf})_3$ are incorrect. These portions of the original publication⁶⁶ have been removed.

^{45}Sc NMR spectra of $\text{Sc}(\text{OTf})_3$ and corresponding analytical simulations are shown in Figure 5.8. Simulations of MAS (Figure 5.8a) and static (Figure 5.8b) patterns yield $C_Q = 4.7$ MHz, $\eta_Q = 0.15$, and $\delta_{\text{iso}} = -28.0$ ppm, $\Omega = 32.0$ ppm and $\kappa = 0.3$. The static spectra possess rounded edges and do not terminate sharply into the baseline. This is most likely due to minor long-range disorder in the sample.

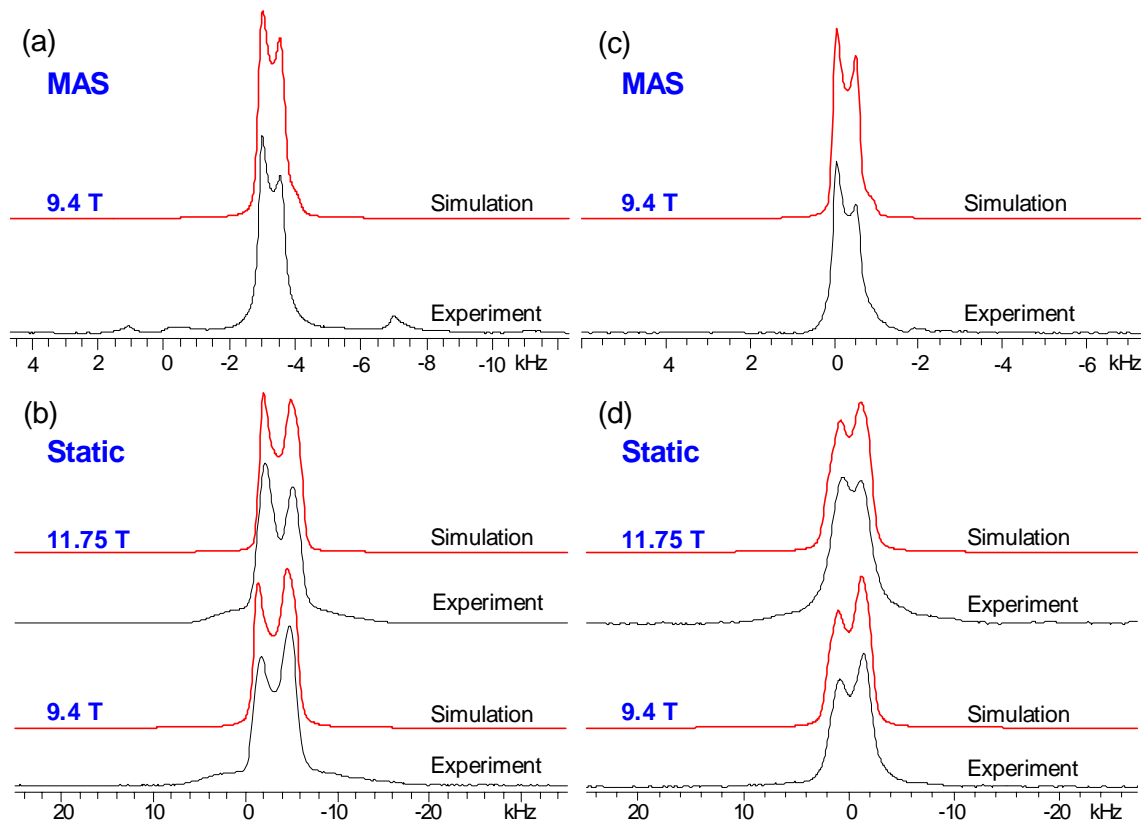


Figure 5.8. Solid-state ^{45}Sc NMR spectra and analytical simulations of $\text{Sc}(\text{OTf})_3$ and $\text{ME Sc}(\text{OTf})_3$. (a) MAS spectrum of $\text{Sc}(\text{OTf})_3$, $\nu_{\text{rot}} = 4$ kHz. (b) Static spectra of $\text{Sc}(\text{OTf})_3$ at 9.4 T and 11.75 T. (c) MAS spectrum of $\text{ME Sc}(\text{OTf})_3$, $\nu_{\text{rot}} = 4$ kHz. (d) Static spectra of $\text{Sc}(\text{OTf})_3$ at 9.4 T (AMDFS-Hahn Echo) and 11.75 T.

There is currently no crystal structure of $\text{Sc}(\text{OTf})_3$; however, the ^{45}Sc NMR data can be used to make structural inferences. The small C_Q suggests that the coordination environment of scandium must be of high symmetry, while the low Ω and negative isotropic chemical shift suggest that there is symmetric coordination by oxygen atoms from one type of ligand. The oxygen atoms should form a nearly idealized octahedron about the scandium centre. Given the similarity of these parameters with those of $\text{Sc}(\text{OAc})_3$ (Table 5.3), $\text{Sc}(\text{OTf})_3$ should have a coordination polymer structure akin to that of $\text{Sc}(\text{OAc})_3$. This is reasonable because triflate and acetate anions are similar in

structure, and can therefore coordinate to Sc in an equivalent manner. This is in accordance with the previously reported IR studies which suggests that the triflate ligands are bridging.⁸⁰ The structure of $\text{Sc}(\text{OAc})_3$ is shown in Figure 5.9 along with a proposed model of a $[\text{Sc}_3(\text{OTf})_6]^{3+}$ unit. In addition, the ^{13}C and ^{19}F NMR spectra only contain one signal apiece (Figure D6), which is also consistent with the proposed structure (one type of carbon and fluorine atom). Thus, ^{45}Sc NMR spectroscopy can be applied as a rapid probe of structure and bonding in the context of the other systems examined within this work.

Table 5.3. Observed ^{45}Sc NMR Parameters of $\text{Sc}(\text{OTf})_3$, $\text{ME Sc}(\text{OTf})_3$, and $\text{Sc}(\text{OAc})_3$.

Compound	C_Q (MHz) ^a η_Q	δ_{iso} (ppm)	Ω (ppm)	κ	α (°)	β (°)	γ (°)	
$\text{Sc}(\text{OTf})_3$	4.7(2)	0.15(5)	-28(1)	32(3)	0.3(1)	75(30)	18(4)	0(25)
$\text{ME Sc}(\text{OTf})_3$	4.2(2)	0.1(1)	1.8(3)	26(8)	-0.1(2)	90(30)	15(5)	0(25)
$\text{Sc}(\text{OAc})_3$	4.6(2)	0.18(6)	-6.2(8)	73(5)	0.65(10)	0(45)	7(3)	90(45)

^aSee Table 5.1 for definitions of parameters.

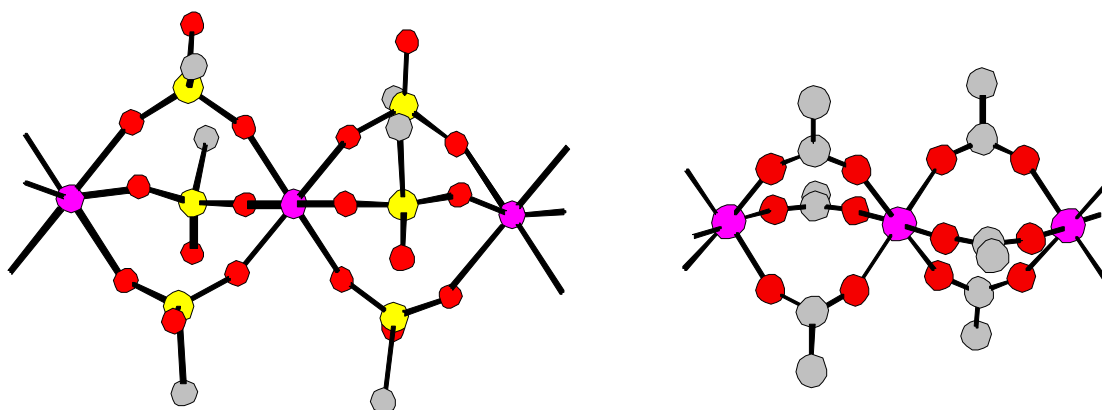


Figure 5.9. Proposed model of $\text{Sc}(\text{OTf})_3$ (left) and the known structure of $\text{Sc}(\text{OAc})_3$ (right). Fluorine and hydrogen atoms have been omitted for clarity.

Solid-state NMR of microencapsulated (ME) Sc(OTf)₃. The ⁴⁵Sc NMR spectra of ME Sc(OTf)₃ reveal spectra similar to those observed from the microcrystalline sample (Figure 5.8c and 5.8d), with $\delta_{\text{iso}} = 1.8$ ppm, $C_Q = 4.2$ MHz, $\eta_Q = 0.1$, $\Omega = 26.0$ ppm and $\kappa = -0.1$. Acquisition of static solid-state ⁴⁵Sc NMR spectra of ME Sc(OTf)₃ without ¹H decoupling results in significant broadening (Figure D7). This strong ¹H-⁴⁵Sc dipolar interaction could not be completely decoupled in the static experiments at 11.75 T (Figure 5.8d), as evidenced by the lack of definition in the pattern. However, the visible discontinuities in the pattern are useful for the confirmation of the parameters obtained from the simulation of the spectrum acquired at 9.4 T. In comparing the ⁴⁵Sc NMR parameters of Sc(OTf)₃ and ME Sc(OTf)₃ (Table 5.3), the latter has a significantly higher chemical shift (scandium is less shielded) and a slightly smaller C_Q . Preliminary ¹³C and ¹⁹F SSNMR spectra have also been acquired (Figure D6). For interpretations of the SSNMR data regarding the structure of ME Sc(OTf)₃ the reader is referred to Chapter 6.

5.4 Conclusions

The ⁴⁵Sc NMR interaction tensor parameters have been measured for a number of well-characterized scandium compounds possessing a broad range of metal coordination environments. For the first time, clear relationships are drawn between the scandium coordination environments and the nature of the ⁴⁵Sc NMR interaction tensors. EFG tensor parameters are primarily affected by the geometry of the scandium coordination environment, while CS tensor parameters are affected by both the symmetry of the coordination environment and nature of bonding in the first coordination sphere.

Anisotropic chemical shielding of the scandium nucleus is observed in all of the systems, and plays a significant role in defining the scandium chemical shift range. Ab initio calculations of the CS and EFG tensor parameters are in very good agreement with experimental data. In addition, the predicted tensor orientations within the molecular frames aids in rationalizing the origin of the observed CS and EFG tensor parameters. Solid-state ^{45}Sc NMR spectroscopy has also been successfully applied to structurally characterize two systems for which single-crystal X-ray diffraction data is unavailable and/or unobtainable. It has been demonstrated that $\text{Sc}(\text{OTf})_3$ is a coordination polymer that possesses a structure similar to $\text{Sc}(\text{OAc})_3$. A distinct chemical shift and significant ^1H - ^{45}Sc dipolar coupling was observed in the ^{45}Sc NMR spectra of ME $\text{Sc}(\text{OTf})_3$.

5.5. Bibliography

- (1) Cotton, S. A., *Polyhedron* **1999**, 18, (12), 1691-1715.
- (2) Meehan, P. R.; Aris, D. R.; Willey, G. R., *Coord. Chem. Rev.* **1999**, 181, 121-145.
- (3) Royset, J.; Ryum, N., *Int. Mat. Rev.* **2005**, 50, (1), 19-44.
- (4) Park, H. S.; Bull, I.; Peng, L. M.; Victor, G. Y. J.; Grey, C. P.; Parise, J. B., *Chem. Mat.* **2004**, 16, (25), 5350-5356.
- (5) Napper, J. D.; Layland, R. C.; Smith, M. D.; zur Loye, H. C., *J. Chem. Cryst.* **2004**, 34, (6), 347-351.
- (6) Perles, J.; Iglesias, M.; Ruiz-Valero, C.; Snejko, N., *J. Mat. Chem.* **2004**, 14, (17), 2683-2689.
- (7) Kolitsch, U.; Tillmanns, E., *Eur. J. Mineral.* **2004**, 16, (1), 143-149.
- (8) Kolitsch, U.; Tillmanns, E., *Mineral. Mag.* **2004**, 68, (4), 677-686.
- (9) Brigden, C. T.; Thompsett, D.; Williams, C. D., *Dalton Trans.* **2004**, (18), 2829-2830.
- (10) Yue, X.; Xiao, D. Q.; Cao, J.; Yuan, X. W.; Yu, G. L.; Xiong, X. B.; Wei, L.; Zhu, J. G., *Ceram. Int.* **2004**, 30, (7), 1905-1908.
- (11) Yamashita, Y. J.; Hosono, Y., *Jpn. J. Appl. Phys., Part 1* **2004**, 43, (9B), 6679-6682.
- (12) Pietraszko, A.; Hilczer, B.; Caranoni, C., *Ferroelectrics* **2004**, 298, 235-241.
- (13) Yoshikawa, Y.; Hanada, T.; Kogai, T., *J. Eur. Ceram. Soc.* **2004**, 24, (6), 1041-1044.
- (14) Maignan, A.; Pelloquin, D.; Flahaut, D.; Caignaert, V., *J. Solid-state Chem.* **2004**, 177, (10), 3693-3699.
- (15) Kurama, S.; Mandal, H., *Key Eng. Mater.* **2004**, 264-268, 1107-1110.
- (16) Kobayashi, S., *Eur J. Org. Chem.* **1999**, 1999, (1), 15-27.
- (17) Kobayashi, S.; Nagayama, S., *J. Am. Chem. Soc.* **1998**, 120, 2985-2986.
- (18) Li, X. F.; Baldamus, J.; Hou, Z., *Angew. Chem. Int. Ed.* **2005**, 44, (6), 962-965.
- (19) Luo, Y. J.; Baldamus, J.; Hou, Z. M., *J. Am. Chem. Soc.* **2004**, 126, (43), 13910-13911.
- (20) Piers, W. E.; Emslie, D. J. H., *Coord. Chem. Rev.* **2002**, 233, 131-155.
- (21) Mountford, P.; Ward, B. D., *Chem. Commun.* **2003**, (15), 1797-1803.

- (22) Melson, G. A.; Olszanski, D. J.; Rahimi, A. K., *Spectrochim. Acta, Part B* **1977**, 33, (3-4), 301-309.
- (23) Haid, E.; Kohnlein, D.; Kossler, G.; Lutz, O.; Messner, W.; Mohn, K. R.; Nothhaft, G.; Vanrickelen, B.; Schich, W.; Steinhauser, N., *Z. Naturforsch., A: Phys. Sci.* **1983**, 38, (3), 317-321.
- (24) Rehder, D., Early Transition Metals, Lanthanides and Actinides. In *Multinuclear NMR*, Mason, J., Ed. 1987; pp 480-482.
- (25) Rehder, D.; Speh, M., *Inorg. Chim. Acta* **1987**, 135, (1), 73-79.
- (26) Rehder, D.; Hink, K., *Inorg. Chim. Acta* **1989**, 158, (2), 265-271.
- (27) Bougeard, P.; Mancini, M.; Sayer, B. G.; McGlinchey, M. J., *Inorg. Chem.* **1985**, 24, (1), 93-5.
- (28) Kirakosyan, G. A.; Tarasov, V. P.; Buslaev, Y. A., *Magn. Reson. Chem.* **1989**, 27, (2), 103-111.
- (29) Randarevich, S. B.; Soloveva, L. G.; Korovin, V. Y.; Nikonov, V. I.; Pastukhova, I. V., *Koord. Khim.* **1989**, 15, (11), 1581-1584.
- (30) Aramini, J. M.; Vogel, H. J., *J. Am. Chem. Soc.* **1994**, 116, (5), 1988-1993.
- (31) Miyake, Y.; Suzuki, S.; Kojima, Y.; Kikuchi, K.; Kobayashi, K.; Nagase, S.; Kainosho, M.; Achiba, Y.; Maniwa, Y.; Fisher, K., *J. Phys. Chem.* **1996**, 100, (23), 9579-9581.
- (32) Meehan, P. R.; Willey, G. R., *Inorg. Chim. Acta* **1999**, 284, (1), 71-75.
- (33) Hill, N. J.; Levason, W.; Popham, M. C.; Reid, G.; Webster, M., *Polyhedron* **2002**, 21, (16), 1579-1588.
- (34) Petrosyants, S. P.; Ilyukhin, A. B., *Koord. Khim.* **2004**, 30, (3), 194-197.
- (35) Gierezyk, B.; Schroeder, G., *Pol. J. Chem.* **2003**, 77, (12), 1741-1745.
- (36) Thompson, A. R.; Oldfield, E., *J. Chem. Soc., Chem. Commun.* **1987**, (1), 27-29.
- (37) Han, J. W.; Chang, C. T.; Torgeson, D. R.; Seymour, E. F. W.; Barnes, R. G., *Phys. Rev. B* **1987**, 36, (1), 615-619.
- (38) Kataoka, H.; Takeda, S.; Nakamura, N., *J. Phys. Soc. Jpn.* **1993**, 62, (5), 1478-1481.
- (39) Koyama, T.; Sugita, H.; Wada, S.; Tsutsumi, K., *J. Phys. Soc. Jpn.* **1999**, 68, (7),

2326-2330.

- (40) Glinchuk, M. D.; Bykov, I. P.; Laguta, V. V.; Nokhrin, S. N., *Ferroelectrics* **1997**, 199, (1-4), 173-185.
- (41) Blinc, R.; Zalar, B.; Gregorovic, A.; Pirc, R.; Glinchuk, M. D., *Ferroelectrics* **2000**, 240, (1-4), 1473-1478.
- (42) Laguta, V. V.; Glinchuk, M. D.; Nokhrin, S. N.; Bykov, I. P.; Blinc, R.; Gregorovic, A.; Zalar, B., *Phys. Rev. B* **2003**, 67, (10).
- (43) Laguta, V. V.; Glinchuk, M. D.; Bykov, I. P.; Blinc, R.; Zalar, B., *Phys. Rev. B* **2004**, 69, (5), 054103.
- (44) Sato, K.; Takeda, S.; Fukuda, S.; Minamisono, T.; Tanigaki, M.; Miyake, T.; Maruyama, Y.; Matsuta, K.; Fukuda, M.; Nojiri, Y., *Z. Naturforsch., A: Phys. Sci.* **1998**, 53, (6/7), 549-551.
- (45) Tien, C.; Charnaya, E. V.; Sun, S. Y.; Wu, R. R.; Ivanov, S. N.; Khazanov, E. N., *Phys. Status Solidi B* **2002**, 233, (2), 222-229.
- (46) Madhu, P. K.; Johannessen, O. G.; Pike, K. J.; Dupree, R.; Smith, M. E.; Levitt, M. H., *J. Magn. Reson.* **2003**, 163, (2), 310-317.
- (47) Morais, C. M.; Lopes, M.; Fernandez, C.; Rocha, J., *Magn. Reson. Chem.* **2003**, 41, (9), 679-688.
- (48) Brauniger, T.; Ramaswamy, K.; Madhu, P. K., *Chem. Phys. Lett.* **2004**, 383, (3-4), 403-410.
- (49) Atwood, J. L.; Smith, K. D., *J. Chem. Soc., Dalton Trans.* **1974**, (9), 921-923.
- (50) Morgan, G. T.; Moss, H. W., *J. Chem. Soc., Trans.* **1914**, 189.
- (51) Yao, Z.; Kwak, H. T.; Sakellariou, D.; Emsley, L.; Grandinetti, P. J., *Chem. Phys. Lett.* **2000**, 327, (1-2), 85-90.
- (52) Kentgens, A. P. M.; Verhagen, R., *Chem. Phys. Lett.* **1999**, 300, (3-4), 435-443.
- (53) Bodart, P. R.; Amoureux, J. P.; Dumazy, Y.; Lefort, R., *Mol. Phys.* **2000**, 98, (19), 1545-1551.
- (54) Eichele, K.; Wasylishen, R. E. *WSolids1: Solid-State NMR Spectrum Simulation*, v. 1.17.30; 2001.

- (55) Bak, M.; Rasmussen, J. T.; Nielsen, N. C., *J. Magn. Reson.* **2000**, 147, (2), 296-330.
- (56) Bennett, A. E.; Rienstra, C. M.; Auger, M.; Lakshmi, K. V.; Griffin, R. G., *J. Chem. Phys.* **1995**, 103, (16), 6951-6958.
- (57) Frisch, M. J. e. a. *Gaussian 03*, Rev. B.03; Gaussian, Inc.: Pittsburgh, 2003.
- (58) Lee, C.; Yang, W.; Parr, R. G., *Phys. Rev. B.* **1988**, 37, 785.
- (59) Huzinaga, S., *Gaussian Basis Sets for Molecular Calculations*. Elsevier: New York, 1984.
- (60) Wolinski, K.; Hinton, J. F.; Pulay, P., *J. Am. Chem. Soc.* **1990**, 112, (23), 8251-8260.
- (61) Ditchfield, R., *Mol. Phys.* **1974**, 27, 789.
- (62) Rudolph, W. W.; Pye, C. C., *J. Phys. Chem. A* **2000**, 104, (8), 1627-1639.
- (63) Kraus, W.; Nolze, G. *PowderCell for Windows*, v. 2.4; Federal Institute for Materials Research and Testing: Berlin, Germany, 2000.
- (64) Cheng, J. T.; Edwards, J. C.; Ellis, P. D., *J. Phys. Chem.* **1990**, 94, (2), 553-561.
- (65) Power, W. P.; Wasylishen, R. E.; Mooibroek, S.; Pettitt, B. A.; Danchura, W., *J. Phys. Chem.* **1990**, 94, (2), 591-598.
- (66) Rossini, A. J.; Schurko, R. W., *J. Am. Chem. Soc.* **2006**, 128, 10391-10402.
- (67) Anderson, T. J.; Neuman, M. A.; Gordon, A. M., *Inorg. Chem.* **1973**, 12, (4), 927-930.
- (68) Lucken, E. A. C., *Nuclear Quadrupole Coupling Constants*. 1969; p 360 pp.
- (69) Cohen, M. H.; Reif, F., Quadrupole effects in nuclear magnetic resonance studies of solids. In *Solid State Physics*, Seitz, F.; Turnbull, D., Eds. Academic Press: New York, 1957; Vol. 5, pp 321-438.
- (70) Fuchs, R.; Strahle, J., *Z.Naturforsch.(B)* **1984**, 39, (12), 1662-1663.
- (71) Medek, A.; Harwood, J. S.; Frydman, L., *J. Am. Chem. Soc.* **1995**, 117, (51), 12779-12787.
- (72) Schurko, R. W.; Hung, I.; Macdonald, C. L. B.; Cowley, A. H., *J. Am. Chem. Soc.* **2002**, 124, (44), 13204-13214.
- (73) Hung, I.; Schurko, R. W., *Solid State Nucl. Magn. Reson.* **2003**, 24, (2-3), 78-93.
- (74) Hung, I.; Schurko, R. W., *J. Phys. Chem. B* **2004**, 108, (26), 9060-9069.

- (75) Willans, M. J.; Schurko, R. W., *J. Phys. Chem. B* **2003**, 107, (22), 5144-5161.
- (76) Widdifield, C. M.; Schurko, R. W., *J. Phys. Chem. A* **2005**, 109, (31), 6865-6876.
- (77) Reynhard, E. C., *J. Phys. C: Solid State Phys.* **1974**, 7, (22), 4135-4142.
- (78) Schurko, R. W.; Wasylishen, R. E.; Foerster, H., *J. Phys. Chem. A* **1998**, 102, (48), 9750-9760.
- (79) Ramsey, N. F., *Phys. Rev.* **1950**, 78, (6), 699-703.
- (80) Hamidi, M. M.; Pascal, J., *Polyhedron* **1993**, 13, (11), 1787-1792.

Chapter 6: Multinuclear Solid-State NMR Studies of Polymer Supported Scandium Triflate Catalysts

6.1 Introduction

Green chemistry is a term used to describe the creation of products or processes in chemistry that will reduce or eliminate hazardous by-products or solvents used in a chemical process or reaction.^{1, 2, 3} One of the simplest ways to attain more environmentally friendly chemical processes is to eliminate potentially toxic and expensive organic solvents and stoichiometric reagents, and replace them with aqueous media and/or catalytic reagents.⁴⁻⁶ For these reasons, there has been intense research in both academic and industrial sectors towards developing water-tolerant reagents and catalysts.⁶

Kobayashi and co-workers have introduced scandium(III) trifluoromethanesulfonate (triflate) $[\text{Sc}(\text{OTf})_3]$ as an effective carbon-carbon bond forming Lewis acid catalyst capable of catalyzing a variety of synthetic organic reactions in aqueous media.⁷⁻¹⁸ This work is part of a larger field of research into water-tolerant Lewis acid catalysts.^{6, 19-21} In 1998, Kobayashi and co-workers introduced microencapsulation as a method of immobilizing $\text{Sc}(\text{OTf})_3$ in polystyrene (PS).²² These microencapsulated (ME) catalysts are recoverable, reusable, often reduce metal leaching and have similar activity to their microcrystalline counterparts; however, they are most often employed with organic solvents.²¹ ME $\text{Sc}(\text{OTf})_3$ has been shown to catalyze many of the same synthetic reactions as microcrystalline $\text{Sc}(\text{OTf})_3$, while imparting the aforementioned beneficial characteristics of ME catalysts.^{21, 23, 24} In some cases, ME $\text{Sc}(\text{OTf})_3$ exhibits superior catalytic activity to $\text{Sc}(\text{OTf})_3$: for example, Lewis acids can be

decomposed by basic aldimines; however, it was shown that ME Sc(OTf)₃ is able to tolerate and activate such aldimines.²¹ In addition, ME Sc(OTf)₃ is able to catalyze Friedel-Crafts alkylation and acylation reactions,²⁵ which are important in large scale reactions that exhibit characteristics desirable for green chemistry.²⁶⁻²⁸

Despite the importance of ME Sc(OTf)₃, the interactions between the microencapsulating polymer and Sc(OTf)₃ is not well understood. Kobayashi and co-workers have characterized ME Sc(OTf)₃ by ⁴⁵Sc solution NMR spectroscopy²⁹ and energy dispersive X-ray (EDX) and scanning electron microscopy (SEM) imaging (in addition to reactivity studies).²² EDX and SEM images showed that the Sc is well dispersed on the surface of the polymer in sub- μm size particles, which suggests the presence of nanocrystalline or molecular-level Sc(OTf)₃ domains in ME Sc(OTf)₃.²² Solution ⁴⁵Sc NMR studies of ME Sc(OTf)₃ revealed a positive chemical shift of *ca.* 18 ppm compared to that of Sc(OTf)₃.²⁹ Furthermore, ⁴⁵Sc NMR of solutions of Sc(OTf)₃ with a “PS analogue” (1,3,5-triphenylpentane) also display a positive chemical shift of *ca.* 14 ppm.²⁹ It was also found that loading levels corresponding to 43% and 0% of the amount of Sc loaded onto PS were obtained with polybutadiene and polyethylene as the support materials, respectively. The positive chemical shift of *ca.* 18 ppm observed in solution ⁴⁵Sc NMR spectra and the higher loading levels observed for PS ME Sc(OTf)₃ and were attributed by Kobayashi to an interaction between the π -electrons of the PS phenyl groups and vacant Sc *d*-orbitals.^{21, 29} It was posited that this electronic interaction is responsible for immobilizing Sc(OTf)₃ in the polymer, although it was also suggested the steric bulk of the polymer may be important as well, i.e., physical envelopment of Sc(OTf)₃ by bulky phenyl groups may play a role in microencapsulation.²²

Solid-state NMR (SSNMR) is an ideal technique for probing the structures of non-crystalline materials, such as polymers,³⁰⁻³² and by extension, polymer based ME catalysts. In addition to SSNMR experiments which employ ubiquitous nuclei, such as ^1H , ^{13}C and ^{19}F , it is also possible to utilize ^{45}Sc ($I = 7/2$, N.A. = 100%) SSNMR to probe the structure of ME $\text{Sc}(\text{OTf})_3$. ^{45}Sc SSNMR has recently been employed to probe the structure of a variety of scandium-containing materials,³³⁻⁴² and the ^{45}Sc quadrupolar interactions and chemical shifts have been found to be very sensitive to the structural differences in local Sc environments.

In our preliminary of $\text{Sc}(\text{OTf})_3$ and ME $\text{Sc}(\text{OTf})_3$,⁴² we observed a single ^{45}Sc powder pattern in the ^{45}Sc SSNMR spectra of both ME $\text{Sc}(\text{OTf})_3$ and $\text{Sc}(\text{OTf})_3$. The δ_{iso} of ME $\text{Sc}(\text{OTf})_3$ was observed to be ca. +30 ppm higher than that of microcrystalline $\text{Sc}(\text{OTf})_3$ (similar to the positive chemical shifts observed in Kobayashi's solution ^{45}Sc NMR studies). Similar electric field gradient (EFG) tensor and chemical shift (CS) tensor parameters were observed in both cases (excepting the difference in isotropic chemical shifts). These preliminary results were consistent with Kobayashi's hypothesis that electronic interactions between the π -electrons of the PS phenyl groups and Sc are partly responsible for microencapsulation.^{21, 29}

Questions still remain regarding the local Sc environments in ME $\text{Sc}(\text{OTf})_3$. This is further exacerbated by the absence of any known single crystal X-ray diffraction structure for $\text{Sc}(\text{OTf})_3$. Hence, further intensive study of $\text{Sc}(\text{OTf})_3$ and ME $\text{Sc}(\text{OTf})_3$ is necessary to understand the mode (and perhaps mechanism) of microencapsulation, as well as the local catalyst structure. To this end, we have acquired ^{45}Sc SSNMR NMR spectra of a series of ME $\text{Sc}(\text{OTf})_3$ samples, freshly prepared under a variety of different

conditions, as well as crystalline and ME $\text{Sc}(\text{OTf})_3 \cdot 8\text{H}_2\text{O}$ (the former features hydrated Sc^{3+} ions). ^1H - ^{45}Sc TRAPDOR NMR experiments were employed in order to probe for possible interactions between the polymer and Sc atoms. In addition, solid-state ^{13}C , ^{19}F , and ^1H NMR experiments, as well as powder X-ray diffraction (PXRD) experiments, were also performed in order to obtain complementary information on the bulk structures of the ME catalysts.

6.2 Experimental

Sample Preparation. Samples of scandium trifluoromethanesulfonate [$\text{Sc}(\text{OTf})_3$] were purchased from Strem Chemicals, Inc. and Sigma-Aldrich Chemicals, Inc. Some of the commercial samples of anhydrous $\text{Sc}(\text{OTf})_3$ were found to be partially hydrated when received, as indicated by solid-state ^{45}Sc NMR and PXRD. Completely anhydrous $\text{Sc}(\text{OTf})_3$ was obtained by drying the powdered sample under vacuum at 160 °C for four hours. $\text{Sc}(\text{OTf})_3 \cdot 8\text{H}_2\text{O}$ and $\text{Sc}(\text{OTf})_3 \cdot 8\text{D}_2\text{O}$ were synthesized by dissolving anhydrous $\text{Sc}(\text{OTf})_3$ in H_2O and D_2O , respectively, followed by drying under vacuum at elevated temperatures (80 °C). PS (PS) ($M_w = 60500$ and 22400) and Deuterated PS (d_8 , $M_w = 66000$, approximately 98% deuterated) were purchased from Polymer Source Inc. and used without purification.

Scandium acetate ($\text{Sc}(\text{OAc})_3$) was purchased from Strem Chemicals, Inc. and purified following a literature procedure to remove water of hydration.⁴³ $\text{Sc}(\text{OAc})_3$ was added to a 5.0 M glacial acetic acid solution and stirred until dissolution. The solvent was then removed by vacuum and the resulting solid was collected and isolated under inert atmosphere. The identity of the purified sample was confirmed by PXRD.

Synthesis of Microencapsulated (ME) Sc(OTf)₃. The synthesis of ME Sc(OTf)₃ was based upon a modified literature procedure.²² All reagents were handled under an inert N₂ atmosphere (except where noted) and all reactions were carried out using Schlenk lines. All solvents were dried by overnight reactions with calcium hydride, followed by distillations, with the exception of acetonitrile, which was obtained from a solvent system. 0.250 g of PS was combined with approximately 6 mL of cyclohexane in a Schlenk flask. The mixture was heated to 40 °C, while stirring, to dissolve the PS. 0.050 g of Sc(OTf)₃ (or Sc(OTf)₃•8H₂O, where indicated) was weighed into a first Schlenk flask. The hot PS/cyclohexane mixture was then cannulated into a second Schlenk flask containing Sc(OTf)₃ and stirred for one hour at 40 °C. The mixture was slowly cooled to 0 °C in an ice bath, during which time PS was observed to precipitate. 8 mL of hexanes were then added in a drop-wise manner to precipitate the remaining PS. After this, the solution was stirred at room temperature for one hour. The solvent was pumped off and the PS was washed several times with dry acetonitrile to remove excess Sc(OTf)₃. After the final washing, the resulting ME Sc(OTf)₃ was dried at 50 °C under vacuum.

Some refinements of the literature procedure are as follows: cooling of the PS/cyclohexane/Sc(OTf)₃ solution to room temperature was done at a slow rate (over ca. 1.5 hours) by allowing the solution to remain in the oil bath used for heating with the hot plate turned off. When the solution reached room temperature it was then placed in a water bath to which ice was slowly added over the span of 0.5 hours until 0 °C was reached. The addition of hexanes to the solution was performed in a drop-wise manner over the course of ca. 20 min.

Solid-state NMR Spectroscopy. Solid-state NMR spectra were obtained on a Varian Infinity Plus NMR Spectrometer with an Oxford 9.4 T ($\nu_0(^1\text{H}) = 399.73$ MHz) wide-bore magnet with $\nu_0(^{45}\text{Sc}) = 97.10$ MHz, $\nu_0(^{13}\text{C}) = 100.52$ MHz and $\nu_0(^{19}\text{F}) = 376.09$ MHz. All samples were ground into powders, packed into 4 mm outer diameter (o.d.) zirconium oxide rotors under an inert atmosphere and sealed with airtight caps. Chemagnetics 4 mm triple-resonance (HXY) or double-resonance (HX) MAS probes were used for all experiments. A detailed list of ^{45}Sc SSNMR acquisition parameters can be found in Tables E1-E6. Scandium chemical shifts were referenced to an aqueous solution of dilute (less than 0.05 M) ScCl_3 ($\delta_{\text{iso}} = 0.0$ ppm).⁴² An echo pulse sequence [$\pi/2 - \tau_1 - \theta_{\text{ref}} - \tau_2 - \text{acquire}$, with $\theta_{\text{ref}} = \pi/2$ or π] was utilized to acquire all ^{45}Sc NMR spectra, and the radiofrequency field of the pulses, $\nu_1(^{45}\text{Sc})$, was set to ca. one-half of the static central-transition powder pattern width.⁴⁴ A double frequency sweep (DFS) sequence^{45, 46} was applied to enhance the signal of some ^{45}Sc echo spectra of the ME samples. ^1H decoupling was applied with $\nu_1(^1\text{H})$ between 22 and 30 kHz, where indicated. Magic-angle spinning (MAS) spectra were acquired with a 90° - 90° echo sequence [$\pi/2 - \tau_1 - \pi/2 - \tau_2 - \text{acquire}$] using high power pulses and large spectral widths. MAS spinning frequencies (ν_{rot}) ranged from 4 kHz to 12 kHz, with inter-pulse delays equal to $1/\nu_{\text{rot}}$. Non-selective pulse widths were adjusted by a factor of $(I + 1/2)^{-1}$ (where $I = 7/2$) in order to achieve central-transition (CT) selective ^{45}Sc pulses for all experiments. A large number of scans were acquired for ME spectra when compared to spectra of the crystalline complexes.

Hydrogen chemical shifts were referenced to tetramethylsilane ($\delta_{\text{iso}} = 0.00$ ppm) via a secondary standard of adamantane ($\delta_{\text{iso}} = 1.85$ ppm). $\pi/2$ pulse widths between 2.30

and 2.40 μs were used corresponding to $\nu_1(^1\text{H}) = 105$ to 109 kHz. A recycle delay of 20 s was applied for all MAS ^1H SSNMR experiments. 32 to 128 scans were obtained for ^1H MAS SSNMR spectra and ν_{rot} ranged from 10 kHz to 13.5 kHz. ^1H TRAPDOR MAS SSNMR experiments were acquired at $\nu_{\text{rot}} = 12.5$ kHz and the first echo dephasing period (τ_1) was set to 240 μs . $\nu_1(^{45}\text{Sc})$ of ca. 108 kHz was applied during the echo dephasing period. The control and dephasing spectra were acquired in an inter-leaved manner, in order to eliminate any variability in spectrometer performance, which could give rise to false reductions in ^1H signal intensity. Deconvolutions of MAS ^1H SSNMR spectra were performed with the line-fitting routine in the Nuts NMR processing software.

Carbon chemical shifts were referenced to tetramethylsilane ($\delta_{\text{iso}} = 0.00$ ppm) by setting the high-field shift of adamantane ($\delta_{\text{iso}} = 38.57$ ppm) as a secondary reference. $^1\text{H} \rightarrow ^{13}\text{C}$ variable amplitude cross-polarization MAS (VACP/MAS) SSNMR experiments utilized a contact time between 1 to 5 ms, a pulse delay of 12 s, and ν_{rot} ranged from 6.5 to 13.5 kHz. ^{19}F chemical shifts were referenced to fluorotrichloromethane ($\delta_{\text{iso}} = 0.00$ ppm) by setting the shift of teflon ($\delta_{\text{iso}} = -122.00$ ppm) as a secondary reference. $^{19}\text{F} \rightarrow ^{13}\text{C}$ VACP/MAS NMR experiments utilized a contact time of 2 ms, a pulse delay of 5 s, and a spectral width of 100 kHz.

Powder X-ray Diffraction. PXRD patterns were acquired using a Bruker AXS HI-STAR system utilizing a General Area Detector Diffractions System (GADDS). A Copper $K\alpha$ radiation source (1.540598 \AA) with area detector 2θ range of ca. $3^\circ - 70^\circ$ was utilized. Powdered samples were packed in 1.0 mm glass capillaries under an inert atmosphere and flame sealed to prevent atmospheric exposure. In order to expose some

of the samples to air, the capillary was broken with a pair of tweezers at the flame sealed (top) side. PXRD patterns were simulated using the Powdercell computer program.⁴⁷

6.3 Results and Discussion

Solid-state ⁴⁵Sc NMR Spectra of Sc(OTf)₃, Sc(OAc)₃, Sc(OTf)₃•8H₂O. Anhydrous crystalline scandium(III) trifluoromethanesulfonate [herein referred to as Sc(OTf)₃] does not have a known crystal structure. For this reason, our research group previously performed ⁴⁵Sc SSNMR and PXRD experiments on Sc(OTf)₃, in order to characterize the scandium coordination environment.⁴² The major findings of this previous study are reviewed at this point in order to clarify some of the structural features of Sc(OAc)₃ and Sc(OTf)₃, and to compare these data to that of Sc(OTf)₃•8H₂O, prior to discussion of the increasingly complex microencapsulated (ME) systems.

Magic angle spinning (MAS) and static (i.e., stationary sample) ⁴⁵Sc SSNMR spectra reveal that the ⁴⁵Sc quadrupolar parameters of Sc(OTf)₃ are similar to those of Sc(OAc)₃ (Figure 6.1, Table 6.1). We have acquired new static NMR spectra of Sc(OTf)₃ at 9.4 T and 11.7 T with a 90°-90° echo sequence (Figure E1). This was done because our previous spectra were acquired with 90°-180° echo sequences and DFS for signal enhancement, which can introduce non-ideal intensities into static ⁴⁵Sc SSNMR spectra. The CS tensor parameters and Euler angles reported herein are slightly different than those previously reported by our research group (Chapter 5).⁴²

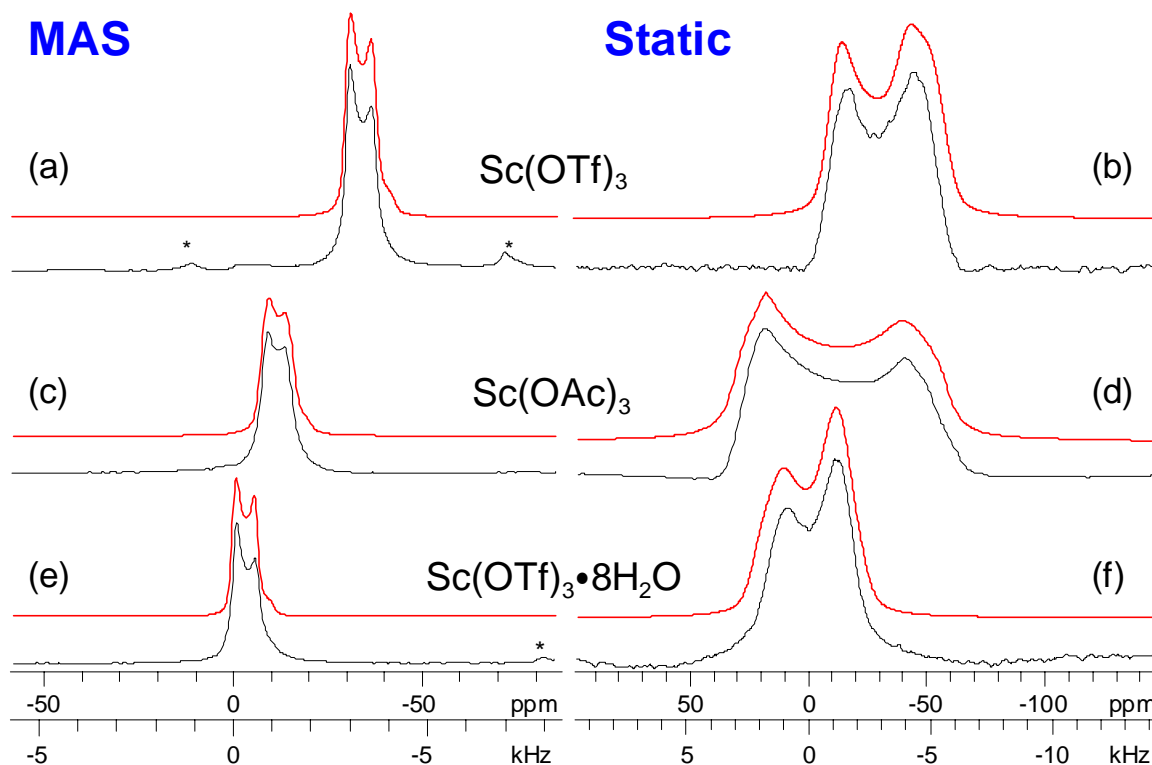


Figure 6.1. MAS (left) and static (right) ^{45}Sc SSNMR spectra acquired at 9.4 T. Analytical simulations of the spectra (red traces) are overlaid on top of the experimental spectra (black traces). (a) MAS spectrum of $\text{Sc}(\text{OTf})_3$ at a sample spinning speed of $v_{\text{rot}} = 4.0$ kHz and (b) static spectrum of $\text{Sc}(\text{OTf})_3$. (c) MAS spectrum of $\text{Sc}(\text{OAc})_3$ at $v_{\text{rot}} = 8.0$ kHz and (d) static spectrum with ^1H decoupling. (e) MAS spectrum of $\text{Sc}(\text{OTf})_3 \cdot 8\text{H}_2\text{O}$ at $v_{\text{rot}} = 8.0$ kHz and (f) static spectrum with ^1H decoupling. Spinning sidebands are indicated with asterisks. ^{45}Sc EFG and CS tensor parameters extracted from simulations are listed in Table 6.1. All static spectra were acquired with a 90° - 90° echo sequence. 90° - 90° echo static spectra of $\text{Sc}(\text{OTf})_3$ and $\text{Sc}(\text{OTf})_3 \cdot 8\text{H}_2\text{O}$ at 11.7 T were acquired in order to confirm the ^{45}Sc CS tensor parameters and Euler angles (Figure E1).

Table 6.1. Experimental ^{45}Sc EFG and CS Tensor Parameters of Crystalline Complexes

Compound	C_Q (MHz) ^a	η_Q ^b	δ_{iso} (ppm) ^c	Ω (ppm) ^d	κ ^e	α (°) ^f	β (°)	γ (°)
$\text{Sc}(\text{OAc})_3$	4.6(2)	0.18(6)	-6.2(8)	73(5)	0.65(10)	0(45)	7(3)	90(45)
$\text{Sc}(\text{OTf})_3$	4.7(2)	0.15(10)	-28(1)	26(5)	0.5(2)	35(20)	20(4)	-5(30)
$\text{Sc}(\text{OTf})_3 \cdot 8\text{H}_2\text{O}$	4.2(2)	0.10(10)	1.8(8)	22(5)	0.1(3)	60(90)	22(20)	-75(30)
ME $\text{Sc}(\text{OTf})_3$	4.2(2)	0.10(10)	1.8(8)	22(5)	0.1(3)	60(90)	22(20)	-75(30)

^a $C_Q = eQV_{33}/h$. ^b $\eta_Q = (V_{11} - V_{22})/V_{33}$. ^c $\delta_{\text{iso}} = (\delta_{11} + \delta_{22} + \delta_{33})/3$. ^d $\Omega = \delta_{33} - \delta_{11}$. ^e $\kappa = 3(\delta_{22} - \delta_{\text{iso}})/\Omega$. ^fThe Rose convention is used to describe the Euler angles.^{48, 49}

Both $\text{Sc}(\text{OTf})_3$ and $\text{Sc}(\text{OAc})_3$ possess similar ^{45}Sc EFG tensor parameters (η_Q and C_Q) and κ values. Their similarity suggests that the Sc coordination environments are comparable for both complexes. A single-crystal X-ray diffraction structure of $\text{Sc}(\text{OAc})_3$ has been previously reported,⁴³ which describes a coordination polymer with bridging acetate groups linking adjacent scandium atoms which reside in pseudo-octahedral coordination environments (Figure 6.2a). The PXRD patterns of $\text{Sc}(\text{OTf})_3$ and $\text{Sc}(\text{OAc})_3$ (Figure 6.2d and 6.2e) have peaks of similar intensity (though peaks are shifted to slightly lower 2θ values for $\text{Sc}(\text{OTf})_3$). Since 2θ is inversely proportional to the d -spacings, this difference in 2θ values suggests that the $\text{Sc}(\text{OTf})_3$ crystal structure has increased spacings between the diffraction planes of the unit cell compared to $\text{Sc}(\text{OAc})_3$, consistent with the triflate ligands being larger in size than the acetate ligands. The combination of the NMR and PXRD data suggest that $\text{Sc}(\text{OTf})_3$ is isomorphous with $\text{Sc}(\text{OAc})_3$ in the solid-state, and that $\text{Sc}(\text{OTf})_3$ has pseudo-octahedral Sc coordination environments which are formed by six oxygen atoms from six separate triflate ligands. The triflate ligands bridge to neighboring Sc sites to form polymeric chains (i.e., a classic *coordination polymer* structure, Figure 6.2b).

Characterization of the hydrated forms of Sc(III) complexes is important, as many of these complexes are hygroscopic and readily form hydrates. For example, several of the commercially purchased samples of anhydrous $\text{Sc}(\text{OTf})_3$ were delivered as the hydrated form $[\text{Sc}(\text{OTf})_3 \cdot 8\text{H}_2\text{O}]$. The solid-state structure of $\text{Sc}(\text{OTf})_3 \cdot 8\text{H}_2\text{O}$ has been extensively investigated by Sandstrom et al.,⁵⁰ who found that nine water molecules are coordinated to the Sc atom; however, the oxygen atoms of the water molecules which cap the rectangular faces of the trigonal prism possess fractional occupancies of 0.67 (labeled

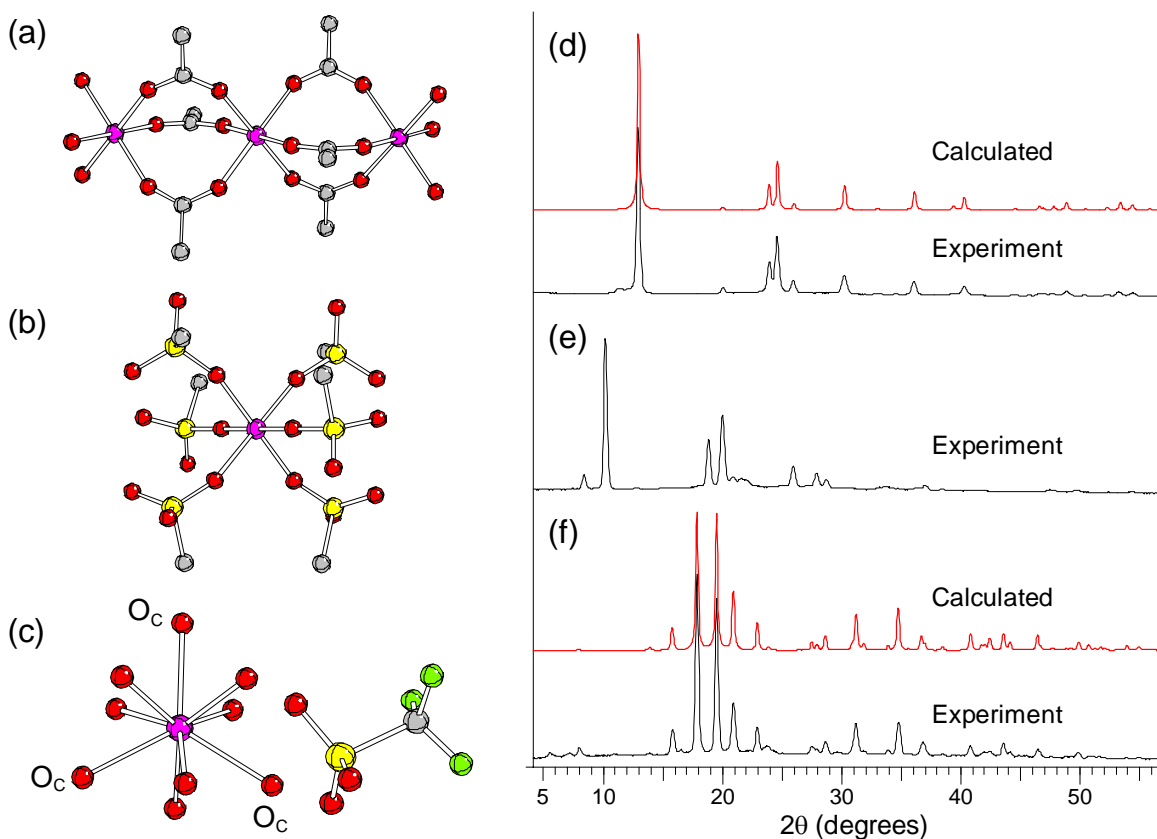


Figure 6.2. Structures of (a) $\text{Sc}(\text{OAc})_3$, (b) $\text{Sc}(\text{OTf})_3$ and (c) $\text{Sc}(\text{OTf})_3 \cdot 8\text{H}_2\text{O}$. Hydrogen and fluorine atoms have been omitted for clarity from the structures of $\text{Sc}(\text{OAc})_3$ and $\text{Sc}(\text{OTf})_3$. Experimental (black trace) powder X-ray diffraction patterns of (d) $\text{Sc}(\text{OAc})_3$, (e) $\text{Sc}(\text{OTf})_3$ and (f) $\text{Sc}(\text{OTf})_3 \cdot 8\text{H}_2\text{O}$. Powder X-ray diffraction patterns calculated (red trace) from the corresponding single crystal X-ray diffraction structures are shown for $\text{Sc}(\text{OAc})_3$ and $\text{Sc}(\text{OTf})_3 \cdot 8\text{H}_2\text{O}$. Single crystal XRD structures of $\text{Sc}(\text{OAc})_3$ and $\text{Sc}(\text{OTf})_3 \cdot 8\text{H}_2\text{O}$ have been previously published [references 43 and 50]. The oxygen atoms labelled O_C possess fractionally occupancies of 0.67 in the single crystal XRD structure of $\text{Sc}(\text{OTf})_3 \cdot 8\text{H}_2\text{O}$, leading to eight-coordinate Sc. There is no crystal structure of $\text{Sc}(\text{OTf})_3$ available. The model of $\text{Sc}(\text{OTf})_3$ presented herein, is based upon our ^{45}Sc SSNMR spectra and the powder X-ray diffraction patterns.

O_C in Figure 6.2),⁵⁰ leading to eight-coordinate Sc atoms. For these reasons, we have acquired ^{45}Sc SSNMR spectra of the crystalline complex $\text{Sc}(\text{OTf})_3 \cdot 8\text{H}_2\text{O}$ (Figure 6.1e and 6.1f). The ^{45}Sc SSNMR spectra of $\text{Sc}(\text{OTf})_3 \cdot 8\text{H}_2\text{O}$ reveal that the ^{45}Sc EFG and CS tensor parameters are similar to those of $\text{Sc}(\text{OTf})_3$ and $\text{Sc}(\text{OAc})_3$, with the exception of δ_{iso} , which is +30 ppm more than that observed for $\text{Sc}(\text{OTf})_3$. Of greater import, the ^{45}Sc

SSNMR spectra of $\text{Sc}(\text{OTf})_3 \cdot 8\text{H}_2\text{O}$ are almost identical in appearance to those of $\text{ME Sc}(\text{OTf})_3$ (*vide infra*). The CS and EFG tensor parameters of $\text{Sc}(\text{OTf})_3 \cdot 8\text{H}_2\text{O}$ were confirmed by acquiring static 90° - 90° echo ^{45}Sc SSNMR spectra at 9.4 T and 11.7 T (Figure E1).

During the course of this work, we also identified a new hydrated phase of $\text{Sc}(\text{OTf})_3$, which we refer to as $\text{Sc}(\text{OTf})_3 \cdot x\text{H}_2\text{O}$. $\text{Sc}(\text{OTf})_3 \cdot x\text{H}_2\text{O}$ possesses a PXRD pattern which is distinct from that of $\text{Sc}(\text{OTf})_3 \cdot 8\text{H}_2\text{O}$ (Figure E2). Further PXRD experiments were performed to identify the order in which the hydrated phases of $\text{Sc}(\text{OTf})_3$ are formed. A sample of anhydrous $\text{Sc}(\text{OTf})_3$ was packed into a sealed glass capillary and a PXRD pattern was acquired. The top of the capillary was then broken open so that the sample would be exposed to atmospheric moisture. A PXRD pattern was then periodically acquired. After ca. 19 hours, the PXRD patterns show complete conversion of $\text{Sc}(\text{OTf})_3$ to the $\text{Sc}(\text{OTf})_3 \cdot x\text{H}_2\text{O}$ phase, and after ca. 29 hours, the PXRD pattern is identical to that of the $\text{Sc}(\text{OTf})_3 \cdot 8\text{H}_2\text{O}$ phase (Figure E2). From these PXRD experiments it is clear that the anhydrous $\text{Sc}(\text{OTf})_3$ readily absorbs water and is first converted into the $\text{Sc}(\text{OTf})_3 \cdot x\text{H}_2\text{O}$ phase, followed by adsorption of additional water to form the previously characterized $\text{Sc}(\text{OTf})_3 \cdot 8\text{H}_2\text{O}$ phase. The $\text{Sc}(\text{OTf})_3 \cdot x\text{H}_2\text{O}$ and $\text{Sc}(\text{OTf})_3 \cdot 8\text{H}_2\text{O}$ phases possess identical MAS and static ^{45}Sc SSNMR spectra (Figure E2b), suggesting that both phases possess very similar eight-coordinate scandium environments. MAS ^1H SSNMR spectra of the two phases are distinct (Figure E2c). The MAS ^1H SSNMR spectra of $\text{Sc}(\text{OTf})_3 \cdot x\text{H}_2\text{O}$ are much broader than those of $\text{Sc}(\text{OTf})_3 \cdot 8\text{H}_2\text{O}$, suggesting that the ^1H nuclei of the water molecules are less mobile in the former. Further investigation of the $\text{Sc}(\text{OTf})_3 \cdot x\text{H}_2\text{O}$ phase is beyond the scope and aim of the current study; however, given the interest in characterizing the hydration state

of Sc(III) ions in aqueous solution and the solid-state,⁵¹⁻⁵⁵ and the role hydrated Sc(III) ions play in aqueous phase catalysis, it merits future study.

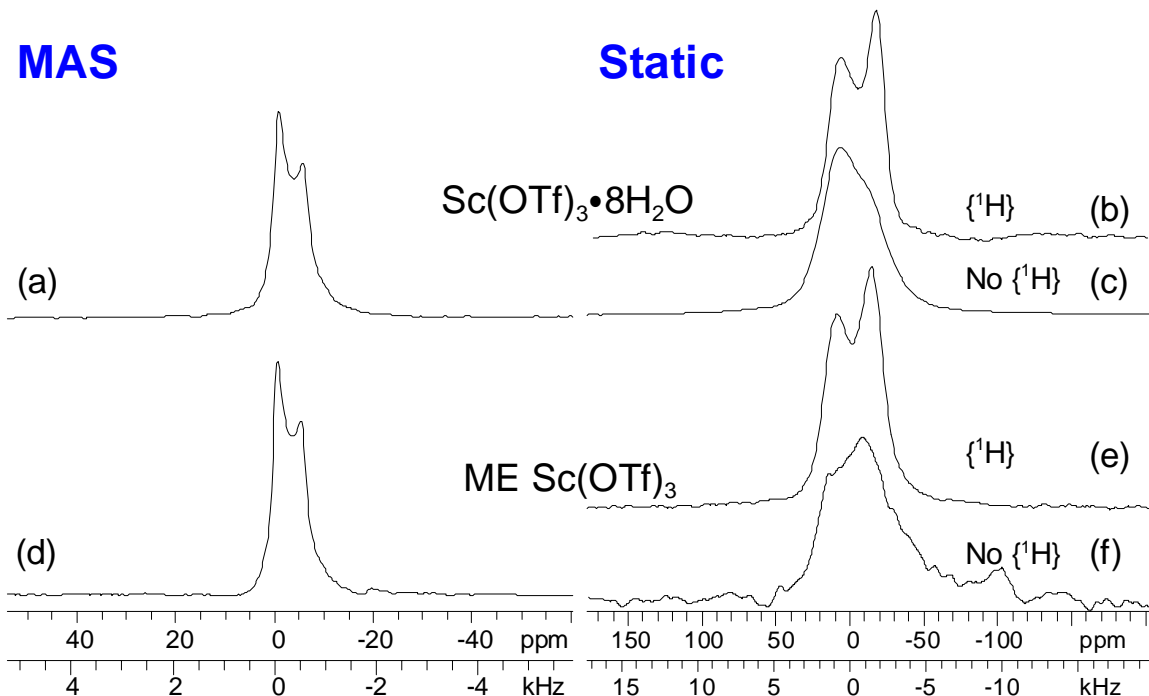


Figure 6.3. MAS and static ^{45}Sc SSNMR spectra of $\text{Sc}(\text{OTf})_3 \cdot 8\text{H}_2\text{O}$ and the commercial sample of $\text{ME Sc}(\text{OTf})_3$ acquired at 9.4 T. (a) MAS spectrum of $\text{Sc}(\text{OTf})_3 \cdot 8\text{H}_2\text{O}$ at a sample spinning speed of $\nu_{\text{rot}} = 8.0$ kHz and (b) static spectra with and (c) without ^1H decoupling. (d) MAS spectrum of $\text{ME Sc}(\text{OTf})_3$ at $\nu_{\text{rot}} = 12.0$ kHz and (e) static spectra with and (f) without ^1H decoupling. All static spectra were acquired with a DFS 90° - 180° echo pulse sequence.

^{45}Sc SSNMR Spectra of Microencapsulated (ME) $\text{Sc}(\text{OTf})_3$. We previously acquired ^{45}Sc SSNMR spectra of $\text{ME Sc}(\text{OTf})_3$ which revealed a distinct ^{45}Sc isotropic chemical shift of $\delta_{\text{iso}} = 1.8$ ppm and a moderate decrease in C_Q in comparison to that of $\text{Sc}(\text{OTf})_3$.⁴² Our new data reveal that the MAS and static ^{45}Sc SSNMR spectra of $\text{ME Sc}(\text{OTf})_3$ are identical to those of $\text{Sc}(\text{OTf})_3 \cdot 8\text{H}_2\text{O}$ (Figure 6.3), as mentioned above. There is a large reduction in the signal to noise of ^{45}Sc SSNMR spectra of $\text{ME Sc}(\text{OTf})_3$ in comparison to $\text{Sc}(\text{OTf})_3 \cdot 8\text{H}_2\text{O}$, consistent with the reduced Sc content of the former (ca. 1 % Sc by mass, *vide infra*). When ^1H decoupling is not applied during the

acquisition of the static ^{45}Sc SSNMR spectra, significant broadening of the static ^{45}Sc central transition powder patterns is observed for both $\text{Sc}(\text{OTf})_3 \cdot 8\text{H}_2\text{O}$ and ME $\text{Sc}(\text{OTf})_3$ (Figure 6.3c, 6.3f). In the case of crystalline $\text{Sc}(\text{OTf})_3 \cdot 8\text{H}_2\text{O}$, this indicates the presence of relatively large ^1H - ^{45}Sc dipolar couplings, which arise from the close spatial proximity of the ^{45}Sc nucleus and the ^1H nuclei of the coordinated water molecules (Sc-H distances of ca. 2.5 to 3.0 Å). All of this data suggests that $\text{Sc}(\text{OTf})_3$ is hydrated during the microencapsulation process and exists as domains of $\text{Sc}(\text{OTf})_3 \cdot 8\text{H}_2\text{O}$ within the polymer, and not as $\text{Sc}(\text{OTf})_3$ as previously suggested (though it is possible that the broadening under conditions of no ^1H decoupling also arises from ^1H nuclei in the surrounding PS, for more discussion *vide infra*).

One initially puzzling aspect of these data was the origin of the hydrating water molecules in the ME $\text{Sc}(\text{OTf})_3$ samples. The commercial sample of ME $\text{Sc}(\text{OTf})_3$ arrived packed under an argon atmosphere, suggesting that it was prepared under inert conditions; however, we are not absolutely certain of this (the manufacturer would not comment) and cannot comment on the origin of the water of hydration for this sample. Further, Kobayashi's synthetic procedures for ME $\text{Sc}(\text{OTf})_3$ do not call for inert atmosphere synthetic techniques, suggesting that water may be absorbed during preparation of the ME systems.²² For all of these reasons, we undertook synthesis of our own samples of ME $\text{Sc}(\text{OTf})_3$, and characterized them with further SSNMR and PXRD experiments, in order to confirm the nature of the hydrated Sc^{3+} environments and posit a source for the hydrating water molecules.

MAS and static ^{45}Sc SSNMR spectra for samples of ME $\text{Sc}(\text{OTf})_3$ prepared under a variety of conditions are shown in Figure 6.4 (all syntheses employed dried solvents). The variations in the synthetic procedure include microencapsulating $\text{Sc}(\text{OTf})_3 \cdot 8\text{H}_2\text{O}$

under an inert atmosphere (ME-1), and microencapsulation of $\text{Sc}(\text{OTf})_3$ under an ambient atmosphere (ME-2) and an inert atmosphere (ME-3). It is clear that regardless of the conditions employed for the synthesis of the ME samples, ^{45}Sc SSNMR spectra similar in appearance to those of $\text{Sc}(\text{OTf})_3 \cdot 8\text{H}_2\text{O}$ and the commercial sample of ME $\text{Sc}(\text{OTf})_3$ are obtained, excepting the spectra of ME-3 (*vide infra*).

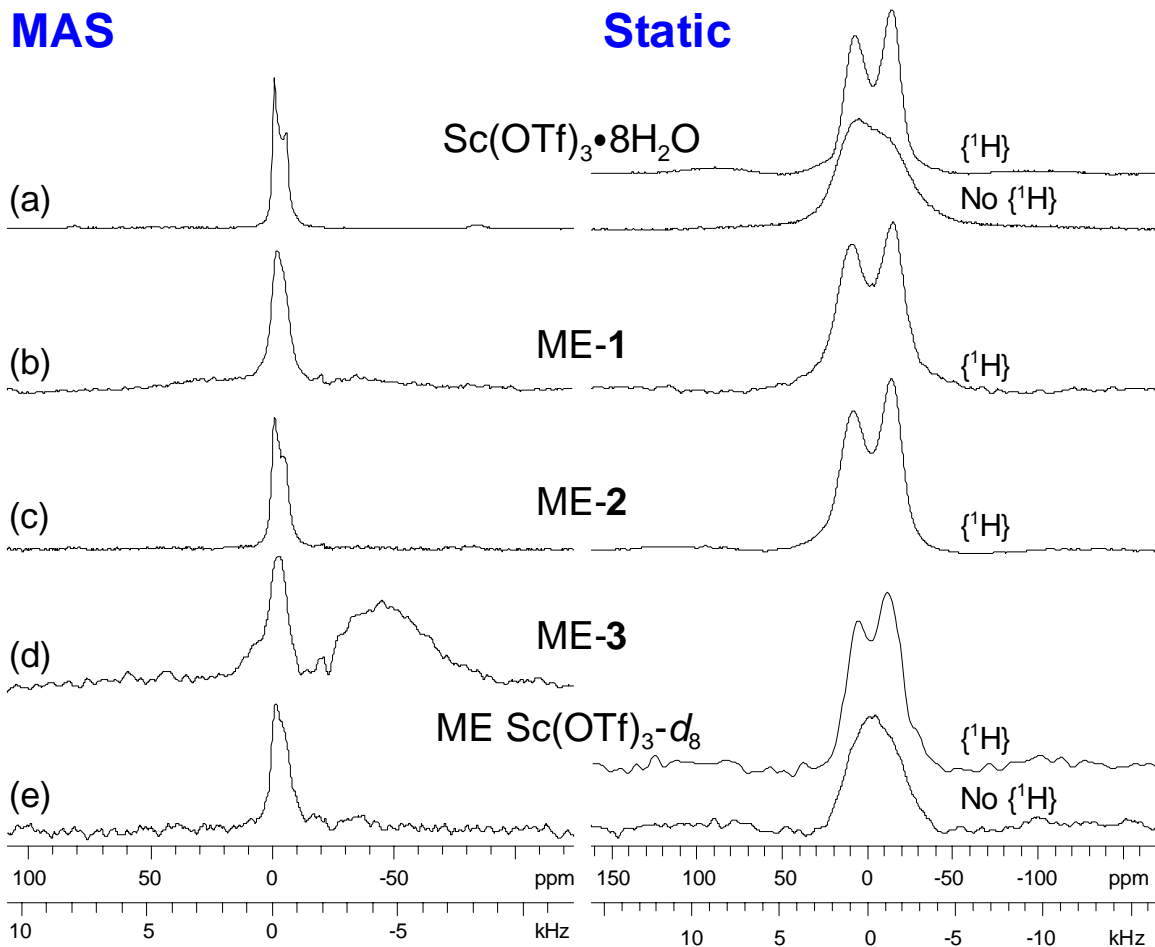


Figure 6.4. MAS (left) and static (right) ^{45}Sc SSNMR spectra of $\text{Sc}(\text{OTf})_3 \cdot 8\text{H}_2\text{O}$ and samples of ME $\text{Sc}(\text{OTf})_3$ prepared with various synthetic procedures. All spectra were acquired at 9.4 T. Spectra of (a) $\text{Sc}(\text{OTf})_3 \cdot 8\text{H}_2\text{O}$, (b) ME $\text{Sc}(\text{OTf})_3$ prepared by microencapsulating $\text{Sc}(\text{OTf})_3 \cdot 8\text{H}_2\text{O}$ in PS under an inert atmosphere (ME-1), (c) ME $\text{Sc}(\text{OTf})_3$ prepared under ambient atmosphere (ME-2), (d) ME $\text{Sc}(\text{OTf})_3$ prepared under inert conditions (ME-3), and (e) ME $\text{Sc}(\text{OTf})_3$ prepared with fully deuterated PS (ME $\text{Sc}(\text{OTf})_3\text{-}d_8$) under ambient conditions. All static spectra were acquired with a DFS $90^\circ\text{-}90^\circ$ echo sequence and ^1H decoupling (except where noted) and all MAS spectra were acquired with a DFS $90^\circ\text{-}180^\circ$ echo sequence. Static ^{45}Sc SSNMR spectra of $\text{Sc}(\text{OTf})_3 \cdot 8\text{H}_2\text{O}$ and ME $\text{Sc}(\text{OTf})_3\text{-}d_8$ acquired without ^1H decoupling are also shown.

Table 6.2. Estimates of Sc Loading Levels of ME Sc(OTf)₃ Samples

Sample	Number of Scans [NS]	Integrated Intensity [II] ^a	II/NS	m _{tot} (mg) ^b	m _{Sc} (mg) ^c	Sc Mass % ^d
Sc(OTf) ₃ •8H ₂ O	64	271	4.234	83	5.87 ^e	7.07 ^e
ME-1	3264	516	0.161	46	0.22	0.49
ME-2	752	265	0.352	54	0.49	0.90
ME-3	3200	719	0.229 ^f	42	0.32	0.27, 0.48 ^f
ME Sc(OTf) ₃ -d ₈	1376	99	0.072	46	0.10	0.22

^a The integral was taken over the central transition of a MAS DFS 90°-180° echo spectrum recorded at $\nu_{\text{rot}} = 8.0$ kHz for all samples. Identical pulse sequence parameters (e.g., recycle delays, pulse widths, receiver gain) were employed for all samples. All MAS experiments were acquired over the course of two days. ^b m_{tot} corresponds to the measured total mass of sample in the rotor. Uncertainties are ± 2 mg. ^c m_{Sc} corresponds to the mass of scandium in the rotor. This was found by the following formula: $m_{\text{Sc}} = 5.87 \times [(\text{II/NS}) \text{ of Sample}] / [(\text{II/NS}) \text{ of Sc(OTf)}_3 \cdot 8\text{H}_2\text{O}]$. ^d Sc Mass % = $100 \times [m_{\text{Sc}}] / [m_{\text{tot}}]$. We estimate uncertainty levels of ca. $\pm 10\%$ for the experimentally determined Sc Mass %. ^e m_{Sc} and the Sc mass % of the sample of crystalline Sc(OTf)₃•8H₂O were calculated from the molecular formula and the measured mass of Sc(OTf)₃•8H₂O in the rotor. ^f This includes integration of the impurity resonance. The first Sc mass % listed corresponds to the resonance attributed to Sc(OTf)₃•8H₂O, while the second Sc mass % listed corresponds to the resonance attributed to anhydrous Sc(OTf)₃. These were determined from the relative integrated intensities of the two resonances in the MAS spectrum.

While the lineshapes of the static and MAS spectra of the ME complexes are similar, the S/N ratios of the spectra are variable. For this reason, we have determined the Sc loading levels of the synthesized samples. The integrated intensity (II) and number of scans (NS) for the MAS ⁴⁵Sc SSNMR spectra of individual samples, acquired under the exact same conditions, are listed in Table 6.2. From these parameters, and knowledge of the total sample mass within the rotor, it is possible to estimate the Sc loading level (Sc mass %) by comparison to the II of MAS ⁴⁵Sc SSNMR spectra of crystalline Sc(OTf)₃•8H₂O. The Sc mass % of the ME Sc(OTf)₃ samples obtained under different synthetic conditions ranges from 0.22 % (ME Sc(OTf)₃-d₈) to 0.90 % (ambient ME Sc(OTf)₃). Unfortunately, we do not have any of the commercial sample of ME Sc(OTf)₃ left over from our previous study in order to determine the Sc mass % by ⁴⁵Sc SSNMR;

however, the manufacturer claims the sample is ca. 13% Sc(OTf)₃ by mass. This corresponds to a Sc mass % of ca. 1.2 %, which is similar to the loading levels determined herein for ME-2.

The ⁴⁵Sc SSNMR spectra indicate the presence of domains of Sc(OTf)₃•8H₂O within the polymer; therefore, it is expected that the Sc loading levels will be low if water of hydration is not supplied during the synthesis. This is clearly the case for ME-3, the sample of ME Sc(OTf)₃ prepared under inert conditions with anhydrous Sc(OTf)₃ (Figure 6.4d), which has a loading level much lower than the other samples (ca. 0.27 Sc mass %). In addition, there is a second broad powder pattern visible in the MAS ⁴⁵Sc SSNMR spectrum of ME-3, which corresponds closely to the spectral region of anhydrous Sc(OTf)₃. This is consistent with a lack of water which is required to form significant amounts of a hydrate phase. The small amount of Sc(OTf)₃•8H₂O visible in ⁴⁵Sc SSNMR spectrum of ME-3 likely results from residual water in the solvents, a minor amount of hydrated Sc(OTf)₃ mixed in with the anhydrous Sc(OTf)₃ and/or from water that entered the reaction flask during the synthetic procedure.

Kobayashi hypothesized that there are bonding interactions between the phenyl groups of PS and the vacant *d*-orbitals of Sc in ME Sc(OTf)₃.^{21, 29} In our previous ⁴⁵Sc SSNMR study of ME Sc(OTf)₃, we incorrectly attributed the origin of the ¹H-⁴⁵Sc dipolar couplings to spatially proximate ¹H nuclei of PS, and proposed that there were domains of crystalline Sc(OTf)₃ encapsulated in the polymer.⁴² In order to further confirm the presence of Sc(OTf)₃•8H₂O, and that the ¹H-⁴⁵Sc dipolar couplings arise from H₂O coordinated to the Sc³⁺ ions, we have prepared a sample of ME Sc(OTf)₃ with a fully deuterated sample of PS (ca. 98 % ²H, we refer to this sample as “ME Sc(OTf)₃-d₈”). The static ⁴⁵Sc SSNMR spectrum of ME Sc(OTf)₃-d₈ acquired without ¹H decoupling are

significantly broadened, indicating that there is still a substantial ^1H - ^{45}Sc dipolar coupling (Figure 6.4e). This confirms that the ^1H - ^{45}Sc dipolar coupling does not arise from proximate ^1H nuclei of PS, but rather, from coupling to the ^1H nuclei of coordinated water molecules. This new data and structural interpretation raise questions about the nature of the interaction between Sc^{3+} and PS in ME samples. It is unlikely that there will be any interactions between the π -systems of the phenyl groups of PS and Sc d -orbitals, as the eight-coordinate hydrated Sc ions are coordinatively saturated. In order to probe for such interactions, we have acquired MAS ^1H and ^1H - ^{45}Sc TRAPDOR SSNMR spectra.

MAS ^1H SSNMR Spectra of ME Sc(OTf) $_3$. In order to aid in properly assigning the resonances observed in the MAS ^1H SSNMR spectra of ME Sc(OTf) $_3$, spectra were obtained from pristine PS, and PS samples which were treated with the organic solvents that are utilized in the synthesis of ME Sc(OTf) $_3$. The solvent-treated PS samples were obtained by following the procedure for the synthesis of ME Sc(OTf) $_3$, without the addition of any Sc(OTf) $_3$ to the polymer-solvent mixtures. All samples were dried under vacuum at 50°C.

The MAS ^1H SSNMR spectrum of PS at a sample spinning speed (v_{rot}) of 13.5 kHz possesses two broad overlapping resonances (Figure 6.5a) attributable to the phenyl protons [$\delta_{\text{iso}}(^1\text{H}) = 6.9$ ppm, FWHH = 2192 Hz] and aliphatic protons [$\delta_{\text{iso}}(^1\text{H}) = 1.4$ ppm, FWHH = 2616 Hz]. It is not possible to fully resolve the aliphatic and aromatic proton resonances in this sample due to the strong ^1H - ^1H homonuclear dipolar couplings and the absence of long-range order. The MAS ^1H SSNMR spectrum of PS treated with cyclohexane (Figure 6.5b) contains an additional, comparatively sharp resonance [$\delta_{\text{iso}}(^1\text{H}) = 1.2$ ppm, FWHH = 582 Hz], which obscures the aliphatic proton resonance of PS. The

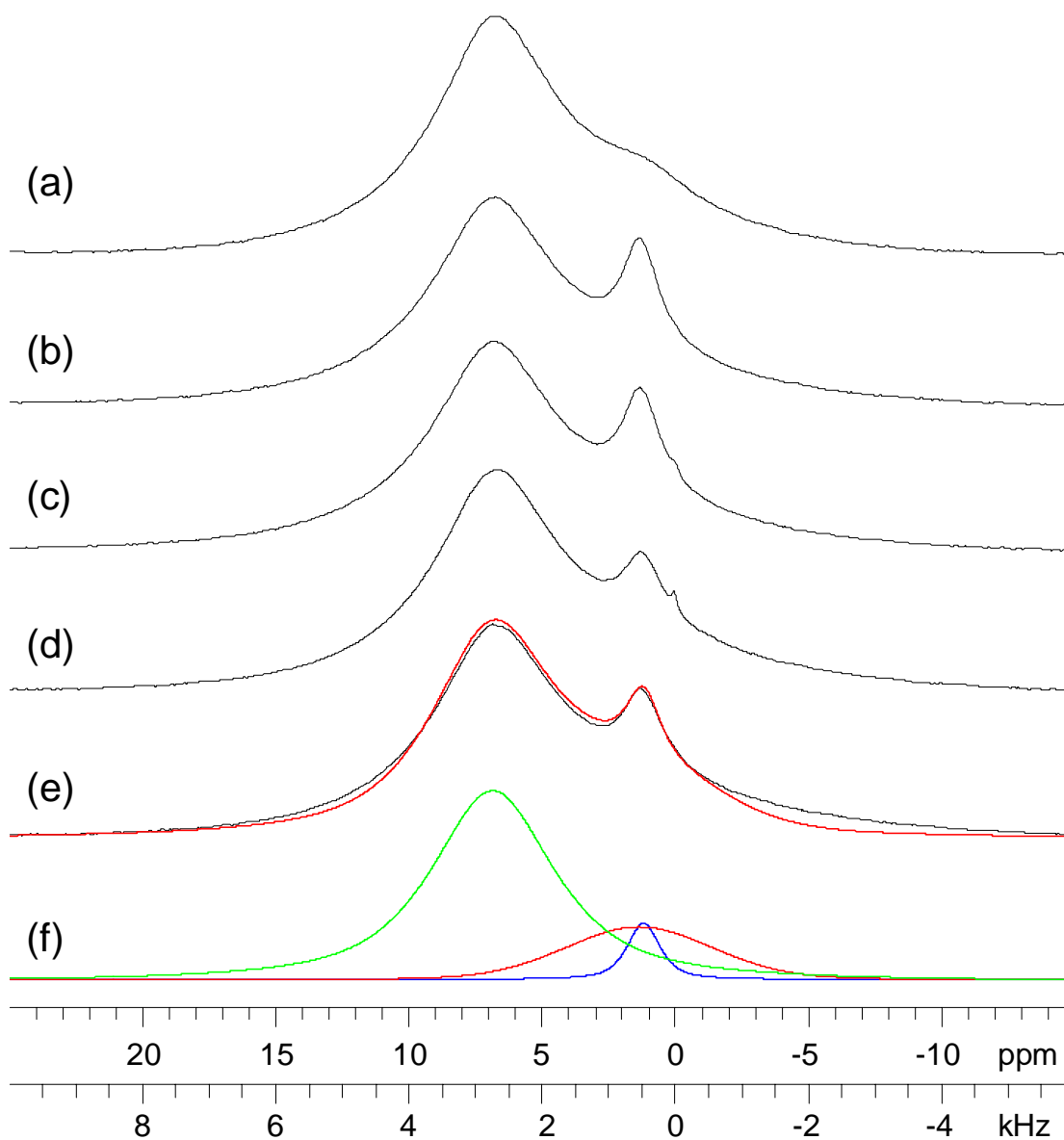


Figure 6.5. MAS ^1H SSNMR spectra of (a) pure PS (PS), (b) PS recovered from cyclohexane, (c) PS recovered from cyclohexane and hexanes, (d) PS recovered from cyclohexane, hexanes, and acetonitrile, and (e) ME-2. A line-fitting simulation (red trace) is overlaid on the experimental spectrum of ME-2 (black trace). (f) Deconvolution of the individual sites employed in the line-fitting simulation. All spectra were acquired with a Bloch decay pulse sequence (90° pulse-acquire), $\nu_{\text{rot}} = 13.5$ kHz, 32 scans and a recycle delay of 20 s which is required to obtain full recovery of longitudinal magnetization.

chemical shift of this resonance correlates well with that of cyclohexane in solution,⁵⁶ and is attributed to cyclohexane absorbed within the polymer. The MAS ^1H SSNMR spectra

of all subsequent solvent treated PS samples and ME Sc(OTf)₃ are similar to that of PS treated with cyclohexane only (compare Figure 6.5b to Figures 6.5c-e). There are no ¹H resonances clearly visible in the methyl region (ca. 0.9 ppm) of the MAS ¹H NMR spectra, suggesting that acetonitrile and hexanes are not substantially adsorbed within the polymer. ¹³C SSNMR spectra of the polymer samples and a ¹H-¹³C dipolar correlation spectrum⁵⁷ of ME-2 confirm this (Figures E3 and E4). The spectrum of PS treated with cyclohexane, hexanes and acetonitrile shows an additional sharp peak at $\delta_{\text{iso}}(^1\text{H}) = 0.1$ ppm (Figure 6.5d), which is attributed to the silicone grease used to seal the joints of the Schlenk flask, which occasionally contaminates some of the samples.⁵⁶

Table 6.3. Chemical Shifts and Integrated Intensities of Resonances Employed for Linefitting of MAS ¹H SSNMR Spectra of ME-2.

	Line 1	Line 2	Line 3
δ_{iso} (ppm)	1.20	1.36	6.86
FWHM (Hz)	582	2616	2192
Π	8	33	100

The MAS ¹H SSNMR spectrum of ME-2 (Figure 6.5e) is similar in appearance to that of the solvent treated PS samples. We have fit the MAS ¹H SSNMR spectra of ME-2 with a line-fitting routine (Figure 6.5). The relative integrated intensities are reported with respect to the aromatic peak which was set to 100 (Table 6.3). From this deconvolution, the ratio of PS ¹H nuclei to cyclohexane ¹H nuclei is ca. 94 : 6, this yields an approximate *molar* ratio of ca. 96 : 4 (PS monomer unit : cyclohexane). It is not necessary to account for signal from the ¹H nuclei of the Sc(OTf)₃•8H₂O domains, due to the breadth of these resonances and their low loading levels (Figure E5). We note that the deconvolutions do not account for intensity dispersed into the spinning sidebands, which may lead to overestimates of the amount of cyclohexane adsorbed in the polymer. In

summary, the MAS ^1H NMR spectra indicate that a substantial amount of cyclohexane is adsorbed within the polymer during the microencapsulation process.

^1H - ^{45}Sc TRAPDOR SSNMR Spectra. In order to determine if there is any interaction between PS/cyclohexane and the domains of $\text{Sc}(\text{OTf})_3 \cdot 8\text{H}_2\text{O}$ within ME $\text{Sc}(\text{OTf})_3$, we have performed ^1H - ^{45}Sc TRAPDOR SSNMR experiments. TRAPDOR is a double resonance pulse sequence which has been extensively used to deduce the spatial proximity of spin-1/2 and quadrupolar nuclei (e.g., ^1H and ^{27}Al).⁵⁸⁻⁶⁰ In the course of a TRAPDOR experiment, two Hahn-echo spectra of the spin-1/2 nucleus (^1H) are acquired.⁶⁰ The first is acquired in the usual manner (90° - τ_1 - 180° - τ_2 -acquire) and serves as the control experiment, while the second is acquired with irradiation of the quadrupolar nucleus (^{45}Sc) during the first dephasing period (τ_1). If the quadrupolar and spin-1/2 nuclei are dipolar coupled (spatially proximate), then a reduction in signal is observed in the second echo spectrum. The attenuation of the ^1H NMR signal will increase with larger dipolar couplings, smaller quadrupolar coupling constants, longer echo dephasing periods (τ_1), slower spinning speeds (ν_{rot}) and higher power irradiation of the quadrupolar nucleus.^{59, 60}

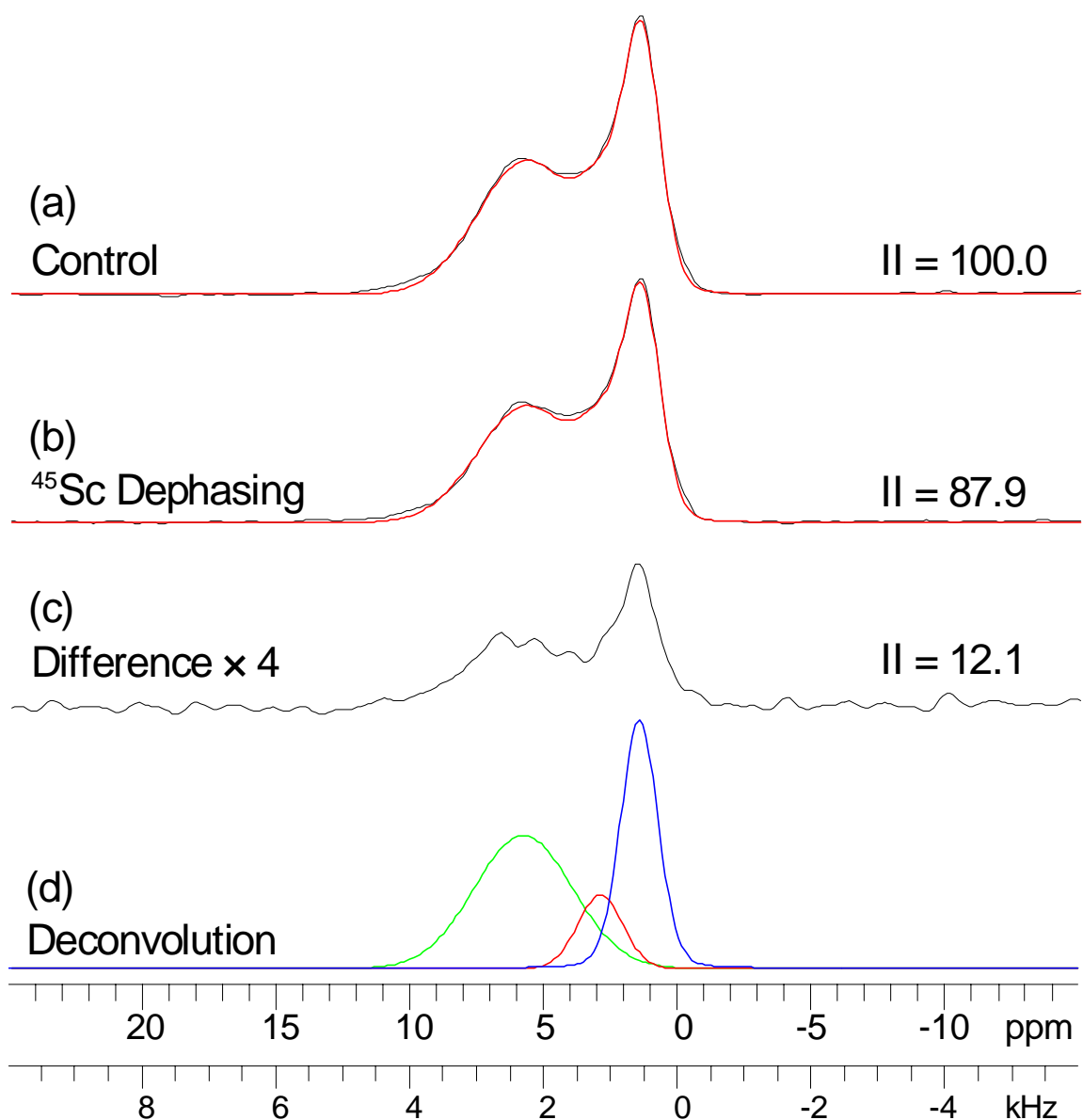


Figure 6.6. MAS ^1H - ^{45}Sc TRAPDOR SSNMR spectra of ME-2. (a) control experiment with no ^{45}Sc irradiation, (b) dephasing experiment with irradiation of ^{45}Sc during the τ_1 period and (c) the difference spectrum resulting from subtraction of the dephasing spectrum from the control spectrum (intensity increased by a factor of 4). Linefitting simulations (red trace) are overlaid on the experimental spectra (black trace). (d) A deconvolution of the three sites employed in the linefitting simulations. $\nu_{\text{rot}} = 12.5$ kHz and a recycle delay of 20 s were employed. A τ_1 value of 240 μs was used, corresponding to 3 rotor cycles, and a ^{45}Sc rf field (ν_1) of 108 kHz was applied during the τ_1 period of the dephasing experiment.

MAS ^1H - ^{45}Sc TRAPDOR SSNMR spectra of ME-2 are shown in Figure 6.6. Spectra were acquired with sample spinning speed of 12.5 kHz because this afforded a nice compromise between resolution of the ^1H spectrum and the amount of dephasing induced by ^{45}Sc irradiation. In addition, with a ν_1 field of ca. 105 kHz, the experiment is well in the adiabatic regime at this spinning speed (adiabaticity parameter, $\alpha \approx 2.4$), where the dephasing efficiencies are high.⁵⁹ The intensity of the broad patterns in the aromatic region of the ^1H - ^{45}Sc TRAPDOR spectra of ME-2 is significantly reduced in comparison to that observed in the Bloch decay spectra of ME-2 (Figure 6.5e). This is because ^1H nuclei which possess short transverse relaxation time constants [$T_2(^1\text{H})$], such as the PS ^1H nuclei, will possess low intensity in the TRAPDOR spectrum due to the relatively long τ_1 value employed (240 μs).

The II of the difference spectrum, obtained by subtracting the ^1H - ^{45}Sc TRAPDOR dephasing spectrum from the control spectrum, is equal to approximately 12% of the II of the control spectrum. This suggests that a substantial fraction of the PS and cyclohexane ^1H nuclei are dipolar coupled to ^{45}Sc nuclei, meaning that a substantial fraction of the cyclohexane and PS ^1H nuclei are spatially proximate to the $\text{Sc}(\text{OTf})_3 \cdot 8\text{H}_2\text{O}$ domains. The relatively low loading level of Sc within the sample (0.90 Sc mass %) and the amount of dephasing observed in the TRAPDOR experiments suggest that the $\text{Sc}(\text{OTf})_3 \cdot 8\text{H}_2\text{O}$ is uniformly dispersed throughout the polymer. At these low Sc loading levels, the $\text{Sc}(\text{OTf})_3 \cdot 8\text{H}_2\text{O}$ must be present as nm scale domains to create a substantial number of dipolar contacts between ^1H and ^{45}Sc nuclei, which lead to significant dephasing in ^1H - ^{45}Sc TRAPDOR experiments. These findings are entirely consistent with Kobayashi's SEM-EDX images of ME $\text{Sc}(\text{OTf})_3$, which show that Sc is

homogeneously dispersed over the polymer surface in sub- μm size domains.²² ^1H - ^{45}Sc TRAPDOR NMR spectra of ME Sc(OTf)₃-d₈ were also acquired since this sample possesses relatively narrow ^1H spectra due to isotopic dilution of the ^1H nuclei (Figure E6). These spectra show a signal decrease in II of *ca.* 9.7 % when ^{45}Sc irradiation is applied, consistent with the decreased Sc content of this sample. In the difference spectrum, it appears as if the degree of dephasing is unequal for the aromatic resonances; however, the spectra have low S/N because of the low ^1H content and lengthy pulse delays required to obtain complete longitudinal relaxation (20 s).

Table 6.4. Chemical Shifts and Integrated Intensities of Resonances Employed for Linefitting of MAS ^1H - ^{45}Sc TRAPDOR NMR Spectra.

	Line 1	Line 2	Line 3
δ_{iso} (ppm)	1.41	2.87	5.74
FWHH (Hz)	650	787	1722
$\text{II}_{\text{Control}}$	25.3	70.4	100.0
$\text{II}_{\text{Dephasing}}$	23.1	61.6	87.3
$\Delta\text{II}^{\text{a}}$	0.13	0.09	0.13

$$\Delta\text{II} = (\text{II}_{\text{Control}} - \text{II}_{\text{Dephasing}})/\text{II}_{\text{Control}}$$

Deconvolutions of the ^1H - ^{45}Sc TRAPDOR spectra of ME-2 were performed to see if the individual ^1H resonances experience differing degrees of dephasing. The ^1H spectra could be effectively fit with three individual resonances, for which the δ_{iso} , FWHH and II of the individual resonances are listed in Table 6.4. Due to T_2 relaxation, the δ_{iso} and II values obtained from deconvolution of the TRAPDOR spectra are significantly different from those obtained from the Bloch decay spectra. From examination of the II values for the control and dephasing experiments, it appears that the signal intensity of the ^1H resonances which correspond to cyclohexane and the PS phenyl groups undergo the greatest degree of dephasing (signal reduction of *ca.* 13%), while, the resonance which

corresponds to the aliphatic PS backbone undergoes a lesser degree of dephasing (signal reduction of *ca.* 9%). This would suggest that the cyclohexane molecules and the phenyl groups of PS make the closest contacts with the Sc(OTf)₃•8H₂O domains; however, given the poor resolution of these experiments and the error inherent to the line fitting routines, these results are not conclusive.

Additional ¹⁹F and ¹³C SSNMR Experiments. Several ²H, ¹³C and ¹⁹F SSNMR experiments were performed on ME Sc(OTf)₃; however, these experiments provided little new information on the molecular structure of the complex (Figures E7 and E8), but are consistent with our hypotheses regarding the molecular structure of ME Sc(OTf)₃. We present a brief discussion of these results in the appendix for the interested reader.

Powder X-ray Diffraction. The static and MAS ⁴⁵Sc SSNMR spectra of ME Sc(OTf)₃ possess sharp spectral features, which are indicative of ordered, crystalline domains of Sc(OTf)₃•8H₂O. PXRD experiments were conducted on ME-1 and ME-2 in order to confirm the presence of crystalline domains within the polymer (Figure 6.7). The PXRD pattern of the two different ME Sc(OTf)₃ samples possess sharp peaks overlaid on a broad underlying peak. The intensity and position of the peaks sharp peaks observed in the PXRD pattern of ME-1 and ME-2 closely match those of the crystalline hydrate phases, Sc(OTf)₃•8H₂O and Sc(OTf)₃•xH₂O, respectively. The shape and position of the broad underlying peak observed in the PXRD pattern of both ME Sc(OTf)₃ samples is similar to that observed in the PXRD pattern of solvent-treated PS (Figure 6.7f). The PXRD patterns of both ME Sc(OTf)₃ samples also indicates the absence of any anhydrous Sc(OTf)₃. In summary, the PXRD experiments are consistent with the incorporation of Sc(OTf)₃ as nanocrystalline domains of Sc(OTf)₃•8H₂O/ Sc(OTf)₃•xH₂O in ME Sc(OTf)₃,

the degree of which is highly dependent upon the exposure to atmospheric moisture, water, etc. (*vide infra*).

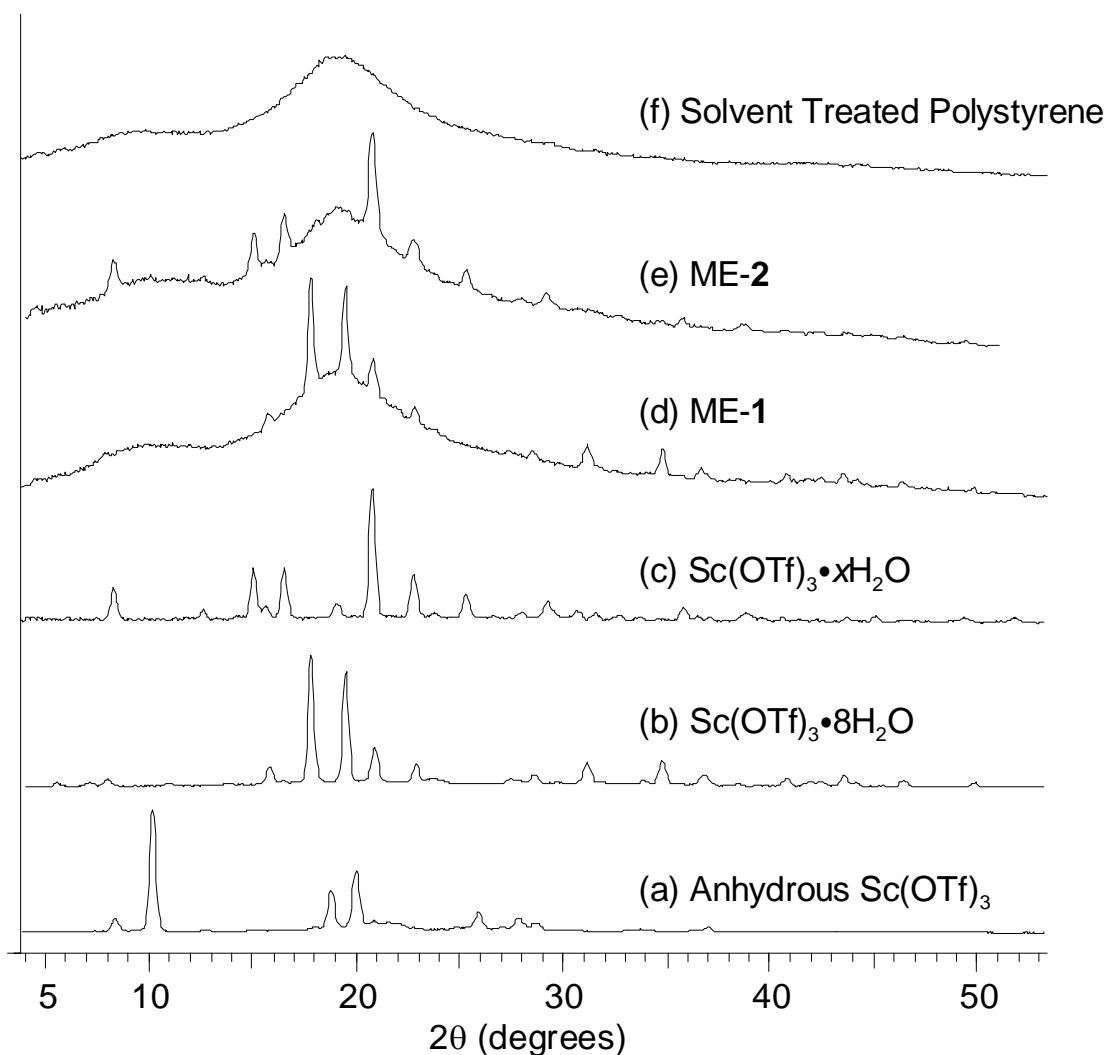


Figure 6.7. Experimental PXRD patterns obtained from (a) anhydrous $\text{Sc}(\text{OTf})_3$, (b) $\text{Sc}(\text{OTf})_3 \cdot 8\text{H}_2\text{O}$, (c) $\text{Sc}(\text{OTf})_3 \cdot x\text{H}_2\text{O}$, (d) ME-1, (e) ME-2, and (f) solvent-treated PS.

Exposure of ME $\text{Sc}(\text{OTf})_3$ to Ambient Moisture. When ME $\text{Sc}(\text{OTf})_3$ is employed as a catalyst, it is anticipated that it will be exposed to water contained in the organic solvents employed as the reaction media, as well as atmospheric moisture. Hydrated ME $\text{Sc}(\text{OTf})_3$ may be more representative of the structure of the working catalyst. While all of the samples of ME $\text{Sc}(\text{OTf})_3$ were handled under an inert atmosphere, it is worthwhile

to examine the influence of moisture adsorption on the catalyst structure. A sample of ME-2 packed into a rotor was exposed to ambient atmosphere by removing the air-tight cap at the top side of the pencil-style rotor. The sample was then left on the bench top for ca. 20 hours, and the sample was then capped and SSNMR spectra were acquired.

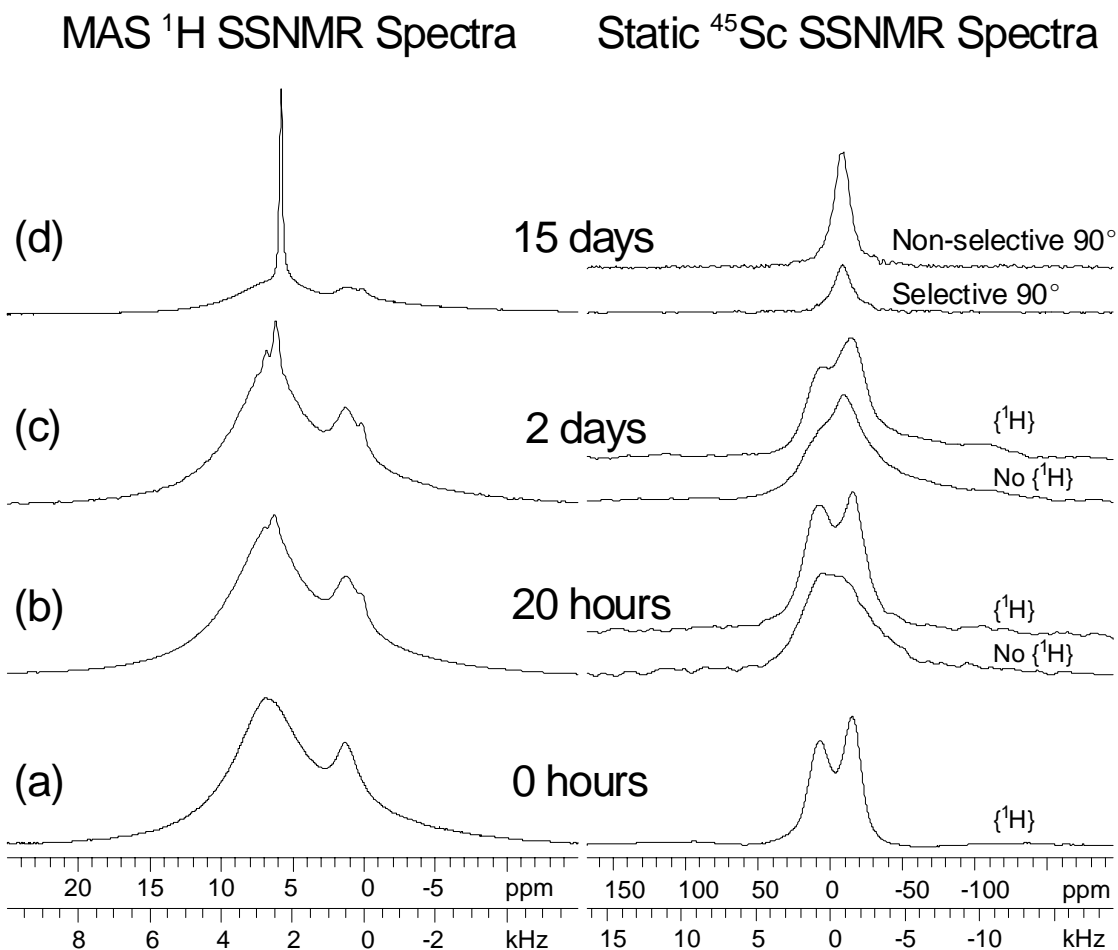


Figure 6.8. MAS ¹H SSNMR spectra (left) and static ⁴⁵Sc SSNMR 90°-180° echo spectra (right) of a sample of ambient ME-2 which has been exposed to air. The sample was exposed to air for total times of (a) 0 hours, (b) 20 hours, (c) 2 days and (d) 15 days. For exposure times of 20 hours and 2 days the static ⁴⁵Sc SSNMR spectra are shown with and without ¹H decoupling. For the exposure time of 15 days, the static ⁴⁵Sc SSNMR spectra were acquired with selective and non-selective 90° and 180° ⁴⁵Sc pulses (and no ¹H decoupling).

^1H and ^{45}Sc SSNMR spectra of this air-exposed sample of ME-2 are shown in Figure 6.8. After 20 hours of air exposure, an additional relatively sharp resonance is visible in the aromatic region of the MAS ^1H SSNMR spectrum ($\delta_{\text{iso}} = 6.3$ ppm), indicating that ME-2 has absorbed water from the atmosphere. The observed δ_{iso} value indicates that the water is associated with the $\text{Sc}(\text{OTf})_3 \cdot 8\text{H}_2\text{O}$ domains, and the narrow width of the resonance intimates that the water possesses significant rotational/translational freedom. The ^{45}Sc SSNMR spectra are similar to those of ME-2 handled under an inert atmosphere (compare Figure 6.8a with 6.8b). ^1H - ^{45}Sc TRAPDOR SSNMR spectra indicate that there is still significant dephasing in the ^{45}Sc irradiation spectrum (Figure E9), suggesting that the $\text{Sc}(\text{OTf})_3 \cdot 8\text{H}_2\text{O}$ domains are still intact and dispersed throughout the polymer.

After two days of total air exposure time the ^1H resonance corresponding to water is further increased in intensity. The static ^{45}Sc SSNMR spectra of ME-2 begin to show differences from those of the pristine ME-2. The static powder patterns are similar, which indicates that the eight-coordinate Sc environments are retained; however, the spectrum of ME-2-acquired without decoupling displays a sharp central feature, which may be indicative of self-decoupling of the ^1H nuclei. The self-decoupling may occur due to rapid exchange of water molecules between the first and second scandium coordination spheres.

Finally, after fifteen days of total exposure time, the MAS ^1H SSNMR spectra indicate that substantially more water has been absorbed. The water resonance is very narrow and intense, and observed at $\delta_{\text{iso}} = 5.8$ ppm, which is closer to that of liquid water (ca. 4.8 ppm). The static ^{45}Sc SSNMR spectra show a single relatively narrow resonance

(FWHH of ca. 1 kHz) with $\delta_{\text{iso}} = -6.3$ ppm. The static ^{45}Sc SSNMR spectra were acquired with central transition selective and non-selective 90° pulses, and it is clear that the non-selective 90° pulses give maximum signal. This indicates that the Sc^{3+} ions have entered a solution-like phase where the quadrupolar interaction is averaged to zero. Further, ^1H - ^{45}Sc TRAPDOR SSNMR spectra show essentially no dephasing when ^{45}Sc irradiation is applied, because the mobility of the $\text{Sc}(\text{III})$ ions efficiently averages ^1H - ^{45}Sc dipolar couplings (Figure E9).

PXRD experiments were also performed on a sample of hydrated ME $\text{Sc}(\text{OTf})_3$. A sample of ME-2 was packed into a flame sealed glass capillary under an inert atmosphere. The capillary was then mounted in the diffractometer, and the top of the capillary was broken open in order to expose the sample to atmospheric moisture. PXRD patterns were acquired periodically (Figure 6.9). Initially, there are crystalline domains of $\text{Sc}(\text{OTf})_3 \cdot x\text{H}_2\text{O}$ within the polymer as indicated by the relatively intense diffraction patterns. After ca. 24 minutes of air exposure, conversion to crystalline domains of $\text{Sc}(\text{OTf})_3 \cdot 8\text{H}_2\text{O}$ occurs. As further moisture is absorbed, the intensities of the diffraction peaks decrease until the pattern matches that of solvent-treated PS (at ca. 13.5 hours), which indicates that the crystalline domains have been converted into amorphous domains. We note that the timings of the structural differences observed by PXRD and SSNMR will be different, since the sample was tightly packed into the rotor for SSNMR experiments, while in the PXRD capillary, the flakes of ME-2 are loosely packed, permitting easy diffusion of air through the PXRD sample and resulting in faster absorption of moisture.

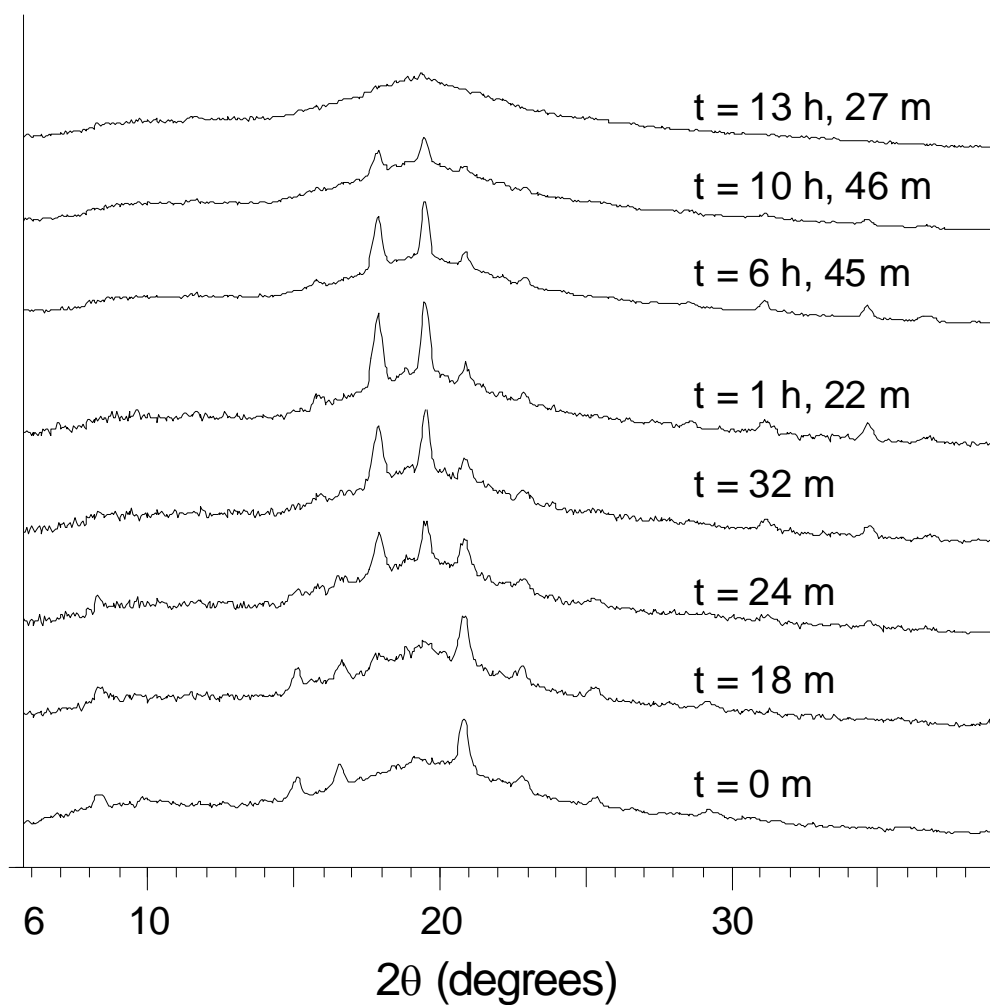


Figure 6.9. PXRD patterns acquired from a sample of ambient $\text{ME Sc}(\text{OTf})_3$ which was exposed to air. The total exposure time is listed to the right of each PXRD pattern.

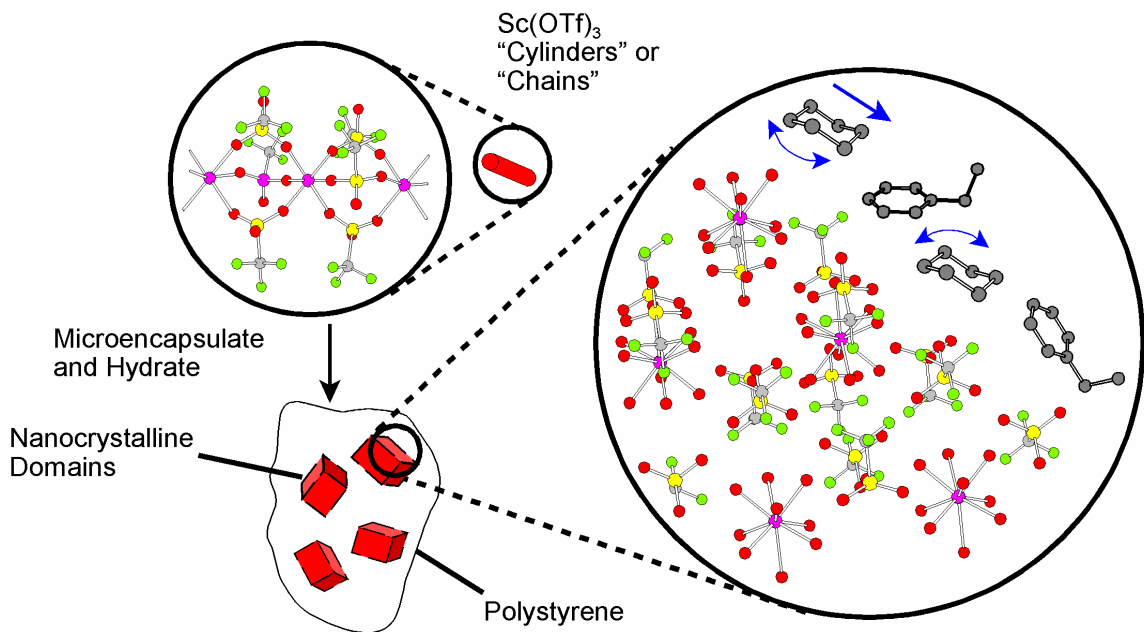


Figure 6.10. Proposed structural model of ME $\text{Sc}(\text{OTf})_3$. This model is highly schematized and qualitative. $\text{Sc}(\text{OTf})_3$ is hydrated when it undergoes microencapsulation in PS. This results in the formation of nanocrystalline domains of $\text{Sc}(\text{OTf})_3 \cdot 8\text{H}_2\text{O}$ in the polymer. The PS groups and cyclohexane molecules are spatially proximate to the surface of the nanocrystalline $\text{Sc}(\text{OTf})_3 \cdot 8\text{H}_2\text{O}$ domains. The cyclohexane molecules undergo translational/rotational motions.

6.4 Conclusions

^{45}Sc SSNMR spectra of the pure crystalline forms of $\text{Sc}(\text{OTf})_3$ and $\text{Sc}(\text{OTf})_3 \cdot 8\text{H}_2\text{O}$ have been acquired, and a new hydrated phase of $\text{Sc}(\text{OTf})_3$, $\text{Sc}(\text{OTf})_3 \cdot x\text{H}_2\text{O}$, has been identified. ME $\text{Sc}(\text{OTf})_3$ has been investigated by multinuclear SSNMR and PXRD experiments, and structural model of the ME $\text{Sc}(\text{OTf})_3$ system is now proposed (Figure 6.10). ^{45}Sc SSNMR spectra indicate that $\text{Sc}(\text{OTf})_3$ is incorporated into PS as domains of $\text{Sc}(\text{OTf})_3 \cdot 8\text{H}_2\text{O}$ and/or $\text{Sc}(\text{OTf})_3 \cdot x\text{H}_2\text{O}$, the relative amounts of which depend upon the level of hydration. There is no evidence of a direct interaction between the phenyl groups of PS and the scandium centres; rather, it is most likely that $\text{Sc}(\text{OTf})_3 \cdot 8\text{H}_2\text{O}$ is stabilized in the PS matrix by physisorption (i.e., physical

envelopment). It is possible, though not confirmed directly through our work, that hydrogen bonding interactions between water molecules at the surface of the $\text{Sc}(\text{OTf})_3 \cdot 8\text{H}_2\text{O} / \text{Sc}(\text{OTf})_3 \cdot x\text{H}_2\text{O}$ domains and the phenyl groups are key to stabilizing the structure of ME $\text{Sc}(\text{OTf})_3$, since contact angle measurements on oriented PS films and AFM studies of PS surfaces indicate that phenyl group surfaces are hydrophilic.^{61,62} ^1H and ^{13}C SSNMR spectra show that a substantial amount of cyclohexane is incorporated into ME $\text{Sc}(\text{OTf})_3$, but other solvents used in preparation of the ME samples are not present in any significant amounts. ^1H - ^{45}Sc TRAPDOR experiments indicate that scandium is dispersed throughout the polymer, consistent with SEM-EDX images previously acquired by Kobayashi. PXRD experiments reveal that the diffraction patterns of ME $\text{Sc}(\text{OTf})_3$ are similar to those of the crystalline complexes, $\text{Sc}(\text{OTf})_3 \cdot 8\text{H}_2\text{O}$ and $\text{Sc}(\text{OTf})_3 \cdot x\text{H}_2\text{O}$, and in combination with the reduced ^1H signal intensities in the TRAPDOR experiments, suggest that there are nanocrystalline domains present. Hence, the structure of this system is best described as a composite material, where nanocrystalline domains of inorganic material are dispersed throughout the polymer.⁶³⁻⁶⁸

The newly proposed structural model for ME $\text{Sc}(\text{OTf})_3$ is clearly different from previous models, and may provide insight into the structure and chemistry of the numerous heterogeneous scandium catalysts which have been prepared utilizing a number of different schemes.^{19, 69-71} The multinuclear SSNMR and PXRD experiments described herein are clearly applicable for the characterization of such systems, and should aid in the future design of new scandium based catalysts, as well a variety of ME catalysts involving different types of metals.⁷²⁻⁷⁸

6.5 Bibliography

- (1) Anastas, P. T.; Heine, L. G.; Williamson, T. C., *Green Chemical Synthesis and Processes*. American Chemical Society: Washington, DC, 2000.
- (2) Anastas, P. T.; Warner, J. C., *Green Chemistry: Theory and Practice*. Oxford University Press: New York, 1998; p 30.
- (3) Anastas, P. T.; Kirchoff, M. M., *Accounts Chem. Res.* **2002**, 35, (9), 686-694.
- (4) Breslow, R., Water as a solvent for chemical reactions. In *Green Chemistry: Frontiers in Benign Chemical Syntheses and Processes*, Anastas, P. T.; Williamson, T. C., Eds. Oxford University Press: New York, 1998.
- (5) Li, C. J., Water as a Solvent for Organic and Material Synthesis. In *Green Chemical Syntheses and Processes*, Anastas P.T., H. L. G., Williamson T.C., Ed. American Chemical Society: Washington D.C., 2000.
- (6) Li, C. J., *Chem. Rev.* **2005**, 105, (8), 3095-3165.
- (7) Hachiya, I.; Kobayashi, S., *J. Org. Chem.* **1993**, 58, (25), 6958-6960.
- (8) Kawada, A.; Mitamura, S.; Kobayashi, S., *Synlett* **1994**, (7), 545-546.
- (9) Kobayashi, S., *Synlett* **1994**, (9), 689-701.
- (10) Kobayashi, S., *Eur. J. Org. Chem.* **1999**, (1), 15-27.
- (11) Kobayashi, S.; Araki, M.; Ishitani, H.; Nagayama, S.; Hachiya, I., *Synlett* **1995**, (3), 233-234.
- (12) Kobayashi, S.; Araki, M.; Yasuda, M., *Tetrahedron Lett.* **1995**, 36, (32), 5773-5776.
- (13) Kobayashi, S.; Hachiya, I.; Ishitani, H.; Araki, M., *Synlett* **1993**, (7), 472-474.
- (14) Kobayashi, S.; Ishitani, H.; Nagayama, S., *Synthesis* **1995**, (9), 1195-&.
- (15) Kobayashi, S.; Ishitani, H.; Nagayama, S., *Chem. Lett.* **1995**, (6), 423-424.
- (16) Kobayashi, S.; Ishitani, H.; Ueno, M., *Synlett* **1997**, (1), 115.
- (17) Kobayashi, S.; Nagayama, S., *J. Am. Chem. Soc.* **1997**, 119, (42), 10049-10053.
- (18) Kobayashi, S.; Sugiura, M.; Kitagawa, H.; Lam, W. W. L., *Chem. Rev.* **2002**, 102, (6), 2227-2302.
- (19) Luo, S. Z.; Zhu, L. H.; Talukdar, A.; Zhang, G. H.; Mi, X. L.; Cheng, J. P.; Wang, P. G., *Mini-Rev. Org. Chem.* **2005**, 2, (2), 177-202.
- (20) Fringuelli, F.; Piermatti, O.; Pizzo, F.; Vaccaro, L., *Eur. J. Org. Chem.* **2001**, (3), 439-455.

- (21) Akiyama, R.; Kobayashi, S., *Chem. Rev.* **2009**, 109, (2), 594-642.
- (22) Kobayashi, S.; Nagayama, S., *J. Amer. Chem. Soc.* **1998**, 120, 2985.
- (23) Schager, F.; Bonwrat, W., *Appl. Catal. A: Gen.* **2002**, 202, 117.
- (24) Suzuki, T.; Watahiki, T.; Oriyama, T., *Tetrahedron Lett.* **2000**, 41, (46), 8903-8906.
- (25) Kobayashi, S.; Komoto, I.; Matsuo, J., *Adv. Synth. Catal.* **2001**, 343, 71.
- (26) Heaney, H., In *Comprehensive Organic Synthesis*, Trost, B. M., Ed. Pergamon Press: Oxford, 1991; Vol. 2, p 733.
- (27) Olah, G. A., *Friedel-Crafts Chemistry*. Wiley-Interscience: New York, 1973.
- (28) Olah, G. A.; Krishnamurti, R.; Prakash, G. K. S., In *Comprehensive Organic Synthesis*, Trost, B. M., Ed. Pergamon Press: Oxford, U.K., 1991; Vol. 3, p 293.
- (29) Kobayashi, S.; Akiyama, R., *Chem. Commun.* **2003**, 449-460.
- (30) Brown, S. P.; Spiess, H. W., *Chem. Rev.* **2001**, 101, (12), 4125-4155.
- (31) Spiess, H. W., *Chem. Rev.* **1991**, 91, (7), 1321-1338.
- (32) Schmidt-Rohr, K.; Spiess, H. W., *Multidimensional Solid-State NMR and Polymers*. Academic Press: London, 1994.
- (33) Balamurugan, S.; Rodewald, U. C.; Harmening, T.; van Wullen, L.; Mohr, D.; Eckert, H.; Pottgen, R., *Z.Naturforsch.(B)* **2010**, 65, (1), 13-17.
- (34) Kim, N.; Stebbins, J. F., *Chem. Mat.* **2009**, 21, (2), 309-315.
- (35) Jayasundera, A. C. A.; Finch, A. A.; Wormald, P.; Lightfoot, P., *Chem. Mat.* **2008**, 20, (21), 6810-6815.
- (36) Huang, H.; Hsieh, C. H.; Kim, N.; Stebbins, J.; Pninz, F., *Solid State Ion.* **2008**, 179, (27-32), 1442-1445.
- (37) Khabibulin, D.; Romanenko, K.; Zuev, M.; Lapina, O., *Magn. Reson. Chem.* **2007**, 45, (11), 962-970.
- (38) Kim, N.; Stebbins, J. F.; Quartieri, S.; Oberti, R., *Am. Miner.* **2007**, 92, (11-12), 1875-1880.
- (39) Lo, A. Y. H.; Sudarsan, V.; Sivakumar, S.; van Veggel, F.; Schurko, R. W., *J. Am. Chem. Soc.* **2007**, 129, (15), 4687-4700.
- (40) Sebastian, C. P.; Zhang, L.; Fehse, C.; Hoffmann, R. D.; Eckert, H.; Pottgen, R., *Inorg. Chem.* **2007**, 46, (3), 771-779.

- (41) Alba, M. D.; Chain, P.; Florian, P.; Massiot, D., *J. Phys. Chem. C* **2010**, 114, (28), 12125-12132.
- (42) Rossini, A. J.; Schurko, R. W., *J. Am. Chem. Soc.* **2006**, 128, (32), 10391-10402.
- (43) Fuchs, R.; Strahle, J., *Z.Naturforsch.(B)* **1984**, 39, (12), 1662-1663.
- (44) Bodart, P. R.; Amoureux, J. P.; Dumazy, Y.; Lefort, R., **2000**, 98, (19), 1545-1551.
- (45) Iuga, D.; Schafer, H.; Verhagen, R.; Kentgens, A. P. M., *J. Magn. Reson.* **2000**, 147, (2), 192-209.
- (46) Kentgens, A. P. M.; Verhagen, R., *Chem. Phys. Lett.* **1999**, 300, (3-4), 435-443.
- (47) Kraus, W.; Nolze, G. *PowderCell for Windows*, Federal Institute for Materials Research and Testing: Berlin, Germany, 2000.
- (48) Arfken, G., *Mathematical Methods for Physicists*. 3rd ed.; Academic Press: New York, 1985.
- (49) Rose, M. E., *Elementary Theory of Angular Momentum*. Wiley: New York, 1957.
- (50) Abbasi, A.; Lindqvist-Reis, P.; Eriksson, L.; Sandstrom, D.; Lidin, S.; Persson, I.; Sandstrom, M., *Chem. Eur. J.* **2005**, 11, (14), 4065-4077.
- (51) Lindqvist-Reis, P.; Persson, I.; Sandstrom, M., *Dalton Trans.* **2006**, (32), 3868-3878.
- (52) Rudolph, W. W.; Pye, C. C., *J. Solut. Chem.* **2000**, 29, (10), 955-986.
- (53) Rudolph, W. W.; Pye, C. C., *J. Phys. Chem. A* **2000**, 104, (8), 1627-1639.
- (54) Rotzinger, F. P., *J. Am. Chem. Soc.* **1997**, 119, (22), 5230-5238.
- (55) Akesson, R.; Pettersson, L. G. M.; Sandstrom, M.; Wahlgren, U., *J. Am. Chem. Soc.* **1994**, 116, (19), 8691-8704.
- (56) Gottlieb, H. E.; Kotlyar, V.; Nudelman, A., *J. Org. Chem.* **1997**, 62, (21), 7513-7514.
- (57) vanRossum, B. J.; Forster, H.; deGroot, H. J. M., *J. Magn. Reson.* **1997**, 124, (2), 516-519.
- (58) Amoureux, J. P.; Trebosc, J.; Delevoye, L.; Lafon, O.; Hu, B.; Wang, Q., *Solid State Nucl. Magn. Reson.* **2009**, 35, (1), 12-18.
- (59) Grey, C.; Vega, A., *J. Am. Chem. Soc.* **1995**, 117, 8232-8242
- (60) van Eck, E. R. H.; Janssen, R.; Maas, W. E. J. R.; Veeman, W. S., *Chem. Phys. Lett.* **1990**, 174, 428.
- (61) Tretinnikov, O. N., *Langmuir* **2000**, 16, (6), 2751-2755.

- (62) Bistac, S.; Schmitt, M.; Ghorbal, A.; Gnecco, E.; Meyer, E., *Polymer* **2008**, 49, (17), 3780-3784.
- (63) Li, Z. H.; Sai, H.; Warren, S. C.; Kamperman, M.; Arora, H.; Gruner, S. M.; Wiesner, U., *Chem. Mat.* **2009**, 21, (23), 5578-5584.
- (64) Fahmi, A.; Pietsch, T.; Mendoza, C.; Cheval, N., *Mater. Today* **2009**, 12, (5), 44-50.
- (65) Munoz-Espi, R.; Jeschke, G.; Lieberwirth, I.; Gomez, C. M.; Wegner, G., *J. Phys. Chem. B* **2007**, 111, (4), 697-707.
- (66) Verploegen, E.; Dworken, B. T.; Faught, M.; Kamperman, M.; Zhang, Y. M.; Wiesner, U., *Macromol. Rapid Commun.* **2007**, 28, (5), 572-578.
- (67) Kim, H. C.; Park, S. M.; Hinsberg, W. D., *Chem. Rev.* **2010**, 110, (1), 146-177.
- (68) Bang, J.; Jeong, U.; Ryu, D. Y.; Russell, T. P.; Hawker, C. J., *Adv. Mater.* **2009**, 21, (47), 4769-4792.
- (69) Choudary, B. M.; Roy, M.; Roy, S.; Kantam, M. L.; Sreedhar, B.; Kumar, K. V., *Adv. Synth. Catal.* **2006**, 348, (12-13), 1734-1742.
- (70) Takeuchi, M.; Akiyama, R.; Kobayashi, S., *J. Am. Chem. Soc.* **2005**, 127, (38), 13096-13097.
- (71) Mantri, K.; Komura, K.; Kubota, Y.; Sugi, Y., *J. Mol. Catal. A-Chem.* **2005**, 236, (1-2), 168-175.
- (72) Gibson, S. E.; Swamy, V. M., *Adv. Synth. Catal.* **2002**, 344, (6-7), 619-621.
- (73) Nagayama, S.; Kobayashi, S., *Angew. Chem.-Int. Edit.* **2000**, 39, (3), 567-+.
- (74) Saladino, R.; Neri, V.; Pelliccia, A. R.; Caminiti, R.; Sadun, C., *J. Org. Chem.* **2002**, 67, (4), 1323-1332.
- (75) Annis, D. A.; Jacobsen, E. N., *J. Am. Chem. Soc.* **1999**, 121, (17), 4147-4154.
- (76) Kobayashi, S.; Endo, M.; Nagayama, S., *J. Am. Chem. Soc.* **1999**, 121, (48), 11229-11230.
- (77) Lattanzi, A.; Leadbeater, N. E., *Org. Lett.* **2002**, 4, (9), 1519-1521.
- (78) Srirattnai, K.; Damronglerd, S.; Omi, S.; Roengsumran, S.; Petsom, A.; Ma, G. H., *Tetrahedron Lett.* **2002**, 43, (25), 4555-4557.

Chapter 7: Probing Lead(II) Bonding Environments in 4-Substituted Pyridine Adducts of (2,6-Me₂C₆H₃S)₂Pb by ²⁰⁷Pb Solid-state NMR

7.1 Introduction

Lead(II) ions are found in a range of materials with interesting optical and electronic properties.¹⁻⁶ For example, lead(II) sulfide (PbS) complexes have many interesting applications in optoelectronic devices as narrow band-gap semi-conducting materials.⁷⁻¹² For this reason, the production of PbS nanocrystals has been extensively studied, and achieved via a variety of synthetic routes.¹³⁻¹⁹ Recently it has been demonstrated that lead(II) thiolates can serve as precursors for the production of thiolate-capped clusters and nanocrystals.²⁰⁻²³ Due to the well known toxicity of lead(II) complexes, there is also much interest in the synthesis of simple thiolate compounds which can be used to model the binding of lead(II) by the cysteine residues of biomolecules.²⁴⁻²⁷ Lead(II) ions may also serve as versatile building blocks for supramolecular frameworks due to the varied coordination geometries observed at the lead(II) centers, with known coordination numbers ranging from three to twelve.^{1, 2, 5, 28-30} Additionally, lead(II) complexes frequently possess stereochemically active electron lone pairs.³⁰ By altering the ligands bound to the lead(II) center it is possible to alter the activity of the electron lone pair, affording the possibility of precisely controlling the symmetry and bonding environment of the lead(II) site.^{1, 2, 5, 6, 28, 29} Therefore, lead(II) centers can act as linkers capable of assuming a number of different geometries and binding modes, which in turn, allows for a variety of structural motifs to be constructed. In this regard, lead(II) thiolates constitute a class of complexes which are known to form

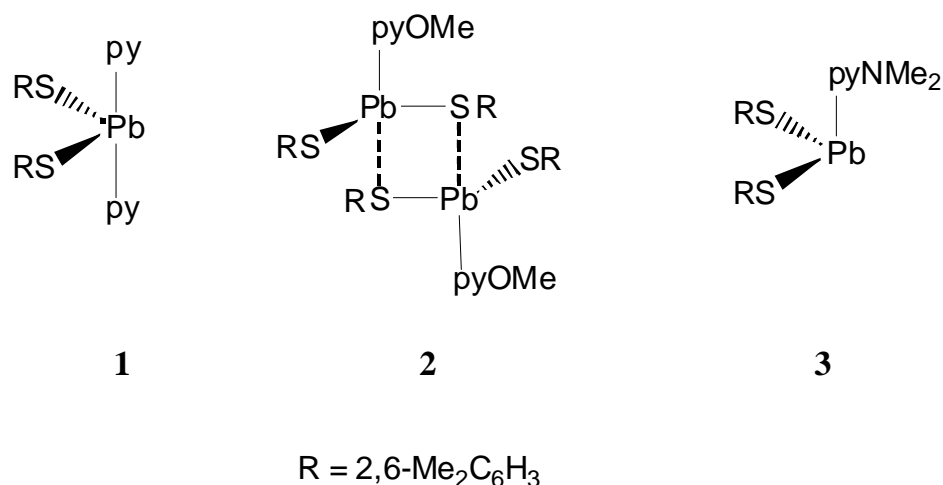
polymeric structures in the solid-state as a result of intermolecular Pb-S contacts.^{20, 21, 31-33}

Many of these polymeric lead(II) complexes are insoluble, and even if they can be dissolved, their polymeric structures do not persist in solution. Therefore, the characterization of lead(II) thiolate complexes in the solid state is of great importance.

While refined single-crystal X-ray diffraction is used to accurately determine molecular structure, solid-state ²⁰⁷Pb NMR spectra can provide information on the electronic environment of the metal atom and the nature of bonding with surrounding ligands. ²⁰⁷Pb ($I = 1/2$) is the only NMR-active isotope of lead and has a receptivity of 11.8 relative to ¹³C.³⁴ The lead chemical shift range is very large, with a difference of approximately 17000 ppm between lead metal and plumbocene.³⁵⁻³⁸ This large chemical shift range is a direct result of the extremely polarizable lead valence orbitals, which give rise to the large lead chemical shielding anisotropies (CSAs) observed in most solid-state ²⁰⁷Pb NMR spectra (with the exception of complexes of high spherical or Platonic symmetry).^{35, 39} Lead chemical shifts are extremely sensitive probes of atomic/molecular environment and subtle molecular changes induced by chemical (e.g., reactions, solvent coordination) and physical (e.g., temperature, stress) changes.^{35, 37, 40, 41}

Once relationships have been established between well-characterized molecular structures and lead chemical shift (CS) tensors, then solid-state NMR can be applied for structural determination of complexes for which single crystal data are not readily available. Given the general insolubility of homoleptic lead(II) thiolate complexes,³¹⁻³³ the lability of their coordination complexes,²⁹ and the well-known sensitivity of lead CS tensors to subtle changes in molecular structure,^{35, 37, 42} solid-state ²⁰⁷Pb NMR should serve as a formidable probe of molecular structure in these systems. To this end, solid-

state ^{207}Pb NMR experiments, in tandem with density functional theory (DFT) calculations of CS tensors, are used to measure and theoretically model lead CS tensors for several lead(II) thiolate pyridine adducts (Scheme 1). All of these complexes possess voids in the lead coordination spheres, indicative of the presence of stereochemically active lone pairs.²⁸ Relationships between the observed ^{207}Pb CS tensor and structure, symmetry and bonding are constructed.



Scheme 7.1. Schematic drawings of lead thiolate structures, including (2,6- $\text{Me}_2\text{C}_6\text{H}_3\text{S}$) $_2\text{Pb}(\text{py})_2$ (**1**), [(2,6- $\text{Me}_2\text{C}_6\text{H}_3\text{S}$) $_2\text{Pb}(\text{pyOMe})$] $_2$ (**2**) and (2,6- $\text{Me}_2\text{C}_6\text{H}_3\text{S}$) $_2\text{Pb}(\text{pyNMe}_2)$ (**3**) (py = pyridine; pyOMe = 4-methoxypyridine; pyNMe $_2$ = 4-dimethylaminopyridine). Additional views of the structures are shown in Figure 7.3.

7.2 Experimental

General Details. The characterization, synthesis and single crystal X-ray diffraction analysis of all complexes is described in the original publication.²⁸

Solid-state NMR Spectroscopy. Solid-state ^{207}Pb NMR spectra were acquired on a Varian Infinity Plus spectrometer with an Oxford 9.4 T wide-bore magnet [$\nu_0(^1\text{H}) = 399.73$ MHz, $\nu_0(^{207}\text{Pb}) = 83.63$ MHz, $\nu_0(^{13}\text{C}) = 100.51$]. Lead chemical shifts were referenced to Me_4Pb ($\delta_{\text{iso}} = 0.0$ ppm) by setting the isotropic shift of a secondary standard

of 0.5 M $\text{Pb}(\text{NO}_3)_2(\text{aq})$ to -2941.0 ppm.⁴² Carbon chemical shifts were referenced to tetramethylsilane ($\delta_{\text{iso}} = 0.0$ ppm) by using the high-frequency peak of adamantane as a secondary reference ($\delta_{\text{iso}} = 38.56$ ppm).⁴³

All solid-state NMR experiments were performed on a double resonance 4 mm HX Varian/Chemagnetics probe. ^1H - ^{207}Pb variable-amplitude cross-polarization/MAS (VACP/MAS)^{44, 45} and cross-polarization/Carr-Purcell-Meiboom-Gill (CP/CPMG)^{46, 47} experiments were optimized on a sample of lead acetate hydrate [$\text{Pb}(\text{OAc})_2 \cdot x\text{H}_2\text{O}$]. All ^1H - ^{207}Pb CP experiments employed $2.0 \mu\text{s}$ $\pi/2$ proton pulses and Hartman-Hahn matching fields of ca. 55 kHz. Individual CP/CPMG sub-spectra were co-added to form the total spectrum (Figure F1). Further details on CP/CPMG experiments are given in the Appendix F (Table F1). Static CP/CPMG ^{207}Pb NMR patterns were simulated using the WSolids program.⁴⁸ ^{207}Pb MAS spectra were simulated with the SIMPSON program.⁴⁹ The TPPM decoupling scheme was employed in all experiments.⁵⁰

DFT Calculations. Theoretical calculations were performed with the EPR and NMR module⁵¹⁻⁵³ of the Amsterdam Density Functional (ADF) program suite.⁵⁴⁻⁵⁶ The VWN-BP functional was used for electron exchange and correlation for all calculations.⁵⁷⁻⁶⁰ Relativistic effects (including spin-orbit) were taken into account with the zeroth-order regular approximation (ZORA).⁶¹⁻⁶⁵ In the current version of ADF, analysis of the contributions to magnetic shielding (MS) from the mixing of molecular orbitals can only be performed for non-relativistic calculations. All-electron gauge including atomic orbitals (GIAO)⁶⁶ triple- ζ singly polarized (TZP) and triple- ζ doubly-polarized (TZ2P) basis sets were employed on all atoms for the non-relativistic calculations and ZORA calculations, respectively. However, the largest basis set

available for lead for the non-relativistic calculations was a frozen-core basis set, where the core was extended to the 4d shell for lead (Pb.4d). All calculations were performed using atomic coordinates from single crystal X-ray structures, with H atoms set to idealized positions (e.g., ideal C-H bond lengths and H-C-H angles). All calculations employed a discrete molecular unit, except for those upon **2** for which a dimer was used. Calculations on Me₄Pb (²⁰⁷Pb chemical shift standard) were performed upon atomic coordinates from the previously published low temperature (150 K) crystal structure.⁶⁷

X-ray Diffraction Experiments. Powder X-ray diffraction patterns were collected using a Bruker AXS HI-STAR system using a General Area Detector Diffractions System. Compounds **1**, **2** and **3** were finely ground, packed into 1.0 mm glass capillary tubes and flame sealed. The X-ray source employed was Cu K α radiation (1.540598 Å) with an area detector using a 2 θ range between 4.0° to 65.0°. Powder X-ray diffraction patterns were simulated with the PowderCell software package.⁶⁸

7.3 Results and discussion

Solid-state ²⁰⁷Pb NMR spectroscopy. In this section we discuss the acquisition and interpretation of solid-state ²⁰⁷Pb NMR spectra of complexes **1**, **2**, and **3**, in order to examine the electronic structure, bonding environment at the lead centre, and presence and/or influence of the lone pair of electrons on the lead CSA. In many cases, it has been observed that direct detection of ²⁰⁷Pb NMR spectra in solids is challenging, since the ²⁰⁷Pb longitudinal relaxation times (T_1) may be very long.^{42, 69-71} In order to circumvent the long ²⁰⁷Pb T_1 constants, ¹H-²⁰⁷Pb variable-amplitude cross-polarization (VACP/MAS) NMR experiments^{44, 45} were performed on compounds **1**, **2** and **3** (Figure 7.1). Normally,

only two spinning speeds are required to differentiate peaks due to spinning sidebands from that of the isotropic chemical shift in the MAS NMR spectra of a spin-1/2 nucleus. However, overlap of spinning sidebands due to large spans (Ω , defined in Table 7.1) requires that the spectrum be acquired at three different spinning speeds (expanded views of spectra given in Figure F2). The isotropic shifts in this series of complexes are similar to that reported from solution ^{207}Pb NMR experiments on $[(\text{PhS})_3\text{Pb}][\text{Ph}_4\text{As}]$, $\delta_{\text{iso}} = 2868$ ppm,⁷² which has an S_3 lead coordination environment, but are clearly distinct from the S_2N environment in $[2\text{-methyl-1-}\{ \text{methyl}(2\text{-pyridin-2-ylethyl})\text{amino}\}\text{propane-2-thiolatolead-Pb}][\text{ClO}_4]$ for which $\delta_{\text{iso}} = 2358$ ppm.²⁵

A temperature-dependent chemical shift is observed for compounds **1** and **2** (Figure F2 and Table F2). This behavior is well known, and was previously observed in the ^{207}Pb NMR spectra of $\text{Pb}(\text{NO}_3)_2$,⁷³⁻⁷⁷ among other lead-containing systems. Minor impurity peaks are visible in the VACP/MAS NMR spectra and are attributed to hydration of the samples since the MAS spectra were acquired *after* the static NMR and powder XRD experiments (Figure F3). Relatively accurate values for δ_{iso} (Table 7.1) can be obtained from the VACP/MAS spectra; however, the large number of spinning sidebands and the poor signal to noise of the spectra makes extraction of the CS tensor parameters by Herzfeld-Berger analysis difficult and potentially inaccurate.

With this in mind, static (i.e., stationary sample) ^1H - ^{207}Pb cross-polarization/Carr-Purcell-Meiboom-Gill (CP/CPMG) experiments were performed.^{46, 47, 78-80} Due to the large breadth of the lead powder patterns, the entire spectrum must be acquired in a piecewise frequency offset fashion (Figure F1), which requires both constant resetting of

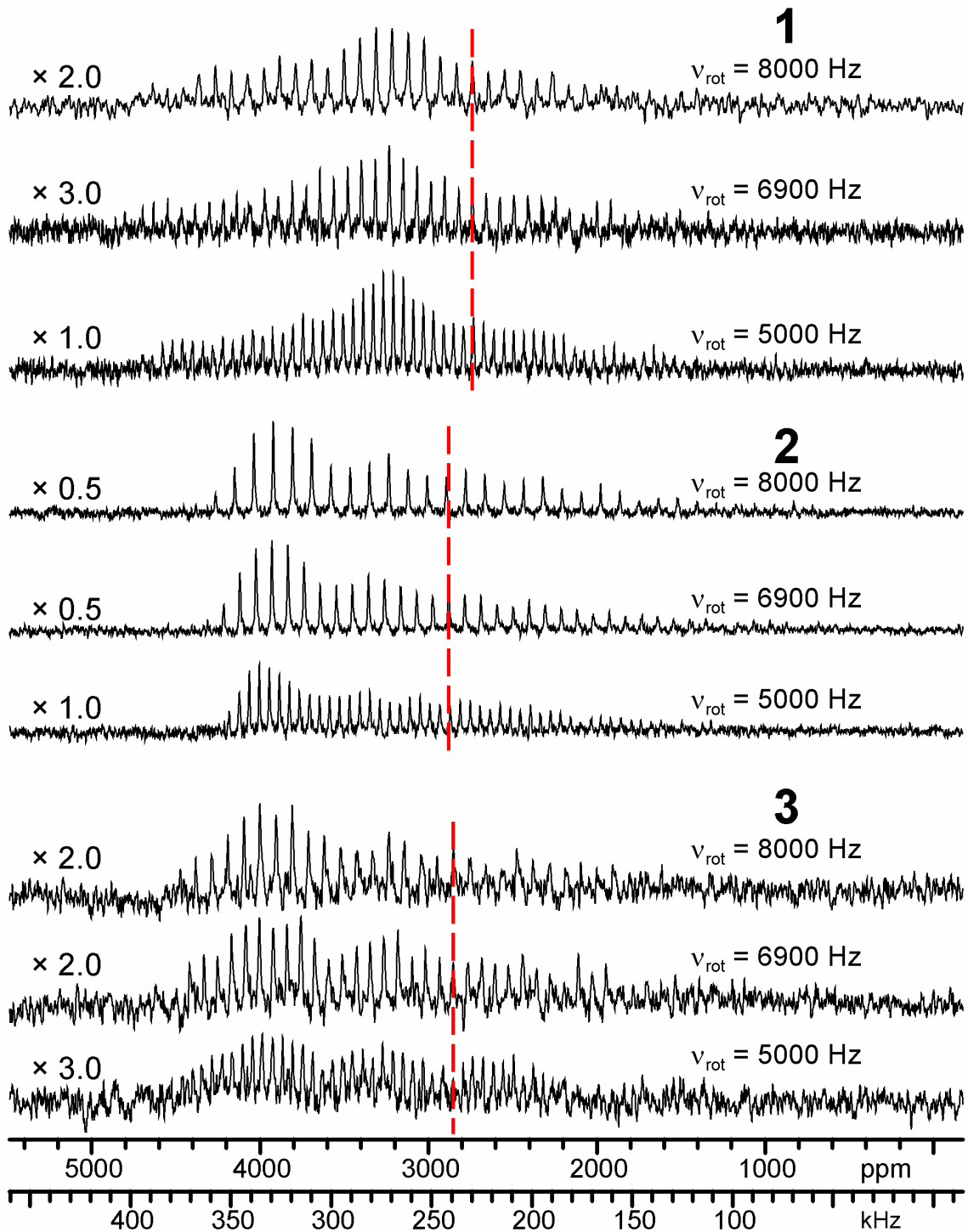


Figure 7.1. ^1H - ^{207}Pb VACP/MAS NMR spectra of **1**, **2** and **3** each acquired at three spinning speeds (ν_{rot}). Dashed lines indicate δ_{iso} . A recycle delay of 10 s was used for all spectra and 2004 to 8428 scans were acquired. The relative vertical scaling of the spectra is given on the left.

Table 7.1. Experimental ^{207}Pb Chemical Shift Parameters.

Complex	δ_{11} (ppm) ^a	δ_{22} (ppm)	δ_{33} (ppm)	δ_{iso} (ppm) ^b	Ω (ppm) ^c	κ ^d
1	4814	3286	114	2733(5) ^e	4700(100)	0.35(7)
2	4256	4022	356	2873(5)	3900(100)	0.88(10)
3	4519	4024	19	2852(5)	4500(100)	0.78(15)

^a The chemical shift tensor is described by three principal components ordered such that $\delta_{11} \geq \delta_{22} \geq \delta_{33}$. Shift values for the individual components are calculated from the values of Ω , κ and δ_{iso} . ^b $\delta_{\text{iso}} = (\delta_{11} + \delta_{22} + \delta_{33})/3$. δ_{iso} is given relative to $(\text{CH}_3)_4\text{Pb}$ [$\delta_{\text{iso}}(^{207}\text{Pb}) = 0.0$ ppm]. All values are taken from VACP/MAS NMR spectra acquired at a spinning speed of 5000 Hz. ^c $\Omega = \delta_{11} - \delta_{33}$. Based upon simulations of the static CP/CPMG spectra. ^d $\kappa = 3(\delta_{22} - \delta_{\text{iso}})/\Omega$, $-1.0 \leq \kappa \leq +1.0$. Based upon simulations of the static CP/CPMG spectra. ^e The uncertainty in the last digit of each value is denoted in brackets. Error bounds in the principal CS tensor components (eg. δ_{11}) are of a similar magnitude to those of Ω .

transmitter frequency and probe retuning. The appearance of “spikelets” in the frequency domain spectra arise from the Fourier transform of the CPMG echo train (alternatively and completely equivalently, one may co-add the echoes and process the summed spin echo to produce a static pattern).⁸¹ Acquisition of static CP/CPMG spectra is not hindered by a partial averaging of the ^1H - ^{207}Pb dipolar interactions that would occur under MAS conditions; hence, high signal to noise static patterns can be acquired very rapidly with respect to VACP/MAS NMR spectra of the same quality. Another clear advantage of the CP/CPMG experiments over their VACP/MAS counterparts is the overall excitation of the ^{207}Pb NMR powder patterns. Simulations of the VACP/MAS spectra employing the CS tensor parameters extracted from the CP/CPMG spectra clearly demonstrate that the former are not uniformly excited and are unsuitable candidates for accurate measurement of CS tensor parameters via Herzfeld-Berger methods (Figure F4). This is in contrast to direct excitation and detection of broad ^{207}Pb NMR powder patterns. For instance, Antzutkin et al. recently measured and simulated ^{207}Pb MAS NMR spectra

of lead patterns with spans close to 4000 ppm and breadths of ca. 300 kHz (acquisition times of ca. 24-48 hours).⁸²

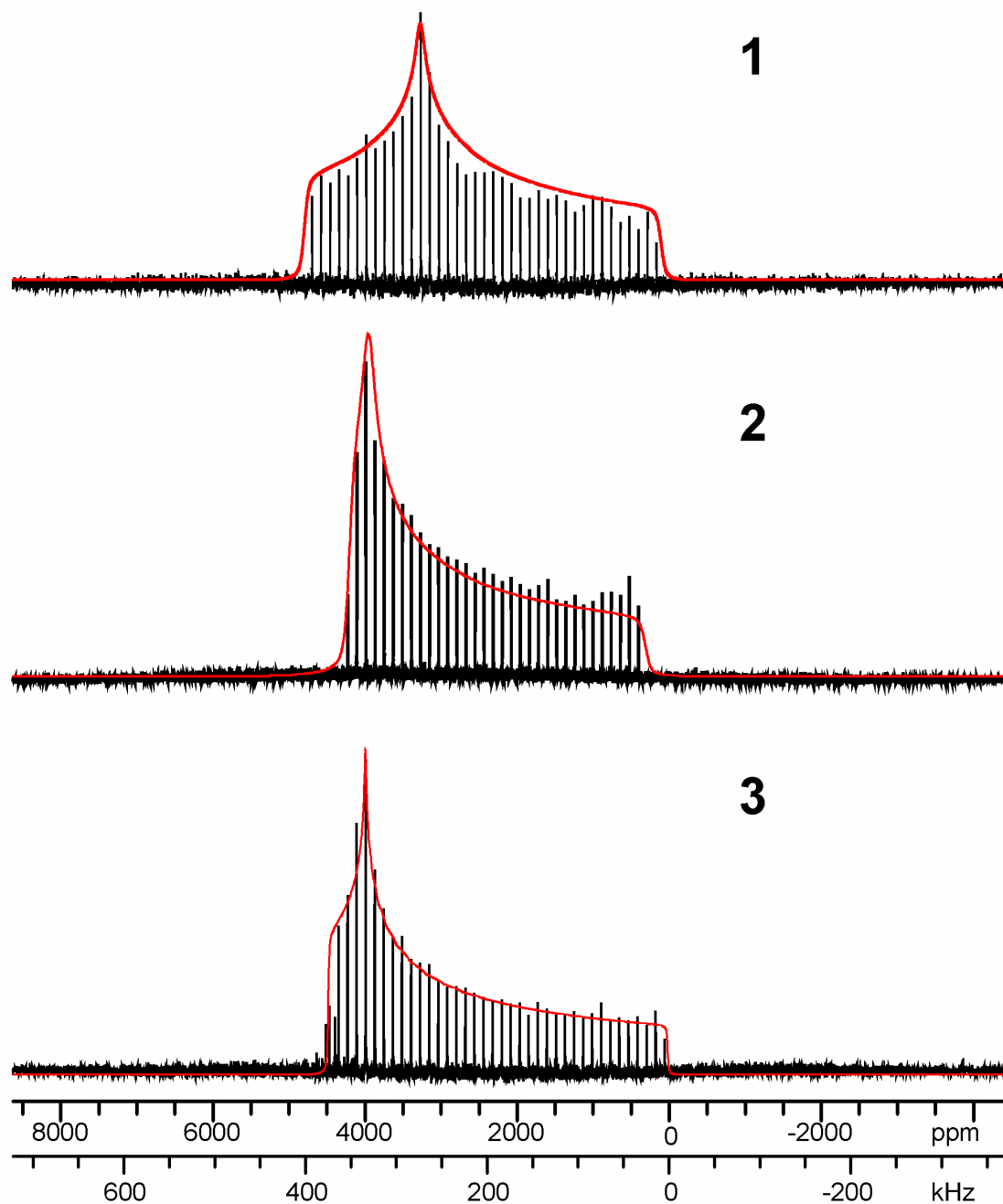


Figure 7.2. ^1H - ^{207}Pb CP/CPMG static NMR spectra (black trace) of compounds **1**, **2**, and **3**. Analytical simulations (solid red trace) are overlaid on the experimental spectra. The CS tensor parameters obtained from the simulations are given in Table 7.1.

Co-addition of the sub-spectra and simulation of the observed patterns (Figure 7.2) yield the lead CS tensor parameters (Table 7.1). The δ_{iso} is located at the centre of gravity of the powder pattern. The Ω and κ describe the breadth of anisotropic chemical shifts (i.e., the “size” of the CSA) and the degree of axial symmetry of the CS tensor. Though the CS tensor parameters are distinct, they do not vary widely in this series of complexes. This suggests that the orientations of the CS tensors in the molecular frames are related among the three complexes, and that the general modes of bonding and electronic environments at the lead centres are very similar. However, there are some interesting trends in these parameters which can be correlated to molecular structure and symmetry.

First, all three patterns have extremely large spans. The Ω values observed for complexes **1** and **3** are several hundred ppm larger than those observed for yellow lead oxide ($\Omega = 3917$ to 3995 ppm) and lead(II) dialkyldithiophosphates ($\Omega = 3840$ ppm), which, to the best of our knowledge, are the largest spans previously reported for lead complexes.^{37, 42, 70, 82} Second, all patterns possess positive skews, denoting δ_{33} as the distinct component in each case, and implying that it must be oriented in a distinct/unique environment within the molecule. Positive skews have previously been observed in the ^{207}Pb NMR spectra of the several lead(II) complexes, which are also thought to have an electron lone pair molecular orbital (MO) localized at the Pb centres.^{2, 37, 41, 42, 70} Since it is well known that CS tensor components orient along/near symmetry elements, and by virtue of the fact that the δ_{33} is the distinct component in each complex, it is very likely that δ_{33} is oriented along/near the direction of the presumed lone pair of electrons. Finally, despite the similarity of the isotropic shifts of **2** and **3**, the spectra of their

respective S_3N and S_2N metal bonding environments are readily distinguished by the differences in Ω and κ (this is visually apparent in comparing these spectra as well, Figure 7.2). With this limited set of structural parameters and NMR data, two observations can be made: (i) decreased Pb-S bond lengths are correlated with larger spans and (ii) the unique four-coordinate environment of **1** leads to a less axial CS tensor.

DFT Calculations of Lead MS Tensors. Ab initio and/or pure DFT computational methods can be used to calculate the nuclear magnetic shielding (MS) tensor parameters, their orientations within the molecular frames and contributions from individual MOs. Ramsey's theory of MS arbitrarily decomposes the total MS (σ) at a nucleus into diamagnetic and paramagnetic terms, such that $\sigma = \sigma_d + \sigma_p$.⁸³⁻⁸⁸ The diamagnetic and paramagnetic terms arise from the circulation of electrons in ground state MOs and mixing of separate MOs, respectively, both of which are induced by the presence of an external magnetic field. Ziegler and co-workers have developed a DFT-GIAO formalism for the calculation of MS which further partitions the paramagnetic terms into contributions from mixing of occupied MOs ($\sigma_p^{\text{occ-occ}}$) and mixing of occupied and virtual MOs ($\sigma_p^{\text{occ-vir}}$),⁵¹⁻⁵³ the details of which are neatly summarized elsewhere.⁸⁹ Furthermore, for heavy nuclei (^{207}Pb , ^{195}Pt , etc.), it is often necessary to include the relativistic contributions to the total MS as described by the spin-orbit coupling term (σ_{so}) in order to improve agreement between experiment and theory.^{52, 61, 62, 83, 90-96}

Table 7.2. ZORA and Non-relativistic (NR) ADF Calculations of ^{207}Pb MS and CS Tensor Parameters.

Complex	Method	Shielding Term	σ_{11} (ppm) ^a	σ_{22} (ppm)	σ_{33} (ppm)	σ_{iso} (ppm)	δ_{iso} (ppm) ^{a,b}	Ω (ppm)	κ	
$(\text{CH}_3)_4\text{Pb}^b$	ZORA	Total	7523.7	7523.8	7546.5	7531.0	0.0	22.8	1.00	
	NR	Total	5447.1	5453.0	5453.0	5451.1	0.0	5.9	-0.99	
1	Expt.	Total ^b	2717	4245	7417	4793	2733	4700	0.35	
	ZORA	Total	4252.6	5301.0	7631.2	5728.27	1803.1	3378.6	0.38	
		σ_{d}	9949.2	9946.1	9940.4	9945.2	-	-8.8	-	
		σ_{p}	-6448.7	-5440.1	-4768.1	-5552.3	-	1680.6	-	
		σ_{so}	752.1	795.1	2458.9	1335.3	-	1706.8	-	
	NR	Total	5131.6	5771.9	6453.9	5785.8	-334.7	1322.3	0.03	
		σ_{d}	10062.3	10059.5	10052.2	10058.0	-	-10.1	-	
		σ_{p}	-4930.7	-4287.6	-3598.2	-4272.2	-	1332.5	-	
	2	Expt.	Total	3275	3509	7175	4653	2873	3900	0.88
		ZORA	Total	4217.4	4341.2	7382.2	5313.6	2217.8	3164.9	0.92
σ_{d}			9948.8	9947.6	9941.4	9945.9	-	-7.4	-	
σ_{p}			-6501.1	-6099.9	-4758.5	-5786.5	-	1742.6	-	
σ_{so}			769.7	493.6	2199.4	1154.2	-	1429.7	-	
NR		Total	5146.9	5231.3	6387.5	5588.6	-137.5	1240.6	0.87	
		σ_{d}	10058.7	10062.6	10052.9	10058.0	-	-5.8	-	
		σ_{p}	-4911.7	-4831.3	-3665.3	-4469.5	-	1246.4	-	
3		Expt.	Total	3012	3507	7512	4677	2852	4500	0.78
		ZORA	Total	3998.3	4341.1	7778.2	5372.5	2158.8	3780.0	0.82
	σ_{d}		9948.5	9947.0	9943.2	9946.2	-	-5.3	-	
	σ_{p}		-6729.2	-6339.1	-4559.0	-5875.8	-	2170.2	-	
	σ_{so}		779.0	733.2	2394.0	1302.1	-	1615.0	-	
	NR	Total	4747.2	5256.2	6473.9	5492.4	-41.3	1726.7	0.41	
		σ_{d}	10060.8	10060.7	10056.5	10059.3	-	-4.3	-	
		σ_{p}	-5313.6	-4804.5	-3582.6	-4566.9	-	1731.0	-	

^a The nuclear magnetic shielding (MS, σ) tensor is described by three principal components ordered such that $\sigma_{11} \leq \sigma_{22} \leq \sigma_{33}$ (lowest to highest *shielding*). The principal chemical *shift* tensor components (δ_{jj}) are related to the principal magnetic *shielding* components (σ_{jj}) by the equation $\delta_{jj} = (\sigma_{\text{iso, ref}} - \sigma_{jj})(10^6)/(1 - \sigma_{\text{iso, ref}}) \approx \sigma_{\text{iso, ref}} - \sigma_{jj}$ where $jj = 11, 22$ or 33 and $\sigma_{\text{iso, ref}}$ refers to the isotropic shielding value of the reference compound ($\sigma_{\text{iso, ref}} = \sigma_{\text{iso}}(\text{Me}_4\text{Pb})$). ^b The experimental shift values have been converted to shielding values by subtracting them from the ZORA calculated value of $\sigma_{\text{iso}}(\text{Me}_4\text{Pb})$; $\sigma_{jj} = 7531.0 - \delta_{jj}$.

Lead MS parameters from calculations performed with the ADF program suite incorporating ZORA⁶³⁻⁶⁵ are shown in Table 7.2. In all cases, the ZORA calculations yield values of κ which are in good agreement with experimental values. Theoretical

values of Ω are lower than experimental values in all cases, which arises from consistent underestimation of deshielding along the directions of σ_{11} and σ_{22} . The errors in the calculated σ_{11} and σ_{22} parameters are unsurprising, given the difficulties associated with accurately calculating the excited electronic states of larger molecules containing Pb atoms. Since the chemical shift range of lead is approximately 17000 ppm, and the spans of the CS tensors are so large, these errors are relatively small (ranging from 15-30%). The calculations also qualitatively predict the relative values of δ_{iso} (the ^{207}Pb nucleus in **1** is predicted to be the most shielded and that in **2** least shielded). While the theoretical tensors are not identical to experimental measurements, they are still extremely useful in understanding the origin of the lead MS in these systems.

Contributions to the principal shielding components of the total shielding tensor have been tabulated for the diamagnetic, paramagnetic and spin-orbit terms for all compounds (Table 7.2). The diamagnetic terms for all compounds are highly isotropic (small Ω values) and do not contribute to the large shielding anisotropies. The paramagnetic term makes much larger contributions to the isotropic shielding values than the spin-orbit term, but both terms contribute relatively equally to the spans of the CS tensors. Comparison of the ZORA and non-relativistic (NR) calculations make it very clear that the inclusion of relativistic effects for calculations of CS tensors for heavy nuclei is absolutely necessary.

The nature of the CS tensor (i.e. the large span and the positive skews) and its relationship to molecular structure can be rationalized by considering the orientation of the CS tensor in the molecular frame. The lead CS tensor orientations generated from the ZORA calculations are presented in Figure 7.3 for complexes **1**, **2** and **3**. In all three

systems, the σ_{33} component is oriented in the presumed direction of the stereochemically active lone pair and close to the plane of the S-Pb-S bonding arrangement. Conversely, the σ_{11} and σ_{22} components are not directed along Pb-S or Pb-N bonds, and are oriented as such due to large paramagnetic deshielding contributions arising from mixing of occupied MOs localized on Pb, S and N atoms with an assortment of low-lying virtual MOs.

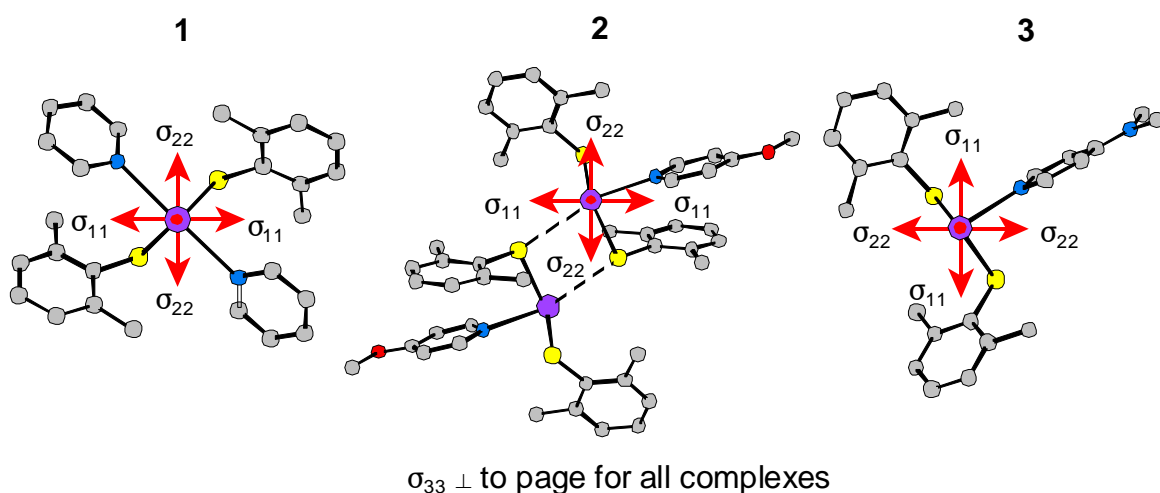


Figure 7.3. Lead CS tensor orientations for complexes **1**, **2** and **3**. The tensor orientations have been generated from the ZORA calculations.

Our hypotheses regarding both the large spans and high positive skews and their relation to molecular structure can be confirmed by analyzing the contributions made by individual MOs to the paramagnetic shielding terms. Analyses of the contributions of particular MOs to paramagnetic shielding in simple molecular systems have previously been demonstrated using both the Gaussian software package⁹⁷⁻⁹⁹ and ADF software.^{51, 89, 100, 101} The NMR/EPR module of the ADF program suite outputs the paramagnetic shielding contributions arising from mixing of individual occupied-virtual and occupied-occupied MO pairs. However, this analysis is only available for NR calculations in the current implementation of ADF. Despite the fact that the NR calculations show poor

quantitative agreement with experiment, the paramagnetic contributions and CS tensor orientations are very similar to those generated from ZORA calculations (Figure F5). Hence, it is reasonable to examine individual contributions from MO pairs to the paramagnetic terms of the lead CS tensor.

Due to the relatively high local symmetry at the lead atom in complex **1**, we have chosen this as the focus of our discussion of MO contributions to MS (a full MO analysis for all systems is beyond the scope of the current chapter). The contributions from mixing of occupied (occ) and virtual (vir) MOs in complex **1** are summarized in Table 7.3 (these MOs are depicted in Figures 7.4 and F6) and account for upwards of 90% of the total isotropic shielding contribution from the paramagnetic term. Therefore, occ-occ mixing will not be considered. Due to the enormous number of MO pairs, only those contributing greater than 2% (~77 ppm) of the total isotropic shielding contribution of occ-vir MO mixing (-3865.1 ppm) are listed. In this way, analysis of MO contributions to paramagnetic shielding can be focused upon a select few MOs that are near the HOMO and/or involved in metal-ligand bonding (e.g., MO pairs involving occ MOs from 1 to 120 contribute to only 8.6% of the occ-vir paramagnetic contribution).

Let us consider a specific example to clarify the data in Table 7.3. The mixing of the occ MO 130 (HOMO -3) with virtual orbitals contributes -894.7 ppm to the total paramagnetic shielding (σ_p) of -4272.2 ppm. Mixing of occ MO 130 with vir MO 138 (denoted as 130-138) accounts for -451.4 ppm of the -894.7 ppm contributed by occ MO 130. The remaining contribution to shielding from occ MO 130 results from its mixing with many other virtual MOs, most notably vir MOs 139 and 144 (an extended data analysis including all occ-vir contributions can be found in the Table F3).

Table 7.3. Contributions to paramagnetic shielding from mixing of occ-vir MOs in **1**.

Occupied MO	σ_{iso} from occ MO (ppm) ^a	Sum of σ_{iso} (ppm)	Major occ-vir Pairs	σ_{iso} of MO Pair (ppm)	σ_{11} (ppm)	σ_{22} (ppm)	σ_{33} (ppm)
1 to 120	-332.7	-332.7	-	-	-	-	-
121	-399.0	-731.7	-	-	-	-	-
122	-323.8	-1055.5	122-138	-81.6	-11.5	-219.6	-13.6
			122-143	-76.4	-27.6	-19.8	-181.8
			Sum	-158.0	-39.1	-239.4	-195.4
123 and 124	-6.3	-1061.7	-	-	-	-	-
125	-428.2	-1489.9	125-143	-135.6	-10.8	-6.7	-389.4
126	-467.5	-1957.4	126-143	-124.8	-318.0	-65.2	8.8
127 to 129	-3.1	-1960.6	-	-	-	-	-
130	-894.7	-2854.3	130-138	-451.4	-468.9	-816.9	-68.3
			130-139	-78.3	12.9	-16.2	-231.5
			130-144	-84.0	-54.4	-156.4	-41.4
			Sum	-613.7	-510.4	-989.5	-341.2
131	-461.8	-3316.0	131-138	-88.6	54.1	-281.7	-38.2
			131-139	199.2	78.5	546.9	-27.8
			131-140	-84.8	-3.2	-315.0	63.8
			131-143	-256.9	-314.5	126.2	-582.5
			Sum	-231.1	-185.1	76.4	-584.7
132	-240.6	-3556.6	132-138	-451.2	-105.5	-1216.4	-31.5
			132-142	-78.9	-86.1	18.3	-169.2
			132-143	231.7	172.6	145.8	376.6
			Sum	-298.4	-19.0	-1052.3	175.9
133 (HOMO)	-308.5	-3865.1	133-139	430.4	45.5	1271.4	-25.8
			133-143	-611.8	-1210.8	-691.5	66.9
			Sum	-181.4	-1165.3	579.9	41.1
			Total	-1743.0	-2247.4	-1696.8	-1284.9

^aThis column corresponds to the sum of isotropic shieldings of the occ-vir MO pairs that contain the specified occ MO.

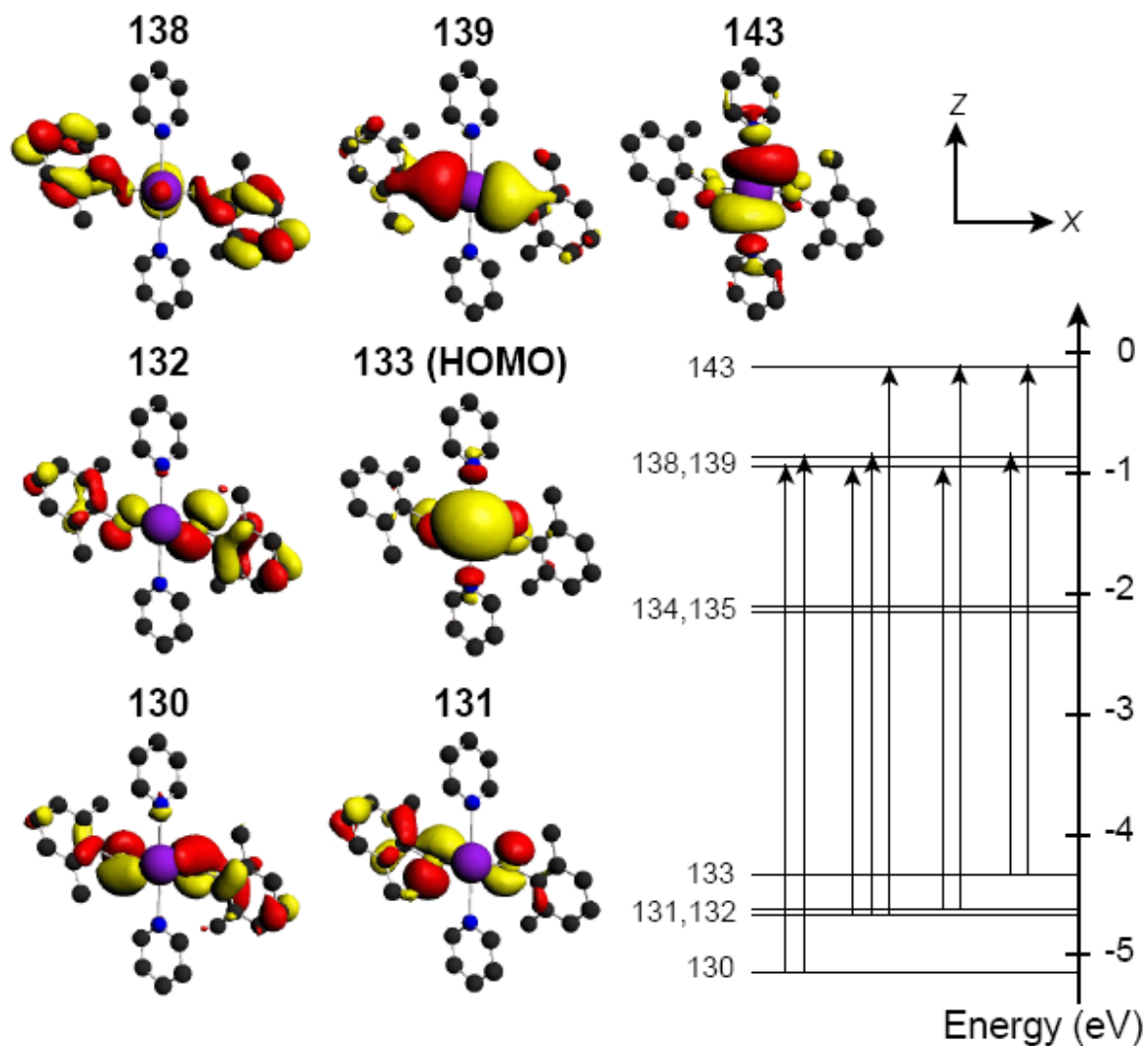


Figure 7.4. The occupied and virtual MOs of **1** that make significant contributions to the paramagnetic shielding term. A partial MO diagram indicating the magnetic-dipole allowed transitions between the occupied and virtual orbitals that are pictured is also shown. The MOs are visualized at the 97% electron density level.

The largest contributions to paramagnetic shielding arise from mixing of a variety of occ MOs with vir MOs 138, 139 and 143 (Table 7.3). These virtual MOs are of high lead *p*-orbital character, as demonstrated by the gross populations contributed by individual AOs (Table F4). MO 138 has relatively high Pb $6p_y$ and slight $6s$ characters, but also has significant contributions from C $2p$ orbitals on the neighbouring aromatic rings. MO 139 and MO 143 are comprised of mixtures of large Pb $6p_x$ and $6p_z$ AO contributions. The occupied MOs which mix with these three virtual MOs vary in their relative amounts of Pb, S, N or C AO character. Large deshielding contributions involve occ MOs 130 to 133 (HOMO -3 to HOMO), as well as occ MOs 121, 122, 125 and 126. MO 133 corresponds to the stereochemically active Pb lone pair, whereas MOs 130, 131 and 132 are largely localized on the S atoms. MO 121 describes Pb-N bonding, MO 122 describes S-C σ -bonding, MO 125 describes Pb-S bonding and S-C π -bonding, and MO 126 describes S-C π -bonding and some degree of localized N $2p$ character. Hence, the origin of the lead chemical shielding tensor is relatively complex, and highly dependent upon the characteristics of the Pb lone pair, $3p$ AOs localized on S atoms, as well as variable types of σ - and π -bonding.

Understanding why certain MO pairs make large paramagnetic (de)shielding contributions can be accomplished through relatively simple visualization. MOs which contribute to shielding along the direction of a particular principal component must be relatively close in energy, but also have the appropriate symmetries to interfere or “overlap” with one another when induced to mix by a magnetic field. This type of mixing can be visualized by rotating the appropriate MOs about the axes defining the principal components of the CS tensor. This concept has previously been demonstrated

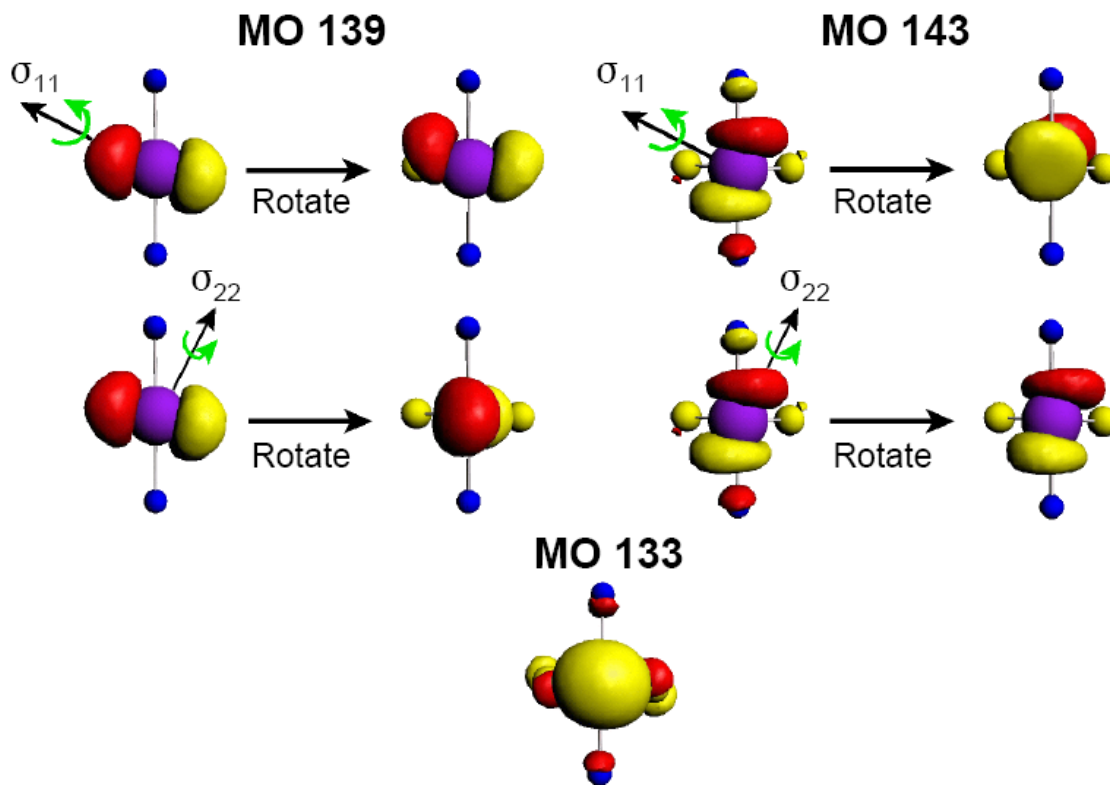


Figure 7.5. A representation of the rotation of vir MOs 139 and 143 of **1**. The axes of rotation correspond to the directions of σ_{11} and σ_{22} in the molecular frame. Only Pb, S and N atoms are shown.

for several relatively simple systems.^{51, 98, 99, 101, 102} We will use the arbitrary convention of right-handed ninety degree rotations of the virtual MOs about their gauge origin (i.e. contributing AOs are rotated in a right-handed fashion at the nuclear site). Rotations resulting in constructive or destructive overlap of MO lobes generate deshielding and shielding contributions, respectively.⁹⁹ The simplest examples to consider are the 133-143 and 133-139 MO pairs (Figure 7.5). The 133-143 MO pair makes significant deshielding contributions along σ_{11} and σ_{22} . A right handed rotation of 143 about the σ_{11} axis results in constructive overlap with 133, and similarly, the same rotation about σ_{22} leads to constructive overlap, but to a lesser extent (and hence the smaller deshielding

contribution). In the case of the 133-139 MO pair, rotation about σ_{11} does not generate any significant overlap, and the deshielding contribution is minimal. On the other hand, right-handed rotation about σ_{22} causes large destructive overlap (i.e. lobes of opposite phase are overlapped), leading to a large shielding contribution. All of the other shielding and deshielding contributions can be rationalized and visualized in this manner, by simple rotations of the virtual orbitals.

7.4 Conclusions

Lead CS tensor parameters have been measured from ^{207}Pb CP/CPMG solid-state NMR spectra for complexes **1**, **2**, and **3**. The CP/CPMG sequence has been demonstrated to be much more efficient and accurate than MAS methods for the acquisition of the ^{207}Pb spectra of extremely broad, CSA-dominated powder patterns. Similar lead isotropic chemical shifts are observed within this series of compounds; however, CS tensor parameters are useful for differentiating the three types of lead coordination environments. DFT calculations that account for relativistic effects adequately reproduce the experimental CS tensor parameters and trends. Examination of the individual MOs generated by non-relativistic calculations provides insight into the molecular origins of lead MS, as well as evidence for the existence and position of the stereochemically active lone electron pair. Experimental measurement and theoretical calculations of lead CS tensor parameters are clearly useful for the elucidation of molecular and electronic structure, bonding and symmetry.

7.5 Bibliography

- (1) Katz, M. J.; Aguiar, P. M.; Batchelor, R. J.; Bokov, A. A.; Ye, Z. G.; Kroeker, S.; Leznoff, D. B., *J. Am. Chem. Soc.* **2006**, 128, (11), 3669-3676.
- (2) Katz, M. J.; Michaelis, V. K.; Agular, P. M.; Yson, R.; Lu, H.; Kaluarachchi, H.; Batchelor, R. J.; Schreckenbach, G.; Kroeker, S.; Patterson, H. H.; Leznoff, D. B., *Inorg. Chem.* **2008**, 47, (14), 6353-6363.
- (3) Kagan, C. R.; Mitzi, D. B.; Dimitrakopoulos, C. D., *Science* **1999**, 286, (5441), 945-947.
- (4) Mitzi, D. B.; Wang, S.; Feild, C. A.; Chess, C. A.; Guloy, A. M., *Science* **1995**, 267, (5203), 1473-1476.
- (5) Davidovich, R. L.; Stavila, V.; Whitmire, K. H., *Coord. Chem. Rev.* **2010**, 254, (17-18), 2193-2226.
- (6) Berenguer, J. R.; Diez, A.; Fernandez, J.; Fornies, J.; Garcia, A.; Gil, B.; Lalinde, E.; Moreno, M. T., *Inorg. Chem.* **2008**, 47, (17), 7703-7716.
- (7) Chang, T. W. F.; Musikhin, S.; Bakueva, L.; Levina, L.; Hines, M. A.; Cyr, P. W.; Sargent, E. H., *Appl. Phys. Lett.* **2004**, 84, (21), 4295-4297.
- (8) Kim, S.; Fisher, B.; Eisler, H. J.; Bawendi, M., *J. Am. Chem. Soc.* **2003**, 125, (38), 11466-11467.
- (9) McDonald, S. A.; Cyr, P. W.; Levina, L.; Sargent, E. H., *Appl. Phys. Lett.* **2004**, 85, (11), 2089-2091.
- (10) McDonald, S. A.; Konstantatos, G.; Zhang, S. G.; Cyr, P. W.; Klem, E. J. D.; Levina, L.; Sargent, E. H., *Nat. Mater.* **2005**, 4, (2), 138-142.
- (11) Sargent, E. H., *J. Mod. Opt.* **2004**, 51, (16-18), 2797-2803.
- (12) Sukhovatkin, V.; Musikhin, S.; Gorelikov, I.; Cauchi, S.; Bakueva, L.; Kumacheva, E.; Sargent, E. H., *Opt. Lett.* **2005**, 30, (2), 171-173.
- (13) Bakueva, L.; Gorelikov, I.; Musikhin, S.; Zhao, X. S.; Sargent, E. H.; Kumacheva, E., *Adv. Mater.* **2004**, 16, (11), 926-929.
- (14) Buckner, S. W.; Konold, R. L.; Jelliss, P. A., *Chem. Phys. Lett.* **2004**, 394, (4-6), 400-404.

- (15) Fernee, M. J.; Watt, A.; Warner, J.; Heckenberg, N.; Rubinsztein-Dunlop, H., *Nanotechnology* **2004**, 15, (9), 1328-1337.
- (16) Hao, E. C.; Yang, B.; Yu, S.; Gao, M. Y.; Shen, J. C., *Chem. Mat.* **1997**, 9, (7), 1598-1600.
- (17) Meehan, E. J.; Erdmann, D. J., *J. Colloid Interface Sci.* **1977**, 62, (1), 8-15.
- (18) Yu, D. B.; Wang, D. B.; Meng, Z. Y.; Lu, J.; Qian, Y. T., *J. Mater. Chem.* **2002**, 12, (3), 403-405.
- (19) Zhao, X. S.; Gorelikov, I.; Musikhin, S.; Cauchi, S.; Sukhovatkin, V.; Sargent, E. H.; Kumacheva, E., *Langmuir* **2005**, 21, (3), 1086-1090.
- (20) Cornacchio, A. L. P.; Jones, N. D., *J. Mater. Chem.* **2006**, 16, (12), 1171-1177.
- (21) Eichhofer, A., *Eur. J. Inorg. Chem.* **2005**, (9), 1683-1688.
- (22) Nenadovic, M. T.; Comor, M. I.; Vasic, V.; Micic, O. I., *J. Phys. Chem.* **1990**, 94, (16), 6390-6396.
- (23) Torimoto, T.; Uchida, H.; Sakata, T.; Mori, H.; Yoneyama, H., *J. Am. Chem. Soc.* **1993**, 115, (5), 1874-1880.
- (24) Fleischer, H.; Schollmeyer, D., *Inorg. Chem.* **2004**, 43, (18), 5529-5536.
- (25) Andersen, R. J.; diTargiani, R. C.; Hancock, R. D.; Stern, C. L.; Goldberg, D. P.; Godwin, H. A., *Inorg. Chem.* **2006**, 45, (17), 6574-6576.
- (26) Magyar, J. S.; Weng, T. C.; Stern, C. M.; Dye, D. F.; Rous, B. W.; Payne, J. C.; Bridgewater, B. M.; Mijovilovich, A.; Parkin, G.; Zaleski, J. M.; Penner-Hahn, J. E.; Godwin, H. A., *J. Am. Chem. Soc.* **2005**, 127, (26), 9495-9505.
- (27) Bharara, M. S.; Kim, C. H.; Parkin, S.; Atwood, D. A., *Polyhedron* **2005**, 24, (8), 865-871.
- (28) Briand, G. G.; Smith, A. D.; Schatte, G.; Rossini, A. J.; Schurko, R. W., *Inorg. Chem.* **2007**, 46, (21), 8625-8637.
- (29) Appleton, S. E.; Briand, G. G.; Decken, A.; Smith, A. S., *Dalton Trans.* **2004**, (21), 3515-3520.
- (30) Shimoni-Livny, L.; Glusker, J. P.; Bock, C. W., *Inorg. Chem.* **1998**, 37, (8), 1853-1867.
- (31) Dean, P. A. W.; Vittal, J. J.; Payne, N. C., *Inorg. Chem.* **1985**, 24, (22), 3594-3597.

- (32) Krebs, B.; Brommelhaus, A.; Kersting, B.; Nienhaus, M., *Eur. J. Solid State Inorg. Chem.* **1992**, 29, 167-180.
- (33) Rae, A. D.; Craig, D. C.; Dance, I. G.; Scudder, M. L.; Dean, P. A. W.; Kmetc, M. A.; Payne, N. C.; Vittal, J. J., *Acta Crystallogr. Sect. B-Struct. Commun.* **1997**, 53, 457-465.
- (34) Harris, R. K.; Becker, E. D.; De Menezes, S. M. C.; Goodfellow, R.; Granger, P., *Pure Appl. Chem.* **2001**, 73, (11), 1795-1818.
- (35) Dybowski, C.; Neue, G., *Prog. Nucl. Magn. Reson. Spectrosc.* **2002**, 41, (3-4), 153-170.
- (36) Janiak, C.; Schumann, H.; Stader, C.; Wrackmeyer, B.; Zuckerman, J. J., *Chem. Ber.-Recl.* **1988**, 121, (10), 1745-1751.
- (37) Kye, Y. S.; Connolly, S.; Herreros, B.; Harbison, G. S., *Main Group Met. Chem.* **1999**, 22, (6), 373-383.
- (38) Mason, J.; Editor, *Multinuclear NMR*. In Plenum Press: New York, 1987; pp 305-333.
- (39) Duncan, T., Michael, *A Compilation of Chemical Shift Anisotropies*. The Farragut Press: Chicago, 1990; p M-23.
- (40) Zwanziger, J. W.; Werner-Zwanziger, U.; Shaw, J. L.; So, C., *Solid State Nucl. Magn. Reson.* **2006**, 29, (1-3), 113-118.
- (41) Hamilton, B. H.; Kelly, K. A.; Wagler, T. A.; Espe, M. P.; Ziegler, C. J., *Inorg. Chem.* **2004**, 43, (1), 50-56.
- (42) Fayon, F.; Farnan, I.; Bessada, C.; Coutures, J.; Massiot, D.; Coutures, J. P., *J. Am. Chem. Soc.* **1997**, 119, (29), 6837-6843.
- (43) Earl, W. L.; Vanderhart, D. L., *J. Magn. Reson.* **1982**, 48, (1), 35-54.
- (44) Peersen, O. B.; Wu, X. L.; Kustanovich, I.; Smith, S. O., *J. Magn. Reson. Ser. A* **1993**, 104, (3), 334-339.
- (45) Peersen, O. B.; Wu, X. L.; Smith, S. O., *J. Magn. Reson. Ser. A* **1994**, 106, (1), 127-131.
- (46) Hung, I.; Rossini, A. J.; Schurko, R. W., *J. Phys. Chem. A* **2004**, 108, (34), 7112-7120.

- (47) Siegel, R.; Nakashima, T. T.; Wasylishen, R. E., *J. Phys. Chem. B* **2004**, 108, (7), 2218-2226.
- (48) Eichele, K.; Wasylishen, R. E. *WSolids: Solid-State NMR Spectrum Simulation*, v. 1.17.30; 2001.
- (49) Bak, M.; Rasmussen, J. T.; Nielsen, N. C., **2000**, 147, (2), 296-330.
- (50) Bennett, A. E.; Rienstra, C. M.; Auger, M.; Lakshmi, K. V.; Griffin, R. G., *J. Chem. Phys.* **1995**, 103, (16), 6951-6958.
- (51) Schreckenbach, G.; Ziegler, T., *J. Phys. Chem.* **1995**, 99, (2), 606-611.
- (52) Schreckenbach, G.; Ziegler, T., *Int. J. Quantum Chem.* **1997**, 61, (6), 899-918.
- (53) Wolff, S. K.; Ziegler, T., *J. Chem. Phys.* **1998**, 109, (3), 895-905.
- (54) Guerra, C. F.; Snijders, J. G.; te Velde, G.; Baerends, E. J., *Theor. Chem. Acc.* **1998**, 99, (6), 391-403.
- (55) Velde, G. T.; Bickelhaupt, F. M.; Baerends, E. J.; Guerra, C. F.; Van Gisbergen, S. J. A.; Snijders, J. G.; Ziegler, T., *J. Comput. Chem.* **2001**, 22, (9), 931-967.
- (56) ADF2005.01 *ADF2005.01*, SCM, Theoretical Chemistry, Vrije Universiteit: Amsterdam.
- (57) Becke, A. D., *Phys. Rev. A* **1988**, 38, (6), 3098-3100.
- (58) Perdew, J. P., *Phys. Rev. B* **1986**, 34, (10), 7406-7406.
- (59) Perdew, J. P., *Phys. Rev. B* **1986**, 33, (12), 8822-8824.
- (60) Vosko, S. H.; Wilk, L.; Nusair, M., *Can. J. Phys.* **1980**, 58, (8), 1200-1211.
- (61) Autschbach, J.; Ziegler, T., Relativistic calculations of spin-spin coupling constants of heavy nuclei. In *Calculation of NMR and EPR Parameters*, Wiley-VCH: Weinheim, 2004; pp 249-264.
- (62) Autschbach, J., Calculation of heavy-nucleus chemical shifts. Relativistic all-electron methods. In *Calculation of NMR and EPR Parameters*, Wiley-VCH: Weinheim, 2004; pp 227-247.
- (63) van Lenthe, E.; Baerends, E. J.; Snijders, J. G., *J. Chem. Phys.* **1993**, 99, (6), 4597-4610.
- (64) van Lenthe, E.; Baerends, E. J.; Snijders, J. G., *J. Chem. Phys.* **1994**, 101, (11), 9783-9792.

- (65) van Lenthe, E.; van Leeuwen, R.; Baerends, E. J.; Snijders, J. G., *Int. J. Quantum Chem.* **1996**, 57, (3), 281-293.
- (66) Ditchfield, R., *Mol. Phys.* **1974**, 27, (4), 789-807.
- (67) Fleischer, H.; Parsons, S.; Pulham, C. R., *Acta Crystallogr. Sect. E.-Struct Rep. Online* **2003**, 59, M11-M13.
- (68) Kraus, W.; Nolze, G. *PowderCell for Windows*, v. 2.4; Federal Institute for Materials Research and Testing: Berlin, Germany, 2000.
- (69) Grutzner, J. B.; Stewart, K. W.; Wasylishen, R. E.; Lumsden, M. D.; Dybowski, C.; Beckmann, P. A., *J. Am. Chem. Soc.* **2001**, 123, (29), 7094-7100.
- (70) Zhao, P. D.; Prasad, S.; Huang, J.; Fitzgerald, J. J.; Shore, J. S., *J. Phys. Chem. B* **1999**, 103, (48), 10617-10626.
- (71) Van Bramer, S. E.; Glatfelter, A.; Bai, S.; Dybowski, C.; Neue, G.; Perry, D. L., *Magn. Reson. Chem.* **2006**, 44, (3), 357-365.
- (72) Dean, P. A. W.; Vittal, J. J.; Payne, N. C., *Inorg. Chem.* **1984**, 23, (25), 4232-4236.
- (73) Bielecki, A.; Burum, D. P., *J. Magn. Reson. Ser. A* **1995**, 116, (2), 215-220.
- (74) Ferguson, D. B.; Haw, J. F., *Anal. Chem.* **1995**, 67, (18), 3342-3348.
- (75) Mildner, T.; Ernst, H.; Freude, D., *Solid State Nucl. Magn. Reson.* **1995**, 5, (3), 269-271.
- (76) Neue, G.; Dybowski, C., *Solid State Nucl. Magn. Reson.* **1997**, 7, (4), 333-336.
- (77) Van Gorkom, L. C. M.; Hook, J. M.; Logan, M. B.; Hanna, J. V.; Wasylishen, R. E., *Magn. Reson. Chem.* **1995**, 33, (10), 791-795.
- (78) Carr, H. Y.; Purcell, E. M., *Phys. Rev.* **1954**, 94, 630.
- (79) Meiboom, S.; Gill, D., *Rev. Sci. Instr.* **1958**, 29, 688-691.
- (80) Larsen, F. H.; Jakobsen, H. J.; Ellis, P. D.; Nielsen, N. C., *J. Phys. Chem. A* **1997**, 101, (46), 8597-8606.
- (81) Lefort, R.; Wiench, J. W.; Pruski, M.; Amoureux, J. P., *J. Chem. Phys.* **2002**, 116, (6), 2493-2501.
- (82) Larsson, A. C.; Ivanov, A. V.; Pike, K. J.; Forsling, W.; Antzutkin, O. N., *J. Magn. Reson.* **2005**, 177, (1), 56-66.

- (83) Autschbach, J., The calculation of NMR parameters in transition metal complexes. In *Principles and Applications of Density Functional Theory in Inorganic Chemistry I*, 2004; Vol. 112, pp 1-48.
- (84) de Dios, A. C., *Prog. Nucl. Magn. Reson. Spectrosc.* **1996**, 29, (3/4), 229-278.
- (85) Fukui, H.; Baba, T.; Inomata, H., *J. Chem. Phys.* **1996**, 105, (8), 3175-3186.
- (86) Ramsey, N. F., *Phys. Rev.* **1950**, 78, 699-703.
- (87) Ramsey, N. F., *Phys. Rev.* **1951**, 83, 540-1.
- (88) Ramsey, N. F., *Phys. Rev.* **1952**, 86, 243-6.
- (89) Harris, K. J.; Bernard, G. M.; McDonald, C.; McDonald, R.; Ferguson, M. J.; Wasylishen, R. E., *Inorg. Chem.* **2006**, 45, (6), 2461-2473.
- (90) Willans, M. J.; Demko, B. A.; Wasylishen, R. E., *Phys. Chem. Chem. Phys.* **2006**, 8, (23), 2733-2743.
- (91) Bagno, A.; Casella, G.; Saielli, G., *J. Chem. Theory Comput.* **2006**, 2, (1), 37-46.
- (92) Jokisaari, J.; Jarvinen, S.; Autschbach, J.; Ziegler, T., *J. Phys. Chem. A* **2002**, 106, (40), 9313-9318.
- (93) Bryce, D. L.; Wasylishen, R. E.; Autschbach, J.; Ziegler, T., *J. Am. Chem. Soc.* **2002**, 124, (17), 4894-4900.
- (94) Rodriguez-Forteza, A.; Alemany, P.; Ziegler, T., *J. Phys. Chem. A* **1999**, 103, (41), 8288-8294.
- (95) Autschbach, J.; Ziegler, T., *J. Chem. Phys.* **2000**, 113, (21), 9410-9418.
- (96) Autschbach, J.; Ziegler, T., *J. Chem. Phys.* **2000**, 113, (3), 936-947.
- (97) Wiberg, K. B.; Hammer, J. D.; Keith, T. A.; Zilm, K., *J. Phys. Chem. A* **1999**, 103, (1), 21-27.
- (98) Wiberg, K. B.; Hammer, J. D.; Zilm, K. W.; Cheeseman, J. R., *J. Org. Chem.* **1999**, 64, (17), 6394-6400.
- (99) Wiberg, K. B.; Hammer, J. D.; Zilm, K. W.; Cheeseman, J. R.; Keith, T. A., *J. Phys. Chem. A* **1998**, 102, (45), 8766-8773.
- (100) Forgeron, M. A. M.; Wasylishen, R. E., *J. Am. Chem. Soc.* **2006**, 128, (24), 7817-7827.
- (101) Feindel, K. W.; Ooms, K. J.; Wasylishen, R. E., **2007**, 9, (10), 1226-1238.

(102) Grutzner, J. B., Chemical Shift Theory. Orbital Symmetry and Charge Effects on Chemical Shifts. In *Recent Advances in Organic NMR Spectroscopy*, Lambert, J. B.; Rittner, R., Eds. Norell Press: Landisville, 1987; pp 17-42.

Chapter 8: The Application of Frequency Swept Pulses for the Acquisition of Nuclear Quadrupole Resonance Spectra

8.1 Introduction

Nuclear quadrupole resonance (NQR) is sometimes referred to as ‘zero-field NMR’ because it involves inducing and observing nuclear spin state transitions in the absence of large static magnetic fields.¹⁻⁴ The NQR phenomenon may be observed for quadrupolar nuclei ($I \geq 1$) in environments which possess non-zero electric field gradients (EFGs). EFGs arise from non-spherically symmetric charge distributions (e.g., from surrounding atoms and bonds) about a nucleus and are described by second-rank tensors which are symmetric and traceless.^{3,4} Diagonalization of the EFG tensor yields three principal components (V_{jj}) which are ordered such that $|V_{11}| \leq |V_{22}| \leq |V_{33}|$. In turn, the diagonalized EFG tensor may be described by two parameters, the quadrupolar coupling constant ($C_Q = eV_{33}Q/h$) and the electric field gradient asymmetry parameter [$\eta_Q = (V_{11}-V_{22})/V_{33}$]. In a pure NQR experiment, the quadrupolar resonance frequencies (ν_Q) are determined by the C_Q and η_Q . For example, there is only one quadrupole resonance frequency for an $I = 3/2$ nucleus which is given by the expression:

$$\nu_Q = \frac{C_Q}{2} \sqrt{1 + \frac{(\eta_Q)^2}{3}}$$

For higher spin nuclei, there are several NQR transitions with distinct values of ν_Q which can be related to C_Q and η_Q via different sets of expressions.⁵

The C_Q and η_Q values are dependent upon the spherical and axial symmetry, respectively, of the ground state electron distribution about the quadrupolar nucleus;

therefore, knowledge of these parameters can lend insight into the structure and symmetry of the local nuclear environment. For these reasons, NQR spectroscopy has found applications in a wide range of areas such as inorganic chemistry, materials science and pharmaceuticals.⁶⁻¹⁵ There is also much interest in the use of NQR for the detection of explosives and illicit narcotics (¹⁴N NQR).¹⁶⁻²² NQR is particularly useful when values of C_Q are extremely large; in such cases, NMR spectra of quadrupolar nuclei are broadened such that detection of an NMR signal can become very difficult.

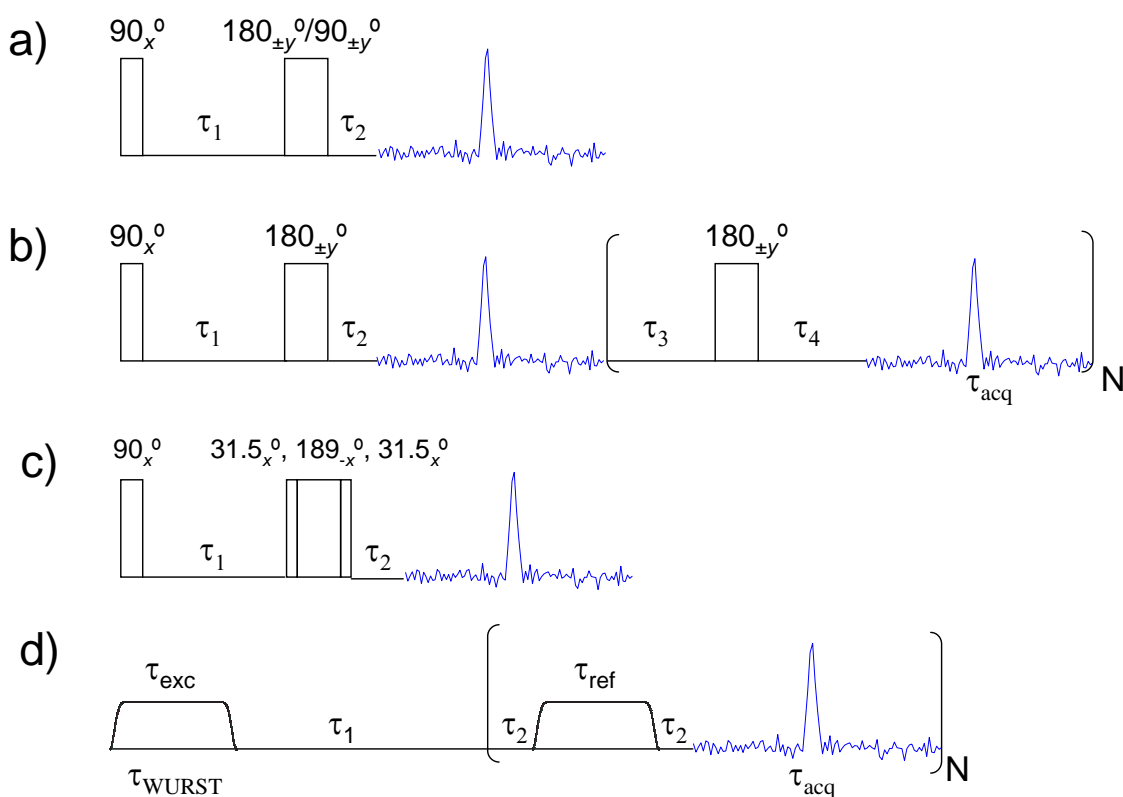


Figure 8.1. Schematic representations of the pulse sequences employed for the acquisition of NQR spectra. (a) Hahn-Echo with 90° excitation pulse and 180° or 90° refocusing pulse. (b) QCPMG sequence with 90° excitation pulse and a train of 180° refocusing pulses (reference 35). (c) The composite echo sequence of Odin (reference 54). (d) WURST-QCPMG sequence with excitation and refocusing pulses with 90° pulses of equal length and sweep rate. Note that for WURST echo spectra the WURST-QCPMG sequence (reference 64) was employed with only a single refocusing pulse and the first echo was acquired ($N = 1$).

In the past, frequency-swept continuous wave irradiation was utilized for acquiring NQR spectra.¹⁻⁴ However, pulsed Fourier transform techniques, such as the standard Hahn-echo sequence²³ and quadrupolar echo sequences²⁴⁻²⁶ (Figure 8.1a), are now the preferred methods for acquiring NQR spectra. Pulse sequences such as the Carr-Purcell Meiboom-Gill (CPMG) sequence²⁷⁻²⁹ (Figure 8.1b) have also been employed for signal enhancement.^{30, 31} These sequences have enabled the acquisition of NQR spectra of nuclei such as ¹⁴N, which typically possesses low resonance frequencies and inherently low signal to noise (S/N).^{21, 22, 32, 33} It should also be noted that CPMG-type sequences have found applications for the signal enhancement of solid-state NMR spectra.³⁴⁻³⁸

While these techniques are successful at increasing the S/N of NQR spectra, there are several commonly encountered problems in NQR spectroscopy. The C_Q and η_Q values are related to the symmetry of the atoms surrounding a nucleus and are characteristic of the particular system under investigation. Therefore, for a given quadrupolar nucleus, resonance frequencies of near 0 MHz to 1000's of MHz are possible. The NQR experiment can be very onerous due to this large range of resonance frequencies, and most often, the experimentalist must spend a great deal of time searching for the NQR resonance(s). If the experimentalist has some prior knowledge of the approximate values of the quadrupolar parameters, the frequency search range may be reduced, and the experimental time decreased. Such information is available from a variety of sources, including previous NQR experiments on analogous systems and from theoretically calculated quadrupolar parameters (i.e., from first principles calculations). However, for many systems, such information is either unavailable or unreliable.

Another commonly encountered problem in NQR spectroscopy is the acquisition of spectra which are severely broadened due to a distribution of resonance frequencies, which most often arise in systems that are disordered at the atomic or molecular level. For example, Taylor et al. have extensively studied arsenic-containing glasses with ^{75}As NQR and have found that the resonances of some samples span several MHz in breadth, as opposed to resonances in ordered solids which are typically several kHz in breadth.³⁹⁻⁴³ The limited excitation bandwidths associated with standard, high-power, rectangular pulses utilized in the Hahn-echo sequence make it necessary to increment the transmitter frequency in order to collect such broad NQR spectra.⁴⁴ Incrementing of the transmitter frequency requires re-tuning and/or re-configuration of the probe, which can be extremely time consuming. Automated NQR systems capable of scanning a wide range of frequencies have been developed to address this problem,⁴⁵⁻⁴⁹ though they are not widely available. Both manual and automated experiments benefit from broadband excitation pulses, which serve to reduce the number of frequency increments, and may aid in mapping out broad distributions of quadrupolar frequencies. In this light, several authors have discussed the development of echo sequences constructed from composite pulses which are capable of exciting broad frequency ranges.⁵⁰⁻⁵⁴ For example, the composite echo sequence of Odin et al. is shown in Figure 8.1c.⁵⁴

Recently, there has been much interest in broadband excitation pulse sequences in solid-state NMR spectroscopy; in particular, the application of *frequency swept* pulses seems to hold significant promise. Bodenhausen et al. first demonstrated the application of echo sequences employing frequency swept pulses for the acquisition of solution ^1H NMR spectra.⁵⁵ Similar pulses have been employed for the excitation and signal enhancement of solid-state NMR spectra of quadrupolar nuclei⁵⁶⁻⁵⁸ and for broadband

decoupling and inversion in solution NMR experiments.⁵⁹⁻⁶² Recently, Bhattacharya and Frydman have demonstrated the application of frequency swept (wideband uniform rate smooth truncated, WURST)⁶¹ pulses for the uniform excitation of wide-line solid-state NMR spectra of quadrupolar nuclei.⁶³ The WURST pulse is applied at a fixed transmitter frequency, with the frequency sweep achieved via simultaneous modulation of the pulse amplitude and phase. WURST pulses differ from conventional rectangular pulses not only in their amplitude and phase modulation over the duration of the pulse, but also because of their generally lower power requirements and longer lengths (typically ca. 50 μ s to several ms). Our research group has recently introduced the WURST-QCPMG pulse sequence (Figure 8.1d).⁶⁴ We have demonstrated that this sequence is useful for acquiring high quality ultra-wide-line NMR spectra of quadrupolar nuclei; this is due in part to the large excitation bandwidths offered by the WURST pulses, and in part to the increased S/N ratios afforded by the CPMG protocol.⁶⁵

Theoretical and experimental investigations have suggested that shaped pulses suitable for NMR experiments can be readily applied to NQR experiments.⁶⁶ For instance, frequency modulated (FM) pulses have previously been applied in NQR experiments by Schurrer and Pérez;⁶⁷ however, these FM pulses possess a non-uniform “zipper”-like excitation profile limited to distinct offset frequencies. Spectral ranges greater than 500 kHz can routinely be uniformly excited with WURST pulses,^{64, 65, 68} with excitation breadth limited by a combination of the resonance frequency and probe bandwidth, suggesting that WURST echo and WURST-QCPMG sequences may find use in NQR experiments for a variety of quadrupolar nuclei.

Herein, we investigate the use of WURST-echo and WURST-QCPMG sequences for the acquisition of NQR spectra. The superior excitation bandwidths of WURST pulse sequences may be helpful in locating NQR resonances during the initial stages of NQR experimentation on samples with unknown resonance frequencies. In order to mimic the search for an NQR signal of unknown frequency, spectra have been acquired with various transmitter offsets (of several hundreds of kHz) from the resonance frequencies. The signals of the NQR spectra obtained with 90° - 90° echo, 90° - 180° echo, Odin's composite echo sequence,⁵⁴ and WURST echo pulse sequences are monitored as a function of transmitter offset frequency. The use of the CPMG protocol for signal enhancement of NQR spectra acquired with WURST pulses is investigated. The utility of the WURST pulses for the acquisition of wide-line NQR spectra is also demonstrated. To this end, we have acquired a portion of the wide-line $^{63/65}\text{Cu}$ NQR spectrum of copper(I) cyanide (CuCN), which is a disordered solid possessing a wide distribution of $^{63/65}\text{Cu}$ nuclear quadrupole resonances.⁶⁹

8.2 Experimental

All samples were purchased from Sigma-Aldrich Inc., and packed into shortened 5 mm glass NMR tubes. All experiments were performed on a Varian Chemagnetics triple resonance T3 MAS NMR probe with a 5 mm coil interfaced with a Varian InfinityPlus console running Spinsight software. Radiofrequency field strengths and pulse lengths were calibrated with on resonance Bloch decay experiments on the respective powdered samples. Note that we refer to the pulses which give maximum signal as " 90° pulses"; however, since all experiments are performed on powdered

samples these actually correspond to pulse angles of ca. 57.3° (1 radian).⁵⁴ All “180°” pulses were double the length of “90°” pulses. For all echo experiments, the interpulse delays, τ_1 and τ_2 , were set such that the full echo was acquired. Hahn-echo and QCPMG sequences employed 16 step phase cycles, while the composite echo sequence employed an 8 step phase cycle. The WURST-QCPMG sequence with N set equal to 1 was used for all WURST echo experiments (Figure 8.1d) and an 8 step phase cycle was employed.⁶³⁻⁶⁵ The required RF field strength (in kHz) for the WURST pulse can be approximated by, $v_{\text{WURST}} = A \cdot R^{1/2} (I + 1/2)^{-1}$, where R is the sweep rate which is equal to 2 times the WURST offset in kHz (e.g., a WURST offset of ± 1000 kHz corresponds to a sweep range of 2 MHz) divided by the pulse length (in ms).⁶⁴ A is a factor which ranges between 0.5 and 0.1 and is inversely proportional to the γ of the nucleus.⁶⁴ For all WURST experiments, the RF field strength of the pulse (v_{WURST}) was experimentally optimized, starting from the theoretical value. The value of v_{WURST} which gave maximum S/N was utilized. In all cases, WURST-80 pulse shapes were used with pulse lengths of 50 μs .⁶¹ The WURST pulses were constructed from 900 individual pulse elements (ca. 55.6 ns in length) whose phases and amplitudes were varied to attain the desired waveform. The minimum pulse element length of the InfinityPlus waveform tool is 50 ns. The value of τ_1 for WURST experiments was set according to the formula $\tau_1 = 0.5 \cdot (\tau_{\text{WURST}} + \tau_{\text{acq}})$, where τ_{WURST} and τ_{acq} are the WURST pulse length and acquisition time of each echo, respectively. Spectral widths of 2 MHz, 1 MHz and 2.5 MHz were employed for ^{35}Cl , $^{63/65}\text{Cu}$, and ^{75}As NQR, respectively. A spectral width of 200 kHz was employed for the point-by-point $^{63/65}\text{Cu}$ NQR spectrum. Recycle delays of 0.2 s, 0.4 s and 0.08 s were employed for ^{35}Cl , ^{75}As and $^{63/65}\text{Cu}$ NQR experiments, respectively.

Recycle delays were experimentally optimized on each sample to ensure complete longitudinal relaxation of the magnetization was obtained. All other relevant experimental parameters are listed in Appendix G (Tables G1-G3). **CAUTION:** Due to the lengths of the WURST pulses and the short recycle delays typical of NQR experiments, the duty cycle of the probe should be carefully monitored. All spectra were processed by applying three zero fills followed by Fourier transformation. For all echo spectra the full echo was acquired and Fourier transformed and the spectrum was then magnitude calculated. The S/N and integrated intensity (II) were measured with the default algorithms in the Spinsight software package. The S/N corresponds to the ratio of the peak intensity of the resonance divided by the average absolute intensity of the baseline regions. The baseline regions on either side of the NQR resonance were employed for S/N measurements. WURST-QCPMG pulse sequences for Varian (InfinityPlus - Spinsight) and Bruker (Avance - TopSpin) spectrometers are available from the authors upon request.

8.3 Results and Discussion

^{35}Cl , $^{63/65}\text{Cu}$ and ^{75}As were chosen for this work due to their high natural abundances and relatively high quadrupolar frequencies (between 34 and 116 MHz) in a variety of structural motifs. The relevant nuclear properties are listed in Table 8.1.⁷⁰ All of the samples discussed herein have previously been characterized by NQR spectroscopy.

Table 8.1. Nuclear Properties⁷⁰

Isotope	Nuclear Spin	Natural Abundance (%)	Quadrupole Moment (Q/fm^2)	Magnetogyric Ratio ($\gamma/10^7 \text{ rad s}^{-1} \text{ T}^{-1}$)
³⁵ Cl	3/2	75.8	-8.2	2.624198
⁶³ Cu	3/2	69.2	-22.0	7.111789
⁶⁵ Cu	3/2	30.8	-20.4	7.60435
⁷⁵ As	3/2	100.0	31.4	4.596163

⁷⁵As NQR. ⁷⁵As NQR spectra of As₂O₃ (arsenolite phase) were previously acquired by Taylor over a range of temperatures.⁷¹ We observed a resonance at 116.234 MHz at 294 K which is close to the frequency of 116.222 MHz (300 K) reported by Taylor. In order to mimic the initial stages of NQR experiments on a sample with unknown resonance frequencies (i.e., searching a large frequency range for a single quadrupolar resonance frequency), ⁷⁵As NQR spectra have been acquired at variable transmitter offset frequencies. The transmitter frequency was incremented in steps of 100 kHz for frequencies close to the NQR frequency, while a larger increment of 200 kHz was employed for offsets of 600 kHz and above. At each transmitter frequency the probe was tuned and ⁷⁵As NQR spectra were then acquired with the four different pulse sequences (spectra are pictured in Fig. G1 for on-resonance irradiation). The integrated intensity (II) of the NQR spectra as a function of transmitter offset is shown in Figure 8.2 (numerical values of S/N and II of the spectra are listed in Table G4).

Before the effects of transmitter offsets are reviewed it is important to discuss the factors which will influence the II and S/N of the NQR spectra acquired with the transmitter on resonance (e.g., the intensity points in Figure 8.2 with 0 kHz transmitter offsets). The main factor which affects the II and S/N of all spectra acquired with echo pulse sequences is the length of time between the excitation and refocusing pulses, during which transverse relaxation (T_2) of the magnetization occurs (i.e., the τ_1 time period in the

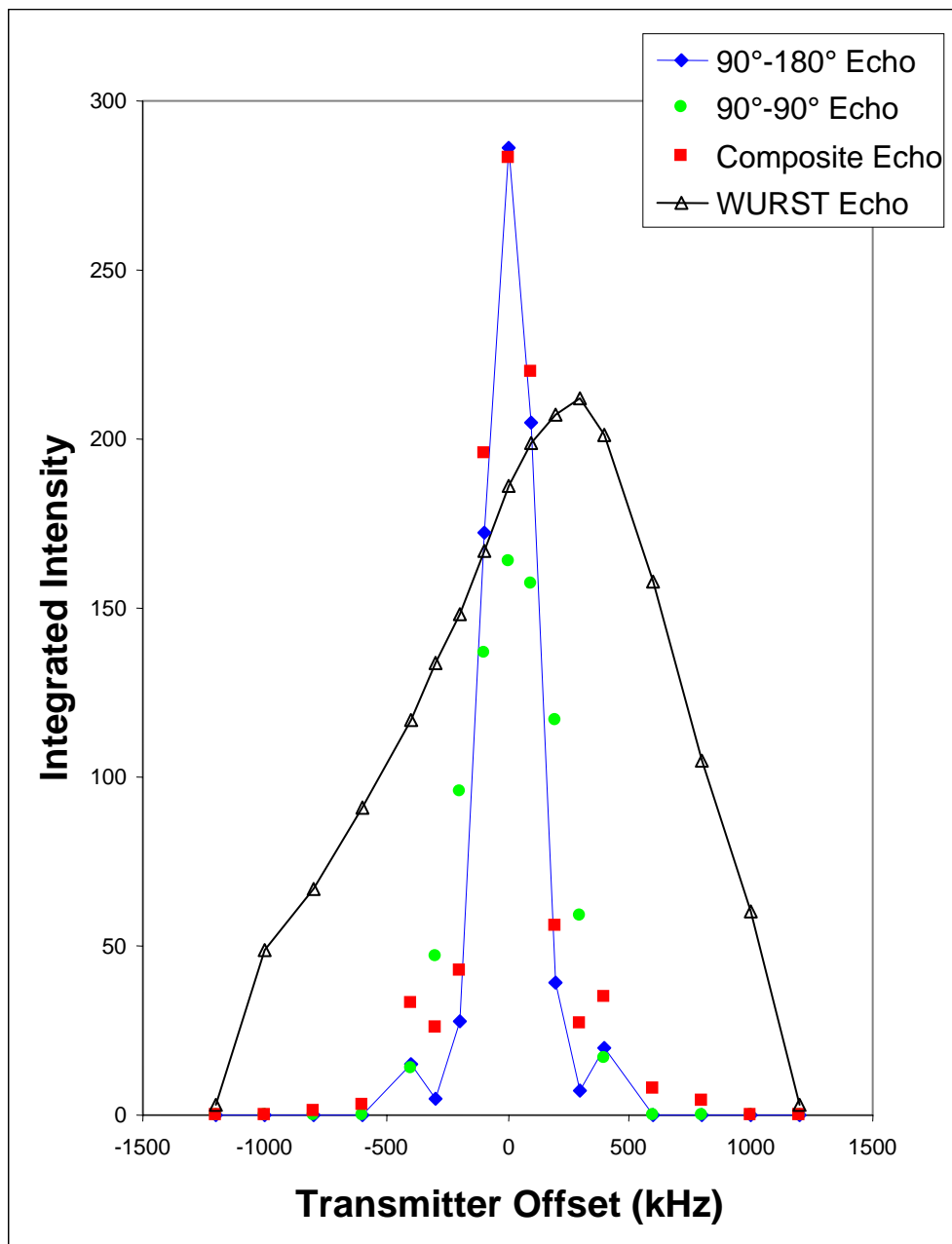


Figure 8.2. Integrated intensity of the ^{75}As NQR spectra of As_2O_3 (arsenolite) as a function of transmitter offset from the resonance frequency for the 90° - 180° echo, 90° - 90° echo, composite echo and WURST echo pulse sequences. For each transmitter offset the probe was tuned using reflected power measurements available in Spinsight, followed by acquisition of the spectra with the five pulse sequences. For clarity the intensity points have been connected by lines for the 90° - 180° echo and WURST echo spectra.

echo sequences, Figure 8.1). The τ_1 values listed in Appendix G are those that were input into the pulse sequences on the spectrometer. These values are corrected within the pulse sequence programs and do not describe the total time for which the signal is allowed to dephase after the excitation pulse. For this reason, we will refer to the total dephasing time period as τ_d . Values of τ_d employed for experiments are also listed in Appendix G.

In the case of the echo sequences employing conventional pulse sequences, τ_d will be close in value to τ_1 due to the relatively short pulse widths of conventional refocusing pulses. However, the WURST echo sequence utilizes pulse widths which are much longer than conventional pulses (i.e., 50 μ s). Subsequently, significantly more transverse relaxation occurs from the time a particular frequency isochromat is excited by a WURST pulse to the time it is refocused by the next WURST pulse, in comparison to conventional echo sequences. For these reasons the τ_1 values are corrected within the pulse sequence to account for lengths of the WURST pulses and for the WURST echo sequence and $\tau_d = \tau_1 + \tau_2$. The S/N and II of the 90°-180° echo sequences and WURST echo sequences with various τ_d times are listed in Table G5. The value of τ_d dramatically affects the II and S/N of the 90°-180° echo and WURST echo spectra due to the relatively short $T_2(^{75}\text{As})$ value for As_2O_3 at room temperature. For example, NQR spectra acquired with the 90°-180° echo sequence using τ_d values of 145.7 μ s and 78.35 μ s, yield II values of 286 and 443, respectively. It should be noted that if τ_d is too short, it is not possible to acquire the full echo, and this truncation leads to lineshape and baseline distortions, making it difficult to obtain meaningful II and S/N measurements. For these reasons, we set τ_d for all echo experiments such that the full echo was acquired and the values of τ_d are approximately equal.

There are several key observations that can be made from Figure 8.2. First, we will consider the case where the transmitter is on resonance or close to the resonance frequency (less than a 100 kHz offset). It is clear that NQR spectra acquired with the 90°-180° echo and composite echo sequences possess higher Π ($\Pi > 280$) and S/N ($S/N > 1200$) than those acquired with the WURST echo sequence ($\Pi = 186$, $S/N = 871$). For the WURST spectra acquired on resonance we tested the effects of the RF field of the WURST pulse on the Π and S/N of NQR spectra. Experiments conducted with variable WURST pulse widths (and different experimentally optimized RF field strengths) show no appreciable variation in Π (Table G6). We therefore attribute the reduced Π and S/N of the WURST echo to the fact that the refocusing pulse is acting as a 90° pulse since it is the same length and power as the initial pulse (e.g., the Π and S/N of the WURST echo sequence are similar to the 90°-90° echo sequence).

In order to try and improve the S/N of the WURST echo spectra we have attempted to implement a 90°-180° WURST echo sequence. Bhattacharya and Frydman previously outlined several approaches for obtaining a WURST 180° (π) refocusing pulse for solid-state NMR of quadrupolar nuclei.⁶³ The first approach is to employ a WURST π -pulse which sweeps over the range of frequencies at double the rate of the excitation pulse ($R_{\text{ref}} = 2R_{\text{exc}}$). This can be accomplished in two ways: (1) by employing a WURST π -pulse which is half the time length of the excitation pulse ($\tau_{\text{exc}} = 2\tau_{\text{ref}}$) and sweeps over the same frequency range, or, (2) by employing a WURST refocusing pulse which is identical in length to the excitation pulse ($\tau_{\text{exc}} = \tau_{\text{ref}}$), but sweeps over double the frequency range. They found that the optimal RF field for the refocusing WURST π -pulse (ν_{ref}) was ca. 4.7 times higher than that of the excitation pulse (ν_{exc}),⁶³ while we

found experimentally optimized ν_{ref} values which were ca. 1.5 to 1.7 times higher than ν_{exc} (Table G7). In both cases, our “90°-180°” WURST echo spectra are similar to the corresponding 90°-90° WURST echo spectra in terms of S/N and II (Table G7). A second approach for obtaining a WURST π -pulse is to utilize a refocusing pulse of the same length ($\tau_{\text{exc}} = \tau_{\text{ref}}$) and same sweep rate ($R_{\text{ref}} = R_{\text{exc}}$); however, ν_{ref} is set to ca. 3.2 times larger than ν_{exc} . In this case, we found that maximum signal is obtained when $\nu_{\text{exc}} \approx \nu_{\text{ref}}$ (identical to a 90°-90° WURST echo spectrum), consistent with our previous results obtained from the solid-state NMR spectra of quadrupolar nuclei.⁶⁴ It is worth noting that the WURST pulses employed herein are much shorter (less than 100 μs) than those employed by Bhattacharya and Frydman (ca. 1 – 2 ms), and hence, the pulses may be operating in different adiabatic regimes (this may account for the differences in ratios of $\nu_{\text{ref}}:\nu_{\text{exc}}$ between our experiments and Frydman’s experiments). It may be possible to obtain WURST π -pulses by employing longer pulse widths, however, this would necessitate the use of much longer echo delays and result in NQR spectra with lower S/N.

At relatively large transmitter offsets (i.e., 200 kHz and greater) the WURST echo sequence affords higher II and S/N NQR spectra than those acquired with conventional echo sequences. For instance, with WURST pulses, NQR spectra with $\text{II} > 48$ are observed for transmitter offsets as large as 1000 kHz. Clearly, the WURST pulses offer superior excitation bandwidths in comparison to the conventional rectangular pulses. Considering these observations, a strategy for the observation of NQR resonances of unknown frequencies emerges. The frequency range of interest can be surveyed with a WURST echo or WURST-QCPMG sequence using large transmitter offset increments. In this case, transmitter increments of ca. 2000 kHz could be reasonably employed with

the WURST echo sequence in the search for an NQR resonance of unknown frequency, while the composite echo sequence would be limited to transmitter increments of ca. 800 kHz. Once the approximate frequency of the NQR resonance is identified, the transmitter could be set to the resonance frequency and a high quality spectrum could then be obtained with a conventional sequence.

Another important observation is the distinct asymmetry in the peak intensities in Figure 8.2. For all of the pulse sequences, higher intensities are observed for spectra acquired with positive transmitter offsets in comparison to those acquired with negative transmitter offsets of the same magnitude. This asymmetry is particularly pronounced for the WURST echo spectra. For example, for the WURST echo spectrum acquired at an offset of +300 kHz, $II = 212$, while at an offset of -300 kHz, $II = 134$. Additionally, the WURST echo NQR spectra unexpectedly possess higher II when the transmitter is +300 kHz from resonance ($II = 212$), rather than when the transmitter is on resonance ($II = 186$).

What is the origin of this asymmetry in II and S/N for equally spaced transmitter offsets of opposite sign? Initially, we thought this asymmetry may be due to the sweep direction of WURST pulses. Given the lengths of the WURST pulses (50 μ s) and the fact that the pulse is linearly swept across the specified frequency range, it is possible that transverse relaxation (T_2) of the resonance may occur if the resonance is excited near the start of the first WURST pulse waveform; however, when a pulse with opposite sweep direction was applied, spectra with an identical intensity profile were obtained (not shown). Our research group has previously observed similar asymmetries in ^{14}N WURST-QCPMG NMR spectra, which were found to result from frequency sweep

induced population transfers.⁶⁸ However, this is very unlikely, given that there are only two quantized energy levels, and that this asymmetry is observed in spectra using WURST pulses with opposite sweep directions. Both of these mechanisms are unlikely, given that this asymmetry in intensities is observed for all of the other pulse sequences, although, the asymmetry is not as pronounced as for the WURST echo spectra.

Therefore, we attribute the asymmetry in Figure 8.2 to a difference in the characteristic impedance values of the excitation circuit and receiver circuit of the spectrometer (which we refer to as an “impedance mismatch”). This phenomenon has recently been reported by Marion and Desvaux⁷² and Muller et al.⁷³ In both manuscripts, the authors describe the observation of an impedance mismatch via the acquisition of spin-noise NMR spectra. It was found the S/N of the spin-noise NMR spectra improved when the probe was detuned (as indicated by standard tuning protocols). This is because the standard tuning procedures available with most commercial spectrometers result in tuning of the probe such that it is optimized for excitation (e.g., matched and tuned to the amplifier circuit), rather than for receiving of signals.^{72,73} These impedance mismatches are readily detected in spin-noise NMR spectra, because they require no excitation pulses and their S/N and phases are only dependent upon impedance matching the probe to the receiver.

In our work the probe was coarsely tuned by observing an impedance-frequency response curve (e.g., a ‘wobble’ curve) and fine tuned by minimizing the level of reflected power. This method optimizes the tuning of the probe for excitation only. Figure 8.2 indicates that there is an approximate difference of 300 kHz between the optimal receiver and excitation tuning of the probe, which is consistent with the

frequency differences of several hundred kilohertz observed by Desvaux and Muller et al.^{72, 73} In order to confirm that there was an impedance mismatch, the probe was tuned in the usual manner to 116.534 MHz, which is 300 kHz *higher* than the resonance frequency. The transmitter frequency was then placed on resonance (116.234 MHz), and spectra with the five different pulse sequences were acquired. This yielded spectra with higher II and S/N, except for the spectrum acquired with 90°-90° echo sequence (Figure 8.3, spectra are shown in Figure G2). Finally, additional experiments were conducted which involved re-calibration of the pulse widths to account for the de-tuning of the probe (the 90° pulse width increases from 1.6 μs to 2.1 μs). These experiments yield S/N and II values which are between 1.3 to 1.4 times larger than those obtained when the probe is tuned to the transmitter frequency (i.e., on-resonance). These gains are observed for all of the pulse sequences (compare first data set to last data set for each pulse sequence in Figure 8.3).

We have also investigated the influence of the receiver gain setting on the II and S/N values when the probe is optimized for excitation (tuned on resonance) and when the probe is optimized for reception (tuned +300 kHz off resonance) and re-calibrated pulse widths are employed (Table G8). The II is observed to steadily increase with the receiver gain level, while the S/N ratio remains constant. Marion and Desvaux have observed that at higher receiver gain settings, the S/N ratio of solution ¹H NMR spectra is progressively lowered and balances the gains in signal (II), due to uniform digitization of the probe noise at higher receiver gain settings.⁷² However, they also point out that if the pre-amplifier noise level is significant, then it is expected that tuning the probe to the receiver optimum will always lead to improved S/N ratios.⁷² This suggests that in our system, the

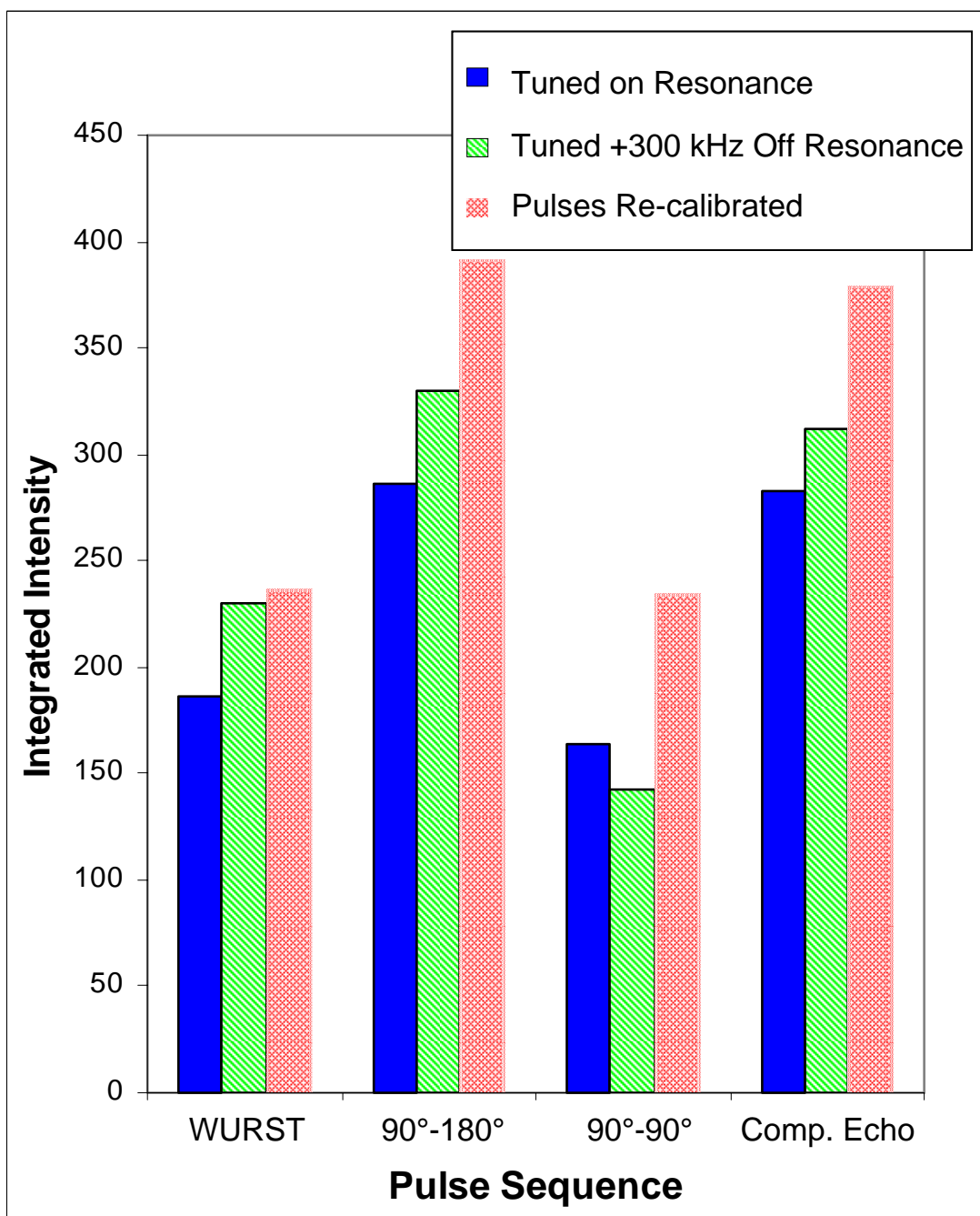


Figure 8.3. Integrated intensity of the ^{75}As NQR spectra of As_2O_3 acquired when the probe has been tuned on resonance (116.234 MHz), tuned +300 kHz off resonance (116.534 MHz), and when the probe is tuned +300 kHz off resonance and the pulse widths have been re-calibrated. The transmitter was set to the resonant frequency (116.234 MHz) in all cases. Spectra were acquired with the four different pulse sequences. When the probe is tuned +300 kHz off resonance and re-calibrated pulses are employed, the II of the NQR spectra is 1.3 to 1.4 times larger.

pre-amplifier is the predominant noise source, as we observe improved S/N ratios when the probe is tuned to the receiver optimum for a range of receiver gain settings.

The superior excitation bandwidths of the WURST pulses enable experiments which allow for the detection of impedance mismatches between reception and excitation pathways, even when the differences are on the order of several hundred kHz. WURST echo spectra could be acquired with variable offsets and the II or S/N can be plotted in a manner similar to that presented herein to detect the optimal receiver tuning. Marion and Desvaux have demonstrated that this mismatch can be eliminated by altering the impedance of the amplifier pathway by changing the lengths of transmission cables.⁷² In the future, we intend to utilize the WURST echo sequence in order to better impedance match our reception and excitation pathways. This approach should be applicable to NQR, as well as solution and solids NMR experiments, and would be much faster than acquiring spin-noise NMR spectra. It would also be possible to detect impedance mismatches by monitoring the S/N of a spectrum acquired with conventional pulses while the transmitter is placed on resonance and the probe tuning frequency is varied. However, if there is a large impedance mismatch, the pulse widths of the conventional pulses will increase due to reflection of power by the probe.⁷² This necessitates time consuming pulse width calibrations for each probe tuning increment. Therefore, WURST pulses should be better suited to detect impedance mismatches.

Signal Enhancement with the CPMG Protocol. Marino and Klainer first demonstrated in 1977 that the CPMG pulse sequence affords large S/N gains in NQR.³¹ CPMG type sequences are now frequently employed in order to enhance the signal of unreceptive NQR nuclei such as ^{14}N .^{18, 21, 22, 30} For these reasons, the S/N of ^{75}As NQR spectra acquired with the QCPMG³⁵ and WURST-QCPMG sequences⁶⁴ (Figure 8.1) are

compared to the corresponding single echo sequences. In order to obtain “spikelet-free” spectra, the spin echoes obtained from the ^{75}As QCPMG and WURST-QCPMG FIDs were summed into a single time domain echo.⁷⁴ These single time domain echoes were then Fourier transformed to produce spectra which are similar in appearance to conventional echo spectra.⁷⁴ The QCPMG and WURST-QCPMG spectra are compared to echo spectra in Figure G3 and II and S/N measurements are shown in Table 8.2. The QCPMG spectra are of higher II and S/N than the WURST-QCPMG when the number of echoes (MG loops) and echo size is the same. This is consistent with the II and S/N observed for the corresponding echo sequences.

Table 8.2. Integrated Intensity and Signal to Noise of Single Echo and QCPMG ^{75}As NQR Spectra

Echo Size	τ_{acq} (μs)	MG Loops (N) ^a	WURST-QCPMG ^b		QCPMG ^c	
			II	S/N	II	S/N
512	204.8	1	186	871	286	2506
512	204.8	8	624	2064	904	3293
256	102.4	24	2294	4700	3834	5741
^d 140	56.0	80	5227	4117	9172	5427

^aThis is the number of refocusing pulses and echoes that were acquired. For the case of MG Loops = 1 the II and S/N from the 90° - 180° echo and WURST echo spectra were used. ^bFor all WURST-QCPMG experiments $\tau_2 = 20 \mu\text{s}$. τ_1 can be determined using the formula given in the Experimental section. ^cFor all QCPMG experiments $\tau_2 = 30 \mu\text{s}$ and $\tau_3 = \tau_4 = 20 \mu\text{s}$. ^dSmall echo sizes lead to truncation of the individual echoes in the time domain. This causes lineshape and baseline distortions leading to skewed II and S/N values.

While the $T_2(^{75}\text{As})$ and $T_1(^{75}\text{As})$ time constants are relatively short for As_2O_3 at room temperature it is possible to acquire multiple echoes for ca. 4.5 ms. It can be readily seen that the acquisition of multiple echoes yields significant improvements in II and S/N of the NQR spectra. For example the acquisition of 8 MG loops leads to ca. three-fold increase in the II values for both the WURST-QCPMG and QCPMG pulse sequences, in

comparison to the corresponding single echo experiments. As expected for CPMG experiments, the largest signal enhancements are obtained when a large number of tightly spaced echoes are acquired. When the echo size is 256 points and 24 echoes are acquired the II is observed to increase by factors of 12.3 and 13.4 for WURST-QCPMG and QCPMG, respectively. Acquisition of 80 echoes (with each echo consisting of 140 points) leads to gains in the II by factors of 28 and 32 for the WURST-QCPMG and QCPMG sequences, respectively (last entries, Table 8.2). However, it should be noted that when the echo size is small, truncation of the individual echoes results in broadening of the NQR resonances as well as baseline distortions (Figure G3), rendering the measured II and S/N values unreliable. Clearly, the CPMG protocol can be used to enhance the signal of NQR spectra acquired with WURST pulses. The WURST-QCPMG sequence can provide significant signal enhancement and should make WURST pulses more competitive with conventional pulses, while still retaining their larger excitation bandwidths.

³⁵Cl NQR. A series of experiments similar to that described above has been conducted for the acquisition of ³⁵Cl NQR spectra of 4-chloropyridine. This was done in order to test the use of WURST pulses for the acquisition of spectra of a less receptive NQR nucleus and the performance of the sequence at a lower resonance frequency. The ³⁵Cl NQR spectrum of 4-chloropyridine at a temperature of 77 K was acquired by Bray et al. and a resonance at 34.789 MHz was observed.⁷⁵ We observed a resonance at 35.352 MHz at a temperature of 294 K. In Figure 8.4, the II of the ³⁵Cl NQR spectra as a function of transmitter offset is shown (II and S/N values given in Table G9) for the four different pulse sequences. Spectra acquired with the four pulse sequences and the transmitter on resonance are pictured in Figure G4. This sample possesses a relatively

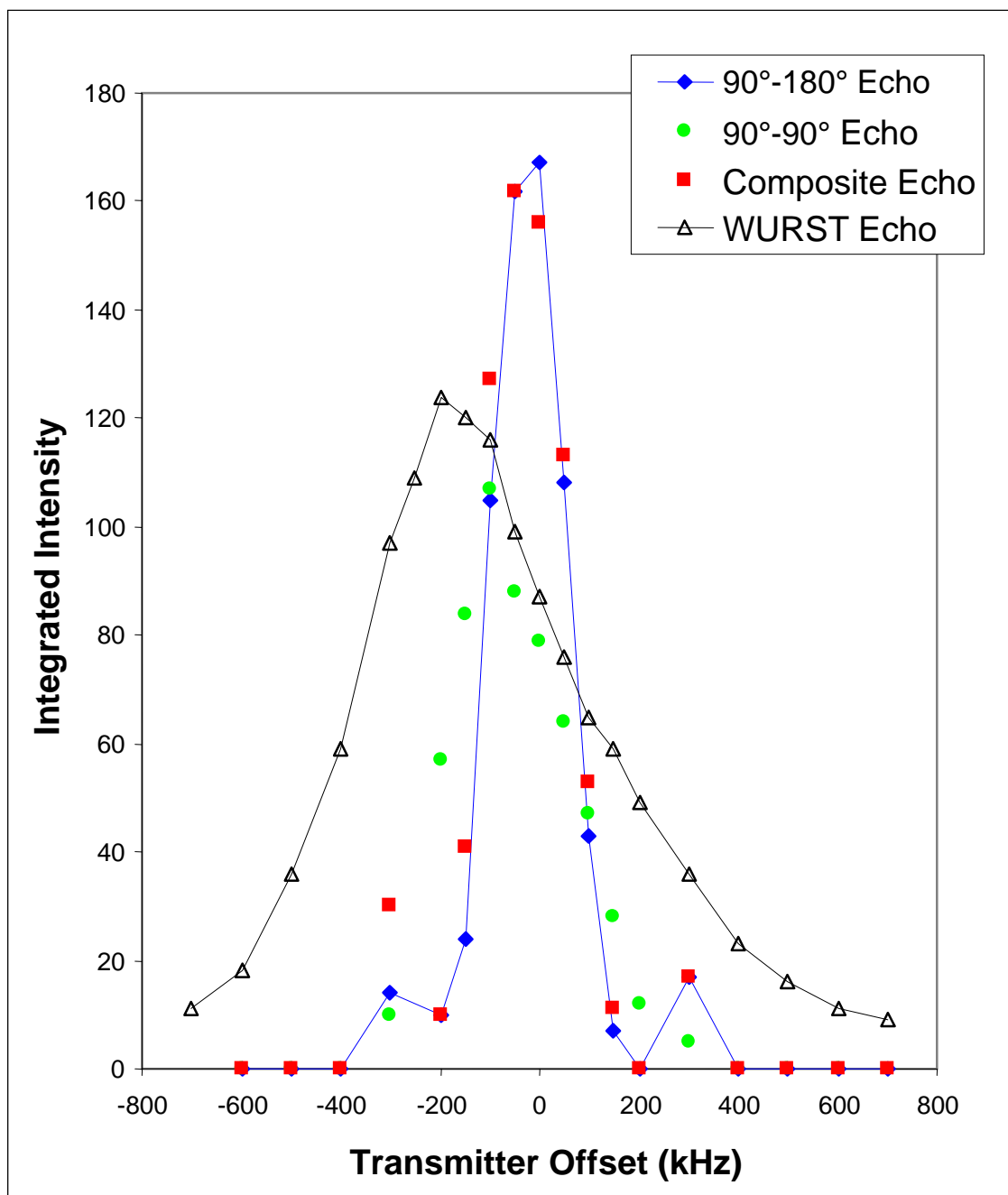


Figure 8.4. Integrated intensity of the ^{35}Cl NQR spectra of 4-chloropyridine as a function of transmitter offset from the resonance frequency for the 90° - 180° echo, 90° - 90° echo, composite echo and WURST echo. For each transmitter offset the probe was tuned using reflected power measurements available in Spinsight. Spectra with the four pulse sequences were then acquired. For clarity the intensity points have been connected by lines for the 90° - 180° echo and WURST echo spectra.

long T_2^* (^{35}Cl), and hence, a fairly long τ_d value (ca. 275 μs) is required to acquire the full echo.

From Figure 8.4 it is once again clear that conventional echo pulse sequences provide superior S/N in comparison to the WURST sequence for spectra acquired with small transmitter frequency offsets (less than 100 kHz). At large frequency offsets (150 kHz and higher) the WURST pulses are much more efficient. ^{35}Cl NQR spectra of II and S/N of 18 and 13, respectively, may be observed with WURST pulses at transmitter offsets as large as 600 kHz. Therefore, in an NQR experiment involving the search for an unknown quadrupolar resonance of a similar frequency to this, it would be possible to use 1.2 MHz transmitter increments to locate the resonance, as opposed to ca. 600 kHz with conventional echoes, effectively reducing the total number of experiments by a factor of two.

The ^{35}Cl NQR configuration of the spectrometer components once again displays an impedance mismatch between the excitation and receiving pathways. In this case the receiving optimum is located at ca. -200 kHz from the excitation optimum as indicated in Figure 8.4. The II was measured for the peaks in the ^{35}Cl NQR spectra acquired with the probe tuned on resonance (35.352 MHz) and tuned -200 kHz off resonance (35.152 MHz), with the transmitter fixed on resonance in both cases (Figure 8.5). II and S/N increases of ca. 1.6 are observed when the probe is tuned to -200 kHz from the resonance frequency and the pulse widths are re-calibrated. These gains in II and S/N are once again relatively constant for a variety of receiver gain settings (Table G10). Although there is a smaller frequency difference between the receiving and excitation optimum for the ^{35}Cl NQR probe configuration, the drop off in signal to noise is more severe than that

observed for the ^{75}As NQR spectra. We attribute this to the decreased bandwidth of the probe for the ^{35}Cl NQR configuration (*vide infra*).

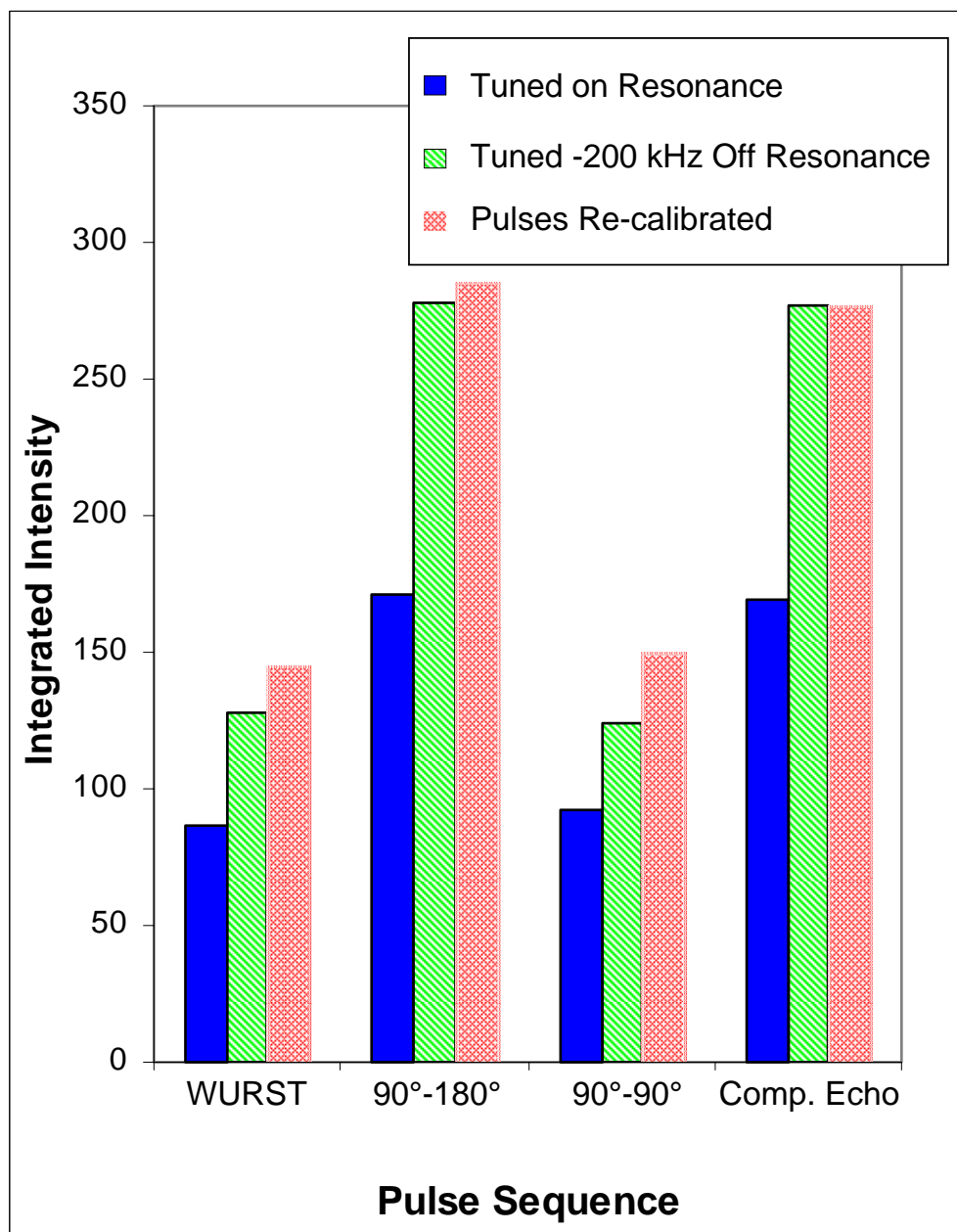


Figure 8.5. Integrated intensity of the ^{35}Cl NQR spectra of 4-chloropyridine acquired when the probe has been tuned on resonance (35.352 MHz), tuned -200 kHz off resonance (35.152 MHz) and when the probe is tuned -200 kHz off resonance and the pulse widths have been re-calibrated. The transmitter was set to the resonant frequency (35.352 MHz) in all cases. Spectra were acquired with the four different pulse sequences. When the probe is tuned -200 kHz off resonance and re-calibrated pulses are employed, the II of the NQR spectra is 1.64 to 1.67 times larger.

Factors Limiting the Excitation Bandwidth of WURST Pulses. While the WURST pulses display impressive excitation bandwidths, it is worthwhile to consider the factors which limit them. For example, ^{35}Cl and ^{75}As NQR experiments employed WURST pulses with a sweep range of ± 1000 kHz and ± 1400 kHz, respectively, while resonances with offsets larger than 600 kHz and 1200 kHz, respectively, possess very low S/N. In these cases, the bandwidth and quality factor (Q-factor) of the probe are the main limitations on the apparent excitation bandwidth of the WURST pulses. The Q-factor of the probe determines the power profile of the probe, which affects both the efficiency of excitation pulses as well as the detection of signal(s).

Muller et al. have suggested that the Q-factor of the probe can be approximated by dividing the resonance frequency (ν_Q) by the FWHH measured from the inflection of the wobble curve.⁷³ For the ^{35}Cl NQR configuration of the probe (35.346 MHz) a FWHH value of approximately 350 kHz was observed in the wobble curve giving a Q-factor of approximately 101 (Figure G6). For the ^{75}As NQR probe configuration (116.234 MHz) a FWHH value of approximately 600 kHz was observed in the wobble curve giving a Q-factor of approximately 194. The large probe bandwidth of the ^{75}As NQR experiments enables resonances to be detected at offsets larger than ± 1000 kHz, whereas the smaller probe bandwidth in the ^{35}Cl configuration limits detection of signals to offsets of ca. ± 600 kHz. For a given resonance frequency lower Q-factor values will lead to larger probe bandwidths; however, the signal is also proportional to the Q-factor of the probe.⁷⁶ For nuclei such as ^{75}As and ^{35}Cl which are highly abundant and typically possess high resonance frequencies (and high S/N), it may be worthwhile to attempt experiments with lower Q-factor probes. This could afford larger excitation and detection bandwidths at

the expense of lower S/N. Aside from limitations imposed by the probe, the required power for the WURST pulses also increases with increasing sweep width, necessitating the use of high powers and/or longer pulses. Large sweep widths and/or long pulse lengths may lead to unacceptably high transmitter duty cycles, although sweep widths of ± 1.5 MHz can be safely achieved for almost all nuclei with 50 μ s WURST pulses.

Acquisition of Wideline NQR Spectra. Systems such as amorphous glasses,¹⁰ semiconductors,⁴³ polymers² and high temperature superconductors^{9, 11, 15} possess varying degrees of disorder at the atomic level which results in distributions in C_Q and η_Q . This in turn gives rise to distributions of NQR frequencies and correspondingly broad NQR spectra. Two methods for acquiring wideline NQR spectra are commonly employed. The traditional method involves stepping the transmitter frequency in evenly spaced increments and acquiring a spin-echo at each frequency (we will refer to this as the “point-by-point” method).⁴³ The echo intensities are then plotted as a function of transmitter frequency and used to construct the NQR spectrum. The second approach is similar to the first approach in that spin-echoes are acquired at evenly spaced transmitter increments; however, each echo is Fourier transformed and then co-added in the frequency domain to form the total spectrum.^{44, 77} Wideline solid-state NMR spectra are frequently acquired in this manner as well.^{78, 79} This method is advantageous because it enables sharp spectral features to be detected while requiring fewer transmitter offsets than the point-by-point method. The superior excitation bandwidths of the WURST pulses should make them ideal for acquiring wideline NQR spectra in a similar manner.

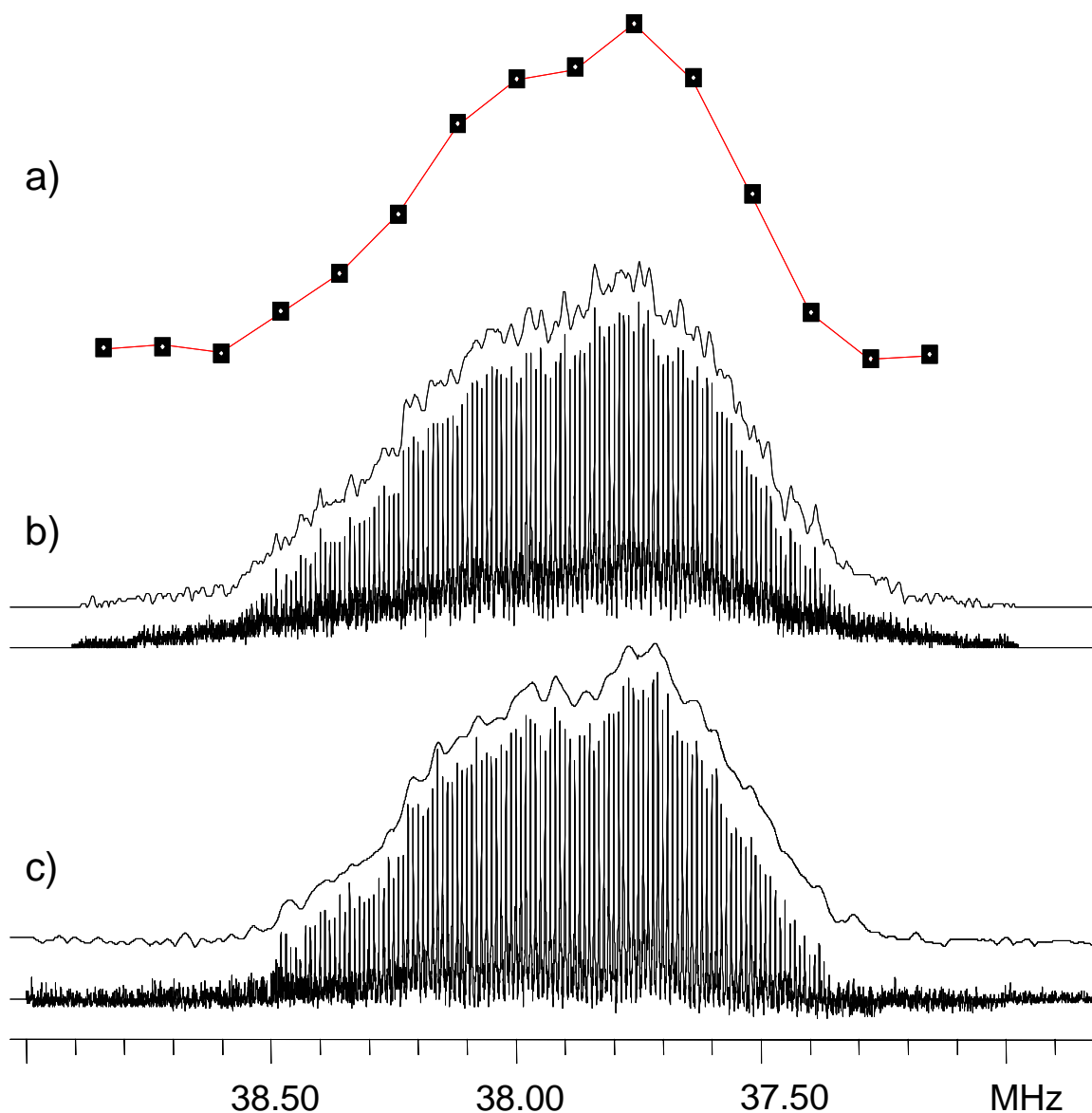


Figure 8.6. Wideline $^{63/65}\text{Cu}$ NQR spectrum of the broad resonance of CuCN centered around 37.9 MHz. (a) “Point-by-point” spectrum (see text for details) acquired with the QCPMG pulse sequence and low power pulses ($10\ \mu\text{s}$ 90° pulse). A transmitter increment of 120 kHz was employed and 15 echoes were acquired (1.3 hours total acquisition time). (b) QCPMG spikelet spectrum and echo spectrum formed from time domain co-addition of the echoes. A transmitter increment of 120 kHz and high-power 90° pulses ($0.7\ \mu\text{s}$) were employed. 12 sub-spectra were required to form the total pattern (1.3 hours total acquisition time). (c) WURST-QCPMG spikelet spectrum and echo spectrum formed from time domain co-addition of the echoes. A transmitter increment of 250 kHz was employed and 6 sub-spectra were required to form the total pattern (0.8 hours total acquisition time).

In order to investigate the utility of WURST pulses for the acquisition of wide-line NQR spectra, we have acquired a portion of the $^{63/65}\text{Cu}$ NQR spectrum of copper(I) cyanide. The $^{63/65}\text{Cu}$ NQR spectrum of CuCN consists of four broad peaks (FWHM > 400 kHz) separated by several MHz with some of the peaks containing overlapping ^{65}Cu and ^{63}Cu resonances from distinct chemical environments.⁶⁹ We have acquired the approximately 1 MHz broad $^{63/65}\text{Cu}$ resonance centered at 37.9 MHz (Figure 8.6). The QCPMG sequence was used to acquire a point-by-point spectrum (Figure 8.6a) by summing the echoes in the QCPMG echo train in the time domain.⁷⁴ The resultant echo was then magnitude calculated and the II was measured and plotted as a function of transmitter frequency. Echo intensities were measured at 15 transmitter offset frequencies, with 4000 scans per sub-spectrum (0.08 s recycle delay) and a total experimental time of 1.3 hours. The asymmetric shape of the point-by-point spectrum is consistent with the previously reported spectrum.⁶⁹

The QCPMG and WURST-QCPMG spectra are shown in Figure 8.6b and 6c, respectively. Both spectra were formed by Fourier transforming the individual sub-spectra and co-adding them in the frequency domain. Spikelet spectra and echo spectra are shown for both pulse sequences. Spikelet spectra were obtained by directly Fourier transforming the train of echoes from the CPMG spectra. Echo spectra were obtained from the QCPMG spectra in the manner described in the “Signal Enhancement with the CPMG Protocol” section. A transmitter increment of 120 kHz was employed for the QCPMG sequence (90° pulses of 0.7 μs); while a transmitter increment of 250 kHz was employed with the WURST-QCPMG sequence (± 1000 kHz sweep ranges). This enabled

the WURST-QCPMG spectrum to be acquired with only 6 sub-spectra while the QCPMG spectrum required 12 sub-spectra to form the total pattern. However, the lower S/N of the WURST spectra required that 6000 scans be acquired for each sub-spectrum, while only 4800 scans were required with the QCPMG sequence to obtain similar S/N ratios. It can also be seen that the spikelet and echo versions of the QCPMG and WURST-QCPMG spectra provide an excellent overall match with the shape of the point-by-point spectrum, indicating that accurate lineshapes can be obtained with either sequence.⁸⁰ However, despite the lower S/N of the WURST-QCPMG spectra the pattern could be acquired in a total time of 0.8 hours, while 1.3 hours of time were required for the QCPMG sequence. This also does not include the additional time required for the spectrometer operator to step the transmitter frequency and re-tune the probe. WURST-QCPMG is clearly the most efficient method for acquiring broad NQR spectra. It should also be noted that due to the high γ of the $^{63/65}\text{Cu}$ nuclei only ca. 100 W of input power were required for the WURST pulses, compared to ca. 750 W of input power utilized for the QCPMG spectra.

8.4 Conclusions

WURST echo and WURST-QCPMG experiments possess several advantages in comparison to standard pulsed experiments for the acquisition of NQR spectra. The large uniform excitation bandwidths of the WURST pulses should enable NQR signals of unknown frequency to be located in a more efficient manner than conventional pulsed NQR experiments. The broadband excitation of the WURST pulses makes them useful for samples which possess broad distributions of NQR frequencies, as evidenced by acquisition of $^{63/65}\text{Cu}$ NQR spectra of CuCN. WURST pulses could also potentially be

useful for examining samples containing multiple sites which possess disparate NQR frequencies that can not be uniformly excited by conventional pulse techniques.

However, WURST pulses are not ideally suited for samples which possess very short transverse relaxation times (T_2) and/or nuclei which possess inherently low signal spectra due to low resonance frequency and/or low natural abundance. Clearly, spectra acquired with WURST pulses are of lower S/N than those acquired with conventional echo sequences; therefore WURST experiments may be limited to nuclei which are highly receptive to NQR experiments. Impedance mismatches between receiving and excitation pathways within NQR and NMR spectrometer systems can also be readily detected with WURST pulse sequences. This may afford a straightforward method for optimizing the performance of a variety of NQR and NMR spectrometers. This is especially important for NMR or NQR experiments performed on unreceptive nuclei where it is desirable to maximize inherently weak signals.

While this work has been limited to $I = 3/2$ nuclei, it is anticipated that WURST pulses may be useful for higher spin nuclei (e.g., $I = 1, 2, 5/2$, etc.); however, due to scaling of the pulse widths, the higher spin nuclei possess inherently shorter 90° pulse widths with large excitation bandwidths. Pre-polarization schemes where the sample is shuttled in and out of high field magnets should also be compatible with WURST pulses. The large excitation bandwidths afforded by the WURST pulses in combination with their low power requirements may also make them attractive for portable NQR systems where small power supplies are desirable and/or for experiments conducted with large-diameter sample coils.

8.5 Bibliography

- (1) Drago, R. S., Nuclear Quadrupole Resonance Spectroscopy. In *Physical Methods in Chemistry*, Saunders College Publishing: 1977; pp 510-529.
- (2) Semin, G. K.; Babushkina, T. A.; Yakobson, G. G., *Nuclear Quadrupole Resonance in Chemistry*. John Wiley and Sons: New York, 1975; p 517.
- (3) Lucken, E. A. C., *Nuclear Quadrupole Coupling Constants*. Academic Press: London, 1969; p 360.
- (4) Das, T. P.; Hahn, E. L., *Nuclear Quadrupole Resonance Spectroscopy*. Academic Press: New York, 1958; Vol. 1, p 223.
- (5) Semin, G. K., *Russ. J. Phys. Chem. A* **2007**, 81, (1), 38-46.
- (6) Rigamonti, A., *Adv. Phys.* **1984**, 33, (2), 115-191.
- (7) Jonsen, P., *Prog. Nucl. Magn. Reson. Spectrosc.* **1995**, 27, 647-727.
- (8) Le Caer, G.; Brand, R. A., *J. Phys.-Condes. Matter* **1998**, 10, (47), 10715-10774.
- (9) Rigamonti, A.; Borsa, F.; Carretta, P., *Rep. Prog. Phys.* **1998**, 61, (10), 1367-1439.
- (10) Bray, P. J., *Inorg. Chim. Acta* **1999**, 289, (1-2), 158-173.
- (11) Hunt, A. W.; Singer, P. M.; Cederstrom, A. F.; Imai, T., *Phys. Rev. B* **2001**, 64, (13), 134525-1-25.
- (12) Lutz, H. D., *J. Mol. Struct.* **2003**, 646, (1-3), 227-236.
- (13) Jerschow, A., *Prog. Nucl. Magn. Reson. Spectrosc.* **2005**, 46, (1), 63-78.
- (14) Latosinska, J. N., *J. Pharm. Biomed. Anal.* **2005**, 38, (4), 577-587.
- (15) Ofer, R.; Keren, A., *Phys. Rev. B* **2009**, 80, (22), 224521-1-8.
- (16) Somasundaram, S. D.; Jakobsson, A.; Smith, J. A. S.; Althoefer, K., *IEEE Trans. Geosci. Remote Sensing* **2007**, 45, (4), 925-933.
- (17) Garroway, A. N.; Buess, M. L.; Miller, J. B.; Suits, B. H.; Hibbs, A. D.; Barrall, G. A.; Matthews, R.; Burnett, L. J., *IEEE Trans. Geosci. Remote Sensing* **2001**, 39, (6), 1108-1118.
- (18) Yesinowski, J. P.; Buess, M. L.; Garroway, A. N.; Ziegeweid, M.; Pines, A., *Anal. Chem.* **1995**, 67, (13), 2256-2263.
- (19) Marino, R. A.; Connors, R. F., *J. Mol. Struct.* **1983**, 111, (DEC), 323-328.
- (20) Blinc, R.; Seliger, J.; Arcon, D.; Cevc, P.; Zagar, V., *Phys. Status Solidi A-Appl. Res.* **2000**, 180, (2), 541-545.

- (21) Rudakov, T. N.; Hayes, P. A.; Flexman, J. H., *Solid State Nucl. Magn. Reson.* **2008**, 33, (3), 31-35.
- (22) Gregorovic, A.; Apih, T., *J. Magn. Reson.* **2009**, 198, (2), 215-221.
- (23) Hahn, E. L.; Maxwell, D. E., *Phys. Rev.* **1952**, 88, 1070-1084.
- (24) Davis, J. H.; Jeffrey, K. R.; Bloom, M.; Valic, M. I.; Higgs, T. P., *Chem. Phys. Lett.* **1976**, 42, (2), 390-394.
- (25) Weisman, I. D.; Bennett, L. H., *Phys. Rev.* **1969**, 181, 1341-1350.
- (26) Solomon, I., *Phys. Rev.* **1958**, 110, 61-65.
- (27) Meiboom, S.; Gill, D., *Rev. Sci. Instrum.* **1958**, 29, 688-91.
- (28) Carr, H. Y., *Phys. Rev.* **1958**, 112, 1693-1701.
- (29) Carr, H. Y.; Purcell, E. M., *Phys. Rev.* **1954**, 94, 630-638.
- (30) Rudakov, T. N.; Belyakov, A. V., *J. Phys. D-Appl. Phys.* **1998**, 31, (10), 1251-1256.
- (31) Marino, R. A.; Klainer, S. M., *J. Chem. Phys.* **1977**, 67, (7), 3388-3389.
- (32) Rudakov, T. N.; Hayes, P. A., *J. Magn. Reson.* **2006**, 183, (1), 96-101.
- (33) Gregorovic, A.; Apih, T., *J. Chem. Phys.* **2008**, 129, (21), 214504-1-7.
- (34) Cheng, J. T.; Ellis, P. D., *J. Phys. Chem.* **1989**, 93, (6), 2549-2555.
- (35) Larsen, F. H.; Jakobsen, H. J.; Ellis, P. D.; Nielsen, N. C., *J. Phys. Chem. A* **1997**, 101, (46), 8597-8606.
- (36) Larsen, F. H.; Jakobsen, H. J.; Ellis, P. D.; Nielsen, N. C., *J. Magn. Reson.* **1998**, 131, (1), 144-147.
- (37) Larsen, F. H.; Skibsted, J.; Jakobsen, H. J.; Nielsen, N. C., *J. Am. Chem. Soc.* **2000**, 122, (29), 7080-7086.
- (38) Siegel, R.; Nakashima, T. T.; Wasylshen, R. E., *Concepts Magn. Reson. Part A* **2005**, 26A, (2), 62-77.
- (39) Rubinstein, M.; Taylor, P. C., *Phys. Rev. B* **1974**, 9, (10), 4258-4276.
- (40) Treacy, D. J.; Taylor, P. C.; Klein, P. B., *Solid State Commun.* **1979**, 32, (6), 423-427.
- (41) Taylor, P. C., *J. Non-Cryst. Solids* **1983**, 59-6, (DEC), 109-116.
- (42) Saleh, Z. M.; Williams, G. A.; Taylor, P. C., *Phys. Rev. B* **1989**, 40, (15), 10557-10563.
- (43) Taylor, P. C., *Z. Naturforsch. Sect. A-J. Phys. Sci.* **1996**, 51, (5-6), 603-610.

- (44) Bussandri, A. P.; Zuriaga, M. J., *J. Magn. Reson.* **1998**, 131, (2), 224-231.
- (45) Hughes, V.; Hartley, F. R., *J. Phys. E: Sci. Instrum.* **1975**, 8, (12), 1027-1030.
- (46) Hoffmann, D.; Pietsch, R.; Kummer, J., *J. Phys. E: Sci. Instrum.* **1979**, 12, (9), 837-840.
- (47) Blauch, A. J.; Schiano, J. L.; Ginsberg, M. D., *J. Magn. Reson.* **2000**, 144, (2), 305-315.
- (48) Schiano, J. L.; Blauch, A. J.; Ginsberg, M. D., *Z. Naturforsch. Sect. A-J. Phys. Sci.* **2000**, 55, (1-2), 67-73.
- (49) Schiano, J. L.; Ginsberg, M. D., *Z. Naturforsch. Sect. A-J. Phys. Sci.* **2000**, 55, (1-2), 61-66.
- (50) Ramamoorthy, A.; Chandrakumar, N.; Dubey, A. K.; Narasimhan, P. T., *J. Magn. Reson. Ser. A* **1993**, 102, (3), 274-286.
- (51) Ageev, S. Z.; Isbister, D. J.; Sanctuary, B. C., *Mol. Phys.* **1994**, 83, (2), 193-210.
- (52) Ramamoorthy, A., *Mol. Phys.* **1997**, 92, (6), 1035-1038.
- (53) Ramamoorthy, A., *Mol. Phys.* **1998**, 93, (5), 757-766.
- (54) Odin, C., *J. Magn. Reson.* **2000**, 143, (2), 299-310.
- (55) Bohlen, J. M.; Rey, M.; Bodenhausen, G., *J. Magn. Res.* **1989**, 84, (1), 191-197.
- (56) Van Veenendaal, E.; Meier, B. H.; Kentgens, A. P. M., *Mol. Phys.* **1998**, 93, (2), 195-213.
- (57) Kentgens, A. P. M., *J. Magn. Reson. Ser. A* **1993**, 104, (3), 302-309.
- (58) Kentgens, A. P. M., *J. Magn. Reson.* **1991**, 95, (3), 619-625.
- (59) Tannus, A.; Garwood, M., *NMR Biomed.* **1997**, 10, (8), 423-434.
- (60) Kupce, E.; Freeman, R., *J. Magn. Reson. Ser. A* **1996**, 118, (2), 299-303.
- (61) Kupce, E.; Freeman, R., *J. Magn. Reson. Ser. A* **1995**, 115, (2), 273-276.
- (62) Garwood, M.; DelaBarre, L., *J. Magn. Reson.* **2001**, 153, (2), 155-177.
- (63) Bhattacharyya, R.; Frydman, L., *J. Chem. Phys.* **2007**, 127, (19), 194503-1-8.
- (64) O'Dell, L. A.; Schurko, R. W., *Chem. Phys. Lett.* **2008**, 464, (1-3), 97-102.
- (65) O'Dell, L. A.; Rossini, A. J.; Schurko, R. W., *Chem. Phys. Lett.* **2009**, 468, (4-6), 330-335.
- (66) Ageev, S. Z.; Sanctuary, B. C., *Chem. Phys. Lett.* **1994**, 225, (4-6), 499-502.
- (67) Schurrer, C.; Perez, S. C., *Appl. Magn. Reson.* **1999**, 16, (1), 135-146.

- (68) O'Dell, L. A.; Schurko, R. W., *J. Am. Chem. Soc.* **2009**, 131, (19), 6658-6659.
- (69) Kroeker, S.; Wasylshen, R. E.; Hanna, J. V., *J. Am. Chem. Soc.* **1999**, 121, (7), 1582-1590.
- (70) Harris, R. K.; Becker, E. D.; De Menezes, S. M. C.; Goodfellow, R.; Granger, P., *Pure Appl. Chem.* **2001**, 73, (11), 1795-1818.
- (71) Treacy, D. J.; Taylor, P. C., *Solid State Commun.* **1981**, 40, (2), 135-138.
- (72) Marion, D. J. Y.; Desvaux, H., *J. Magn. Reson.* **2008**, 193, (1), 153-157.
- (73) Nausner, M.; Schlagnitweit, J.; Smrecki, V.; Yang, X.; Jerschow, A.; Muller, N., *J. Magn. Reson.* **2009**, 198, (1), 73-79.
- (74) Lefort, R.; Wiench, J. W.; Pruski, M.; Amoureux, J. P., *J. Chem. Phys.* **2002**, 116, (6), 2493-2501.
- (75) Bray, P. J.; Moskowitz, S.; Hooper, H. O.; Barnes, R. G.; Segel, S. L., *J. Chem. Phys.* **1958**, 28, (1), 99-102.
- (76) Fukushima, E.; Roeder, S. B. W., *Experimental Pulse NMR: A Nuts and Bolts Approach*. Addison-Wesley Publishing Company: Reading, Massachusetts, 1981; p 539.
- (77) Veglio, N.; Zuriaga, M. J., *Appl. Magn. Reson.* **2005**, 28, (1-2), 107-113.
- (78) Tong, Y. Y., *J. Magn. Reson. Ser. A* **1996**, 119, (1), 22-28.
- (79) Massiot, D.; Farnan, I.; Gautier, N.; Trumeau, D.; Trokiner, A.; Coutures, J. P., *Solid State Nucl. Magn. Reson.* **1995**, 4, (4), 241-248.
- (80) T_2 was measured for several QCPMG sub-spectra acquired at different transmitter frequencies (Table G11) and T_2 values were found to be relatively constant, suggesting that the shape of the pattern is not strongly influenced by T_2 .

Chapter 9: General Conclusions and Future Outlook

In this thesis it is demonstrated that multinuclear solid-state NMR (SSNMR) can be employed as a powerful probe of structure and bonding in inorganic and organometallic complexes, and can be readily applied to characterize complex heterogeneous catalyst systems. As detailed in Chapter 6, multinuclear SSNMR experiments, complemented by powder XRD data, have allowed for the development of a structural model for microencapsulated (ME) $\text{Sc}(\text{OTf})_3$ catalysts, which will provide much needed insight for the preparation and development of improved ME catalytic systems. Similarly, the combination of ^{35}Cl and ^{91}Zr SSNMR can act as a powerful probe of structure for zirconocene-based catalysts, as demonstrated in Chapters 2 and 3. Quantum chemical calculations of NMR interaction tensors, when taken along side of experimental SSNMR data of well-characterized systems, enable the NMR spectroscopist to gain a deep comprehension not only of the origin of the NMR interactions, but also an understanding of the relationships between these interactions and molecular structure and symmetry. This in turn can be used to make structural predictions for systems with unknown or ambiguous structures, as well as shedding light on the local electronic structure, including details like molecular orbitals, bonding and internuclear distances. This approach is demonstrated in Chapter 7, where the experimentally determined lead chemical shift anisotropies were demonstrated to arise from the presence of stereochemically active electron lone pairs centred on the lead atoms. It is hoped that this thesis will encourage the more general application of SSNMR for the characterization of inorganic and organometallic complexes, and related catalysts.

A continuing goal of the research presented herein will be to demonstrate that multinuclear SSNMR can be applied to probe the structure of heterogeneous catalysts which possess ambiguous molecular structures. In this regard, metallocenes serve as an ideal system to demonstrate this approach. As recounted in Chapters 2 and 3, the exact nature and structure of both homogeneous and heterogeneous activated metallocene olefin polymerization catalysts remain poorly understood.¹⁻³ The difficulties in probing the structure of these complexes arise from the fact that highly active catalysts are only obtained when the metallocenes have been treated with a stoichiometric excess of methylaluminoxane (MAO). Furthermore, heterogeneous versions of the catalysts are especially challenging to study due their lack of long-range order and the small number of active sites which reside at the surface of the support material. Given the inherent insensitivity of SSNMR experiments, the dilution of the active sites/species currently represents a considerable challenge for NMR spectroscopists. This is not terribly problematic when acquiring SSNMR spectra of highly receptive nuclei and/or nuclei which possess relatively narrow resonances or powder patterns. For example, in Chapter 6, it was shown that ⁴⁵Sc SSNMR spectra of ME Sc(OTf)₃ samples (which are ca. 1 % Sc by mass) could be acquired in several hours at a moderate magnetic field strength of 9.4 T. However, many important catalysts possess unreceptive nuclei; in these cases, the dilution of the active catalyst or precursor in the abundant support material can lead to unreasonably lengthy experiment times if signal enhancement techniques are not employed.

The signal of the NMR experiment is described by the following equation:

$$S = \frac{N\gamma^3\hbar^2B_0^2}{4kT} \quad (1)$$

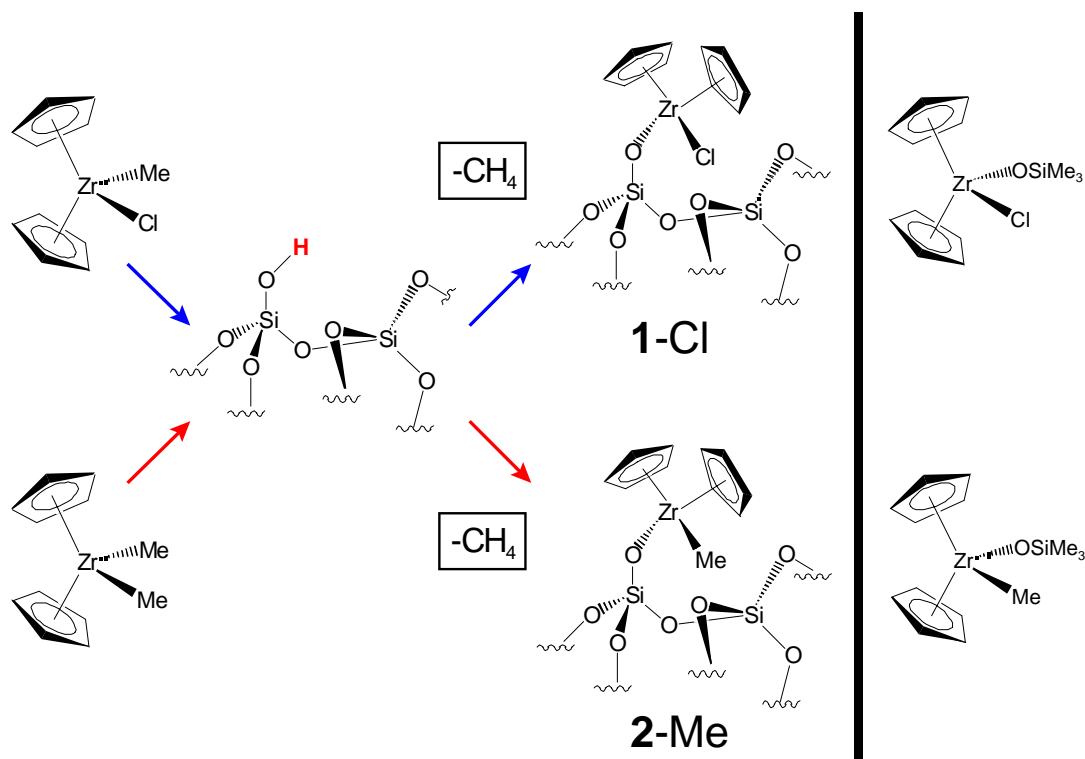
Hence, it is clear that the application of high magnetic fields and/or very low temperatures can lead to large signal enhancements. Herein, it was demonstrated that SSNMR spectra of unresponsive nuclei, such as ^{35}Cl and ^{91}Zr , in crystalline metallocenes, can be acquired in times on the order of minutes at high magnetic fields. For zirconocenes possessing narrow powder patterns (such as Cp_2ZrCl_2), a high quality ^{91}Zr SSNMR spectrum can be acquired with a standard quadrupolar echo sequence in a matter of minutes at 21.1 T. However, we have also demonstrated that it is very likely that many SSNMR spectra of quadrupolar nuclei in heterogeneous catalysts will possess ultra-wideline (UW) powder patterns. UW SSNMR spectra are very challenging to acquire due to dispersion of the NMR signal intensity over the broad powder patterns. In Chapters 2 and 3, it was shown that the QCPMG and WURST-QCPMG pulse sequences allow for the acquisition of ^{91}Zr and ^{35}Cl UW SSNMR spectra of metallocenes in a matter of minutes at 21.1 T. This suggests that the examination of heterogeneous catalysts with dilute nuclear contents and broad powder patterns is feasible; however, depending upon the exact dilution factors and natures of the systems, it will be a considerable challenge.

9.1 Preliminary Characterization of Model Heterogeneous Catalysts by ^{91}Zr SSNMR Spectroscopy

In the remaining portions of this final chapter, a recently initiated ^{91}Zr SSNMR

study of model heterogeneous zirconocene catalysts consisting of zirconocenes immobilized on silica, is described. This study is being conducted in collaboration with Drs. Paul Ellis and Andrew Lipton (Pacific Northwest National Labs, Richland WA) and Prof. Christophe Copéret (CNRS, Lyon, France and ETH Zurich).

The two model catalysts were obtained by contacting Cp_2ZrMeCl and Cp_2ZrMe_2 with the silica surface (Scheme 9.1). A reaction between the methyl groups of the zirconocene complexes and the hydroxyl groups of the surface occurs, leading to the formation of Zr-O bonds. The surface species have been characterized by ^1H MAS SSNMR and IR spectroscopy (results not shown). The structures shown in Scheme 9.1 are consistent with this data and previously proposed structures.²⁻⁷



Scheme 9.1. Preparation of surface-supported zirconocenes. Molecular analogs of the surface-supported species are shown to the right.

Elemental analysis (EA) indicates that **1-Cl** and **2-Me** are 3.02 % Zr by mass and 1.99 % Zr by mass, respectively, which are ca. one tenth of those of the crystalline species, Cp_2ZrCl_2 (31.2 % Zr by mass) and Cp_2ZrMe_2 (36.3 % Zr by mass). As a result, ^{91}Zr SSNMR experiments on **1-Cl** and **2-Me** will be challenging. In addition to the direct reduction in Zr mass %, a further reduction of Zr occurs in **1-Cl** and **2-Me** due to low densities of the support material (tamped densities of ca. 0.3 g/cm^3); for comparison, the densities predicted from the single crystal X-ray structures of Cp_2ZrCl_2 and Cp_2ZrMe_2 are 1.82 g/cm^3 and 1.46 g/cm^3 , respectively. Therefore, the number of ^{91}Zr spins in the **1-Cl** and **2-Me** samples is reduced by a factor of ca. 30-60, depending upon the tamped densities of the powdered crystalline samples. One might naively assume that the reduction in Zr content could be made up by acquiring more transients, however, the signal to noise of NMR experiments is proportional to the square root of the number of transients. Therefore, in order to acquire ^{91}Zr SSNMR spectra of similar S/N to those of the crystalline complexes, 900 to 3600 times the number of transients would be needed. Clearly, signal enhancement techniques are absolutely necessary for any ^{91}Zr SSNMR experiments conducted on such systems.

In this regard, Ellis and Lipton have previously demonstrated that the SSNMR spectra of unresponsive metal nuclei in metalloproteins can be acquired by employing cryogenic temperatures, in conjunction with NMR experiments which employ cross-polarization (CP) from ^1H and the QCPMG pulse sequence (CP/QCPMG).⁸⁻¹⁴ For example, when this pulse sequence was utilized on isotopically enriched samples at 10 K, it was possible to acquire ^{67}Zn SSNMR spectra of a 32 kDa protein (0.21 % Zn by mass)

and ^{25}Mg SSNMR spectra of 35 kDa protein (0.07% Mg by mass). A similar approach was employed for the acquisition of the ^{91}Zr SSNMR spectra of **1-Cl** and **2-Me**.

The ^{91}Zr QCPMG SSNMR spectra of **1-Cl** and **2-Me** acquired at 10 K with direct polarization of the ^{91}Zr nuclei are shown in Figure 9.1. Cooling the sample to 10 K provides signal enhancement of a factor of ca. 30, which partially offsets the loss in signal from reduced Zr content. A preliminary ^{91}Zr SSNMR spectrum of a molecular analog to the surface supported species, $\text{Cp}_2\text{ZrClOSiMe}_3$, was also acquired at 9.4 T (Figure 9.1c). The synthesis and characterization of a corresponding methyl derivative, $\text{Cp}_2\text{ZrMe(OSiMe}_3)$, is currently underway. Spectra were acquired in a piece-wise manner, with 11 and 13 sub-spectra acquired for **1-Cl** and **2-Me**, respectively. A 30 s pulse delay was employed for all experiments and the complete UW SSNMR spectra of **1-Cl** and **2-Me** were acquired in total experiment times of ca. 2 days each. Cross-polarization from ^1H was attempted, as this could provide a theoretical signal gain of $\gamma_{^1\text{H}}/\gamma_{^{91}\text{Zr}} \approx 17$. Unfortunately, signal was not observed, most likely due to an increase in the ^1H longitudinal relaxation times [$T_1(^1\text{H})$] at 10 K. It was possible to acquire ^1H - ^{91}Zr CP/QCPMG SSNMR spectra of crystalline Cp_2ZrCl_2 ; however, CP could only be observed at temperatures below ca. 200 K, presumably due to an increase in the rotating frame relaxation time constants [$T_{1\rho}(^{91}\text{Zr})$]. Measurements of the optimal ^1H recycle delays for crystalline Cp_2ZrCl_2 at 140 K reveal that recycle delays of ca. 12 s are necessary to obtain complete longitudinal relaxation. This is consistent with our hypothesis that the $T_1(^1\text{H})$ is very long for **1-Cl** and **2-Me** at 10 K. Future experiments should be attempted with pentamethylcyclopentadienyl (Cp^*) complexes, as the presence of mobile methyl

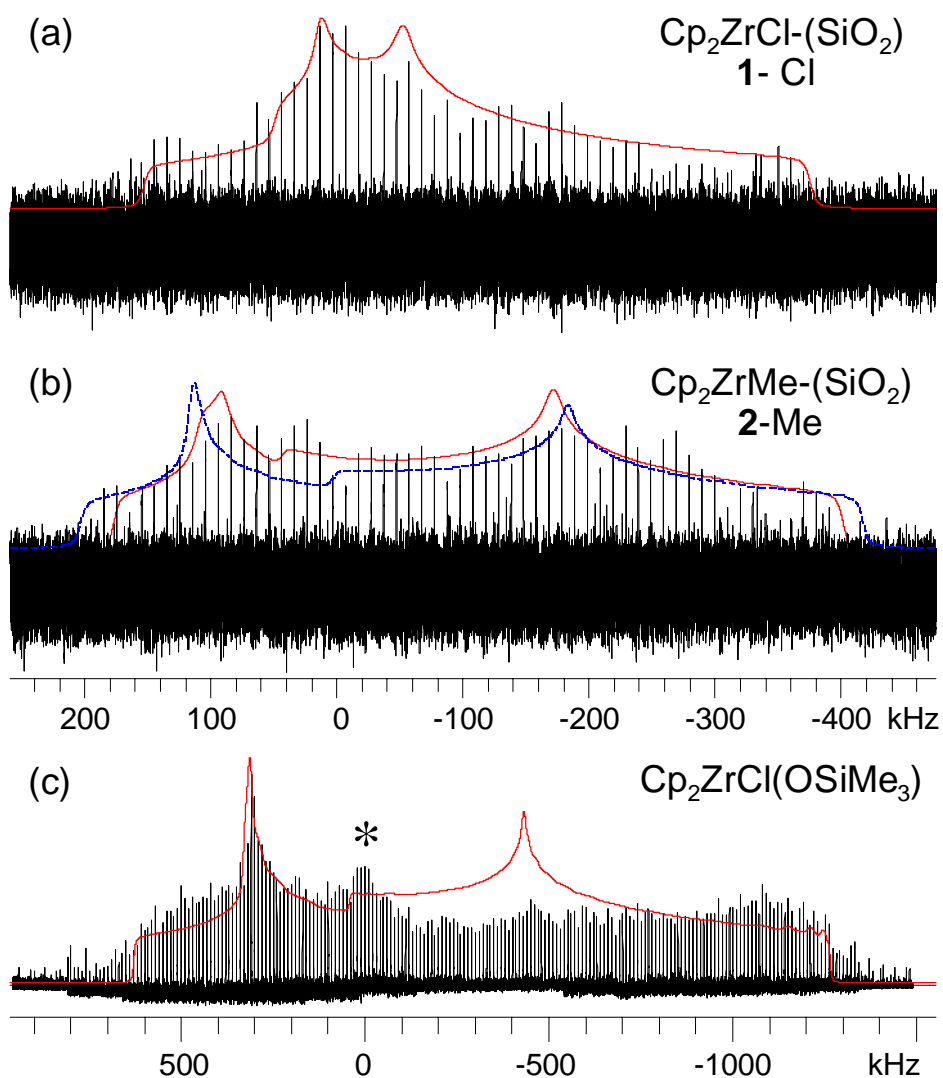


Figure 9.1. Static ^{91}Zr SSNMR spectra of (a) $\text{Cp}_2\text{ZrCl}-(\text{SiO}_2)$ (**1-Cl**) and (b) $\text{Cp}_2\text{ZrMe}-(\text{SiO}_2)$ (**2-Me**) acquired at 18.8 T. Analytical simulations are overlaid on the experimental spectra (solid red traces). Both spectra were acquired with sample temperatures of 10 K, 30 second recycle delays and 512 transients (4.3 hours) per sub-spectrum (50 kHz transmitter offset). 11 sub-spectra and 13 sub-spectra were acquired to form the total spectra of $\text{Cp}_2\text{ZrCl}-(\text{SiO}_2)$ and $\text{Cp}_2\text{ZrMe}-(\text{SiO}_2)$, respectively. A simulation with $\Omega = 0$ ppm (dashed blue trace) is shown for $\text{Cp}_2\text{ZrMe}-(\text{SiO}_2)$. (c) Static ^{91}Zr SSNMR WURST-QCPMG spectrum of $\text{Cp}_2\text{ZrCl}(\text{OSiMe}_3)$ at 9.4 T (black trace). The asterisk denotes a small amount of Cp_2ZrCl_2 . Partway through the acquisition of sub-spectra it was necessary to alter the probe configuration, resulting in uneven intensities in the individual sub-spectra, and leading to intensity differentials between the experimental and simulated spectra.

Table 9.1. Experimental and Calculated ^{91}Zr EFG and CS Tensor NMR Parameters^a

Compound	δ_{iso} (ppm)	C_Q (MHz) ^b	η_Q ^c	Ω (ppm) ^d	κ ^e	α (°)	β (°)	γ (°)
Cp₂ZrCl₂ (site 1)	21(5)	6.2(3)	0.18(10)	340(40)	-0.6(3)	90(35)	86(10)	2(10)
Cp₂ZrCl₂ (site 2)	21(5)	6.5(3)	0.30(10)	350(40)	-0.7(3)	90(35)	86(10)	3(10)
Cp₂ZrMeCl (site 1)	230(100)	23.3(10)	0.35(10)	900(500)	-0.6(8)	5(70)	15(45)	85(70)
Cp₂ZrMeCl (site 2)	230(100)	20.0(30)	0.75(15)	1000(500)	0.8(9)	80(40)	20(20)	5(40)
Cp₂ZrMe₂	475(40)	28.0(3)	0.40(4)	1750(300)	-0.9(3)	80(40)	90(5)	0(5)
[Cp₂ZrMe][MeB(C₆F₅)₃]	350(100)	39.0(8)	0.76(6)	1000(400)	0.2(5)	90(10)	80(15)	86(40)
Cp₂ZrCl(OSiMe₃)	-200(400)	39.6(20)	0.50(15)	-	-	-	-	-
Cp ₂ ZrCl(OSiMe ₃) (X-ray)	-238	33.1	0.50	318	-0.2	0	77	-90
Cp ₂ ZrCl(OSiMe ₃) (geom)	-192	31.8	0.62	320	-0.3	-2	71	90
Cp₂ZrCl-SiO₂ (1-Cl)	-250 ^f	27.0(30)	0.85(15)	-	-	-	-	-
Cp ₂ ZrCl-SiO ₂ (geom)	-186	27.0	0.63	286	0.1	-3	71	94
Cp₂ZrMe-SiO₂ (2-Me)	-100 ^f	33.0(30)	0.40(15)	1000 ^f	-0.2 ^f	151 ^f	89 ^f	0 ^f
Cp ₂ ZrMe-SiO ₂ (geom)	-14	-35.2	0.28	931	-0.1	151	89	0

^a The complex name has been bolded for experimental values. The “X-ray” and “geom” labels indicate that calculations were performed with atomic coordinates taken from single crystal X-ray structures and geometry optimized models, respectively. ^b $C_Q = eQV_{33}/h$. Only the magnitude of C_Q can be obtained from SSNMR experiments, while the sign of C_Q is obtainable only from theoretical calculations. ^c $\eta_Q = (V_{11} - V_{22})/V_{33}$. ^d $\Omega = \delta_{33} - \delta_{11}$. ^e $\kappa = 3(\delta_{22} - \delta_{\text{iso}})/\Omega$. ^f The uncertainties associated with the CS tensor parameters and Euler angles are very large; however, inclusion of parameters similar to those obtained from calculated values results in improved fits of the experiment spectra.

groups may afford more efficient ^1H relaxation and enable CP experiments to be performed.

From the simulations of the static ^{91}Zr SSNMR spectra of **1-Cl**, **2-Me** and $\text{Cp}_2\text{ZrCl}(\text{OSiMe}_3)$ it is possible to obtain the ^{91}Zr electric field gradient (EFG) tensor parameters (C_Q and η_Q , Table 9.1). The lineshapes of static powder patterns are also influenced by the chemical shift (CS) tensor parameters (Ω , κ and δ_{iso}) and Euler angles; however, given the magnitude of the quadrupolar interactions in **1-Cl**, **2-Me** and $\text{Cp}_2\text{ZrCl}(\text{OSiMe}_3)$, and the low S/N of the spectra of **1** and **2**, it is difficult to obtain accurate values for these parameters. For comparison, the ^{91}Zr CS and EFG tensor parameters of several previously studied crystalline zirconocene complexes (Chapter 3) are also listed in Table 9.1.

Large values of C_Q are obtained for all complexes, and can most likely be attributed to the relatively short O-Zr bond lengths (ca. 1.90 to 2.00 Å, *vide infra*). In Chapter 3, it is demonstrated that C_Q increases for Cp_2ZrX_2 complexes ($X = \text{Cl}, \text{Me}$) as the Zr-X bond lengths are shortened. Therefore, from the values of C_Q obtained from the spectra of **1-Cl** and **2-Me**, and the similarly large value of C_Q observed for $\text{Cp}_2\text{ZrCl}(\text{OSiMe}_3)$, one can conclude that there is an interaction between the Zr centres and surface oxygen atoms in **1-Cl** and **2-Me**. The η_Q value of **1-Cl** is near 1 ($\eta_Q = 0.85$), while those of **2-Me** and $\text{Cp}_2\text{ZrCl}(\text{OSiMe}_3)$ are closer to 0.50 ($\eta_Q = 0.40$ and 0.50, respectively). The differences in the η_Q values for **1-Cl** and **2-Me** can probably be attributed to differences in the Zr-Cl and Zr-Me bond lengths, but the origin of the differences in the C_Q and η_Q values for **1-Cl** and $\text{Cp}_2\text{ZrCl}(\text{OSiMe}_3)$ is not immediately

clear.

Quantum chemical calculations were performed in order to obtain structural models of **1-Cl** and **2-Me**. There is no known crystal structure for $\text{Cp}_2\text{ZrCl}(\text{OSiMe}_3)$; however, a structure for the closely related $\text{CpZrCl}(\text{OSiMe}_2(\text{CH}_2\text{Cl}))$ complex is known.¹⁵ Atomic coordinates for calculations on $\text{Cp}_2\text{ZrCl}(\text{OSiMe}_3)$ were obtained by replacing the Cl atom in $\text{CpZrCl}(\text{OSiMe}_2(\text{CH}_2\text{Cl}))$ with an H atom. Calculations of NMR tensor parameters were performed on this model, as well as a model in which all atomic positions were optimized (Figure 9.2). In both cases the calculations successfully predict the large C_Q values and the intermediate η_Q values that were obtained from simulations of the spectra, although C_Q is slightly underestimated in each case.

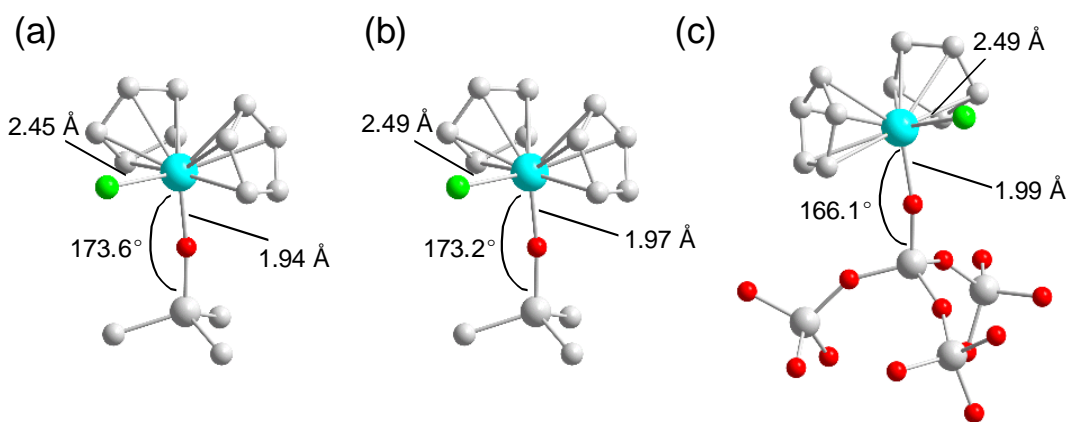


Figure 9.2. (a) Structure of $\text{Cp}_2\text{ZrCl}(\text{OSiMe}_3)$ with coordinates based upon the single crystal XRD structure of $\text{Cp}_2\text{ZrCl}(\text{OSiMe}_2(\text{CH}_2\text{Cl}))$. (b) Geometry optimized structure of $\text{Cp}_2\text{ZrCl}(\text{OSiMe}_3)$. (c) Geometry optimized model of **1-Cl**. The Cp_2ZrCl fragment was bonded to a SiO_2 cluster based upon the structure of β -cristabollite. Atomic coordinates for the SiO_2 fragment were taken from Blanc et al.⁶ Each of the terminal oxygen atoms was capped with a single H atom.

Eisenstein and Coperet have recently presented computational studies of organometallic complexes bound to silica surfaces.^{6,7} One of the major findings of these studies is that the SiO₂ surface essentially acts as a sterically congested anionic ligand. Quantum chemical calculations were performed on models of **1**-Cl and **2**-Me constructed by binding the metallocene fragments to the surface oxygen atom of an SiO₂ cluster derived from the (110) surface structure of β-cristabollite. These calculations predict that there are relatively minor differences in the O-Zr bond lengths and Zr-O-Si angles of **1**-Cl and Cp₂ZrCl(OSiMe₃). The slight differences in this angle may explain the differences in the observed C_Q and η_Q values for **1**-Cl and Cp₂ZrCl(OSiMe₃), although additional calculations are required to test this. The quantum chemical calculations also predict that **2**-Me should possess a larger value of C_Q and lower value of η_Q than **1**-Cl.

Future Work

Silica is one of the most commonly employed support materials for heterogeneous organometallic catalysts; therefore, investigating the structures of silica-supported catalysts is of great importance.^{2-4,6} In the future, it will be worthwhile to attempt experiments on surface-supported Cp* zirconocenes, as the methyl groups may lead to efficient ¹H relaxation, which may enable ¹H-⁹¹Zr CP experiments. This could result in substantial increases in S/N bringing total experiment times down to the order of hours.

Another exciting possibility is the application of dynamic nuclear polarization (DNP) for signal enhancement.¹⁶⁻²⁰ In DNP experiments the spin polarization of unpaired electrons is transferred to ¹H nuclei by irradiating the sample with microwave frequencies.

In order to accomplish this the sample is usually dissolved into a solution which is doped with a stable radical species. The solutions are then frozen and DNP SSNMR experiments are conducted. The low temperatures are also necessary in order to obtain efficient DNP enhancements. In order to apply this approach to heterogeneous catalysts it would be necessary to develop sample preparation protocols which are capable of bringing the polarization transfer agent in contact with the catalyst surface. While the development of these protocols would be a non-trivial, the potential signal enhancements available from DNP experiments warrant their development.

The theoretical signal gain of DNP experiments is proportional to γ_e/γ_X where, γ_e is the gyromagnetic ratio of the electron. For ^1H this ratio is equal to -658 , while for ^{91}Zr this ratio is equal to 7051 . Recently, commercial DNP SSNMR spectrometers operating at fields of 9.4 T and 14.1 T have become available.¹⁷ With these systems, ^1H DNP signal enhancement factors of 30 to 60 are typical. Therefore, if the polarization of the ^1H nuclei could be enhanced and then subsequently transferred to ^{91}Zr nuclei via CP, ^{91}Zr signal enhancement factors of ca. 321 to 642 are feasible. These DNP SSNMR experiments would not be limited to zirconium, as many of the other transition metals possess NMR active nuclei with low receptivities (e.g., $^{47/49}\text{Ti}$, ^{53}Cr , ^{57}Fe , ^{67}Zn , ^{95}Mo , ^{99}Ru , ^{109}Ag , ^{183}W and ^{189}Y).²¹ Therefore, DNP experiments could enable the characterization of a variety of heterogeneous catalysts by SSNMR spectroscopy of unreceptive metal nuclei.

9.5 Bibliography

- (1) Chen, E. Y. X.; Marks, T. J., *Chem. Rev.* **2000**, 100, (4), 1391-1434.
- (2) Hlatky, G. G., *Chem. Rev.* **2000**, 100, (4), 1347-1376.
- (3) Severn, J. R.; Chadwick, J. C.; Duchateau, R.; Friederichs, N., *Chem. Rev.* **2005**, 105, (11), 4073-4147.
- (4) Coperet, C.; Chabanas, M.; Saint-Arroman, R. P.; Basset, J. M., *Angew. Chem.-Int. Edit.* **2003**, 42, (2), 156-181.
- (5) Jezequel, M.; Dufaud, V.; Ruiz-Garcia, M. J.; Carrillo-Hermosilla, F.; Neugebauer, U.; Niccolai, G. P.; Lefebvre, F.; Bayard, F.; Corker, J.; Fiddy, S.; Evans, J.; Broyer, J. P.; Malinge, J.; Basset, J. M., *J. Am. Chem. Soc.* **2001**, 123, (15), 3520-3540.
- (6) Blanc, F.; Basset, J. M.; Coperet, C.; Sinha, A.; Tonzetich, Z. J.; Schrock, R. R.; Solans-Monfort, X.; Clot, E.; Eisenstein, O.; Lesage, A.; Emsley, L., *J. Am. Chem. Soc.* **2008**, 130, (18), 5886-5900.
- (7) Solans-Monfort, X.; Filhol, J. S.; Coperet, C.; Eisenstein, O., *New J. Chem.* **2006**, 30, (6), 842-850.
- (8) Lipton, A. S.; Heck, R. W.; de Jong, W. A.; Gao, A. R.; Wu, X. J.; Roehrich, A.; Harbison, G. S.; Ellis, P. D., *J. Am. Chem. Soc.* **2009**, 131, (39), 13992-13999.
- (9) Lipton, A. S.; Heck, R. W.; Primak, S.; McNeill, D. R.; Wilson, D. M.; Ellis, P. D., *J. Am. Chem. Soc.* **2008**, 130, (29), 9332-9341.
- (10) Lipton, A. S.; Heck, R. W.; Hernick, M.; Fierke, C. A.; Ellis, P. D., *J. Am. Chem. Soc.* **2008**, 130, (38), 12671-12679.
- (11) Lipton, A. S.; Sears, J. A.; Ellis, P. D., *J. Magn. Reson.* **2001**, 151, (1), 48-59.
- (12) Lipton, A. S.; Buchko, G. W.; Sears, J. A.; Kennedy, M. A.; Ellis, P. D., *J. Am. Chem. Soc.* **2001**, 123, (5), 992-993.
- (13) Lipton, A. S.; Heck, R. W.; Sears, J. A.; Ellis, P. D., *J. Magn. Reson.* **2004**, 168, (1), 66-74.
- (14) Ellis, P. D.; Lipton, A. S., Low-temperature solid-state NMR spectroscopy. A strategy for the direct observation of quadrupolar nuclides of biological interest. In *Annual*

Reports on NMR Spectroscopy, Vol 60, 2007; Vol. 60, pp 1-38.

- (15) Enders, M.; Fink, J.; Maillant, V.; Pritzkow, H., *Z. Anorg. Allg. Chem.* **2001**, 627, (9), 2281-2288.
- (16) Griffin, R. G.; Prisner, T. F., *Phys. Chem. Chem. Phys.* **2010**, 12, (22), 5737-5740.
- (17) Rosay, M.; Tometich, L.; Pawsey, S.; Bader, R.; Schauwecker, R.; Blank, M.; Borchard, P. M.; Cauffman, S. R.; Felch, K. L.; Weber, R. T.; Temkin, R. J.; Griffin, R. G.; Maas, W. E., *Phys. Chem. Chem. Phys.* **2010**, 12, (22), 5850-5860.
- (18) Barnes, A. B.; De Paepe, G.; van der Wel, P. C. A.; Hu, K. N.; Joo, C. G.; Bajaj, V. S.; Mak-Jurkauskas, M. L.; Sirigiri, J. R.; Herzfeld, J.; Temkin, R. J.; Griffin, R. G., *App. Magn. Reson.* **2008**, 34, (3-4), 237-263.
- (19) Maly, T.; Debelouchina, G. T.; Bajaj, V. S.; Hu, K. N.; Joo, C. G.; Mak-Jurkauskas, M. L.; Sirigiri, J. R.; van der Wel, P. C. A.; Herzfeld, J.; Temkin, R. J.; Griffin, R. G., *J. Chem. Phys.* **2008**, 128, (5).
- (20) Lewandowski, J. R.; De Paepe, G.; Griffin, R. G., *J. Am. Chem. Soc.* **2007**, 129, (4), 728-729.
- (21) Harris, R. K.; Becker, E. D.; De Menezes, S. M. C.; Goodfellow, R.; Granger, P., *Pure Appl. Chem.* **2001**, 73, (11), 1795-1818.

Appendix A: Supplementary Figures and Tables for Chapter 2

Table A1. QCPMG Acquisition Parameters For Spectra Acquired at 9.4 T

	1^a	2	3	4	5	6	7	8	9	10
Number of sub-spectra acquired ^b	72	25	38	35	37	20	28	52	69	39
Number of scans per sub-spectrum	2816	2816	160	1200	1200	2976	800	976	976	800
Transmitter offset per piece (kHz)	40.0	60.0	60.0	60.0	60.0	60.0	50.0	60.0	60.0	60.0
Recycle Delay (s)	0.5	0.5	1.0	1.0	1.0	1.0	0.8	1.0	1.0	1.0
Number of Meiboom-Gill loops [N]	81	162	163	81	40	19	81	163	163	81
Real points per loop	100	50	100	100	100	100	50	100	100	100
Spectral window of sub-spectra (kHz)	1000	1000	1000	1000	1000	1000	500	1000	1000	1000
Dwell (μ s)	1.0	1.0	1.0	1.0	1.0	1.0	2.0	1.0	1.0	1.0
Spikelet separation (kHz) [1/ τ_a]	10.0	20.0	10.0	10.0	10.0	10.0	10.0	10.0	10.0	10.0
Acquisition length (number of points)	8k	8k	16k	8k	4k	2k	4k	16k	16k	8k
90° pulse width [$\pi/2$] (μ s)	1.5	1.45	1.45	1.5	1.5	1.62	1.45	1.45	1.45	1.5
180° pulse widths [π] (μ s)	3.0	2.90	2.90	3.0	3.0	3.24	2.90	2.90	2.90	3.0
Ring-down delays [$\tau_1 = \tau_2 = \tau_3 = \tau_4$] (μ s)	60.0	60.0	60.0	60.0	60.0	60.0	60.0	60.0	60.0	60.0

^a**1** = Cp₂TiCl₂, **2** = CpTiCl₃, **3** = Cp₂ZrCl₂, **4** = Cp*₂ZrCl₂, **5** = Cp₂HfCl₂, **6** = Cp₂ZrMeCl, **7** = (Cp₂ZrCl)₂ μ -O, **8** = Cp*ZrCl₃, **9** = CpZrCl₃, **10** = Cp₂ZrHCl

^bThis includes sub-spectra that were acquired in the region of the ³⁵Cl satellite transitions.

Table A2. QCPMG Acquisition Parameters For Spectra Acquired at 21.1 T

	^a 2	3	^b 8	10
Number of sub-spectra acquired	13	14	10	16
Number of scans per sub-spectrum	64	32	3600	512
Transmitter offset per piece (kHz)	60.0	60.0	70.0	60.0
Recycle Delay (s)	1.0	1.0	1.0	1.0
Number of Meiboom-Gill loops [N] ^c	41	81	-	19
Real points per loop	100	100	-	100
Spectral window of sub-spectra (kHz)	500	500	1000	500
Dwell (μ s)	2.0	2.0	1.0	2.0
Spikelet separation (kHz) [$1/\tau_a$]	5000	5000	-	5000
Acquisition length (number of points)	8k	16k	1k	4k
90° pulse width [$\pi/2$] (μ s)	2.30	2.30	2.30	2.30
180° pulse widths [π] (μ s)	4.60	4.60	4.60	4.60
Ring-down delays [$\tau_1 = \tau_2 = \tau_3 = \tau_4$] (μ s)	100.0	100.0	100.0	100.0

^a**2** = CpTiCl₃, **3** = Cp₂ZrCl₂, **8** = Cp*ZrCl₃, **10** = Cp₂ZrHCl

^bThe spectrum of this compound was acquired with a hahn-echo type sequence in a piecewise manner.

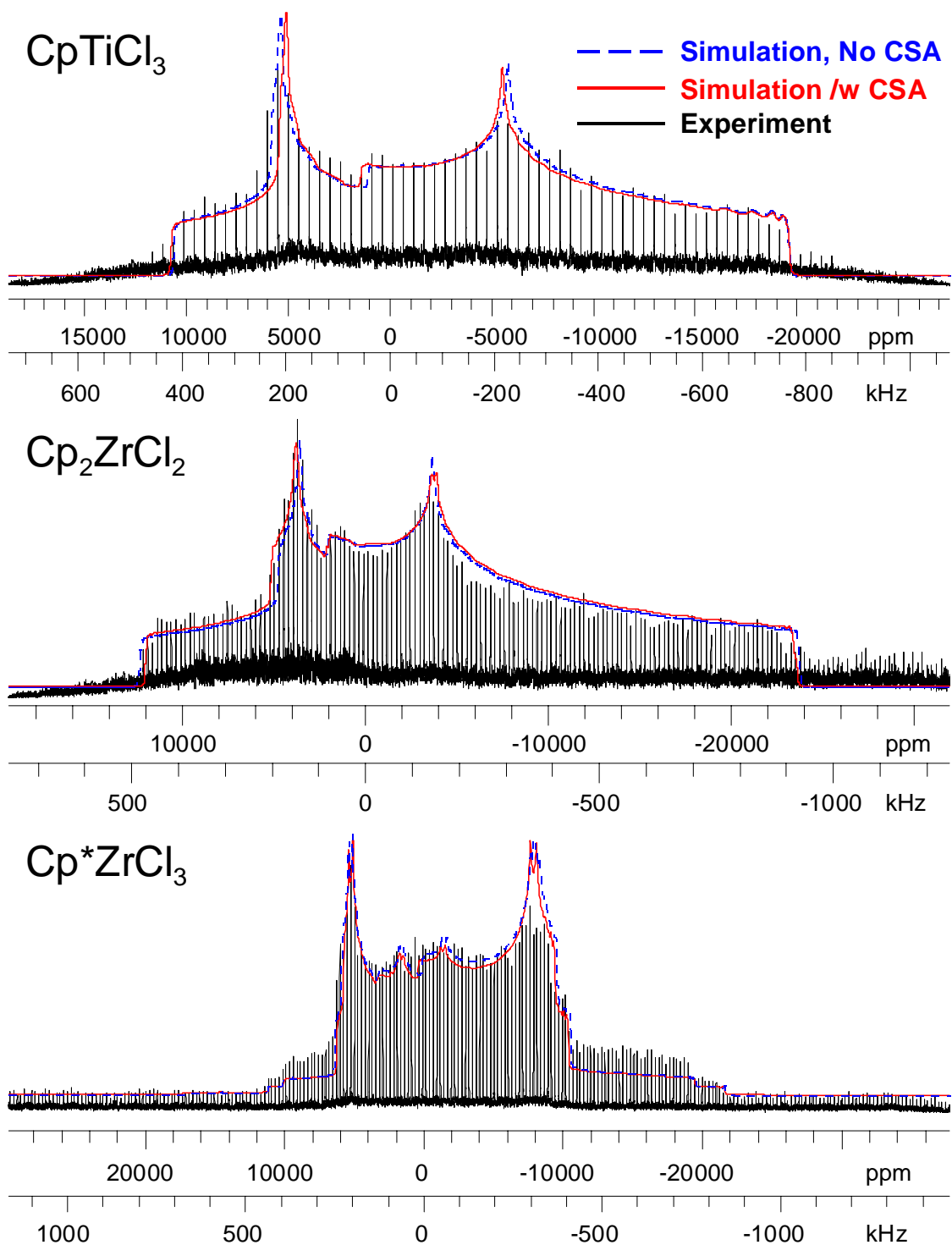


Figure A1. Static ^{35}Cl NMR spectra acquired at 9.4 T and a comparison of simulations. The dashed traces are simulations which include the effects of CSA, while the solid trace does not include CSA. At this field there is very little difference between the two simulations for all spectra. The fit with four independent sites is shown for Cp*ZrCl₃.

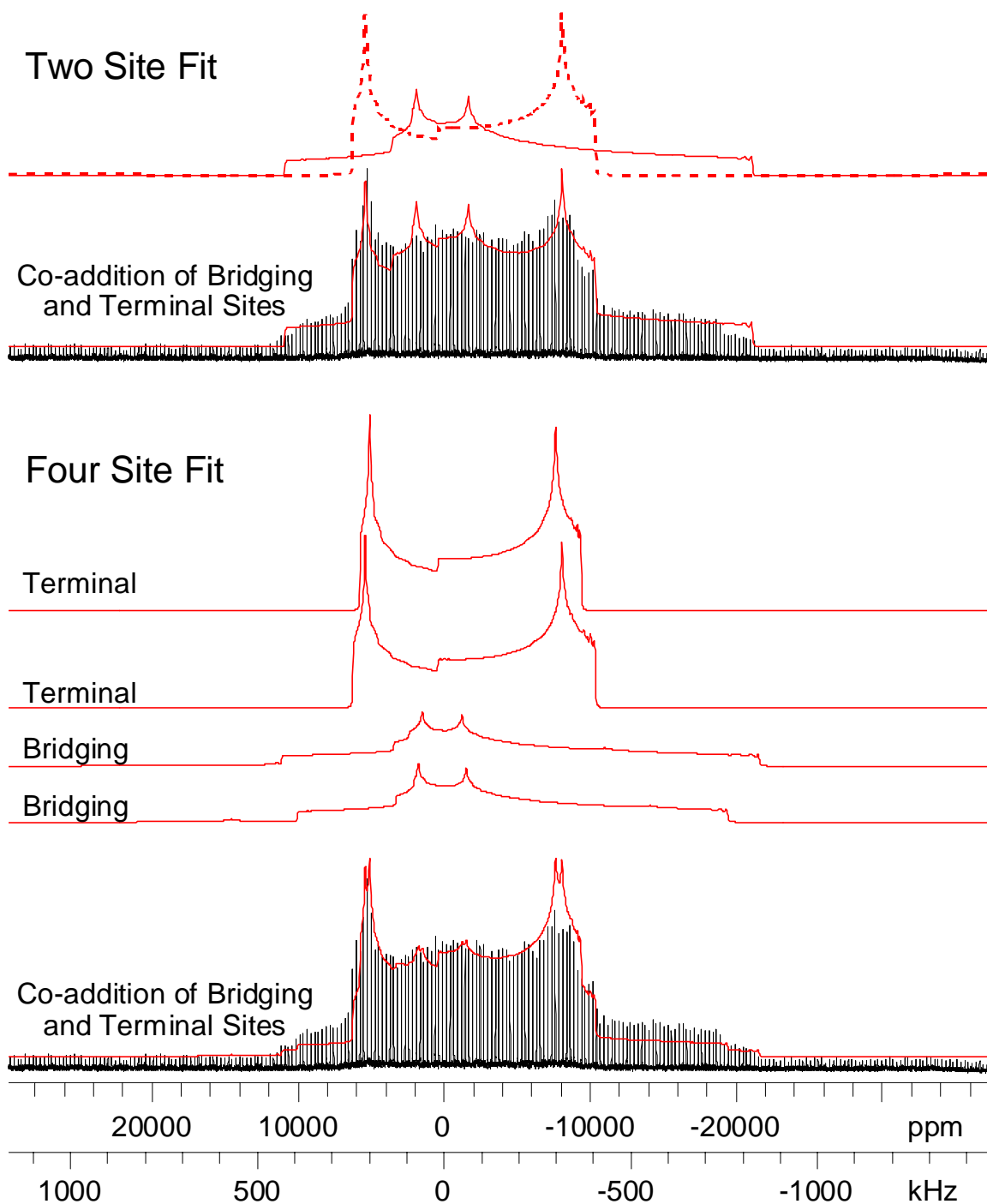


Figure A2. The ^{35}Cl spectrum of Cp^*ZrCl_3 and a comparison of simulations which utilize two sites (one bridging and one terminal) and four independent sites (two bridging and two terminal). In the two site fit the terminal site is shown with the dashed trace. The simulation which uses four sites provides a better fit of the intensity in the central part of the pattern and reproduces the “shoulder” features at both sides of the central transitions. In both the two and four site fits the intensity of the bridging sites has been set to half of those of the terminal sites.

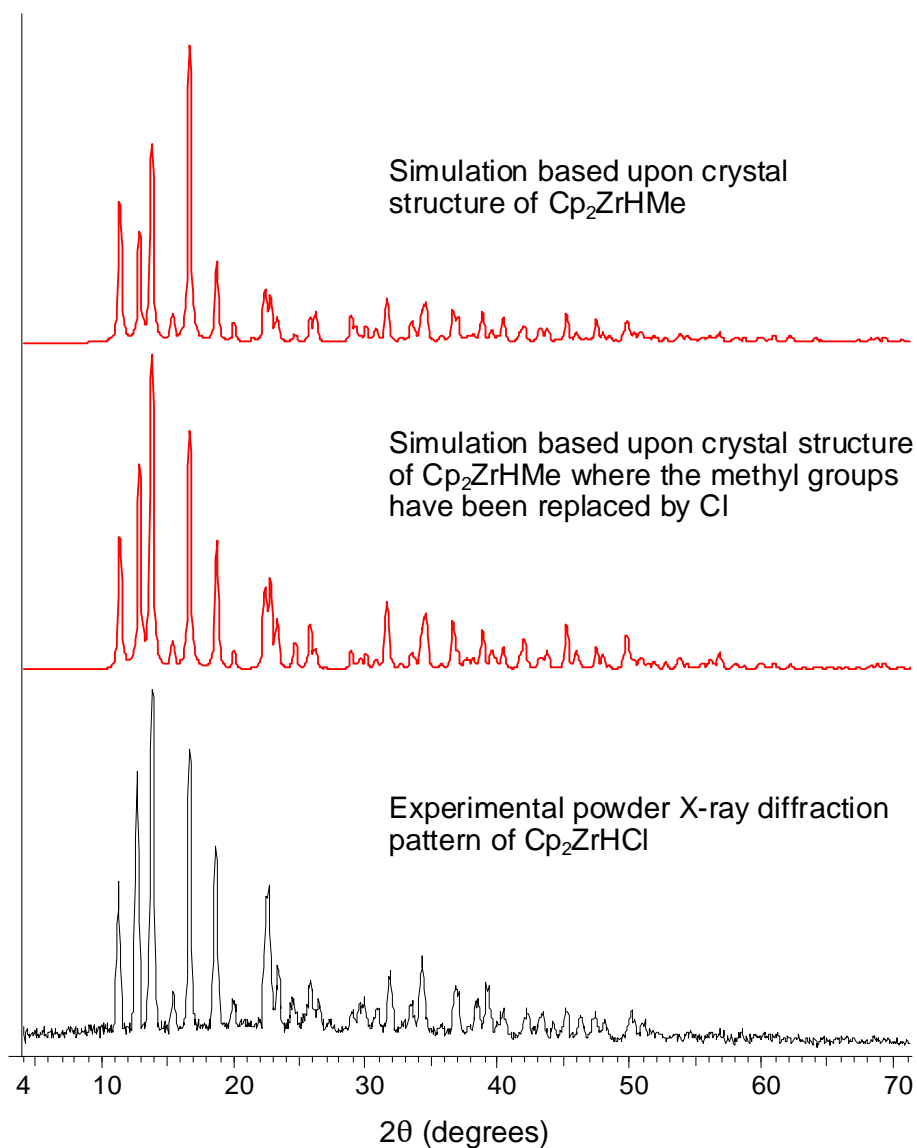


Figure A3. Experimental powder X-ray diffraction pattern of Cp₂ZrHCl. The top simulation is based upon the single-crystal X-ray diffraction structure of Cp₂ZrHMe. The middle trace is a simulation based upon the structure Cp₂ZrHMe where the methyl group has been removed and a chlorine atom has been placed at the position of the methyl carbon. The middle trace provides an excellent match with the experimental pattern.

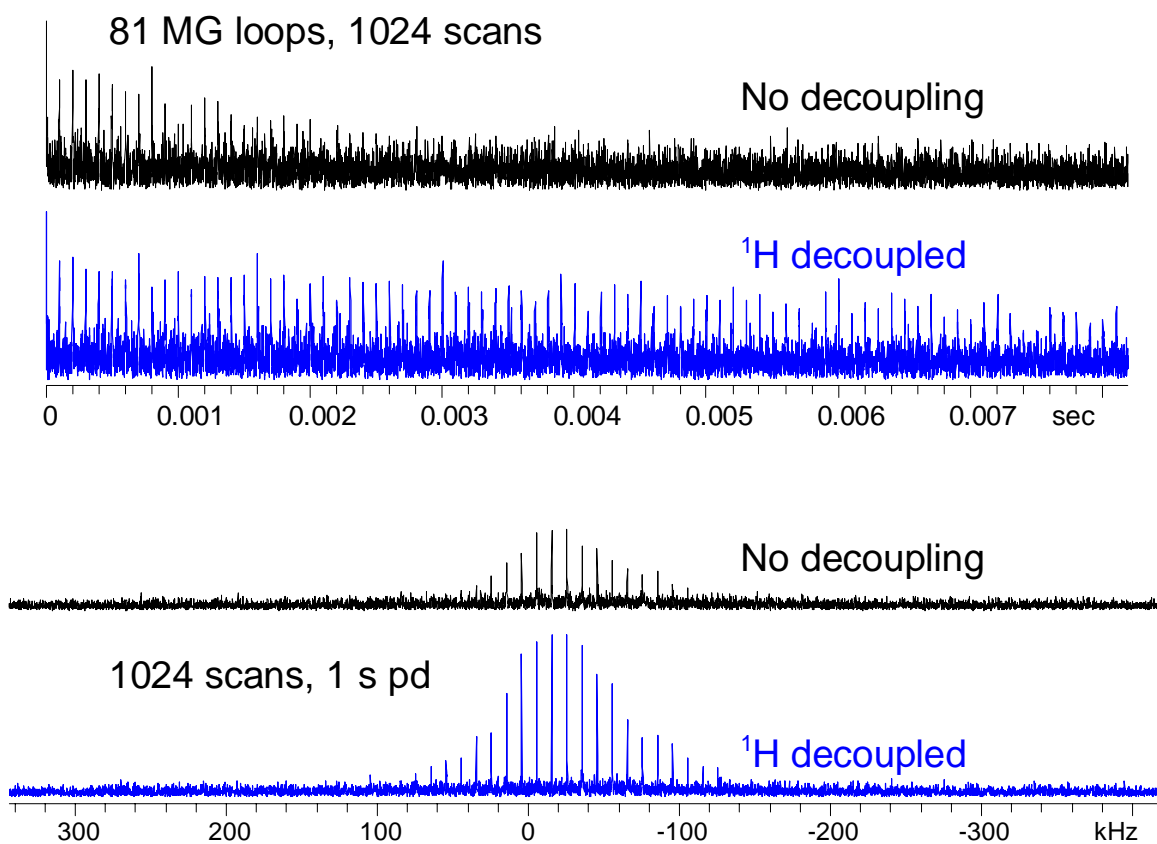


Figure A4. FIDs and the corresponding fourier transformed ^{35}Cl NMR spectra of Cp_2ZrHCl . The FIDs have been magnitude calculated in order to make the echo tops more visible. The application of ^1H decoupling greatly increases the number of echoes which may be acquired and results in large gains in signal to noise.

Appendix B: Supplementary Figures and Tables for Chapter 3

Table B1. Acquisition Parameters for ^{91}Zr MAS SSNMR Spectra Acquired at 9.4 T

	1	2	3	4	5
Pulse Sequence ^a	Echo	Echo	DFS/Echo	DFS/Echo	FAM/Echo
Number of scans	26000	10000	78720	6528	90112
Recycle Delay (s)	1.0	1.0	0.75	0.75	0.75
Dwell (μs)	25.0	25.0	12.5	20.0	10.0
Spectral width (kHz)	40.0	40.0	80.0	50.0	100
Spinning Speed (Hz)	10000	10000	11000	10000	10000
Acquisition length (number of points)	1024	1024	256	1024	512
90° pulse width [$\pi/2$] (μs)	2.0	1.86	5.5	5.5	5.5
180° pulse widths [π] (μs)	4.0	3.72	11.0	11.0	11.0
Ring-down delays [τ_1] (μs)	100.0	100	90.91	200	200
Ring-down delays [τ_2] (μs)	50	50	53.41	60	40
DFS Start Frequency (MHz)	-	-	0.900	0.65	-
DFS End Frequency (MHz)	-	-	0.150	0.12	-
Length of DFS Sweep (ms)	-	-	0.800	0.600	-
Number of Steps in DFS Waveform	-	-	1800	1800	-
DFS Step Length (μs)	-	-	0.44	0.33	-

^aEcho refers to a 16-step Hahn echo sequence. DFS/Echo or FAM/Echo refers to a sequence where the Hahn echo portion is prefaced by a double frequency sweep (DFS) waveform or fast amplitude modulated (FAM) waveform [see main text for references].

Table B2. Acquisition Parameters for Static ^{91}Zr SSNMR Spectra Acquired at 9.4 T

	Cp₂ZrCl₂	1	2	4	5
Pulse Sequence ^a	DFS/Echo	DFS/Echo	Echo	DFS/Echo	DFS/Echo
Number of scans	153600	90167	110608	54000	64800
Recycle Delay (s)	0.75	1.0	1.0	1.0	0.8
Dwell (μs)	3.5	25.0	5.0	5.0	5.0
Spectral width (kHz)	285.71	40	200	200	200
Acquisition length (number of points)	256	512	512	2048	2048
90° pulse width [$\pi/2$] (μs)	1.17	2.00	1.86	4.16	2.71
180° pulse widths [π] (μs)	2.34	4.00	3.72	4.16 ^b	5.42
Ring-down delays [τ_1] (μs)	84.5	100	65	100	100
Ring-down delays [τ_2] (μs)	53.0	50	35	40	40
DFS Start Frequency (MHz)	2.000	0.800	-	1.000	1.250
DFS End Frequency (MHz)	0.185	0.110	-	0.100	0.100
Length of DFS Sweep (ms)	0.800	0.700	-	1.250	1.600
Number of Steps in DFS Waveform	5920	2380	-	6400	6400
DFS Step Length (μs)	0.135	0.294	-	0.195	0.25

^aEcho refers to a 16-step Hahn echo sequence. DFS/Echo or FAM/Echo refers to a sequence where the Hahn echo portion is prefaced by a double frequency sweep (DFS) waveform or fast amplitude modulated (FAM) waveform [see main text for references].

^bIn this case the a 90°-90° echo was employed.

Table B3. Acquisition Parameters for Ultra-wideline ^{91}Zr SSNMR Spectra Acquired at 9.4 T

	6	7	8
Pulse Sequence	QCPMG	WURST-QCPMG	WURST-QCPMG
Number of scans per sub-spectrum	70000	36000	10800
Transmitter offset per piece (kHz)	80	192	200
Number of sub-spectra acquired	40	6	6
Recycle delay (s)	0.2	0.4	0.5
Number of Meiboom-Gill loops [N]	24	16	163
Real points per loop	40	50	100
Spectral width of sub-spectra (kHz)	800	800	1000
Dwell (μs)	1.25	1.25	1.0
Spikelet separation (kHz) [$1/\tau_a$]	20.0	16.0	10.0
Acquisition length (number of points)	980	800	16300
90° pulse width [$\pi/2$] (μs)	1.95	50	50
180° pulse widths [π] (μs)	3.90	50	50
QCPMG ring-down delays [$\tau_1 = \tau_2 = \tau_3 = \tau_4$] (μs)	40	-	-
WURST-QCPMG ringdown delay [τ_1] (μs)	-	56.25	75
WURST-QCPMG ringdown delay [$\tau_2 = \tau_3$] (μs)	-	10	10
Offset of WURST pulse (kHz)*	-	800	1000
Sweep Rate of WURST pulse (MHz/ms)	-	32	40

*The WURST pulse sweeps over a total frequency range equal to two times the offset of the WURST pulse.

Table B4. Acquisition Parameters for Static ^{91}Zr SSNMR Spectra Acquired at 21.1 T

	Cp₂ZrCl₂	1	2	5
Pulse Sequence ^a	Echo	Echo	Echo	Echo
Number of scans	1024	9832	12730	28816
Recycle Delay (s)	0.5	1.0	1.0	2.0
Dwell (μs)	10.0	5.0	2.0	4.0
Spectral width (kHz)	100.0	200.0	500.0	250.0
Acquisition length (number of points)	1024	512	256	512
90° pulse width [$\pi/2$] (μs)	4.2	5.7	2.3	2.0
180° pulse widths [π] (μs)	4.2	5.7	4.6	2.0
Ring-down delays [τ_1] (μs)	100	30	30	98
Ring-down delays [τ_2] (μs)	50	10	10	10

^aEcho refers to a 16-step Hahn echo sequence. DFS/Echo or FAM/Echo refers to a sequence where the Hahn echo portion is prefaced by a double frequency sweep (DFS) waveform or fast amplitude modulated (FAM) waveform [see main text for references].

^bIn this case the a 90°-90° echo was employed.

Table B5. Acquisition Parameters for Wideline ^{91}Zr SSNMR Spectra Acquired at 21.1 T

	4	6	7	8	9
Pulse Sequence	WURST-QCPMG	WURST-QCPMG	WURST-QCPMG	WURST-QCPMG	WURST-QCPMG
Number of scans per sub-spectrum	19161	40960	32768	8192	8192
Transmitter offset per piece (kHz)	-	-	-	-	200.0
Number of sub-spectra acquired	1	1	1	1	8
Recycle delay (s)	2.0	0.5	0.5	0.5	0.5
Number of Meiboom-Gill loops [N]	25	32	32	32	32
Real points per loop	200	250	250	500	125
Spectral width of sub-spectra (kHz)	500	1000	1000	1000	1000
Dwell (μs)	2.0	1.0	1.0	1.0	1.0
Spikelet separation (kHz) [$1/\tau_a$]	2.5	4.0	4.0	2.0	8.0
Acquisition length (number of points)	5000	8000	8000	16000	4000
WURST pulse width (μs)	50	50	50	50	50
WURST-QCPMG ringdown delay [τ_1] (μs)	130	112	112	192	2.5
WURST-QCPMG ringdown delay [$\tau_2 = \tau_3$] (μs)	20	30	30	30	10
Offset of WURST pulse (kHz)*	1000	1000	1000	1000	1000
Sweep Rate of WURST pulse (MHz/ms)	40	40	40	40	40

*The WURST pulse sweeps over a total frequency range equal to two times the offset of the WURST pulse.

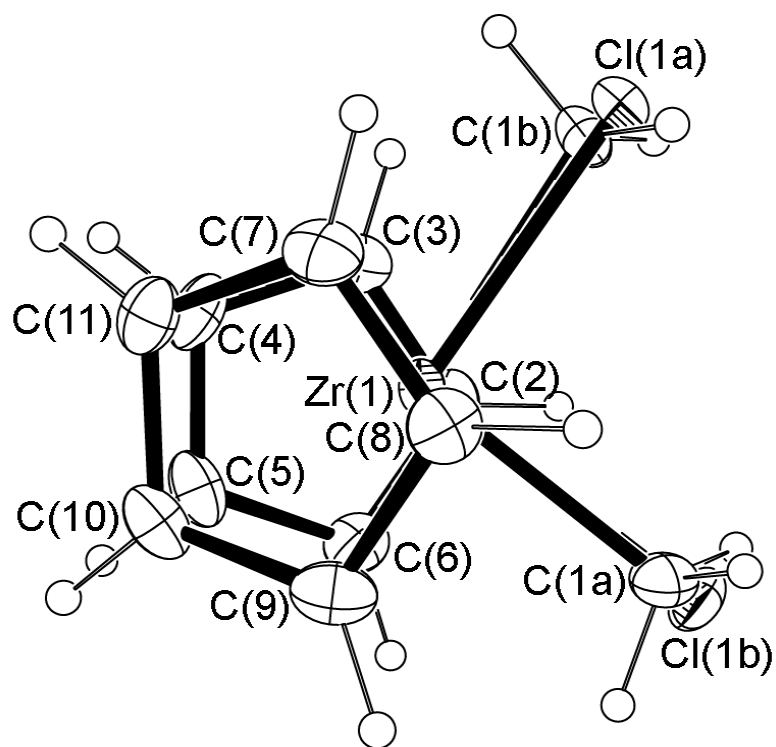


Figure B1. ORTEP depiction of the solid-state molecular structure of Cp_2ZrMeCl shown with 30% probability thermal ellipsoids. The structure features a ~60:40 occupational disorder of the Cl and CH_3 sites, with a greater occupation of Cl at the Cl(1a) site. Bonds between the cyclopentadienyl carbons and Zr are omitted for clarity.

Table B6. Crystal Data and Structure Refinement for Cp₂ZrMeCl (7).

Empirical formula	C ₁₁ H ₁₃ ClZr	
Formula weight	271.88	
Temperature	173(2) K	
Wavelength	0.71073 Å	
Crystal system	Monoclinic	
Space group	P2(1)/n	
Unit cell dimensions	a = 6.7624(6) Å	α = 90°.
	b = 11.7215(10) Å	β = 92.3670(10)°.
	c = 13.6347(11) Å	γ = 90°.
Volume	1079.84(16) Å ³	
Z	4	
Density (calculated)	1.672 mg/m ³	
Absorption coefficient	1.216 mm ⁻¹	
F(000)	544	
Crystal size	0.42 × 0.4 × 0.19 mm ³	
Theta range for data collection	2.99 to 27.47°.	
Index ranges	-8 ≤ h ≤ 8, -15 ≤ k ≤ 14, -17 ≤ l ≤ 17	
Reflections collected	11766	
Independent reflections	2447 [R(int) = 0.0234]	
Completeness to theta = 27.47°	98.6 %	
Absorption correction	Semi-empirical from equivalents	
Max. and min. transmission	0.794 and 0.653	
Refinement method	Full-matrix least-squares on F ²	
Data / restraints / parameters	2447 / 0 / 139	
Goodness-of-fit on F ²	1.047	
Final R indices [I > 2σ(I)]	R1 = 0.0226, wR2 = 0.0509	
R indices (all data)	R1 = 0.0261, wR2 = 0.0532	
Largest diff. peak and hole	0.623 and -0.391 e.Å ⁻³	

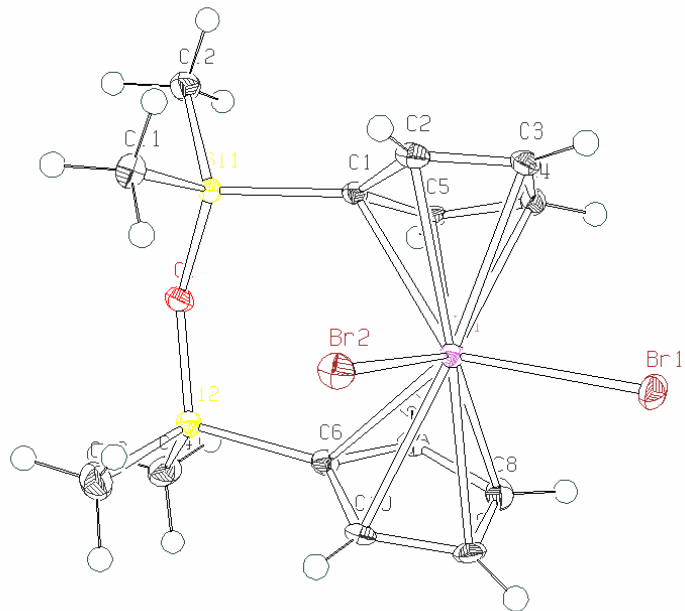


Figure B2. ORTEP depiction of the solid-state molecular structure of $\text{O}(\text{Me}_2\text{SiC}_5\text{H}_4)_2\text{ZrBr}_2$ (**4**) shown with 50% probability thermal ellipsoids.

Table B7. Crystal data and structure refinement for O(Me₂SiC₅H₄)₂ZrBr₂ (**4**).

Identification code	cs905	
Empirical formula	C ₁₄ H ₂₀ Br ₂ OSi ₂ Zr	
Formula weight	511.52	
Temperature	100(2) K	
Wavelength	0.71073 Å	
Crystal system	Monoclinic	
Space group	<i>P</i> 2 ₁ / <i>c</i>	
Unit cell dimensions	<i>a</i> = 13.5792(5) Å	<i>α</i> = 90°.
	<i>b</i> = 8.5955(3) Å	<i>β</i> = 96.587(3)°.
	<i>c</i> = 15.3894(5) Å	<i>γ</i> = 90°.
Volume	1784.40(10) Å ³	
<i>Z</i>	4	
Density (calculated)	1.904 Mg/m ³	
Absorption coefficient	5.222 mm ⁻¹	
F(000)	1000	
Crystal size	0.44 x 0.21 x 0.12 mm ³	
Theta range for data collection	4.18 to 30.03°.	
Index ranges	-16 ≤ <i>h</i> ≤ 19, -12 ≤ <i>k</i> ≤ 8, -21 ≤ <i>l</i> ≤ 21	
Reflections collected	16281	
Independent reflections	5194 [R(int) = 0.0444]	
Completeness to theta = 30.03°	99.7 %	
Absorption correction	Gaussian	
Max. and min. transmission	0.583 and 0.293	
Refinement method	Full-matrix least-squares on F ²	
Data / restraints / parameters	5194 / 0 / 185	
Goodness-of-fit on F ²	0.867	
Final R indices [I > 2σ(I)]	R1 = 0.0286, wR2 = 0.0537	
R indices (all data)	R1 = 0.0459, wR2 = 0.0554	
Largest diff. peak and hole	1.165 and -0.623 e.Å ⁻³	

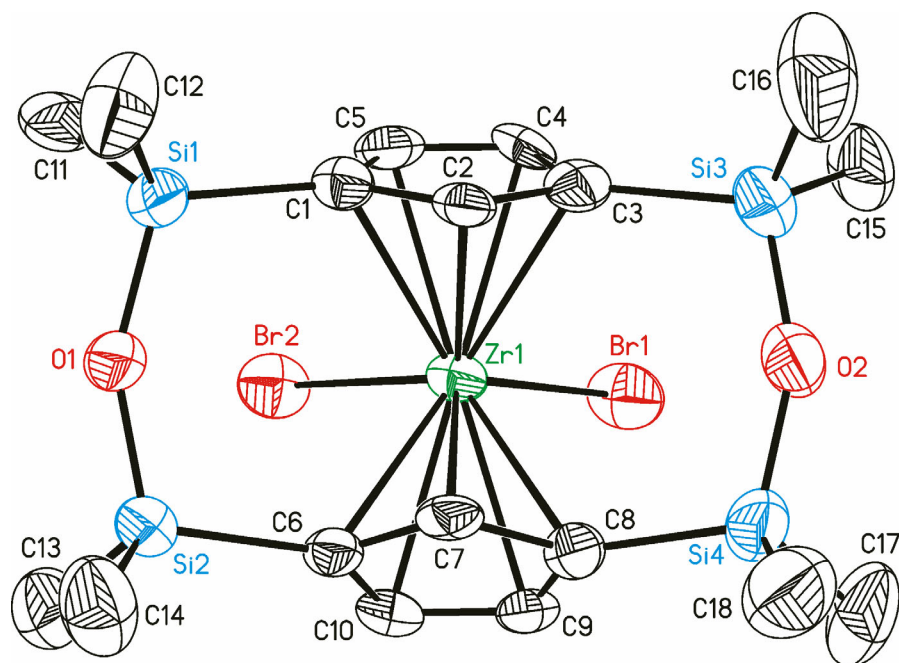


Figure B3. ORTEP depiction of the solid-state molecular structure of (1,3-C₅H₃)(SiMe₂OSiMe₂)₂(1,3-C₅H₃)ZrBr₂ (**5**) shown with 50% probability thermal ellipsoids.

Table B8. Crystal Data and Structure Refinement for
(1,3-C₅H₃)(SiMe₂OSiMe₂)₂(1,3-C₅H₃)ZrBr₂ (**5**)

Table 1. Crystal data and structure refinement for JSM-STRAP2.

Identification code	strap2	
Empirical formula	C ₁₈ H ₃₀ Br ₂ O ₂ Si ₄ Zr	
Formula weight	641.82	
Temperature	298(2) K	
Wavelength	0.71073 Å	
Crystal system	Orthorhombic	
Space group	<i>P b c a</i>	
Unit cell dimensions	<i>a</i> = 14.9355(13) Å	$\alpha = 90^\circ$.
	<i>b</i> = 14.682(3) Å	$\beta = 90^\circ$.
	<i>c</i> = 24.174(2) Å	$\gamma = 90^\circ$.
Volume	5301.0(12) Å ³	
Z	8	
Density (calculated)	1.608 Mg/m ³	
Absorption coefficient	3.622 mm ⁻¹	
F(000)	2560	
Crystal size	0.6 x 0.2 x 0.08 mm ³	
Theta range for data collection	2.12 to 22.50°.	
Index ranges	-1<= <i>h</i> <=16, -1<= <i>k</i> <=15, -26<= <i>l</i> <=1	
Reflections collected	3879	
Independent reflections	3202 [R(int) = 0.0548]	
Completeness to theta = 22.50°	92.5 %	
Absorption correction	Empirical	
Max. and min. transmission	0.8107 and 0.3614	
Refinement method	Full-matrix least-squares on F ²	
Data / restraints / parameters	3202 / 0 / 253	
Goodness-of-fit on F ²	0.993	
Final R indices [I>2sigma(I)]	R1 = 0.0508, wR2 = 0.0788	
R indices (all data)	R1 = 0.1200, wR2 = 0.0966	
Extinction coefficient	0.00061(6)	
Largest diff. peak and hole	0.415 and -0.430 e.Å ⁻³	

Table B9. Calculated ^{91}Zr EFG and CS Tensor Parameters for Cp_2ZrCl_2 using Coordinates Determined from Single Crystal X-ray Structures (Site 1 Only)

Zr Basis	Method	Cl Basis	σ_{iso} (ppm)	Ω (ppm)	κ	V_{33} (a.u.)	C_Q (MHz)	η_Q
EXPERIMENT			-	340	-0.60	0.150	6.2	0.18
12s11p7d								
	RHF	aug-cc-pCVDZ	2543	422	-0.65	-0.3050	-12.61	0.16
	RHF	aug-cc-pVDZ	2543	421	-0.65	-0.3041	-12.57	0.16
	RHF	cc-pVDZ	2534	439	-0.63	-0.2389	-9.88	0.16
	RHF	cc-pVTZ	2547	435	-0.66	-0.3047	-12.60	0.14
	RHF	cc-pVQZ	2555	430	-0.67	-0.3314	-13.71	0.17
	RHF	cc-pV5Z	2563	427	-0.68	-0.3271	-13.53	-0.15
	B3LYP	aug-cc-pCVDZ	1826	647	-0.59	-0.2500	-10.34	0.25
	B3LYP	aug-cc-pVDZ	1826	648	-0.59	-0.2489	-10.29	0.25
	B3LYP	cc-pVDZ	1816	687	-0.58	-0.2228	-9.21	0.40
	B3LYP	cc-pVTZ	1825	664	-0.59	-0.2515	-10.40	0.26
	B3LYP	cc-pVQZ	1836	653	-0.59	-0.2675	-11.06	0.21
	B3LYP	cc-pV5Z	1843	648	-0.60	-0.2613	-10.80	0.22
12s11p7d - ii								
	RHF	aug-cc-pCVDZ	2567	424	-0.66	-0.2846	-11.77	0.18
	RHF	aug-cc-pVDZ	2567	423	-0.65	-0.2834	-11.72	0.18
	RHF	cc-pVDZ	2560	435	-0.67	-0.2784	-11.51	0.18
	RHF	cc-pVTZ	2568	439	-0.68	-0.3146	-13.01	0.15
	RHF	cc-pVQZ	2574	436	-0.67	-0.3168	-13.10	0.15
	RHF	cc-pV5Z	2581	431	-0.67	-0.3079	-12.73	0.14
	B3LYP	aug-cc-pCVDZ	1857	646	-0.59	-0.2377	-9.83	0.25
	B3LYP	aug-cc-pVDZ	1857	647	-0.59	-0.2377	-9.83	0.25
	B3LYP	cc-pVDZ	1853	664	-0.60	-0.2391	-9.89	0.25
	B3LYP	cc-pVTZ	1858	660	-0.60	-0.2557	-10.57	-0.23
	B3LYP	cc-pVQZ	1865	653	-0.60	-0.2581	-10.67	0.24
	B3LYP	cc-pV5Z	1873	647	-0.60	-0.2493	-10.31	0.25
12s7p4d								
	RHF	aug-cc-pCVDZ	2585	424	-0.69	-0.3136	-12.97	0.16
	RHF	aug-cc-pVDZ	2585	423	-0.69	-0.3126	-12.93	0.17
	RHF	cc-pVDZ	2576	446	-0.67	-0.2485	-10.28	0.15
	RHF	cc-pVTZ	2588	438	-0.69	-0.3140	-12.99	0.00
	RHF	cc-pVQZ	2595	433	-0.70	-0.3439	-14.22	0.18
	RHF	cc-pV5Z	2601	430	-0.71	-0.3413	-14.11	0.16
	B3LYP	aug-cc-pCVDZ	1888	635	-0.61	-0.2533	-10.47	0.24
	B3LYP	aug-cc-pVDZ	1888	636	-0.61	-0.2520	-10.42	0.25
	B3LYP	cc-pVDZ	1877	685	-0.61	-0.2316	-9.58	0.38
	B3LYP	cc-pVTZ	1887	655	-0.61	-0.2584	-10.69	0.25
	B3LYP	cc-pVQZ	1897	642	-0.61	-0.2771	-11.46	0.19
	B3LYP	cc-pV5Z	1903	638	-0.62	-0.2728	-11.28	0.20
12s9p5d								
	RHF	aug-cc-pCVDZ	2594	425	-0.67	-0.2833	-11.72	0.18
	RHF	aug-cc-pVDZ	2594	424	-0.67	-0.2822	-11.67	0.18
	RHF	cc-pVDZ	2585	440	-0.69	-0.2820	-11.66	0.00
	RHF	cc-pVTZ	2594	440	-0.70	-0.3168	-13.10	0.16

	RHF	cc-pVQZ	2600	436	-0.69	-0.3191	-13.20	0.15
	RHF	cc-pV5Z	2605	432	-0.69	-0.3110	-12.86	0.15
	RHF	6-31G** on C,H,Cl	-	-	-	-0.2801	-11.58	0.18
	B3LYP	aug-cc-pCVDZ	1897	640	-0.60	-0.2344	-9.69	0.26
	B3LYP	aug-cc-pVDZ	1897	641	-0.60	-0.2344	-9.70	0.26
	B3LYP	cc-pVDZ	1890	661	-0.62	-0.2403	-9.94	0.25
	B3LYP	cc-pVTZ	1897	653	-0.62	-0.2560	-10.59	0.23
	B3LYP	cc-pVQZ	1905	645	-0.61	-0.2586	-10.69	0.24
	B3LYP	cc-pV5Z	1911	641	-0.61	-0.2510	-10.38	0.25
	B3LYP	6-31G** on C,H,Cl	-	-	-	-0.2266	-9.37	0.26
<hr/>								
6s3p3d	RHF	aug-cc-pCVDZ	2568	388	-0.59	-0.3625	-14.99	0.26
	RHF	aug-cc-pVDZ	2568	387	-0.58	-0.3625	-14.99	0.26
	RHF	cc-pVDZ	2556	382	-0.36	-0.1129	-4.67	0.92
	RHF	cc-pVTZ	2565	408	-0.48	-0.1643	-6.79	0.28
	RHF	cc-pVQZ	2576	424	-0.57	-0.3096	-12.80	0.23
	RHF	cc-pV5Z	2605	405	-0.63	-0.3544	-14.65	0.29
	RHF	6-31G** on C,H,Cl	-	-	-	0.0983	4.07	0.77
	B3LYP	aug-cc-pCVDZ	1919	497	-0.66	-0.2470	-10.22	0.09
	B3LYP	aug-cc-pVDZ	1920	496	-0.67	-0.2416	-9.99	0.00
	B3LYP	cc-pVDZ	1903	499	-0.52	-0.2487	-10.28	0.22
	B3LYP	cc-pVTZ	1908	514	-0.58	-0.1933	-7.99	0.33
	B3LYP	cc-pVQZ	1944	541	-0.68	-0.1057	-4.37	0.79
	B3LYP	6-31G** on C,H,Cl	-	-	-	-0.1497	-6.19	0.51
<hr/>								
Zr-5F3 (Huzinaga)	RHF	aug-cc-pCVDZ	2592	285	-0.57	-0.3720	-15.38	0.17
	RHF	aug-cc-pVDZ	2592	283	-0.57	-0.3737	-15.45	0.17
	RHF	cc-pVDZ	2574	323	-0.27	-0.1898	-7.85	0.21
	RHF	cc-pVTZ	2590	322	-0.38	-0.1932	-7.99	0.19
	RHF	cc-pVQZ	2602	303	-0.64	-0.2331	-9.64	0.13
	RHF	cc-pV5Z	2642	272	-0.83	-0.1732	-7.16	0.75
	RHF	6-31G** on C,H,Cl	-	-	-	-0.1439	-5.95	0.32
	B3LYP	aug-cc-pCVDZ	2045	344	-0.61	-0.2938	-12.15	0.10
	B3LYP	aug-cc-pVDZ	2044	344	-0.61	-0.2938	-12.15	0.11
	B3LYP	cc-pVDZ	2017	392	-0.46	-0.3312	-13.70	0.14
	B3LYP	cc-pVTZ	2032	385	-0.48	-0.2310	-9.55	0.11
	B3LYP	cc-pVQZ	2069	373	-0.68	0.1016	4.20	0.81
	B3LYP	cc-pV5Z	2118	344	-0.83	-0.1945	-8.04	0.10
	B3LYP	6-31G** on C,H,Cl	-	-	-	-0.2238	-9.26	0.15

The 6-311G** basis set was employed on C and H unless otherwise noted. For some of the calculations CS tensor parameters were not calculated. All calculations were performed with Gaussian 03. References and explanations of the basis set labels can be found in the main text.

Table B10. Calculated ^{91}Zr EFG and CS Tensor Parameters for Cp_2ZrBr_2 (**2**) Using Coordinates Determined from Single Crystal X-ray Structures (Both Sites)

Zr Basis/Site	Method	Br Basis	σ_{iso} (ppm)	Ω (ppm)	κ	V_{33} (a.u.)	C_Q (MHz)	η_Q
Experiment			-	550	-0.55	0.058	2.4	0.40
Site 1								
6s3p3d	RHF	Br-1S2	2421	447	-0.25	-0.236	-9.77	0.85
	RHF	6-31G**	2495	562	-0.58	0.162	6.69	0.72
	B3LYP	Br-1S2	1760	637	-0.34	0.124	5.14	0.87
	B3LYP	6-31G**	1820	821	-0.59	-0.158	-6.53	0.91
	B3LYP	6-311G**	1806	811	-0.58	-0.151	-6.25	0.86
	B3LYP	Br-11s7p4d- QZV	1817	821	-0.61	-0.141	-5.82	0.93
	B3LYP	Br-8s6p2d	1786	843	-0.58	-0.173	-7.13	0.71
	B3LYP	Br-cc-pVTZ	1806	837	-0.62	0.136	5.62	0.90
Zr-5F3	RHF	Br-1S2	2417	451	-0.20	0.141	5.82	-0.97
	RHF	6-31G**	2530	499	-0.52	0.122	5.03	0.64
	B3LYP	Br-1S2	1858	534	-0.29	-0.180	-7.45	0.54
	B3LYP	6-31G**	1952	689	-0.55	-0.212	-8.75	0.36
12s9p5d	RHF	Br-1S2	2483	587	-0.72	0.154	6.38	0.48
	RHF	6-31G**	2531	609	-0.75	-0.181	-7.50	1.00
	B3LYP	Br-1S2	1743	888	-0.64	0.174	7.20	0.82
	B3LYP	6-31G**	1794	950	-0.69	0.192	7.93	0.79
Site 2/Cp Conformation 1								
6s3p3d	RHF	Br-1S2	2420	415	-0.20	-0.244	-10.09	0.89
	RHF	6-31G**	2494	528	-0.56	0.143	5.90	0.97
	B3LYP	Br-1S2	1754	551	-0.43	0.127	5.27	0.64
	B3LYP	6-31G**	1816	734	-0.67	0.148	6.11	0.68
	B3LYP	6-311G**	1802	728	-0.67	0.137	5.65	0.67
	B3LYP	Br-11s7p4d- QZV	1817	740	-0.68	0.127	5.25	0.69
	B3LYP	Br-8s6p2d	1780	758	-0.66	0.144	5.96	0.86
	B3LYP	Br-cc-pVTZ	1805	754	-0.70	0.130	5.38	0.53
Zr-5F3	RHF	Br-1S2	2410	384	-0.17	0.149	6.14	0.92
	RHF	6-31G**	2522	443	-0.51	0.114	4.72	0.29
	B3LYP	Br-1S2	1848	420	-0.40	-0.141	-5.85	0.92
	B3LYP	6-31G**	1943	589	-0.65	-0.176	-7.29	0.59
12s9p5d	RHF	Br-1S2	2482	549	-0.72	0.163	6.75	0.49
	RHF	6-31G**	2530	574	-0.74	0.151	6.25	0.75
	B3LYP	Br-1S2	1747	836	-0.66	0.186	7.69	0.83
	B3LYP	6-31G**	1799	901	-0.71	0.161	6.66	0.54
Site 2/Cp Conformation 2								
6s3p3d	RHF	Br-1S2	2408	397	-0.17	0.283	11.70	0.61
	RHF	6-31G**	2487	526	-0.53	0.138	5.71	0.72
	B3LYP	Br-1S2	1732	540	-0.40	0.088	3.63	0.69
	B3LYP	6-31G**	1797	742	-0.63	0.041	1.71	0.67
	B3LYP	6-311G**	1781	728	-0.63	0.030	1.24	0.58
	B3LYP	Br-11s7p4d-	1797	748	-0.65	-0.027	-1.12	0.93

		QZV						
	B3LYP	Br-8s6p2d	1761	758	-0.63	-0.042	-1.74	0.87
	B3LYP	Br-cc-pVTZ	1786	761	-0.66	-0.034	-1.40	0.92
Zr-5F3	RHF	Br-1S2	2401	402	-0.14	0.177	7.31	0.45
	RHF	6-31G**	2521	456	-0.47	0.072	2.96	0.31
	B3LYP	Br-1S2	1831	437	-0.34	-0.053	-2.20	0.48
	B3LYP	6-31G**	1933	606	-0.59	-0.090	-3.71	0.34
12s9p5d	RHF	Br-1S2	2478	550	-0.64	0.153	6.32	0.06
	RHF	6-31G**	2528	579	-0.67	-0.034	-1.40	0.26
	B3LYP	Br-1S2	1727	827	-0.63	0.184	7.60	0.38
	B3LYP	6-31G**	1781	898	-0.68	0.039	1.62	0.24

Note: There are two crystallographic sites for Cp_2ZrBr_2 . One Cp ring of site 2 has been modelled with disorder and possesses two conformations. Calculations are shown for both conformations.

Table B11. Calculated ^{91}Zr EFG and CS Tensor Parameters for Cp_2ZrCl_2 using Coordinates With Idealized Cp Rings (Both Sites)

Zr Basis	Method	Cl Basis	Site	σ_{iso} (ppm)	Ω (ppm)	κ	V_{33} (a.u.)	C_Q (MHz)	η_Q
Experiment			1	-	340	-0.60	0.150	6.2	0.18
Experiment			2		350	-0.70	0.158	6.5	0.30
6s3p3d									
	RHF	cc-pVDZ	1	2562	343	-0.41	0.0142	0.59	0.88
	RHF	cc-pVDZ	2	2562	349	-0.42	0.0188	0.78	0.42
	RHF	cc-pVTZ	1	2573	371	-0.55	0.0677	2.80	0.59
	RHF	cc-pVTZ	2	2573	378	-0.56	0.0812	3.36	0.71
6-31G** on C,H									
	RHF	6-31G**	1	-	-	-	0.0589	2.43	0.68
	B3LYP	cc-pVDZ	1	1918	454	-0.58	-0.1343	-5.56	0.22
	B3LYP	cc-pVDZ	2	1917	456	-0.58	-0.1472	-6.09	0.30
	B3LYP	cc-pVTZ	1	1925	471	-0.65	-0.0823	-3.40	0.39
	B3LYP	cc-pVTZ	2	1925	474	-0.65	-0.0948	-3.92	0.48
6-31G** on C,H									
	B3LYP	6-31G**	1	-	-	-	-0.0405	-1.67	0.40
Zr-5F3 (Huzinaga)									
	RHF	cc-pVDZ	1	2581	260	-0.32	0.0861	3.56	0.45
	RHF	cc-pVDZ	2	2582	265	-0.34	0.0980	4.05	0.55
	RHF	cc-pVTZ	1	2598	263	-0.45	0.0930	3.84	0.66
	RHF	cc-pVTZ	2	2599	268	-0.47	0.1049	4.34	0.74
6-31G** on C,H									
	RHF	6-31G**	1	-	-	-	-0.0200	-0.83	0.97
	B3LYP	cc-pVDZ	1	2034	327	-0.52	-0.2115	-8.74	0.49
	B3LYP	cc-pVDZ	2	2036	330	-0.52	-0.2234	-9.24	0.51
	B3LYP	cc-pVTZ	1	2051	324	-0.52	-0.1178	-4.87	0.63
	B3LYP	cc-pVTZ	2	2052	326	-0.53	-0.1293	-5.35	0.65
6-31G** on C,H									
	B3LYP	6-31G**	1	-	-	-	-0.1203	-4.98	0.22

The 6-311G** basis set was employed on C and H unless otherwise noted. For some of the calculations CS tensor parameters were not calculated. All calculations were performed with Gaussian 03.

Table B12. Calculated ^{91}Zr EFG and CS Tensor Parameters for Cp_2ZrBr_2 (**2**) Using Coordinates With Idealized Cp rings (Both Sites)

Zr Basis/Site	Method	Br Basis	σ_{iso} (ppm)	Ω (ppm)	κ	V_{33} (a.u.)	C_Q (MHz)	η_Q
Experiment			-	550	-0.70	0.058	2.4	0.40
Site 1								
6s3p3d	RHF	Br-1S2	2407	380	-0.13	0.308	12.75	0.27
	RHF	6-31G**	2486	501	-0.55	0.155	6.41	0.15
	B3LYP	Br-1S2	1733	520	-0.42	0.118	4.88	0.18
	B3LYP	6-31G**	1799	711	-0.68	-0.021	-0.88	0.69
	B3LYP	6-311G**	1783	700	-0.68	-0.032	-1.33	0.57
	B3LYP	Br-11s7p4d- QZV	1800	721	-0.70	-0.047	-1.94	0.47
	B3LYP	Br-8s6p2d	1762	727	-0.68	-0.026	-1.05	0.85
	B3LYP	Br-cc-pVTZ	1788	734	-0.71	0.048	2.00	0.79
Zr-5F3	RHF	Br-1S2	2395	373	-0.12	0.202	8.37	0.07
	RHF	6-31G**	2515	423	-0.51	0.092	3.81	0.94
	B3LYP	Br-1S2	1827	409	-0.38	0.033	1.35	0.79
	B3LYP	6-31G**	1929	571	-0.66	0.073	3.02	0.62
12s9p5d	RHF	Br-1S2	2477	508	-0.74	0.187	7.74	0.53
	RHF	6-31G**	2527	534	-0.77	0.047	1.92	-0.59
	B3LYP	Br-1S2	1732	799	-0.67	0.220	9.08	0.09
	B3LYP	6-31G**	1786	865	-0.72	-0.042	-1.75	0.91
Site 2/Cp Conformation 1								
6s3p3d	RHF	Br-1S2	2411	379	-0.14	0.310	12.83	0.20
	RHF	6-31G**	2490	493	-0.56	0.154	6.37	0.06
	B3LYP	Br-1S2	1747	515	-0.43	0.120	4.97	0.31
	B3LYP	6-31G**	1811	698	-0.68	-0.025	-1.03	0.31
	B3LYP	6-311G**	1797	692	-0.68	-0.038	-1.57	0.39
	B3LYP	Br-11s7p4d- QZV	1813	708	-0.71	-0.058	-2.40	0.18
	B3LYP	Br-8s6p2d	1775	718	-0.68	0.030	1.25	0.77
	B3LYP	Br-cc-pVTZ	1801	722	-0.72	-0.053	-2.18	0.79
Zr-5F3	RHF	Br-1S2	2400	345	-0.09	0.202	8.34	0.12
	RHF	6-31G**	2517	399	-0.52	-0.099	-4.10	0.83
	B3LYP	Br-1S2	1839	380	-0.36	0.042	1.73	0.19
	B3LYP	6-31G**	1938	545	-0.67	0.082	3.38	0.40
12s9p5d	RHF	Br-1S2	2479	501	-0.75	0.199	8.22	0.59
	RHF	6-31G**	2529	528	-0.78	-0.080	-3.33	0.43
	B3LYP	Br-1S2	1742	794	-0.67	0.232	9.60	0.19
	B3LYP	6-31G**	1796	861	-0.73	-0.057	-2.36	0.67
Site 2/Cp Conformation 2								
6s3p3d	RHF	Br-1S2	2402	386	-0.16	0.299	12.35	0.22
	RHF	6-31G**	2483	513	-0.57	0.148	6.14	0.07
	B3LYP	Br-1S2	1726	523	-0.44	0.107	4.42	0.36
	B3LYP	6-31G**	1793	721	-0.69	-0.046	-1.92	0.17
	B3LYP	6-311G**	1777	707	-0.69	-0.049	-2.03	0.16
	B3LYP	Br-11s7p4d-	1794	730	-0.71	-0.059	-2.45	0.16

		QZV						
	B3LYP	Br-8s6p2d	1756	735	-0.68	-0.054	-2.24	0.45
	B3LYP	Br-cc-pVTZ	1783	742	-0.71	0.047	1.96	-0.86
Zr-5F3	RHF	Br-1S2	2394	383	-0.14	0.194	8.02	0.11
	RHF	6-31G**	2517	434	-0.53	-0.098	-4.06	0.76
	B3LYP	Br-1S2	1825	413	-0.39	-0.065	-2.68	0.53
	B3LYP	6-31G**	1929	577	-0.67	-0.091	-3.75	0.93
12s9p5d	RHF	Br-1S2	2475	522	-0.74	0.172	7.13	0.72
	RHF	6-31G**	2525	549	-0.77	-0.085	-3.51	0.54
	B3LYP	Br-1S2	1725	806	-0.67	0.204	8.42	0.21
	B3LYP	6-31G**	1780	876	-0.72	-0.062	-2.57	0.35

Note: There are two crystallographic sites for Cp_2ZrBr_2 . One Cp ring of site 2 has been modelled with disorder and possesses two conformations. Calculations are shown for both conformations.

Table B13. Calculated ^{91}Zr NMR Tensor Parameters for $\text{Cp}^*_2\text{ZrCl}_2$ (**1**) Using Coordinates From the Single Crystal X-ray Structure of $(\text{CpMe}_4\text{Et})_2\text{ZrCl}_2$ and Structures With Idealized Cp rings

Zr Basis	Method	Cl Basis	σ_{iso} (ppm)	Ω (ppm)	κ	V_{33} (a.u.)	C_Q (MHz)	η_Q
Experiment			-	225	-0.90	0.063	2.6	0.22
X-ray Coordinates								
6s3p3d	RHF	cc-pVDZ	2486	192	-0.71	-0.095	-3.92	0.72
	B3LYP	cc-pVDZ	1759	251	-0.77	-0.117	-4.85	0.56
Zr-5F3	RHF	cc-pVDZ	2488	113	-1.00	-0.117	-4.82	0.28
	B3LYP	cc-pVDZ	1880	156	-0.51	-0.201	-8.31	0.15
12s9p5d	RHF	cc-pVDZ	2509	283	-0.87	-0.166	-6.88	0.14
	B3LYP	cc-pVDZ	1712	402	-0.83	-0.109	-4.51	0.75
Idealized Cp Rings								
6s3p3d	RHF	cc-pVDZ	2492	203	-0.54	-0.088	-3.64	0.27
	B3LYP	cc-pVDZ	1774	286	-0.52	0.072	2.97	0.23
Zr-5F3	RHF	cc-pVDZ	2505	166	-0.29	-0.046	-1.91	0.55
	B3LYP	cc-pVDZ	1895	201	-0.16	-0.147	-6.07	0.17
12s9p5d	RHF	cc-pVDZ	2519	288	-0.91	-0.088	-3.65	0.40
	B3LYP	cc-pVDZ	1725	433	-0.66	0.071	2.92	0.84

Table B14. Calculated EFG Tensor Parameters for the Central Molecule of a 12 Molecule Cluster of Cp_2ZrMeCl .

Structure	V_{33} (a.u.)	C_Q (MHz)	η_Q
Cluster 1	-0.829515	-34.30	0.66
Cluster 2	0.805366	33.31	0.04
Isolated Molecule (site 2)	0.806216	33.34	0.11

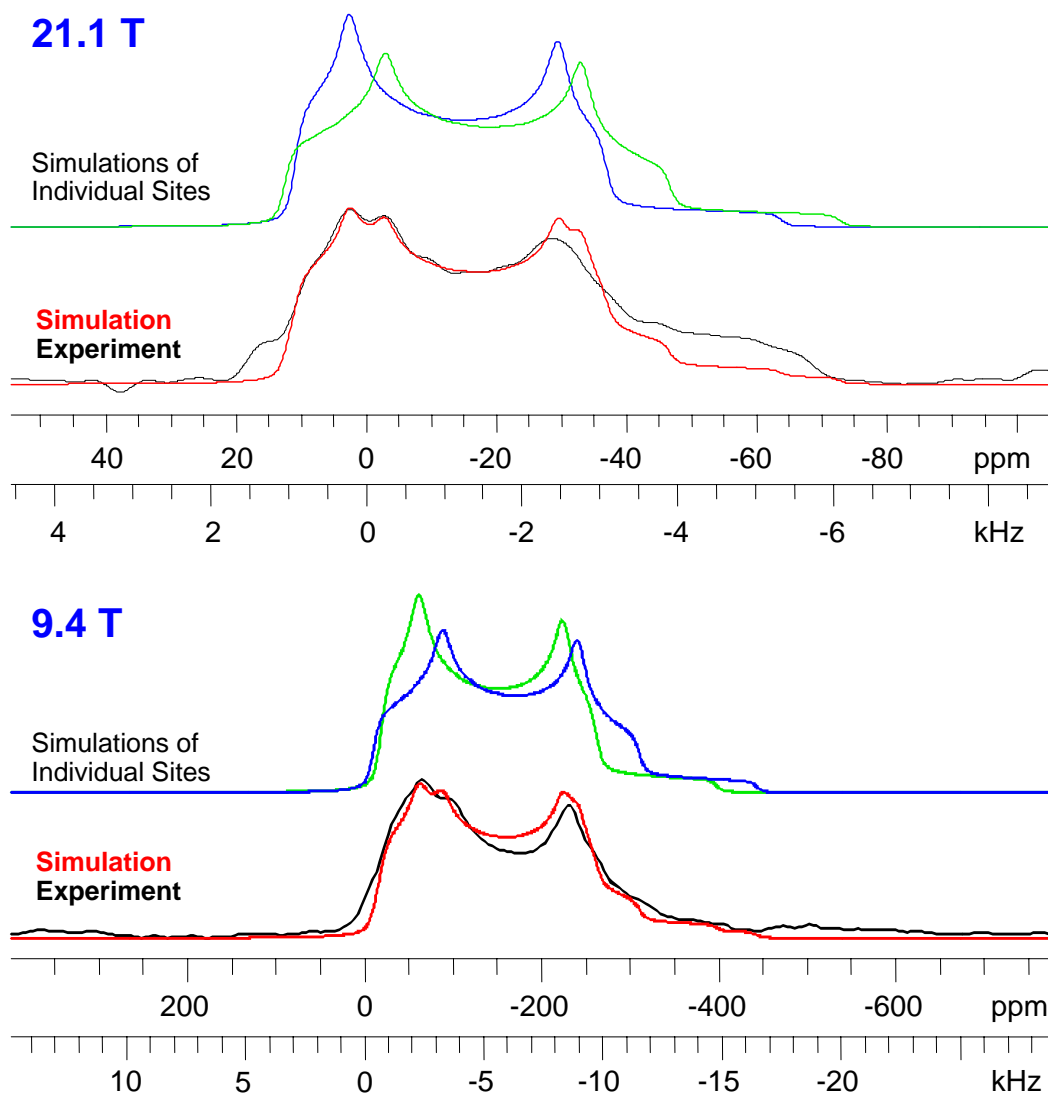


Figure B4. MAS ^{91}Zr SSNMR spectra of Cp_2ZrCl_2 acquired at 21.1 T (top) and 9.4 T (bottom). Analytical simulations are overlaid on top of the experimental spectra. Two sites were employed in the simulations. A de-convolution of the individual simulated sites is also shown for both fields. The spectrum acquired at 21.1 T was acquired with a sample spinning speed (ν_{rot}) of 10 kHz.

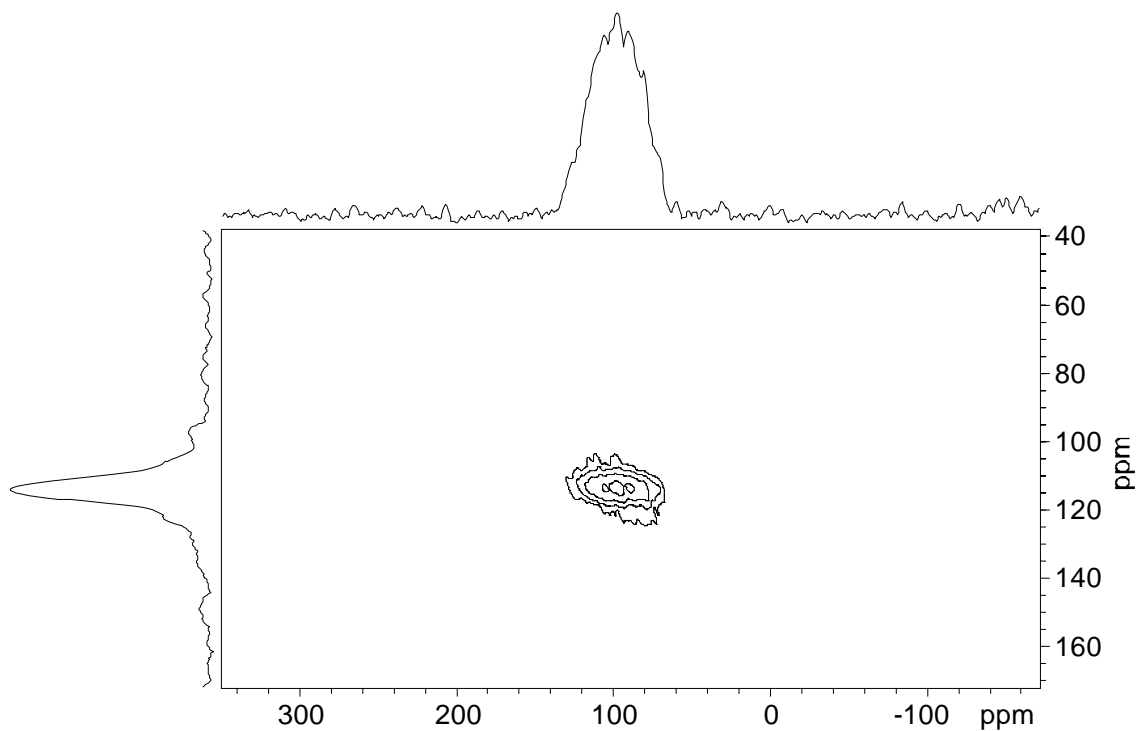


Figure B5 ^{91}Zr triple quantum-MQMAS NMR spectrum of Cp_2ZrBr_2 at 9.4 T. Although the direct dimension clearly exhibits NMR patterns for more than one ^{91}Zr site, it is not possible to separate them at an applied magnetic field of 9.4 T. A spinning speed of $\nu_{\text{rot}} = 10000$ Hz was employed.

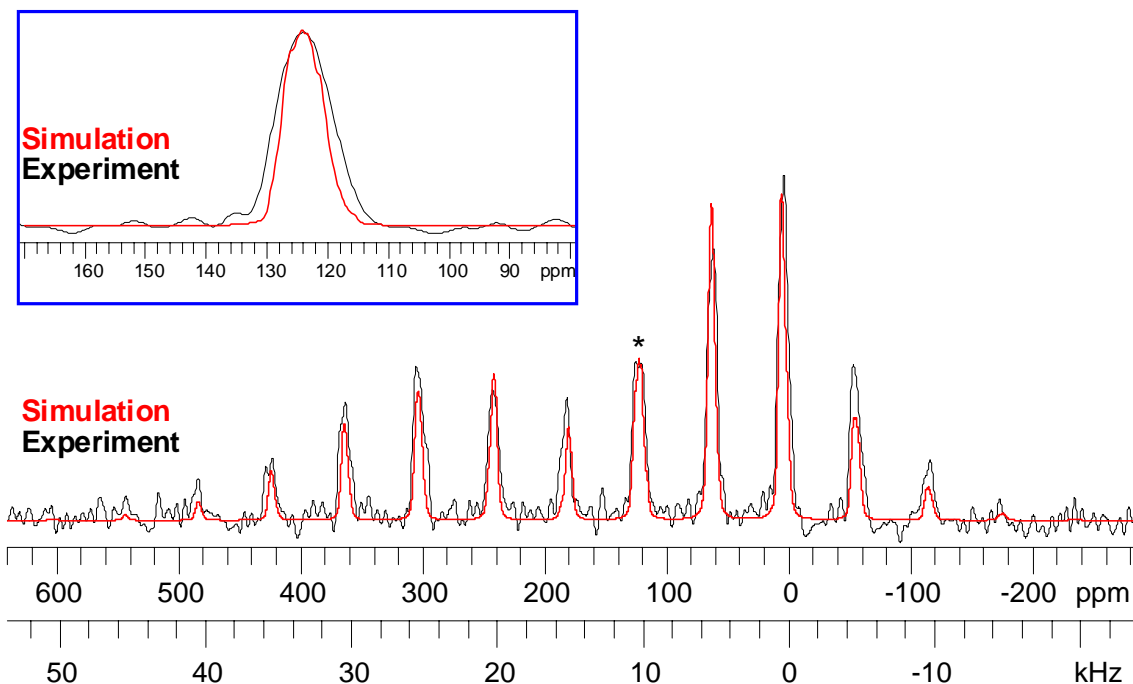


Figure B6. MAS ^{91}Zr SSNMR spectrum of Cp_2ZrBr_2 (**2**) acquired at a sample spinning speed (v_{rot}) of 5000 Hz at 21.1 T. The asterisk denotes the isotropic peak. All other peaks are spinning sidebands. A numerical simulation performed with the SIMPSON program is overlaid on top of the experimental spectrum. The simulation employs the CS tensor parameters and Euler angles obtained from the static spectra. Inset: The spectrum that results from adding each of the spinning sidebands to the isotropic peak. An analytical simulation generated with the WSolids program is overlaid on the experimental spectrum. The simulation employs two sites which possess the same EFG tensor parameters as those employed for simulations of the 9.4 T MAS spectrum. δ_{iso} values of 128 ppm and 130 ppm were employed for the two sites in the simulation.

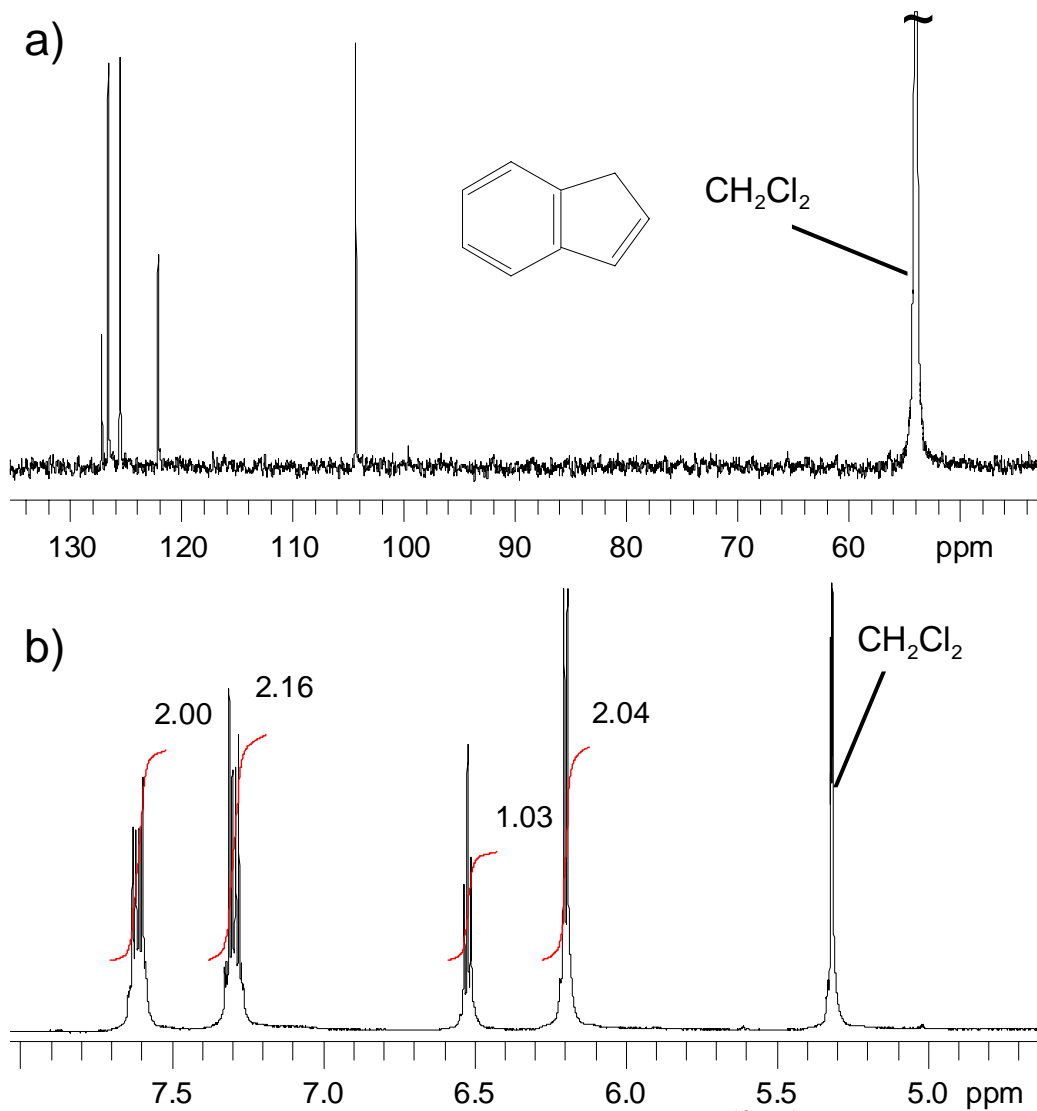


Figure B7. Solution NMR spectra of $\text{Ind}_2\text{ZrCl}_2$ (**6**). (a) $^{13}\text{C}\{^1\text{H}\}$ NMR spectrum in CH_2Cl_2 . The indenyl ligand fragment is pictured. (b) ^1H NMR spectrum in CD_2Cl_2 .

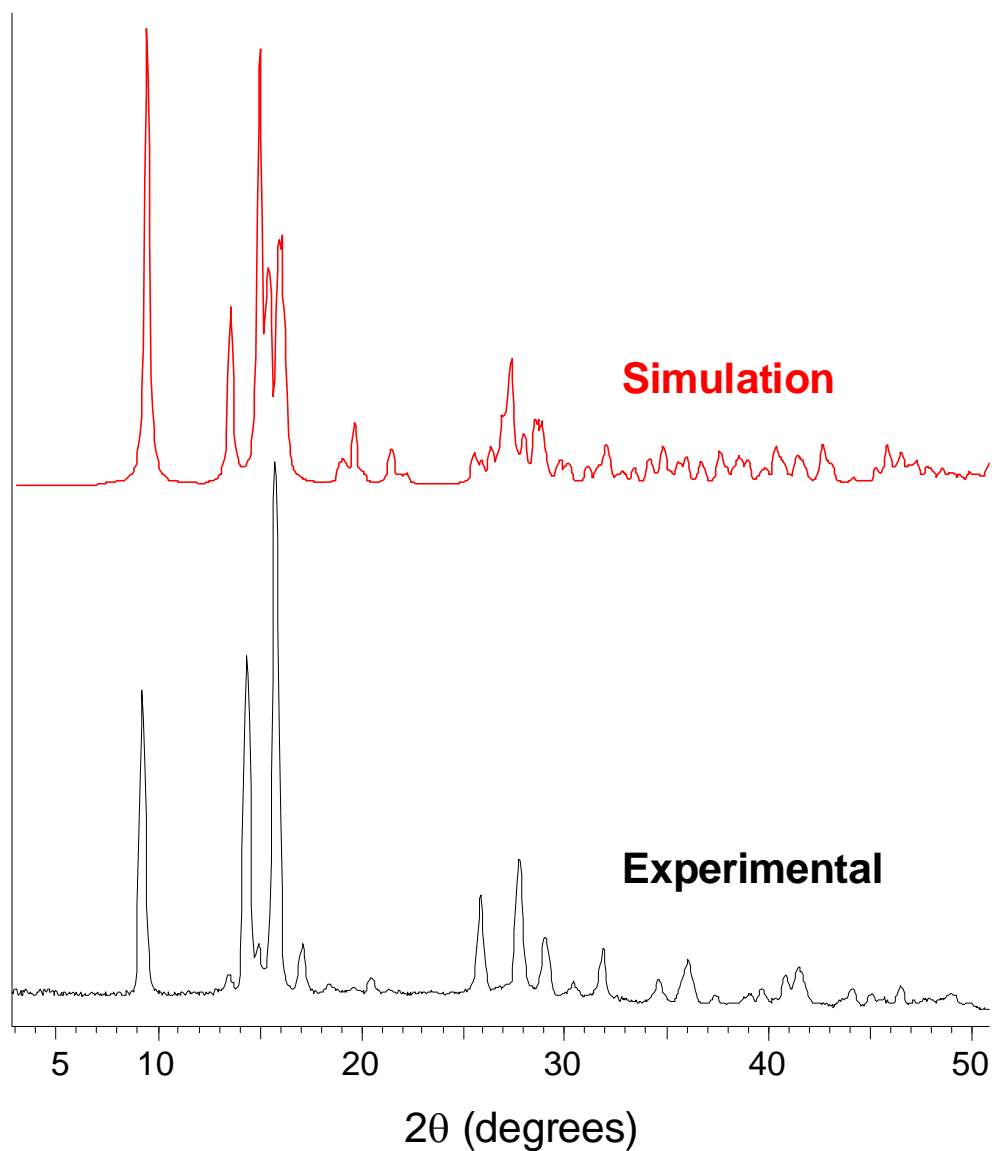


Figure B8. Experimental powder X-ray diffraction pattern (bottom trace) measured from **6** at room temperature. The simulated powder pattern (top trace) has been calculated from the previously determined single crystal X-ray diffraction structure (Repo, T.; Klinga, M.; Mutikainen, I.; Su, Y.; Leskela, M.; Polamo, M., *Acta Chem. Scand.* **1996**, *50*, (12), 1116-1120). The single crystal X-ray diffraction structure was determined at a temperature of 153 K. Temperature dependent polymorphism may account for the discrepancy in the measured and observed powder patterns.

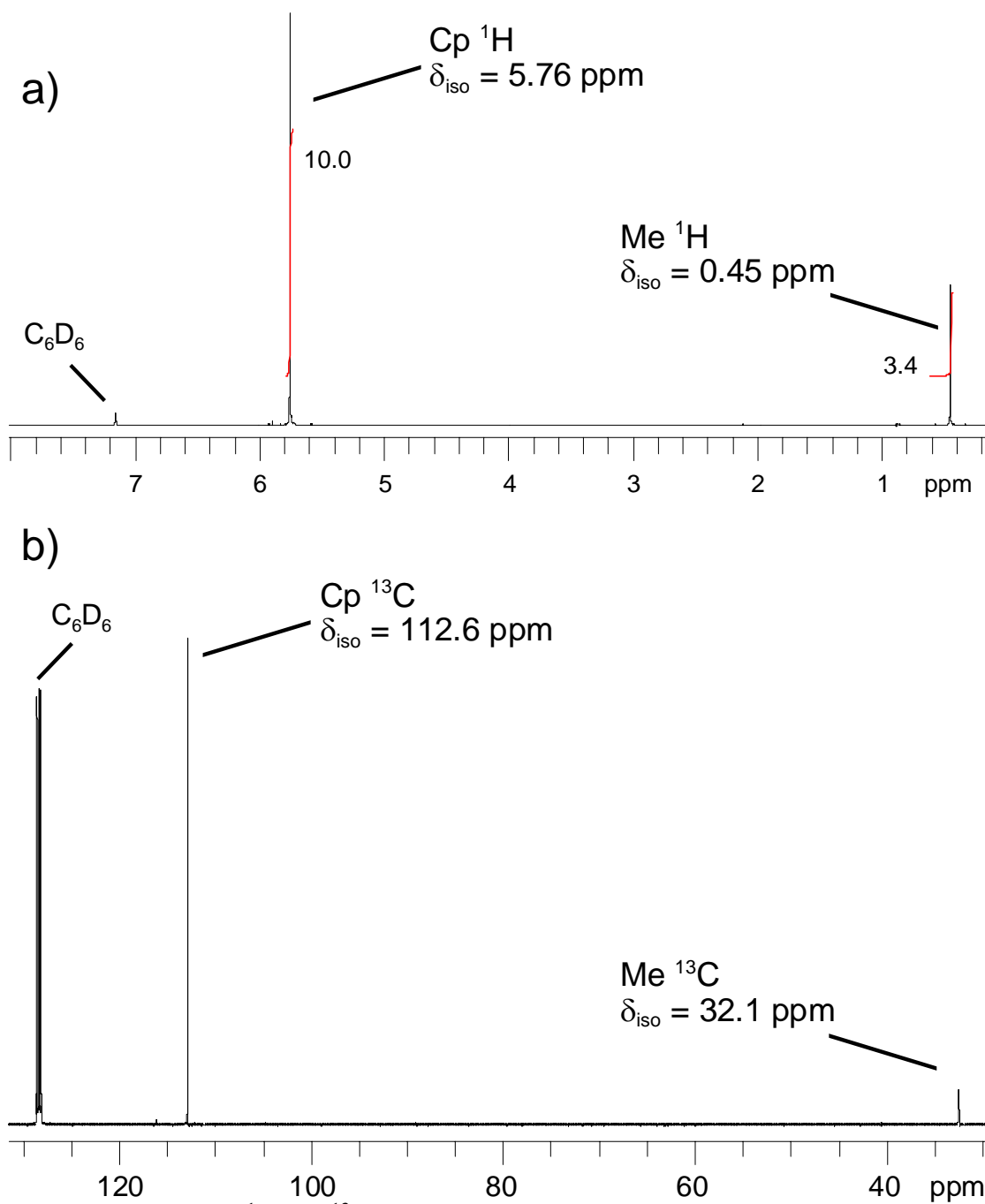


Figure B9. Solution ^1H and ^{13}C NMR spectra of **7** in C_6D_6 . These spectra were collected immediately after the sample was synthesized. (a) ^1H NMR (b) ^{13}C NMR.

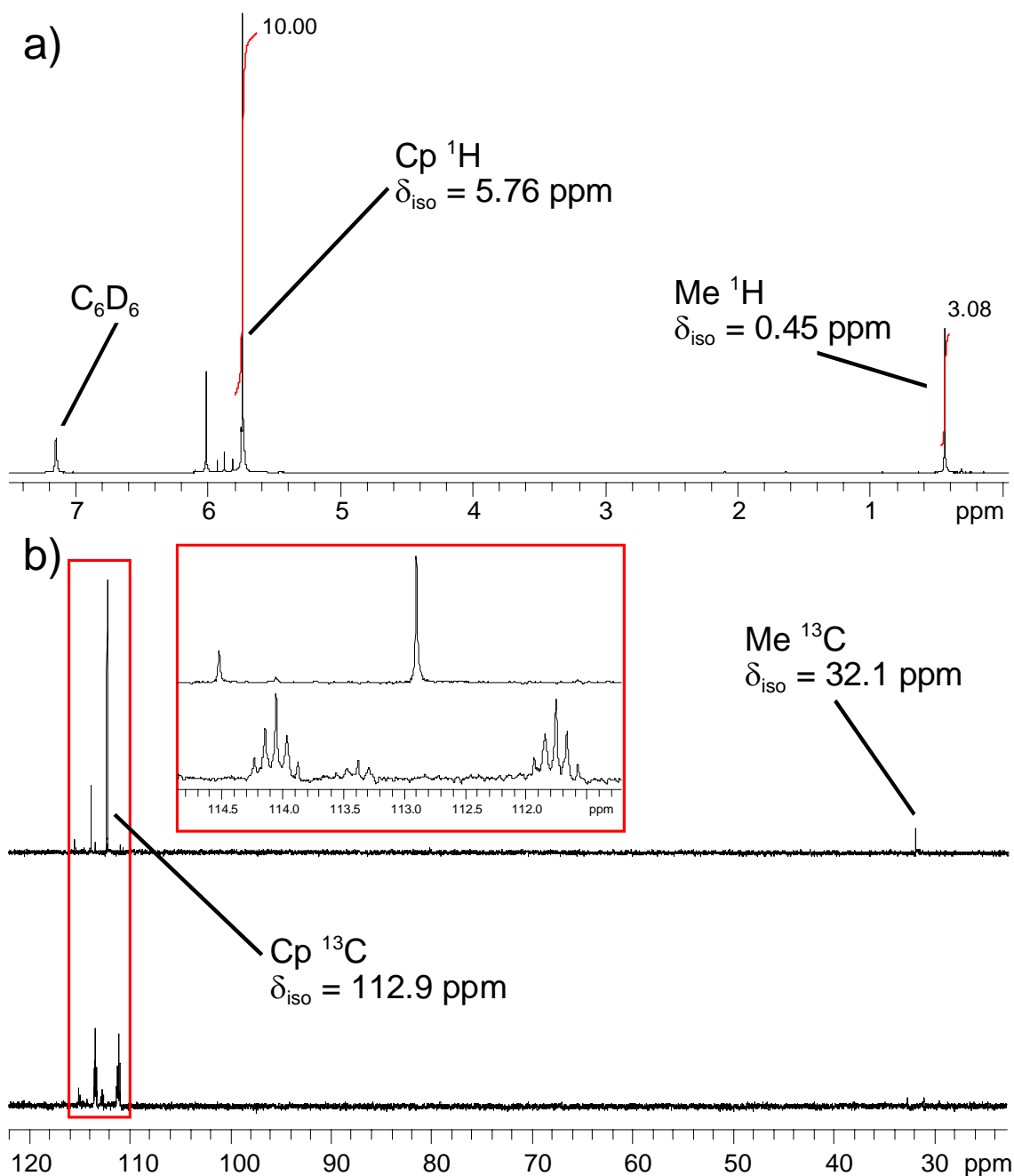


Figure B10. ^1H and ^{13}C solution NMR spectra of the sample of **7** which was employed for experiments at 21.1 T. These spectra were acquired several months after the solid-state ^{91}Zr NMR spectrum had been acquired. (a) ^1H NMR spectrum. (b) ^{13}C NMR spectra with and without ^1H decoupling are shown. C_6D_6 was employed as the solvent. The methyl peak is not visible in the ^{13}C NMR spectrum without decoupling due to low signal to noise.

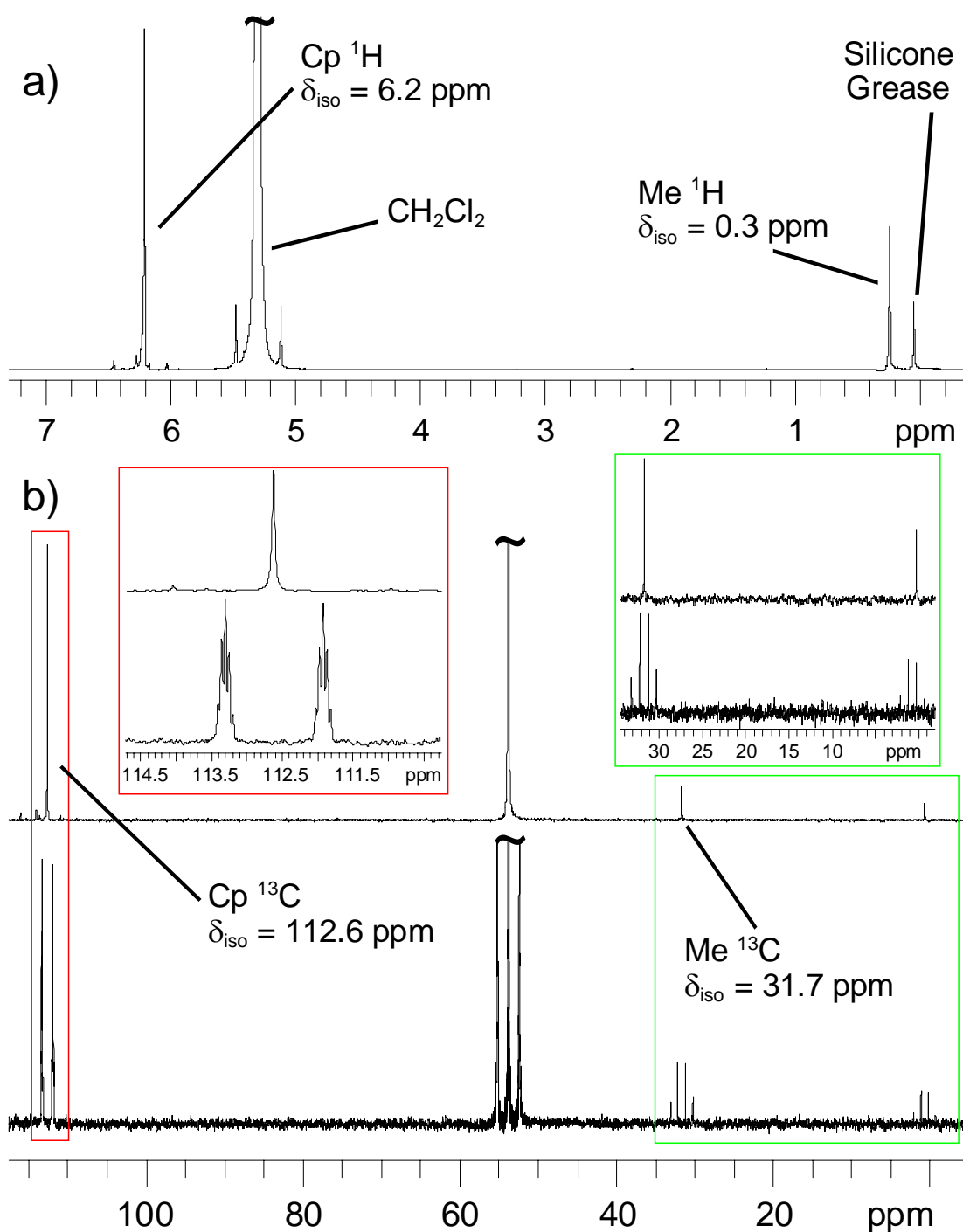


Figure B11. ^1H and ^{13}C solution NMR spectra of the sample of **7** which was employed for experiments at 9.4 T. These spectra were recorded after the sample had been characterized by ^{91}Zr SSNMR. (a) ^1H NMR spectrum. (b) ^{13}C NMR spectra with and without ^1H decoupling are shown. The peaks visible at $\delta_{\text{iso}}(^1\text{H}) = 0.05$ ppm and $\delta_{\text{iso}}(^{13}\text{C}) = 1.04$ ppm are attributed to silicone grease which was used to seal the top of glass tubes used for SSNMR experiments. CH₂Cl₂ was employed as the solvent. All CH₂Cl₂ resonances have been truncated.

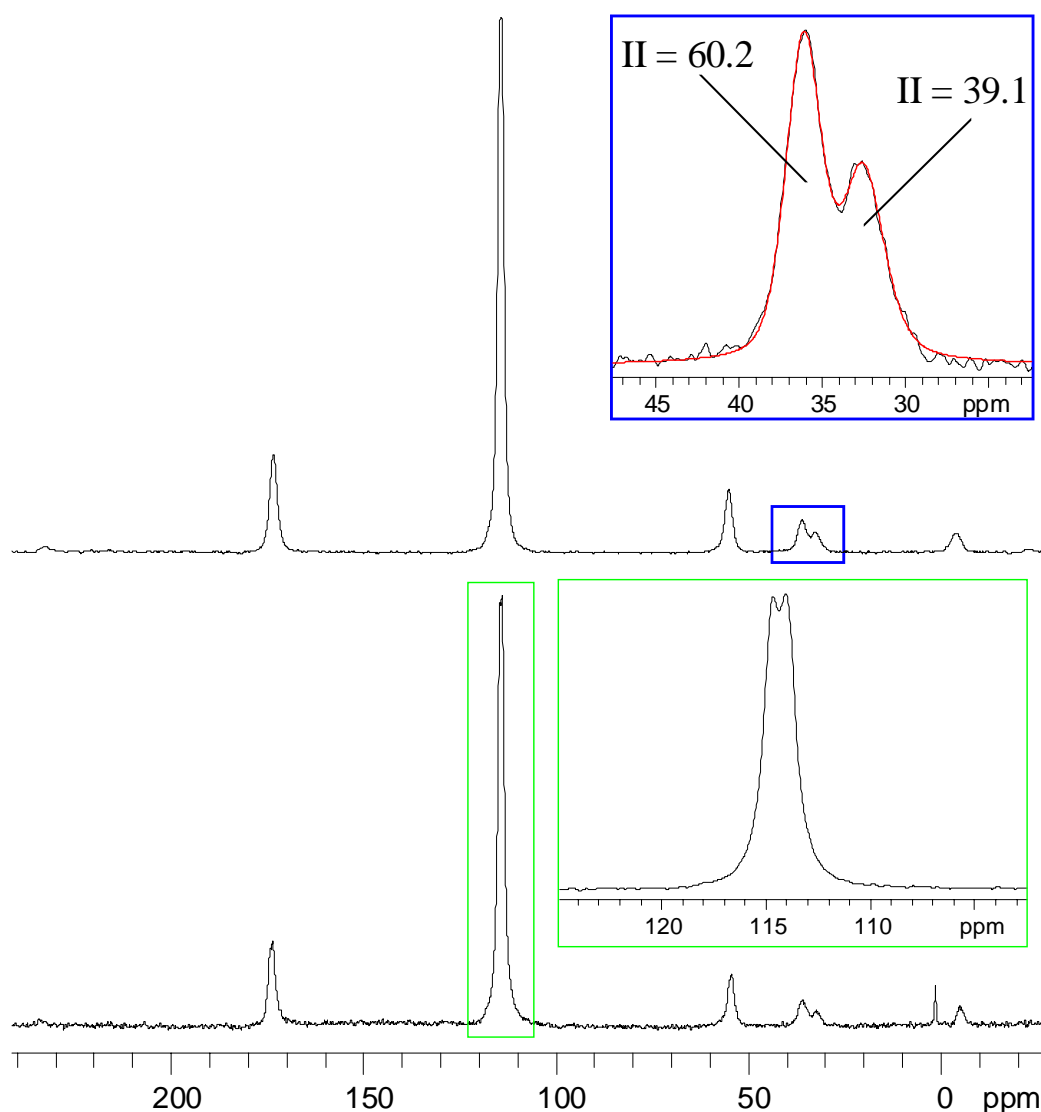


Figure B12. Solid-state ^{13}C NMR spectra of **7** acquired with the variable amplitude cross-polarization sequence (top trace) and the Bloch decay sequence (bottom trace). Spectra were acquired from the sample employed for experiments at 9.4 T. Both spectra were acquired with spinning speeds of $\nu_{\text{rot}} = 6000$ Hz. The silicone grease signal observed in the solution ^{13}C NMR spectra is visible near 0 ppm in the solid-state ^{13}C Bloch decay NMR spectrum. The silicone grease signal is not visible in the cross-polarization spectrum due to the averaging of ^1H - ^{13}C dipolar coupling by translational/rotational motion of the grease molecules. Two peaks corresponding to cyclopentadienyl carbons are visible (114.7 and 114.1 ppm, shown in bottom inset). Two peaks in the methyl region are visible (36.1 ppm and 32.6 ppm). The top inset shows an expansion of the methyl region with a linefitting simulation overlaid. The integrated intensity of the two methyl peaks matches that expected from the fractional occupancies listed in the single crystal X-ray diffraction structure.

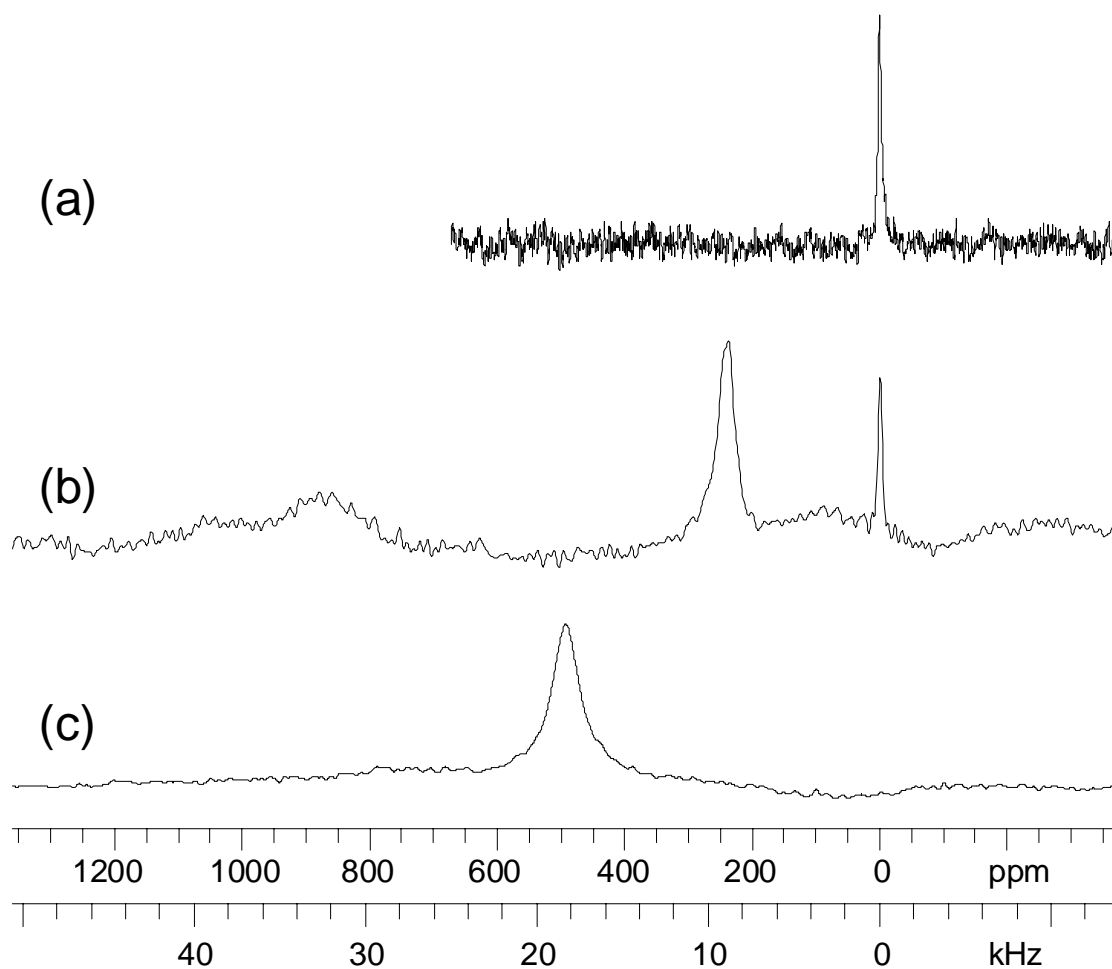


Figure B13. Solution ^{91}Zr NMR spectra of zirconocenes dissolved in CH_2Cl_2 . (a) Cp_2ZrCl_2 [$\delta_{\text{iso}} = 0.0$ ppm, FWHM = 224 Hz]. (b) Cp_2ZrMeCl (**7**) [$\delta_{\text{iso}} = 240.4$ ppm, FWHM = 1214 Hz]. (c) Cp_2ZrMe_2 (**8**) [$\delta_{\text{iso}} = 493$ ppm, FWHM = 2524 Hz]. Based upon solution ^{91}Zr NMR spectra there appears to be a significant amount of Cp_2ZrCl_2 within the sample of Cp_2ZrMeCl . Integration of the peaks in the ^{91}Zr spectrum reveals an approximate ratio of 100:21 of Cp_2ZrMeCl to Cp_2ZrCl_2 , however, this ratio is misleading as the narrower ^{91}Zr signal of Cp_2ZrCl_2 will decay much more slowly due to a much longer T_2 . This leads to a relatively high intensity for the Cp_2ZrCl_2 resonance; much of the signal corresponding to Cp_2ZrMeCl is lost during ring down delays. Solution ^1H NMR spectra indicated that the ratio of Cp_2ZrMeCl to Cp_2ZrCl_2 is closer to 100:2.

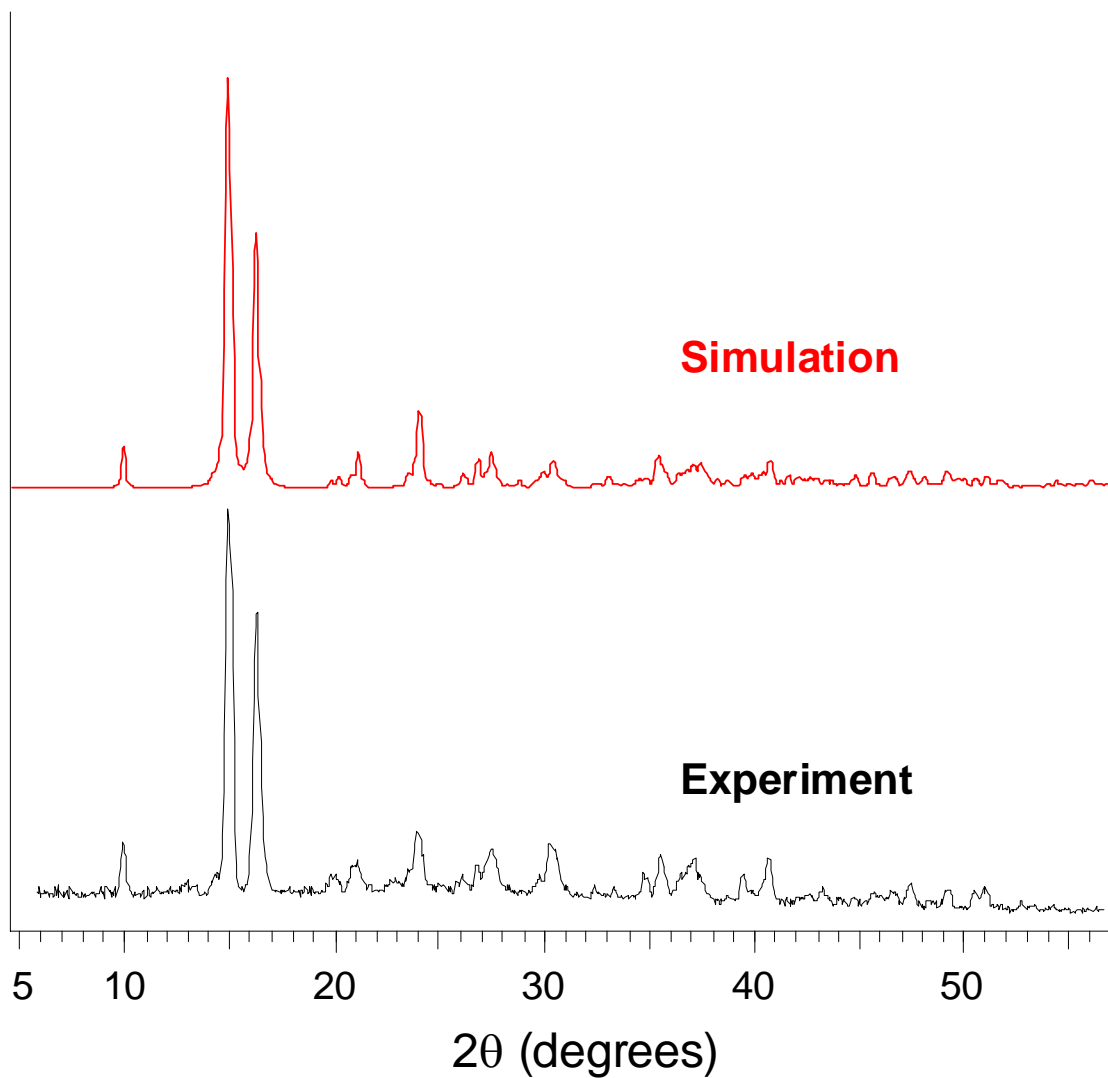


Figure B14. Experimental powder X-ray diffraction pattern (bottom trace) measured from **7** at room temperature. The simulated powder pattern (top trace) has been calculated with the single crystal X-ray diffraction structure reported in this work. These diffraction patterns were acquired before solid-state NMR spectra had been acquired.

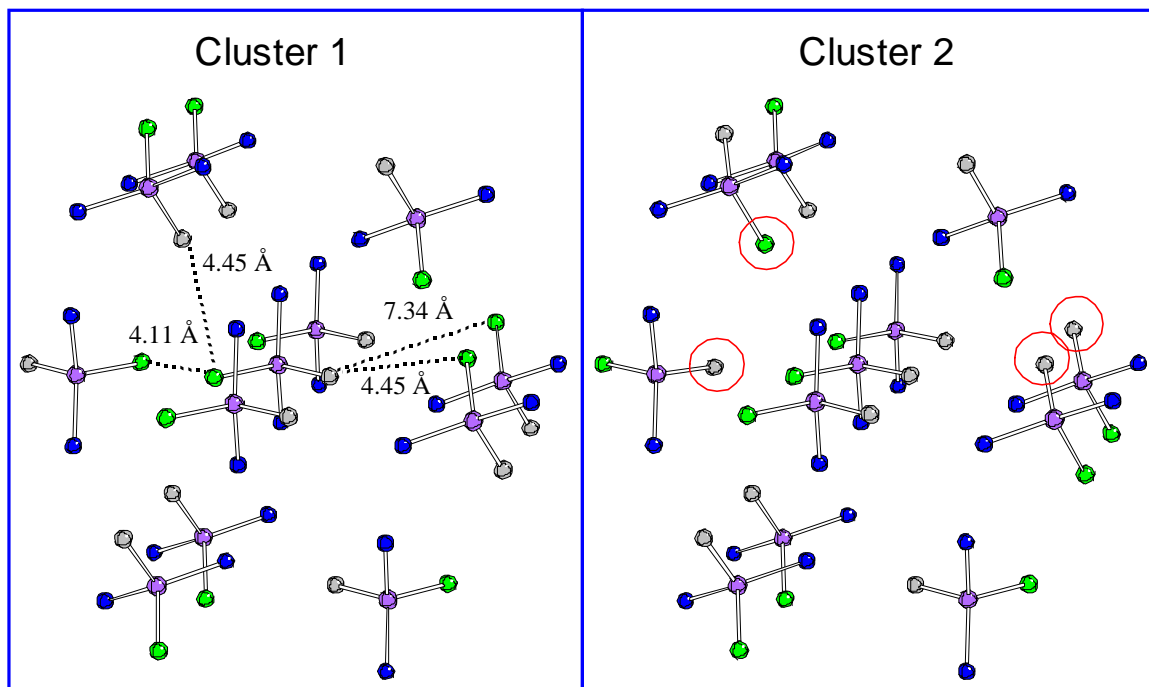


Figure B15. The two different 12-molecule clusters employed for the calculation of ^{91}Zr EFG tensor parameters of **7**. The cyclopentadienyl (Cp) ligands have been removed and the centroids (blue) of the Cp rings are included for clarity. The position of some of the Me carbon (grey) and Cl atoms (green) vary between the two clusters. The Me carbon and Cl atoms which are located in different positions in Cluster 2 are circled. Interatomic distances are shown for these Me carbon and Cl distances. The EFG tensor parameters for the central atom are reported in Table B14.

Appendix C: Supplementary Figures and Tables for Chapter 4

Table C1. Acquisition Parameters for MAS $^{47/49}\text{Ti}$ SSNMR Spectra Acquired at 21.1 T^a

	1	2	3	4
Pulse Sequence ^b	Echo	Echo	Echo	Echo
Number of scans	4474	31870	1008	3974
Recycle Delay (s)	1.0	1.0	4.0	1.0
Dwell (μs)	4.0	4.0	10.0	4.0
Spectral width (kHz)	250.0	250.0	100.0	250.0
Spinning Speed (Hz)	12500	10000	10000	10000
Acquisition length (number of points)	1024	1024	1024	1024
90° pulse width [$\pi/2$] (μs)	1.30	1.30	1.30	1.30
180° pulse widths [π] (μs)	2.60	2.60	2.60	2.60
Ring-down delays [τ_1] (μs)	80.0	100.0	100.0	100.0
Ring-down delays [τ_2] (μs)	20.0	20.0	20.0	20.0

^aAll MAS spectra acquired at 21.1 T were acquired on a Bruker 4mm HX MAS probe. ^bEcho refers to a 16-step Hahn echo sequence.

Table C2. Acquisition Parameters for MAS $^{47/49}\text{Ti}$ SSNMR Spectra Acquired at 9.4 T

	3	4
Probe ^a	4 mm HXY	5 mm HXY
Pulse Sequence ^b	DFS/Echo	DFS/QCPMG
Number of scans	3680	25000
Recycle Delay (s)	2.0	3.0
Dwell (μs)	12.5	4.0
Spectral width (kHz)	80.0	250.0
Spinning Speed (Hz)	13000	8000
Acquisition length (number of points)	512	13125
90° pulse width [$\pi/2$] (μs)	2.0	2.50
180° pulse widths [π] (μs)	4.0	5.00
Ring-down delays [τ_1] (μs)	153.85	125.0
Ring-down delays [τ_2] (μs)	66.35	250.0
Number of Meiboom-Gill loops [N]	-	10
Real points per loop	-	1250
Spikelet Separation [$1/\tau_a$] (Hz)	-	200.0
DFS Start Frequency (MHz)	1.150	0.900
DFS End Frequency (MHz)	0.140	0.200
Length of DFS Sweep (ms)	0.650	1.200
Number of Steps in DFS	2158	1229
Waveform		
DFS Step Length (μs)	0.301	0.976

^aMAS spectra at 9.4 T were acquired on Chemagnetics T3 MAS probes. ^bDFS/Echo and DFS/QCPMG refers to a sequence where the Hahn echo and QCPMG portions, respectively, are prefaced by a double frequency sweep (DFS) waveform [see main text for references].

Table C3. Acquisition Parameters for Static $^{47/49}\text{Ti}$ SSNMR Spectra Acquired at 21.1 T

	1	2	3	4
Probe	5 mm	7 mm	4 mm	7 mm
Pulse Sequence ^a	Echo	Echo	Echo	Echo
Number of scans	8898	20951	35218	16764
Recycle Delay (s)	1.0	2.0	1.0	2.0
Dwell (μs)	2.5	5.0	10.0	5.0
Spectral width (kHz)	400.0	200.0	100.0	200.0
Acquisition length (number of points)	1024	512	1024	512
90° pulse width [$\pi/2$] (μs)	2.1	1.4	8.4	1.4
180° pulse widths [π] (μs)	4.2	2.8	16.8	2.8
Ring-down delays [τ_1] (μs)	100.0	80.0	60.0	80.0
Ring-down delays [τ_2] (μs)	20.0	10.0	10.0	10.0

^aStatic spectra at 21.1 T were acquired on a Bruker 4mm MAS probe or a home built single channel 5mm coil or 7 mm coil static transverse coil probes. ^bDFS/Echo and DFS/QCPMG refers to a sequence where the Hahn echo and QCPMG portions, respectively, are prefaced by a double frequency sweep (DFS) waveform [see main text for references].

Table C4. Acquisition Parameters for Static $^{47/49}\text{Ti}$ SSNMR Spectra Acquired at 9.4 T

	1	2	3	4
Probe	5 mm static	5 mm static	5 mm static	5 mm static
Pulse Sequence ^a	DFS/QCPMG	DFS/QCPMG	Echo	DFS/Echo
Number of scans	30592	30240	150752	34644
Recycle Delay (s)	2.0	2.0	4.0	4.0
Dwell (μs)	10.0	6.2	5.0	6.2
Spectral width (kHz)	100.0	160.0	200.0	160.0
Acquisition length (number of points)	2048	4096	1024	4096
90° pulse width [$\pi/2$] (μs)	2.50	2.10	6.00	2.75
180° pulse widths [π] (μs)	5.00	4.20	12.00	5.50
Ring-down delays [τ_1] (μs)	100.0	100.0	100.0	140.0
Ring-down delays [τ_2] (μs)	100.0	100.0	60.0	60.0
Number of Meiboom- Gill loops [N]	19	25	-	-
Real points per loop	100	160	-	-
Spikelet Separation [$1/\tau_a$] (Hz)	1000.0	1000.0	-	-
DFS Start Frequency (MHz)	1.000	1.300	-	1.000
DFS End Frequency (MHz)	0.250	0.320	-	0.250
Length of DFS Sweep (ms)	0.200	1.800	-	0.200
Number of Steps in DFS Waveform	800	7200	-	800
DFS Step Length (μs)	0.25	0.25	-	0.25

^aDFS/Echo and DFS/QCPMG refers to a sequence where the Hahn echo and QCPMG portions, respectively, are prefaced by a double frequency sweep (DFS) waveform [see main text for references].

Table C5. Quantum Chemical Calculations of ^{49}Ti CS and EFG Tensor Parameters for **1** with Variable Ti Basis Sets.

Site 1 – RHF Calculations								
Structure	Ti Basis	σ_{iso} (ppm)	δ_{iso} (ppm)	Ω (ppm)	κ	C_Q (MHz)	η_Q	
Ideal Cp	cc-pVTZ	559	-600	109	0.9	2.55	0.80	
X-ray Cp	cc-pVTZ	585	-642	170	0.3	6.44	0.32	
Ideal Cp	cc-pVQZ	558	-596	107	0.9	3.61	0.64	
X-ray Cp	cc-pVQZ	584	-637	168	0.3	7.60	0.30	
Ideal Cp	ahlrichs-pVDZ	409	-689	166	0.7	-6.14	0.21	
X-ray Cp	ahlrichs-pVDZ	437	-737	252	0.2	-2.05	0.55	
Ideal Cp	ahlrichs-VTZ	564	-623	148	0.5	2.09	0.48	
X-ray Cp	ahlrichs-VTZ	591	-667	216	0.0	6.64	0.15	
Ideal Cp	6-311G**	572	-630	143	0.4	2.10	0.55	
X-ray Cp	6-311G**	599	-674	209	0.0	6.75	0.18	
Site 1 – B3LYP Calculations								
Structure	Ti Basis	σ_{iso} (ppm)	δ_{iso} (ppm)	Ω (ppm)	κ	C_Q (MHz)	η_Q	
Ideal Cp	cc-pVTZ	-98	-690	473	-0.2	1.86	0.97	
X-ray Cp	cc-pVTZ	-62	-744	538	-0.3	5.60	0.35	
Ideal Cp	cc-pVQZ	-112	-690	472	-0.2	-1.83	0.85	
X-ray Cp	cc-pVQZ	-76	-744	536	-0.3	5.43	0.41	
Ideal Cp	ahlrichs-pVDZ	-90	-678	526	-0.3	3.85	0.16	
X-ray Cp	ahlrichs-pVDZ	-57	-729	588	-0.4	7.82	0.07	
Ideal Cp	ahlrichs-VTZ	-82	-688	520	-0.3	-2.42	0.48	
X-ray Cp	ahlrichs-VTZ	-45	-743	585	-0.4	5.84	0.58	
Ideal Cp	6-311G**	-97	-701	517	-0.3	-2.45	0.41	
X-ray Cp	6-311G**	-60	-757	583	-0.4	5.61	0.67	
Site 2 – RHF Calculations								
Structure	Ti Basis	σ_{iso} (ppm)	δ_{iso} (ppm)	Ω (ppm)	κ	C_Q (MHz)	η_Q	
Ideal Cp	cc-pVTZ	560	-602	112	0.9	2.46	0.71	
X-ray Cp	cc-pVTZ	565	-622	156	0.5	7.40	0.22	
Ideal Cp	cc-pVQZ	560	-597	111	0.9	3.53	0.57	
X-ray Cp	cc-pVQZ	564	-618	153	0.5	8.35	0.21	
Ideal Cp	ahlrichs-pVDZ	412	-691	168	0.7	-6.02	0.16	
X-ray Cp	ahlrichs-pVDZ	415	-715	230	0.3	4.24	0.95	
Ideal Cp	ahlrichs-VTZ	566	-625	150	0.5	1.99	0.29	
X-ray Cp	ahlrichs-VTZ	571	-647	198	0.2	7.80	0.09	
Ideal Cp	6-311G**	573	-631	145	0.5	1.99	0.35	
X-ray Cp	6-311G**	579	-654	192	0.1	7.98	0.11	
Site 2 – B3LYP Calculations								
Structure	Ti Basis	σ_{iso} (ppm)	δ_{iso} (ppm)	Ω (ppm)	κ	C_Q (MHz)	η_Q	
Ideal Cp	cc-pVTZ	-96	-692	476	-0.2	-1.81	0.91	
X-ray Cp	cc-pVTZ	-85	-721	522	-0.3	6.82	0.29	
Ideal Cp	cc-pVQZ	-110	-692	475	-0.2	-1.82	0.70	
X-ray Cp	cc-pVQZ	-99	-721	521	-0.2	6.72	0.33	
Ideal Cp	ahlrichs-pVDZ	-88	-680	530	-0.3	3.80	0.12	
X-ray Cp	ahlrichs-pVDZ	-78	-708	576	-0.3	8.32	0.04	
Ideal Cp	ahlrichs-VTZ	-80	-690	522	-0.3	-2.43	0.35	
X-ray Cp	ahlrichs-VTZ	-68	-720	569	-0.3	7.30	0.44	
Ideal Cp	6-311G**	-95	-703	519	-0.3	-2.47	0.31	
X-ray Cp	6-311G**	-84	-733	567	-0.3	7.24	0.49	

Table C6. Quantum Chemical Calculations of ^{49}Ti CS and EFG Tensor Parameters for **2** with Variable Ti Basis Sets.

RHF Calculations								
Structure	Ti Basis	σ_{iso} (ppm)	δ_{iso} (ppm)	Ω (ppm)	κ	C_Q (MHz)	η_Q	
Ideal Cp	cc-pVTZ	364	-405	94	0.1	2.71	0.48	
X-ray Cp	cc-pVTZ	347	-404	117	-0.2	7.44	0.40	
Ideal Cp	cc-pVQZ	368	-405	98	0.1	3.77	0.38	
X-ray Cp	cc-pVQZ	351	-404	118	-0.2	8.00	0.33	
Ideal Cp	ahlricks-pVDZ	198	-478	101	-0.1	-5.86	0.40	
X-ray Cp	ahlricks-pVDZ	180	-479	138	-0.4	-6.49	0.42	
Ideal Cp	ahlricks-VTZ	384	-443	72	-0.3	-3.03	0.45	
X-ray Cp	ahlricks-VTZ	367	-443	98	-0.6	7.29	0.66	
Ideal Cp	6-311G**	395	-453	63	-0.3	-3.09	0.56	
X-ray Cp	6-311G**	379	-453	90	-0.5	7.67	0.61	
B3LYP Calculations								
Structure	Ti Basis	σ_{iso} (ppm)	δ_{iso} (ppm)	Ω (ppm)	κ	C_Q (MHz)	η_Q	
Ideal Cp	cc-pVTZ	-402	-386	287	0.0	3.68	0.66	
X-ray Cp	cc-pVTZ	-418	-388	276	0.2	-6.13	0.58	
Ideal Cp	cc-pVQZ	-415	-387	282	0.0	4.36	0.31	
X-ray Cp	cc-pVQZ	-431	-389	270	0.2	-6.07	0.51	
Ideal Cp	ahlricks-pVDZ	-369	-399	327	-0.1	-3.99	0.67	
X-ray Cp	ahlricks-pVDZ	-385	-401	317	0.1	6.39	0.83	
Ideal Cp	ahlricks-VTZ	-371	-399	316	-0.1	5.38	0.74	
X-ray Cp	ahlricks-VTZ	-387	-402	304	0.0	-7.27	0.47	
Ideal Cp	6-311G**	-386	-413	312	-0.1	5.79	0.68	
X-ray Cp	6-311G**	-402	-415	301	0.0	-7.52	0.46	

Table C7. Quantum Chemical Calculations of ^{49}Ti CS and EFG Tensor Parameters for **3** with Variable Ti Basis Sets.

RHF Calculations								
Structure	Ti Basis	σ_{iso} (ppm)	δ_{iso} (ppm)	Ω (ppm)	κ	C_Q (MHz)	η_Q	
Ideal Cp	cc-pVTZ	129	-170	113	-0.8	9.06	0.17	
X-ray Cp	cc-pVTZ	125	-182	111	-0.7	9.00	0.24	
Ideal Cp	cc-pVQZ	129	-166	115	-0.8	9.92	0.17	
X-ray Cp	cc-pVQZ	125	-178	112	-0.7	9.84	0.23	
Ideal Cp	ahlricks-pVDZ	-80	-200	44	-0.5	3.76	0.46	
X-ray Cp	ahlricks-pVDZ	-86	-214	42	-0.2	3.84	-0.60	
Ideal Cp	ahlricks-VTZ	96	-155	171	-0.8	9.06	0.22	
X-ray Cp	ahlricks-VTZ	91	-168	168	-0.8	9.02	0.31	
Ideal Cp	6-311G**	92	-151	181	-0.9	9.33	0.21	
X-ray Cp	6-311G**	88	-163	177	-0.8	9.28	0.30	
B3LYP Calculations								
Structure	Ti Basis	σ_{iso} (ppm)	δ_{iso} (ppm)	Ω (ppm)	κ	C_Q (MHz)	η_Q	
Ideal Cp	cc-pVTZ	-531	-257	344	-0.8	7.96	0.20	
X-ray Cp	cc-pVTZ	-535	-271	337	-0.8	7.87	0.27	
Ideal Cp	cc-pVQZ	-545	-256	343	-0.8	8.18	0.21	
X-ray Cp	cc-pVQZ	-550	-270	336	-0.8	8.07	0.27	
Ideal Cp	ahlricks-pVDZ	-529	-239	375	-0.8	8.54	0.19	
X-ray Cp	ahlricks-pVDZ	-533	-253	369	-0.8	8.54	0.24	
Ideal Cp	ahlricks-VTZ	-528	-242	404	-0.9	8.11	0.25	
X-ray Cp	ahlricks-VTZ	-532	-256	396	-0.8	8.03	0.32	
Ideal Cp	6-311G**	-558	-240	407	-0.9	8.08	0.24	
X-ray Cp	6-311G**	-563	-254	400	-0.9	7.99	0.32	

Table C8. Quantum Chemical Calculations of ^{49}Ti CS and EFG Tensor Parameters for **4** with Variable Ti Basis Sets.

RHF Calculations								
Structure	Ti Basis	σ_{iso} (ppm)	δ_{iso} (ppm)	Ω (ppm)	κ	C_Q (MHz)	η_Q	
Ideal Cp	cc-pVTZ	-8	-33	238	0.8	4.48	0.57	
X-ray Cp	cc-pVTZ	-24	-33	258	0.9	4.41	0.34	
Ideal Cp	cc-pVQZ	-4	-33	230	0.8	5.06	0.53	
X-ray Cp	cc-pVQZ	-20	-33	249	0.9	4.96	0.31	
Ideal Cp	ahlrichs-pVDZ	-247	-33	394	0.9	1.25	0.62	
X-ray Cp	ahlrichs-pVDZ	-267	-33	414	1.0	1.40	0.57	
Ideal Cp	ahlrichs-VTZ	-26	-33	186	0.8	3.24	0.87	
X-ray Cp	ahlrichs-VTZ	-43	-33	208	0.9	3.00	0.55	
Ideal Cp	6-311G**	-25	-33	158	0.7	3.55	0.87	
X-ray Cp	6-311G**	-42	-33	179	0.9	3.31	0.54	
B3LYP Calculations								
Structure	Ti Basis	σ_{iso} (ppm)	δ_{iso} (ppm)	Ω (ppm)	κ	C_Q (MHz)	η_Q	
Ideal Cp	cc-pVTZ	-755	-33	127	0.7	2.60	0.81	
X-ray Cp	cc-pVTZ	-773	-33	161	0.8	2.26	0.64	
Ideal Cp	cc-pVQZ	-769	-33	127	0.7	2.34	0.87	
X-ray Cp	cc-pVQZ	-787	-33	161	0.7	1.87	0.77	
Ideal Cp	ahlrichs-pVDZ	-735	-33	102	0.7	2.57	0.77	
X-ray Cp	ahlrichs-pVDZ	-753	-33	137	0.7	2.12	0.62	
Ideal Cp	ahlrichs-VTZ	-737	-33	54	0.2	2.20	0.87	
X-ray Cp	ahlrichs-VTZ	-755	-33	88	0.5	-1.44	0.93	
Ideal Cp	6-311G**	-766	-33	44	0.0	2.24	0.87	
X-ray Cp	6-311G**	-784	-33	78	0.4	-1.44	0.82	

Table C9. Plane-wave Calculations of ^{49}Ti NMR Tensor Parameters (CASTEP)^a

Complex	σ_{iso} (ppm)	δ_{iso} (ppm)	Ω (ppm)	κ	C_Q (MHz)	η_Q
1 (site 1)	-127	-819	406	-0.1	5.40	0.33
1 (site 2)	-106	-798	411	0.0	-2.81	0.13
2	-436	-510	284	-0.1	-6.61	0.38
3	-519	-427	320	0.8	3.96	0.25
4	-913	-33	685	0.2	2.02	0.25

^aAb initio plane-wave density functional theory calculations for **1-4** were performed with the CASTEP NMR program in the Materials Studio 5.0 environment. Ultrasoft pseudopotentials were used for ^{49}Ti EFG calculations with a plane wave basis set cutoff of 350 eV for fine accuracy basis sets with Monkhorst-Pack k -space grid sizes of $(3 \times 1 \times 1)$, $(1 \times 2 \times 1)$, $(2 \times 1 \times 2)$, and $(2 \times 1 \times 1)$ employed for **1**, **2**, **3** and **4**, respectively. The Perdew, Burke and Ernzerhof (PBE) functionals were used in the generalized gradient approximation (GGA) for the exchange-correlation energy.^{1,2} The magnetic shielding (MS) for ^{49}Ti was calculated with fine accuracy using the projector-augmented wave method (GIPAW) implemented in the CASTEP code.^{3,4} The previously reported single crystal X-ray diffraction structures were employed for all calculations. Prior to EFG and MS calculations the H atom positions were optimized.

(1) Perdew, J. P.; Burke, K.; Ernzerhof, M., *Phys. Rev. Lett.* **1998**, 80, (4), 891-891.(2) Perdew, J. P.; Burke, K.; Ernzerhof, M., *Phys. Rev. Lett.* **1996**, 77, (18), 3865-3868.(3) Yates, J. R.; Pickard, C. J.; Mauri, F., *Phys. Rev. B* **2007**, 76, (2).(4) Pickard, C. J.; Mauri, F., *Phys. Rev. B* **2001**, 63, (24).

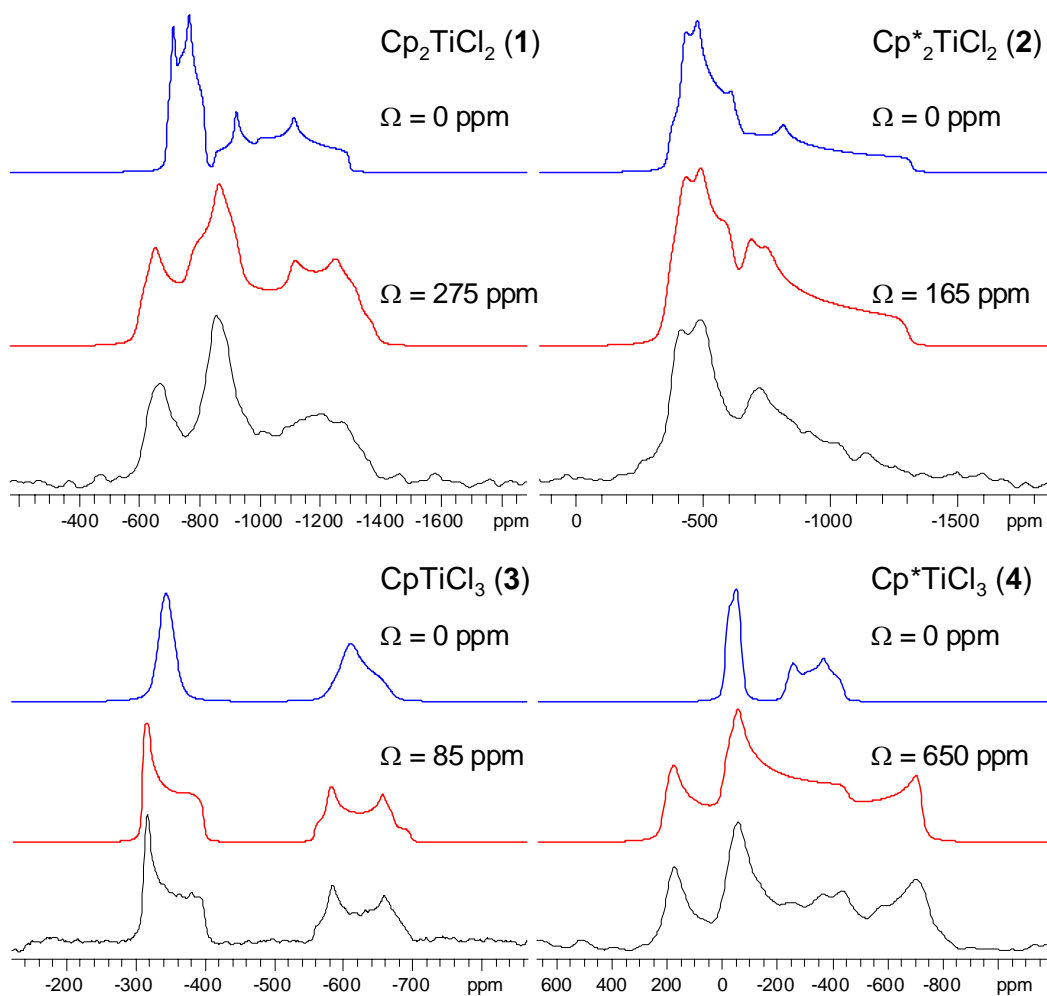


Figure C1. Experimental (black traces) and simulated (blue and red traces) static $^{47/49}\text{Ti}$ SSNMR spectra of **1-4** acquired at 21.1 T. The top simulations (blue traces) employ $\Omega = 0$ ppm, while the bottom simulations (red traces) employ the Ω value determined from fits of the static spectra at both fields. From these simulations it is clear that titanium CSA is substantial for **1-4**.

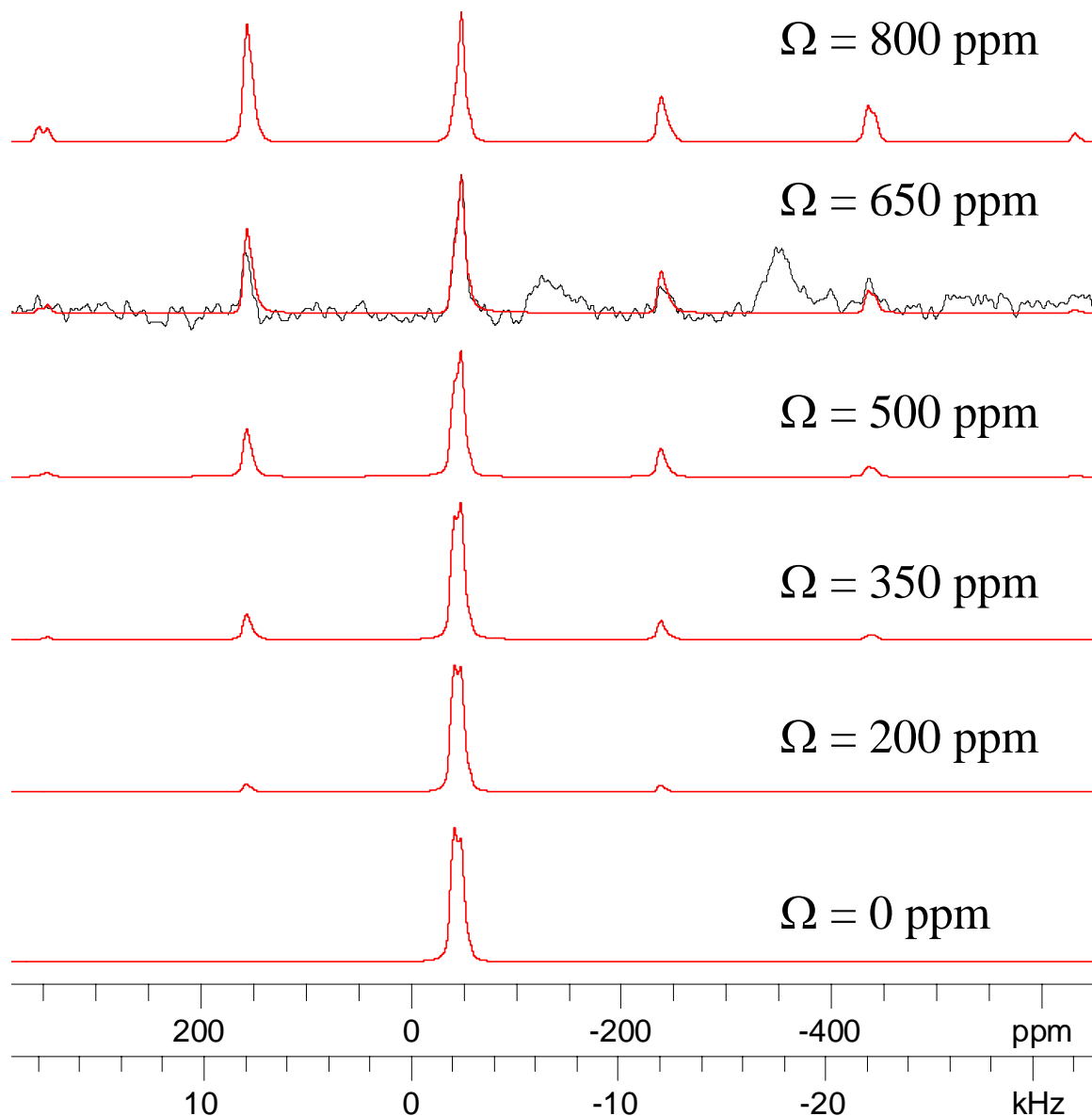


Figure C2. SIMPSON simulations of the MAS $^{47/49}\text{Ti}$ spectra of **4**. The value of Ω was changed for each simulation while all other parameters were fixed to those given in Table 4.1. This shows the sensitivity of the lineshape of the isotropic peak and spinning sideband manifold to the magnitude of the $^{47/49}\text{Ti}$ CSA.

Appendix D: Supplementary Figures and Tables for Chapter 5

Table D1. Experimental Pulse Sequence Settings

Parameter	Values Employed
Solid-state ^{45}Sc NMR experiments	
$\pi/2$ pulse widths (μs)	1.5 to 6.5
ν_1 , Rf fields (kHz)	41.7 to 9.7
Recycle Delays (s)	0.5 to 4.0
ν_{rot} , Sample spinning speeds (kHz)	5.0 to 15.0
Spectral widths for static spectra (kHz)	50.0 to 400.0
Spectral widths for MAS spectra (kHz)	200 to 1000
Number of scans for static spectra	1700 to 125000
Number of scans for MAS spectra	192 to 9800
Solid-state ^{13}C MAS NMR experiments	
^{13}C $\pi/2$ pulse width (μs)	1.75 to 2.2
Recycle delay (s)	10.0
ν_{rot} , Sample spinning speeds (kHz)	10.0 to 14.0
Spectral widths (kHz)	50.0 to 100.0
Number of scans	320 to 864
$^1\text{H}/^{19}\text{F}$ decoupling fields (kHz)	Same as corresponding VACP/MAS expt.
Solid-state $^1\text{H} \rightarrow ^{13}\text{C}$ VACP/MAS NMR experiments	
^1H $\pi/2$ pulse widths (μs)	4.0 to 4.5
Hartman-Hahn matching fields (kHz)	54 kHz and 60 kHz
Recycle delays (s)	2.0 to 4.0
ν_{rot} , Sample spinning speeds (kHz)	4.0 to 11.0
Spectral widths (kHz)	40.0 to 60.0
Number of scans	24 to 708
^1H decoupling fields (kHz)	34 to 66
Solid-state $^{19}\text{F} \rightarrow ^{13}\text{C}$ VACP/MAS NMR experiments	
^{19}F $\pi/2$ pulse widths (μs)	2.1 to 4.5
Hartman-Hahn matching fields (kHz)	56 to 63
Recycle delays (s)	2.0 to 4.0
ν_{rot} , Sample spinning speeds (kHz)	5.0 to 13.0
Spectral widths (kHz)	50.0 to 80.0
Number of scans	320 to 1386
^{19}F decoupling fields (kHz)	46 to 74
Solid-state ^{19}F MAS NMR experiments	
^{19}F $\pi/2$ pulse width (μs)	2.2
Recycle delay (s)	3.0
ν_{rot} , Sample spinning speeds (kHz)	8.0 to 12.0
Spectral width (kHz)	100
Number of scans	1696 to 15856

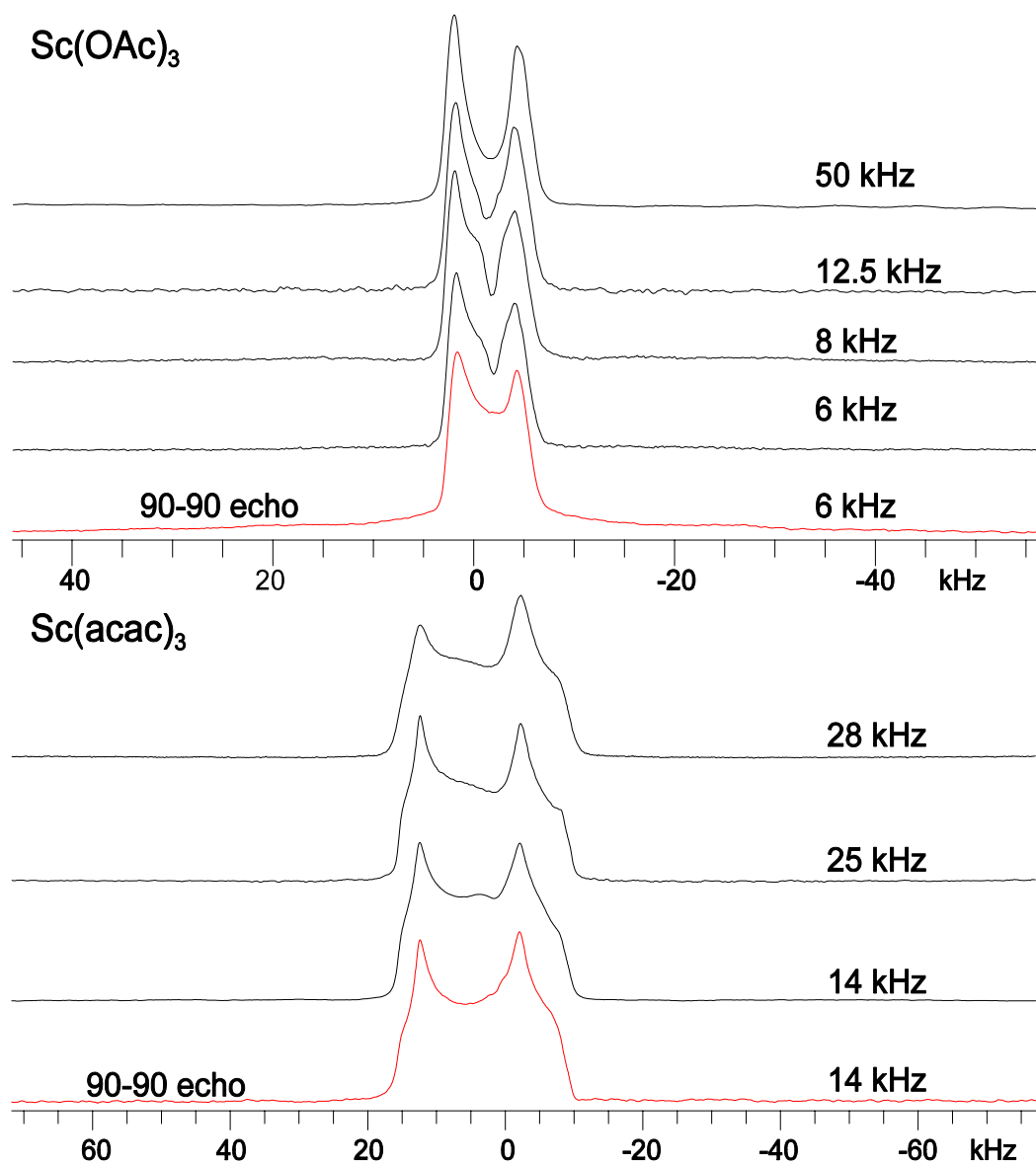


Figure D1. Static ^{45}Sc Spectra of $\text{Sc}(\text{OAc})_3$ and $\text{Sc}(\text{acac})_3$. The rf field used to acquire the spectra is shown to the right of each spectrum. The bottom (red) spectrum has been acquired with a Hahn echo of the form $\{\pi/2 - \tau - \pi/2 - \tau - \text{acquire}\}$, denoted as $90^\circ - 90^\circ$ echo in the figure. All other spectra were acquired with an echo of the form $\{\pi/2 - \tau - \pi - \tau - \text{acquire}\}$. The sensitivity of the spectra to the rf field and pulse sequence is visible. For these samples a $90^\circ - 90^\circ$ echo employing an rf field equal to approximately half the width of the static pattern produces the best lineshape.

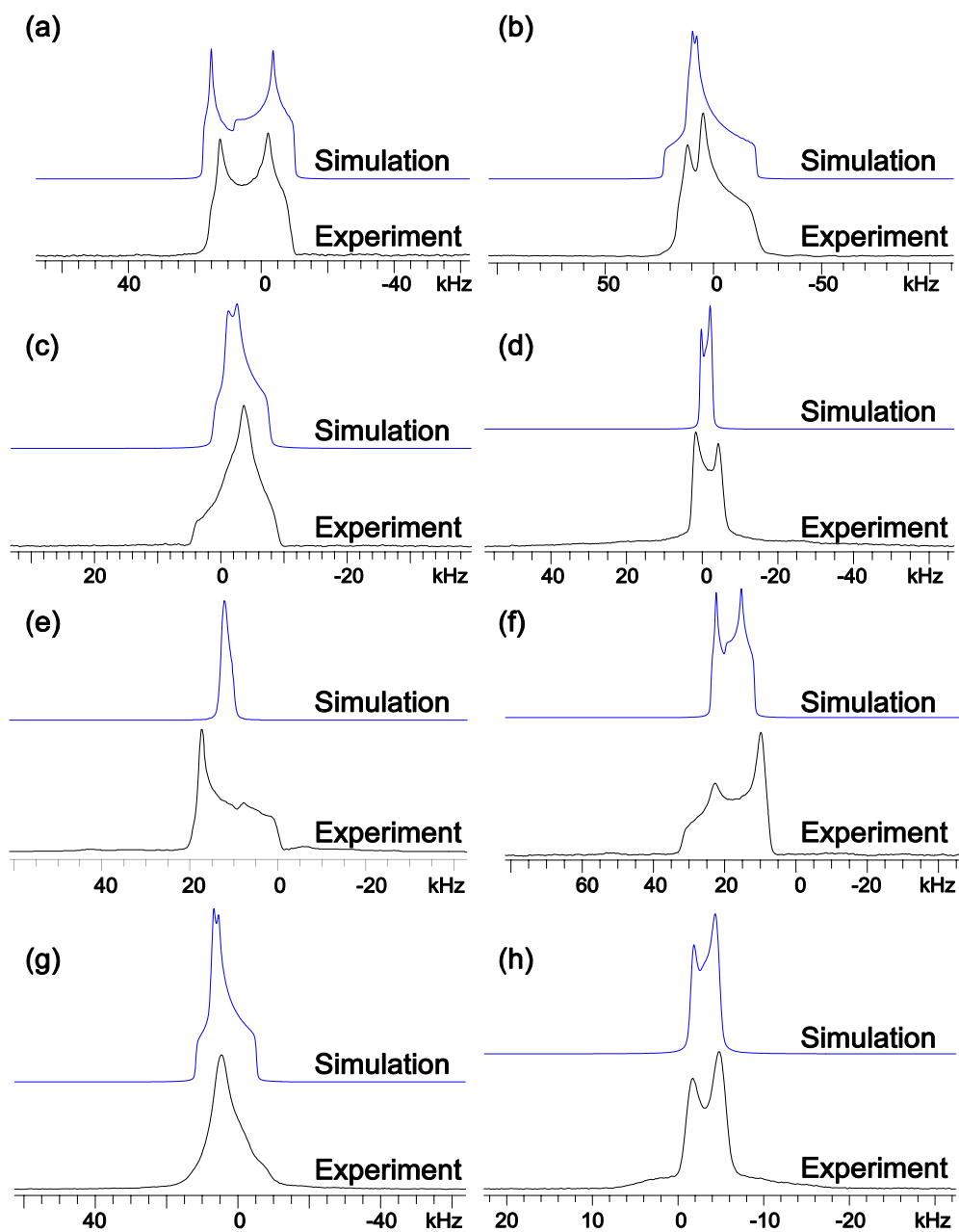
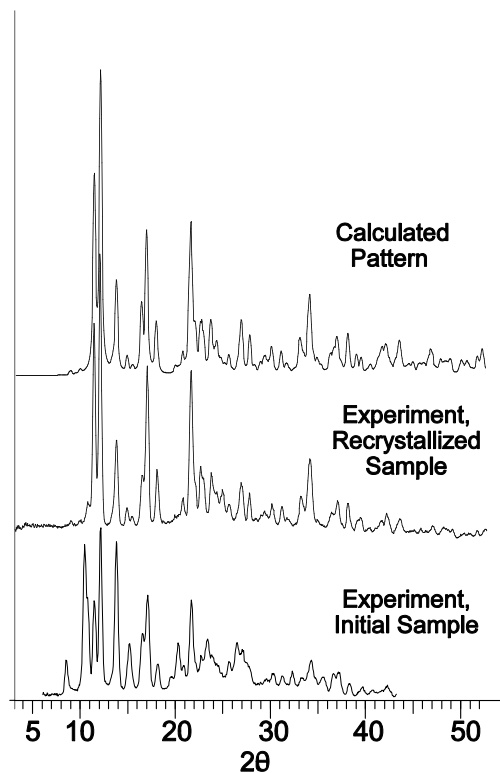


Figure D2. Static ^{45}Sc NMR spectra at 9.4 T and simulations. All simulations neglect the effects of scandium CSA ($\Omega = 0$ ppm), illustrating that scandium CSA is substantial for all complexes. (a) $\text{Sc}(\text{acac})_3$ (b) $\text{Sc}(\text{TMHD})_3$ (c) $\text{Sc}(\text{OAc})_3$ (d) $\text{Sc}(\text{NO}_3)_3 \cdot 5\text{H}_2\text{O}$, (e) $\text{ScCl}_3 \cdot 6\text{H}_2\text{O}$ (f) $\text{ScCl}_3 \cdot 3\text{THF}$ (g) ScCp_3 (h) $\text{Sc}(\text{OTf})_3$.

Powder X-Ray Diffraction of
 $\text{ScCl}_3 \cdot 3\text{THF}$



Powder X-Ray Diffraction of
 $\text{Sc}(\text{OAc})_3$ and $\text{Sc}(\text{OTf})_3$

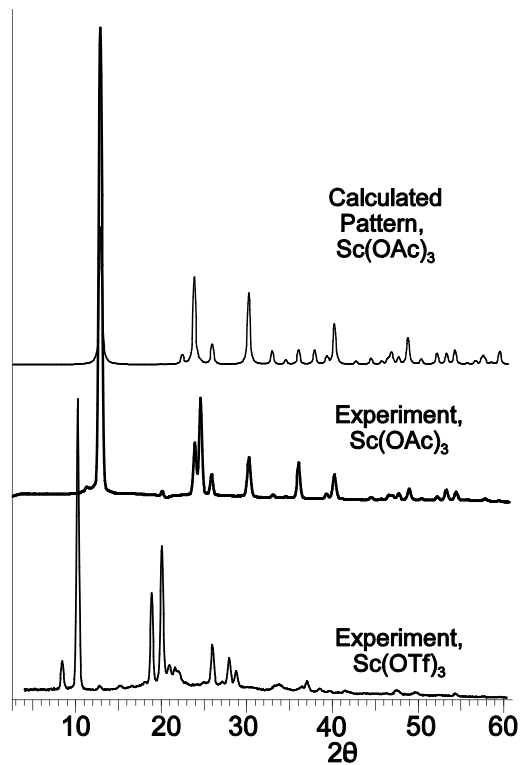


Figure D3. Powder X-Ray diffraction patterns of $\text{ScCl}_3 \cdot 3\text{THF}$, $\text{Sc}(\text{OAc})_3$ and $\text{Sc}(\text{OTf})_3$. The calculated patterns were generated from known single crystal X-ray structures using the PowderCell computer program.

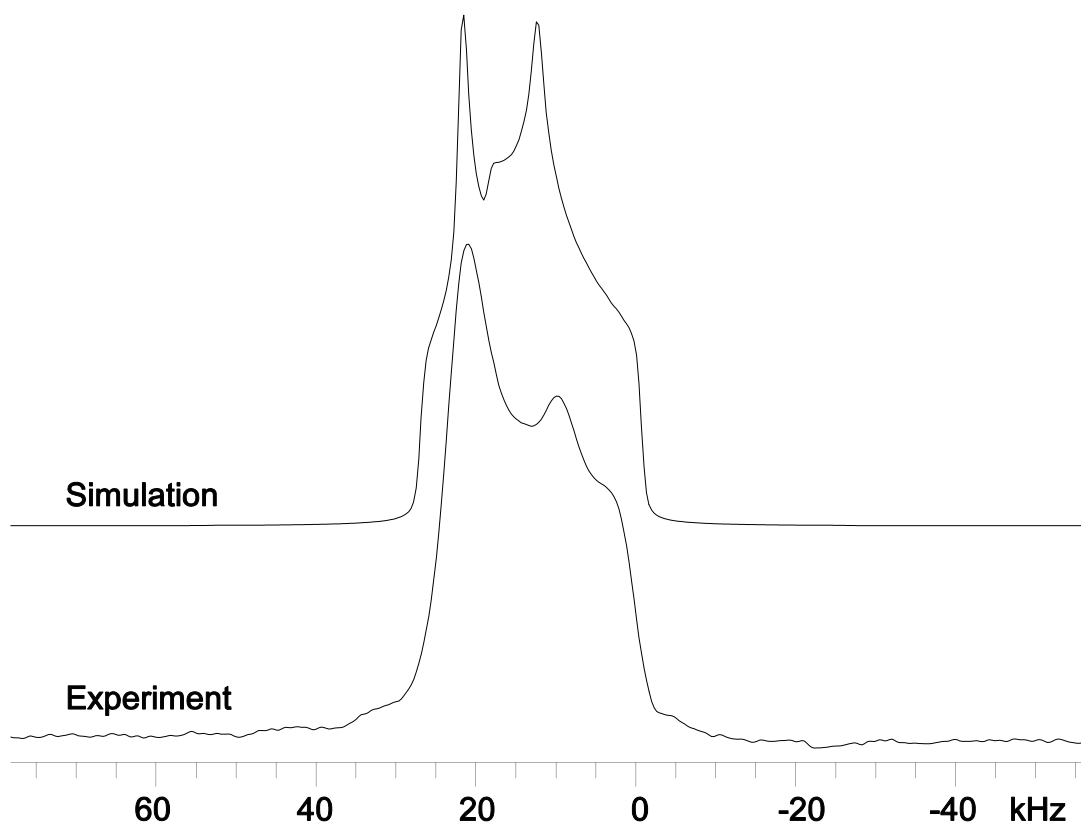


Figure D4. Static ^{45}Sc NMR spectrum of $\text{ScCl}_3 \cdot 6\text{H}_2\text{O}$ without ^1H decoupling at 11.7 T. The simulation parameters are $C_Q = 13.0$, $\eta_Q = 0.55$, $\delta_{\text{iso}} = 145.0$ ppm. Without the acquisition of MAS spectra and/or ^1H decoupled static spectra incorrect ^{45}Sc NMR parameters could be obtained from simulation.

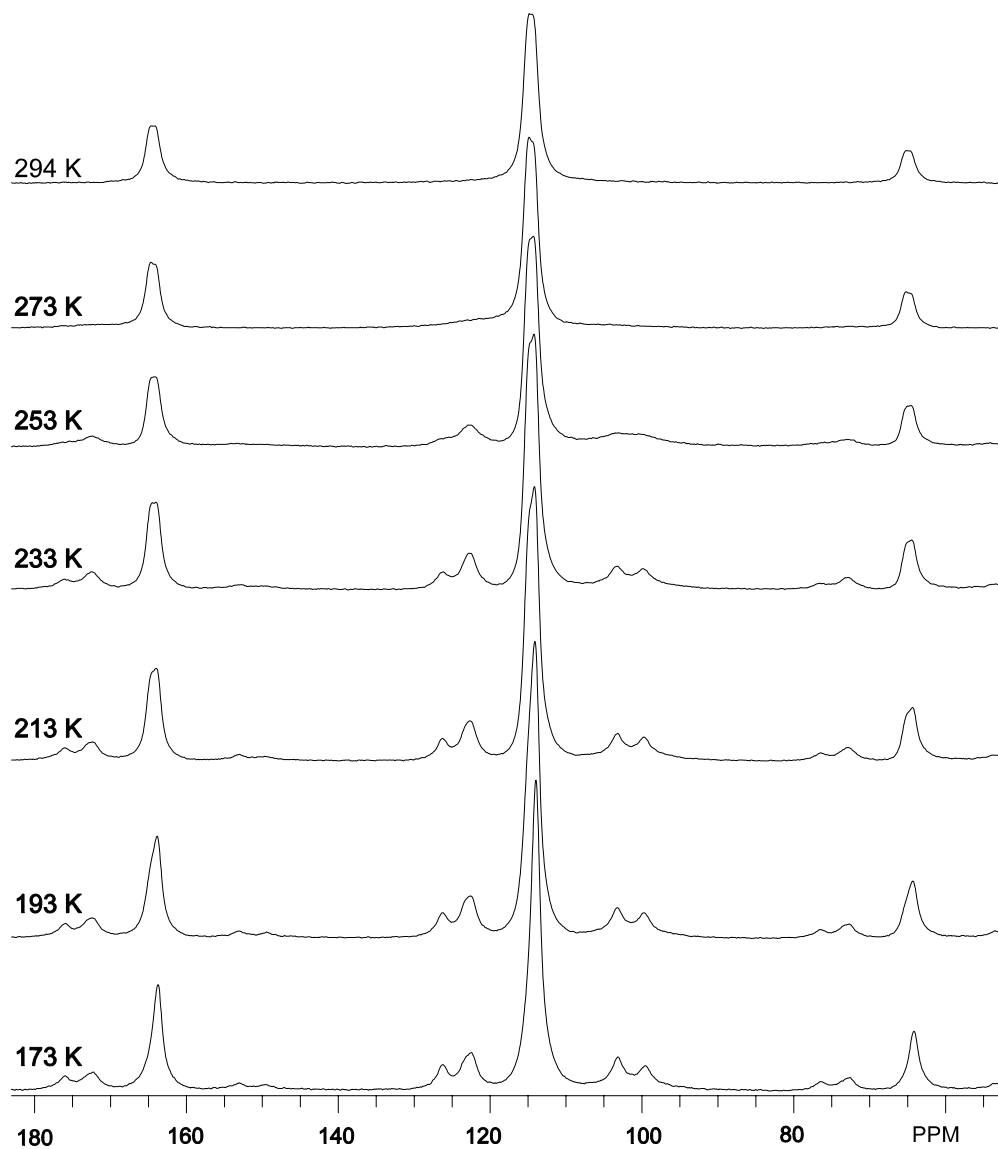


Figure D5. Variable Temperature ^{13}C VACP/MAS NMR spectra of ScCp_3 at 9.4 T with a spinning speed of 5 kHz. Spinning sidebands are visible at the both sides of the spectra. These spectra indicate that there is fluxional motion of the Cp ligands.

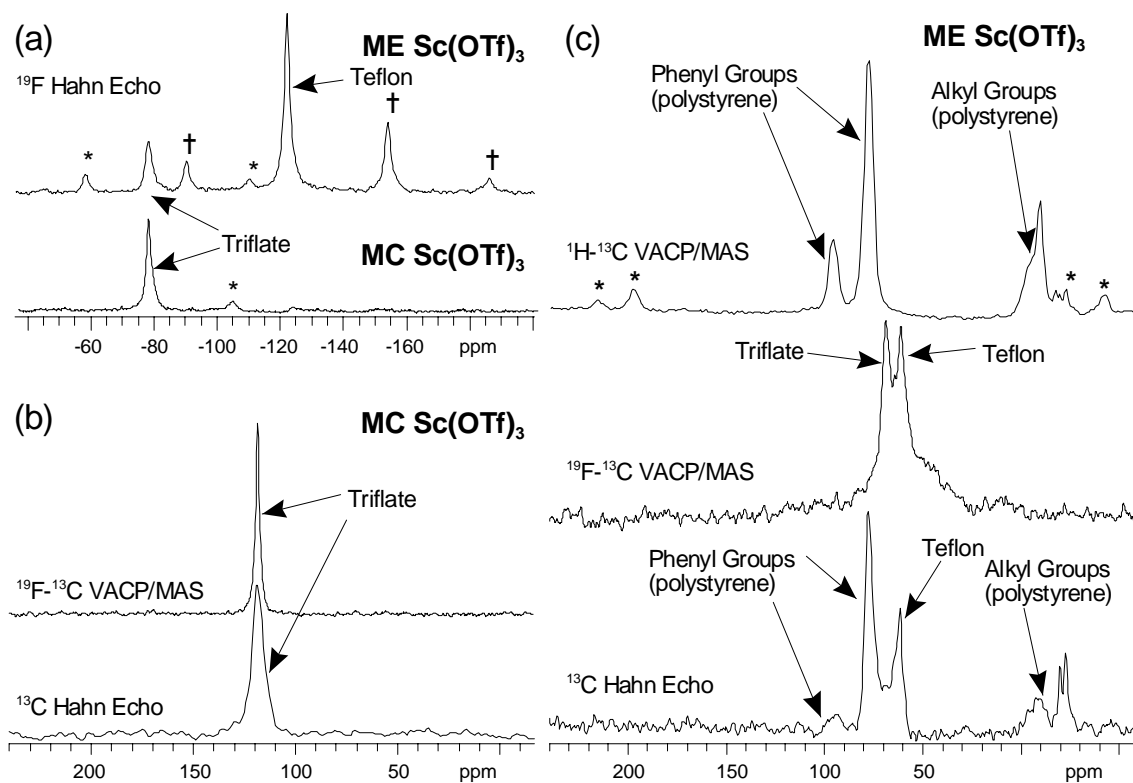


Figure D6. ^{19}F and ^{13}C NMR spectra at 9.4 T. Asterisks and crosses denote spinning sidebands. (a) ^{19}F Hahn-echo MAS spectra of $\text{ME Sc}(\text{OTf})_3$ (top) and $\text{Sc}(\text{OTf})_3$ (bottom) at spinning speeds of 12 kHz and 10 kHz, respectively. (b) ^{13}C NMR spectra of $\text{Sc}(\text{OTf})_3$; ^{19}F - ^{13}C VACP/MAS at 5 kHz (top); Hahn-Echo at 10 kHz (bottom). (c) ^{13}C NMR spectra of $\text{ME Sc}(\text{OTf})_3$; ^1H - ^{13}C VACP/MAS at 13 kHz (top); ^{19}F - ^{13}C VACP/MAS at 5 kHz (middle); ^{13}C Hahn-Echo at 14 kHz (bottom). The loading level of $\text{Sc}(\text{OTf})_3$ in the polystyrene is approximately 10% by mass, which accounts for the observation of the normally weak Teflon signal of the rotor spacer in the ^{13}C and ^{19}F spectra.

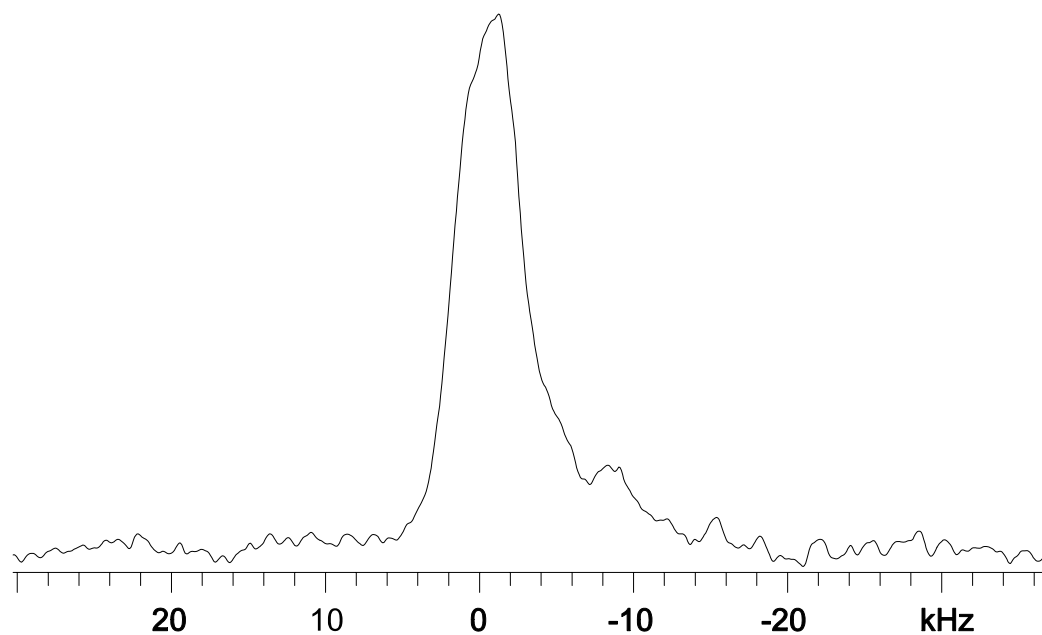


Figure D7. Static ^{45}Sc NMR spectrum of ME $\text{Sc}(\text{OTf})_3$ without ^1H decoupling at 9.4 T. The spectrum is the result of ~ 35000 scans. The strong ^1H - ^{45}Sc dipole coupling indicates the relatively close proximity of protons to the scandium nucleus.

Appendix E: Supplementary Figures and Tables for Chapter 6

Table E1. Acquisition Parameters for MAS ^{45}Sc SSNMR Spectra Acquired at 9.4 T (Figure 6.1)

Sample	$\text{Sc}(\text{OAc})_3$	$\text{Sc}(\text{OTf})_3$	$\text{Sc}(\text{OTf})_3 \cdot 8\text{H}_2\text{O}$
Pulse Sequence ^a	Echo	Echo	Echo
Number of scans	128	64	64
Recycle Delay (s)	2.0	2.0	2.0
Dwell (μs)	1.0	2.0	2.5
Spectral width (kHz)	1000.0	500.0	400.0
Spinning Speed (Hz)	8000	5000	8000
Acquisition length (number of points)	32768	65536	16384
90° pulse width [$\pi/2$] (μs)	0.60	2.90	2.90
180° pulse widths [π] (μs)	1.20	2.90	2.90
Ring-down delays [τ_1] (μs)	125.0	200.0	125.0
Ring-down delays [τ_2] (μs)	75.0	30.0	30.0

^aEcho refers to a 16-step echo sequence.

Table E2. Acquisition Parameters for Static ^{45}Sc SSNMR Spectra Acquired at 9.4 T (Figure 6.1)

Sample	$\text{Sc}(\text{OAc})_3$	$\text{Sc}(\text{OTf})_3$	$\text{Sc}(\text{OTf})_3 \cdot 8\text{H}_2\text{O}$
Pulse Sequence ^a	Echo	Echo	Echo
Number of scans	3392	1024	96
Recycle Delay (s)	2.0	2.0	2.0
Dwell (μs)	5.0	2.0	2.5
Spectral width (kHz)	200.0	500.0	100.0
Acquisition length (number of points)	2048	4096	2048
90° pulse width [$\pi/2$] (μs)	10.00	5.80	2.90
180° pulse widths [π] (μs)	10.00	5.80	2.90
Ring-down delays [τ_1] (μs)	60.0	140.0	100.0
Ring-down delays [τ_2] (μs)	25.0	20.0	20.0

^aEcho refers to a 16-step echo sequence.

Table E3. Acquisition Parameters for MAS ^{45}Sc SSNMR Spectra Acquired at 9.4 T (Figure 6.3)

Sample	$\text{Sc}(\text{OTf})_3 \cdot 8\text{H}_2\text{O}$	$\text{ME Sc}(\text{OTf})_3$
Pulse Sequence ^a	Echo	Echo
Number of scans	64	115568
Recycle Delay (s)	2.0	0.5
Dwell (μs)	2.5	20.0
Spectral width (kHz)	400.0	50.0
Spinning Speed (Hz)	8000	12000
Acquisition length (number of points)	16384	2048
90° pulse width [$\pi/2$] (μs)	2.90	1.50
180° pulse widths [π] (μs)	2.90	3.00
Ring-down delays [τ_1] (μs)	125.0	83.33
Ring-down delays [τ_2] (μs)	30.0	43.33

^aEcho refers to a 16-step echo sequence.

Table E4. Acquisition Parameters for Static ^{45}Sc SSNMR Spectra Acquired at 9.4 T (Figure 6.3)

Sample	$\text{Sc}(\text{OTf})_3 \cdot 8\text{H}_2\text{O}$	$\text{ME Sc}(\text{OTf})_3$
Pulse Sequence ^a	DFS/Echo	DFS/Echo
Number of scans	256	44272
Recycle Delay (s)	1.5	0.5
Dwell (μs)	12.5	12.5
Spectral width (kHz)	80.0	80.0
Acquisition length (number of points)	512	512
90° pulse width [$\pi/2$] (μs)	3.30	5.00
180° pulse widths [π] (μs)	6.60	10.00
Ring-down delays [τ_1] (μs)	75.0	75.0
Ring-down delays [τ_2] (μs)	20.0	25.0
DFS Start Frequency (MHz)	1.600	1.600
DFS End Frequency (MHz)	0.100	0.100
Length of DFS Sweep (μs)	60	60
Number of Steps in DFS Waveform	1024	1024
DFS Step Length (μs)	0.059	0.059

^aDFS/Echo refers to a sequence where the Hahn echo portion is prefaced by a double frequency sweep (DFS) waveform [see main text for references].

Table E5. Acquisition Parameters for MAS ^{45}Sc SSNMR Spectra Acquired at 9.4 T (Figure 6.4)

Sample	$\text{Sc}(\text{OTf})_3 \cdot 8\text{H}_2\text{O}$	ME-1	ME-2	ME-3	ME $\text{Sc}(\text{OTf})_3\text{-}d_8$
Pulse Sequence ^a	DFS/Echo	DFS/Echo	DFS/Echo	DFS/Echo	DFS/Echo
Number of scans	32	752	304	1040	720
Recycle Delay (s)	2.0	2.0	2.0	2.0	2.0
Dwell (μs)	2.5	2.5	2.5	5.0	2.5
Spectral width (kHz)	400.0	400.0	400.0	200.0	400.0
Spinning Speed (Hz)	8000	10000	8000	10000	10000
Acquisition length (number of points)	4096	4096	4096	4096	4096
90° pulse width [$\pi/2$] (μs)	2.90	2.90	2.90	2.90	2.90
180° pulse widths [π] (μs)	5.80	5.80	5.80	5.80	5.80
Ring-down delays [τ_1] (μs)	125.0	100.0	125.0	100.0	100.0
Ring-down delays [τ_2] (μs)	30.0	30.0	30.0	30.0	30.0
DFS Start Frequency (MHz)	1.100	1.100	1.100	1.100	1.100
DFS End Frequency (MHz)	0.100	0.100	0.100	0.100	0.100
Length of DFS Sweep (μs)	2000	2000	2000	2000	2000
Number of Steps in DFS Waveform	4000	4000	4000	4000	4000
DFS Step Length (μs)	0.50	0.50	0.50	0.50	0.50

^aDFS/Echo refers to a sequence where the Hahn echo portion is prefaced by a double frequency sweep (DFS) waveform [see main text for references].

Table E6. Acquisition Parameters for Static ^{45}Sc SSNMR Spectra Acquired at 9.4 T (Figure 6.4)

Sample	$\text{Sc}(\text{OTf})_3 \cdot 8\text{H}_2\text{O}$	ME $\text{Sc}(\text{OTf})_3 \cdot 8\text{H}_2\text{O}$	Ambient ME $\text{Sc}(\text{OTf})_3$	ME $\text{Sc}(\text{OTf})_3 \cdot d_8$
Pulse Sequence ^a	DFS/Echo	DFS/Echo	DFS/Echo	DFS/Echo
Number of scans	208	3120	3400	44272
Recycle Delay (s)	2.0	2.0	2.0	0.5
Dwell (μs)	10.0	10.0	10.0	12.5
Spectral width (kHz)	100.0	100.0	100.0	80.0
Acquisition length (number of points)	1024	1024	1024	1024
90° pulse width [$\pi/2$] (μs)	2.90	2.90	2.90	5.00
180° pulse widths [π] (μs)	2.90	2.90	2.90	10.00
Ring-down delays [τ_1] (μs)	125.0	100.0	100.0	75.0
Ring-down delays [τ_2] (μs)	25.0	30.0	30.0	25.0
DFS Start Frequency (MHz)	1.100	1.100	1.100	1.600
DFS End Frequency (MHz)	0.100	0.100	0.100	0.100
Length of DFS Sweep (μs)	2000	2000	2000	60
Number of Steps in DFS Waveform	4000	4000	4000	1024
DFS Step Length (μs)	0.50	0.50	0.50	0.059

^aDFS/Echo refers to a sequence where the Hahn echo portion is prefaced by a double frequency sweep (DFS) waveform [see main text for references].

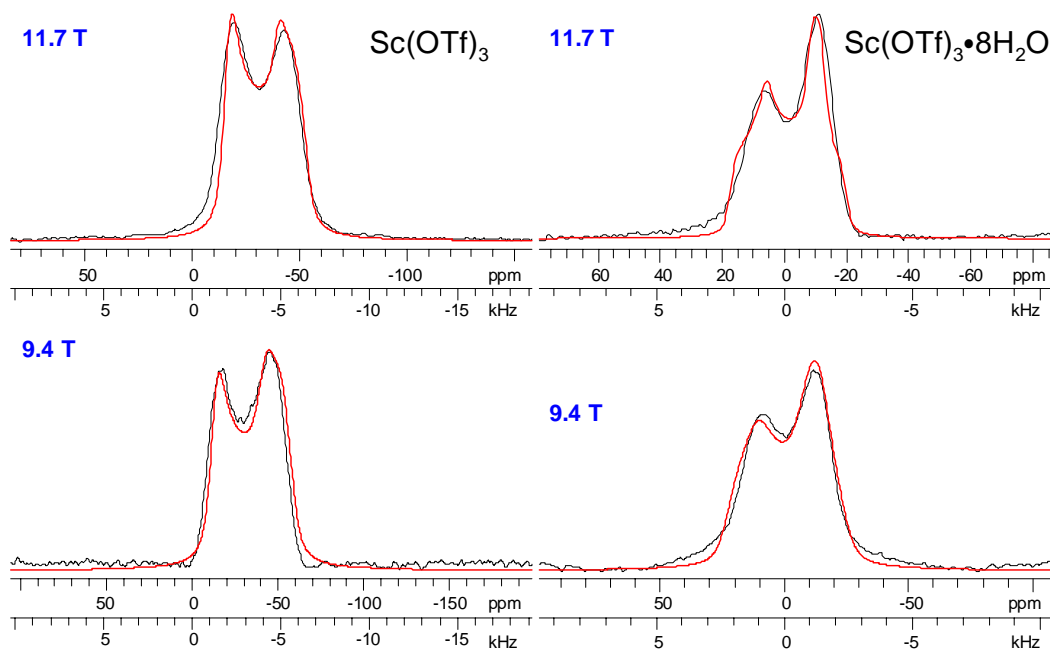


Figure E1. Static solid-state ^{45}Sc NMR spectra of $\text{Sc}(\text{OTf})_3$ and $\text{Sc}(\text{OTf})_3 \cdot 8\text{H}_2\text{O}$ acquired at magnetic fields of 11.7 T and 9.4 T. The EFG and CS tensor parameters and Euler angles employed for the simulations are given in Table 1 of the manuscript. All spectra were acquired with 90° - 90° echo sequences. It should be noted that a sample of $\text{Sc}(\text{OTf})_3 \cdot 8\text{D}_2\text{O}$ was employed for experiments at 11.7 T in order to reduce the effects of ^1H dipolar coupling on the static ^{45}Sc powder pattern. The 11.7 T spectrometer did not possess an amplifier capable of fully removing the effects of dipolar coupling to ^1H . For this reason the deuterated compound was employed. Both spectra were acquired with 90° - 90° echo sequences.

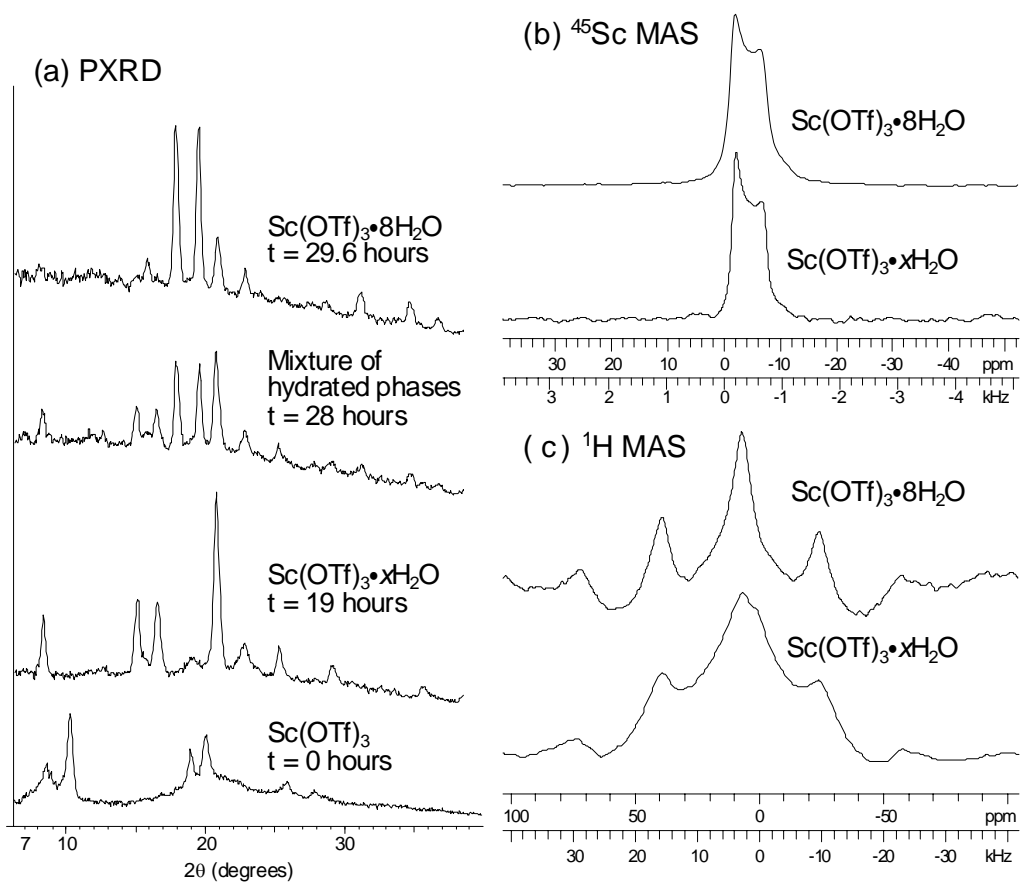


Figure E2. (a) Powder X-ray diffraction (PXRD) patterns of a sample of $\text{Sc}(\text{OTf})_3$ acquired with a capillary which is open to air. The times listed next to the PXRD patterns correspond to the amount of time for which the sample was exposed to air. From the PXRD patterns it is clear that anhydrous $\text{Sc}(\text{OTf})_3$ adsorbs water and is converted to $\text{Sc}(\text{OTf})_3 \cdot x\text{H}_2\text{O}$ followed by adsorption of additional water to form $\text{Sc}(\text{OTf})_3 \cdot 8\text{H}_2\text{O}$. (b) MAS ^{45}Sc SSNMR spectra of $\text{Sc}(\text{OTf})_3 \cdot x\text{H}_2\text{O}$ and $\text{Sc}(\text{OTf})_3 \cdot 8\text{H}_2\text{O}$. The MAS spectra of the two phases are identical in appearance. Static ^{45}Sc SSNMR spectra of the two phases are also identical in appearance (not shown). (c) MAS ^1H SSNMR spectra of $\text{Sc}(\text{OTf})_3 \cdot x\text{H}_2\text{O}$ and $\text{Sc}(\text{OTf})_3 \cdot 8\text{H}_2\text{O}$ acquired with $\nu_{\text{rot}} = 12500$ Hz and a 20s pulse delay. The MAS ^1H SSNMR spectrum of $\text{Sc}(\text{OTf})_3 \cdot x\text{H}_2\text{O}$ is substantially broader than that of $\text{Sc}(\text{OTf})_3 \cdot 8\text{H}_2\text{O}$.

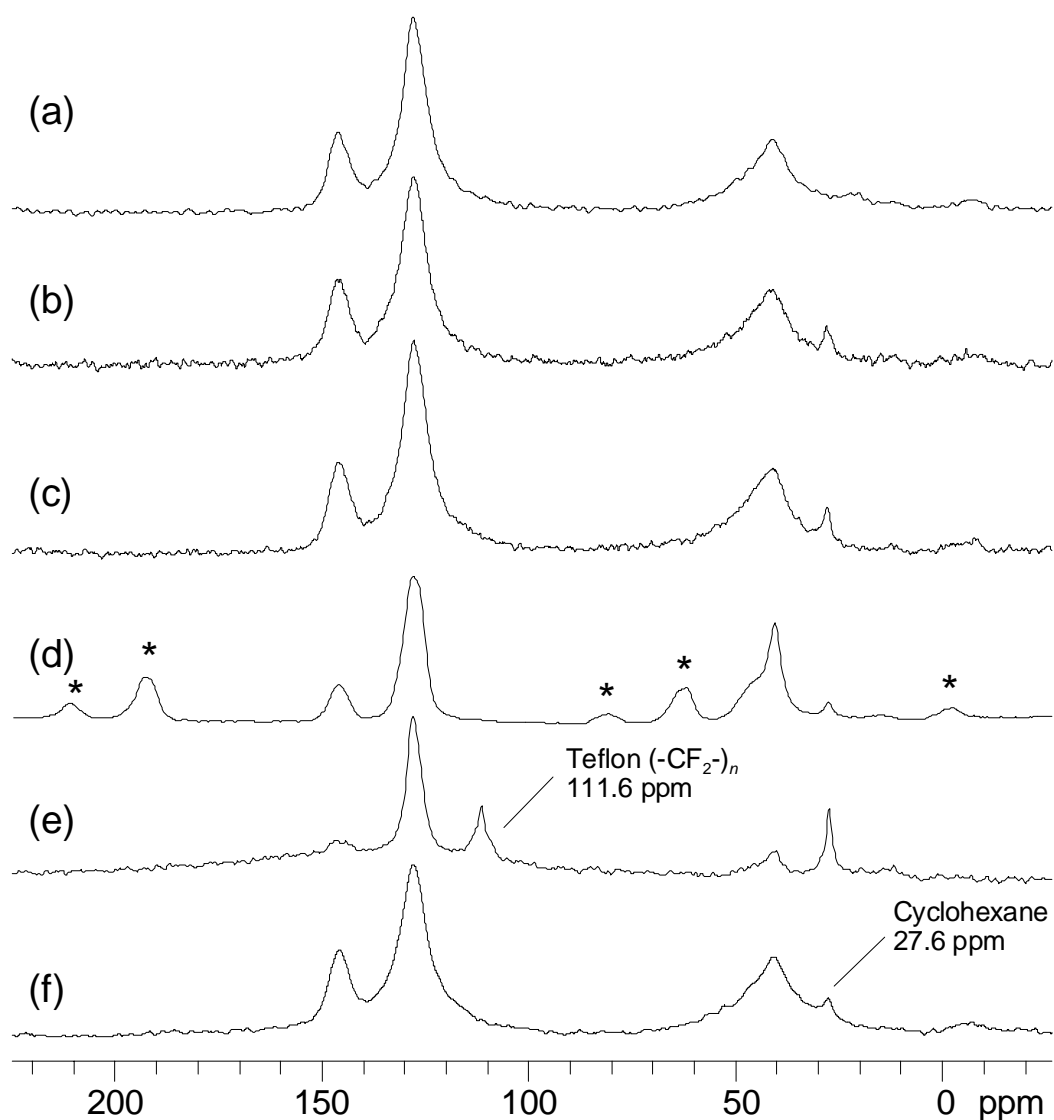


Figure E3. MAS ^{13}C SSNMR spectra of polystyrene samples treated with various solvents and ME Sc(OTf) $_3$. (a) pure polystyrene (PS), $\nu_{\text{rot}} = 13500$ Hz, (b) PS recovered from cyclohexane, $\nu_{\text{rot}} = 13500$ Hz (c) PS recovered from cyclohexane and hexanes, $\nu_{\text{rot}} = 13500$ Hz (d) PS recovered from cyclohexane, hexanes, and acetonitrile, $\nu_{\text{rot}} = 6500$ Hz and (e) PS recovered from cyclohexane, hexanes, and acetonitrile, $\nu_{\text{rot}} = 11500$ Hz, and (f) ME-2. The spectrum depicted in (e) was acquired with a Bloch decay pulse sequence (90° pulse-acquire) and a recycle delay of 4 s and all other spectra were acquired with VACP. A 1 ms contact time was employed for all VACP experiments. These spectra show that cyclohexane is adsorbed by the polystyrene and is present in the samples of ME Sc(OTf) $_3$.

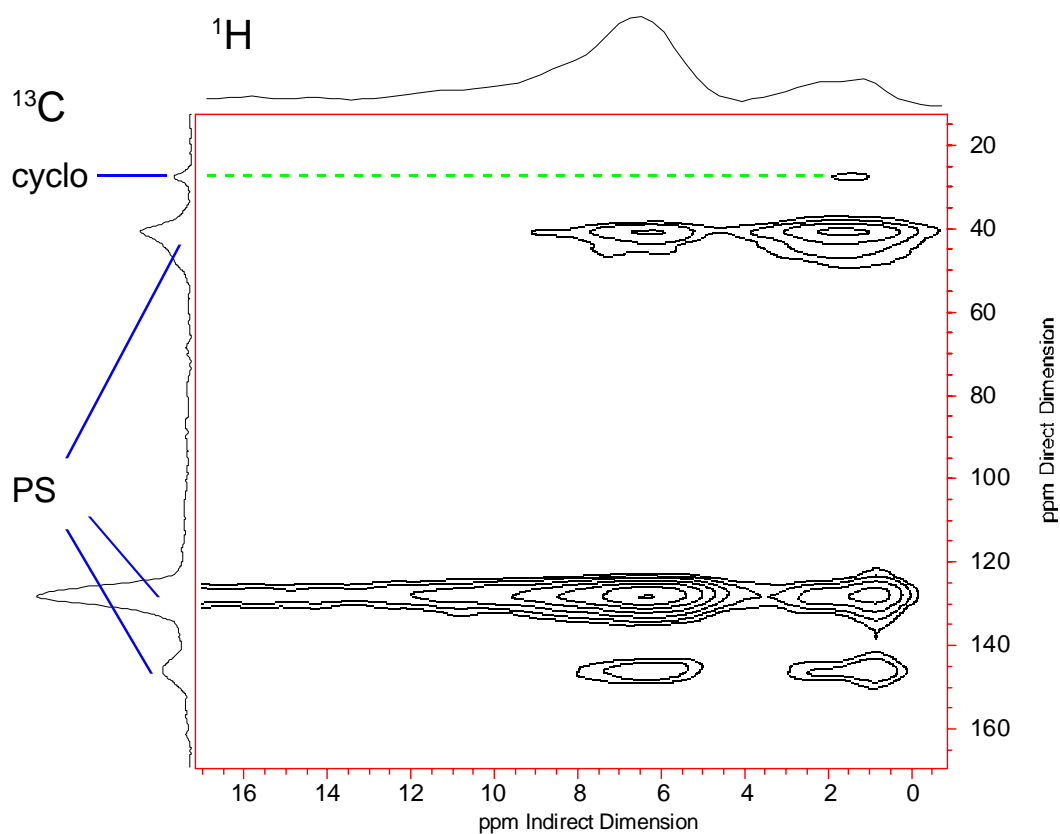


Figure E4. ^1H - ^{13}C dipolar correlation spectrum of ME-2 acquired with $\nu_{\text{rot}} = 13669$ Hz. Frequency switched Lee-Goldberg (FSLG) was applied during the t_1 evolution period in order to provide homonuclear ^1H decoupling. The spectrum was acquired with a 12 s pulse delay and a 1 ms contact time. 48 t_1 increments were acquired. TPPI phase cycling was employed to obtain absorption lineshapes.

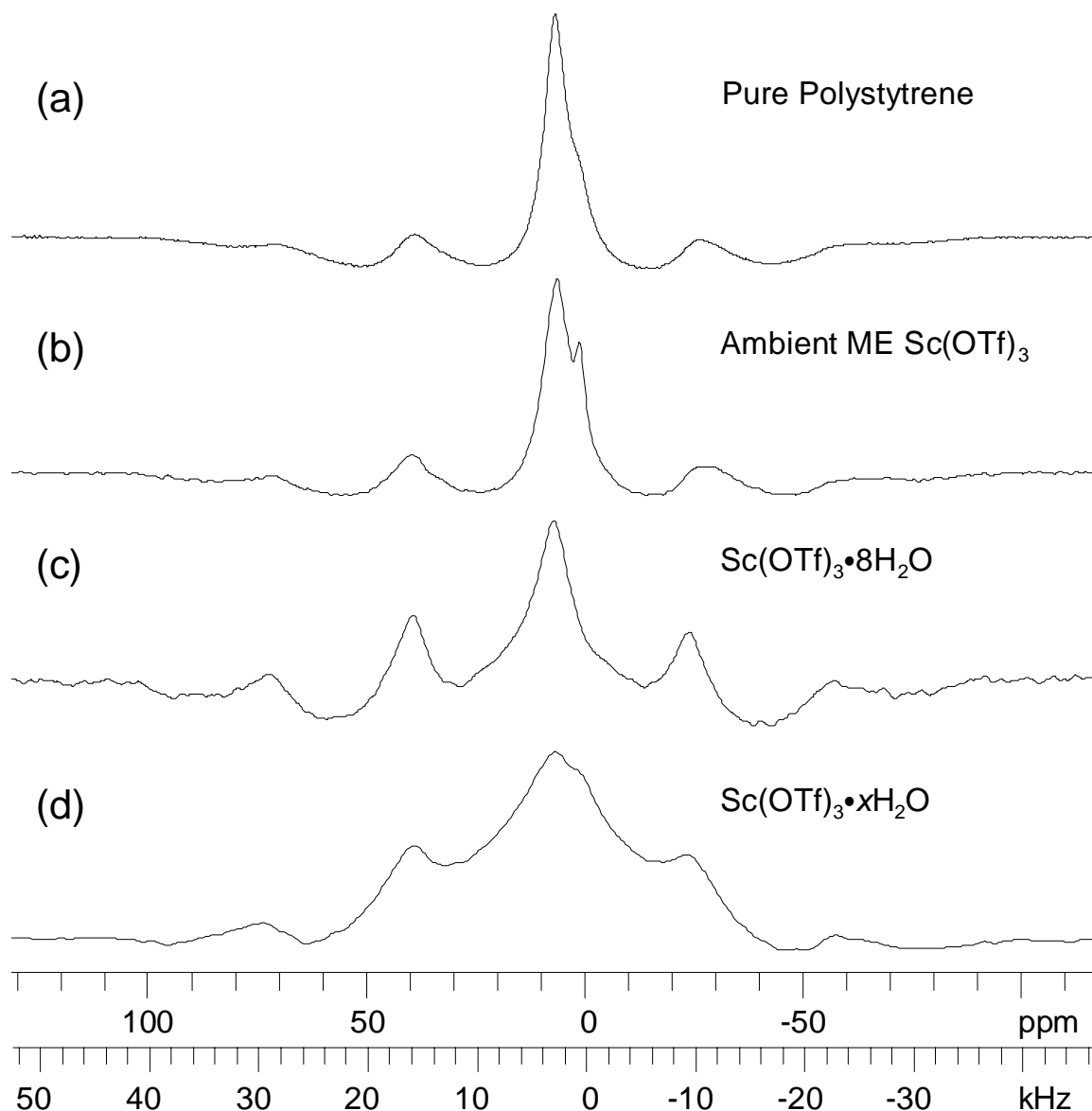


Figure E5. MAS ^1H SSNMR spectra acquired with $\nu_{\text{rot}} = 12500$ kHz. (a) pure polystyrene, (b) ambient ME $\text{Sc}(\text{OTf})_3$, (c) $\text{Sc}(\text{OTf})_3 \cdot 8\text{H}_2\text{O}$, (d) $\text{Sc}(\text{OTf})_3 \cdot x\text{H}_2\text{O}$. The resonances of the water ^1H nuclei are extremely broad in comparison to those of the polystyrene and cyclohexane resonances. Given the relatively low loading levels of $\text{Sc}(\text{OTf})_3 \cdot 8\text{H}_2\text{O}$ within ambient ME $\text{Sc}(\text{OTf})_3$ it is anticipated that the water ^1H nuclei will contribute negligible amounts of signal to the ^1H SSNMR spectrum of ambient ME $\text{Sc}(\text{OTf})_3$. Therefore, it can be assumed that all signal observed in the MAS ^1H SSNMR spectrum of ambient ME $\text{Sc}(\text{OTf})_3$ can be attributed to the ^1H nuclei of polystyrene and cyclohexane.

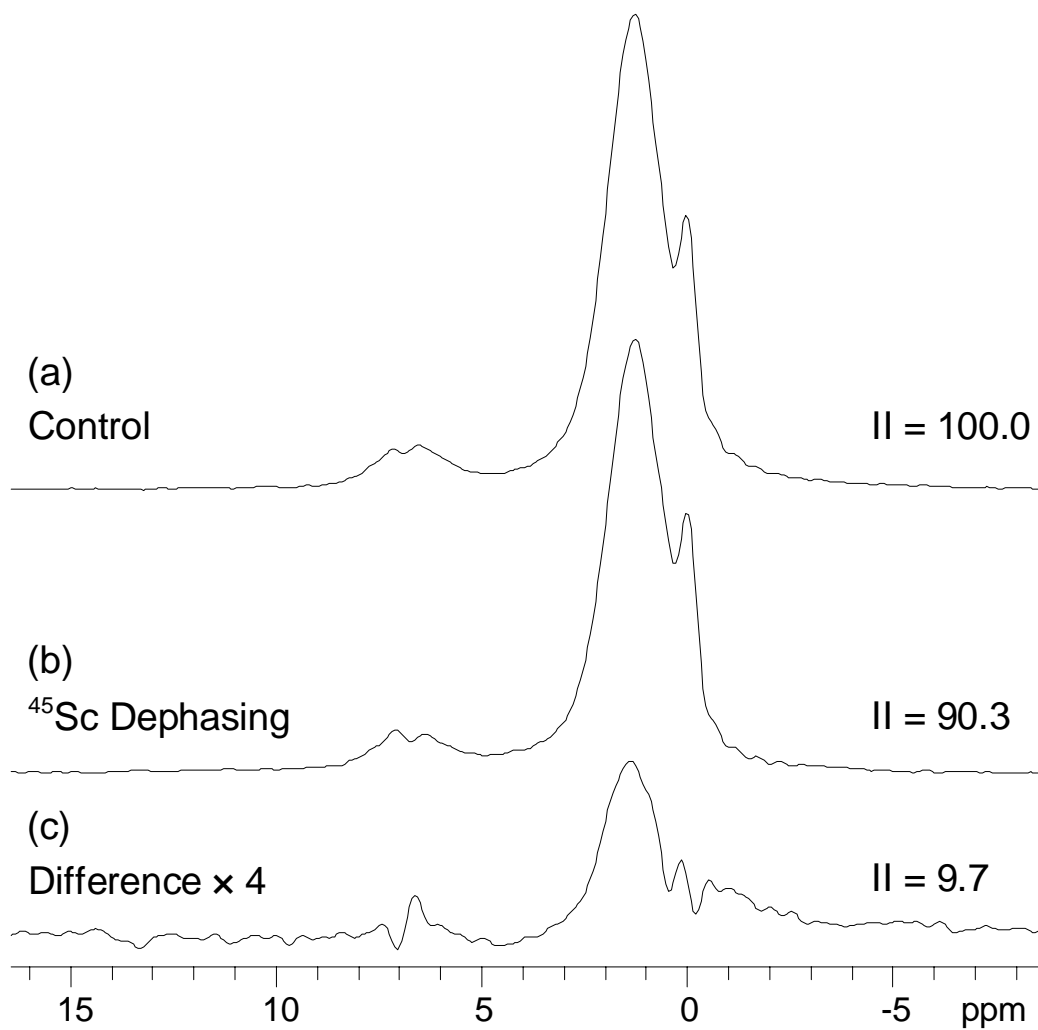


Figure E6. MAS ^1H - ^{45}Sc TRAPDOR SSNMR spectra of ME $\text{Sc}(\text{OTf})_3\text{-}d_8$. All pulse sequence parameters were identical to those employed to acquire the TRAPDOR MAS spectrum of ambient ME $\text{Sc}(\text{OTf})_3$. Integrated intensities are shown to the right of each spectrum. The most intense resonance at ca. 1.4 ppm corresponds to cyclohexane.

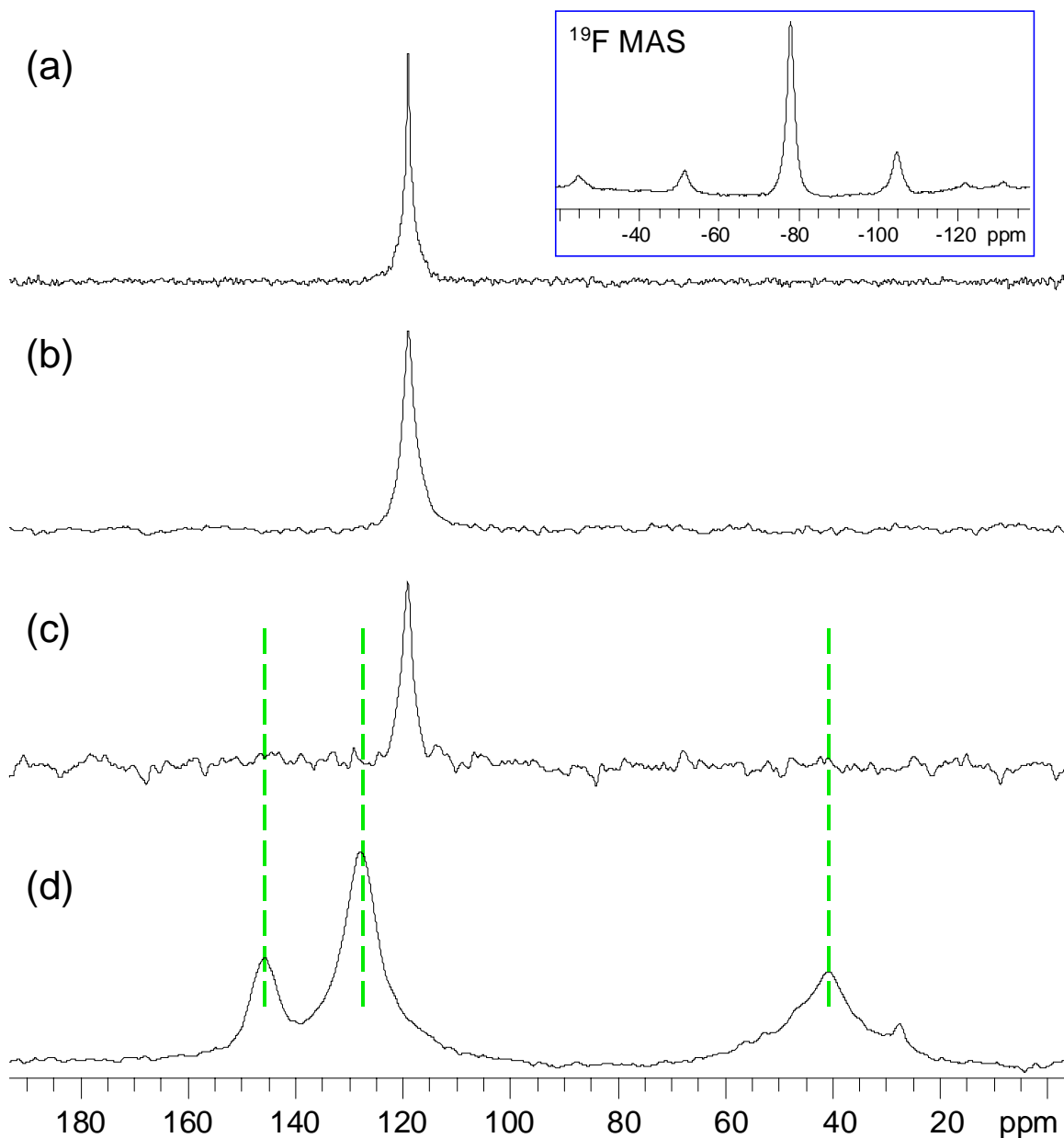


Figure E7. VACP/MAS $^{19}\text{F} \rightarrow ^{13}\text{C}\{^{19}\text{F}\}$ SSNMR spectra of (a) $\text{Sc}(\text{OTf})_3 \cdot 8\text{H}_2\text{O}$ (MAS ^{19}F SSNMR spectrum inset), (b) ambient ME $\text{Sc}(\text{OTf})_3$ and (c) ME $\text{Sc}(\text{OTf})_3\text{-}d_8$. A broad resonance centered around the ^{13}C phenyl group resonances is visible in the spectrum of ME $\text{Sc}(\text{OTf})_3\text{-}d_8$. A contact time of 2 ms, $\nu_{\text{rot}} = 10000$ Hz and a recycle delay of 5 s were employed for all VACP/MAS $^{19}\text{F} \rightarrow ^{13}\text{C}$ spectra. 13260 and 17880 transients were collected for the spectra of ambient ME $\text{Sc}(\text{OTf})_3$ and ME $\text{Sc}(\text{OTf})_3\text{-}d_8$, respectively. (d) The $^1\text{H} \rightarrow ^{13}\text{C}\{^1\text{H}\}$ SSNMR spectrum of ambient ME $\text{Sc}(\text{OTf})_3$ is shown for comparison.

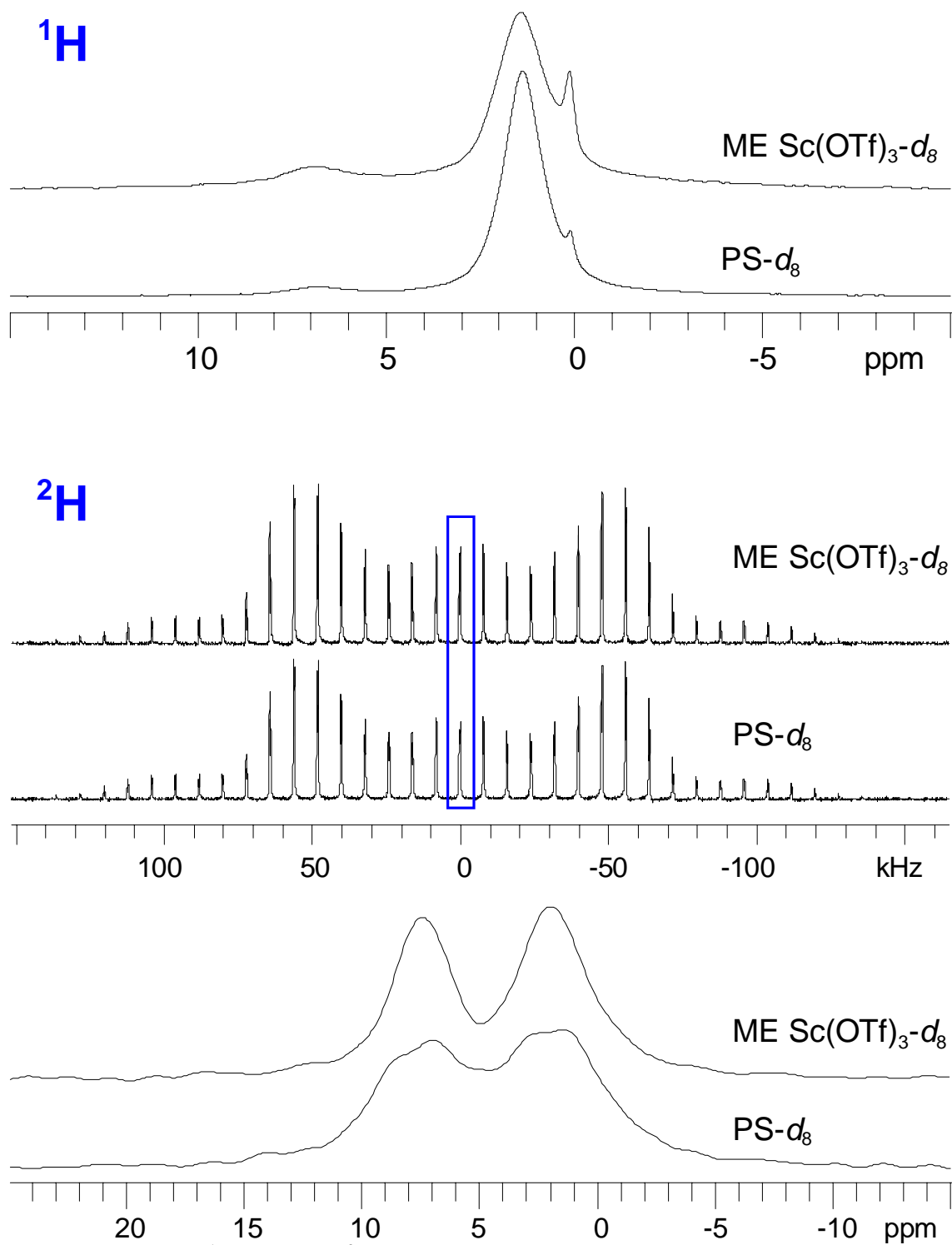


Figure E8. MAS ^1H (top) and ^2H (bottom) SSNMR spectra of ME $\text{Sc}(\text{OTf})_3-d_8$ and PS- d_8 . MAS ^1H SSNMR spectra were acquired with $\nu_{\text{rot}} = 12.5$ kHz and a 20 s recycle delay. MAS ^2H spectra of both complexes were acquired with $\nu_{\text{rot}} = 8$ kHz. An expansion of the isotropic peaks is shown in the bottom set of ^2H spectra.

¹⁹F-¹³C Cross-polarization experiments. VACP/MAS ¹⁹F→¹³C{¹⁹F} SSNMR experiments were conducted on ME Sc(OTf)₃-d₈ because ¹H nuclei directly bound to ¹³C nuclei will be absent; this eliminates the need to apply ¹H decoupling to observe any potential cross-polarization from the ¹⁹F nuclei of the triflate groups to the ¹³C nuclei of polystyrene. MAS ¹³C{¹⁹F} Bloch decay SSNMR spectra of ME Sc(OTf)₃-D₈, Sc(OTf)₃•8H₂O, and ambient ME ScOTf₃ are shown in Figure E7. However, There are no resonances visible in the phenyl regions or aliphatic regions of the VACP/MAS ¹⁹F→¹³C{¹⁹F} SSNMR spectrum of ME Sc(OTf)₃-d₈. The ¹⁹F spectra of Sc(OTf)₃•8H₂O are relatively narrow, indicative of substantial rotational motion of the -CF₃ groups. This suggests that the lack of polystyrene signals in the VACP/MAS ¹⁹F→¹³C spectrum can most likely be attributed to the efficient averaging of ¹⁹F-¹³C dipolar interactions by rotational motion of the triflate groups.

MAS ¹H and ²H SSNMR Experiments on ME Sc(OTf)₃-d₈. MAS ²H SSNMR is often employed to acquire high resolution MAS SSNMR spectra of deuterated species. MAS ²H SSNMR spectra are particularly useful because the ²H chemical shifts (δ_{iso}) are approximately identical to those observed in the ¹H SSNMR spectra of the same complex. Therefore, the ²H SSNMR spectrum can serve as a “high-resolution” ¹H SSNMR spectrum of the complex. The MAS ²H and ¹H SSNMR spectra of the sample of pristine deuterated polystyrene (PS-d₈) and ME Sc(OTf)₃ prepared with deuterated polystyrene (ME Sc(OTf)₃-d₈) are shown in Figure E8. The spectra of the deuterated complexes show two distinct chemical shifts which correspond to those expected for aromatic and aliphatic deuterons. The isotropic ²H resonances of ME Sc(OTf)₃-d₈ are substantially narrowed in comparison to those of PS-d₈. This suggests that ME Sc(OTf)₃-d₈ is more crystalline than PS-d₈. This increased crystallinity probably arises from the dissolution and subsequent precipitation of the PS which occurs during the synthetic procedure of ME Sc(OTf)₃.

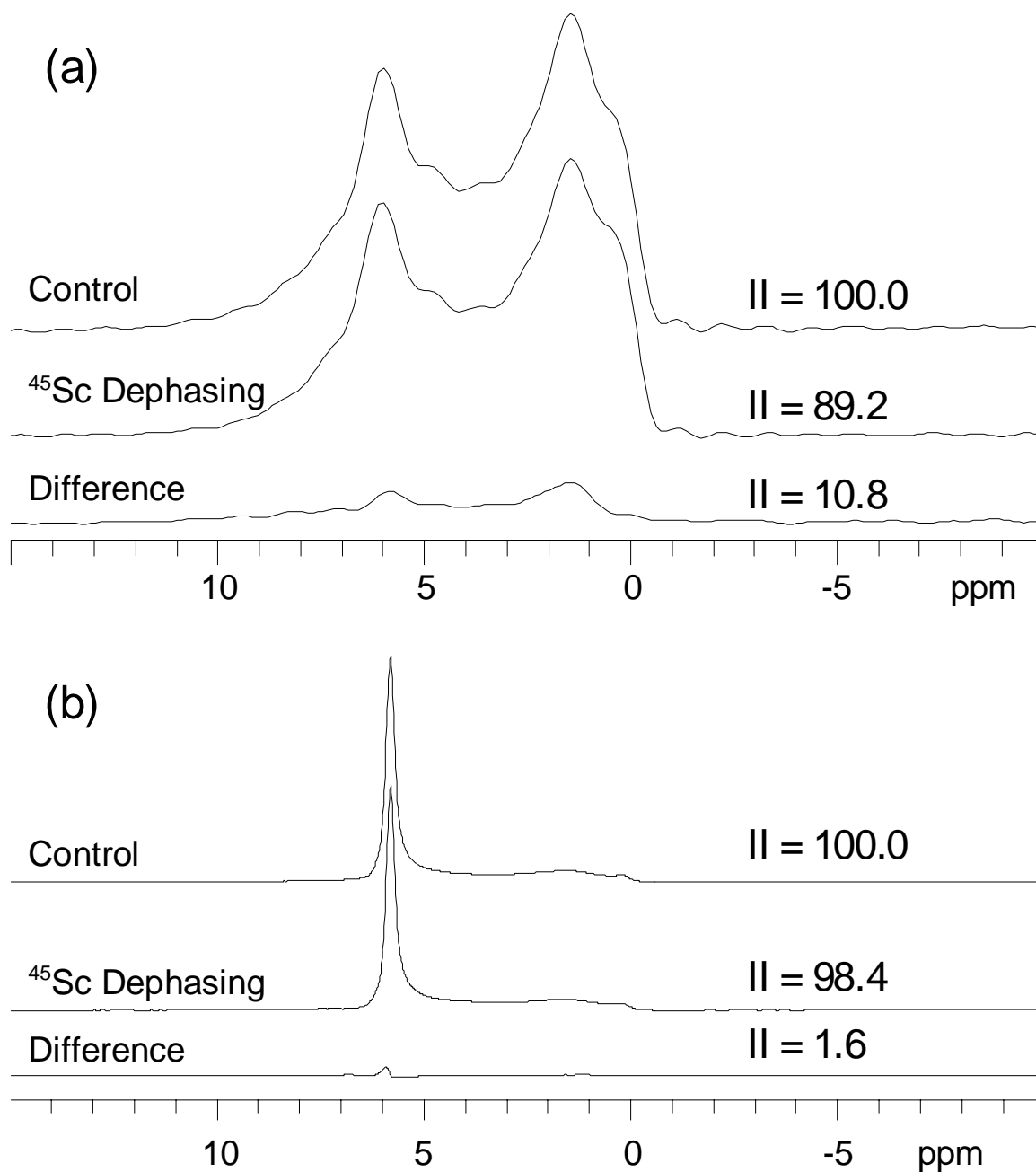


Figure E9. ^1H - ^{45}Sc TRAPDOR SSNMR spectra of a sample of ME-2 which has been exposed to air for (a) 20 hours and (b) 15 days. Integrated intensities are shown to the right of each spectrum.

Appendix F: Supplementary Figures and Tables for Chapter 7

Table F1. CP/CPMG Acquisition Parameters

Parameter	Compound		
	1	2	3
Number of sub-spectra acquired	16	15	17
Number of scans per sub-spectrum	80	144	64
Transmitter offset per piece (kHz)	30.0	30.0	30.0
Recycle Delay (s)	20.0	20.0	40.0
Number of Meiboom-Gill loops [N]	163	163	163
Real points per loop	100	100	100
Spectral window of sub-spectra (kHz)	1000.0	1000.0	1000.0
Dwell (μ s)	1.0	1.0	1.0
Spikelet separation (kHz) [$1/\tau_a$]	10.0	10.0	10.0
Acquisition length (number of points)	16384	16384	16384
Proton 90° pulse width [$\pi/2$] (μ s)	1.9	2.0	2.0
Lead 180° pulse widths [π] (μ s)	4.0	3.3	3.3
Contact time (ms)	13.0	12.0	9.0
Ring-down delays [$\tau_1 = \tau_2 = \tau_3 = \tau_4$] (μ s)	40.0	30.0	30.0

Elements in square-brackets [] are defined in the schematic of the CP/CPMG sequence (Figure S2).

Table F2. ^{207}Pb isotropic chemical shift of $(2,6\text{-Me}_2\text{C}_6\text{H}_3\text{S})_2\text{Pb}(\text{py})_2$ (**1**) and $[(2,6\text{-Me}_2\text{C}_6\text{H}_3\text{S})_2\text{Pb}(\text{pyOMe})_2]$ (**2**) at three spinning speeds.

Spinning Speed (Hz)	Temperature (K) ^a	δ_{iso} of 1 (ppm) ^b	δ_{iso} of 2 (ppm)
5000	293.5	2733	2873
6900	296.5	2740	2878
8000	298.0	2741	2882

^a The temperature of the sample in the rotor was calibrated by recording the ^{119}Sn spectrum of $\text{Sn}_2\text{Sm}_2\text{O}_7$ at various spinning speeds according to the procedure given by Grimmer, A.; Kretschmer, A.; Cajipe, V. B. *Magnetic Resonance in Chemistry* **1997**, 35, 86. ^b Given the breadth of the peaks in the MAS spectra there are significant errors of approximately 5 ppm for all of the listed shifts.

Table F3. Paramagnetic shielding arising from mixing of occ.-vir. MOs in **1**.

Occ. MO	Vir. MO	σ_{iso}	Occ. MO	Vir. MO	σ_{iso}	Occ. MO	Vir. MO	σ_{iso}
48	143	-23.435	122	138	-81.601	130	350	20.43
48	144	11.838	122	139	19.602	131	134	3.932
48	145	-4.696	122	143	-76.395	131	138	-88.629
48	146	28.675	122	144	-39.537	131	139	199.183
49	139	-24.882	122	145	-29.738	131	140	-84.824
49	143	-21.408	122	147	20.57	131	141	-15.821
49	146	15.539	122	149	-29.603	131	142	-25.99
50	210	4.346	122	154	-7.962	131	143	-256.911
53	210	-5.516	122	155	13.617	131	144	7.756
54	144	-8.208	122	156	17.947	131	145	-1.33
54	334	-9.329	122	157	-45.666	131	146	-29.943
56	139	1.217	122	163	-10.073	131	156	17.737
75	139	8.357	122	164	-8.018	131	157	-12.95
76	144	-7.298	122	192	-33.844	131	161	-0.818
87	139	17.161	122	193	-8.519	131	191	6.789
87	148	-9.575	122	252	-0.633	131	194	-14.328
93	139	-5.472	125	138	19.687	131	209	1.743
93	143	28.958	125	139	34.247	131	309	-1.684
94	139	8.451	125	143	-135.605	132	138	-451.157
95	138	6.406	125	144	-64.748	132	139	-30.445
96	143	-1.829	125	145	-19.491	132	140	47.294
98	143	29.049	125	146	-7.528	132	142	-78.946
99	139	10.021	125	147	-16.791	132	143	231.689
99	143	-43.08	125	152	-12.349	132	144	-33.977
105	139	3.688	125	154	4.583	132	145	-17.905
105	146	10.502	125	155	-23.511	132	149	-22.725
106	139	4.072	125	157	-18.003	132	152	7.226
109	143	1.707	125	158	1.013	132	154	6.93
110	138	-16.494	125	161	3.78	132	157	31.198
110	143	-34.799	125	162	-20.665	132	162	-22.549
111	138	-10.351	125	164	18.043	132	164	-17.674
111	144	-5.881	125	165	-20.259	132	192	19.868
111	146	-14.569	125	166	14.425	132	193	19.458
111	155	-5.907	125	167	-26.601	132	295	-8.764
112	143	-25.374	125	169	7.378	133	134	5.253
114	138	-45.568	125	188	-27.022	133	139	430.36
114	144	6.5	125	191	25.93	133	140	-155.367
114	152	1.966	125	209	5.069	133	141	-14.686
118	143	-18.34	125	220	-1.774	133	142	-45.895
119	139	-20.134	125	246	9.879	133	143	-611.812
119	143	2.838	125	248	2.097	133	144	-54.507
120	138	29.184	125	252	4.256	133	146	13.92
120	139	-125.88	125	262	10.816	133	148	3.626
120	143	-44.645	125	295	-7.298	133	151	-3.336
120	144	15.106	125	307	-5.455	133	152	-13.54
120	147	38.461	125	324	-26.28	133	154	27.459
120	148	-6.895	125	351	5.401	133	156	27.553
120	153	-14.679	125	353	-1.232	133	157	-21.832
120	155	56.185	125	359	-13.12	133	158	-14.106
120	156	-39.049	126	138	-33.903	133	164	27.122

120	161	41.549	126	139	-41.408	133	165	-3.925
120	162	26.59	126	140	9.86	133	166	-44.892
120	164	-21.534	126	141	7.627	133	169	-27.185
120	192	27.45	126	142	24.024	133	170	-5.568
120	194	-25.002	126	143	-124.824	133	173	11.79
120	243	19.534	126	144	-27.115	133	174	35.433
121	134	3.387	126	146	-61.333	133	175	-7.849
121	138	-43.367	126	148	-7.31	133	179	-11.981
121	139	21.177	126	194	-5.906	133	188	52.173
121	143	4.86	127	138	5.041	133	190	-28.071
121	144	-31.988	127	139	-72.964	133	192	38.849
121	145	55.502	127	143	48.604	133	193	-33.448
121	147	-61.664	127	144	-5.433	133	195	20.202
121	148	-7.221	130	138	-451.383	133	197	-19.564
121	149	-0.009	130	139	-78.316	133	204	-11.9
121	151	3.946	130	140	-43.538	133	209	-15.134
121	154	-23.565	130	142	1.207	133	211	-19.142
121	155	-46.459	130	143	-40.019	133	216	17.206
121	156	6.146	130	144	-84.027	133	218	-0.449
121	161	-40.07	130	145	-8.263	133	219	4.091
121	162	-17.169	130	146	13.683	133	221	35.363
121	163	-6.633	130	147	-16.634	133	225	21.651
121	164	-25.44	130	149	-12.12	133	226	-6.784
121	170	-11.012	130	152	-8.556	133	231	6.275
121	171	-11.342	130	154	1.442	133	234	14.738
121	177	-20.293	130	155	-10.93	133	239	17.672
121	188	-4.281	130	158	-33.515	133	249	20.099
121	194	-28.683	130	162	-53.547	133	252	-4.446
121	195	-45.091	130	164	1.949	133	273	-7.678
121	208	-27.798	130	169	43.887	133	285	-4.074
121	210	-30.674	130	174	-7.851	133	290	6.075
121	211	59.053	130	175	11.397	133	293	-18.311
121	216	1.006	130	176	-12.968	133	306	-0.962
121	219	25.057	130	192	11.703	133	309	35.571
121	221	10.08	130	209	1.973	133	325	35.72
121	225	-5.555	130	210	2.268	133	328	8.882
121	246	12.584	130	220	-0.853	133	339	7.044
121	256	-14.083	130	238	-4.691	133	344	1.165
121	257	-22.33	130	244	0.615	133	350	1.349
121	265	-12.976	130	248	0.956	133	351	11.14
121	277	16.968	130	250	-31.83	133	353	-9.944
121	295	-22.008	130	295	-6.774	133	357	-4.361
121	299	-7.245	130	299	-20.114	133	396	6.012
121	306	33.217	130	307	-10.923	133	681	14.623
121	315	23.809	130	324	-7.804	133	682	-0.078
121	340	-28.298	130	339	-0.175			

Table F4. Composition of the MOs of **1** from NR calculations.

MO	Energy (eV)	Occ. of MO ^a	Composition of MO (%)	SFO (first member) ^b	Occ. of SFO	Fragment ^c
121	-7.423	2.00 ^d	16.57	2p _z	1.00	N1
			16.51	2p _z	1.00	N2
			5.79	6p _z	0.67	Pb
122	-7.265	2.00	9.21	3p _z	1.33	S2
			7.82	3p _x	1.33	S2
			3.58	2p _z	0.67	C2
			3.45	3p _x	1.33	S1
			2.71	2p _y	0.67	C2
			2.70	3p _z	1.33	S1
125	-6.855	2.00	14.25	3p _y	1.33	S2
			13.08	3p _y	1.33	S1
			5.57	6p _z	0.67	Pb
			4.92	2p _x	0.67	C1
			4.82	3p _x	1.33	S1
			4.79	2p _x	0.67	C2
			4.67	3p _x	1.33	S2
126	-6.660	2.00	11.73	2p _z	1.00	N2
			9.58	2p _z	1.00	N1
			8.28	3p _y	1.33	S1
			8.16	3p _y	1.33	S2
			4.07	2p _x	0.67	C1
			3.76	2p _x	0.67	C2
130	-5.179	2.00	15.55	3p _y	1.33	S1
			15.00	3p _y	1.33	S2
			12.50	3p _z	1.33	S1
			10.62	3p _z	1.33	S2
			6.52	6p _x	0.67	Pb
131	-4.692	2.00	24.70	3p _x	1.33	S1
			21.63	3p _z	1.33	S1
			12.67	3p _z	1.33	S2
			9.77	3p _x	1.33	S2
132	-4.618	2.00	26.01	3p _x	1.33	S2
			16.79	3p _z	1.33	S2
			8.85	3p _x	1.33	S1
			4.27	3p _z	1.33	S1
133	-4.365	2.00	26.78	6s	2.00	Pb
			21.95	6p _y	0.67	Pb
			14.31	3p _y	1.33	S2
			12.73	3p _y	1.33	S1
			5.74	3p _z	1.33	S2
			3.34	3p _z	1.33	S1

138	-0.969	0.00	18.09	6p _y	0.67	Pb
			7.45	2p _y	0.67	C2
			7.10	2p _x	0.67	C2p ^e
			6.50	2p _x	0.67	C1p
			6.19	2p _y	0.67	C1
			5.96	2p _y	0.67	C2p
			5.53	2p _x	0.67	C2
			5.40	2p _x	0.67	C1
			5.26	2p _y	0.67	C1p
			3.27	2p _x	0.67	C1o
			3.26	2p _x	0.67	C2o
			3.11	2p _y	0.67	C1o
			2.62	2p _y	0.67	C2o
2.46	6s	2.00	Pb			
139	-0.843	0.00	51.70	6p _x	0.67	Pb
			21.67	6p _z	0.67	Pb
			2.69	3p _x	1.33	S1
			2.26	3p _x	1.33	S2
143	-0.143	0.00	66.69	6p _z	0.67	Pb
			24.55	6p _x	0.67	Pb
			-3.20	3p _z	0.00	N2
			-3.11	3p _z	0.00	N1
			2.69	2p _z	1.00	N2
			2.50	2p _z	1.00	N1

^aOcc stands for occupancy. ^bSFO: symmetrized fragment orbitals. ^cC1 and C2 are bound to S1 and S2 respectively. *p* and *o* refer to carbon atoms *para* and *ortho* to C1 and C2. ^dOccupied MOs are fully occupied by two electrons, vir MOs contain no electrons. ^eThe “*p*” and “*o*” labels refer to the carbon atoms *ortho* and *para* to the carbon bound to sulfur. The “2” in “C2p” indicates that it is located in the phenyl group bound to “S2”.

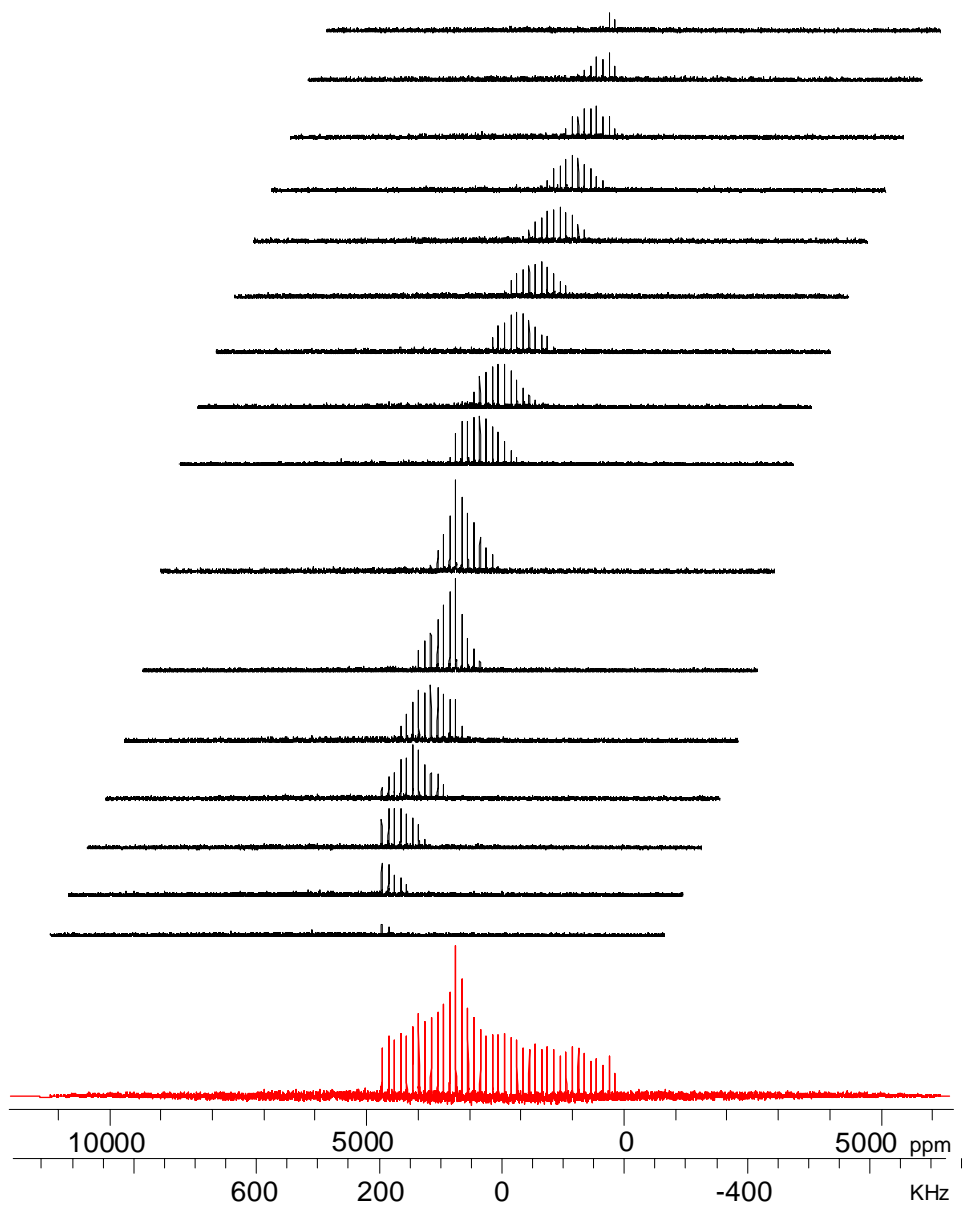


Figure F1. Sixteen CP/CPMG sub-spectra of compound **1** are shown along with the resultant spectrum produced by co-addition of the individual pieces.

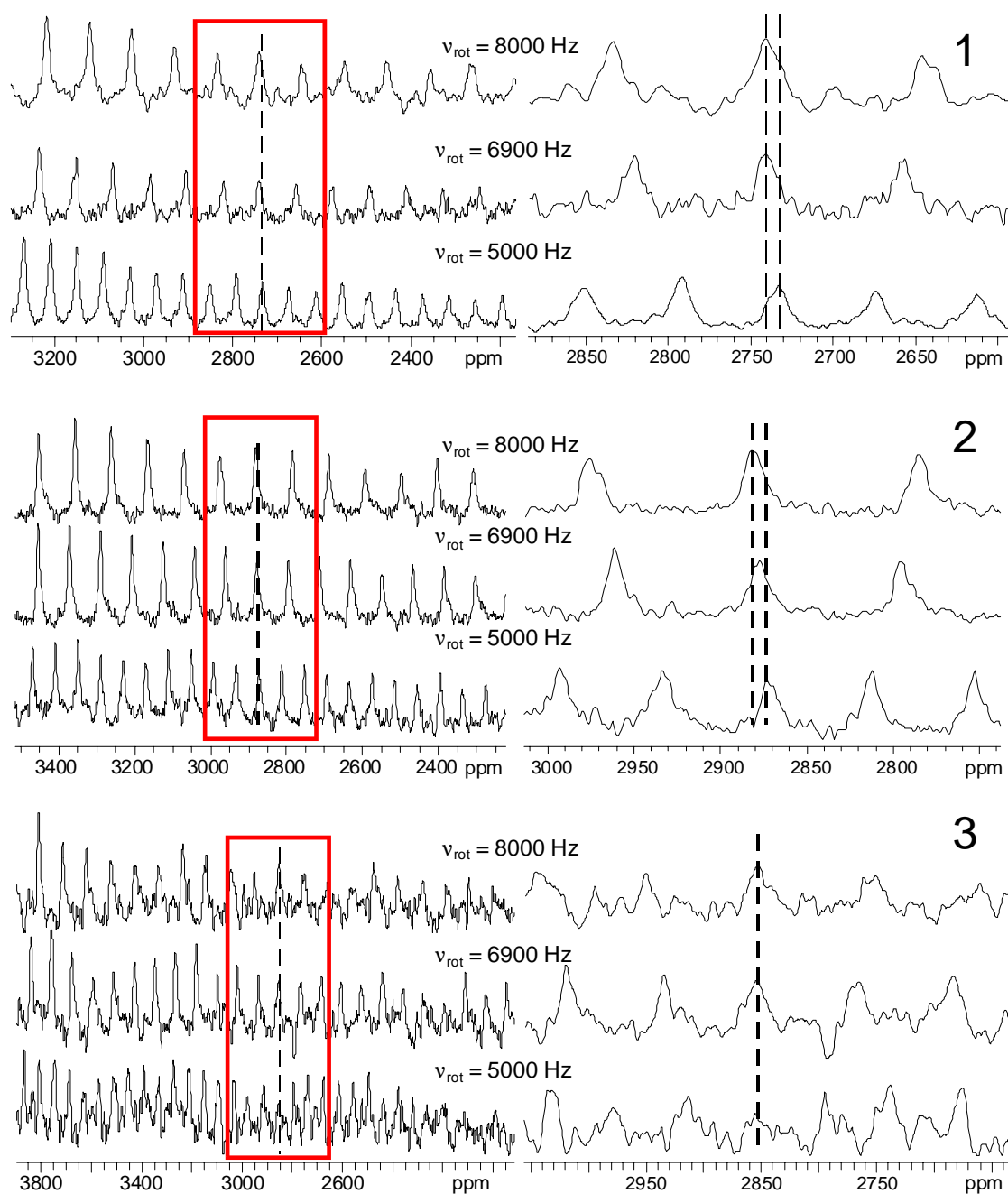


Figure F2. Magnified views of the ^1H - ^{207}Pb VACP/MAS NMR spectra of **1**, **2** and **3** found in Figure 5 of the manuscript. Further expansions of the areas highlighted in the boxed areas are shown in the right columns of the figure. The dependence of the isotropic chemical shifts of **1** and **2** on the temperature (spinning speed) of the sample is evident (Table F2). Minor impurities that are visible are believed to result from hydration of the samples, since the VACP/MAS NMR spectra were acquired 21 days after the static spectra. The width of the peaks is increased by the amount of gaussian line broadening applied in processing (minimum 300 Hz).

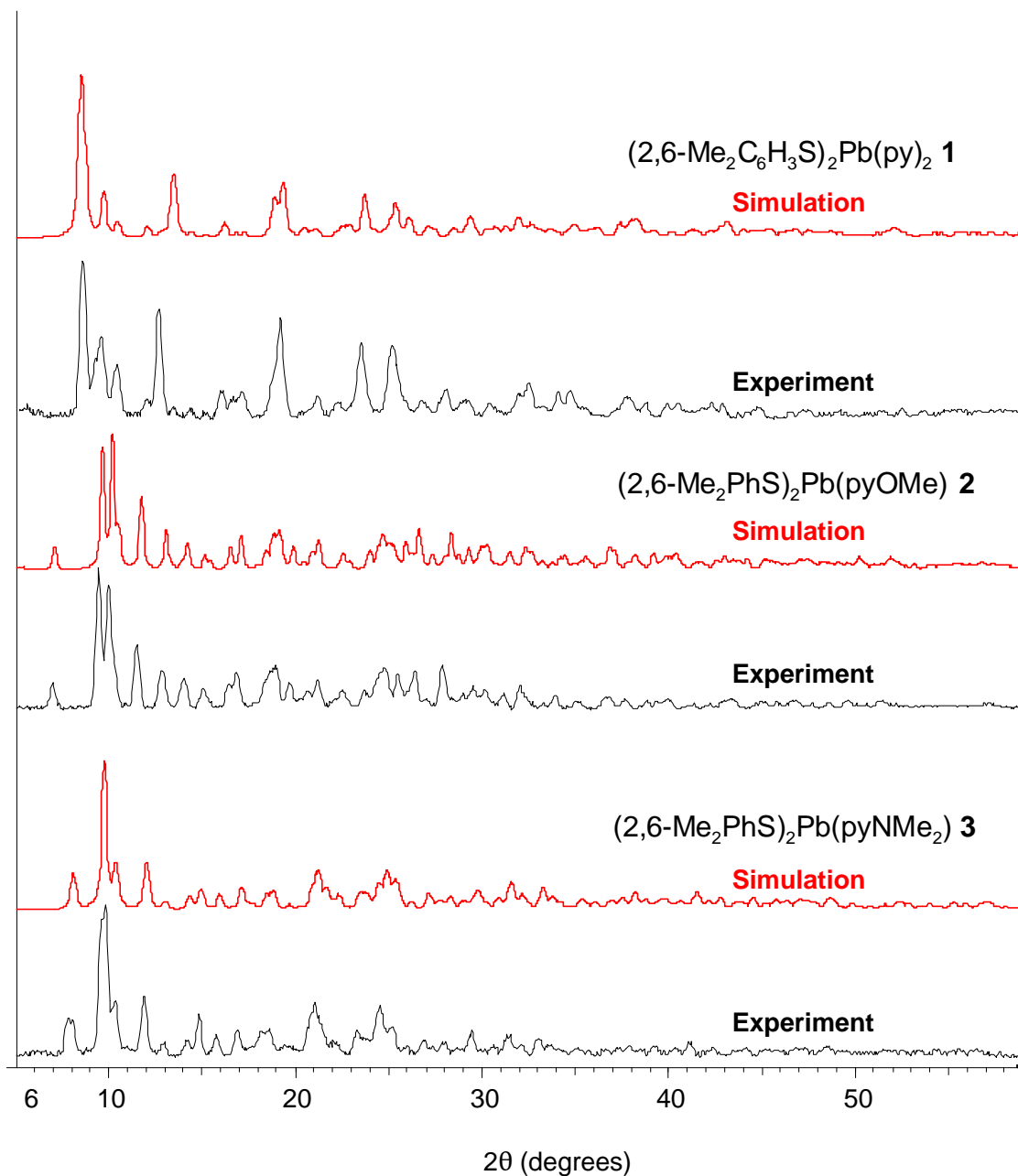


Figure F3. Powder X-ray diffraction patterns of compounds **1**, **2** and **3**. Simulated patterns were generated from the single crystal X-ray diffraction structures with the Powdercell program.

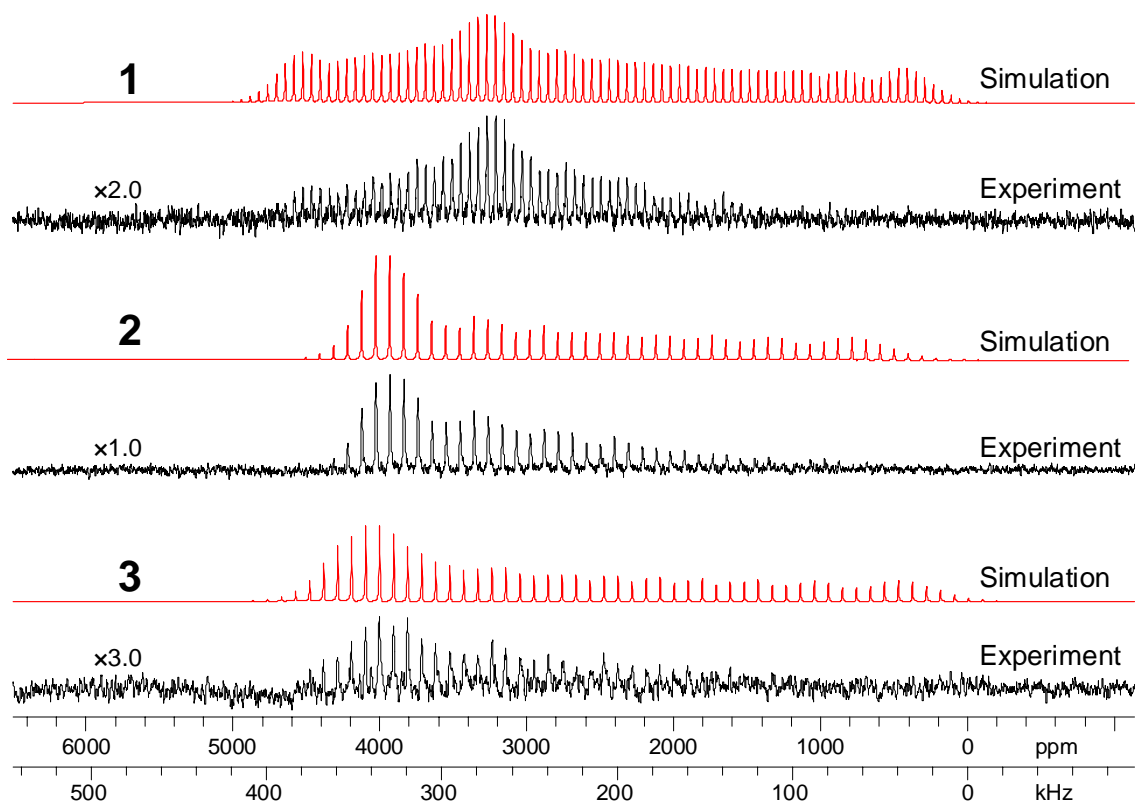
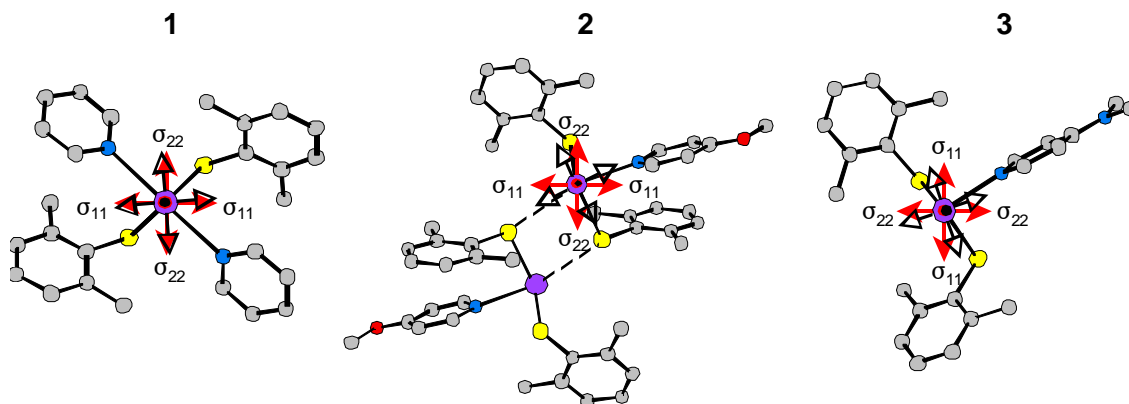


Figure F4. SIMPSON simulations of the VACP/MAS spectra employing the CS tensor parameters extracted from simulation of the CP/CPMG spectra. The simulations employ ideal pulses. The vertical scaling factors of the experimental spectra are indicated in the figure. In all instances the experimental spectra display incomplete excitation and/or lack of signal to noise for resolving lower-intensity portions of the patterns. The discontinuities (eg. high and low points of the sideband manifolds) of the experimental spectra match those of the simulations. The incomplete excitation arises from a combination of the large chemical shielding anisotropy and small excitation profiles characteristic of cross-polarization experiments.



$\sigma_{33} \perp$ to page for all complexes

Figure F5. Chemical shielding tensor orientations generated from ZORA [closed-head (\blacktriangleright) red arrows] and non-relativistic (NR) [open-head (\triangleright) black arrows] ADF calculations for complexes **1**, **2** and **3**. For all cases the position of σ_{33} is placed in approximately the same direction by the NR and ZORA calculations; the $\sigma_{33}(\text{ZORA})\text{-Pb-}\sigma_{33}(\text{NR})$ angles are $\sim 0^\circ$, 8° and 6° for **1**, **2**, and **3** respectively. In complex **2** the positions of σ_{11} and σ_{22} generated by the NR calculations are switched relative to those produced by the ZORA calculation [i.e., $\sigma_{11}(\text{NR})$ is directed closer to $\sigma_{22}(\text{ZORA})$ than $\sigma_{11}(\text{ZORA})$].

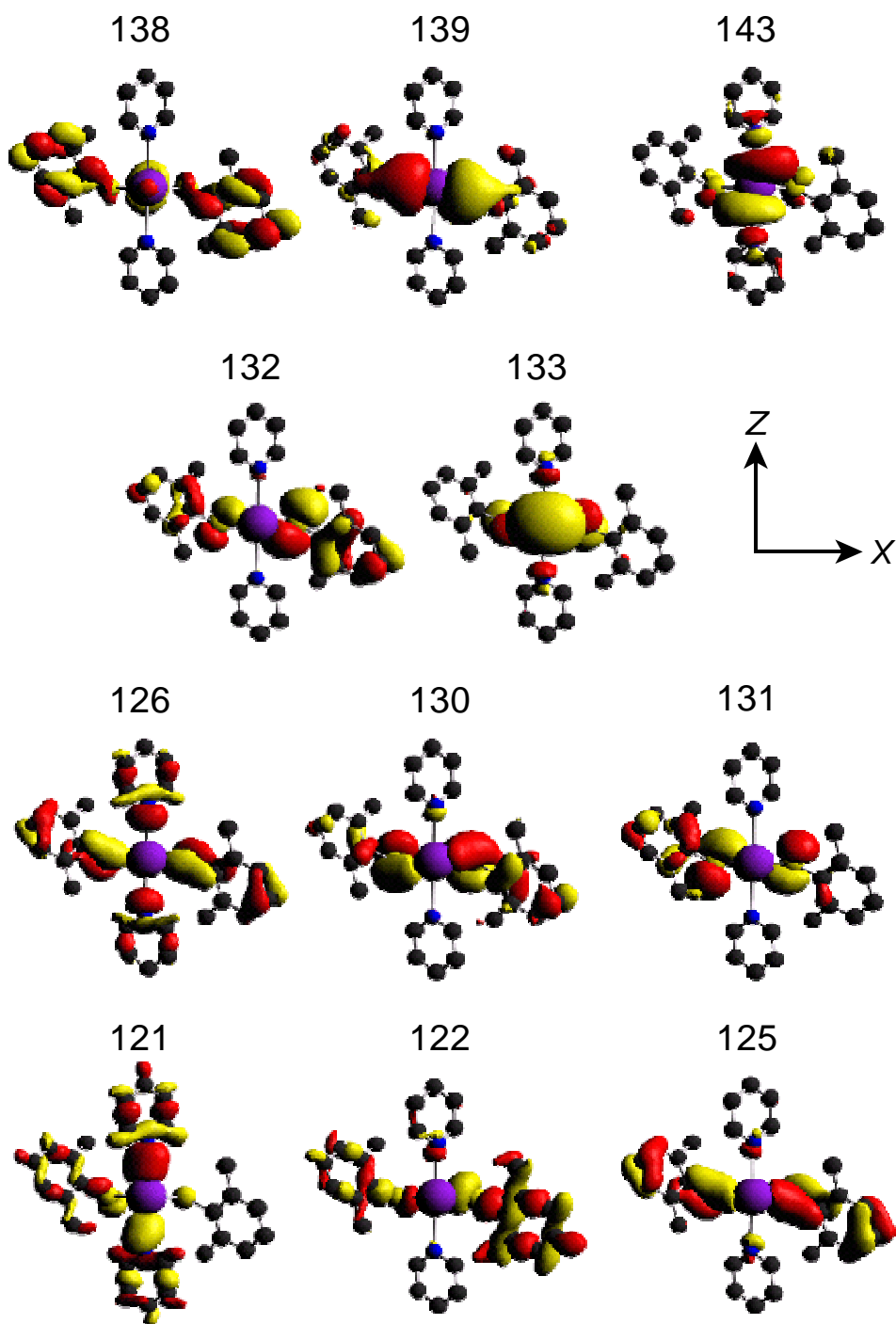


Figure F6. MOs generated from non-relativistic DFT calculations on complex **1**. The MOs pictured make large contributions to the paramagnetic shielding term, and are visualized at the 97% electron density level with the ADFview program. Hydrogen atoms omitted for clarity.

A Note on the Generation of the Contributions of the Individual Shielding Terms to the Total Principal Shielding Components

The ADF program outputs principal shielding components for the diamagnetic (σ^d), paramagnetic (σ^p), and spin-orbit terms (σ^{so}). In order to determine the contributions from the individual shielding terms (e.g. paramagnetic) to the principal components of the total shielding tensor (σ) the principal components of the shielding terms as output by the ADF program cannot be used. This is because the principal axis system (PAS) of each of the individual shielding terms is not necessarily coincident with the PAS of the total shielding tensor; if one tries to sum the principal components of each of the individual shielding terms the values of the principal components of the total tensor will *not* be obtained. In order to gauge the contributions of the individual shielding terms to the principal components of σ one must translate the individual shielding terms into the PAS of the total shielding tensor. This is done by determining the eigenvectors (which correspond to the columns of the 3 x 3 matrix X) of the total shielding tensor. Eigenvectors for the total shielding tensor can be found in ADF output file and are labelled as “Principal Axis System” near the tensor output. Alternatively they can be found by solving for the eigenvalues of the total shielding tensor with a standard mathematical computing program.

$$\sigma X = \sigma_{PAS} X$$

$$\text{where, } \sigma = \begin{pmatrix} \sigma_{xx} & \sigma_{xy} & \sigma_{xz} \\ \sigma_{xy} & \sigma_{yy} & \sigma_{yz} \\ \sigma_{xz} & \sigma_{yz} & \sigma_{zz} \end{pmatrix} \sigma_{PAS} = \begin{pmatrix} \sigma_{11} & 0 & 0 \\ 0 & \sigma_{22} & 0 \\ 0 & 0 & \sigma_{33} \end{pmatrix}$$

The inverse of the eigenvectors (X^{-1}) then needs to be found. The product of X^{-1} , σ and X will yield the principal shielding components of the total CS tensor (the diagonal elements of σ_{PAS}).

$$X^{-1} \sigma X = \sigma_{PAS}$$

The contributions to the principal components of the total shielding tensor from the individual shielding terms can then be determined by finding the product of X , σ^x and X^{-1} (where σ^x corresponds to the tensor of the shielding term in question).

$$X^{-1} \mathbf{\sigma}^x X = \mathbf{\sigma}^x_{PAS}$$

The diagonal elements of the 3 x 3 matrix $\mathbf{\sigma}^x_{PAS}$ correspond to the contributions to the principal components of the total shielding tensor from the tensor $\mathbf{\sigma}^x$.

By applying this routine to the diamagnetic, paramagnetic, and spin-orbit shielding tensors their contributions to the principal components of the total shielding tensor can be determined. This same procedure is also applied to determine the contributions of the individual MO pairs (Table 5 of the manuscript) to the total shielding tensor.

Appendix G: Supplementary Figures and Tables for Chapter 8

Table G1. Experimental ^{75}As NQR Parameters

Pulse Sequence	Bloch Decay	90°-180° Echo	90°-90° Echo	Composite Echo	WURST Echo
Number of Scans	32	32	32	32	32
Recycle Delay (s)	0.4	0.4	0.4	0.4	0.4
90° Pulse Width (μs)	1.65	1.65	1.65	1.65	50
180° Pulse Width (μs)	-	3.30	1.65	0.58, 3.47*	50
Spectral Width (kHz)	2500	2500	2500	2500	2500
Dwell (μs)	0.4	0.4	0.4	0.4	0.4
τ_1 (μs)	-	147.4	147.4	147.4	127.4
τ_2 (μs)	-	40	40	40	20
τ_d (μs) [!]	-	145.75	146.58	145.1	147.4
Ring down delay (μs)	20	-	-	-	-
Acquisition Length (# of points)	512	512	512	512	256
Receiver Gain	20.0	20.0	20.0	20.0	20.0
WURST offset (kHz)	-	-	-	-	1400
WURST sweep rate (kHz/ms)	-	-	-	-	56000
WURST rf field (kHz)	-	-	-	-	57

*The first time listed for the 180° pulse width corresponds to the length of the 31.5° pulse and the second time listed gives the length of the 189° pulse.

! τ_d is the total time between excitation of a signal and the time at which it is refocused. For WURST echo experiments $\tau_d = \tau_1 + \tau_2$. For the echo sequences $\tau_d = \tau_1 - 0.5*(180^\circ \text{ pulse width})$.

Table G2. Experimental ^{35}Cl NQR Parameters

Pulse Sequence	Bloch Decay	90°-180° Echo	90°-90° Echo	Composite Echo	WURST Echo
Number of Scans	256	256	256	256	256
Recycle Delay (s)	0.2	0.2	0.2	0.2	0.2
90° Pulse Width (μs)	2.20	2.20	2.20	2.20	50
180° Pulse Width (μs)	-	4.40	2.20	0.76, 4.62*	50
Spectral Width (kHz)	2000	2000	2000	2000	2000
Dwell (μs)	0.5	0.5	0.5	0.5	0.5
τ_1 (μs)	-	276	276	276	281
τ_2 (μs)	-	24	24	24	24
τ_d (μs)	-	273.8	274.8	272.9	305.0
Ring down delay (μs)	20	-	-	-	-
Acquisition Length (# of points)	512	1024	1024	1024	1024
Receiver Gain	120.0	120.0	120.0	120.0	120.0
WURST offset (kHz)	-	-	-	-	1000
WURST sweep rate (kHz/ms)	-	-	-	-	40000
WURST rf field (kHz)	-	-	-	-	57

*The first time listed for the 180° pulse width corresponds to the length of the 31.5° pulse and the second time listed gives the length of the 189° pulse.

! τ_d is the total time between excitation of a signal and the time at which it is refocused. For WURST echo experiments $\tau_d = \tau_1 + \tau_2$. For the echo sequences $\tau_d = \tau_1 - 0.5*(180^\circ \text{ pulse width})$.

Table G3. Experimental $^{63/65}\text{Cu}$ NQR Parameters

Pulse Sequence	QCPMG (Point-by Point)	QCPMG (Co-Add of FT Spectra)	WURST-QCPMG (Co-Add of FT Spectra)
Number of Scans	4000	4800	600
Recycle Delay (s)	0.08	0.08	0.08
Total Number of Sub-Spectra	15	12	6
Transmitter Increment (kHz)	120	120	250
90° Pulse Width (μs)	10.0	0.7	50.0
180° Pulse Width (μs)	20.0	1.4	50.0
Spectral Width (kHz)	200	1000	1000
Dwell (μs)	5.0	1.0	1.0
τ_1 (μs)	50	40	25
τ_2 (μs)	50	40	24
$\tau_3 = \tau_4$ (μs)	50	40	-
Echo Size (# points)	20	100	100
MG Loops (N)	20	20	16
Acquisition Length (# of points)	400	2000	1600
Receiver Gain	40.0	40.0	40.0
WURST offset (kHz)	-	-	1000
WURST sweep rate (kHz/ms)	-	-	40000
WURST rf field (kHz)			48

*The first time listed for the 180° pulse width corresponds to the length of the 31.5° pulse and the second time listed gives the length of the 189° pulse.

Table G4. Integrated Intensity and Signal to Noise of ^{75}As NQR Spectra of As_2O_3 as a Function of Transmitter Offset

Transmitter Frequency (MHz)	Offset from Resonance (kHz)	90-180 Echo		90-90 Echo		Comp. Echo		WURST Echo		Bloch Decay	
		II	S/N	II	S/N	II	S/N	II	S/N	II	S/N
115.034	-1200	0	0	0	0	0	0	3	20	2	9
115.234	-1000	0	0	0	0	0	0	49	240	10	40
115.434	-800	0	0	0	0	1	6	67	363	13	65
115.634	-600	0	0	0	0	3	13	91	465	9	37
115.834	-400	15	87	14	72	33	172	117	571	53	187
115.934	-300	5	30	47	257	26	134	134	684	80	353
116.034	-200	28	143	96	496	43	212	148	710	102	417
116.134	-100	172	804	137	670	196	876	167	781	117	489
116.234	0	286	1242	164	734	283	1246	186	871	137	503
116.334	100	205	862	157	792	220	1025	199	919	148	550
116.434	200	39	170	117	530	56	240	207	982	151	503
116.534	300	7	35	59	270	27	122	212	844	131	478
116.634	400	20	92	17	80	35	155	201	885	95	358
116.834	600	0	0	0	0	8	21	158	567	16	62
117.034	800	0	0	0	0	4	11	105	400	27	104
117.234	1000	0	0	0	0	0	0	60	254	15	57
117.434	1200	0	0	0	0	0	0	3	15	3	10

Table G5. Integrated Intensity and Signal to Noise of ^{75}As NQR Spectra of As_2O_3 as a Function of the Echo Delay (τ_d)

τ_d	WURST Echo	
	II	S/N
245	73	250
225	91	352
205	112	457
185	136	554
165	160	690
147.4	186	871
τ_d	90°-180° Echo	
	II	S/N
198.4	180	623
158.4	259	858
145.7	286	1242
118.4	399	1300
*78.35	443	1200
*58.35	491	604
*38.35	399	1300

*When τ_d becomes short only a portion of the full echo is acquired (e.g., the echo is truncated in the time domain). This leads to baseline and lineshape distortions which make II and S/N measurements unreliable.

Table G6. Integrated Intensity and Signal to Noise of ^{75}As NQR Spectra of As_2O_3 as a Function of WURST Pulse Width

WURST Pulse Width (μs)	RF Field of Pulse (kHz)	Echo Size (# of points) *	τ_1 (μs)	τ_2 (μs)	τ_d (μs)	II	S/N
50	57	1024	229.8	20	249.8	69	250
100	44	900	230.0	20	250.0	72	271
200	31	650	230.0	20	250.0	72	312

*The echo size was decreased for longer pulse widths in order to retain similar values of τ_1 and τ_d .

Table G7. Pulse Sequence Parameters and Performance of 90° - 180° and 90° - 90° WURST Echo Sequences for the Acquisition of ^{75}As NQR Spectra.

Experimental Parameters ^a	WURST Pulse Sequence				
	90° - 90°	90° - 90°	90° - 180°	90° - 180°	90° - 180°
τ_{exc} (us)	50	100	100	100	100
τ_{ref} (us)	50	100	100	100	50
Offset _{exc} (kHz)	800	800	800	800	800
Offset _{ref} (kHz)	800	800	800	1600	800
R_{exc} (kHz/ms)	32000	16000	16000	16000	16000
R_{ref} (kHz/ms)	32000	16000	16000	32000	32000
ν_{exc} (kHz)	52	37	37	37	37
ν_{ref} (kHz)	52	37	37^b	56	63
τ_d (us)	147.4	172.4	172.4	172.4	147.4
II	149	116	$-^b$	122	153^c
S/N	730	541	-	579	753

^aAll other experimental parameters not listed here were the same as those listed in Table S1.

^bThe rf field of the refocusing pulse was experimentally optimized and it was found that using an rf field equal in magnitude to the excitation pulse gave maximum signal. Therefore, the sequence and resulting spectra are identical to the corresponding 90° - 90° WURST echo case.

^cThis 90° - 180° WURST echo sequence yields II and S/N comparable to that obtained from the 90° - 90° sequence, which employs an identical echo dephasing period (τ_d).

Table G8. S/N and II of ^{75}As NQR WURST Echo Spectra at Different Receiver Gain Settings.

Receiver Gain	Probe Tuned on Resonance		Probe Tuned +300 kHz Off Resonance ^a	
	II	S/N	II	S/N
10	98	950	125	1190
20 ^b	186	955	237	1295
30	299	950	377	1181
40	377	944	479	1106
50	473	910	600	1243
70	596	950	758	1266
80	757	838	969	1180
90 ^c	904	934	1146	1212

^aRe-calibrated pulse widths were also employed (the 90° pulse was found to increase from 1.65 μs to 2.1 μs).

^bThis receiver gain setting was employed for all other experiments in the manuscript.

^cAt a receiver gain setting greater than 90 the signal saturates the digitizer.

Table G9. Integrated Intensity and Signal to Noise of ^{35}Cl NQR Spectra of 4-chloropyridne as a Function of Transmitter Offset

Transmitter Frequency (MHz)	Offset from Resonance (kHz)	90°-180° Echo		90°-90° Echo		Comp. Echo		WURST Echo		Bloch Decay		
		II	S/N	II	S/N	II	S/N	II	S/N	II	S/N	II*
36.052	700	0	0	0	0	0	0	6	0	6	8	2
35.952	600	0	0	0	0	0	0	8	0	8	9	3
35.852	500	0	0	0	0	0	0	9	0	9	10	4
35.752	400	0	0	0	0	0	0	14	0	14	15	14
35.652	300	17	16	5	6	17	20	24	20	24	20	64
35.552	200	0	0	12	10	0	0	42	0	42	31	108
35.502	150	7	8	28	25	11	9	46	9	46	37	148
35.452	100	43	32	47	40	53	45	53	45	53	44	167
35.402	50	108	84	64	51	113	90	65	90	65	55	182
35.352	0	167	120	79	57	156	112	83	112	83	60	199
35.302	-50	162	120	88	71	162	122	94	122	94	70	234
35.252	-100	105	89	107	83	127	101	115	101	115	82	256
35.202	-150	24	19	84	63	41	37	124	37	124	96	238
35.152	-200	10	7	57	48	10	6	121	6	121	86	220
35.052	-300	14	9	10	3	30	20	93	20	93	61	95
34.952	-400	0	0	0	0	0	0	56	0	56	38	14
34.852	-500	0	0	0	0	0	0	33	0	33	26	6
34.752	-600	0	0	0	0	0	0	18	0	18	13	6
34.652	-700	0	0	0	0	0	0	15	0	15	9	7

II* correspond to II values which have been corrected by multiplying the measured II values by the ratio of the FWHH of the echo spectra to the Bloch decay spectra [e.g., a scaling factor of (3.7 kHz/4.7 kHz = 0.80) has been applied].

Table G10. S/N and II of ^{35}Cl NQR WURST Echo Spectra at Different Receiver Gain Settings.

Receiver Gain	Probe Tuned on Resonance		Probe Tuned +300 kHz Off Resonance ^a	
	II	S/N	II	S/N
10	7	60	10	89
70	41	61	68	90
130 ^b	89	64	142	92
190	138	58	206	89
250	188	58	283	90
310	228	58	351	89
490 ^c	284	60	460	90

^aRe-calibrated pulse widths were also employed (the 90° pulse was found to increase from 2.2 μs to 2.5 μs).

^bThis receiver gain setting was employed for all other experiments in the manuscript.

^cAt a receiver gain setting greater than 90 the signal saturates the digitizer.

Table G11. Transverse Relaxation (T_2) Time Constants as a Function of Resonance Frequency for $^{63/65}\text{Cu}$ NQR of CuCN.

Frequency (MHz)	T_2 (μs)	Deviation (χ^2 , μs)
37.64	500	76
37.88	498	77
38.12	474	84
38.36	532	96

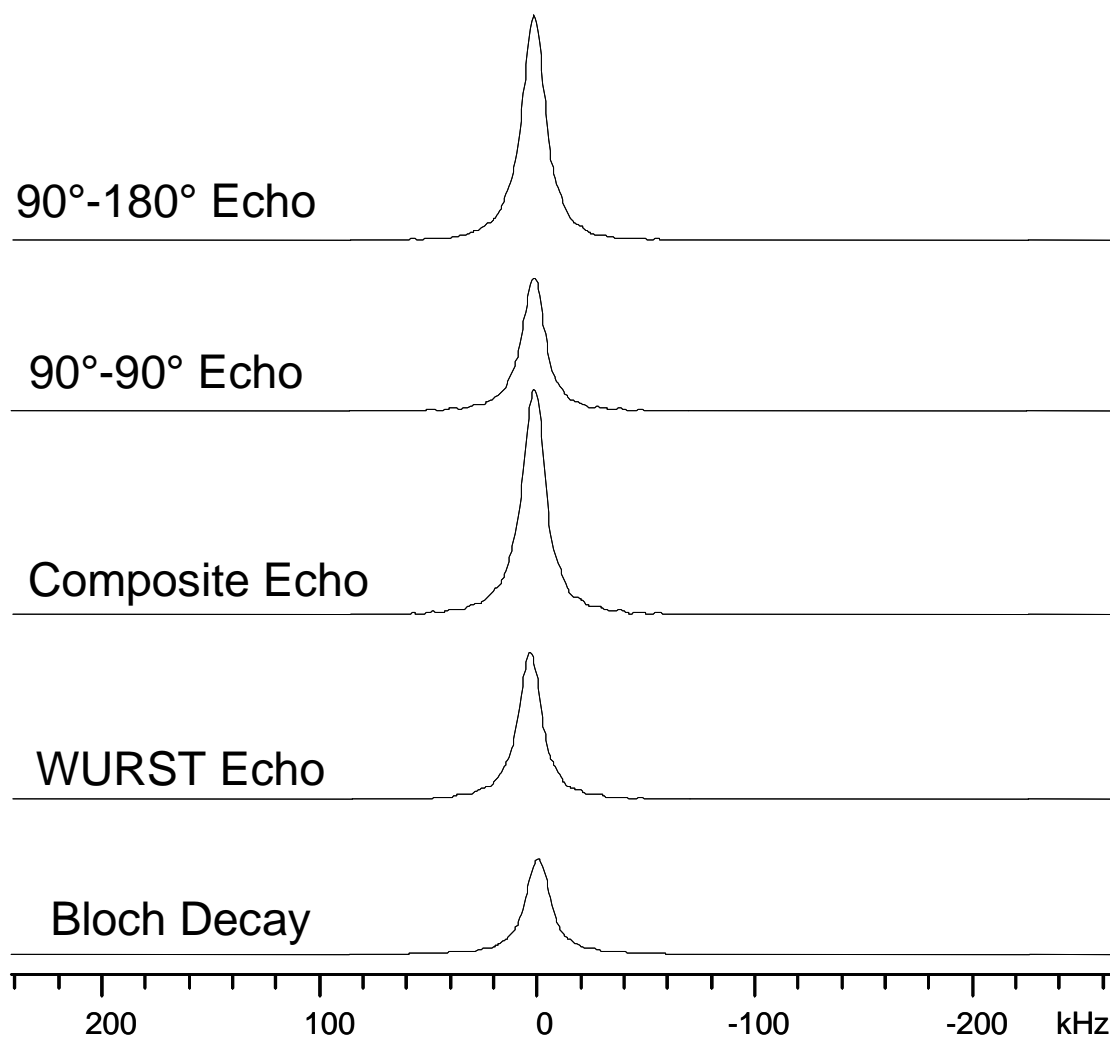


Figure G1. ^{75}As NQR spectra of As_2O_3 acquired with the transmitter on resonance and the probe tuned to the resonance frequency. Spectra acquired with five different pulse sequences are shown. The vertical scaling of the spectra has not been altered. The full width at half height (FWHH) of the resonance is approximately 13 kHz in all spectra.

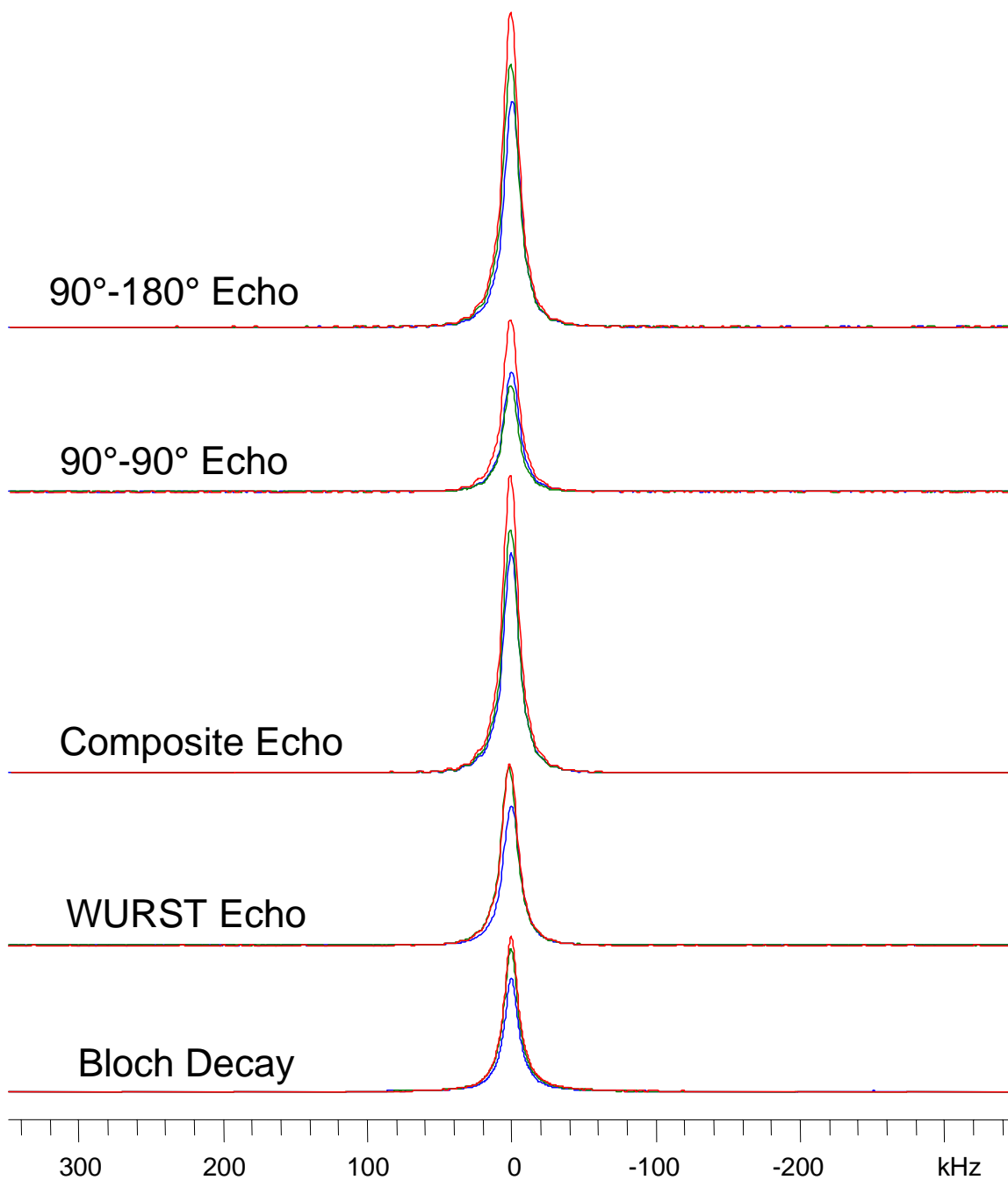


Figure G2. ^{75}As NQR spectra of As_2O_3 acquired with the transmitter on resonance. Spectra acquired with the probe tuned to the resonance frequency (blue spectra) are compared to spectra acquired with the probe tuned to a frequency +300 kHz from the resonance frequency (green spectra), and the probe tuned +300 kHz off resonance and with re-calibrated pulse widths (red spectra). The S/N and II of the spectra are between 1.3 to 1.4 times higher when the probe is tuned +300 kHz off resonance and re-calibrated pulses are employed than when the probe is tuned on resonance.

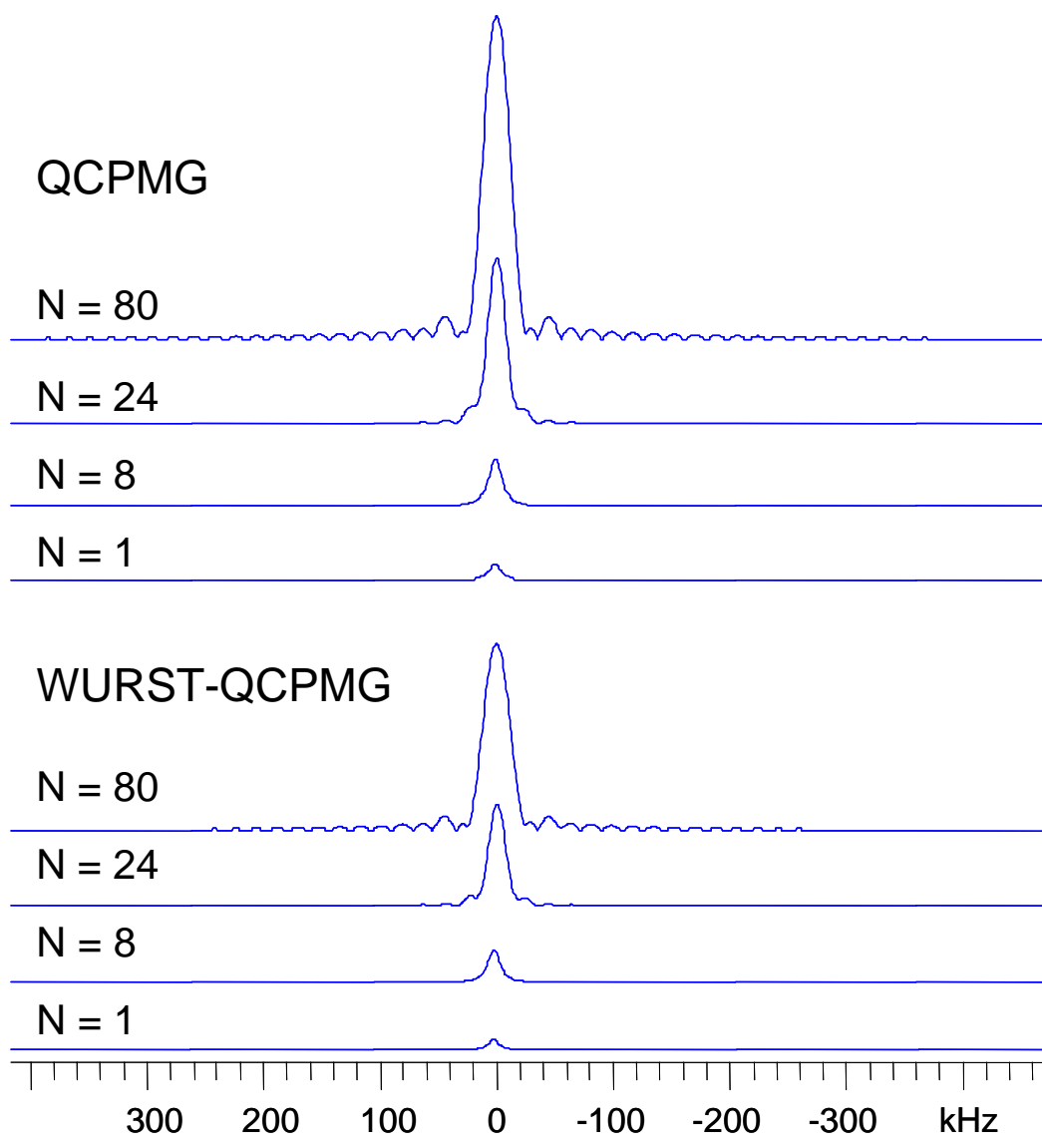


Figure G3. ^{75}As QCPMG and WURST-CPMG NQR spectra. The numbers of refocusing pulses and echoes acquired are given next to the spectra. Large gains in signal are realized for both QCPMG and WURST-QCPMG when 80 echoes are acquired, however truncation of the individual echoes leads to broadening of the signal and lineshape distortions.

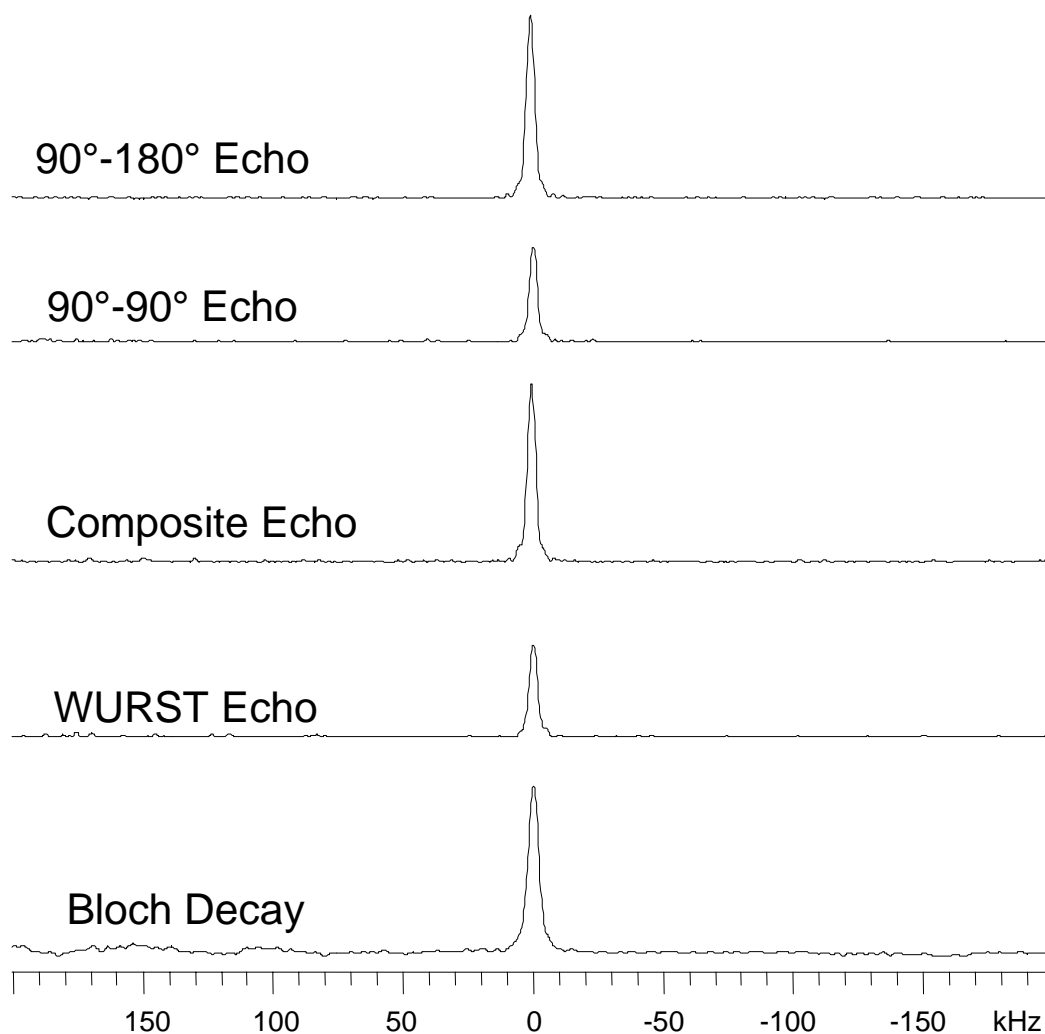


Figure G4. ^{35}Cl NQR spectra of 4-chloropyridine acquired with the transmitter on resonance and the probe tuned to the resonance frequency. Spectra acquired with five different pulse sequences are shown. The vertical scaling of the spectra has not been altered. The full width at half height (FWHH) of the resonance is approximately 3.6 kHz for all echo spectra. The FWHH of the Bloch decay spectra is approximately 4.7 kHz. This will lead to artificially higher II values for Bloch decay spectra. From comparison of the spectra above it is clear that the intensity of the Bloch decay spectra is actually similar to that of the $90^\circ\text{-}180^\circ$ echo spectra.

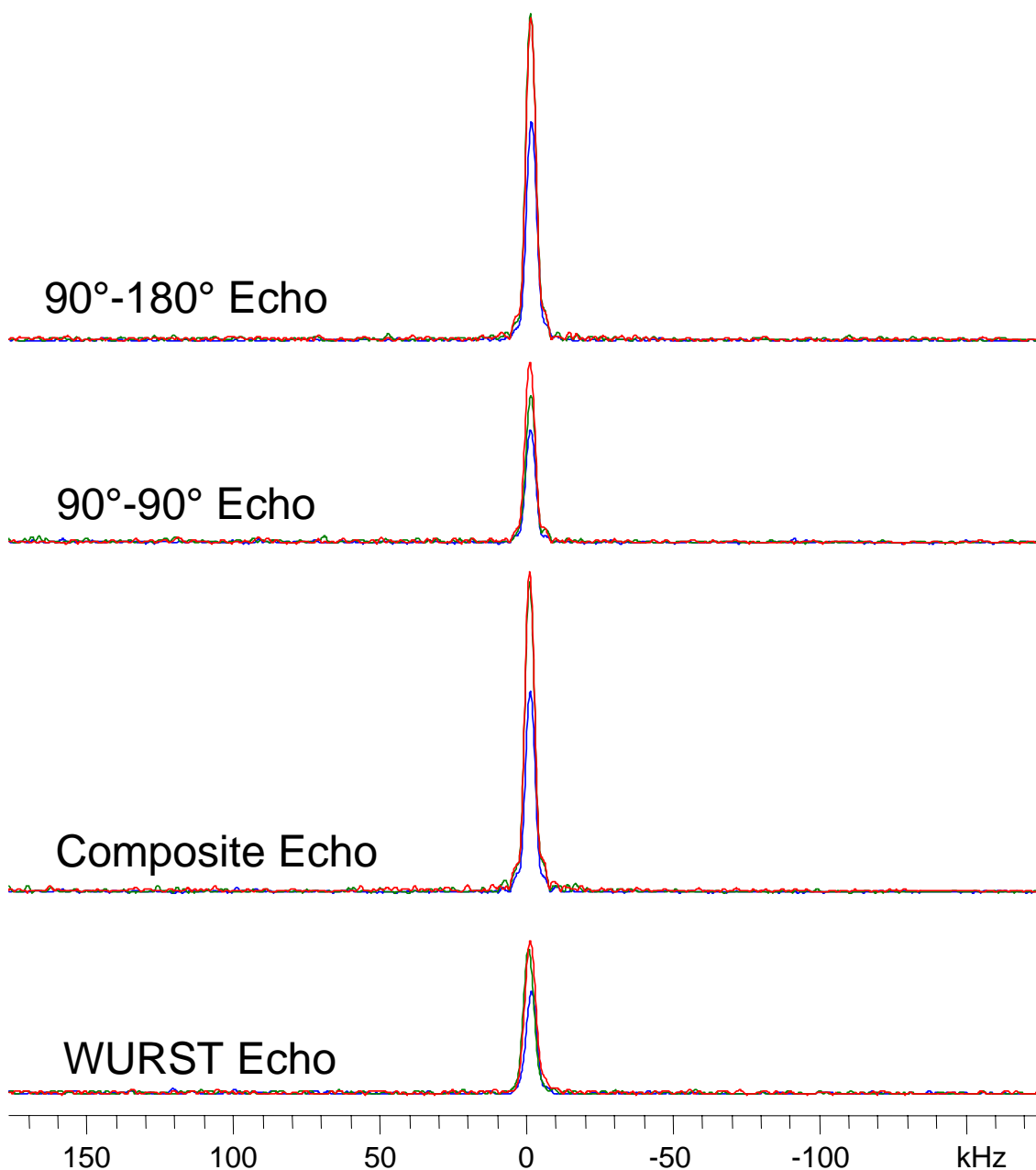


Figure G5. ^{35}Cl NQR spectra of 4-chloropyridine acquired with the transmitter on resonance. Spectra acquired with the probe tuned to the resonance frequency (blue spectra) are compared to spectra acquired with the probe tuned to a frequency +300 kHz from the resonance frequency (green spectra), and the probe tuned +300 kHz off resonance and with re-calibrated pulse widths (red spectra). The S/N and II of the spectra are ca. 1.6 times higher when the probe is tuned -200 kHz off resonance and re-calibrated pulses are employed than when the probe is tuned on resonance.

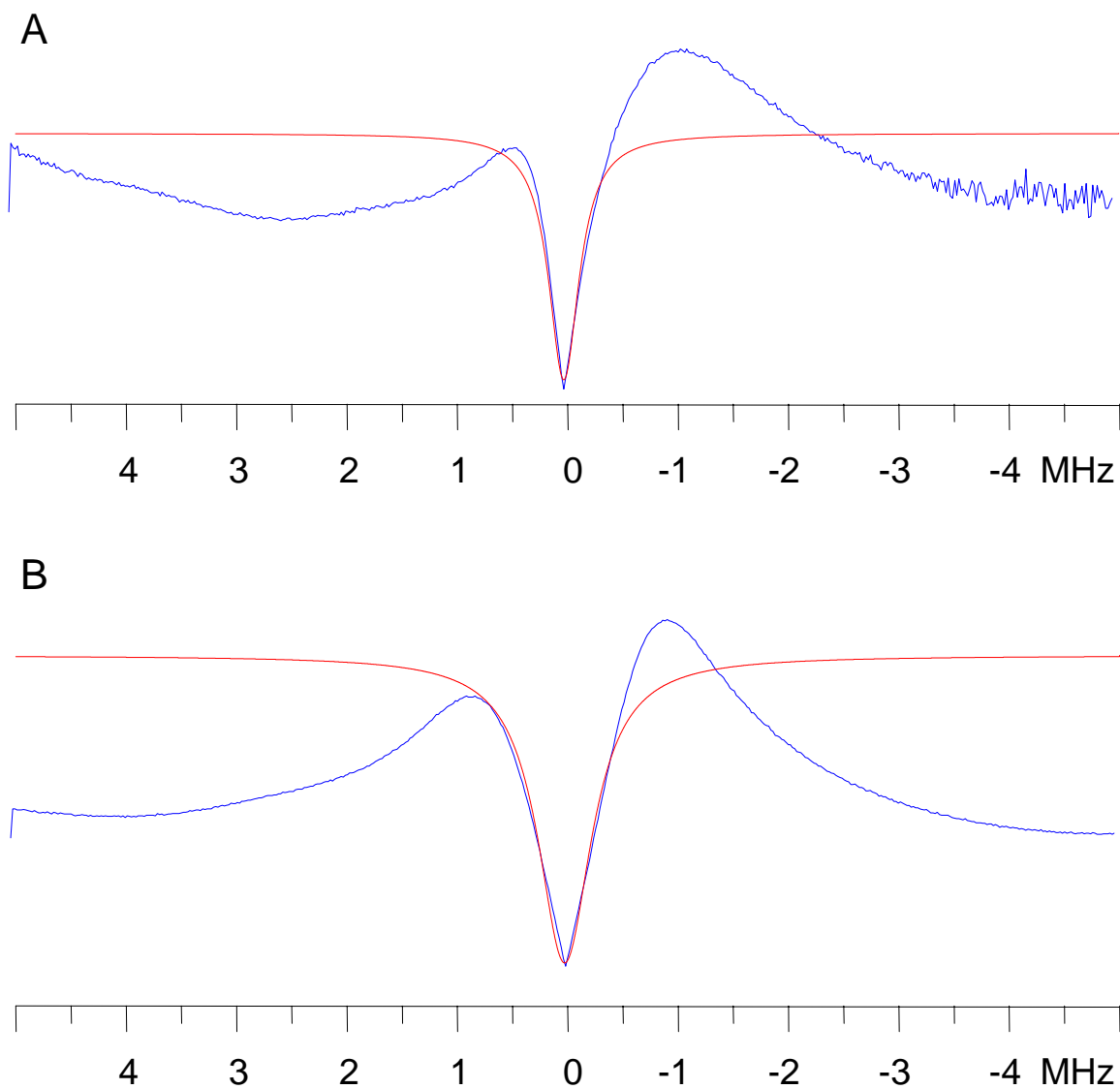


Figure G6. The wobble curves (blue trace) obtained from the NQR probe when it was configured for (A) ^{35}Cl (35.346 MHz) and (B) ^{75}As (116.234 MHz). Lorentzian line fits (red trace) generated with the NUTS NMR processing software are overlaid on the wobble curves (blue trace). The full widths at half maximum of the fits are approximately 350 kHz and 600 kHz for ^{35}Cl and ^{75}As , respectively.

Vita Auctoris

Aaron J. Rossini was born in Brantford, Ontario, Canada. He graduated from St. Anne's High School in Tecumseh, Ontario in June of 2001, and the University of Windsor in May 2005 with a B.Sc. (Honours) in Chemistry. He is currently a PhD. candidate at the University of Windsor and is planning on graduating in October 2010.

Publications:

- 8.) Rossini, A.J., Hung, I. and Schurko, R.W.. Solid-State $^{47/49}\text{Ti}$ NMR of Titanocene Chlorides. *J. Phys. Chem. Lett.*, **2010**, DOI: 10.1021/jz1012017.
- 7.) Rossini, A.J., Hamaed, H. and Schurko, R.W. The Application of Frequency Swept Pulses for the Acquisition of Nuclear Quadrupole Resonance Spectra. *J. Magn. Reson.*, **2010**, *206*, 32-40.
- 6.) Bandyopadhyay, R., Cooper, B.F.T., Rossini, A.J., Schurko, R.W. and Macdonald, C.L.B. Crown Ether Complexes of Tin(II) Trifluoromethane-sulfonate. *J. Organomet. Chem.*, **2010**, *695*, 1012-1018.
- 5.) Rossini, A.J., Mills, R.W., Briscoe, G.A., Norton, E.L., Geier, S.J., Hung I., Zheng, S., Autschbach, J. and Schurko, R.W. Solid-State Chlorine NMR of Group IV Transition Metal Organometallic Complexes. *J. Am. Chem. Soc.*, **2009**, *131*, 3317-3330.
- 4.) O'Dell, L.A., Rossini, A.J. and Schurko, R.W. Acquisition of Ultra-Wideline NMR Spectra from Quadrupolar Nuclei by Frequency-Stepped WURST-QCPMG. *Chem. Phys. Lett.*, **2009**, *468*, 330-335.
- 3.) Briand, G.G., Smith, A.D., Schatte, G., Rossini, A.J. and Schurko, R.W. Probing Lead(II) Bonding Environments in 4-Substituted Pyridine Adducts of $(2,6\text{-Me}_2\text{C}_6\text{H}_3\text{S})_2\text{Pb}$: An X-ray Structural and Solid-State ^{207}Pb NMR Study. *Inorg. Chem.*, **2007**, *46*, 8625-8637.
- 2.) Rossini, A.J. and Schurko, R.W. Experimental and Theoretical Studies of ^{45}Sc NMR Interactions in Solids. *J. Am. Chem. Soc.*, **2006**, *128*, 10391-10402.
- 1.) Hung, I., Rossini, A.J. and Schurko, R.W. Application of the Carr-Purcell Meiboom-Gill Pulse Sequence for the Acquisition of Solid-State NMR Spectra of Spin-1/2 Nuclei. *J. Phys. Chem. A*, **2004**, *108*, 7112-7120.